AD NUMBER

AD893748

NEW LIMITATION CHANGE

TO

Approved for public release, distribution unlimited

FROM

Distribution authorized to U.S. Gov't. agencies only; Test and evaluation; Apr 1972. Other requests shall be referred to Air Force Rocket Propulsion Lab, Edwards AFB, CA, 93523.

AUTHORITY

AFRPL ltr, 31 Jan 1974

AD-893748-L

FINAL REPORT

SOLID PROPELLANT STRUCTURAL

TEST VEHICLE PROGRAM

H. LEEMING

et al

APRIL 1972

BEST AVAILABLE COPY

FOREWORD

This program was sponsored by the

Air Force Rocket Propulsion Laboratory
Research and Technology Division
Edwards, California
Air Force Systems Command, United States Air Force

This work was accomplished under Contract No. F04611-70-C-0061 between 1 May 1970 and 30 September 1971 by Lockheed Propulsion Company, Redlands, California. The Air Force Project Engineer was Capt. R. T. Schuder.

This program was conducted during the third and final year of work initiated in May 1967 under Contract No. F04611-67-C-0100 and reported in Technical Report AFRPL-TR-68-130, and continued in August 1968 under Contract No. F04611-69-C-0002 and reported in Technical Report AFRPL-TR-70-10. These programs represent a continuing integrated approach to the problems of solid propellant structural integrity. The work was primarily concerned with experimental measurement of grain stress and strains using instrumented Structural Test Vehicles (STVs).

In this third-year effort the main emphasis was on developing a greater understanding of the embedded gage performance in simple test fixtures under known loadings. A combined analytical and experimental approach was employed.

Major contributors to this report were Professor M. L. Williams and W. S. Brown (University of Utah), Professors K. Pister and R. Taylor (University of California at Berkeley), Professors R. A. Schapery and W. D. Webb (Texas A&M), and Professor W. G. Knauss (California Institute of Technology). Dr. H. Leeming (Leeming & Associates) was Principal Investigator.

This Technical Report has been reviewed and is approved.

R. T. Schuder, Capt., USAF
AFRPL Project Engineer

ABSTRACT

Results of the third year of the Structural Test Vehicle (STV) Program conducted by Lockheed Propulsion Company for AFRPL are presented. Improvements in computer codes THVINC and CXL 450 resulted in improved cost-effectiveness. THVINC is for transient thermoviscoelastic analysis of incompressible solids and CXL 450 is for isothermal steady-state vibration of viscoelastic solids. The improved codes were used for viscoelastic analyses of a diaphragm gage in a uniaxial propellant specimen subject to constant stress, constant strain, and cyclic tests. Predicted gage performance is qualitatively similar to experimental results. Analysis of the gage response to shock suggests it is not effective for shock wave measurements. However, experimental tests show reasonable response to shock pulses in the millisecond time range. A three-dimensional computer code was used to analyze a shear cube under simple loading conditions and to confirm experimental findings that the interference problem is minimal and that a slight cross sensitivity exists. Experimental data show the performance of shear gages in a biaxial (diametral compression) stress field and under cyclical shear loading. Results of restrained cooling and heating tests are presented and compared with analysis. Usually analytical stresses are lower (at least 2 times) than experimental stresses. Embedded diaphragm gages indicate thermal stresses close to those measured. Modifications to the "reduced time" definition to incorporate rate-of-temperature change do not result in significant changes in predicted stresses. Later experiments using a block (2 x 2 x 6 in.) of STV propellant show good agreement between analysis and experiment, suggesting that low-strain, large-specimen test data are more useful in predicting thermal stresses. Dilatational experimental and analytical work performed at Texas A&M University shows significant nonlinear behavior in the STV propellant and suggests an improved approach for the determination of thermal strain in a circular port grain. Improved material characterization techniques are also described. Results of thermal cycling and cooling experiments on 4-point-star, inert-propellant STV No. 6 are given. No motor failure was detected after thermal cycling from 150 to -100°F. Gage readings measured during the tests are discussed and compared with analysis. A technique for removal of gages from old motors and STVs by chemical milling is discussed. Finally a modified system is described for coding microfilm data of STV, and inert propellant and gage calibration data.

(The reverse is blank)

CONTENTS

CONTENTS (Continued)

CONTENTS (Continued)

CONTENTS (Continued)

CONTENTS (Continued)

CONTENTS (Continued)

CONTENTS (Continued)

ILLUSTRATIONS

ILLUSTRATIONS (Continued)

ILLUSTRATIONS (Continued)

ILLUSTRATIONS (Continued)

ILLUSTRATIONS (Continued)

ILLUSTRATIONS (Continued)

ILLUSTRATIONS (Continued)

ILLUSTRATIONS (Continued)

ILLUSTRATIONS (Continued)

ILLUSTRATIONS (Continued)

TABLES

TABLES (Continued)

(The reverse is blank)

SECTION I

INTRODUCTION AND SUMMARY

1. PROGRAM OBJECTIVES

Lockheed Propulsion Company (LPC) has completed the third and final year of a theoretical and experimental program concerned with the development of Solid Propellant Structural Test Vehicles and the necessary instrumentation for measuring propellant grain stress, strain, and temperature. This work originated under AFRPL Contract No. F04611-67-C-0100 in May of 1967 and was continued under AFRPL Contracts No. F04611-69-C-0002 and F04611-70-C-0061. The overall objectives of the work were as follows:

- The design, manufacture, and testing of instrumented structural test vehicles to investigate the utility of available stress/strain instrumentation for solid propellant grains, and to investigate the accuracy of currently available motor structural analysis techniques based upon infinitesimal elastic theory and linear viscoelastic material behavior.

- The development of improved analysis procedures and material characterization techniques as required to obtain good agreement between experimentally measured stresses and strains and calculated values.

2. PROGRAM SUPPORT

Lockheed Propulsion Company retained the services of Dr. H. Leeming to continue as Principal Investigator after he left LPC at an early stage of this final program year. Mr. Dalton Cantey took over the responsibility of Program Manager after Dr. Leeming left LPC.

Professor Karl Pister and his colleagues at Mathematical Sciences NorthWest continued their work in the areas of:

- Improved analysis codes for thermal and vibration problems

- Detailed diaphragm gage-calibration fixture analysis

- Analysis of an embedded shear gage

Professor R. A. Schapery and Professor D. Webb of Texas A&M University continued their investigations into the nonlinear analysis of propellant and methods for determining these properties.

Professor W. G. Knauss of the California Institute of Technology developed a much improved version of his uniaxial transient thermal stress analysis code.

-1-

Professor M. L. Williams was absent from the country for most of this year's work but managed to perform a closed form solution for a shear gage embedded in an elastic material.

A subcontract was also arranged with Mr. E. R. Frost to assist LPC with the classification and copying of the STV propellant and gage calibration data on microfiche.

3. SUMMARY OF PROGRESS MADE IN EARLIER YEARS

During the first year of the STV program, techniques for the manufacture of instrumented solid propellant motors were developed and the available instrumentation for measuring stress and strain within a grain was evaluated. It was demonstrated that the thermal analysis of a propellant bar or sheet under nonisothermal conditions was a real problem and that available analytical techniques were not accurate in predicting stresses under this condition. Errors of the order of several hundred per cent were encountered, the analysis predicting much lower stress levels than were measured.

The second year of the program included the development of the THVISC, Transient Thermal Viscoelastic Computer Code, and the CX450, Cyclical Viscoelastic Computer Code. Although these programs were written in the first year of the program, they were not debugged and properly working until the end of the second year.

A comparison between the experimental results from the STV vibration tests and the predicted results from the CX450 program led to the conclusion that in most real vibration problems involving motors, the only way to determine reliably the magnitudes of dynamic stresses and strains was to measure them. This results not so much from errors or problems with the analysis as from the complex coupling between various modes which occurs in practice and which completely invalidates the calculations.

The use of THVISC computer code to predict transient thermal STV stresses showed that it was still much too expensive to run for most purposes and that a considerable effort should be made to improve the cost-effectiveness of the program.

Analysis of an STV under thermal cooldown conditions was conducted using a one-dimensional analysis code developed at Aerojet-General Corporation. A comparison between the experimental data and the analysis revealed that there was a problem at the case-liner-propellant interface. Agreement was not obtained between analysis and experiment until a layer of insulation was introduced into the analysis at the case-grain interface. Once this artificial barrier was introduced, the temperatures throughout the grain could be made to agree with the measured values, and, when the temperatures were in agreement, the bore strain history agreed with that measured. The predicted thermal stress values were still much lower than those measured even when the temperatures and the strains were satisfactory.

The results of a series of tests of small test motors to failure under a variety of loading environments showed that the predictions of failure were in most instances not very precise. In many instances, it was predicted that the motors should fail and they did not, which confirms the conservative nature of most approaches to failure prediction.

In this context, one of the most satisfying results to come from the second-year STV program was the demonstration that even under transient thermal cooldown conditions, when analytical predictions were greatly in error, the embedded 25-psi gage gave stress values that were very close to those measured experimentally.

4. SUMMARY OF THIRD-YEAR RESULTS

a. Improved Analysis Codes

In the area of improvements to computer analysis codes, the emphasis during the third year of the STV program was to improve the cost-effectiveness of the new programs, THVISC, CX450, and the Knauss Uniaxial Thermal Stress Analysis Program, which had been developed but were too expensive for normal routine analysis problems.

One of the approaches to improving the cost-effectiveness of the THVISC code was not strictly a programming approach, but consisted rather of using an improved method of handling the Prony Series terms used to describe the propellant relaxation modulus. In the integration procedure, it was found that only four of the whole series of terms (which may number up to 15) were involved in the integration process. Reduced computation was therefore effected by a search procedure to ascertain those terms that would be involved, and only those were subject to the computation procedure. The time taken for the search is much less costly than the approach of simply calculating the integration with all the terms in the series, which was the normal method in earlier programs.

Another advantage of the new procedure is that it is now possible to use a large number of terms in the Prony Series to obtain a good fit to the experimental data without worry about the cost involved in the computation.

The transient thermal viscoelastic computer code modified for near-incompressible material properties, as required by most propellants, is referred to as THVINC. The program has been extensively modified to eliminate the use of taping operations as much as possible. Small problems can now be handled within the computer core, which eliminates a great deal of the cost.

The treatment of boundary conditions has been improved to allow for time dependence. Thus, the thermal environment history may now be used directly as an input to the program.

The improved version of the steady-state vibration program is known as CXL450. Reduced costs in running this program were effected by improvements in two areas: (1) formulation of the finite element matrices, and (2) solution of the resulting system of algebraic equations. The breakdown of the running times for the improved code is presented in a later section of this report.

The earlier computer code devised by Professor Knauss for solving thermoviscoelastic problems made use of existing subroutines as a programming convenience. The code was made to adjust the calculations automatically to within a specified error band by means of a series of iterations. The time consumed in these iterations was very costly. Therefore, in the revised thermoviscoelastic code, the iterations were eliminated by the incorporation of the approximation error into the program as a specified input parameter. Improved cost-effectiveness was achieved in this case by improved preprogramming to eliminate the time and cost of the computer iterations.

In reporting the effect of the programming improvements, Professor Knauss told of short test runs with the old and the new programs. A reduction of running time on the computer from minutes to seconds was obtained, an improvement of the order of 100 times.

Professor Pister, in reporting the effects of the changes in THVINC, stated that the plane strain transient thermal analysis of the STV, detailed on pages 229 through 234 of Reference 1, last year's final report, had been rerun with the improved code. The data obtained had been of similar accuracy to that obtained last year, and with a running time on the computer of only 1/5 of that required earlier. Thus there is no doubt that striking improvements in program cost-effectiveness have been achieved during the year's work.

b.   Normal Diaphragm Stress Gage

Professor Pister and his colleagues have continued the analysis of the diaphragm gage embedded within a propellant uniaxial calibration test fixture for loadings such as steady-state vibration, constant stress and strain, and shock loads. They have been able to confirm most of the experimental results generated over the last three years and, furthermore, they have been able to synthesize the viscoelastic calibration curves from the propellant's relaxation modulus curves and the assumption of temperature-time equivalence. The existence of the gage transfer function was implicit in the empirical gage data analysis technique developed during the earlier STV work, and Professor Pister has now shown the form of this function and its relationship to the other material parameters.

For the gage in an elastic material, the gage output θ is related to the average normal stress on the gage $\bar{\sigma}_p$ and the propellant modulus E_p through the expression:

$$\frac{\theta}{\bar{\sigma}_p} = a_1 + b_1 E_p$$

-4-

where a_1 and b_1 are calibration coefficients; a_1 depending on the stress state at the gage, whereas b_1 is a constant.

The extension of this analysis to the case of the gage in a viscoelastic material leads to the relationship:

$$\frac{\theta}{\bar{\sigma}_p} = \frac{a_2 + b_2 E_p}{K(t)}$$

where $K(t) = K(t/a_T)$ is the transfer function relating the average normal stress on the gage to the free field normal stress. In the latter expression, the term b is a constant and the term a depends upon the gage neighborhood stress state.

The results of the analysis of the diaphragm gage in a viscoelastic material subject to a sinusoidal loading showed that the gage response varies considerably with the propellant modulus, making it highly frequency-dependent and showing that there may be resonances within the frequency range of interest. It is also shown that because of the manner in which the frequency term enters into the equation of motion, the results of the tests cannot be shifted to include other temperatures.

Additional brief analyses show that a diaphragm gage cannot respond to a shear load across its face, and suggest that the diaphragm device is not well suited to the measurement of shock loads.

These analytical predictions are, in general, supported by the results of experimental tests carried out on gages embedded within uniaxial propellant test fixtures.

c.   Embedded Shear Gage

A preliminary analysis of a shear gage embedded within a cube of propellant was conducted using a rather coarse numerical model. It was determined that the interference problem was minimal and that a slight cross-sensitivity exists. These results confirm the experimental data measured on shear gages in previous years. Additional experimental data were obtained for the vibration loading of a shear gage in a simple shear test fixture. Another series of experiments was conducted to determine the response of shear gages at the center of a diametral disc subject to a vertical compressive loading. Rotation of the disc containing the shear gages enables different values of shear stress to be applied to the gages.

The test results confirm the anticipated shear distribution within the specimen and show that the gages will perform well in complex biaxial stress fields.

d.   Nonisothermal Testing and Analysis

Nonisothermal tests, i. e., thermal cooling and heating tests, were again performed during the third year of the program. Experiments were carried out with three types of uniaxial specimen: the original STV

propellant uniaxial specimen containing a 25-psi diaphragm gage, an inert specimen containing a 150-psi diaphragm gage, and a third specimen made from inert propellant containing three 150-psi diaphragm gages.

An additional set of interesting experiments was later carried out with a large STV propellant block (2 by 2 by 6-in. long) as a uniaxial test specimen.

The results of the majority of the experimental tests supported the data obtained earlier in the program. Thus, the experimental test data gave thermal stresses greater than those predicted on the basis of conventional linear viscoelastic theory and with the thermorheological simplicity postulate assumed. When the most favorable modulus values from conventional test data were used (usually inverse creep compliance data), the error in the calculations was of the order of two times, i.e., the theory calculated stress values of about one-half that measured. Higher errors in the predicted stress values could frequently be found.

Because the errors in calculating the stresses under isothermal conditions are, in general, much lower (of the order of 40 percent under the worst conditions), it was believed that the fault in the analysis resided in the method of calculating the "reduced time" from the isothermal temperature data. The conventional approach is to make use of Morland and Lee's postulate that the reduced time may be defined by means of the equation:

$$\xi = \int_0^t \frac{dt'}{a_T} \qquad \text{(Reference 2)}$$

where a_T is the time-temperature shift factor. This equation does reduce to the form $\xi = t/a_T$ for isothermal test conditions and for this reason it has not been seriously questioned for many years. However, it appeared that the above equation is inadequate and should be replaced by a more meaningful expression.

Experiments suggested that there was a larger discrepancy between the calculated stress values and the experimental data at relatively high cooling rates. Under very slow cooling conditions commonly found in large motors the discrepancy could be very small. For this reason the expression for reduced time should contain some function of rate of temperature change as well as simply the temperature.

Two approaches to this problem were evaluated in this work. The first approach makes use of the standard definition of reduced time for a thermorheologically simple material, $\xi = t/a_T = t \cdot \phi_T$ where $\phi_T = 1/a_T$. Differentiation of this expression leads to the following equation for reduced time under varying temperature conditions:

$$\xi(t) = \int_0^t \phi_T \, dt' + \int_0^t t' \, \frac{\partial \phi_T}{\partial T} \cdot \left(\frac{dT}{dt}\right) \cdot dt'$$

This equation contains two parts, the first being identical with the Morland and Lee definition of reduced time, and the second depending on

the rate of change of temperature. In most instances this expression is not sufficient to make the calculated stress values agree with the experimental data.

The second approach to the problem was suggested by Professor Pister. He defined a modified reduced time ξ_m by the equation:

$$\frac{d\xi_m(t)}{dt} = \phi_T(T, \dot{T}) = \phi_T(T) \cdot \psi_{\dot{T}}(\dot{T})$$

where the assumption is made that the effects of temperature and rate of change of temperature are separable into two independent functions, ϕ_T and $\psi_{\dot{T}}$. The first function is the shift factor under constant temperature conditions, i.e., the inverse of a_T.

Reduced time under transient thermal histories is given by the equation:

$$\xi_m(t) = \int_0^t \phi_T\left[T(t')\right] \psi_{\dot{T}}\left[\frac{dT}{dt}\right] dt'$$

Experiments so far with this equation have made use of a simple functional form for the factor $\psi_{\dot{T}}$, having the form:

$$\psi_{\dot{T}} = 1 + K_1 \dot{T} + K_2 \dot{T}^2$$

The use of this modified reduced time definition results in larger thermal stress values in tests where the rate of temperature change is a significant quantity. Unfortunately, in the majority of cases considered, the rate of temperature change is insufficient to produce a significant change in stress value. However, this is not to say that the reduced time is independent of rate of temperature change. The problem is one of determining a realistic series of experiments that can unequivocally demonstrate the effect(s) of rate of temperature change on the thermally induced stresses.

The last series of experiments performed in connection with the measurement of thermal cooling stresses made use of the large STV propellant block as a specimen. The experiments were performed primarily for the purpose of demonstrating that repeated tests could be performed and would result in meaningful data, providing that small enough strain levels were employed. The main reason for these tests was to demonstrate the validity of the gage calibration technique in which a gage was embedded within a propellant specimen that was then subjected to a series of tests at various temperatures. It was argued that the calibration tests were invalid because the repeated use of a single propellant specimen would modify the gage-propellant interaction, as the propellant became damaged.

The primary result of the tests on the large block specimen was the verification that no detectable damage was measured as a result of creep tests carried out at load levels sufficiently low so that the strain in the specimen was never greater than 0.5 percent. After the completion of

this series of creep tests, it was decided to perform thermal cooling tests on the large propellant block and to calculate the anticipated thermal stresses based on the low strain creep test data. The agreement between the experimentally measured thermal stresses on the block and the calculated values based on conventional thermal analysis techniques, i.e., standard Morland and Lee reduced time, is extremely good. (The rate of cooling that could be achieved with this large block was insufficient to investigate rate of temperature change effects.)

However, as a result of this series of tests, it seems that at least a part of the problem of predicting the thermally induced stresses in solid propellant rocket motors can be eliminated by measuring the propellant modulus values at low strain values, of the order of 0.5 percent.

The results of the thermal cooling tests on specimens containing gages (both 25 and 150 psi) showed that the gage readings gave an accurate indication of the real thermal stress value, as measured experimentally with the load cell. Thus, nonlinear propellant behavior does not significantly affect the stress values obtained from embedded gages. Furthermore, standard data reduction techniques based on linear viscoelasticity have proved adequate for the accurate interpretation of the 25-psi gage data. The 150-psi gage data, in most instances, may be reduced by means of a simple constant gage sensitivity factor, even under thermal cooling conditions.

e. Nonlinear Propellant Behavior

The conclusions arrived at as a result of the internal LPC thermal cooling work are supported by the work of Professor Schapery at Texas A&M University. They show that the properties of the STV propellant are nonlinear, and that the use of constitutive equations, which are in themselves linear, enables stresses to be predicted at values close to those observed experimentally. The constitutive equations are based on a nonequilibrium thermodynamic theory developed in an earlier Air Force-sponsored program, and they are only slightly more involved than the constitutive equations currently used by solid rocket structural analysis.

A simple method for predicting nonlinear thermal strains and deformations in long, case-bonded circular port grains is presented. The nonlinear phenomena of vacuole dilatation and large strains are included. This theory closely predicts the experimentally measured bore strains reported in the first year STV program work (Ref 1). It also provides a means for determining the propellant bulk properties in a realistic stress state.

The experimental techniques necessary for determining the propellant creep, relaxation, and thermal properties in multiaxial stress states are also described.

f.   Failure Testing of STV No. 6

Toward the end of the current contract, STV No. 6 was subjected to thermal cycling to increasingly severe conditions and eventually from +150 to -100°F. It was found that there was no apparent damage either by cracking at the star valleys or by unbonding at the ends of the grain. Even allowing for the excellent physical properties of the inert propellant used in the STV, the motor should have failed by all methods of predicting failure in use today. The fact that it did not simply reinforces the obvious conclusion that methods of failure prediction must be improved, especially when used in conjunction with modern propellants with a large amount of dewetting before final rupture.

g.   Removal of Gages from Old STVs

At the onset of the program it was decided to attempt to remove some of the miniature diaphragm gages from the old STVs and to recalibrate them in accordance with the latest techniques. Thus, the data already measured on the early STVs could have been reinterpreted in the light of the new calibrations.

Eventually, after considerable time and expense, the sections of the STVs containing the gages were chemically milled from the old STVs. At this stage it was still necessary to trim the propellant away from the gage and to connect the broken lead wires to the power supply and output device. It was therefore decided not to spend any more time and effort on this particular project. The work already performed had demonstrated the feasibility of cutting the STVs into sections by chemical milling techniques and it was clearly feasible to proceed and remove the gage from the STV section. The extra effort in manpower and cost was not believed worthwhile for the information that could be obtained at this stage.

h.   Microfilming the STV Propellant and Gage Calibration Data

The Air Force Rocket Propulsion Laboratory (AFRPL) wished to make use of the STV propellant data as the start of a physical properties data bank. For convenience, the data were to be copied onto microfilm and filed in accordance with the system developed by Mr. E. R. Frost as described in AFRPL Report AFRPL-TR-69-177. However, this storage, filing, and data retrieval system was not entirely satisfactory, so that Mr. Frost was retained by LPC to amend the system until it would work with the type of data available.

The STV propellant data were selected by AFRPL for the initiation of this project because a considerable amount of work had been performed not only by LPC during the STV program but by Aerojet-General Corporation and Rocketdyne, Solid Rocket Division, under the Cumulative Damage contracts.

Modifications to the data storage and retrieval system were carried out by Mr. Frost and Dr. Leeming, and the available data from LPC, AGC, and NAR were copied and placed onto microfiche. Details of the modified system are presented in the text of this report.

(The reverse is blank)

-9-

SECTION II

MODIFICATIONS TO COMPUTER PROGRAMS

1. INTRODUCTION

Under earlier contracts associated with the Structural Test Vehicle Program, computer programs were developed to perform elastic and visco-elastic analysis of the STVs as well as typical solid propellant motors. These programs were still in their development phase and not yet ready for routine production work. The first tasks completed under the third-year program involved updating and improving the efficiency of two programs: THVISC, a program for transient thermoviscoelasticity (modified to THVINC) and CX450, a program for isothermal steady-state vibration of viscoelastic solids (modified to CXL450). Included here are brief descriptions of these program modifications. The programs, along with descriptive information for the user, are given in the supplement to this report.

Another matter bearing on the problem of program efficiency is that of characterizing the viscoelastic moduli on the basis of experimental data. This factor is discussed first.

2. CHARACTERIZATION OF VISCOELASTIC MODULI

In the program THVINC (Thermoviscoelastic Analysis of Incompressible Solids), the shear relaxation modulus is represented by the series:

$$G(t) = G_0 + \sum_{i=1}^{15} G_i e^{-t/\lambda_i} \tag{1}$$

where λ_i are relaxation times, usually selected at about one decade time increments, G_i are shear modulus coefficients, and G_0 is an equilibrium modulus. During computation, the solution involves integration of integral equations by a one-step-forward integration algorithm (Ref 3). If a specific time increment Δt is used in the integration process, the solution depends upon:

$$g_i = e^{-\Delta t/\lambda_i}$$

and

$$h_i = \frac{\lambda_i}{\Delta t} \left[1 - e^{-\Delta t/\lambda_i} \right] \tag{2}$$

These two functions are plotted in Figure 1. It is observed that their effect is limited to about three and four decades of time, respectively. Thus, in equation (1), for a specific time step only four of the fifteen terms are used to incorporate history effects during the integration process (assuming one decade separation of the λ_i). If the reduced time ξ is used to include the temperature effect on relaxation rates, then Δt must be replaced by $\Delta \xi$ in

-11-
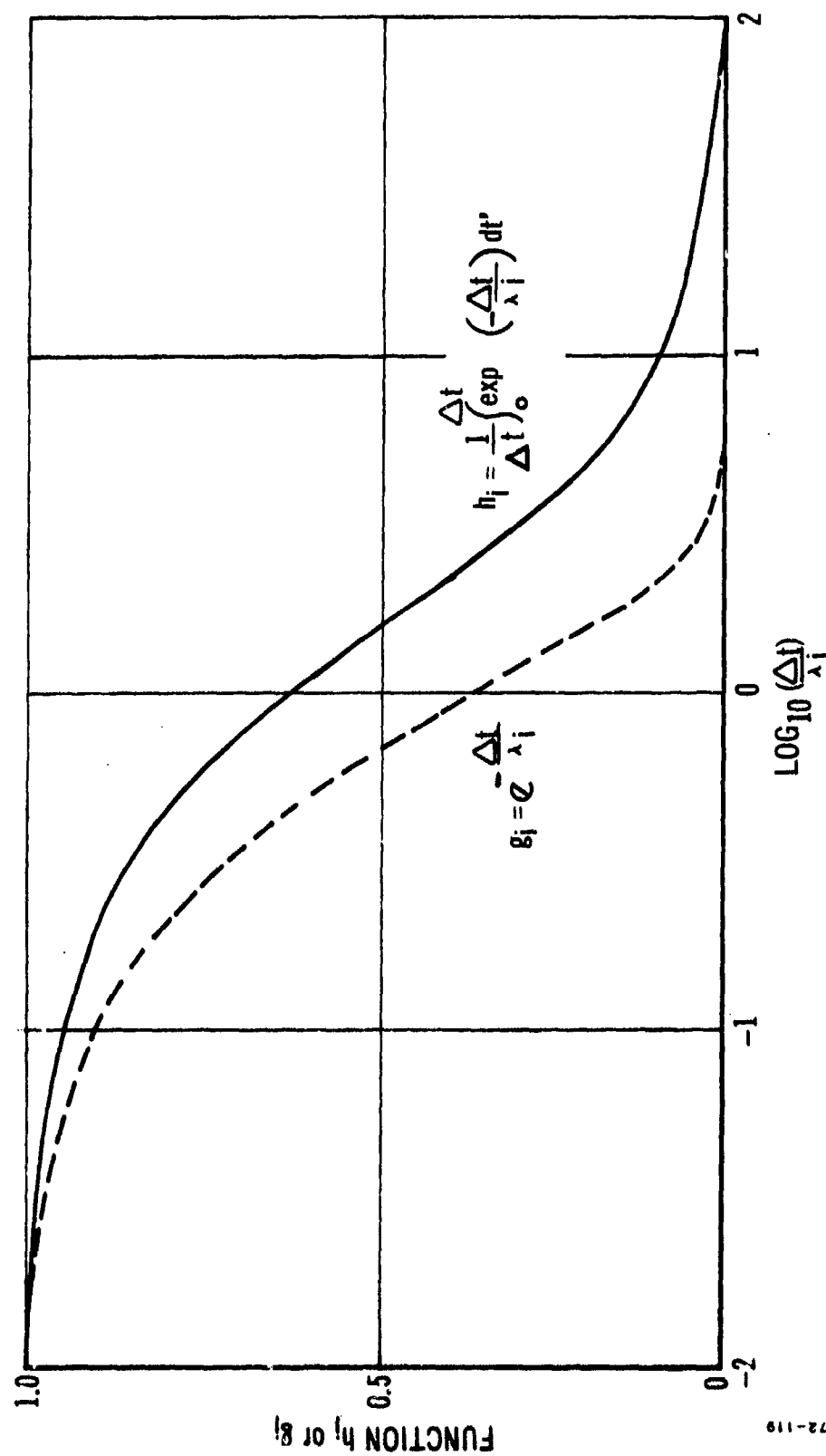
Figure 1. Functions h_i and g_i versus $\text{Log}\left(\frac{\Delta t}{\lambda i}\right)$.

$$h_i = \frac{1}{\Delta t}\int_o^{\Delta t}\exp\left(\frac{-\Delta t}{\lambda i}\right)dt'$$

$$g_i = \mathcal{C}^{-\frac{\Delta t}{\lambda i}}$$

FUNCTION h_i or g_i

$\text{LOG}_{10}\left(\frac{\Delta t}{\lambda i}\right)$

72-119

the above; consequently, during the solution process a search must be made to find the terms to be used.

Using the above methods, the analyst need not worry that a large number of terms in the series will lead to correspondingly large computation times. Experience has shown that the search for the proper terms is insignificant compared with the actual computations involved with any one term. The computation behaves as if only four terms were used.

3. MODIFICATIONS TO THE THERMOVISCOELASTIC FINITE ELEMENT CODE (THVISC)

A program for thermoviscoelastic stress analysis of solids (THVISC) was developed during the first year of the STV program (Ref 1). The program was subsequently modified to account for the near-incompressibility of most propellant characterizations. This program is referred to as THVINC. Effort was expended under the current contract to improve the cost-effectiveness of the program. In addition to the improvement discussed above, the program was extensively restructured to achieve a more efficient use of taping operations. This was accomplished by using the variable dimensioning feature of FORTRAN and combining history effects for groups of elements together on a single record. By these means optimal use of available storage space was achieved for all problems whether large or small; small problems are handled in-core, thus eliminating costly tape operations. In addition, the program is adaptable to larger or smaller computers by changing only two cards that control the total amount of storage to be used.

The treatment of boundary conditions by the program has been restructured to allow for their time dependence. The thermal boundary conditions can be made time dependent by specifying their time variations by a series of straight-line segments. These time-temperature data are stored in a table and accessed as required during the analysis. Several such environments can be stored so that measured thermal responses can be directly utilized in the viscoelastic analysis. In addition, prescribed forces and displacements can be specified as time dependent functions in the table. Finally, it is now possible to change the convection boundary condition with time. Thus, bodies passing from a cold to a hot environment can be accommodated.

Using the data from Figure 115 and Table XXV in Reference 2, together with the measured bore and case temperature histories shown in Figure 116, the temperature at 3.35 inches of radius was predicted with THVINC. The predicted results coincide with the measured data given in Figure 116 of Reference 2.

These improvements allow the program to follow imposed temperature conditions accurately regardless of their time variations. By using the actual data it has not been necessary to use derived heat transfer coefficients. Furthermore, it is no longer necessary to use the artificially induced liner (insulator) by using all three measurements as input data to the program. The ability of the program to predict accurate mechanical

-13-

response (displacements, strains, and stresses) depends strongly on the accuracy of the computed temperatures. Consequently, whenever possible, measured thermal responses should be directly used in the analysis if the best linear thermoviscoelastic estimates to the mechanical response are to be obtained.

4. MODIFICATIONS TO THE STEADY-STATE DYNAMIC VISCOELASTIC FINITE ELEMENT PROGRAM

A program for the viscoelastic analysis of a solid/shell, CX450, was also developed and reported during the first year of the STV Program (Ref 1). During the current contract this program has been modified to improve its cost-effectiveness as well as its reliability with a wider class of problems. The significant costs encountered in using the program resulted principally from two sources: (1) formulation of the finite element matrices, and (2) solution of the resulting system of algebraic equations. The data input-output constituted a minor portion of the overall solution effort. The routines involved in setting up the algebraic problem have been rewritten in a more efficient format for computer evaluation. This has been achieved at the expense of a slightly greater storage requirement. The solution algorithm has been modified to allow for subsequent computation of different forcing functions on the same structure without the necessity of reformulation and a complete refactoring of the algebraic equations. Typical computation times on a CDC 6400 computer are indicated below for a 420-element mesh with 465 nodal points (15 by 31 grid). As may be observed the main effort is now concentrated on the initial solution to the algebraic equations. Whenever possible all loading combinations at a certain frequency should be performed before proceeding to the next frequency (which constitutes a new problem).

TIMING FOR CXL450 ON CDC 6400 COMPUTER

	Time (sec)
Input data for first load case	3.08
Form element matrices	22.13
Solve equations	131.77
Output answers for first load case	15.96
Input data for second load case	5.07
Solve for new load case	10.03
Output answers for second load case	15.98

5. MODIFICATIONS TO UNIAXIAL THERMOVISCOELASTIC PROGRAM

The following section derives a numerical scheme for evaluating the hereditary integral equation, which is fundamental to all calculations involving thermoviscoelastic responses of linearly viscoelastic materials. Experience with the analysis code developed earlier for this purpose (Ref 2) showed that if standard computer integration routines are used, the calculations may be extremely expensive. The main reason for this expense is that integration routines are set up for very general types of functions and

have to cover many different cases. With most viscoelastic materials of concern, a very specific function and error analysis may therefore be cheaper if tailored to this special condition.

The thermoviscoelastic integral equation may be written

$$\sigma(t) = \int_0^t E_{rel}(ARG) \frac{d}{d\xi}\left[\epsilon(\xi) - \alpha\, T(\xi)\right] d\xi \tag{3}$$

where $E_{rel}(s)$ = the relaxation function (it may be given as numerical or graphical data)

$\epsilon(s)$ = the uniaxial mechanical strain

$T(s)$ = the temperature

α = the linear coefficient of thermal expansion (it may be a function of temperature, and through temperature may depend on time)

$ARG = \int_\xi^t \dfrac{d\tau}{a_T\ T(\tau)}$ with a_T the shift factor as a function

of temperature.

Consider first the integral

$$I_1(t) = \int_0^t E_{rel}(ARG)\, d\xi \tag{4}$$

and refer to Figure 2 where there are plotted, schematically, the logarithm of the relaxation modulus versus the logarithm of the ARG. It is desired to perform the integration so that the total error does not exceed a certain value, e %.

A stepped approximation to the relaxation modulus will be used, primarily to keep the algebra and the programming unsophisticated. (The advantage of this does not become apparent until later.)

The integral, Equation (4), can be written

$$I_1(t) = \sum_{i=0}^{i=n} \int_{t_i}^{t_{i+1}} E_{rel}(ARG)\cdot d\xi, \quad t_o = 0, \tag{5}$$

where, according to Figure 2 the t_i are arguments of $E_{rel}(s)$, which are yet to be defined.

Consider now a single term of the summation

$$\int_{t_i}^{t_{i+1}} E_{rel}(ARG)\, d\xi \tag{6}$$

-15-
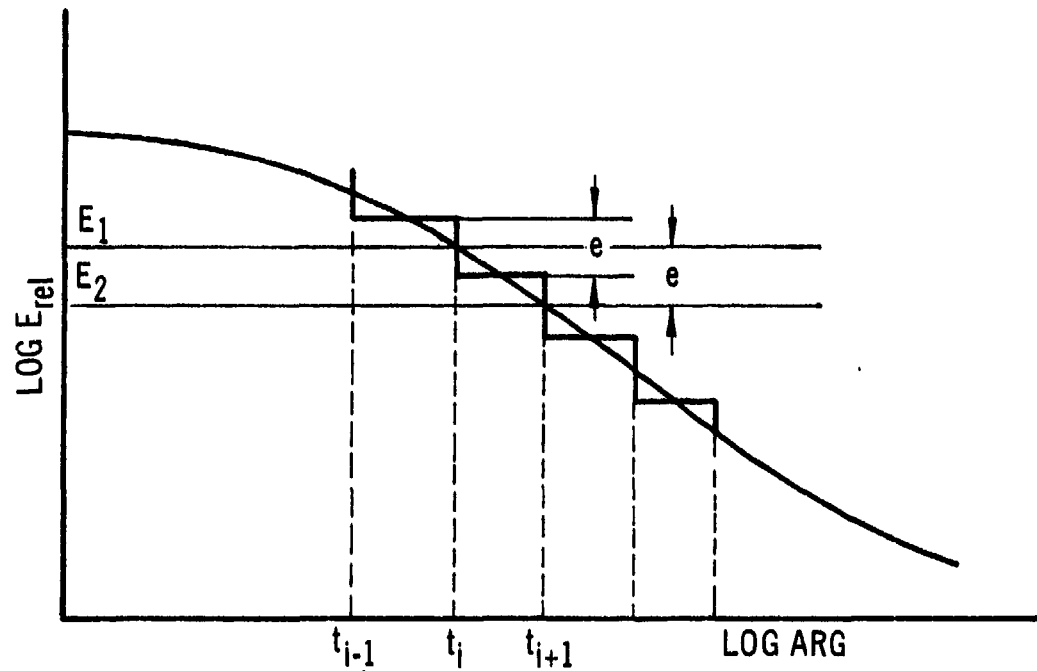
Figure 2. Log Relaxation Modulus versus Log ARG
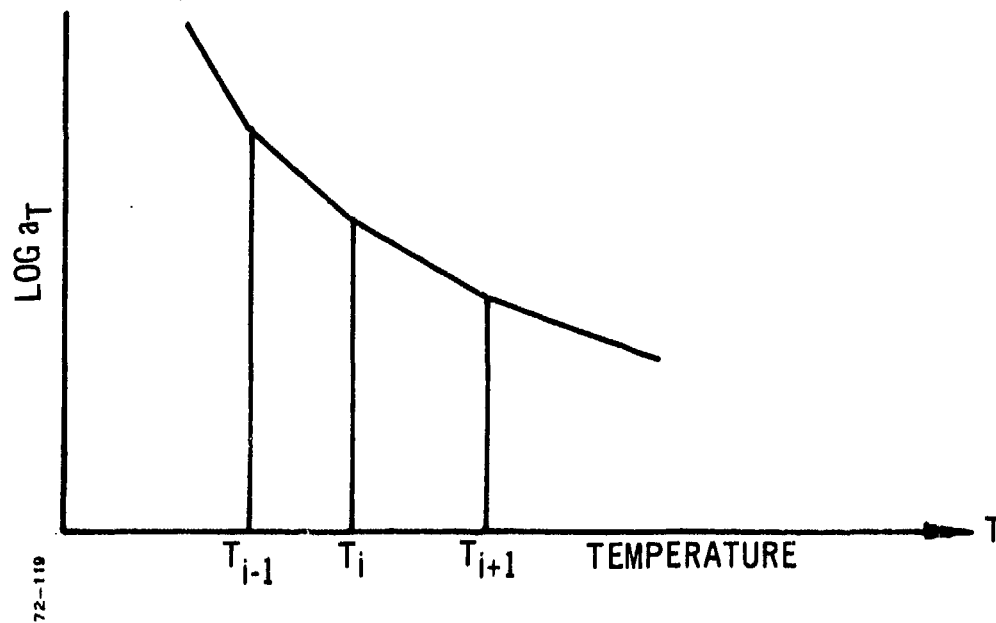
Figure 3. Log a_T Shift Factors versus Temperature.

-16-

If ARG = constant in $t_i \leqslant \xi \leqslant t_{i+1}$ then that integral is equal to

$$E_{rel}(t_{i+1})(t_{i+1} - t_{i-1}) \tag{7}$$

In reality, ARG changes between t_i and t_{i+1} so that the integrand varies between

$$E_{rel}(t_i) \quad \text{and} \quad E_{rel}(t_{i+1})$$

but the error of substituting the constant value of $E_{rel}(t_{i+1})$ for the integrand is always less than

$$e = \frac{E_{rel}(t_i)}{E_{rel}(t_{i+1})} - 1 \tag{8}$$

Dividing then the log E_{rel} scale into equal intervals of magnitude e, (Figure 2), the end points of these intervals determine time intervals t_i as shown. Indeed, from now on the values of t_i can be considered to be defined in this way. Specification of the integration error, e, to be below a certain minimum, say 2 percent, will fix the number of intervals in both log E_{rel} and log ARG. As a matter of fact, the error can be made much smaller than that specified by using the average value of E_{rel} in the interval $t_i \leqslant ARG \leqslant t_{i+1}$. Further refinement can be introduced by calling on the mean value theorem.

Next the specification of the temperature and its effect on ARG will be considered. First consider the representation of log a_T as a function of the temperature T. In Figure 3, the plot of log a_T versus temperature T is subdivided into segments such that each can be represented well with a linear relationship in that plot, or such that

$$\log a_T = A_i + B_i T$$
$$\text{for } T_i \leqslant T \leqslant T_{i+1} \tag{9}$$
$$a_T = \exp(A_i + B_i T)$$

Furthermore, let the temperature history be broken down into a sequence of linear segments as shown in Figure 4. Note that the values of the T_n in Figure 4 are not necessarily the same as those of the T_i in Figure 3. In fact, let the values of T_i from Figure 3 be interposed between the T_n of Figure 4 to give the plot shown in Figure 5.

Now in any interval, say t_{n-1} and t_i, the temperature is given by the equation:

$$T = C_n \cdot t + D_n \tag{10}$$

while a_T is given in the same interval by

$$a_T = \exp(A_i + B_i T) \tag{9}$$
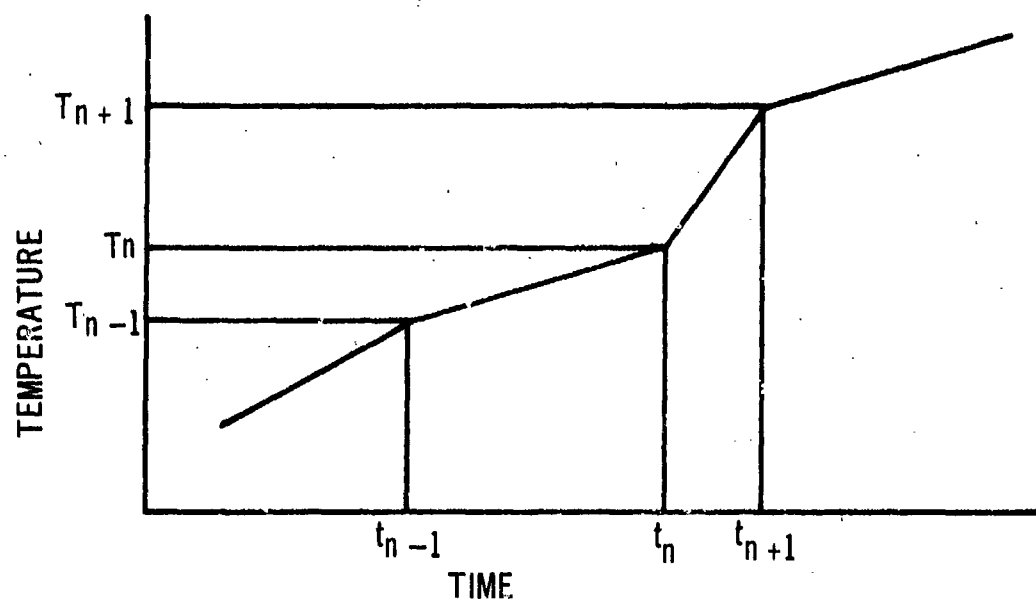
Figure 4. Temperature History versus Time.
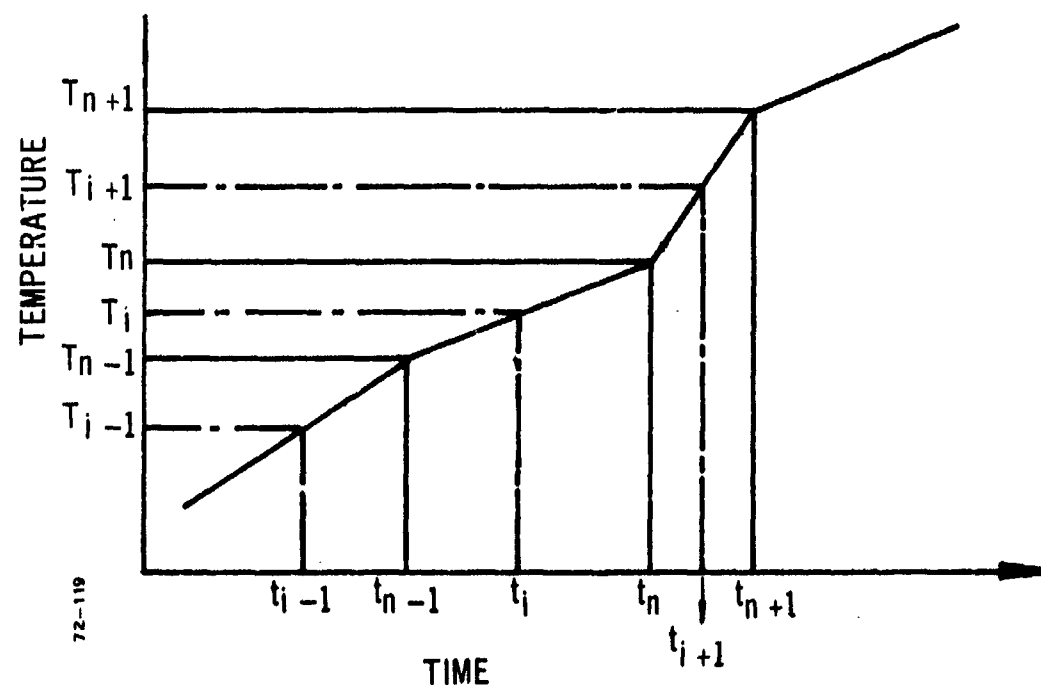
Figure 5. Temperature History with Time Intervals Interposed.

-18-

and, therefore, in any one time interval in Figure 5, a_T is given by:

$$a_T = \exp\left[A_i + B_i\left(C_n \cdot t + D_n\right)\right] \tag{11}$$

and the integral

$$ARG = \int_s^{s'} \frac{dT}{a_T\left[T(\tau)\right]} \tag{12}$$

becomes, in that interval,

$$ARG = \int_s^{s'} \exp\left\{-\left[(A_i + D_nB_i) + B_iC_n\tau\right]\right\} \, d\tau \tag{13}$$

$$= \exp\left[\left\{-(A_i + D_nB_i)\right\} - B_iC_nS'\left\{\frac{1 - \exp\left[-B_iC_n(S-S')\right]}{-B_iC_n}\right\}\right] \tag{14}$$

Recalling that we wished to evaluate the integral

$$\int_0^t E_{rel}\left[ARG(t, \xi)\right] \alpha \frac{dT}{d\xi} \cdot d\xi \tag{15}$$

then let the upper limit of the integral be one of the times t_n or t_i in Figure 5, i.e., a time determined by the temperature history or by the decomposition of a_T. Then, automatically, the upper limit of the argument

$$ARG(t \cdot \xi) = \int_\xi^t \frac{d\tau}{a_T\left[T(\tau)\right]} \tag{16}$$

is also fixed. Let t be equal to t_n in Figure 5; then $ARG(t \cdot \xi)$ defined in Equation (16), consists of an integral from ξ to t_n, where ξ has to range from zero to t_n, according to Equation (15).

We can evaluate Equation (16) for those intervals given by adjacent time numbers like t_i and t_n or t_{i+1} and t_{n+1} in Figure 5. That evaluation is given by equation (14), where the constants A_i, B_i, C_n, D_n, are appropriate for each interval. Thus,

$$ARG(t_n, t_i) = \exp\left[-(A_i + D_nB_i) - B_iC_nt_n\left\{\frac{1 - \exp\left\{B_iC_n(t_n-t_i)\right\}}{B_iC_n}\right\}\right] \tag{17}$$

while,

$$ARG(t_i, t_{n-1}) = \exp\left[-(A_i' + D_n'B_i') - B_i'C_n't_i\left\{\frac{1 - \exp\left[B_i'C_n'(t_i-t_{n-1})\right]}{B_i'C_n'}\right\}\right] \tag{18}$$

where the primes denote the appropriate constants for this interval. It follows that

$$ARG(t_n, t_{n-1}) = \int_{t_{n-1}}^{t_n} = \int_{t_{n-1}}^{t_i} + \int_{t_i}^{t_n} \tag{19}$$

$$= ARG(t_i, t_{n-1}) + ARG(t_n, t_i)$$

which is the sum of Equations (17) and (18).

This process can be continued until we have $ARG(t_n, 0)$. It appears advantageous, therefore, to compute the arguments ARG for each of the sub-intervals of the time scale in Figure 5 and to store these numbers in memory. The argument of the relaxation function in Equation (15) can then be quickly calculated by simple addition.

Let us now return to the integration of Equation (15) and consider a re-plot of Figure 2 as shown in Figure 6. We assume that we know the values of all $ARG(t_n, s)$, where s is any recursive time number on the time scale in Figure 5 that is less than t_n. Therefore we know, for example, the values of:

$$ARG(t_n, t_{i+1})$$

$$ARG(t_n, t_i)$$

$$ARG(t_n, t_{i-1})$$

$$\cdot$$
$$\cdot$$
$$\cdot$$

$$ARG(t_n, 0)$$

Let us denote the differences between two successive ARG values ΔARG, as given by

$$\Delta ARG(t_i, t_{i+1}) = \int_{t_i}^{t_{i+1}} \frac{d\tau}{a_T [T(\tau)]} \tag{20}$$

which, according to Equation (19), is one of the summands of ARG(   ). Thus,

$$\Delta ARG(t_i, t_{i+1}) = ARG(t_n, t_i) - ARG(t_n, t_{i+1}) \tag{21}$$

Suppose we enter all the values of $ARG(t_n, t_i -...)$, as calculated from the pertinent times of Figure 5 via Equations (19) and (20), into Figure 6. Associated with each ΔARG there is a definite time increment $(t_{i+1} - t_i)$.
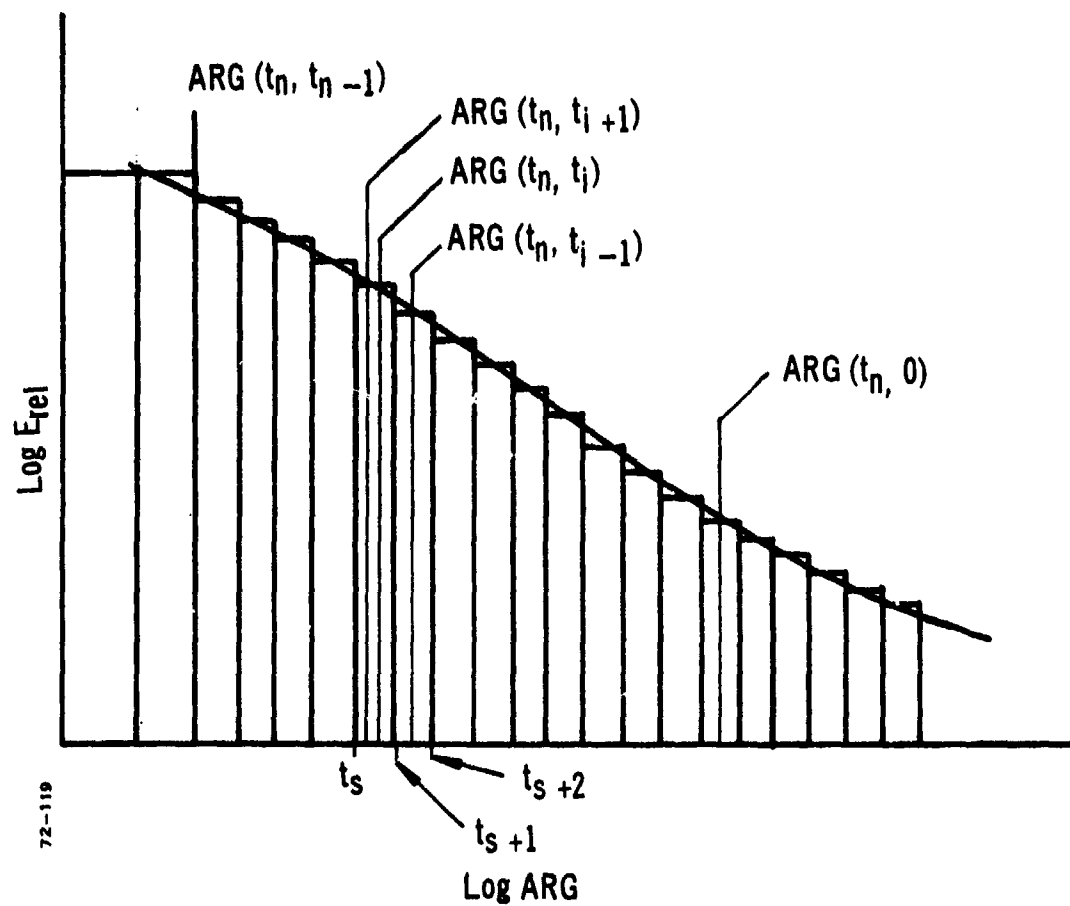
Figure 6. Replot of Log E_{rel} versus Log ARG To Show Time Increments.

Assume for the moment that ARG (t_n, t_{i+1}) and ARG (t_n, t_i) both fall inside the ARG interval that was determined in the beginning so that in that interval the modulus could be assumed constant (bounded by t_s and t_{s+1} in Figure 6). In that interval bounded by ARG (t_n, t_{i+1}) and ARG (t_n, t_i) the modulus is constant also, therefore the integral ΔI (t_n) a function of t_n written as

$$\Delta I \ (t_n) = \int_{t_{i+1}}^{t_i} E_{rel} \left[ARG (t_n, \xi) \right] \frac{dT}{d\xi} \ d\xi \tag{22}$$

may be rewritten as

$$\Delta I \ (t_n) = E_{rel} \left[ARG \ (t_n, \frac{t_i + t_{i+1}}{2} \right] \int_{t_{i+1}}^{t_i} \frac{dT}{d\xi} \ d\xi \tag{23}$$

If $dT/d\xi$ is also constant in the interval $t_i \leqslant t \leqslant t_{i+1}$, then

$$\Delta I \ (t_n) = E_{rel} \left[ARG \right] \frac{dT}{d\xi} \bigg|_{t_i} (t_{i+1} - t_i) \tag{24}$$

The incremental integral equation (24) is one of the summands in the series that represents the integral equation (15). The point to note is that the time increment $(t_{i+1} - t_i)$ is known because the incremental argument ΔARG corresponding to the time interval fell within that of t_s and t_{s+1}. Let ARG (t_n, t_{i+1}) fall within $t_{s+1} \leqslant t \leqslant t_{s+2}$ and assume that:

$$\frac{E_{rel}(t_{s+1})}{E_{rel}(t_{s+2})} - 1 > e \tag{25}$$

Then to stay within the prescribed error, we have to use t_{s+1} as one time point for subdivision, i.e., we have to write another incremental integral equation like (23) and (24) but now for the interval between ARG (t_n, t_i) and t_{s+1}. E_{rel} is still constant in that interval and we may also assume that $dT/d\xi$ is constant, for the present. Because t_{s+1} is a value of ARG not of a known time, we must find out what its corresponding value of time is. In other words, we know from the Equation (20) written for unknown $t_i = t$ and $t_{i+1} \geqslant t_i$

$$\Delta ARG (t, t_i) = ARG \ (t_n, t) - ARG(t_n, t_i) \tag{26}$$

Since $t_{s+1} = ARG \ (t_n, t)$ we can solve for t by using Equations (17) or (18).

$$t_{s+1} = exp \left[-(A_i + D_n B_i) - B_i C_n t_n \left\{ \frac{1 - exp \left[B_i C_n (t_n - t) \right]}{B_i C_n} \right\} \right] \tag{27}$$

-22-

We can assume that the constants $A_i \ldots C_n$ are chosen for the appropriate interval. Then we obtain:

$$\exp\left[B_i C_n (t_n - t)\right] = 1 - B_i C_n t_{s+1} \exp\left[A_i + D_n B_i + B_i C_n t_n\right] \qquad (28)$$

and therefore,

$$t_n - t = \frac{1}{B_i C_n} \ln\left[1 - B_i C_n t_{s+1} \exp\left\{A_i + D_n B_i + B_i C_n t_n\right\}\right] \qquad (29)$$

This value is readily obtained on the computer provided ln can be evaluated with sufficient accuracy. We will have to include a test to see whether or not the argument of ln comes too close to unity or zero. In that event one would be better off using the expansion

$$\ln z = 2\left[\frac{1-z}{1+z} + \frac{1}{3}\left(\frac{1-z}{1+z}\right)^3 + \frac{1}{5}\left(\frac{1-z}{1+z}\right)^5 + \ldots\right] \qquad (30)$$

and to write

$$\ln(1+\Sigma) = 2\left[\frac{\Sigma}{2+\Sigma} + \frac{1}{3}\left(\frac{\Sigma}{2+\Sigma}\right)^3 + \frac{1}{5}\left(\frac{\Sigma}{2+\Sigma}\right)^5 + \ldots\right] \qquad (31)$$

which converges fast and efficiently.

We have thus determined the time t and can write now the incremental integral

$$\Delta I(t_n) = \int_{t_i}^{t} E_{rel}\left[ARG\left(t_n, \frac{t+t_i}{2}\right)\right] \frac{dT}{d\xi} \, d\xi \qquad (32)$$

$$= E_{rel}[ARG] \frac{dT}{d\xi}\bigg|_t (t_i - t) \qquad (33)$$

In principle we now can calculate all the incremental integrals which, when summed, give the value of Equation (15). We have defined in Figure 6 all times that need to be considered in the subdivision of either the temperature history, Figure 5, or the accurate integration of E_{rel}, Figures 2 or 6.

If simultaneous straining and cooling occur, we divide the strain and temperature history into the same time divisions, i.e., we treat $\epsilon - \alpha T$ now as we have treated T before.

The effects of preprogramming the thermoviscoelastic integral equations with such care have been to produce a tremendous saving in the running time of the program. Furthermore, this is the same program that

is readily adaptable for interpreting gage output data as discussed in a later section of this report. When the gage problems were run on the computer during last year's work, the problems ran for a considerable time and cost approximately $70.00 per point. The same problems rerun with the modified program took only minutes to run at a cost of only a few dollars for all six values required.

SECTION III

NORMAL DIAPHRAGM STRESS GAGE: CALIBRATION AND RESPONSE WITH STATIC LOADS

1.   INTRODUCTION TO PROBLEM

This section of the report is concerned with the miniature diaphragm gage employe in a propellant grain to measure the normal stress at the case-grain interface or within the propellant grain itself. The earlier final STV reports, References 1 and 2, presented detailed descriptions of the various types of gage developed for this work, together with a certain amount of analytical work showing how the gage should respond in an idealized environment.

Emphasis during the third year of the STV program has been removed from the purely practical aspects of using the gages in STVs and has been placed on determining a better understanding of the gage behavior under calibration conditions in uniaxial test fixtures. Although this approach is certainly not as dramatic or inspiring as the testing of new STV designs, it was high time that the complete calibration procedure was examined in detail. Only by a careful and meticulous approach could the problem areas be resolved and the doubts associated with the use of stress gages in STVs be laid to rest.

Professor Pister has frequently referred to the calibration of a gage as something more than merely embedding the device within some type of test fixture and proceeding to apply a series of load increments. It involves in general a complete analysis of the gage, the test fixture, and the propellant, and not until a complete reconciliation of the analytical and the experimental work across the whole environmental spectrum to which the gage may be subjected has been achieved, can the calibration procedure be considered complete.

It is obviously unnecessary to perform such a comprehensive calibration procedure very often, but until it has been performed at least once, doubts as to the veracity of the gage data must exist.

It is the purpose of this section of the report to demonstrate the results of a comprehensive calibration of the miniature diaphragm gage embedded with a uniaxial test fixture.

2.   CALIBRATION APPARATUS AND TECHNIQUES

a.   Uniaxial Test Fixture

Figure 7 shows a sketch of the type of uniaxial test fixture that was developed at LPC for the calibration of the miniature diaphragm gages. Usually, the gages are bonded to the end pieces of the fixture and these may be made of different materials, if required, so that the performance of the gage may be examined in conjunction with different case materials.

PLEXIGLASS END

150 PSI DIAPHRAGM
GAGES

INERT PROPELLANT

STEEL END

END PIECE

72-119
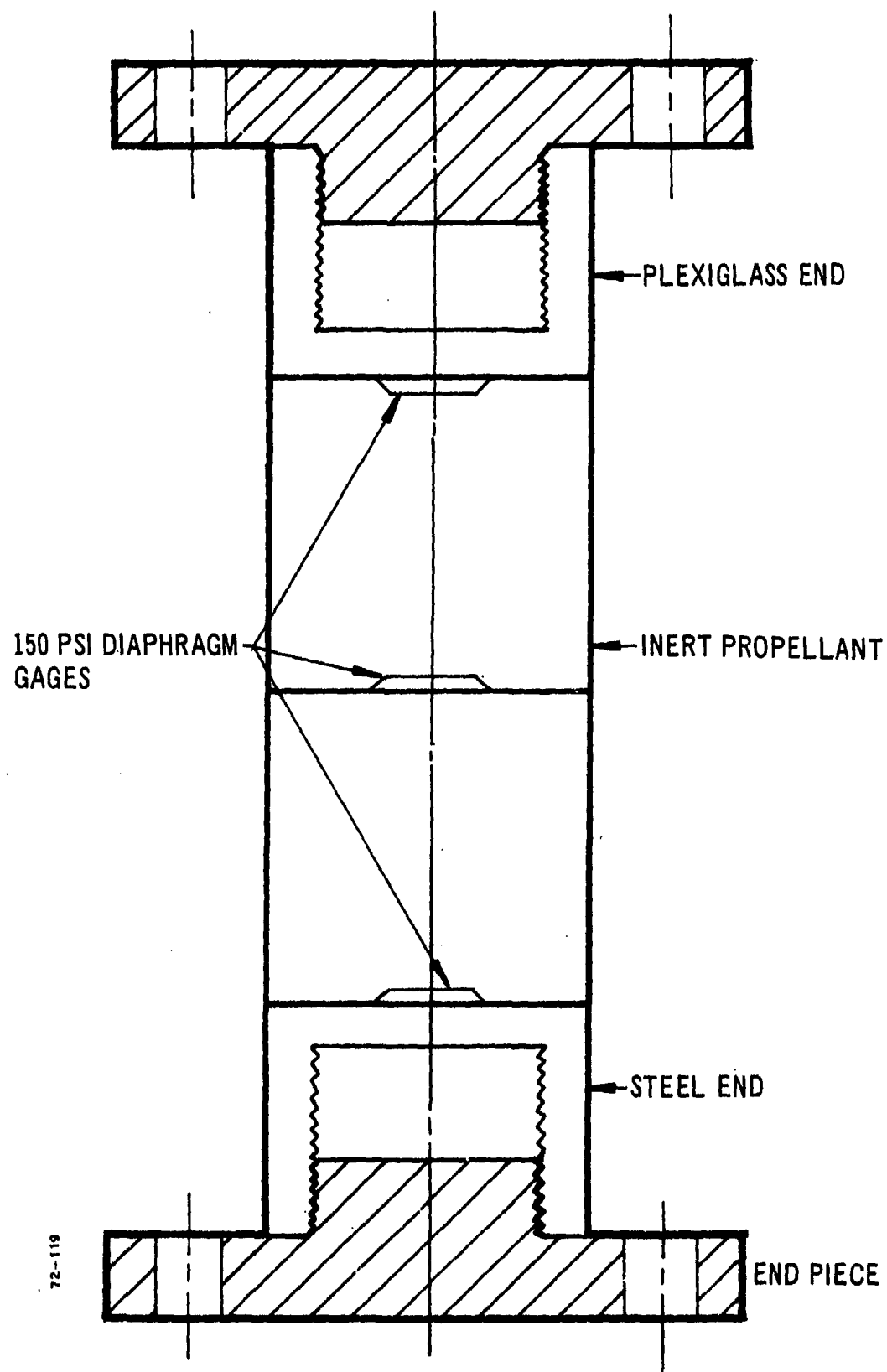
Figure 7. Uniaxial Test Fixture for Gage Calibration.

A third gage was embedded at the center of the propellant specimen to evaluate the performance of the gage when removed from close proximity to the case.

Screw-in end connections are employed with the calibration fixture so that different types may be used for tension or compression testing. The sketch shows the type of end fittings used for compression tests.

The uniaxial test specimen is made at LPC with a diameter between 1.5 and 2.0 inches, and a length between 4.0 and 6.0 inches. The important thing is not the absolute specimen size but its size relative to the gage size. The diameter must be at least four times the diameter of the gage itself so that the gage does not "know" that the specimen has finite dimensions. The minimum length of the specimen will be such that the end effects of the two end pieces do not interfere with each other. A minimum length equal to the diameter will be sufficient to ensure that this condition is met. It should be noted that a poker chip type of specimen is not a good vehicle for calibrating gages. The compliance of the gage will seriously interfere with the stress distribution throughout the poker chip and, of course, the gage will not be subjected to a simple stress field.

b.   Test Setup for Tensile and Compression Testing

The initial test procedures employed with the gage test fixtures closely resembled those used for the testing of propellant specimens. During the third year of the program, however, it was found that a more elaborate test procedure was necessary to make sure of obtaining accurate calibration data.

Data scatter obtained in a series of creep tests on the uniaxial test fixture led to an investigation of its causes. It appeared that the scatter was associated with the initial zero reading of the gage before a load is applied to the specimen. Because we are concerned with changes in gage signal caused by the change in stress, the gage signals measured during the loading phase are converted to output signal changes from the zero gage reading (prior to loading). Therefore, an error in the gage zero load reading will cause all the gage signal change values to be incorrect and will produce errors in the gage sensitivity values.

The initial gage zero reading may be greatly influenced by handling during the test setup procedure, especially at the lower temperatures. For instance, if a test is begun and then stopped, the gage zero reading will have changed and, if a new test is begun within a short time interval, the measured signal changes will be incorrect. This is because a viscoelastic material has a memory for earlier events, and a gage embedded within a viscoelastic material "remembers" earlier loading histories.

The solution to this problem is to perform the calibration tests in such a manner as to minimize the effects of earlier tests. Thus, the single-step tests performed as routine calibration procedures are inadequate, and multi-step loading tests are required. Further, it is recommended that alternating tensile and compressive loads be applied to the specimen, as

shown in Figure 8. The anticipated gage readings from such a test sequence are also shown in this figure.

Figure 9 shows a sketch of the simple apparatus developed for applying alternating tensile and compressive loads to a uniaxial test specimen. The load application is controlled by means of the crosshead of the testing machine; movement in an upwards direction causes a compressive load (W_2) to be applied, whereas movement of the crosshead downward from the unloaded position causes the tensile load (W_1) to be applied.

A minor problem with this apparatus is the existence of two different zero load conditions. One is the tensile zero load condition and the other is the compressive zero load condition. These two zero load conditions are illustrated in Figure 10, wherein it will be noted the real zero load on a gage depends on its location in the test fixture. However, once this fact is appreciated, there is no further problem in dealing with the calibration data. Changing between the tensile zero load condition and the compressive zero load condition has to be treated like any other step change in load with a sufficient time interval in between to allow near-equilibrium to be attained.

Figure 11 shows typical data obtained from a series of tension and compression tests on the uniaxial inert propellant test specimen containing three 150-psi gages. The repeatability of the data is excellent and there is no doubt as to the proper location of either of the two zero load conditions. Another interesting aspect of the data of Figure 11 is the performance of gage No. 20, which is located in the middle of the propellant. It performed very well indeed and there seemed to be no particular problems associated with the use of a diaphragm gage removed from an interface. At a later stage in the testing, the lead wires to this gage became broken and could not be repaired, but up to this time the gage performed in a manner identical to that of the other two gages located at the ends.

c. Apparatus for Pressure and Complex Loads Calibration

In addition to the uniaxial tension and compression testing of the test fixture, it was necessary to calibrate the device with hydrostatic pressure. The apparatus sketched in Figure 12 was developed for this purpose. It consists of a pressure cylinder, 7.0 inches in diameter, into which the test fixture is placed, and it is attached to a load cell that is firmly mounted to the top end closure of the cylinder. The gage lead wires and other electrical wiring are taken out through a sealed plug in the upper end cap.

For simple pressure testing of the test fixture, the unit is mounted inside the pressure cell and the bottom cap is screwed in place. Nitrogen gas pressure may then be applied to the cylinder and the output signals from the gages can be monitored.

This apparatus may also be used for the application of uniaxial loads, tension or compression, in addition to the pressure loading. By this means the performance of the gages in a complex stress field can be examined. The load cell and the displacement LVDT are used for these complex load tests.
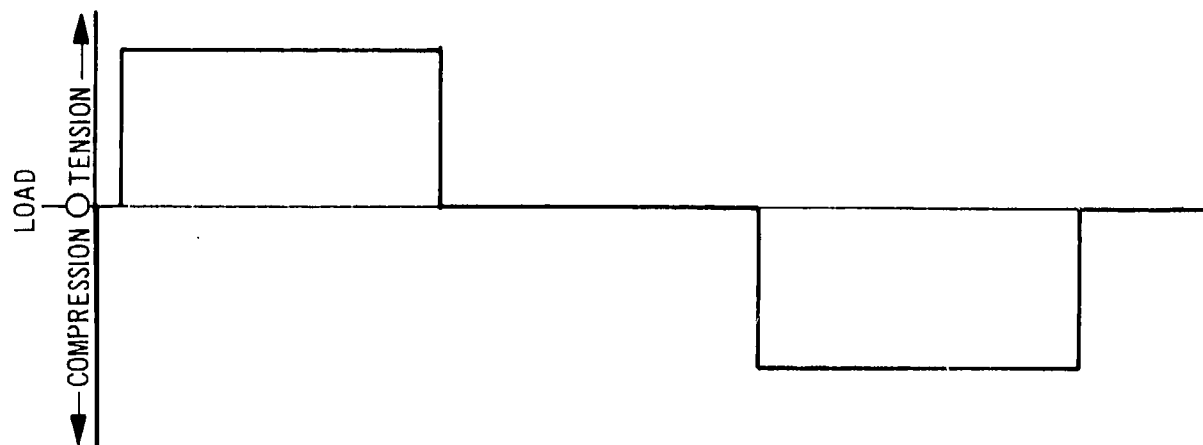
a.   Load versus Time History
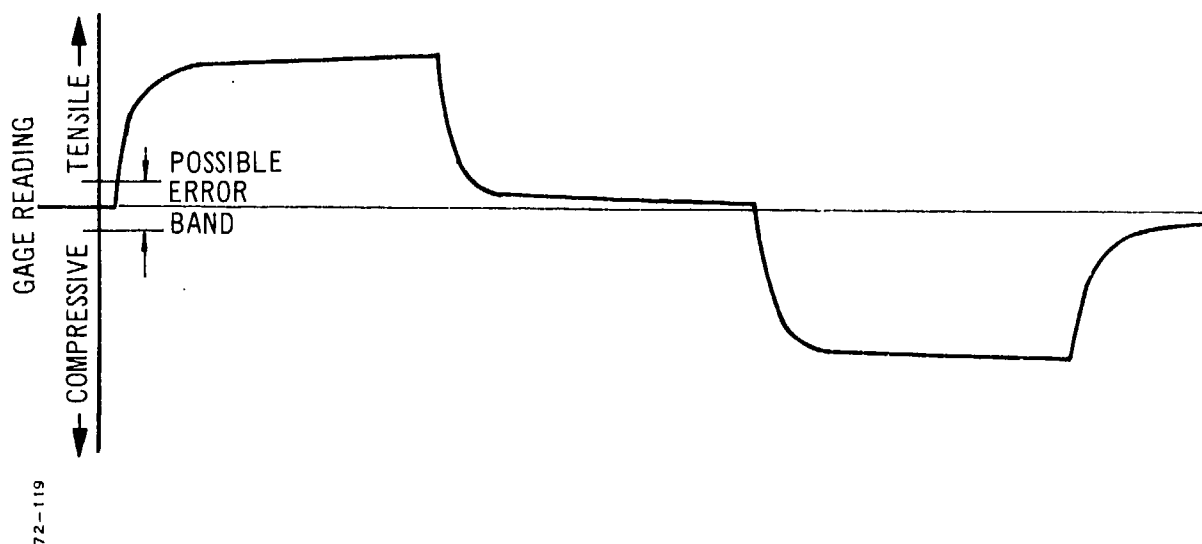
b.   Gage Reading versus Time for Alternating Tension,
     Compression Loading Sequence

Figure 8   Alternating Tensile and Compressive Loading and
           Anticipated Gage Response.
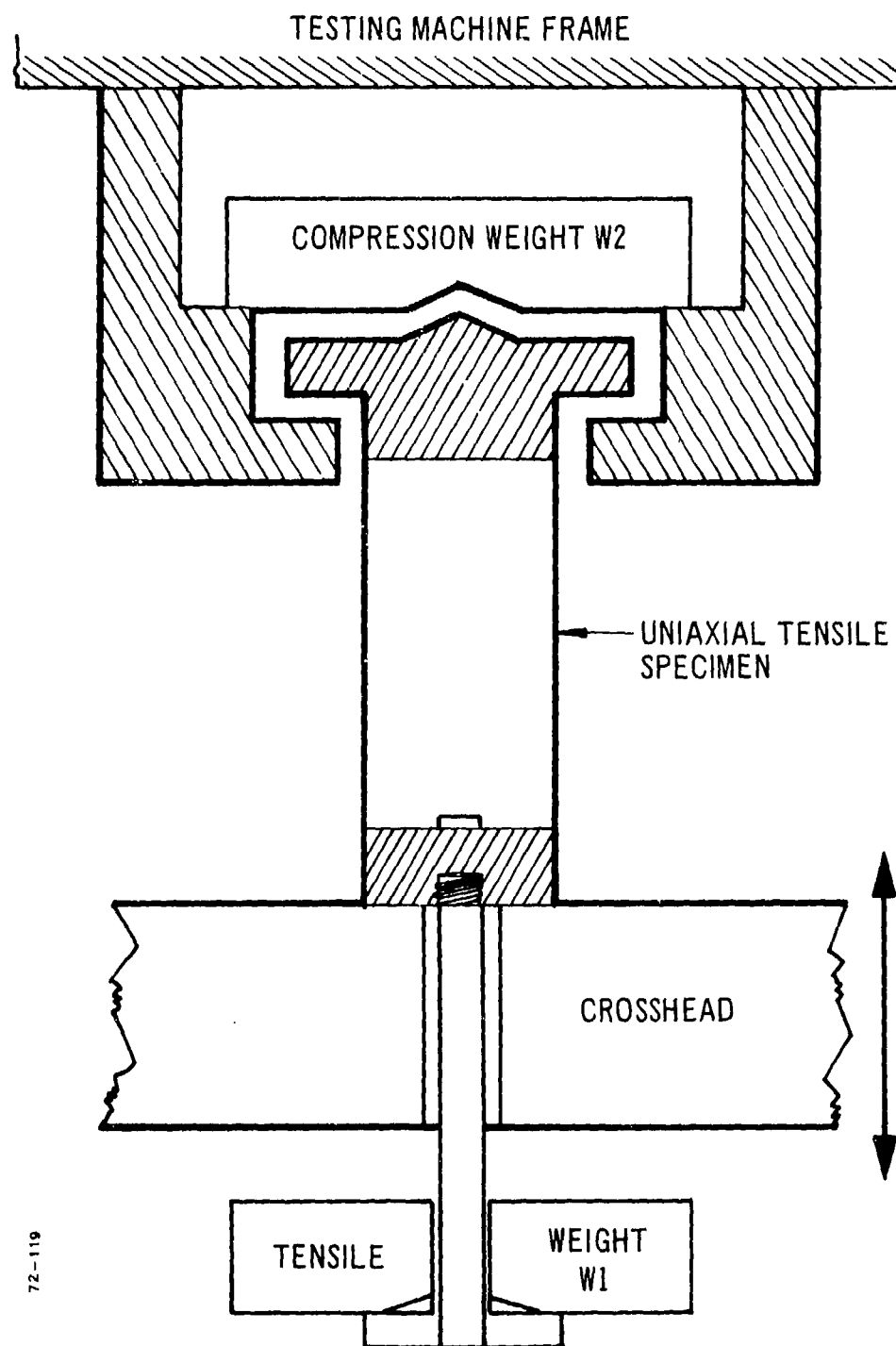
Figure 9. Apparatus for Application of Alternating Tensile and
Compressive Loads to Uniaxial Test Fixture.
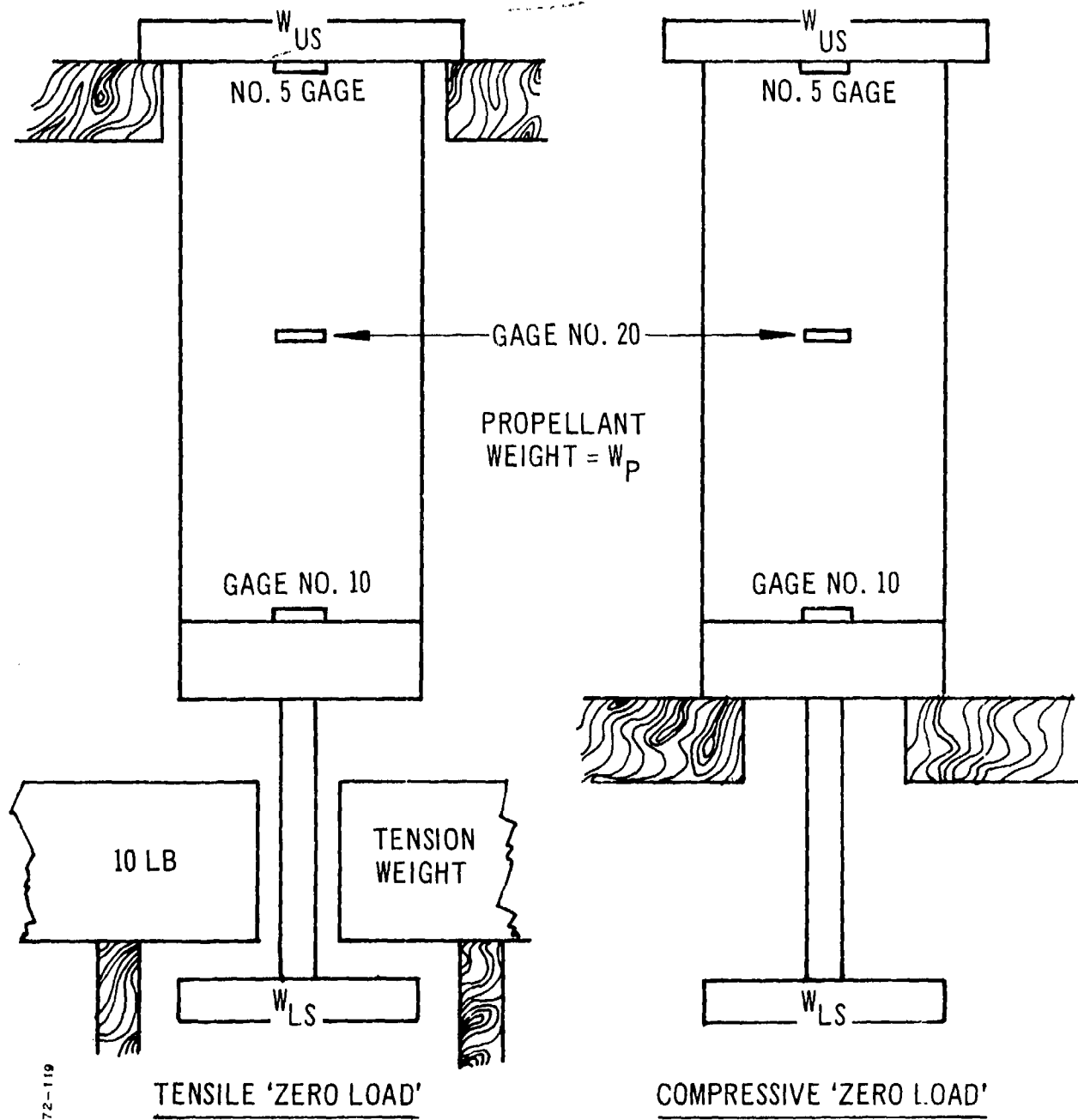
Figure 10. Tensile and Compressive Zero Load Conditions.

-31-
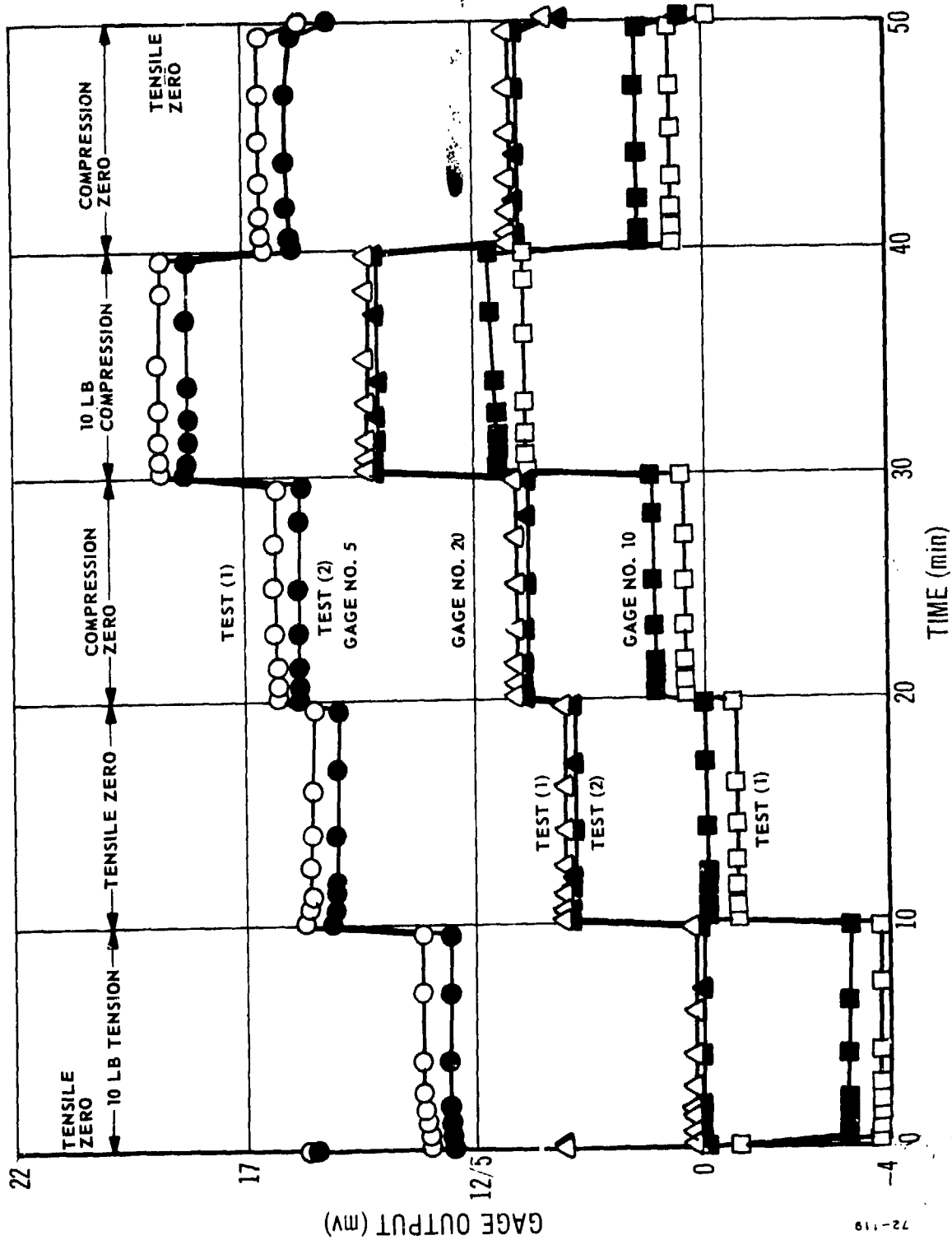
Figure 11. Uniaxial Test Fixture No. 2: Alternating Tension and Compression Data.

-32-

TO INSTRON FRAME

TO GALVANOMETER
CHART RECORDER

LOAD
CELL

PRESSURE
VESSEL

GAGE

PRESSURE
SEAL

UNIAXIAL
TEST FIXTURE

TO PRESSURIZED
NITROGEN CYLINDER

LVDT

ELECTRICAL
PRESSURE
TRANSDUCER

TO GALVANOMETER
CHART RECORDER

72—119

TO INSTRON
CROSSHEAD
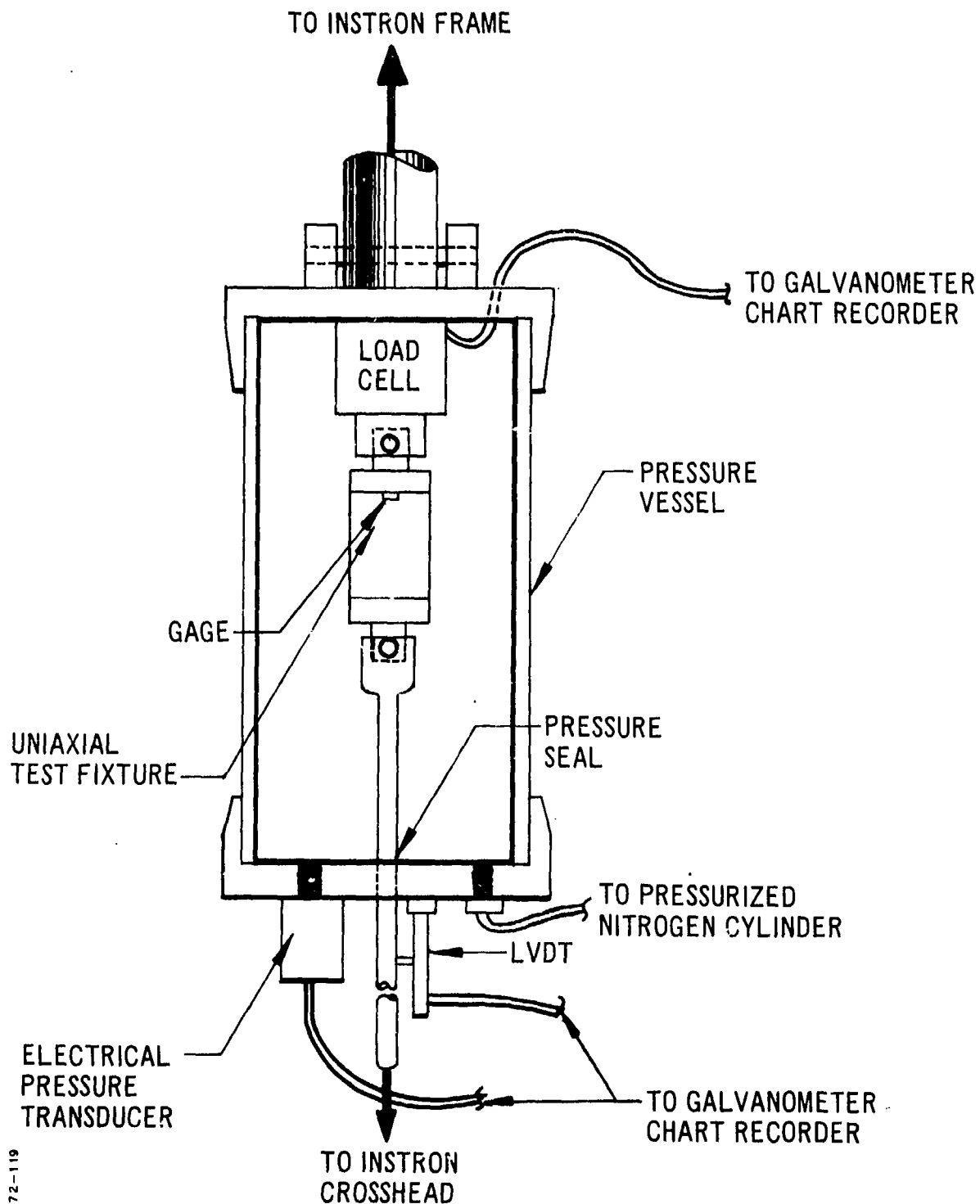
Figure 12. Apparatus for Pressure and Complex Loading of
Uniaxial Test Fixture.

3. GAGE CALIBRATION ANALYSES FOR STATIC LOADS

a. Review of Elastic Calibration for Static Loading

The principles of gage calibration were discussed previously in References 1 and 2. It was pointed out there that calibration of a gaged depends on the ability to perform analysis of the gage fixture used for calib·ation. The purpose of such analysis is to determine the effect of the gage on the existing stress field as well as to determine calibration functions for the gage. The analysis of the test fixture involves the solution of an initial boundary value problem for which it is necessary to know the material properties, geometry, and prescribed loads. The initial conditions of the fixture are normally taken as the conditions existing at the initiation of testing and in themselves are often difficult or impossible to evaluate. The manufacturing process and assembly of the fixture may introduce conditions that cannot be evaluated. Care must be taken to keep these unknown factors at a minimum if reliable calibrations are to be obtained from experiments and analysis.

In Reference 2, analyses of the uniaxial calibration apparatus were undertaken with an assumed linear elastic behavior of an initially undisturbed system. The analysis considered both incompressible ($\nu = 0.5$) and nearly incompressible ($\nu = 0.49$) properties for the propellant and analyzed a range of extensional moduli, E_p, between 200 and 1000 psi. Only static loadings were considered. In the third year of work, those analyses were extended to cover both linear elastic and linear viscoelastic characterizations of the propellant. In addition, both dynamic and quasi-static loading conditions were considered. Because of the complexity of the initial-boundary value problem for the test fixture, it was necessary to use numerical methods for their solution. The methods used here consist of a set of finite element programs (two of which are THVINC and CXL450, discussed earlier), which can treat complex two- and three-dimensional problems. These programs are in themselves approximate methods of limited storage capacity, and it is therefore necessary to use less accurate modeling of the fixture as the complexity of the problem increases. Consequently, it has not been possible in all analyses to provide explicit data for use in calibration. It has, however, been possible to indicate whether or not calibration analyses are feasible.

b. Additional Static Analyses of the 150-psi Diaphragm Gage

A continuation of the static analysis of the 150-psi diaphragm gage embedded within the calibration test fixture has been completed. The propellant was represented as a linear, isotropic, incompressible elastic solid, and studies were undertaken to ascertain the effect of varying the propellant extensional modulus (E_p) over the range of 50 to 15,000 psi. The analyses were performed using the ANL 800 computer code, which employs standard finite element procedures. The finite element idealization used in these analyses is identical to that used earlier, and is shown in Figure 13.

Numerical results for axial and hydrostatic loading conditions are depicted in Figures 14 through 17. Figures 14 and 15 illustrate the normal pressure distribution across the radial dimension of the gage. The
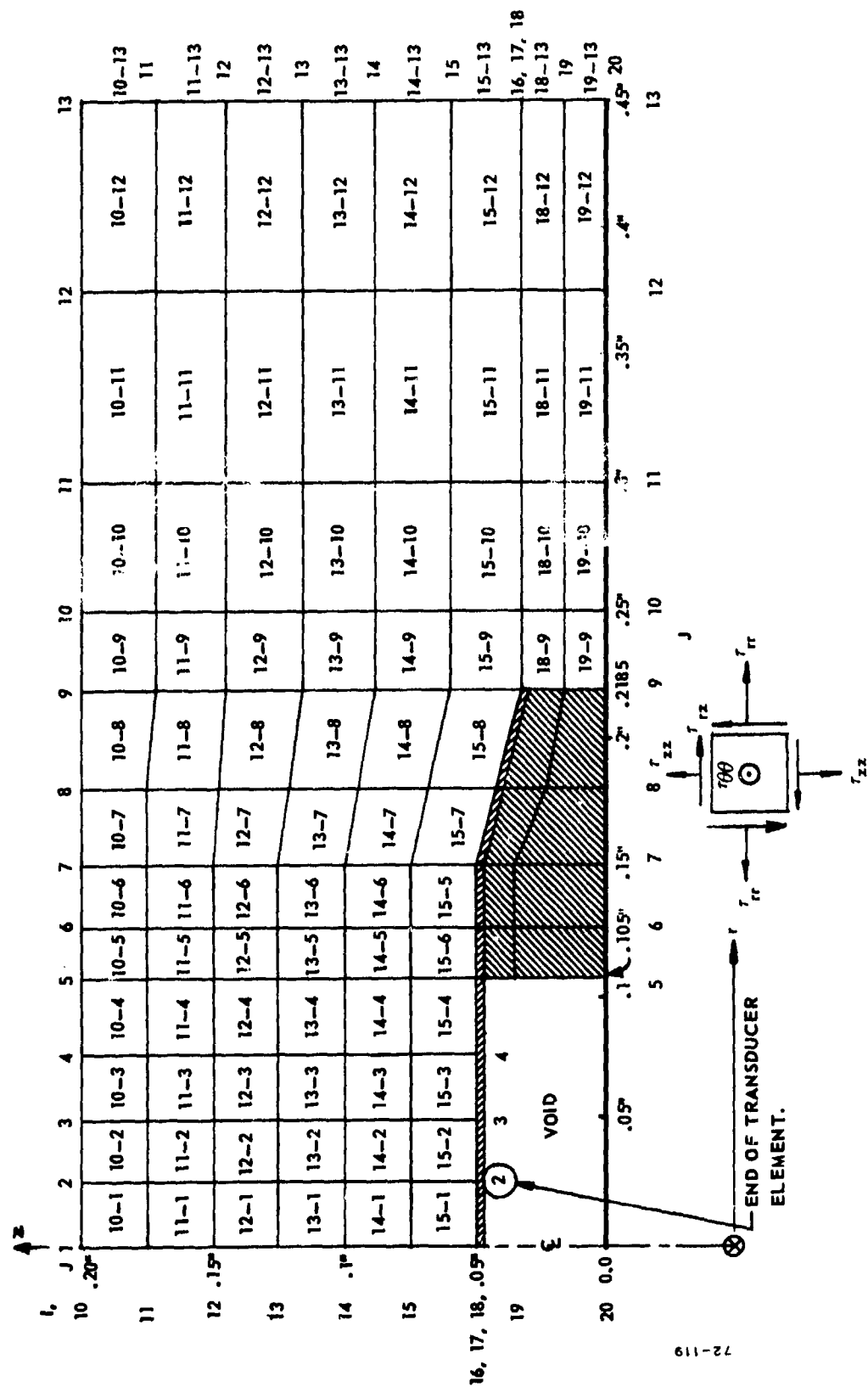
Figure 13. Finite Element Idealization of Gage Neighborhood.

-35-
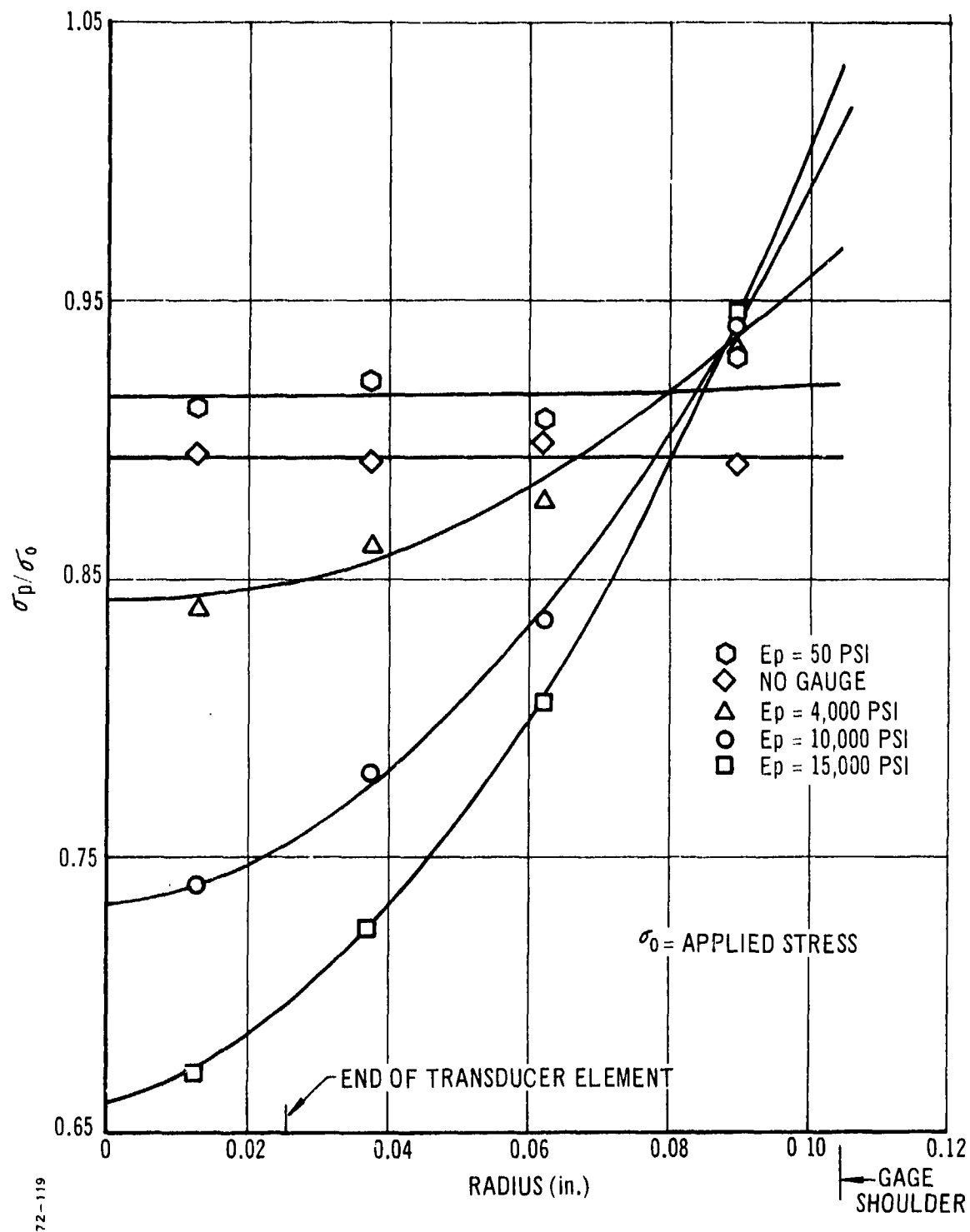
Figure 14.   150-psi Diaphragm Gage in Uniaxial Calibration Fixture under Axial Load.

-36-
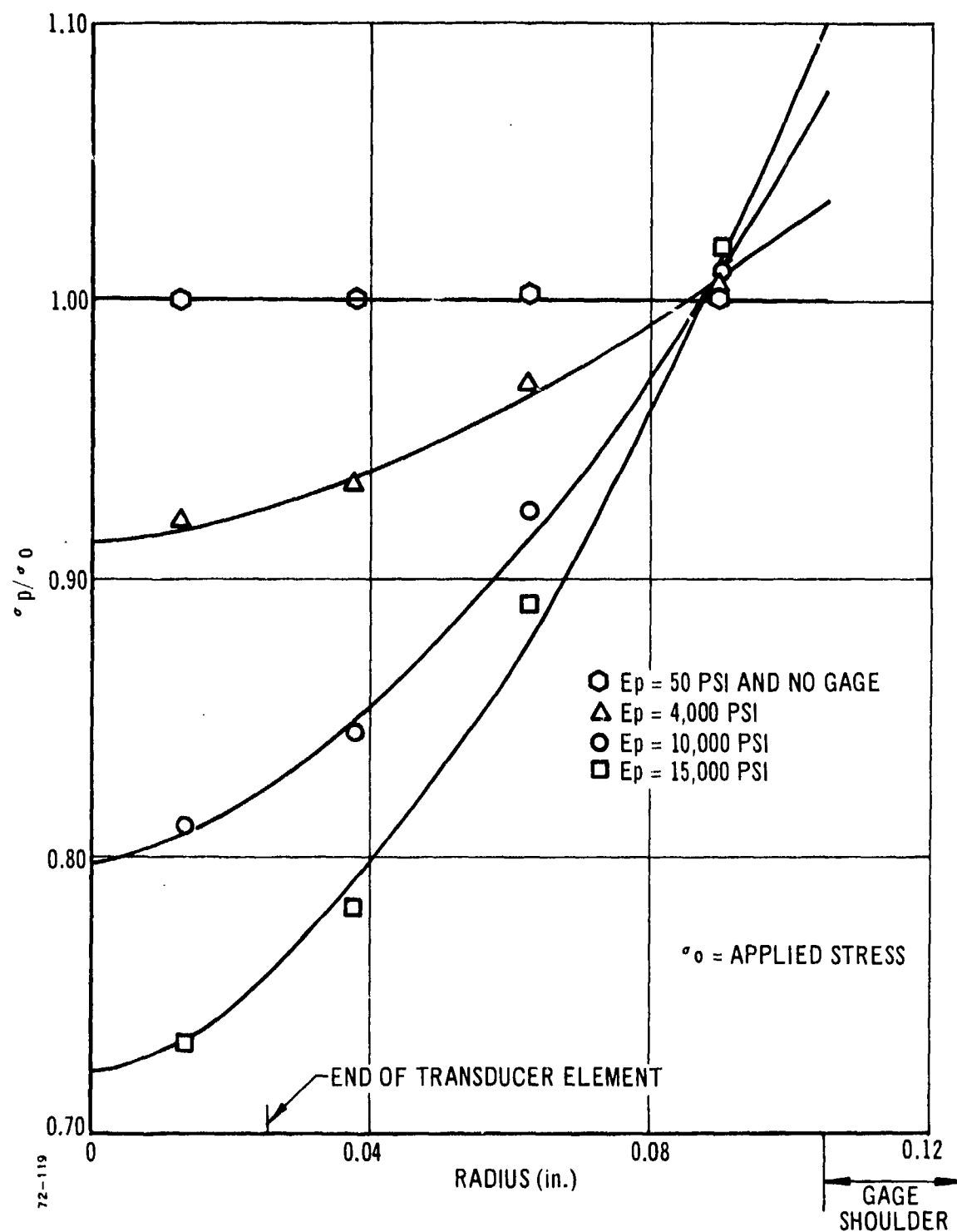
Figure 15. 150-psi Diaphragm Gage in Uniaxial Fixture under Hydrostatic Load.
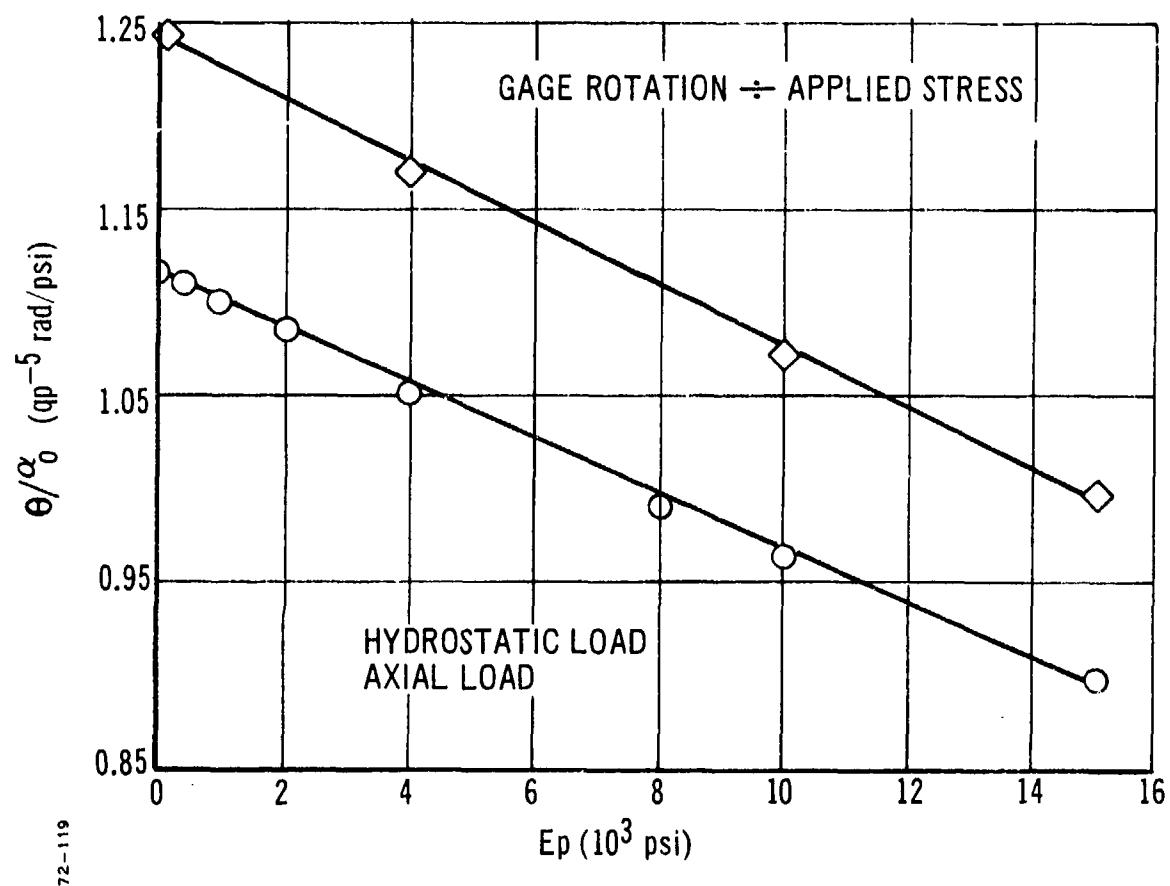
Figure 16. 150-psi Diaphragm Gage Rotation (r = 0.0255 inch)/
Applied Stress versus Propellant Modulus

-38-
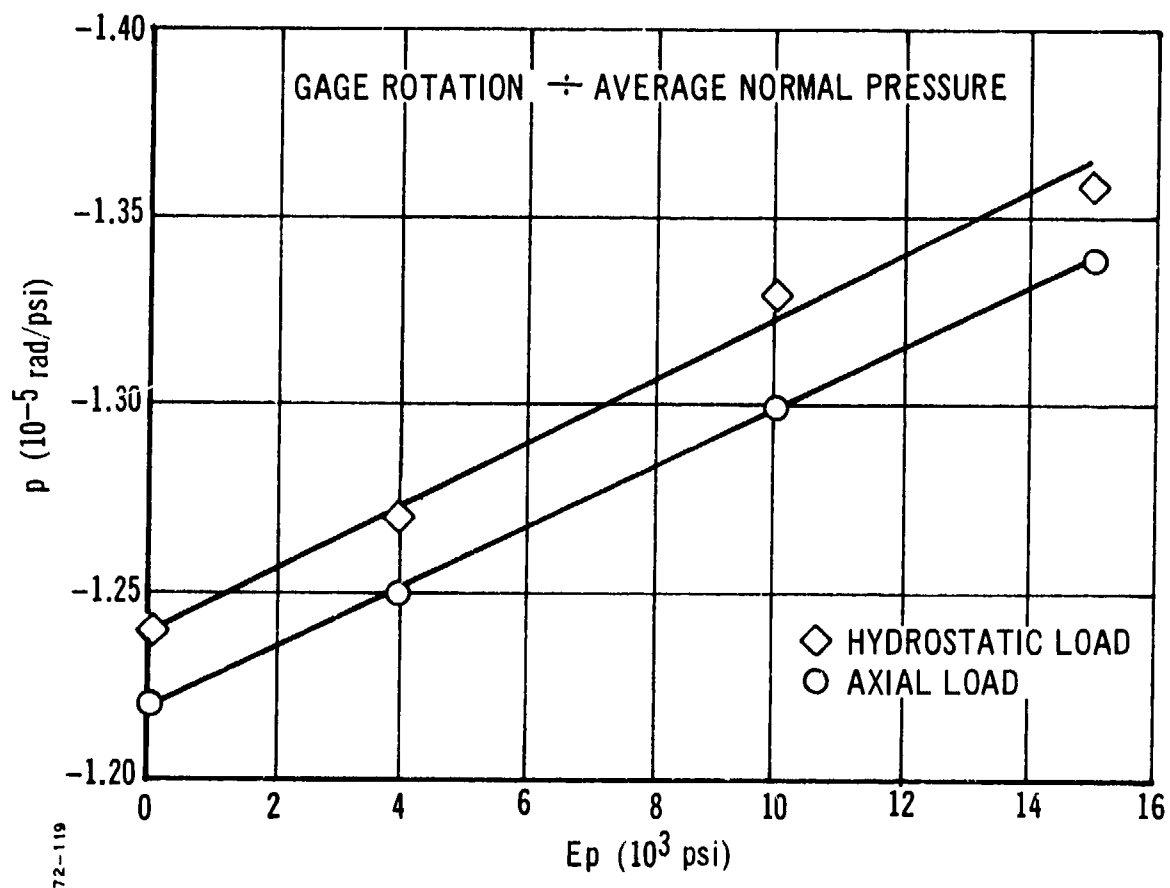
Figure 17. 150-psi Diaphragm Gage Rotation (r = 0.0255 inch)/
Average Normal Pressure versus Propellant Modulus

-39-

results indicate a greater sensitivity of the pressure distribution (with respect to modulus) than previously expected from analyses carried out over a more narrow range of moduli (100 to 1000 psi). Furthermore, the ratio of maximum (or average) pressure on the gage with respect to applied stress is very sensitive to changes in propellant modulus. Finally, the gage interference problem is much more important for the high E_p range. These curves are essential to the interpretation of gage output signals to make conversions to "stress at gage" in motor applications. These comments apply both to uniaxial and hydrostatic loading of the test fixture.

In Figure 16 the gage rotation (θ) at the radial distance 0.0255 inch, i.e., at the end of the strain gage on the diaphragm, which also corresponds to the gage output signal, is plotted over the spectrum of E_p values. Figure 17 shows the gage rotation at the same location normalized by inner element normal pressures from Figures 14 and 15, and plotted over the range of E_p values.

The data in Figures 16 and 17 reveal several interesting aspects of the gage performance. First, the data show conclusively that there is a difference in the sensitivity of the gage to a uniaxial stress and to a hydrostatic stress. This difference was noted in last year's analysis, but the more extensive data presented here reveal that the difference in sensitivity is constant over the whole range of E_p values and does not change, as was considered possible, with the propellant properties. The data predict the gage-in-propellant to be more sensitive to hydrostatic loads than to uniaxial loads by a factor of 1.111:1.

The second significant aspect of the analytical data is the linear form of the relationship between the gage sensitivity and the propellant modulus. Thus, Figure 16 shows that the gage sensitivity to the applied stress (σ_o) decreases linearly with increasing propellant modulus, and may therefore be represented by means of the equation

$$\theta/\sigma_p = A - B.E_p \tag{34}$$

for uniaxial loads, and

$$\theta/\sigma_p = K(A - B.E_p) \tag{35}$$

for hydrostatic loads. A, B, and K are constants with values of

$$A = 1.116$$
$$B = 1.44 \times 10^{-5}$$
$$K = 1.111$$

This format represents the way in which the experimentalist will observe gage behavior. Thus, gage sensitivity to applied stress in the test fixture will decrease as the modulus of the propellant increases.

Figure 17, however, shows another aspect of gage sensitivity as a function of propellant modulus. It will be noted that when gage output is expressed as a function of the average normal stress over the gage, the gage sensitivity increases with increasing propellant modulus. Again the relationship is linear and may be expressed by the equation

$$\theta / \sigma_p = a + b.E_p \tag{36}$$

where now b is a constant for both the hydrostatic and the axial loading cases, but a varies with the type of loading. The values of these factors are: a = 1.22 for axial loads and 1.24 for hydrostatic loads and b = 0.8 x 10^{-5}.

c. Viscoelastic Calibration, Quasi-Static Loading

The basic concepts involved in calibration of a diaphragm gage embedded in a linear viscoelastic solid are briefly discussed in Reference 2. The test fixture input is now a time-dependent stress or strain; the resulting normal stress distribution on the gage diaphragm is both time- and space-dependent. Parameters affecting the dependence are, $E(t)$, $v(t)$, for the propellant and E_g, v_g, for the gage. Just as in elastic calibration, once the normal stress distribution on the gage is known, the voltage output is merely a coefficient multiplied by the average normal stress on the gage.

When this distribution is time-dependent, the coefficient is also time-dependent. This is the core of the calibration problem. To put these ideas in quantitative terms, the solution of the viscoelastic quasi-static boundary value problem can be put in the form

$$\sigma_p (r, t) = \int_0^t k (r, t - \tau) \frac{d\sigma}{d\tau} . d\tau \tag{37}$$

where σ_p is the normal stress on the gage, $\sigma(\tau)$ is the test fixture applied stress history, and k is an influence function for the problem. In actuality, k depends on the factors described above, i.e.

$$k = f\left[r, E_g, E(t), v(t), v_g\right] \tag{38}$$

In the sequel we assume $v(t) = \frac{1}{2}$, fix the values of v_g, E_g, and express Equation (38) as:

$$k = f\left[r, E(t)\right] = k\left[r.t\right] \tag{39}$$

We can also define an average normal stress over the gage,

$$\bar{\sigma}_p (t) = \frac{1}{\pi a^2} \int_0^a \sigma_p (r, t) . 2 \pi r . dr$$

$$= \frac{2}{a^2} \int_0^a \left[\int_0^t k (r, t - \tau) \frac{d\sigma}{d\tau} d\tau \right] r.dr$$

$$= \int_0^t K (t - \tau) \frac{d\sigma}{d\tau} . d\tau \qquad (40)$$

where we have defined a gage transfer (calibration) function

$$K (t - \tau) = 2/a^2 \int_0^a k (r, t - \tau) r.dr \qquad (41)$$

The purpose of the following numerical analysis is to evaluate this transfer function K (t) for uniaxial and hydrostatic loading cases. First, it is convenient to note that when $\sigma = \sigma_0 H (t)$, corresponding to a step pressure input,

$$\frac{\bar{\sigma}_p (t)}{\sigma_0} = K (t) \qquad (42)$$

This ratio is shown for both axial and hydrostatic loading in Figure 17; details are discussed at the end of this section.

It is also possible to define a gage transfer function based on prescribed strain history in the test fixture. Analogous to Equation (40) we have:

$$\bar{\sigma}_p (t) = \int_0^t M (t - \tau) \frac{d\epsilon}{d\tau} . d\tau \qquad (43)$$

where

$$M (t - \tau) = 2/a^2 \int_0^a m (r, t - \tau) r.dr. \qquad (44)$$

If a step function strain input $\epsilon (t) = \epsilon_0 H (t)$ is substituted in the above,

$$\bar{\sigma}_p (t) = M (t) \epsilon_0 \qquad (45)$$

Equations (42) and (45) defining gage calibration functions K (t), M (t) can be related by taking the Laplace transforms of Equations (42) and (45) and equating:

$$K^* \sigma^* = M^* \epsilon^* \qquad (46)$$

But, σ^*, ϵ^* are related by the viscoelastic constitutive equation

$$\sigma^* = p\,E^*\epsilon^* = \frac{\epsilon^*}{p\,J^*} \tag{47}$$

where $J(t)$ is the uniaxial creep compliance corresponding to relaxation modulus $E(t)$. Substitution of Equation (47) into (46) gives the alternative forms

$$M(t) = \int_0^t K(t-\tau)\frac{dE}{d\tau}\cdot d\tau$$

$$K(t) = \int_0^t M(t-\tau)\frac{dJ}{d\tau}\cdot d\tau \tag{48}$$

This determines the relation between calibration functions corresponding to arbitrary input histories in the calibration experiments. When step function inputs are used in both creep and relaxation experiments, Equations (42) and (45) can be related by substituting $\sigma_o = \epsilon_o\,E(t)$ into (45) and comparing:

For Stress Input   For Strain Input

$$\frac{\sigma_p(t)}{\sigma_o} = K(t) \qquad\qquad \frac{\sigma_p(t)}{\sigma_o} = \frac{M(t)}{E(t)} \tag{49}$$

In order to determine the calibration functions $K(t)$, $M(t)$, defined above, quasi-static viscoelastic numerical analyses of the calibration fixture were conducted using the THVINC computer code discussed earlier in this report. Because of size limitations of THVINC, the finite element discretization used in the static analyses (Figure 13) could not be successfully handled. Instead, the coarser model shown in Figure 18 was used.

THVINC does not contain a shell element; thus, a simulation with elastic continuum elements had to be employed to model the diaphragm. As shown in Figure 18, three continuum elements, with the indicated boundary conditions, were used for this purpose. A Poisson's ratio of 0.3 was selected and the shear modulus was calculated by matching z-deflections of the circled node in Figure 18 with that of the 150-psi diaphragm gage, when both were subjected to uniform transverse pressure. The shoulder area was assumed rigid in this simulation. Thermal properties of the three "gage" elements were assumed identical to those of the propellant, following indications from previous work discussed in Reference 1.

The following material properties were used for the propellant:

Density ($lb/in.^3$)   0.064

Thermal conductivity ($Btu/min\text{-}in.\text{-}^\circ F$) 2.7×10^{-4}
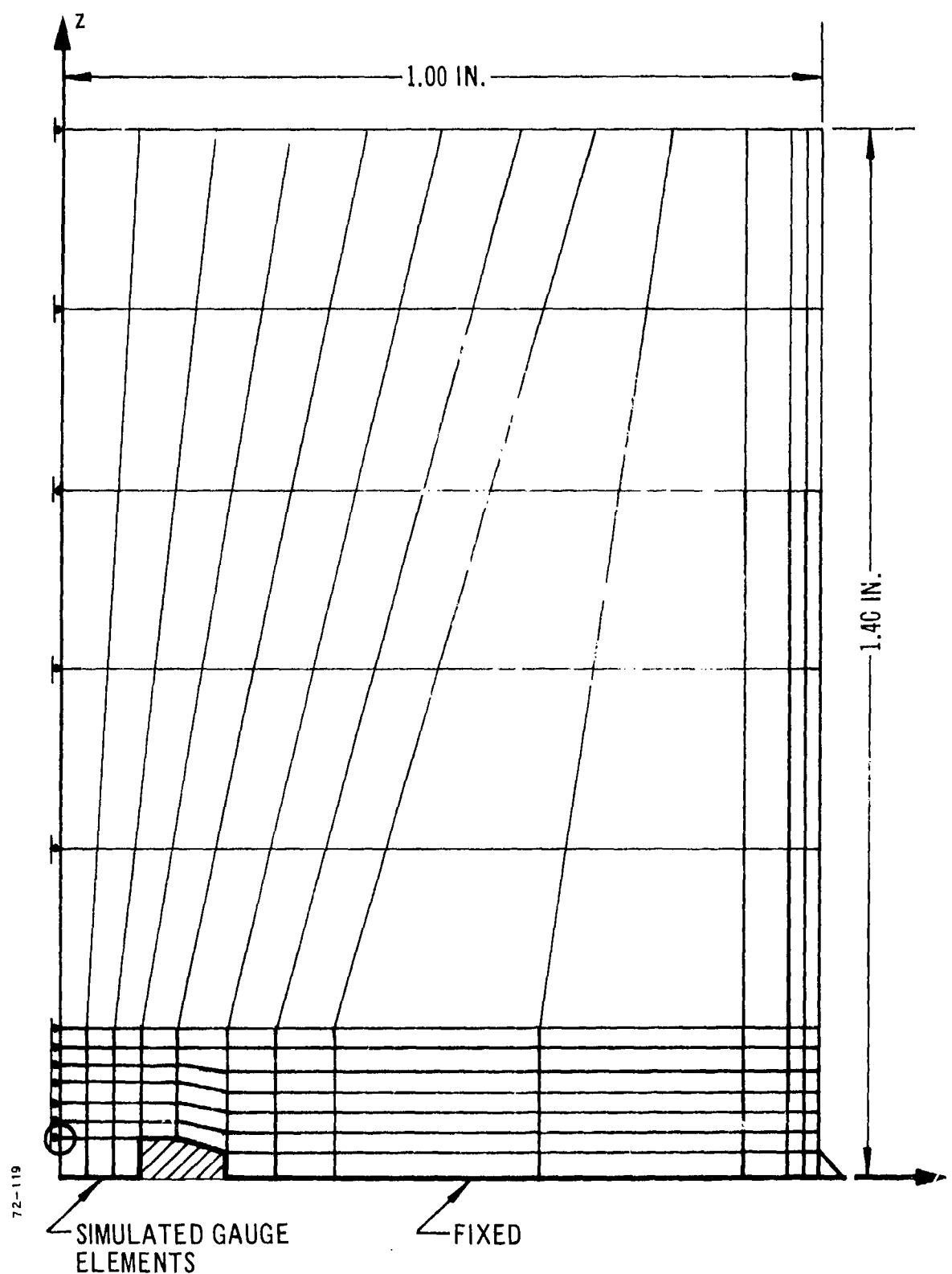
Figure 18. Finite Element Idealization of Uniaxial Calibration Fixture for Viscoelastic Analysis.

Specific heat (Btu/lb-^{0}F)   0.249

Coefficient of thermal expansion (in./in.-^{0}F) 5.67×10^{-5}

Poisson's ratio   0.5

The shear moduli G_o, G_i and the relaxation time β_i defined through the relation

$$G(\xi) = G_o + \sum_{i=1}^{15} G_i \exp(-\xi/\beta_i,$$

(where G is the viscoelastic shear modulus) are given in Table I.

Four analyses were performed. The first three were strictly mechanical, in which the specimen was subjected to uniform uniaxial stress, uniform uniaxial displacement, and hydrostatic stress. Normal stresses above the gage for the uniaxial load condition were virtually identical to those obtained from the uniaxial displacement analysis after normalizing by the average z-stress at z = 1.4 inches. Results, with the three elements over the gage averaged, are presented in Figure 19. It will be noted that the curves K(t) for uniaxial and hydrostatic leading are virtually identical except for a vertical shift which corresponds to the difference between the ratios of applied stress and stress at the gage diaphragm in the two loading cases. (This was noted previously for elastic calibration.)

Calibration analyses were repeated for a prescribed displacement input, corresponding to Equations (45) and (49). The numerical results indicated that for those test conditions,

$$K(t) \approx \frac{M(t)}{E(t)} \tag{50}$$

i. e. , a simple relation approximating the solution of the integral equations (48) is obtained.

Finally, it should be noted that the calibration curves can be used for a range of temperatures by using the thermorheologically simple shift postulate.

The analytical result given in Equation (50) is particularly important when considering the inversion of the gage calibration data in order to determine the stress value from the gage output signal. This problem is dealt with in the next section of this report.

d.   Interpretation of Gage Output Data

The basic integral equation for interpreting gage output data as stress or strain was discussed in last year's final report. Reference 2

TABLE I

SHEAR RELAXATION AND SHIFT
FACTOR DATA FOR STV PROPELLANT

$$G_o = 66.67 \text{ psi}$$

i	G_i (psi)	β_i (min)
1	663.10	10^{-12}
2	637.20	10^{-11}
3	579.90	10^{-10}
4	524.60	10^{-9}
5	471.30	10^{-8}
6	420.00	10^{-7}
7	370.70	10^{-6}
8	323.40	10^{-5}
9	278.10	10^{-4}
10	234.70	10^{-3}
11	193.40	10^{-2}
12	154.00	10^{-1}
13	116.62	1
14	81.23	10
15	47.83	10^{2}

The following log shift factor data versus temperature were used:

Temperature (^{0}F)	Log $\emptyset$ Shift Factor
-80	-8.6
-60	-7.3
-40	-5.8
-20	-4.0
0	-3.0
20	-2.0
40	-1.0
70	0
100	1.0
130	2.0
160	3.0
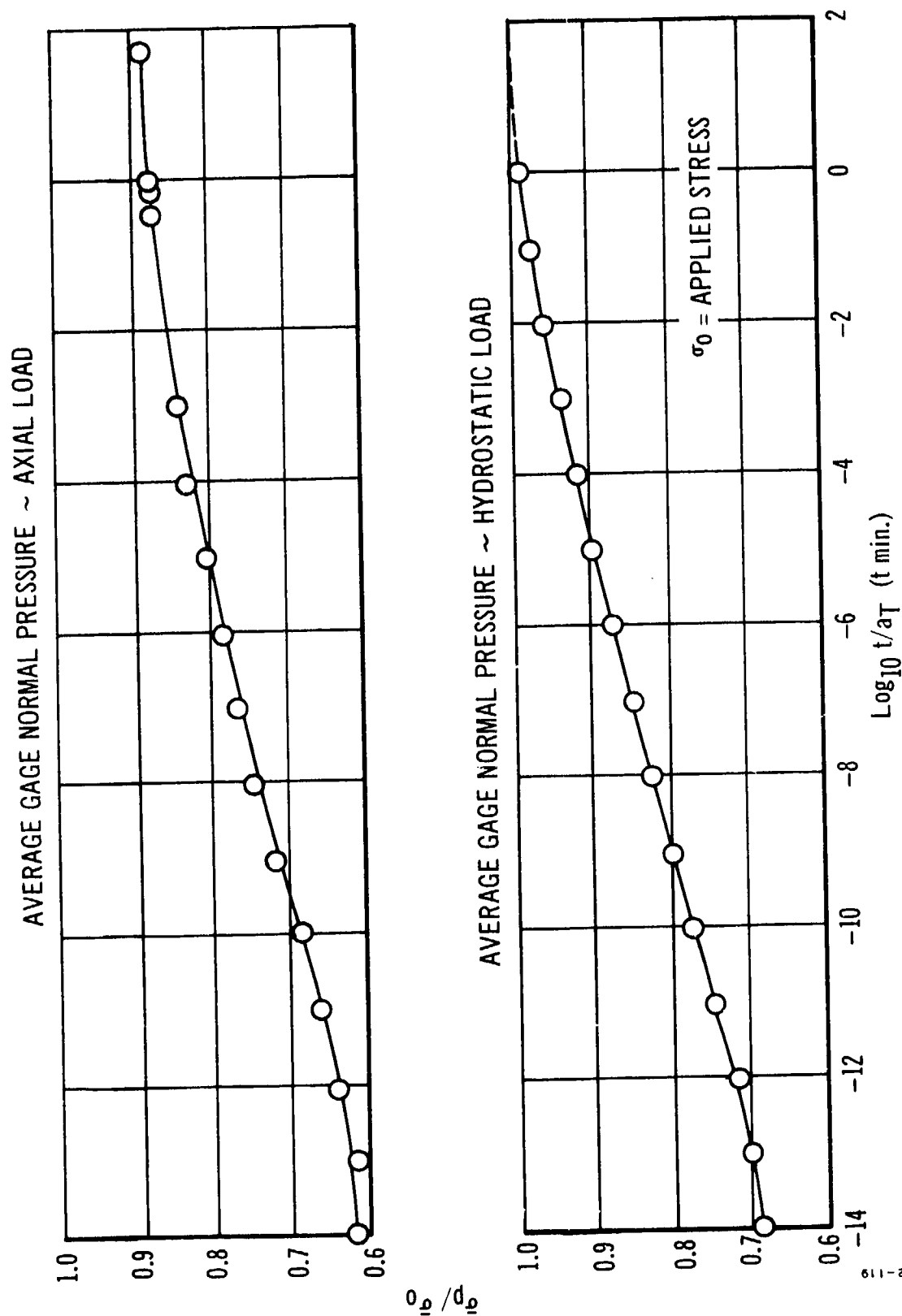
Figure 19. Simulated 150-psi Diaphragm Gage in Uniaxial Calibration Fixture, Gage Transfer Functions versus Log Reduced Time.

A gage transfer function relating the gage output $S(t)$ for a step stress input σ_o was defined as:

$$\psi(t) = \frac{S(t)}{\sigma_o} \qquad (mv/psi) \qquad (51)$$

To interpret the gage output data, the inversion of the Laplace transforms of Equation (51) is required. However, the analytical results presented above show that there will be very little error in simply inverting the expression for $\psi(t)$ to obtain the required transfer function $\phi(t)$, where this is defined by the equation

$$\phi(t) = \frac{\sigma(t)}{S_o} \qquad (52)$$

which may therefore be approximated by the reciprocal of $\psi(t)$, i.e.,

$$\phi(t) \approx 1/\psi(t) \approx \frac{\sigma_o}{S(t)} \qquad (53)$$

The applied stress producing the gage signal may then be determined from the output signal by means of the equation

$$\sigma(t) = \int_0^t \phi(t-\tau) \frac{dS(\tau)}{d\tau} . d\tau \qquad (54)$$

It remains to show the relationship between the gage transfer functions $\phi(t)$ and $\psi(t)$ and the analytical transfer functions derived earlier in this section.

Clearly, the gage output signal S is a direct function of the diaphragm rotation θ and this may be written as

$$S = q.\theta \qquad (55)$$

where q is a constant involving such factors as the gage resistance, bridge voltage, and strain gage factor, as well as some geometric terms.

Equations (34) and (35) present the relationship between the diaphragm rotation and the propellant modulus for a gage embedded within an elastic material:

$$\theta/\sigma_o = A - B.E_p$$

or

$$\theta/\sigma_o = K(A - B.E_p)$$

for axial loading and hydrostatic loading, respectively.

These equations may be extended to the problem of a gage in a viscoelastic material as follows:

$$\theta\,(t)/\sigma_o \;=\; K\left[A - B.\Gamma_p\,(t)\right] \tag{56}$$

where K may be taken as unity for the axial load case.

Substituting from Equation (55) for $\theta\,(t)$ in terms of S (t), we obtain

$$S\,(t)/\sigma_o \;=\; q.K\left[A - B.E_p\,(t)\right] \tag{57}$$

and clearly, by definition

$$S\,(t)/\sigma_o \;=\; \psi(t)$$

therefore

$$\psi\,(t) \;=\; q.K\left[A - B.E_p\,(t)\right]$$

and the approximate equation for $\emptyset\,(t)$ is as follows:

$$\emptyset\,(t) \;=\; \frac{1}{q.K\,\left[A - B.E_p\,(t)\right]} \tag{58}$$

4. EXPERIMENTAL CREEP AND PRESSURE DATA AND COMPARISON WITH ANALYSIS

a. Experimental Creep Data

A series of constant load creep tests was performed on the inert propellant uniaxial test specimen containing the three 150-psi diaphragm gages for normal stress measurement. The alternating tension-compression test apparatus described earlier and shown in Figure 9 was used and results typified by those given in Figure 11 were obtained.

The tensile gage sensitivity data for Gage No. 10 are presented in Figure 20 against reduced time, $\log\,(t/a_T)$. Note that the compression data are very similar but are not shown for clarity.

Examination of the curves of Figure 20 reveals the following facts:

- The 150-psi normal stress gage shows variation in response with time for temperatures between 140 and -32^0F.

- The various response curves obtained at the different temperatures do not shift horizontally, i. e., along the log time axis, to produce a smooth single curve.

-49-
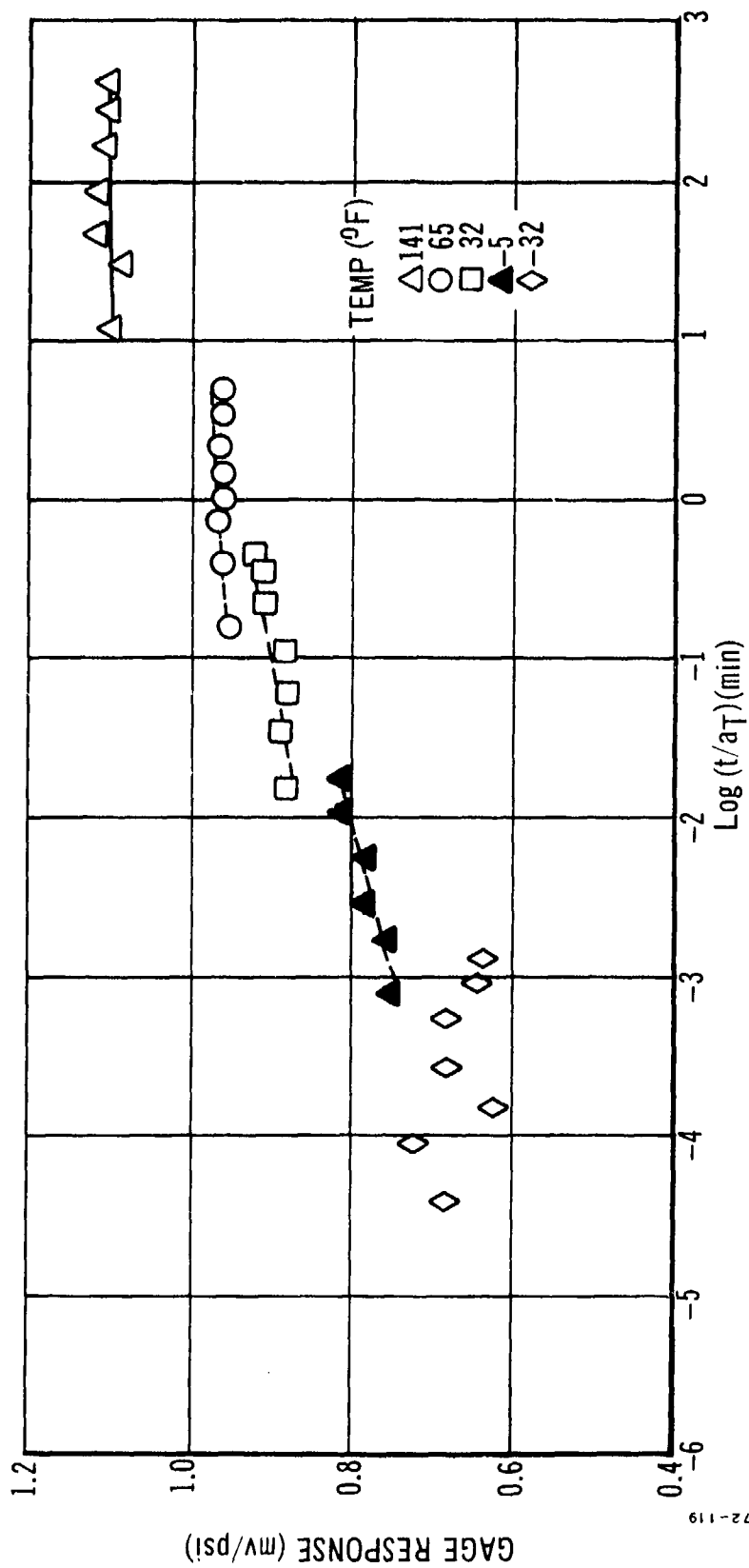
Figure 20. Response of Diaphragm Gage No. 10 to Normal Tensile Stress as a Function of Reduced Time.

- A vertical shift is required to align all the curves
  for each gage into a single response curve.

The suggestion that a vertical shift factor was required to
obtain a smooth reduced variable curve is not new. During the examination
of data from the 25-psi gage embedded in STV propellant (discussed in
Report 966-P-5, Reference 3), it was shown that, in addition to the normal
log a_T shift factor, a vertical shift factor was required to produce a smooth
data curve.

Thus, the need for a vertical shift factor had been apparent
without any clear indication as to why it was necessary. The 25-psi gage
showed distinct changes in response with temperature, necessitating the use
of a log a horizontal shift, and it appeared that a simple alternative to the
use of an additional vertical shift was to use slightly different log a_T values
so as to produce a smooth, continuous response curve. This was in fact
done to the response data for the 25-psi gage presented in last year's final
report (966-F). However, the data from the 150-psi gages, which are
almost completely time-independent, cannot be made into a smooth continu-
ous curve by the use of different log a_T values; a vertical shift log b_T must
be employed.

Once the fact is established that the magnitude of the gage
response varies with temperature, the causes of this variation are not
difficult to find. Two major contributors for semiconductor-type resistance
strain gage systems are:

- The variation in gage resistance with temperature

- The variation in "gage factor" (i.e., the change in
  gage resistance for a given change in applied strain)
  with temperature

Both of these effects are significant and, although they can be
minimized by careful circuit design, they cannot be eliminated completely.
Furthermore, the variation in gage sensitivity with temperature will be
different for each gage, and therefore there need be no similarity in the
vertical shift factor curves for similar types of gage.

An important aspect of the causes of change in gage response
discussed above is that they are dependent simply upon temperature alone.
From an analytical viewpoint this is important because the equation

$$\text{Gage response } \psi(t) = \text{function } (t/a_T) \tag{58}$$

for a gage with no vertical shift required, becomes simply

$$\text{Gage response } \psi'(t) \cdot b_T = \text{function } (t/a_T)$$

or

$$\text{Gage response } \psi'(t) = \left| \text{function } (t/a_T) \right| (1/b_T) \tag{59}$$

-51-

Equation (57), which determines the function for ψ (t), must be modified to include this vertical shift term as follows:

$$(S\,(t)/\sigma_o)' \;=\; \psi'(t) \;=\; q.K\left[A - B.E_p\,(t)\right]\,(1/b_T \tag{60}$$

and therefore, Equation (58) for ϕ (t) must also be changed to:

$$\phi\,(t) \;=\; \frac{b_T}{q.K\left[A - B.E_p\,(t)\right]} \tag{61}$$

To determine the stress from the gage output signals, the term ϕ (t) in Equation (54) must be replaced by the modified term from the inverse of Equation (59), i.e.,

$$\sigma\,(t) \;=\; \int_o^t b_T\,.\;\phi\,(t-\tau)\,\frac{dS\,(\tau)}{d\tau}\,.\;d\tau \tag{62}$$

where $b_T\left[T\,(\tau)\right]$ must be used in the above equation.

Returning to the experimental data, Figure 21 shows the response data of Figure 20 for the 150-psi gage No. 10, reduced by the vertical shift factor b_T and plotted against reduced time. The vertical shift factors are presented in Figure 22, which also shows the shift factors required by the other two gages, No. 5 and No. 20. Figure 23 shows the reduced sensivitity data for the three gages for both tension and compression loading modes; the similarity in gage sensitivity for these two modes is obvious, despite the scatter at -32°F.

b.   Comparison with Analysis

Once the changes in gage sensitivity due simply to inherent thermal effects have been eliminated by means of the vertical shift term, the reduced plot may then be compared with the analytical predictions from Equation (60). To eliminate some of the unknowns from this equation, we may nondimensionalize by dividing by the gage response in a fluid (E_p = 0) at the reference temperature (so that b_T = 1). Calling the relative gage response ratio R_g, we find that

$$R_g \;=\; \left[A - B.E_p\,(t)\right]/A \tag{63}$$

The predicted gage response from Equation (63) is plotted against log reduced time in Figure 24 and against extensional modulus in Figure 25. The modulus-versus-reduced time data from Figure 26 and the log a_T shift factors versus temperature of Figure 27 were used to obtain these data plots. The experimental data are also plotted in Figures 24 and 25, and it will be noted that the measured response of the gage is not as good as the predicted response. This was noted before in comparing the response of the 25-psi diaphragm gage with the experimental data (see Figure 136 of Reference 1). The plots in Figure 25 show exactly the same type of
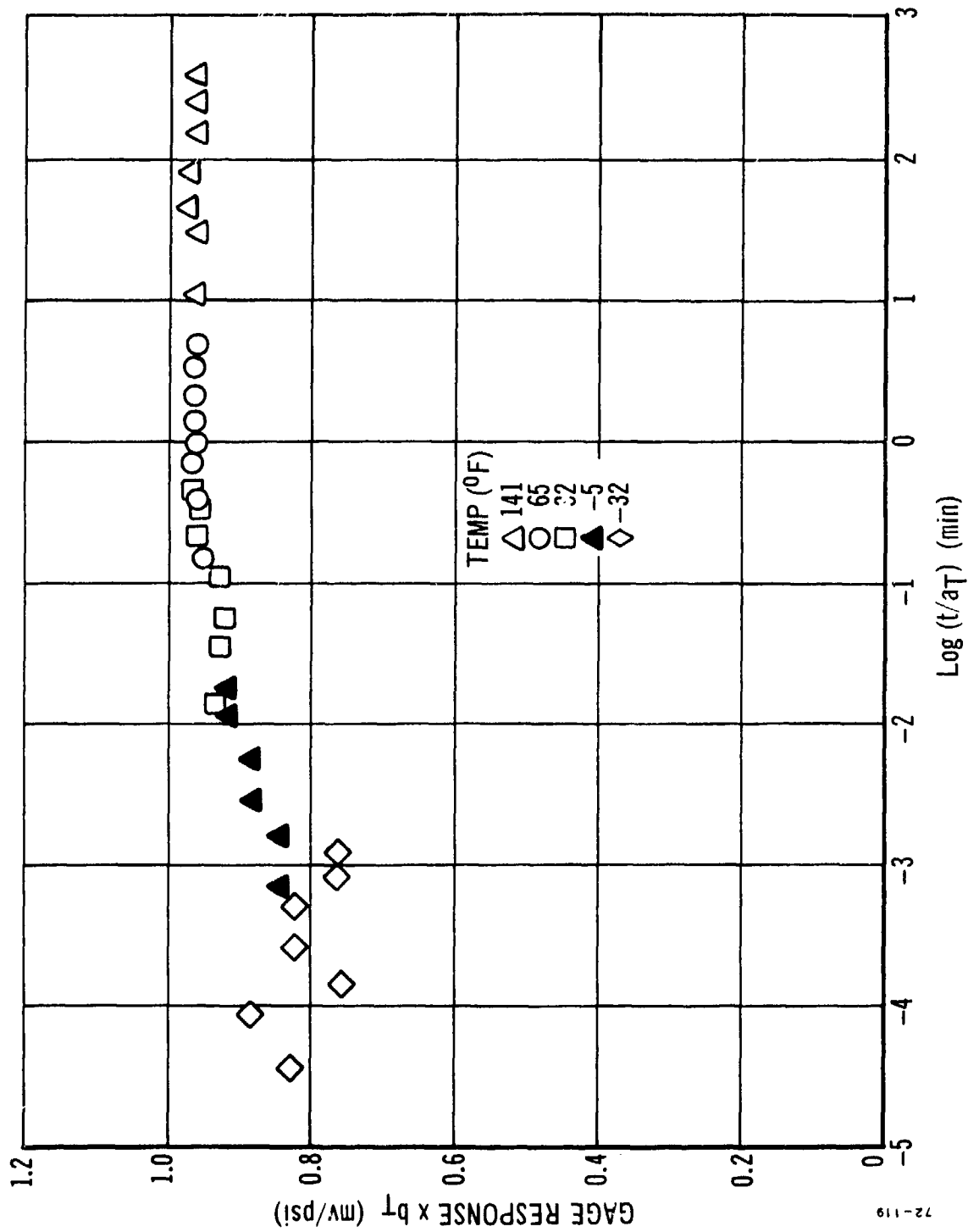
Figure 21. Response of 150-psi Diaphragm Gage No. 10 to Normal Tensile Stress Times Vertical Shift Factor b_T as a Function of Reduced Time.

72-119
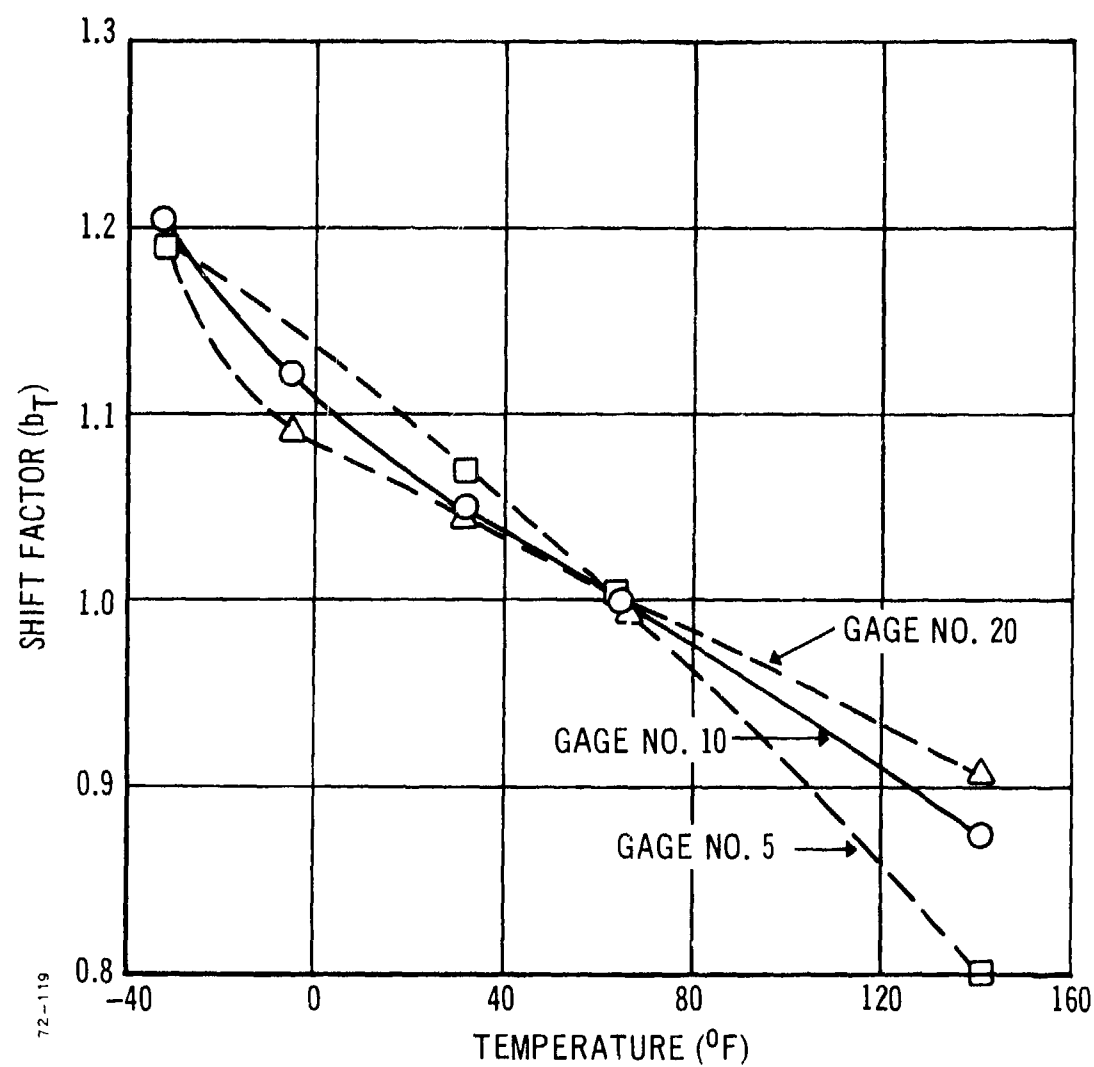
Figure 22. Vertical Shift Factors versus Temperature.
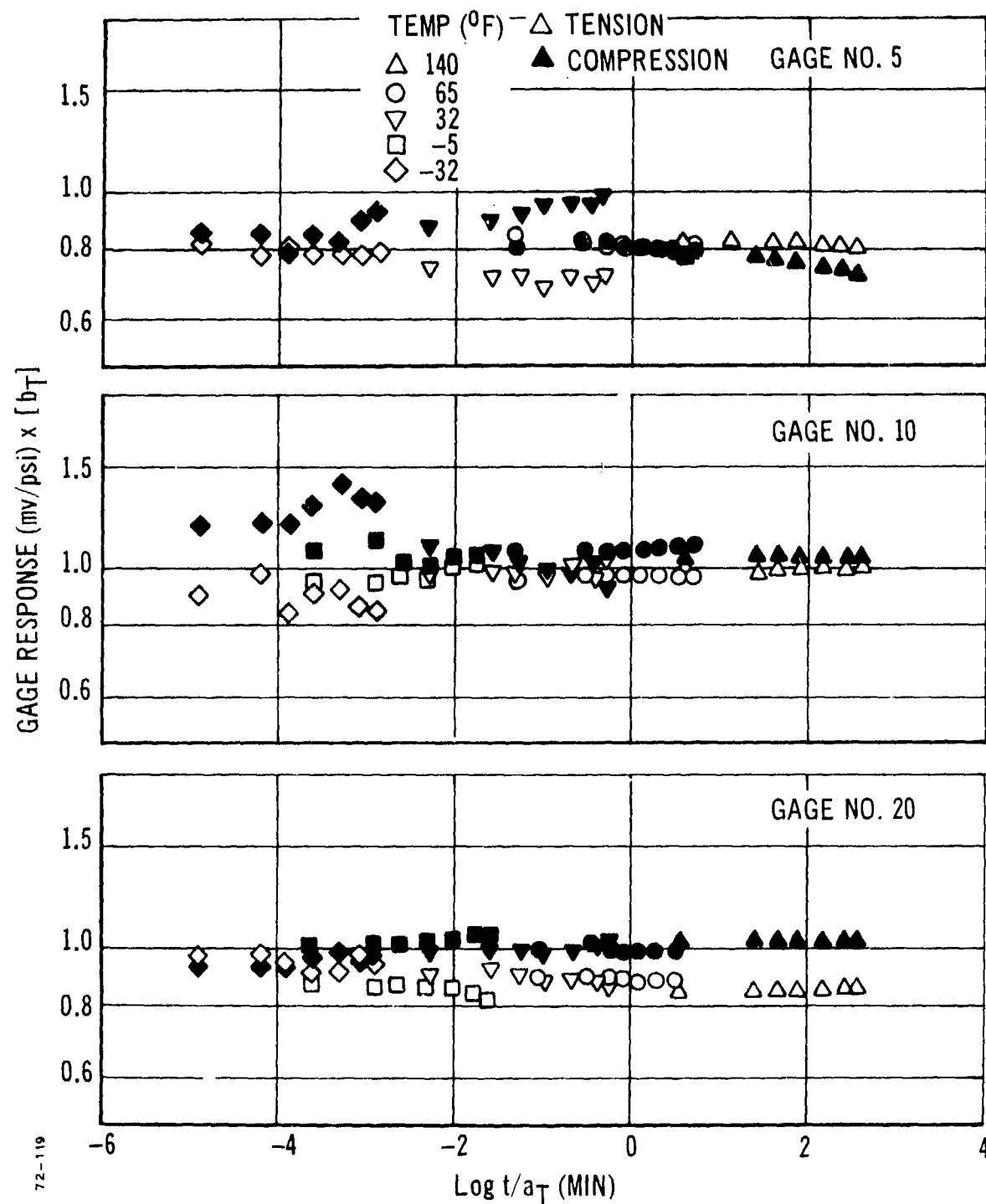
Figure 23. Shifted Gage Response versus Reduced Time, 150-psi Gages, Uniaxial Test Fixture No. 2, Tension and Compression.

-55-
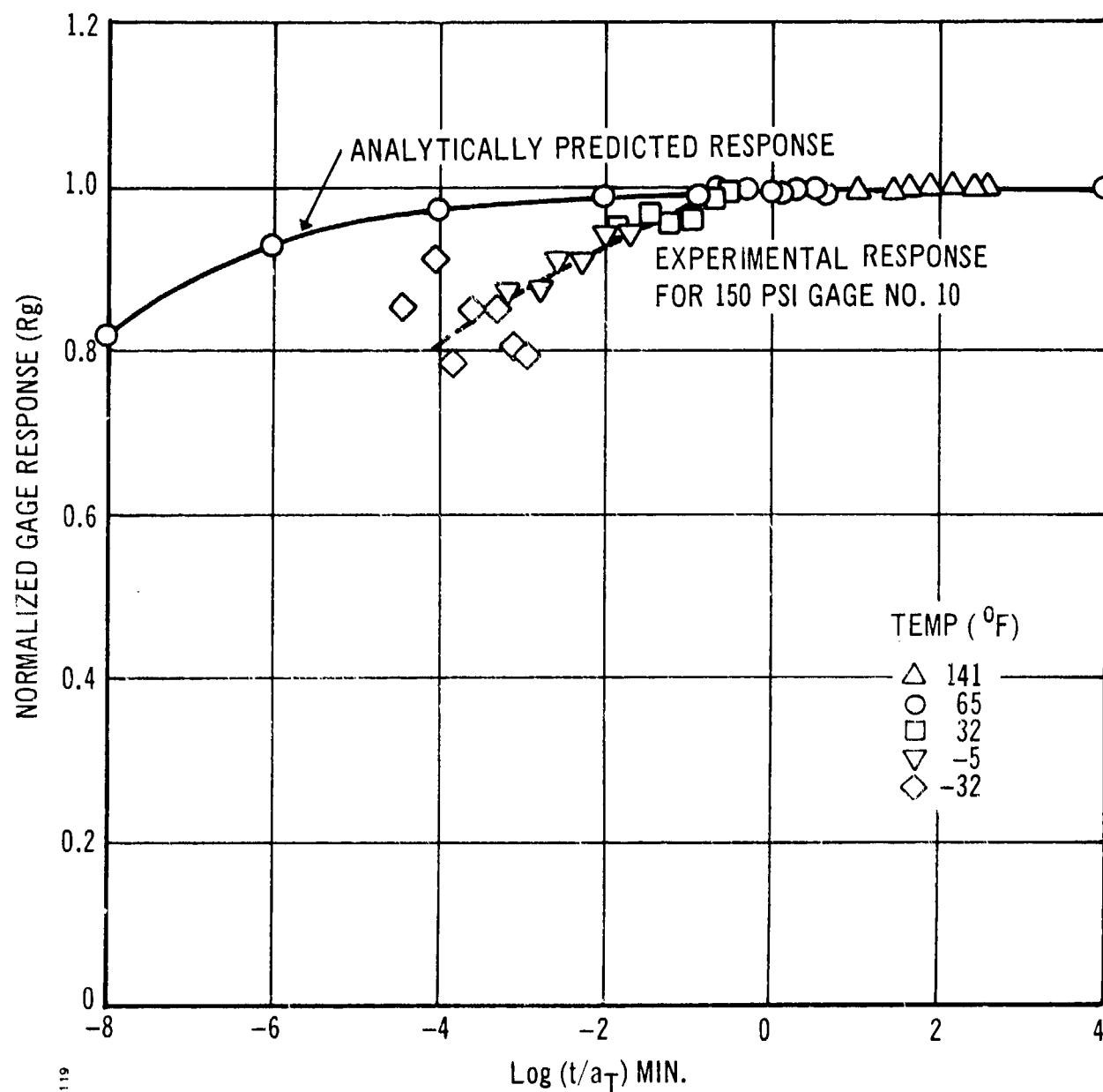
Figure 24. Normalized Diaphragm Gage Response versus Reduced Time, Experimental and Analytical.
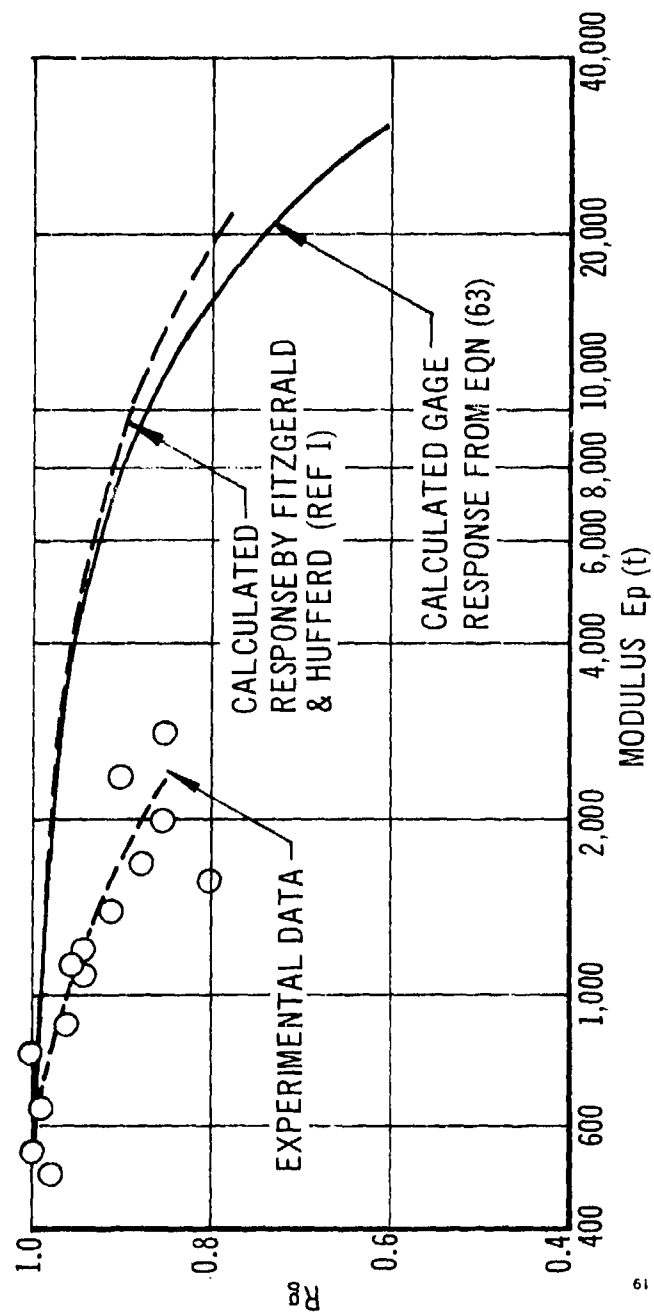
Figure 25. Normalized Diaphragm Gage Response versus Propellant Modulus, Experimental and Analytical.
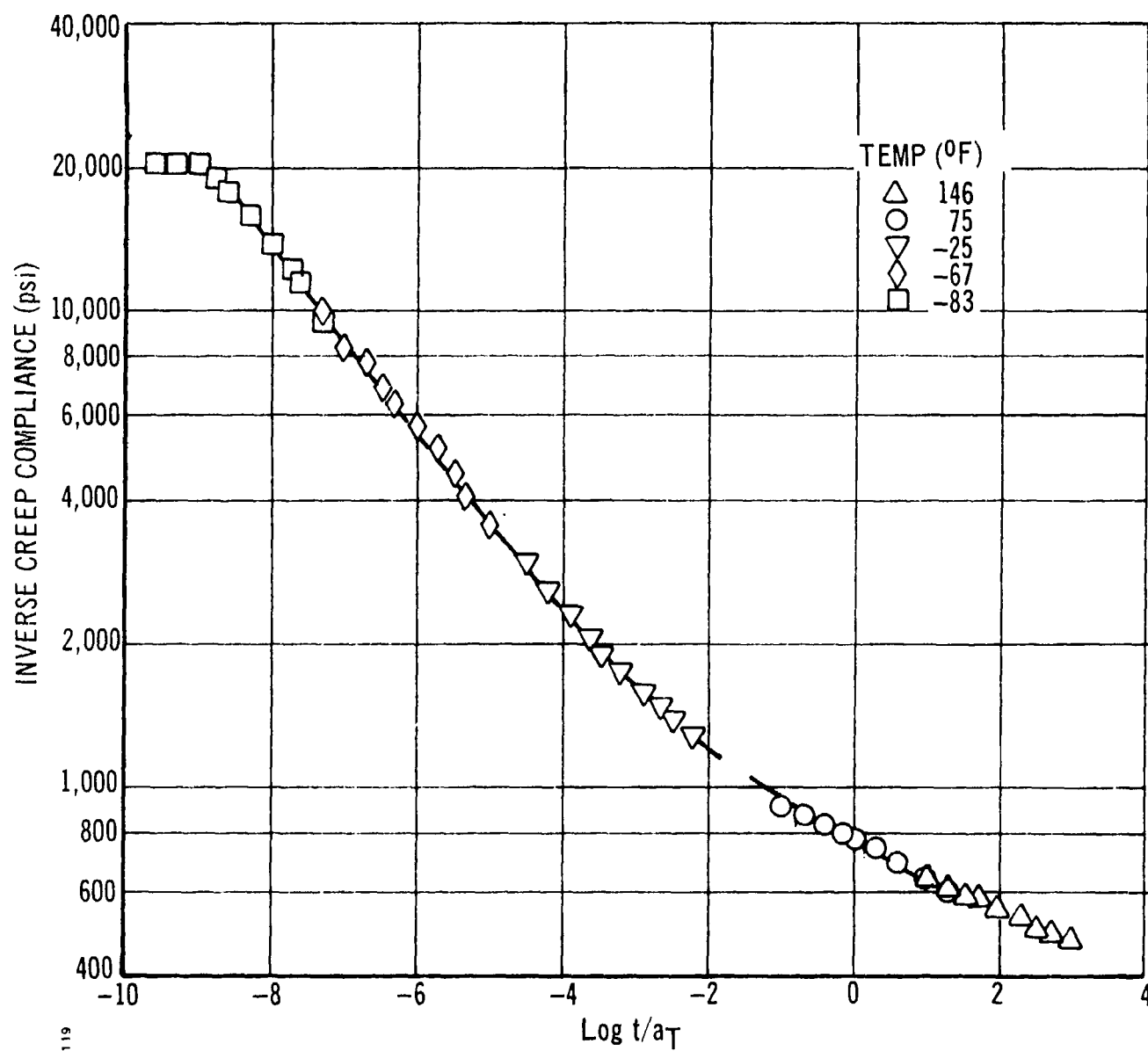
Figure 26. Inert Propellant Uniaxial Test Fixture, Inverse Creep
Compliance versus Reduced Time.
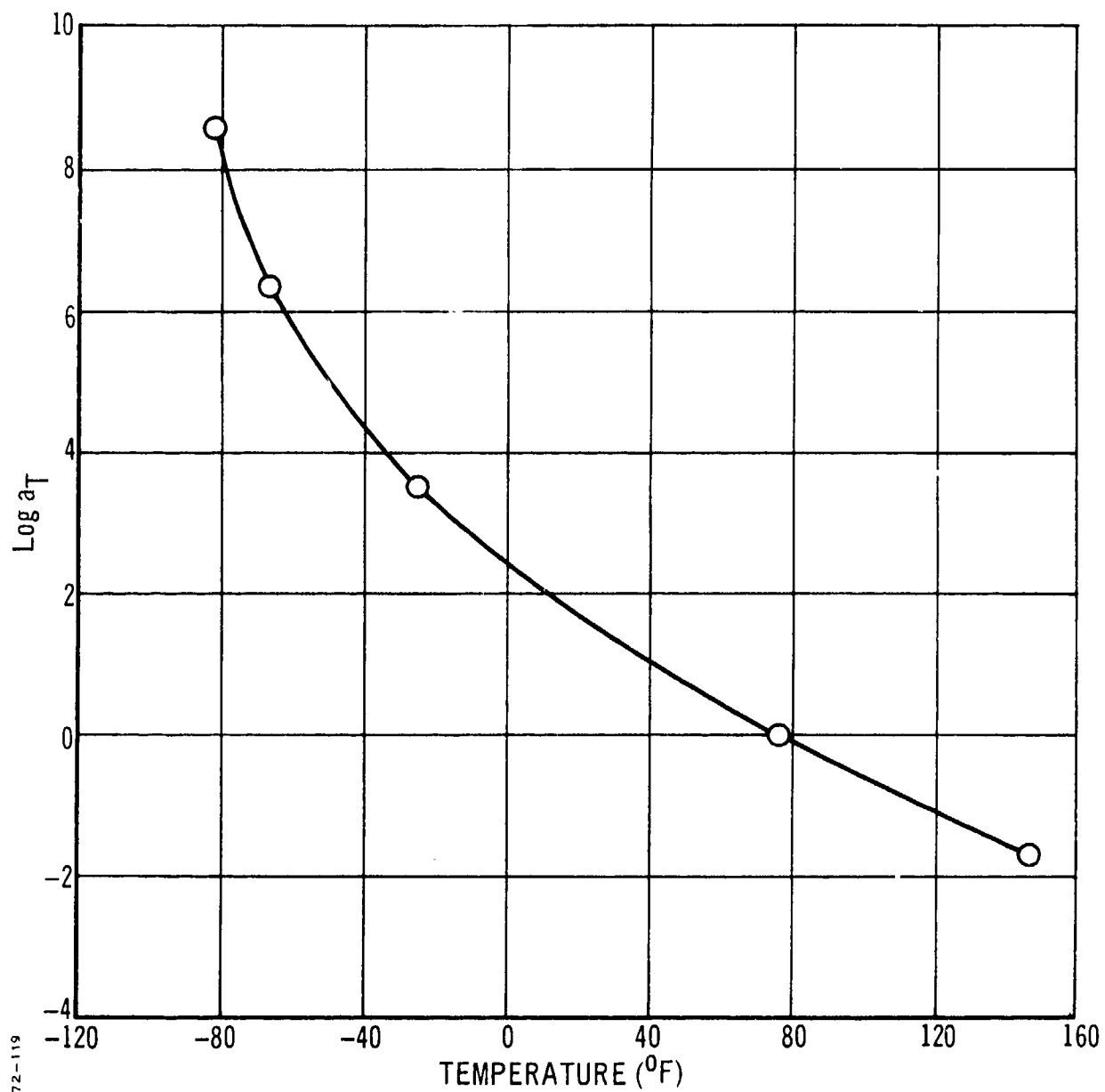
Figure 27. Inert Propellant Uniaxial Test Fixture, Shift Factors versus
       Temperature.

comparison between the experimental data and the analytical data as those of Figure 136, Reference 1. It seems that the gage experiences a much larger modulus than is measured in the stress relaxation or creep compliance tests used to obtain the experimental modulus data.

Figure 25 also shows the predicted gage response from the Fitzgerald-Hufferd analysis detailed in the first-year STV Final report, Reference 1. The close agreement between the two analytical response curves derived from greatly different approaches gives increased confidence in the data. The only factor that can produce such poor agreement between experiment and theory is the value of the "effective modulus" that the gage experiences. As in the case of the thermal cooling tests, the modulus values obtained from normal experimental test procedures do not permit good correlation between theory and experiment.

c. Data Scatter in Gage Calibration Tests

Examination of the experimental data obtained from a series of gage calibration tests based on the latest experimental techniques and conducted with great care revealed what seemed to be an unacceptable amount of data scatter. (The -32^0F data in Figure 20 are typical of much of the experimental data obtained.) As a consequence, the causes of this data scatter were sought and the principal problem areas are believed to be those listed below:

- The use of small loads or small displacements in the tests to prevent damage to the propellant, resulting in small output signals

- Small variations in the digital measuring device employed, resulting from drift, and other causes

- The use of conditioning boxes employing liquid CO_2 as a cooling medium

The third of these problems is an obvious nuisance that is particularly troublesome at the lower temperatures. The use of a refrigerated cooling chamber with no CO_2 blasts is the only way to avoid the trouble.

The first two problem areas become serious in combination, as discussed in the following paragraphs.

Let the creep test be performed using a stress level of 3.0 psi with the gage response equal to 1.0 mv/psi. Thus, if the gage reading is initially zero mv, then application of the stress will produce a gage reading of 3.00 mv. Now, if the variation in measuring the gage output amounts to merely ±0.10 mv, which is a relatively small reading error for most instruments, then the gage sensitivity will be measured as either $2.90/3.00 = 0.967$ mv/psi or as $3.10/3.00 = 1.033$ mv/psi. Although this is a small variation in measurement, it causes a considerable error in the resulting gage sensitivity values, from 0.967 to 1.033 mv/psi. Thus, a variation of only ±0.1 mv will be quite sufficient to produce a serious scatter in the gage sensitivity data and perhaps prevent a smooth reduced data plot from being produced.

The same error in measuring the sensitivity of the shear cubes, which produce an output of approximately 30 mv/psi, will not be noticeable in the resulting data.

To keep the data scatter from measuring devices within close limits, say ±1.0 percent for propellant gage applications. the change in gage output signal must not be less than 10.0 mv, equivalent to a stress of approximately 10 psi.

Another problem with measuring devices is long-term drift. Many digital devices need periodic adjustments to their zero control to maintain a proper zero reading. If the instrument drifts during a creep or relaxation test, the effect will be to produce either too great a change in output with time (too great a slope to the output-time record) or too small a change in signal. In either case the resulting data will not fit the pattern established by the other (accurate) data and the test will have to be repeated.

If these reasonable precautions are observed in the calibration of the diaphragm normal stress gages and in the measurement of the gage output data in later use, there should be little problem in measuring the stress magnitudes to within ±10 percent, for stress values greater than 2.0 psi; at the lower stress levels, the probable error will be approximately ±0.5 psi.

d. Experimental Pressure, Vacuum, and Complex Load Tests

(1) Pressure Tests

Uniaxial test fixture No. 1, containing one 150-psi gage in inert propellant, was used for a series of pressure, vacuum, and pressure-plus-tension tests. The test fixture used for these tests was described earlier and sketched in Figure 12.

In an initial experiment to determine the gage response to pressure at 75°F, a series of pressure steps was applied to the test fixture starting at zero pressure and increasing to 20 psig. The resulting gage output data are shown in Figure 28. There was virtually no drift in the gage readings with time because viscoelastic effects are minimal at this temperature. The pressure calibration curve was linear, with a sensitivity (slope) of 1.15 mv/psi.

The sensitivity of the gage to a normal tensile stress was measured for comparison and found to be 1.028 mv/psi. The ratio of the hydrostatic load sensitivity to the axial load sensitivity is therefore 1.15:1.028 = 1.142. This compares very favorably with the value of 1.111 predicted theoretically.

(2) Pressure and Vacuum Tests

The question of the validity of using in situ pressure step tests to calibrate the embedded gage for a tensile stress has often been raised. This problem hinges on the relative sensitivity of the embedded gage to tensile, compressive, and hydrostatic stresses.

-61-
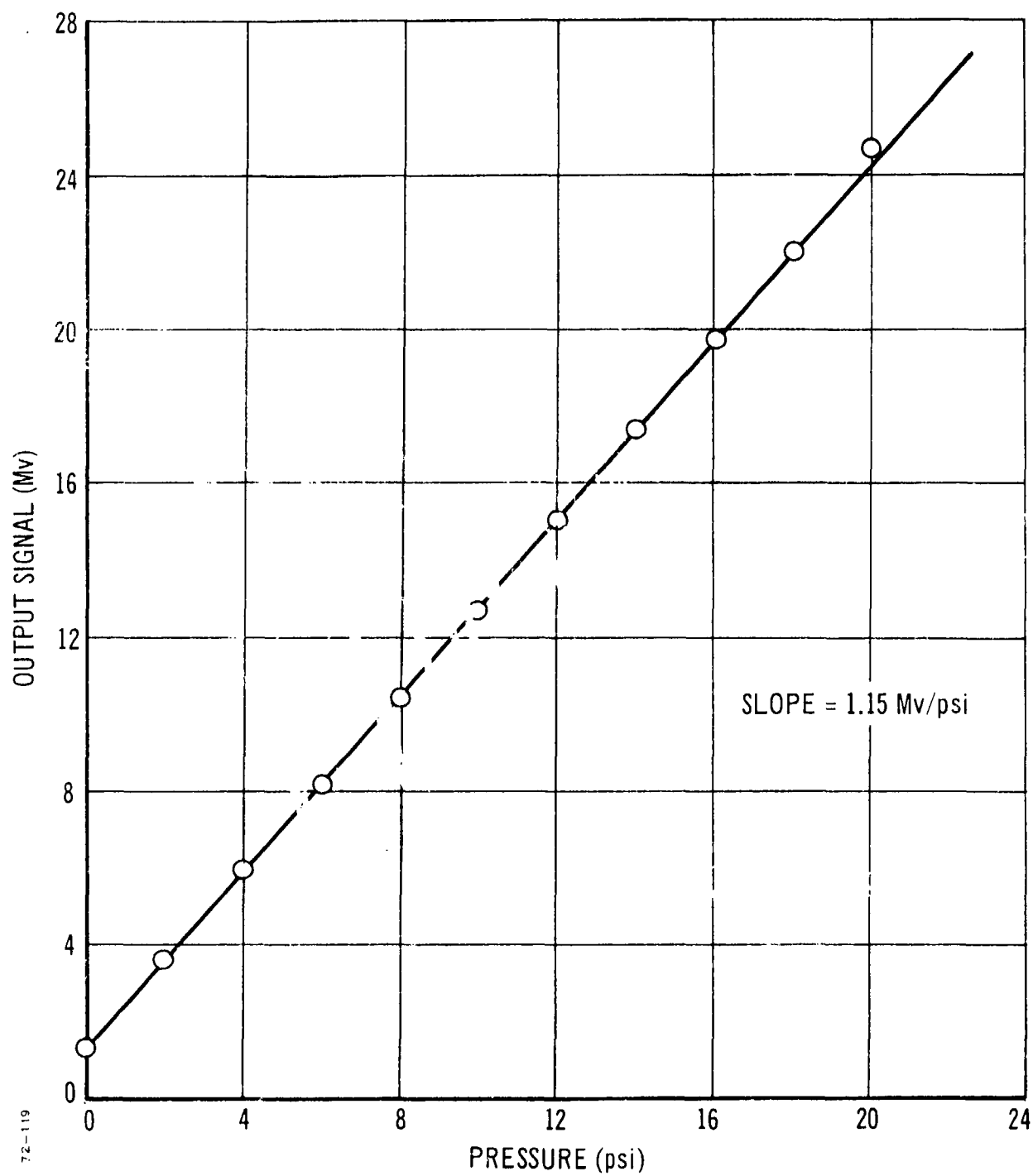
Figure 28. Pressure Calibration of 150-psi Gage in Inert Propellant Test
Fixture, $T = 75^0F$.

Tension and compression and tension and hydrostatic pressure having been compared, the case of hydrostatic tension was next examined. A series of alternating pressure and vacuum steps was applied to the fixture, the pressure or vacuum being held for 5 minutes, then removed for 5 minutes, and subsequently followed by another vacuum or pressure step. The reason for returning to zero load between each pressure and vacuum step was to prevent any long-term zero shifts during the course of the testing.

The test data are presented in Figure 29. Close examination of these data suggests that there is a slight difference between the sensitivity of the embedded gage to pressure and to vacuum, although this is somewhat obscured by the drift in the zero pressure reading. However, the error involved in using the single linear gage sensitivity curve (shown dashed in Figure 29) is extremely small. The slope of the gage output versus pressure line is 1.15 mv/psi, which is exactly the same as that of the data in Figure 28, obtained for pressure alone.

It was concluded, therefore, that the embedded gage will have essentially the same sensitivity to hydrostatic tension as to hydrostatic pressure. Thus, the use of hydrostatic pressure steps on gages embedded within motors is a valid method of calibration even for different stress systems. The sensitivity of the gage to a uniaxial normal stress will be approximately $1/1.11$ of the gage sensitivity to hydrostatic pressure, and therefore the normal stress causing the gage reading can be evaluated.

(3) Restrained Pressure and Vacuum Testing

One of the major tasks of the third-year STV program was to investigate the response of the diaphragm gage under complex three-dimentional stress/strain fields. Two approaches to this problem were adopted: (1) a series of pressure and vacuum steps was applied to the uniaxial test specimen with the ends held fixed, and (2) combinations of pressure plus tension loadings were applied. The first of these complex load tests is considered here.

The test fixture was located in the pressure chamber and the specimen ends were firmly attached to the chamber end-caps. Pressure and vacuum steps were applied sequentially to the chamber and the gage readings were noted. The loading conditions were as follows:

Stress field: $\sigma_1 = \sigma_2 = -p$

$\sigma_3 =$ unknown (measured by gage)

Strain field: $\epsilon_3 = 0$ and $\epsilon_2 = \epsilon_1$
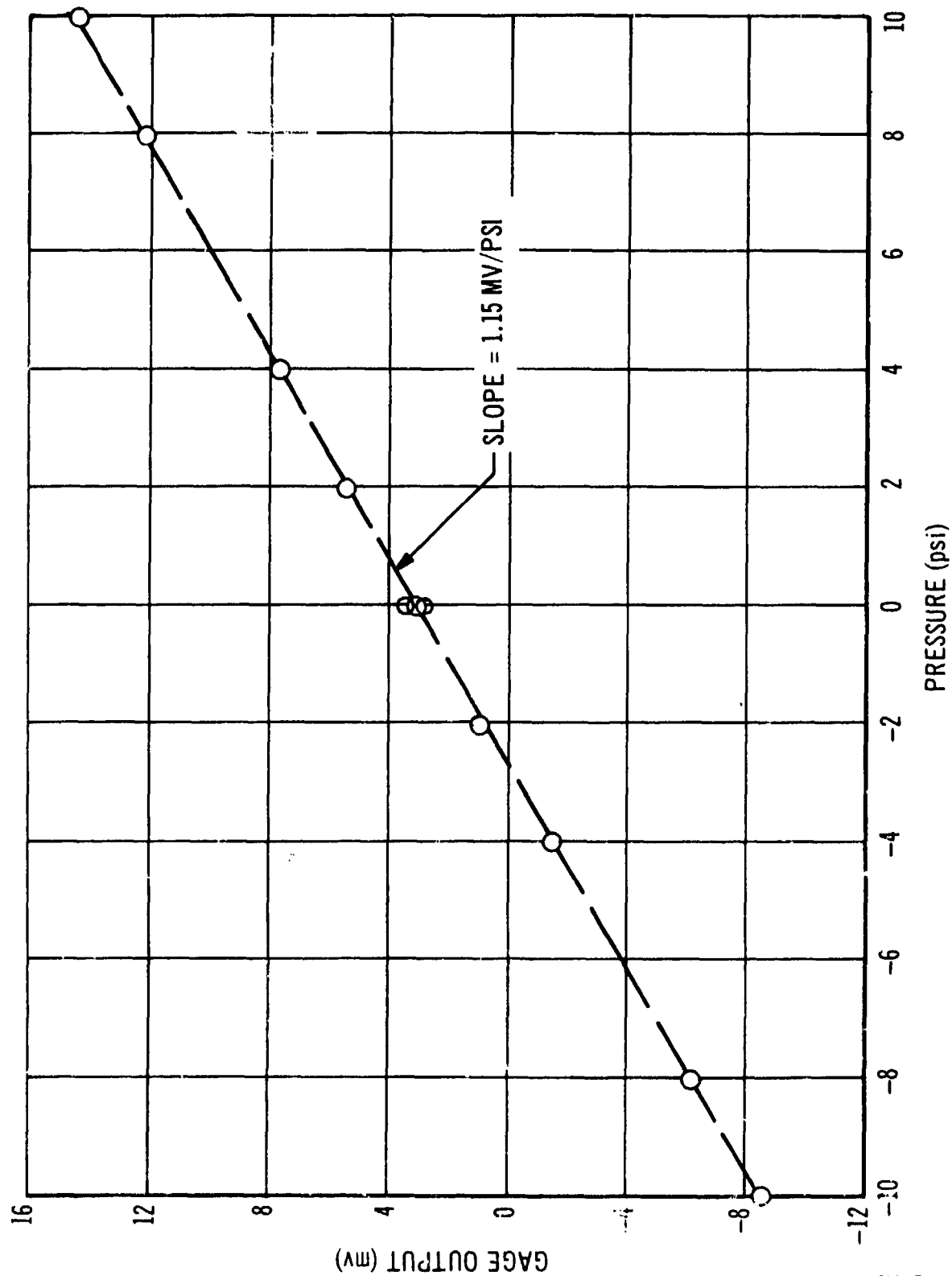
Figure 29. 150-psi Gage in Inert Propellant Uniaxial Test Fixture: Response to Pressure and Vacuum.

72-119

-64-

From the stress-strain relations it is found that

$$\sigma_3 = 2 \nu p$$

where ν = Poisson's ratio. Thus, for an incompressible material

$$\nu = 0.5$$

and therefore

$$\sigma_3 = -p$$

This test condition is therefore a means of determining how close to incompressible the propellant really is. The test results are shown in Figure 30, where they are compared with the test results obtained under hydrostatic pressure (from Figure 29). It will be noted that the slopes of the two response lines are identical, implying a value of $\nu = 0.5$. The slight vertical displacement of the two lines is caused by a small difference in the test temperatures.

Thus there is little doubt that the diaphragm gage responds correctly under the restrained pressure and vacuum test conditions.

(4) Combined Pressure and Tension Loading

The combined pressure and tension loading test was first employed during the second-year program, with the 25-psi gage embedded in the 0064-61E live (STV) propellant test fixture. Separate pressure and creep testing of the specimen had shown a 2 to 1 difference in response between pressure, and tension and the combined tests showed the same results (Ref 2).

The initial pressure tests on the 150-psi gage in the inert propellant test fixture at 70^0F gave a response of 1.15 mv/psi under hydrostatic pressure and a response of 1.028 mv/psi under tension in the test fixture. (Analysis of the test fixture and gage showed that the stress at the gage location is only 90 percent of the mean stress in the specimen. Therefore, if the gage response is 1.15 mv/psi, it should be 1.15 x 0.9 = 1.035 mv/psi under a tensile load.)

With these data it is possible to predict the gage output for various loading conditions and to compare the experimental data with the predictions. This comparison gives some idea of the accuracy of the gage under various types of loading condition. The data also illustrate some of the problems of obtaining precise test data. For instance, holding pressure to exactly 10 psi for long periods of time can be difficult, and many digital monitoring systems exhibit long-term drift, which can produce spurious gage signals. Both of these problems are to be found in the curves shown in Figure 31, where two sets of test data are given.
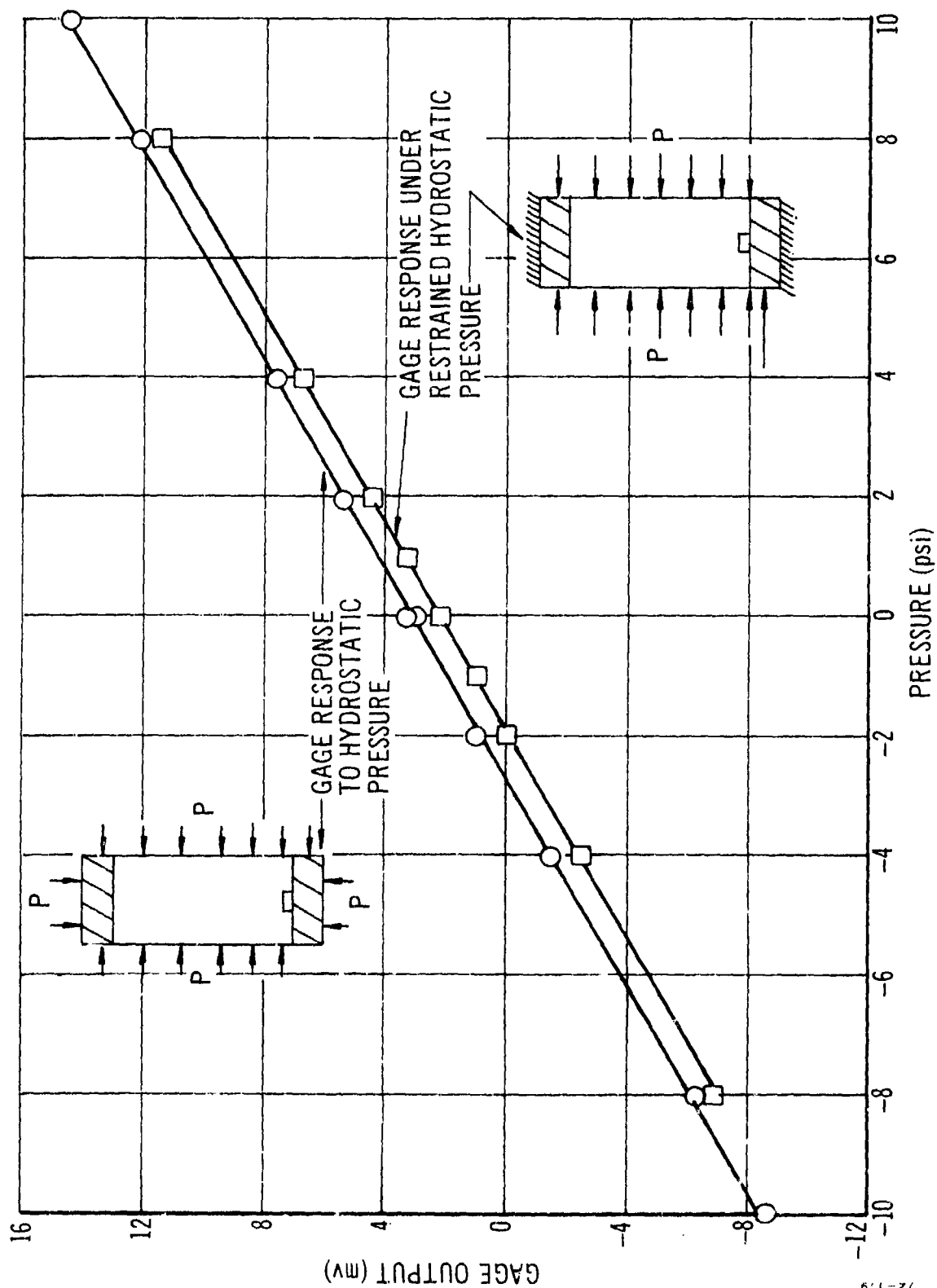
Figure 30. Inert Propellant Uniaxial Test Fixture, 150-psi Gage Response
Comparison.
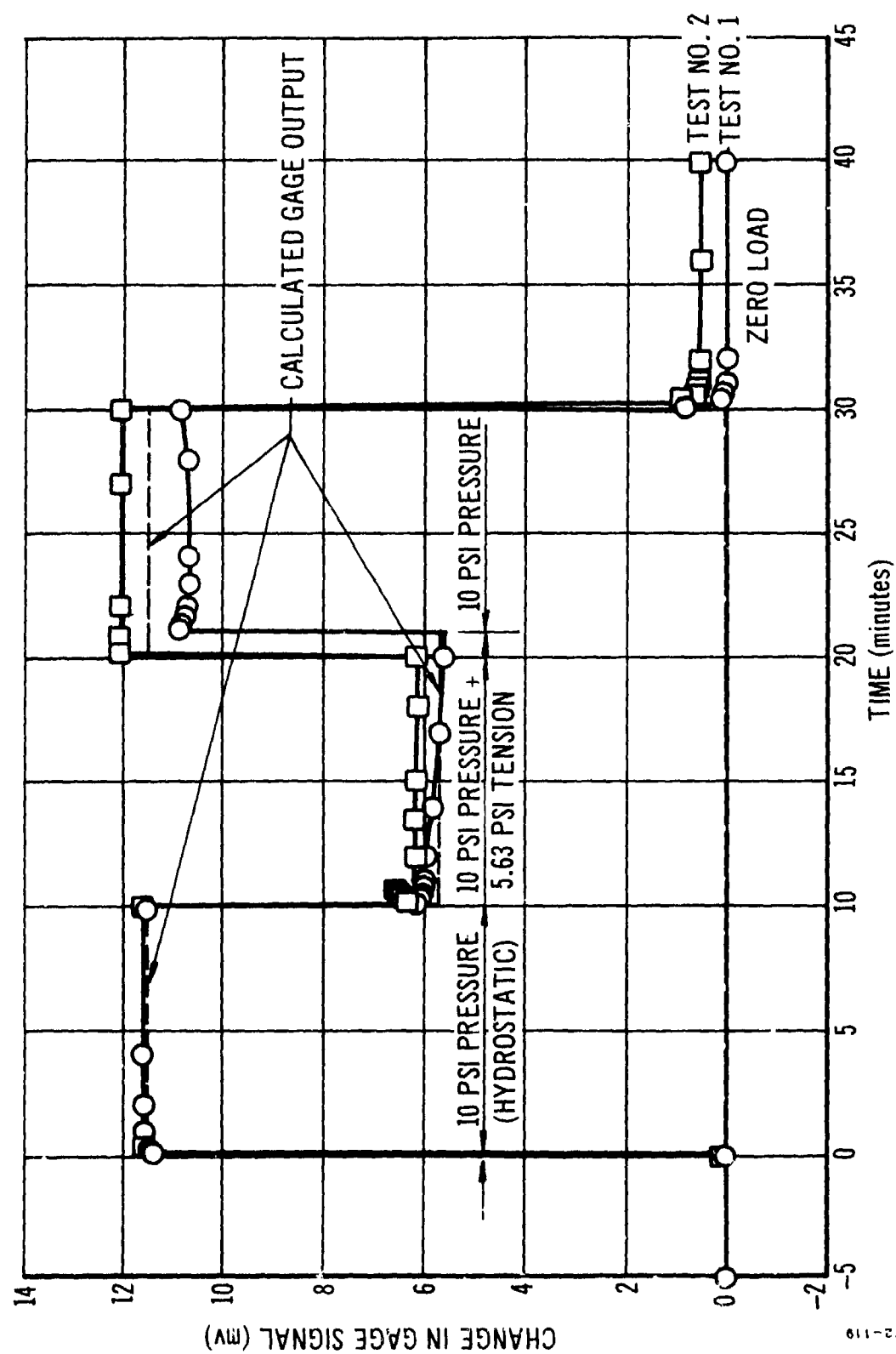
Figure 31. Uniaxial Test Specimen No. 1, Combined Pressure and Tension Loading at 70°F.

The test sequence consisted of a 10-psi pressure step (from zero load) held for 10 minutes. A tensile stress of 5.625 psi (equivalent to a 10-pound deadweight) was then applied in addition to the pressure and held for 10 or 11 minutes. The tensile load was then removed and the pressure held for another 9 or 10 minutes, after which the pressure was reduced to zero, and the gage response was monitored for another 10 minutes. The calculated gage response was as follows:

10-psi pressure at 1.15 mv/psi	=	+11.5 mv
5.625-psi tension at -1.15 x 0.9 mv/psi	=	-5.82 mv
Thus, 10-psi pressure plus 5.625-psi tension	=	+5.68 mv

It will be seen from Figure 31 that both tests gave excellent gage readings during the initial 10-psi pressure step phase. During the tensile creep test, pressure was not maintained at exactly 10 psi during the first test, as was noted when the tensile load was released. The gage reading increased to 10.7 to 10.8 mv, indicating a reduced pressure. When the pressure was released, the gage response fell to 0 mv.

Because of the loss in pressure during Test 1, a second test was performed. In this test, however, the digital meter monitoring the gage output drifted and read 0.50 mv when all load was removed. For this reason the gage reading was high during the combined pressure plus tension phase (6.1 to 6.2 mv) and during the second pressure-alone phase (12.0 mv).

However, despite these difficulties the gage performed well within the ±10-percent error band, which is believed acceptable for a propellant stress gage. This does not excuse poor test technique, but demonstrates the fact that reasonably accurate stress values can be obtained under normal field conditions.

The 150-psi gage has not shown any problems under the complex stress fields considered to date. The rigid construction of the new 150-psi gage has probably prevented the distortion under transverse loads that was obtained with the early 25-psi gage and that led to the large discrepancy between the tensile and hydrostatic pressure calibrations.

Probably the only additional complexity in the stress/strain field that occurs in practice and that has not been evaluated either experimentally or analytically is the condition of a stress gradient over the gage face. If the gage is located near an end of a grain, then a significant stress gradient can occur and this may affect gage performance. Under most normal situations, however, it is not believed that such stress gradients will cause much trouble.

5. ANALYSIS OF DIAPHRAGM GAGE UNDER SHEAR LOADING

The effects of the application of shear loads to a diaphragm gage embedded in a uniaxial calibration fixture can be ascertained by subjecting

the end of the fixture to a rigid translation relative to the other end. Using a Fourier analysis, the end displacements may be written as

$$
\left.
\begin{aligned}
u_r &= A \sin \theta \\
v_\theta &= A \cos \theta \\
w_z &= 0
\end{aligned}
\right\} \tag{64}
$$

The axisymmetric geometry of the boundary value problem suggests a formulation in cylindrical coordinate. Solution of the boundary value problem posed in cylindrical coordinate can be formulated by Fourier analyses. As a result of the nature of the loading, expressed in Equation (64), the deformations and stresses in a linear elastic formulation will depend only on the first harmonic of the expansion. Consequently, the gage response will be asymmetric as opposed to the symmetric responses obtained in the other analyses reported here. Unless the sensing strain gage is mounted asymmetrically on the diaphragm, the gage should register no response during asymmetric loadings (e.g., shear). To calibrate the gage for shear loads, the precise eccentricity of the sensing element must be known. Furthermore, the orientation of the gage element relative to the shearing load must be specified. This is clearly not a variable that can be determined by calibration. Thus, the only practical solution is to discard gages with eccentrically mounted strain gages on the diaphragm, if ever they are encountered.

In practice, the eccentricity of the strain gage elements will be extremely small and the response of the diaphragm gage to shear will be negligible, as determined by Dureli in Reference 4.

6. GAGE CALIBRATION ANALYSIS FOR STEADY-STATE VIBRATION LOADS

To ascertain the amount of interference the diaphragm gage imparts under steady-state harmonic excitation of one end of the uniaxial calibration apparatus, a numerical investigation was undertaken. The test fixture and gage were modeled and analyzed by means of the finite element program CXL450.

In modeling the system, quadrilateral elements of axisymmetric geometry were used for the propellant, and axisymmetric plate elements were used for the diaphragm gage. The mesh details adjacent to and remote from the gage are shown in Figure 32.

For loading, six excitation frequencies were employed, which covered the practical range of data given in Figure 22 of Reference 1 at a temperature of $70^0 F$. These frequencies and the corresponding complex moduli are listed in Table II.

For each frequency the system was solved first with the top excited by a harmonic axial displacement and the bottom held fixed. Then the system was resolved with the input excitation switched to the bottom and the top
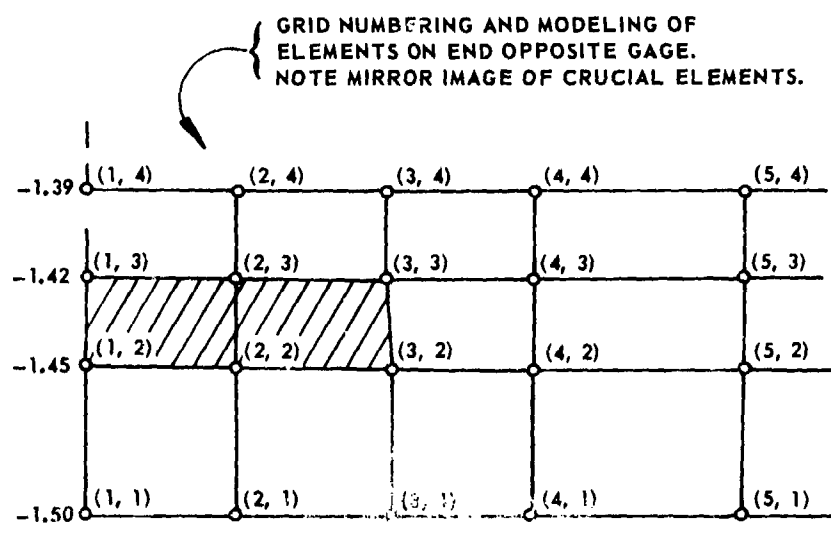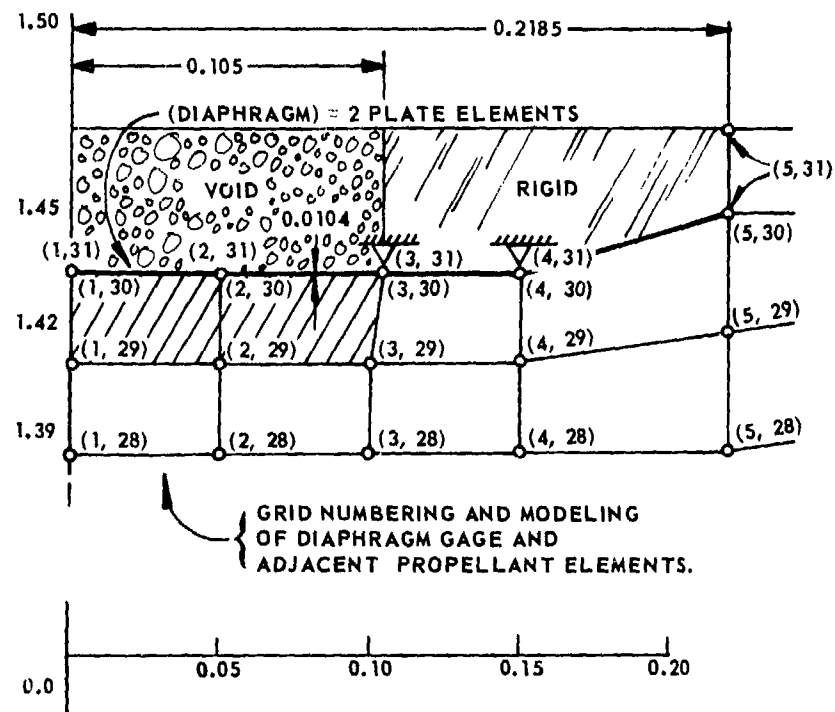
Figure 32. Finite Element Mesh, Near to and Remote from Gage.

TABLE II

MATERIAL PROPERTIES VERSUS FREQUENCY AT 70°F

Frequency		Real Shear Modulus	Imaginary Shear Modulus	Poisson's Ratio = 0.5	
ω (rads/sec)	cps			Real Young's Modulus	Imaginary Young's Modulus
10^2	15.9	1,050	410	3,150	1,230
10^3	1.59×10^2	2,000	740	6,000	2,200
10^4	1.59×10^3	3,500	1,250	10,500	3,750
10^5	1.59×10^4	6,100	2,050	18,300	6,150
10^6	1.59×10^5	9,600	3,200	28,800	9,600
10^7	1.59×10^6	15,000	4,700	45,000	14,100
10^8	1.59×10^7	22,000	6,200	66,000	18,600
10^9	1.59×10^8	32,000	6,100	96,000	18,300
10^{10}	1.59×10^9	39,000	2,300	117,000	6,900

was held fixed. In this manner the interference factor can be determined by comparing the mechanical behavior in the propellant immediately adjacent to the gage with the corresponding behavior of the mirror image of the location and loading on the bottom side, which is modeled with no gage.

The results for the magnitude and phase angle of the stress normal to the diaphragm gage (σ_z) are tabulated in Table III for the frequencies analyzed at 70^0F. The magnitude of the gage interference is plotted in Figure 33 as a function of frequency of excitation. Because only a selected few frequencies were considered and because resonances are likely in the specimen, the results are presented as a histogram. The response between these frequencies can be confirmed only by further numerical studies. In particular it is likely that a resonance occurs near an excitation frequency of 10^4 rad/sec and that calibration of the gage near these frequencies may be meaningless in other applications. For excitation frequencies below 1000 rad/sec, calibration at room temperature (based on further numerical results) may be feasible.

To calibrate the gage over a wide range of temperatures, further analysis is necessary. For each temperature of interest the model must be subjected to excitations over the frequency domain.

It is not possible to apply shift principles to the results presented here. This can be verified by considering the form of the equations used in the finite element analysis, e.g., Equation (101) in Reference 1.

$$\left[K^*_{in} (\omega, T) - \omega^2 M_{in} \right] V^*_n = R^*_n \tag{65}$$

where

K^*_{in} = the complex modulus stiffness matrix

M_{in} = the mass matrix

V^*_n = the complex nodal displacement vector

R^*_n = the complex force vector

ω = the frequency

T = the temperature

If the thermorheologically simple postulate is used and a shift factor a_T is established, then

$$K^*_{in} (\omega, T) = K^*_{in} (\omega a_T, T_o) \tag{66}$$

Thus, K^*_{ij} can be calculated by means of the shift function. However, the frequency ω appears in an explicit manner in the inertia term. Consequently, the notion of shifting the results for various temperatures fails in the dynamic problem, and each temperature must be analyzed independently.

TABLE III

MAGNITUDE OF CYCLIC AXIAL STRESS AT 70°F

Frequency (Hz)		Bottom Excitation				Top Excitation			
		Element (1, 2)	Element (2, 2)	Element (1, 29)	Element (2, 29)	Element (1, 2)	Element (2, 2)	Element (1, 29)	Element (2, 29)
1.59 x 10¹	(1)	5.2956E-02	4.9756E-02	1.4201E-03	1.2898E-03	1.4223E-03	1.3515E-03	5.3586E-02	5.9155E-02
	(2)	-122.1	-120.9	-164.7	-163.8	-163.44	-163.42	-124.46	-133.90
	(3)	0.9991E-00	0.9996E-00	2.3905E-03	1.4985E-03	2.0123E-03	1.1653E-03	0.9996E-00	0.9997E-00
1.59 x 10²	(1)	3.0356E-04	2.9981E-04	1.5365E-03	1.3900E-03	1.5749E-03	1.5603E-03	2.6886E-04	2.9094E-04
	(2)	-21.17	-20.04	-47.75	-49.38	-52.02	-49.50	-24.79	-19.98
	(3)	0.9511E-00	0.99765	2.4706E-03	1.5485E-03	3.2715E-03	3.7078E-03	1.0510E-00	1.0322E-00
1.59 x 10³	(1)	3.6724E-06	3.6621E-06	8.5237E-03	7.2139E-03	5.0310E-03	4.7443E-03	7.3690E-06	6.3871E-06
	(2)	-8.737	-8.690	-14.11	-4.578	+11.70	+9.60	-40.30	-29.30
	(3)	0.8955E-00	0.9794E-00	1.8766E-02	1.1683E-02	7.0363E-04	5.4068E-04	17.6951E-00	11.352E-00
1.59 x 10⁴	(1)	7.8197E-07	7.8465E-07	8.9629E-04	8.7847E-04	1.1947E-05	1.1962E-05	5.1279E-07	4.1918E-07
	(2)	-8.687	-8.243	-5.689	-9.493	-14.5	-14.6	-2.80	-2.72
	(3)	1.7193E-00	0.9039E-00	4.5153E-03	6.5889E-03	1.200E-04	2.6622E-04	5.4657E-00	5.0359E-00
1.59 x 10⁵	(1)	1.02060E-10	1.0233E-10	1.1122E-07	1.2328E-07	1.9787E-07	1.9735E-07	4.0538E-09	5.2058E-09
	(2)	-0.063	-0.062	-0.064	-0.089	-0.01	-0.01	0.00	0.00
	(3)	1.4146E-00	0.9058E-00	3.3152E-03	8.7969E-03	3.0306E-05	2.5491E-04	1.7054E-00	3.8331E-00
1.59 x 10⁶	(1)	1.0294E-12	1.0266E-12	1.1164E-09	1.2450E-09	1.9919E-09	1.9867E-09	4.1009E-11	5.2484E-11
	(2)	0.00	0.00	0.00	0.00	0.00	0.00	0.00	0.00
	(3)	1.4118E-00	C.9052E-00	3.4213E-03	8.7592E-03	3.0135E-05	2.5506E-04	1 5175E-00	3.8224

NOTE:
(1) Magnitude of Z-stress: psi
(2) Phase angle of Z-stress: degrees
(3) Magnitude of Z-displacement: inches
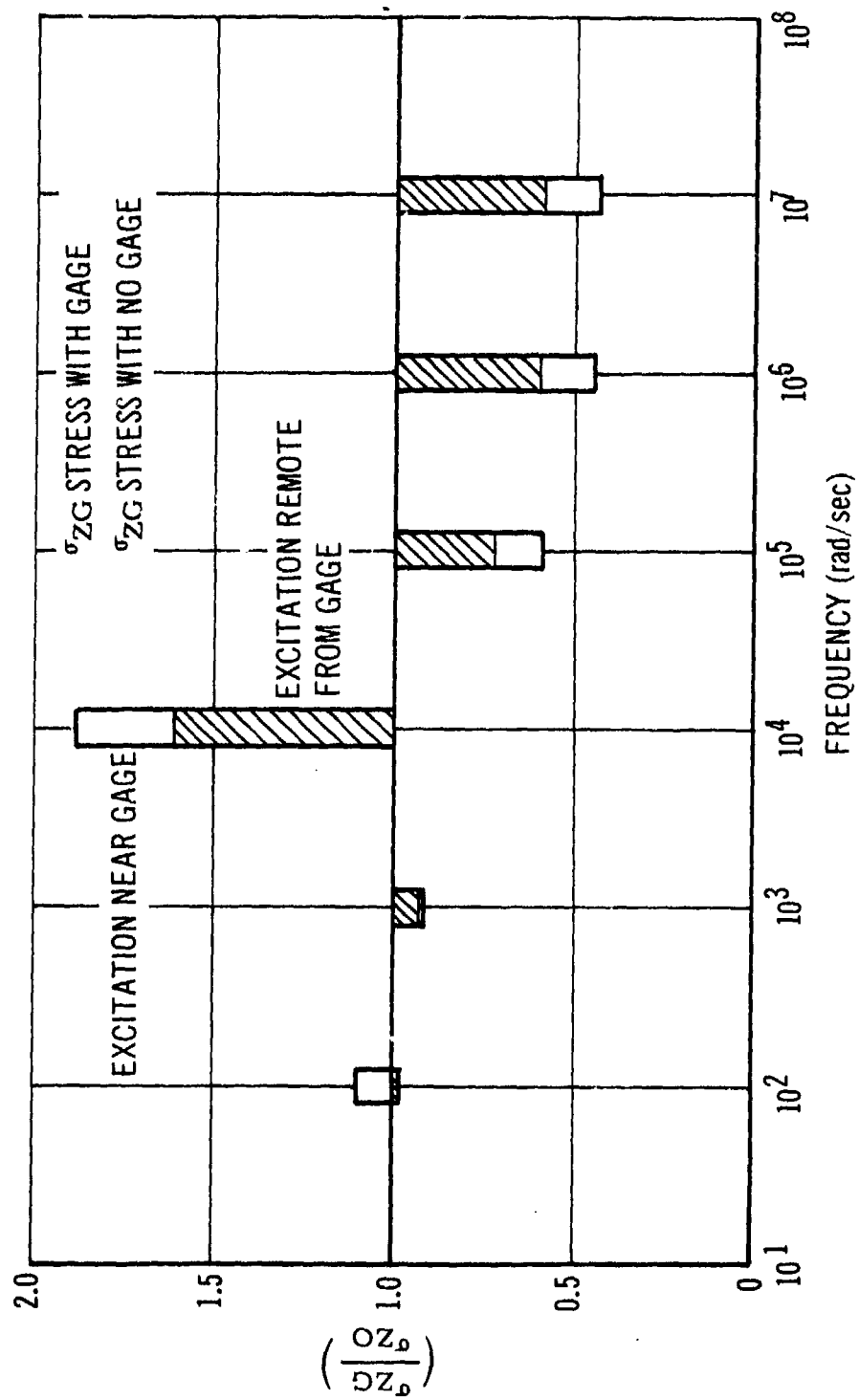
Figure 33. Gage Interference for Steady-State Excitations Near to and Remote from Gage.

72-119

-74-

This harmonic excitation analysis, and that presented later for the response of the gage to shock, suggest strongly that the diaphragm gage will not be an effective instrument for high-frequency measurement.

7. EXPERIMENTAL CYCLIC LOAD TEST DATA AND COMPARISON WITH ANALYSIS

a. Introduction

On the surface it would seem that vibration testing of the uni-axial test fixture should not present much of a problem. All that is necessary, after all, is to mount the device in a rigid structure and to apply a cyclic load by means of an electrodynamic exciter. In practice, however, the problem is much more difficult than it appears. The major difficulties can be listed as follows:

- There is a distinct shortage of "rigid" or stiff test fixtures for vibration testing. All available structures were found to exhibit some deflection at certain frequencies.

- The uniaxial test fixture itself is a resonant system, with a resonant frequency within the range of interest.

- Very few instruments such as accelerometers, displacement transducers, or load cells will function properly across a frequency range from 1 to 10,000 Hz. Even if it is claimed that the device will perform satisfactorily, there is usually no calibration data to support the contention.

Despite difficulties such as those listed above, vibration tests were performed on the uniaxial test fixture No. 2 containing three 150-psi diaphragm gages. Unfortunately, a lead wire to gage No. 20, in the middle of the specimen, broke before the vibration testing commenced and no data were obtained from this gage. However, a considerable amount of data was obtained with the two remaining devices.

The area of vibration testing of the embedded gages, both normal stress sensors and shear stress sensors, was of particular impor-tance during the third year of the STV program. Little work had been per-formed in the way of verifying that the gages would work properly within the propellant and there was, by now, considerable pressure to make use of the devices in operational situations where vibration loads would be encountered. For this reason, the combined analytical and experimental program was undertaken. At the very least, the data would point out problem areas and illustrate any obvious shortcomings of the available gages.

b. Experimental Apparatus

When the vibration testing was initiated, the experimental apparatus was arranged on the frame of an Instron testing machine as shown

-75-

in Figure 34. The sketch shows the apparatus arranged for vibration testing of the shear specimen, but the uniaxial specimen was also tested in this apparatus.

The results of some preliminary tests with the apparatus showed that it was not sufficiently rigid for the purpose. The Instron crosshead was found to deflect a significant amount when the vibrator was supposedly applying force to the specimen.

Later, a new apparatus was assembled, as sketches in Figure 35. This device employed large, 2-inch-thick aluminum plates for the framework and the unit was bolted together as shown. Although this apparatus was better, resonances were still obtained in the framework and it was later found to be too small to house additional apparatus such as a load cell, accelerometer, or LVDT for displacement monitoring.

Finally, therefore, the apparatus sketched in Figure 36 was designed and built for the vibration tests. The frame consisted of welded channel section (steel) and the fixture was designed to hold the vibrator and load cell, and either the uniaxial or the shear test specimen. Although larger than the earlier apparatus, it was small enough to fit inside a conditioning chamber to enable tests to be performed at several temperatures.

c. Experimental Vibration Test Data

Preliminary vibration tests were conducted on the Instron vibration apparatus with the inert propellant uniaxial test fixture No. 2, with two working 150-psi gages. The current through the vibrator coil was monitored as a measure of the force input. The resulting data from tests at 75^0F are given in Table IV and in Figure 37.

Because of the presence of resonances in the system, these data were not regarded as particularly satisfactory. Thus, both gages show a peak in sensitivity at 100 Hz and gage No. 10 appears to show another at 800 Hz. Above 1000 Hz, gage No. 10 shows a rapid loss in sensitivity, whereas gage No. 5 retains an almost constant response from 1000 to 3000 Hz.

At the low frequencies, the phase angle between the input force and the gage signal is small, 15 to 20 degrees at 10 Hz, and this phase lag increases to 90 degrees at approximately 200 Hz, continuing to increase with higher excitation frequencies and reaching a maximum of about 360 degrees at 700 Hz.

It was not certain what the causes of the apparent resonances in the gage response were, and there seemed to be no method of eliminating them. Therefore, further vibration testing was postponed until the final test apparatus (Figure 36) was available.

First, the load transmitted through the specimen and measured on the load cell was monitored and compared with the input force as measured with the driver coil current.
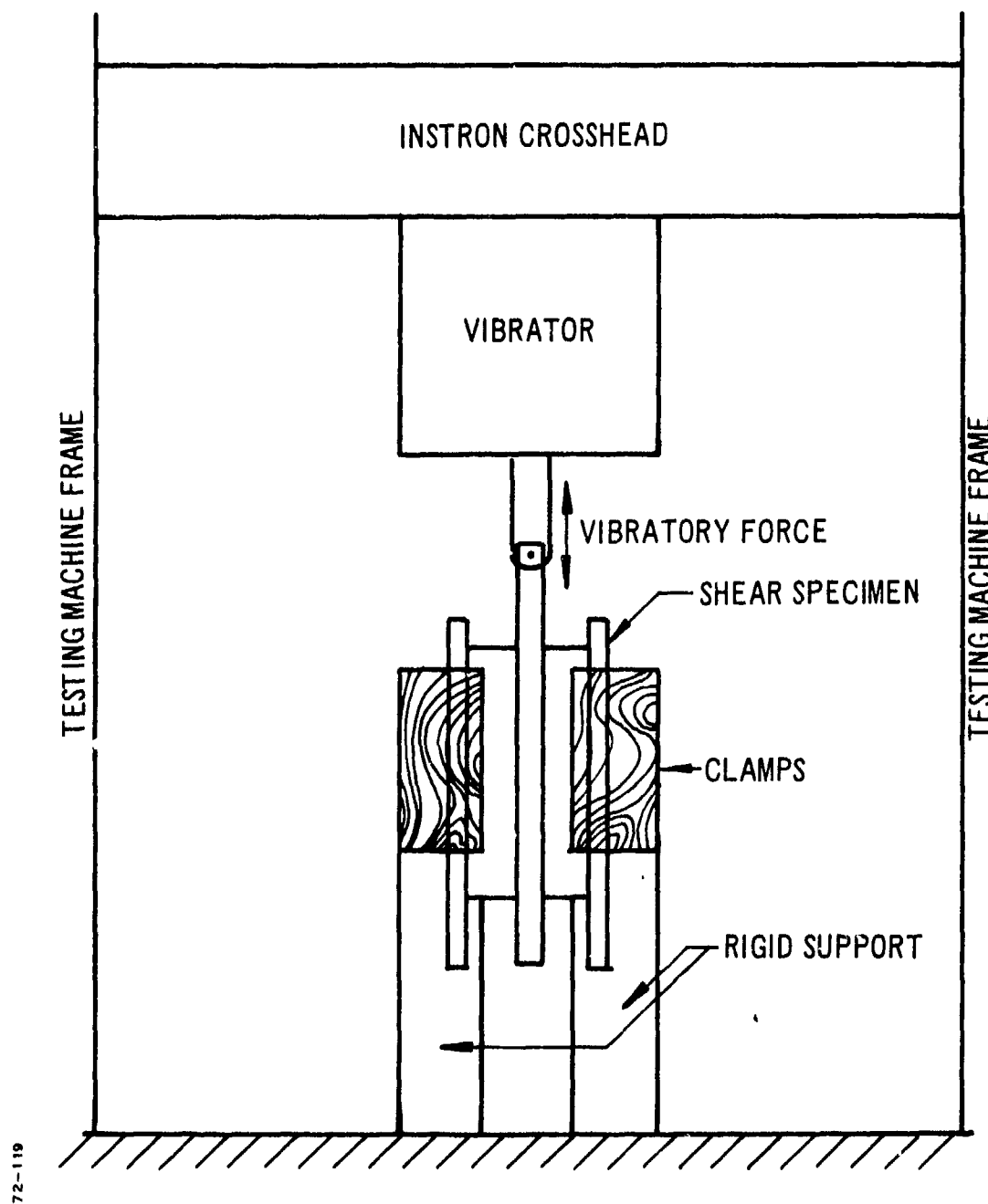
Figure 34. Experimental Test Apparatus for Dynamic Shear Tests.
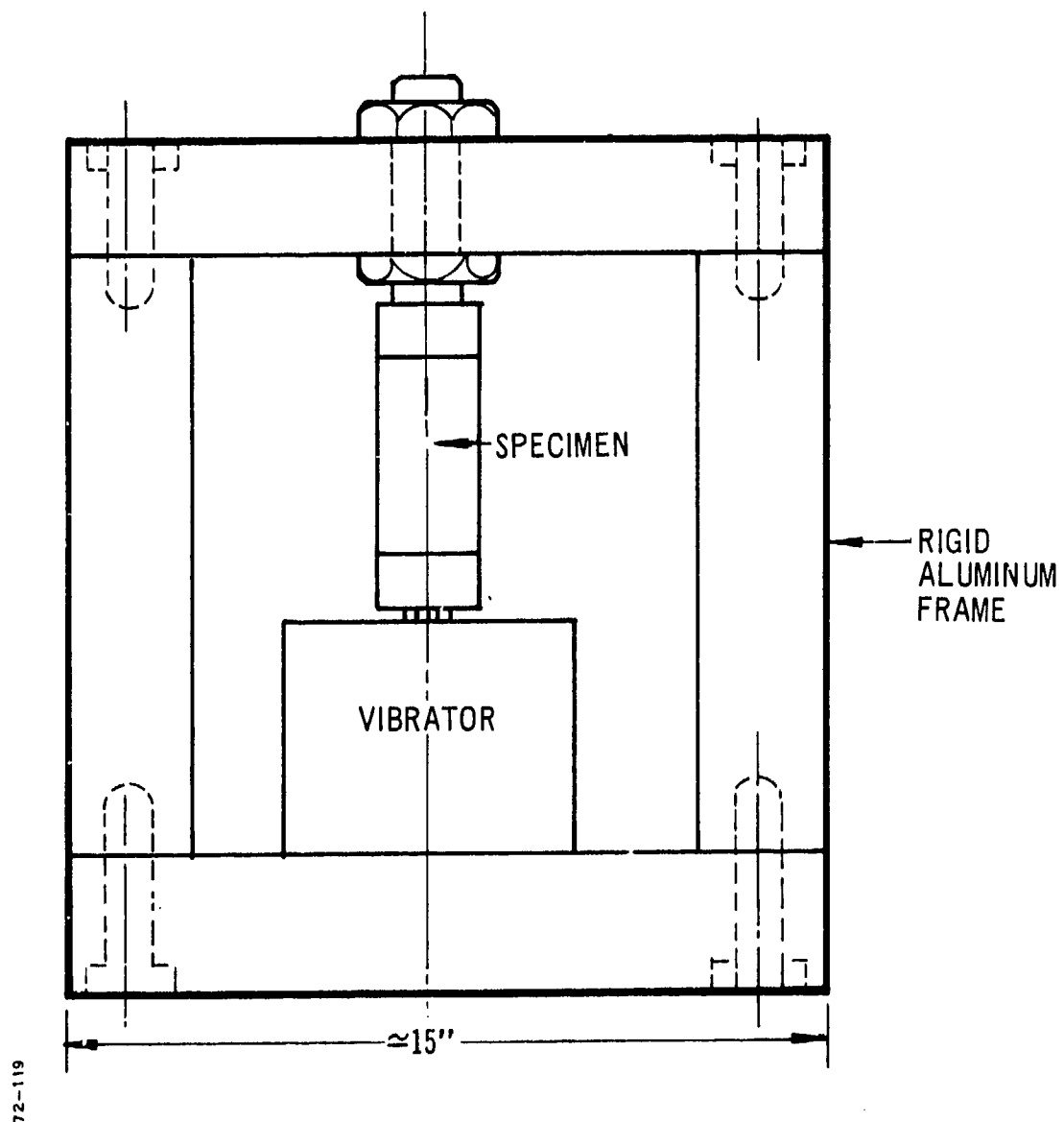
Figure 35. Sketch of New Vibration Test Fixture.
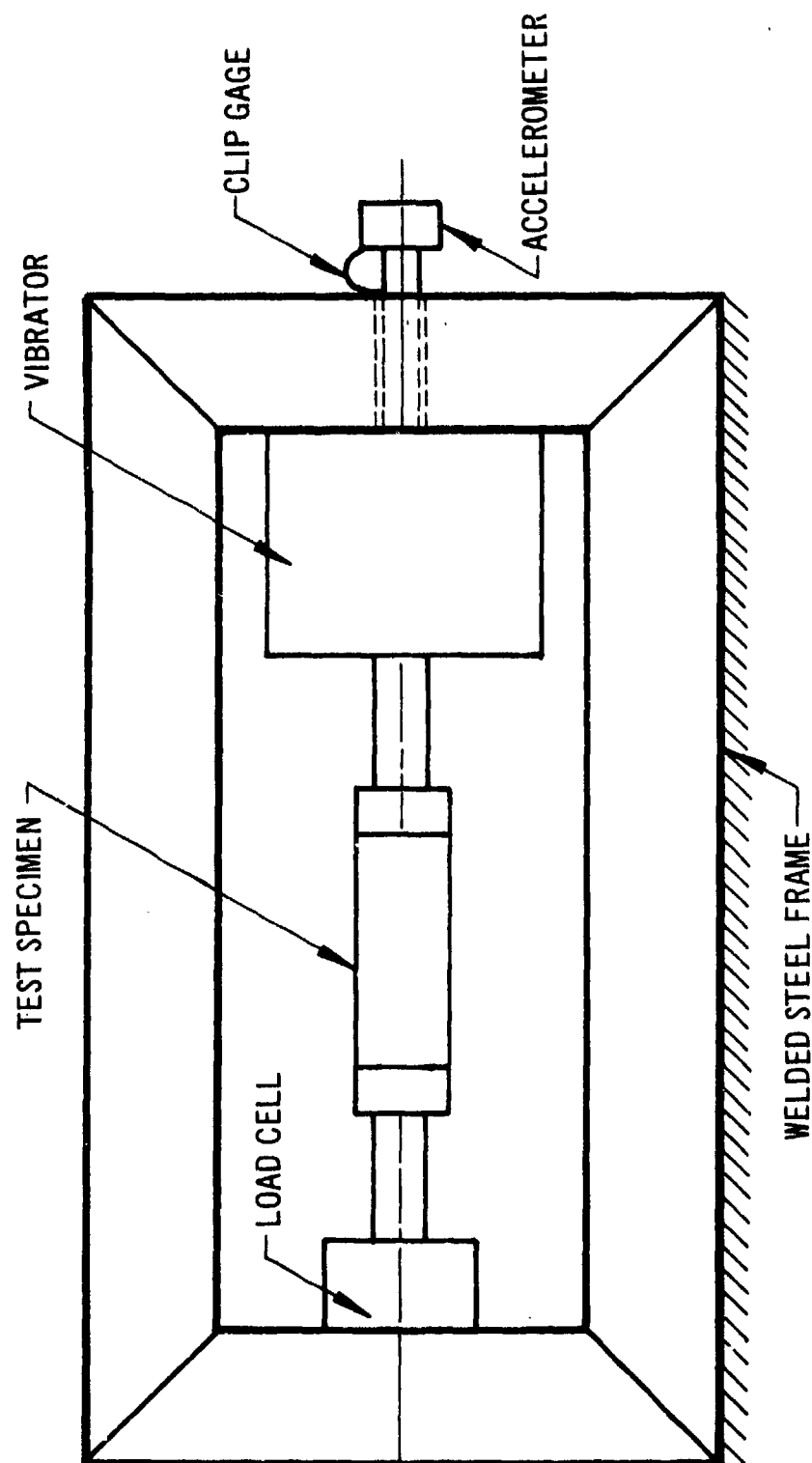
Figure 36. Sketch of Revised Vibration Test Fixture.

72-119

TABLE IV

DIAPHRAGM GAGE RESPONSE TO CONSTANT CYCLIC INPUT FORCE AT 75°F

(Early Test in Instron Machine)

Frequency (Hz)	Input Force (lb)	Stress (psi)	Gage No. 5			Gage No. 10		
			Output (mv)	Phase Angle (deg)	Response (mv/psi)	Output (mv)	Phase Angle (deg)	Response (mv/psi)
10	10	3.18	2.6	14	0.82	3.0	22	0.95
20	10	3.18	2.5	22	0.79	2.8	36	0.88
50	10	3.18	2.9	27	0.91	3.3	36	1.04
100	10	3.18	4.8	43	1.51	5.3	57	1.67
200	10	3.18	0.4	57	0.13	1.15	100	0.36
300	10	3.18	0.48	338	0.15	0.9	131	0.28
500	10	3.18	0.72	323	0.23	0.62	162	0.20
700	10	3.18	0.94	38	0.30	0.84	244	0.26
1000	10	3.18	0.98	49	0.31	0.80	352	0.25
2000	~8	~2.54	~0.66	50	0.26	0.15	316	0.054
3000	~6	~1.88	~0.6	79	0.27	0.02	207	0.011

Gage No. 5 = input gage; Gage No. 10 = output gage

Static Calibration Test Data:

Gage No. 5: 10-lb wt ≡ 3.18 psi ≡ 2.8 mv ≡ 0.88 mv/psi

Gage No. 10: 10-lb wt ≡ 3.18 psi ≡ 3.6 mv ≡ 1.13 mv/psi
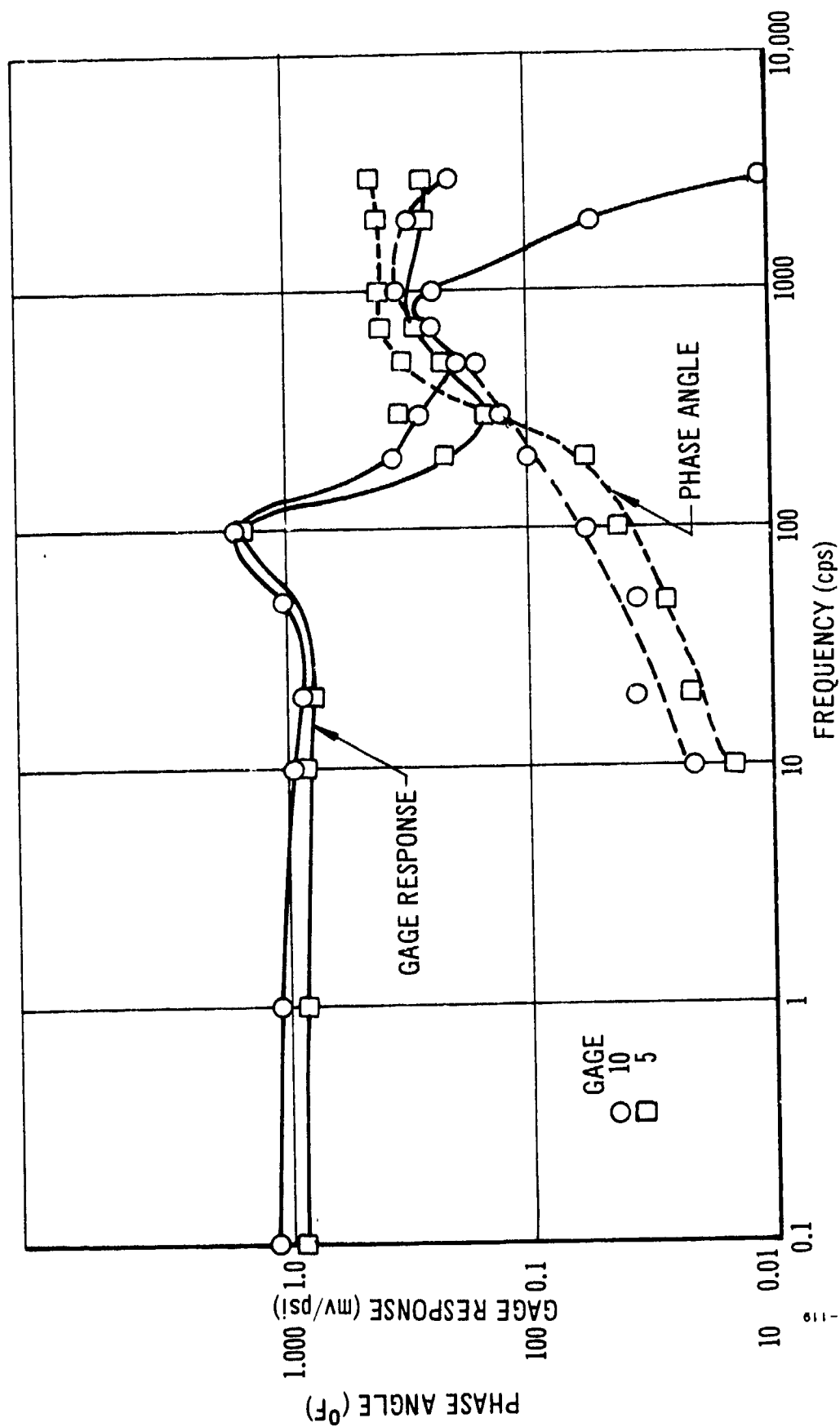
Figure 37. Dynamic Response Curves for 150-psi Gages in Inert Propellant Uniaxial Test Fixture.

The resulting data are shown in Table V and Figure 38. Preliminary tests at the standard frequencies showed the presence of three resonances. A search was made to ascertain the precise resonant frequencies; these were found to be 150, 540, and 975 Hz. There seems little doubt that the three frequencies represent the fundamental and harmonic modes of the resonance of the system as a simple mass-spring system, as illustrated in Figure 39.

The uniaxial test fixture acts as a damped spring and the mass of the moving parts of the vibrator (the linkage, etc) act as a lumped mass and give the fundamental resonance mode of 150 Hz. The damping, which is clearly present in the fundamental resonant mode, appears less effective at the higher mode (540 Hz) and seems almost nonexistent at the highest resonant mode of 975 Hz.

It was clear that this was far from an ideal system to investigate the response of the diaphragm gages, but there seemed to be no way around the problem at this stage. It was decided to carry on with the vibration tests in the hope that the data obtained would at least provide some insight into the performance of the gages under dynamic test conditions.

The presence of two gages at opposite ends of the specimen should have provided information about the gage behavior, especially from a comparison between their performance. The fact that the force transmitted through the specimen was so drastically different from the input force, as the system went through the various resonances, meant that the performance of the output gage should be much different from that of the input gage, if the gages were working properly. The input gage should follow the input force reasonably closely, whereas the output gage should more closely follow the output force as measured on the load cell.

The data obtained from a series of tests at 75°F are given in Table VI, and are shown in Figure 38, 40, 41, and 42. The output/input force ratios are presented in Figure 38 for comparison with the earlier test data. The first test sequence was obtained under constant output force conditions, whereas the second test series was conducted under constant acceleration conditions. The data comparison shows little difference in the resonant frequencies, particularly the two higher modes.

Figure 40 compares the response of the two gages for the later test series with those of the earlier tests conducted in the Instron apparatus and illustrated in Figure 37. Again, it will be clear that there is a difference between the two sets of data from the two tests. However, this difference is not especially significant. Probably the most significant aspect of the data shown in Figure 40 is the fact that the uniaxial test specimen was assembled for testing with gage No. 5, the input gage in the first test sequence, whereas gage No. 10 was the input gage in the last series of tests. The difference in the input and output performance of the gage may be noted as follows:

- After the fundamental resonant mode has been attained, in input gage response always diminishes faster than the output gage response.

TABLE V

CYCLIC FORCE TRANSMISSION THROUGH UNIAXIAL
SPECIMEN AT 75°F
(Later Test in Welded Steel Rig)

Frequency (Hz)	Input Force (lb)	Output Force (lb)	Phase	Output ÷ Input	Remarks
10	12.7	9.5	0	0.75	
20	12.8	9.5	0	0.74	
50	12.2	9.5	0	0.78	
100	7.2	10.0	21	1.40	
150	5.8	10.0	85	1.73	Resonance
200	11.8	10.0	147	0.85	
400	30.2	10.0	166	0.33	
500	15.8	10.0	198	0.64	
700	32.5	10.0	50	0.31	
900	23.2	3.5	161	0.15	
540	9.1	10.0	270	1.1	Resonance
975	18.0	9.0	0	0.5	Resonance
1,000	18.5	2.8	42	0.15	
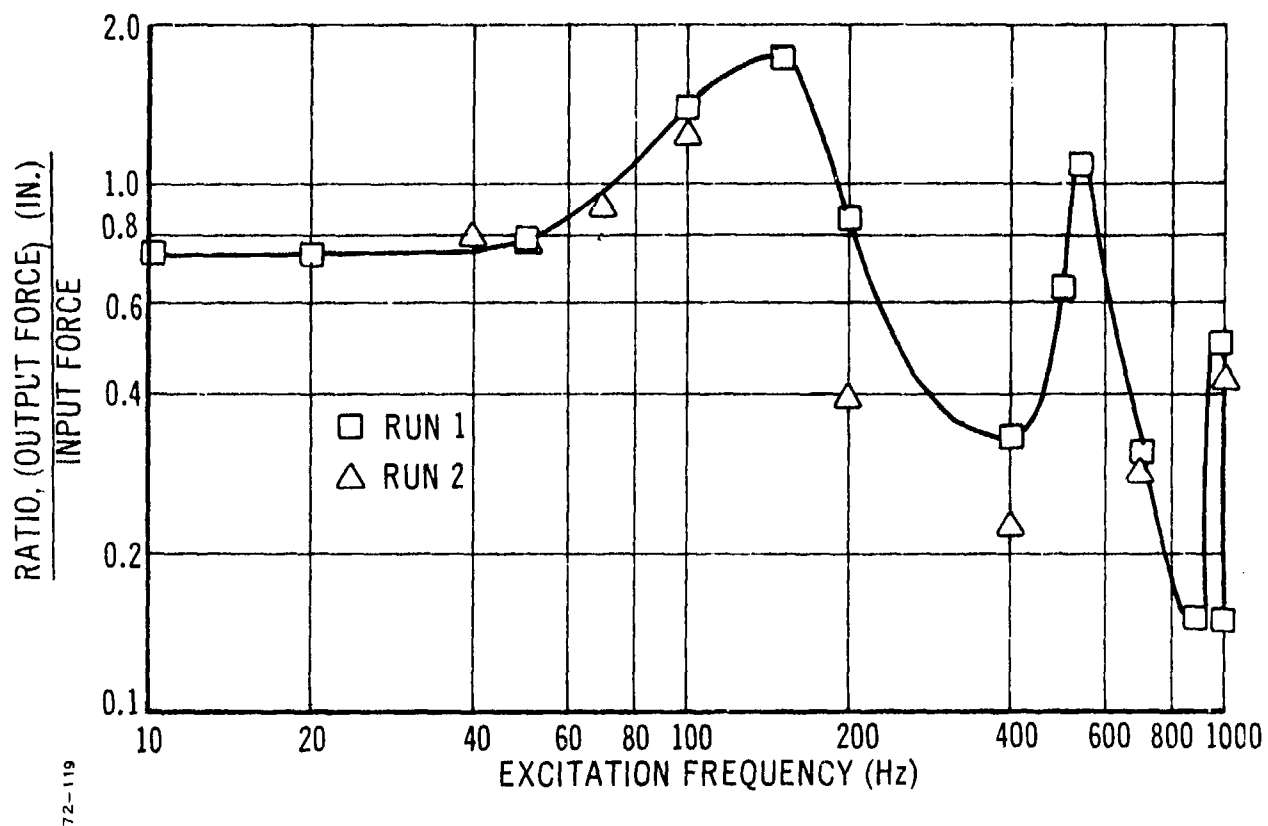
Figure 30. Ratio of Output Force to Input Force versus Excitation at 75°F.
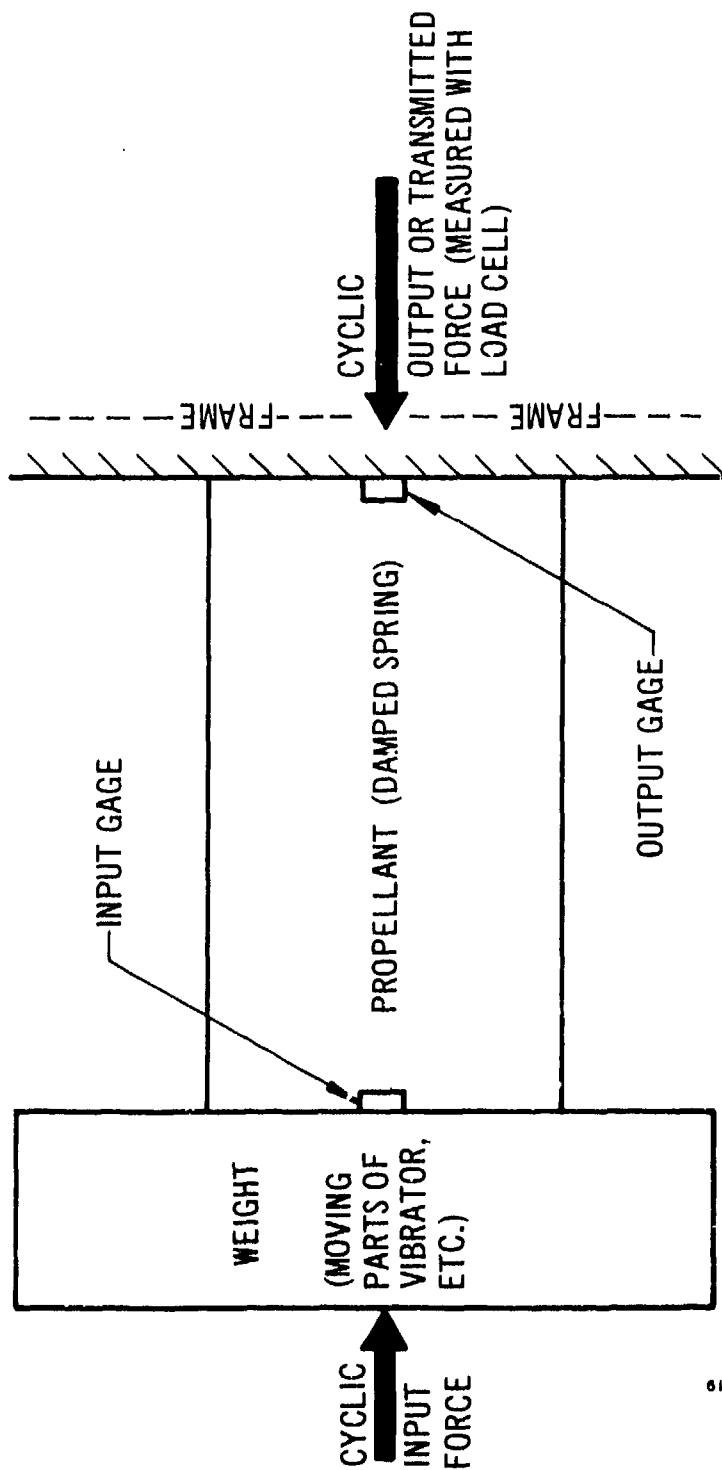
Figure 39. Equivalent System for Dynamic Uniaxial Tests.

-85-

TABLE IV

DIAPHRAGM GAGE RESPONSE TO INPUT AND OUTPUT FORCES AT 75°F

Frequency (Hz)	With Respect to Input Force				With Respect to Output Force			
	Gage No. 5		Gage No. 10		Gage No. 5		Gage No. 10	
	Response (mv/psi)	Phase Angle (deg)	Response (mv/psi)	Phase Angle (deg)	Response (mv/psi)	Phase Angle (deg)	Response (mv/psi)	Phase Angle (deg)
40	0.81	0	0.99	15	1.01	0	1.24	15
50	0.72	8.5	0.72	13	0.93	-4	0.92	0
70	0.77	-12	0.94	-12	0.85	0	1.04	0
100	1.0	18	1.07	18	0.82	0	0.88	0
114					0.80	0	0.84	0
165					0.72	-5	0.61	-6
200	0.28	108	0.22	100	0.74	0	0.51	-8
400	0.12	162	0.08	4	0.54	0	0.34	202
570					0.15	10	0.19	160
700	0.114	175	0.18	5	0.40	170	0.63	0
850					1.57	150	1.39	315
1000	0.21	324	0.26	48	0.50	310	0.63	34

Gage No. 10 = input gage; Gage No. 5 = output gage
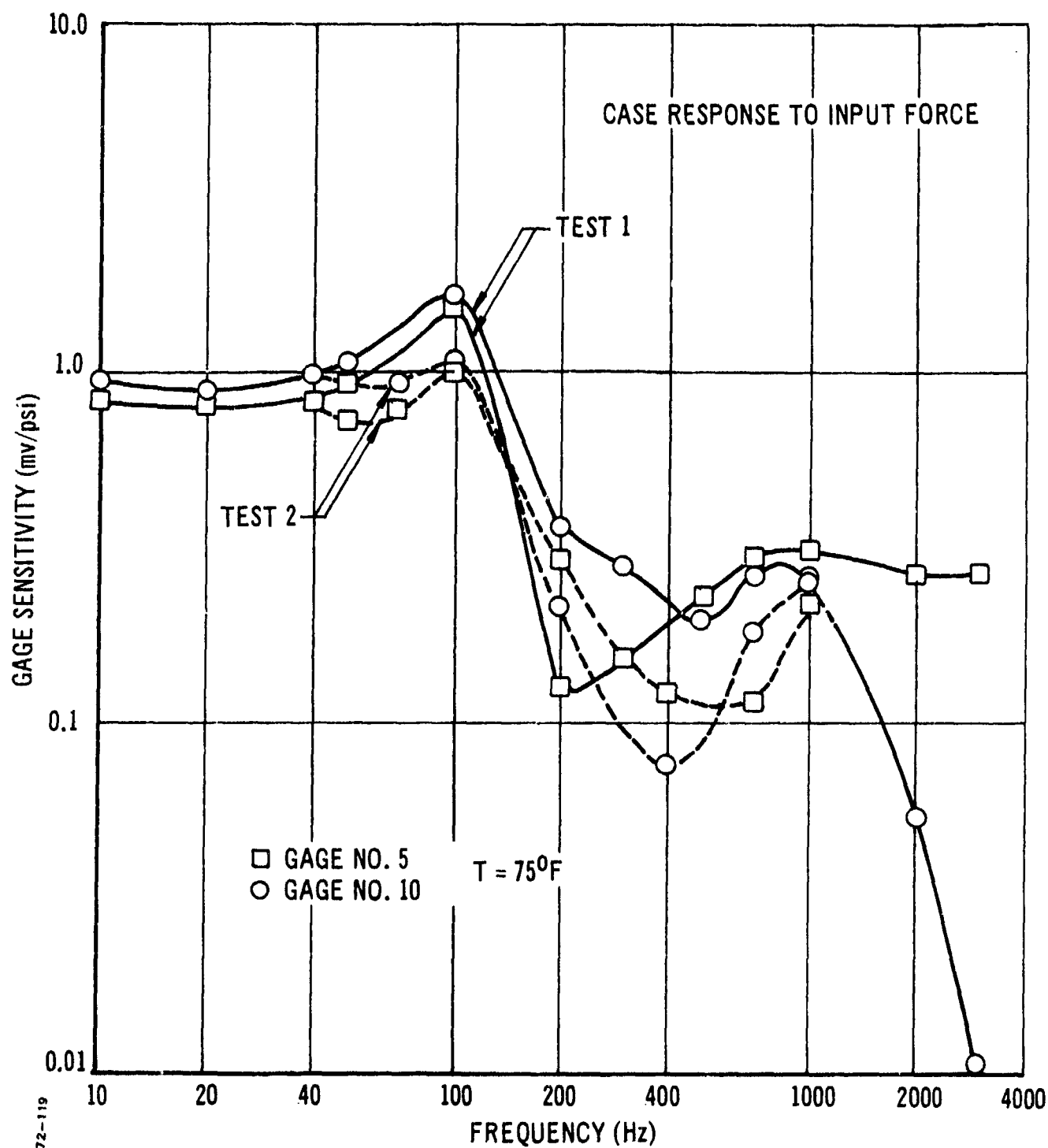
Figure 40. Comparison Between Gage Response to Input Force Ratio for Two Test Runs.
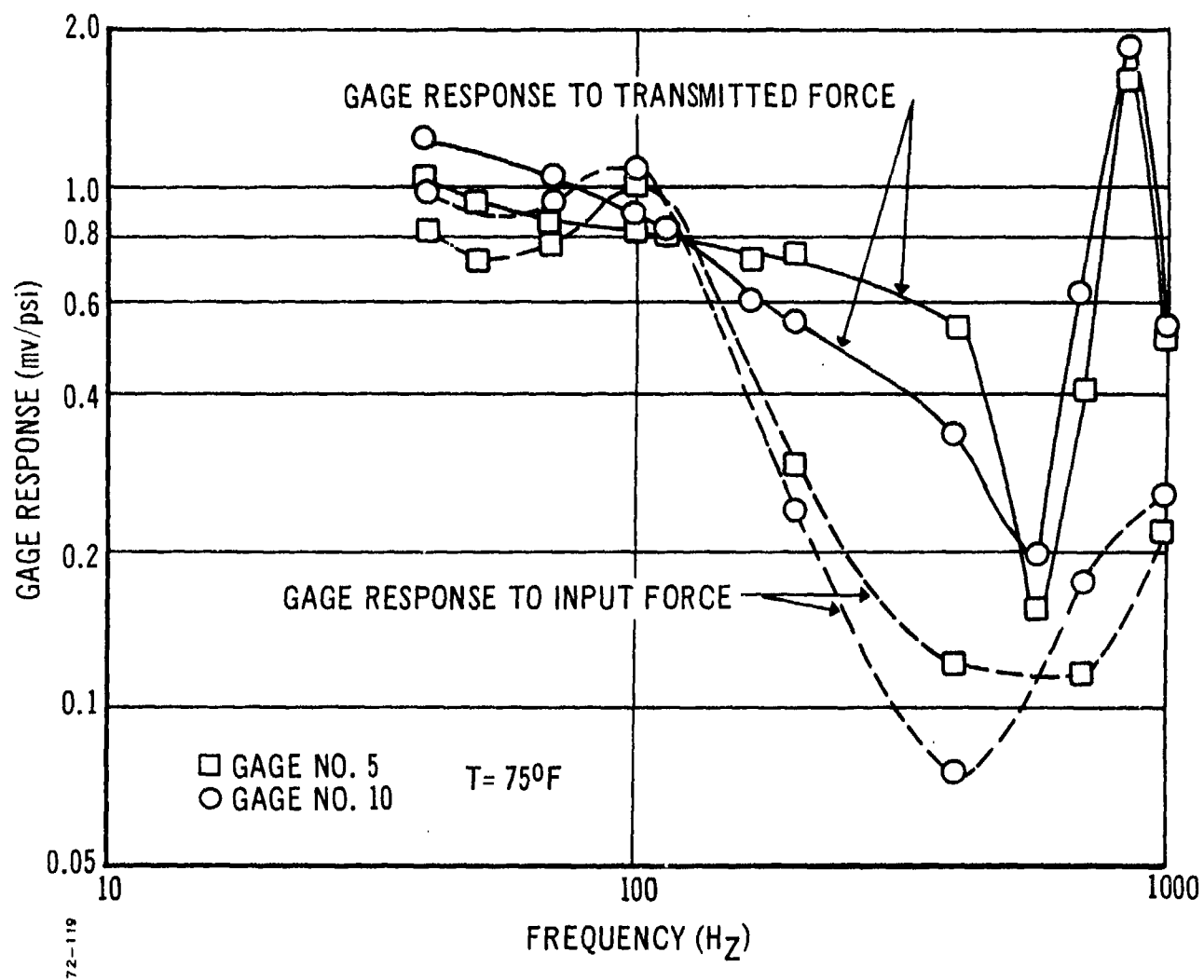
Figure 41. Comparison Between Gage Response to Input and Output
Force, 75°F Vibration Tests.
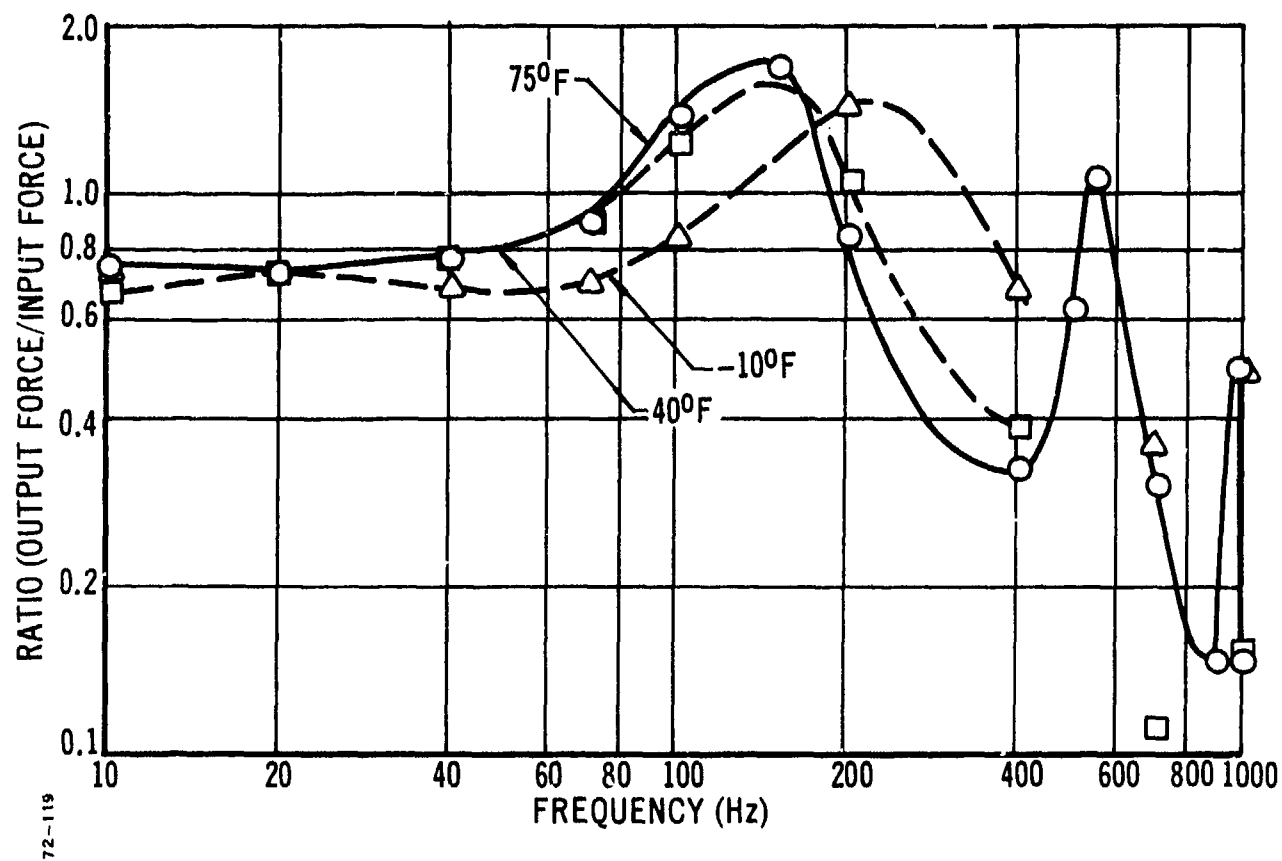
Figure 42. Output/Input Force Ratio versus Frequency; 75, 40, and -10°F
Uniaxial Vibration Tests.

- The input gage also recovers its response more rapidly, and then maintains its response at the higher frequencies, i.e., above 1000 Hz.

- The output gage shows almost no output at the higher frequencies because no force is transmitted through the test specimen.

Both sets of data show that the slight peak obtained at 100 Hz is not a pro or resonance because there is no accompanying change in phase angle. It is possible that the real peak in the response data would have been noted at 150 Hz, which is where the phase angle changes to 90 degrees, this being the system resonance. The behavior of the two gages is quite different after the initial resonance, as will be observed from the phase angle values given in Table VI. Gage No. 10, the input gage in this test series, remains in phase with the input force at all frequencies except 200 Hz. Most probably, the phase angle would have been observed to have shifted from 18 degrees at 100 Hz, through 90 and 180 degrees before coming back into phase with the input force at 400 Hz. There is also insufficient data to show if the gage response changed significantly when the frequency passed through the higher resonance frequencies.

Gage No. 5, the output gage, is in phase with the input force at the low frequencies below 150 Hz. Above this resonance, the phase angle shifts to the 180-degree value that should be obtained if the input of the specimen and the output have just passed through a resonance. Between 700 and 1000 Hz this gage also shows a 180-degree phase change, whereas the input gage does not appear to show any change.

Bearing in mind the performance of the two gages with respect to the input force, it is interesting to note their behavior with respect to the output force as shown in Figure 41. The response relative to the input force is also shown in this figure to aid the comparison. The most important aspect of these data is the absence of any peak in the response data for both gages during the fundamental resonant mode at 150 Hz. There is no peak and there is no phase change, and the test was conducted to investigate this resonance. It appears, therefore, that the gages are following the force transmitted through the specimen at the lower test frequencies. This was expected in the case of the output gage (No. 5) but was not anticipated for gage No. 10, attached to the input end of the specimen.

These data suggest that the fundamental resonant mode is one in which the whole of the propellant of the test fixture acts as a simple spring with the external mass resonating on the spring.

Gage No. 5 (output gage) remains in phase with the output force through the 570-Hz resonance, although it shows a dip in the response curve at this frequency. The input gage (No. 10) meanwhile showed a 180-degree change in phase angle from 200 to 400 Hz, which suggests that a resonance was in fact missed between these frequencies. Furthermore, both gages then show a 180-degree phase change between 570 and 700 Hz, corresponding to the minima in both response curves. A pronounced peak in the response

curves of both gages was obtained at 850 Hz with, however, only gage No. 10 showing a marked phase change. It is possible that the resonance for the output gage (No. 5) occurred at a slightly higher frequency than 850 Hz, inasmuch as the phase change from 850 to 1000 Hz was 160 degrees.

The higher resonances in the uniaxial test fixture appear to include the mass of the propellant in the mode as an inertia term, so that the ends of the specimen become 180 degrees out of phase at resonance. Also, the fact that the gages at both ends of the specimen show a reduction in sensitivity suggests that most of the output force in this frequency range is inertial and does not affect the gages.

It is possible that the pronounced resonance obtained at or near 850 Hz is related to the pronounced force ratio peak observed at 975 Hz. However, this is not certain; the only sure thing about the data in this frequency range is that both input and output gages are affected almost identically, which would seem to preclude the gage itself as the cause of the resonance.

In fact, close examination of the gage response data obtained from this test series does not indicate a problem area with the diaphragm gages. It is, of course, entirely possible that the specimen-vibrator resonances were so strong that they obscured any effects of the gages alone. It is also possible that the tests were not continued to a sufficiently high frequency. Unfortunately, testing at frequencies higher than 1000 Hz proved extremely difficult and the data obtained did not seem to warrant the trouble required.

Similar series of vibration tests were performed at two additional temperatures: +40 and -10°F. The tests were conducted with the latest experimental apparatus arranged as for the last series of 75°F tests just described. Thus, gage No. 10 was the input gage and gage No. 5 was the output gage. The test data obtained are presented in Tables VII through X and in Figures 42 through 44.

Figure 42 shows the output force/input force ratio as a function of frequency for all three temperatures. At the lower frequencies it seems that there is little difference between the 75 and 40°F data, unless there is a slight increase in the resonant frequency. The -10°F data show conclusively that there is a real upward trend in the resonant frequencies, no doubt caused by the increasing propellant modulus at the lower frequencies. The precise resonances were not followed in these tests, so that the higher frequency resonances were not determined. An examination of the data of Figure 42 suggests that the analysts may be correct in predicting that the system response at different temperatures may not be derived from the use of "shift principles". The shapes of the curves for the three temperatures are sufficiently different that merely translating them along the log frequency axis will not produce superposition.

The gage response curves for 40 and -10°F are presented in Figures 43 and 44, respectively. Examination of these figures will show that the gage response does not change drastically with temperature; the trends

TABLE VII

CYCLIC FORCE TRANSMISSION THROUGH UNIAXIAL
SPECIMEN AT 40°F

Frequency (Hz)	Input Force (lb)	Output Force (lb)	Phase Angle (deg)	Output ÷ Input
10	15.0	10.0	0	0.67
.20	16.0	11.5	0	0.72
40	17.1	13.5	0	0.79
70	18.0	16.0	0	0.89
100	17.8	22.0	14	1.24
200	25.0	26.0	130	1.04
400	25.6	10.0	173	0.39
700	24.4	2.75	180	0.11
1000	9.75	1.50	330	0.15

TABLE VIII

DIAPHRAGM GAGE RESPONSE TO INPUT AND OUTPUT
FORCES AT 40°F

Freq (Hz)	Gage No. 5 Response (mv/psi)	Gage No. 5 Phase Angle (deg)	Gage No. 10 Response (mv/psi)	Gage No. 10 Phase Angle (deg)	Gage No. 5 Response (mv/psi)	Gage No. 5 Phase Angle (deg)	Gage No. 10 Response (mv/psi)	Gage No. 10 Phase Angle (deg)
	◄─── Relative to Input Force ───►				◄── Relative to Output Force ───►			
10	0.60	0	0.90	0	0.89	0	1.35	0
20	0.52	0	0.77	0	0.72	0	1.07	0
40	0.58	0	0.81	0	0.95	0	1.02	0
70	0.72	26	0.94	13	0.81	26	1.05	13
100	1.01	14	1.01	22	0.82	0	0.82	7
200	0.83	130	0.55	144	0.80	0	0.53	14
400	0.18	173	0.08	43	0.46	0	0.20	227
700	0.12	206	0.14	51	1.06	26	1.28	231
1000	0.30	302	0.24	94	1.94	330	1.53	124

Gage No. 10 = input; Gage No. 5 = output

TABLE IX

CYCLIC FORCE TRANSMISSION THROUGH UNIAXIAL
SPECIMEN AT -10°F

Frequency (Hz)	Input Force (lb)	Output Force (lb)	Phase Angle (deg)	Output ÷ Input
10	15.9	12.0	0	0.76
20	16.4	12.0	0	0.73
40	17.5	12.0	0	0.68
70	18.52	13.0	0	0.70
100	17.85	15.0	14	0.84
200	25.6	37.0	36	1.45
400	26.3	18.0	158	0.68
700	25.0	9.0	310	0.36
1000	10.0	5.0	298	0.50

TABLE X

DIAPHRAGM GAGE RESPONSE TO INPUT AND OUTPUT
FORCES AT -10°F

Freq (Hz)	Gage No. 5		Gage No. 10		Gage No. 5		Gage No. 10	
	Response (mv/psi)	Phase Angle (deg)	Response (mv/psi)	Phase Angle (deg)	Response (mv/psi)	Phase Angle (deg)	Response (mv/psi)	Phase Angle (deg)
	← Relative to Input Force →				← Relative to Output Force →			
10	0.52	0	0.60	0	0.68	0	0.79	0
20	0.58	0	0.58	10	0.79	0	0.79	0
40	0.54	0	0.57	19	0.78	0	0.84	0
70	0.51	0	0.44	13	0.73	0	0.63	0
100	0.65	0	0.53	22	0.78	14	0.63	-7
200	1.11	43	0.77	43	0.77	-7	0.53	-7
400	0.31	158	0.06	115	0.45	0	0.087	43
700	0.13	154	0.088	103	0.35	156	0.25	207
1000	0.22	194	0.16	58	0.44	200	0.31	240

Gage No. 10 = input; Gage No. 5 = output
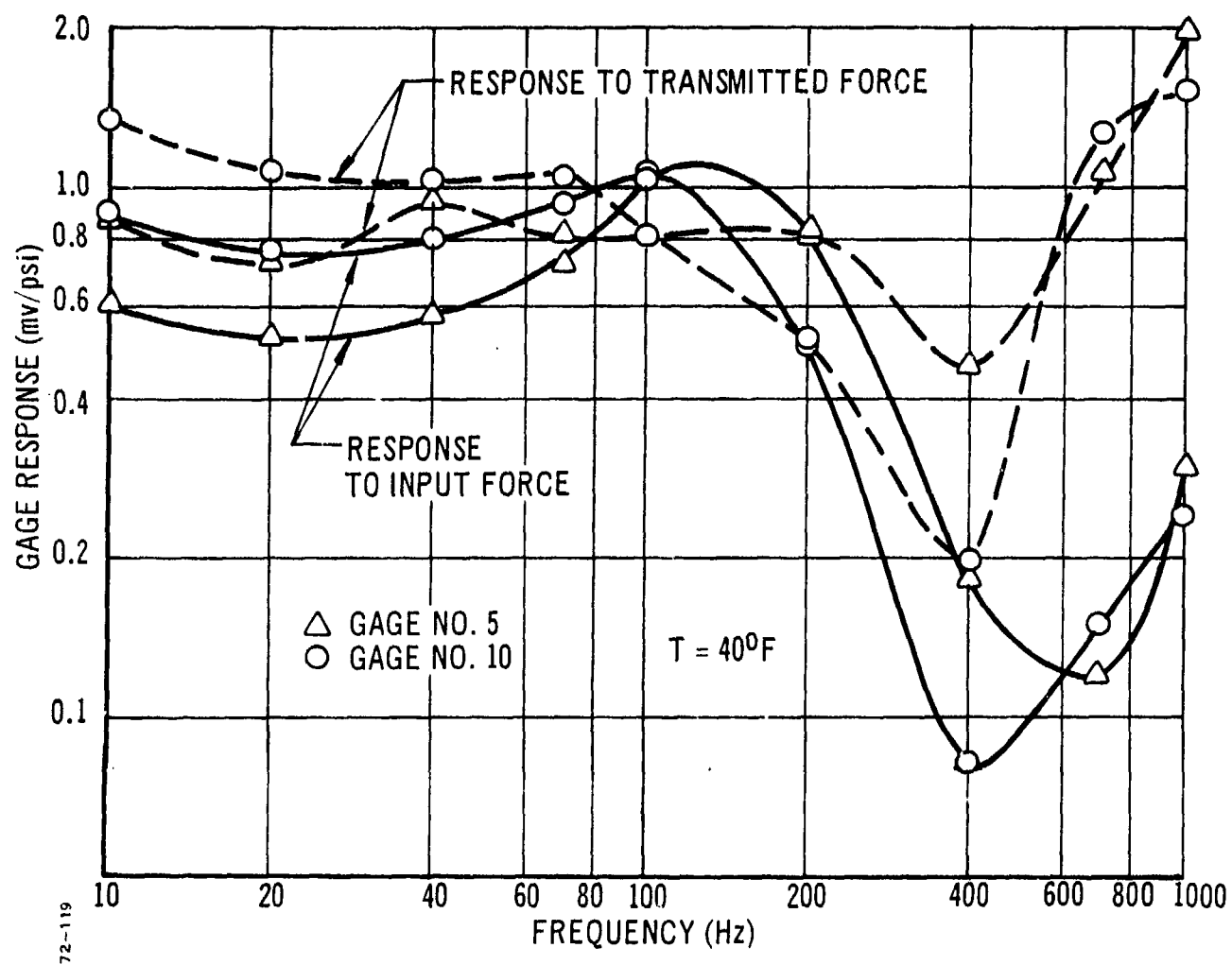
Figure 43. Gage Response to Input and Output Force versus Frequency,
Uniaxial Vibration Tests at 40°F.
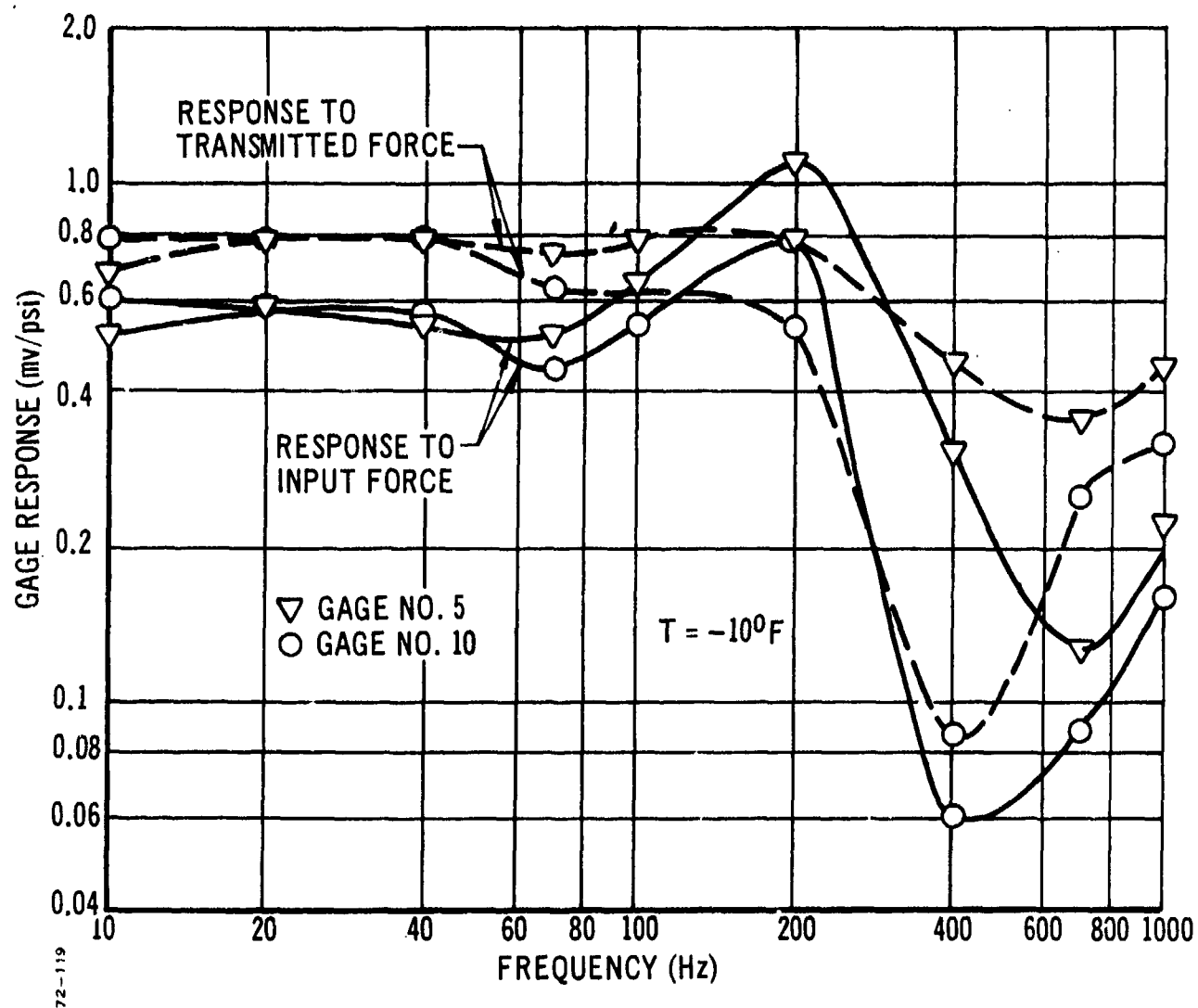
Figure 44. Gage Response to Input and Output Force versus Frequency, Uniaxial Vibration Tests at -10°F.

noted for the 75°F data and discussed at some length are also found in the lower-temperature data.

The gage response is found to be less at -10°F, as would have been predicted on the basis of the higher modulus for the propellant. Also, in general, there seems to be less difference between the gage response curves for the input force and the output force. However, it should be remembered that this may possibly be due to the fact that the tests were not conducted at the system resonances, as were the 75°F tests. Certainly, though, it may be stated that there does not seem to be a greater problem in obtaining the dynamic test data at the lower temperatures than there was at ambient temperature.

d. Comparison with Analysis

The analysis of the uniaxial test fixture containing the diaphragm gage unfortunately did not include the additional inertia terms caused by the moving parts of the vibrator and the coupling rods. This is not surprising in view of the fact that these terms were unknown before the tests were begun. Consequently, the analysis predicts that the important system resonances should occur at much higher frequencies than were obtained experimentally. The experimental data did show that the diaphragm gages would in fact work very well over the frequency range from 10 to 1000 Hz, even under relatively trying conditions with real-life resonant modes occurring. As well as can be determined, and as predicted, the gages do not seem to have either modified the system resonances or to have created new resonances. This is difficult to be dogmatic about because the tests were not continued into the high frequency range where theory predicts that the resonance should occur. Also, the experimental data are difficult to interpret.

The data and the analysis have suggested that there should be a reasonable range of frequencies over which the diaphragm gage embedded in propellant should work very well. This frequency range would appear to extend to 1000 Hz at ambient and relatively moderate cold temperatures (-10°F)

8. WAVE PROPAGATION STUDIES WITH DIAPHRAGM GAGE

a. Introduction

Wave propagation analyses of the gage neighborhood were performed, in which the gage was considered to be rigid and the 150-psi diaphragm gage was modeled. Both the gage and the propellant were assumed to be linearly elastic. The gage was titanium and the following material properties were used for the propellant:

Shear modulus, G (psi)	= 10,000
Poisson's ratio, ν	= 0.485
Mass density, ρ (lb-sec^2/in.^{4})	= 0.0001603

Figure 45 depicts the finite element model of the rigid gage inclusion, and Figure 45A illustrates the idealization, including the gage modeled as a thin
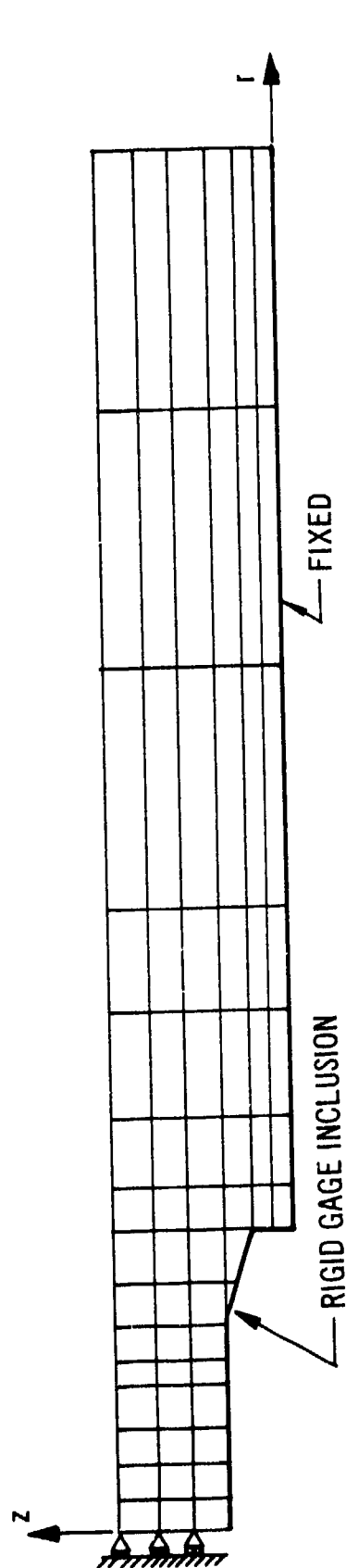
Figure 45. Finite Element Model of Gage Neighborhood, Rigid Gage.
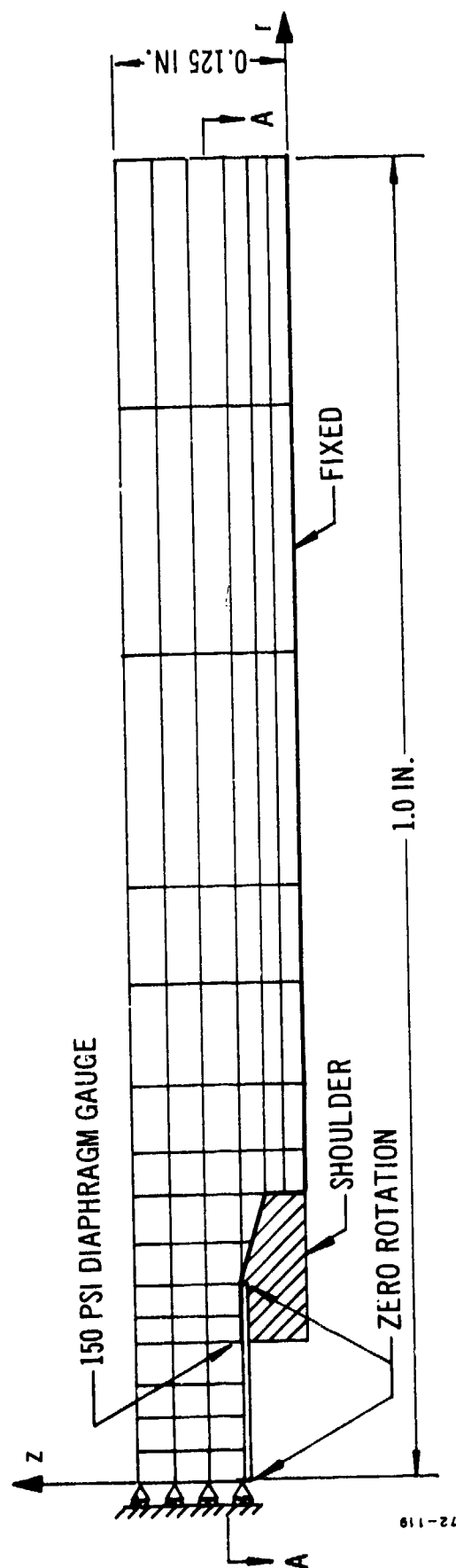
Figure 45A. Finite Element Model of Gage Neighborhood, Flexible Gage.

72-118

-46-

LOCKHEED PROPULSION COMPANY

plate. The diaphragm was modeled with plate elements and there is some kinematic incompatibility in interconnecting them with continuum elements. (Such incompatibility exists in all analyses performed with plate elements modeling the diaphragm.) In both analyses the input is a step pressure of 1 psi applied to the upper edge and propagated down toward the gage. A time increment of 54×10^{-6} sec was used and each analysis was carried out for six time steps. A dilatational wave transverses 0.025 inch, the axial dimension of each of the upper three elements, in one time step. Thus, the duration of the analysis permits the pressure wave to impinge upon the gage, reflect, and return to the free edge. The analyses were run on the DYNA 2D Program, which has been described in an earlier report, Reference 5. The equations of motion were solved by means of an explicit algorithm.

b.   Rigid Gage Model

Because of the geometry of the rigid gage inclusion configuration, one would expect the region immediately above the gage to behave as if a one-dimensional wave had reflected off a fixed boundary, in which the reflected wave superimposes, with like sign, upon the incident wave, causing in the case of a step pressure input, a doubling of the axial stress component. The analysis corroborates this, indicating that dispersive waves originating in the shoulder area play no significant effect in disturbing the pattern of a one-dimensional response during the duration of the computer analysis. In fact, the four interior elements immediately above the gage experience exactly the doubling of the step pressure, causing an axial stress of -2.0 psi after reflection. The radial and tangential components register values of -1.88 psi after reflection, due to the Poisson effect. There is no shear stress.

c.   Elastic Gage Model

Modeling the diaphragm as an elastic plate presents computational problems, because the successful capturing of wave propagation phenomena depends heavily upon the regularity of the finite element grid. The thinness of the plate compared with the axial dimension of the continuum elements above it and, in addition, the faster wave speed in titanium, cause the detailed response occurring immediately after impingement upon the diaphragm to be lost in the computer analysis. However, exploiting the geometry, we may perform a one-dimensional wave analysis in the region of the gage to obtain qualitative short-time results.

The gage diaphragm is modeled as a layer of material bonded to the free surface of a propellant half-space, in which a plane wave propagates in a direction perpendicular to the interface surface. A step pressure wave will cancel itself upon reflection from a free surface, and doubles when reflected off a rigid boundary. The effect, in our case, of the diaphragm is to initially reflect the pressure wave, amplifying it approximately 1.85 times. That is, the properties of titanium make the plate appear to be almost rigid compared with the propellant. The wave transmitted into the gage reflects off the free boundary and reimpinges upon the interface, reducing the existing value of axial stress there by 15 percent. The wave in the diaphragm continues to reflect, each time reducing its magnitude and that in the propellant as it impinges upon the interface. The effect is illustrated in

-98-

Figure 46. Thus it is obvious that the diaphragm very quickly changes the character of the solution from that of a fixed boundary to approximately that of a free boundary. In this case, the stress state corresponding to the absence of a diaphragm is completely altered by the presence of the gage.

d. Numerical Analysis Results

Numerical finite element results are presented in Figures 47 and 48, depicting the pressure wave in the row of elements above the diaphragm. Figure 47 shows the axial stress as the discontinuity surface impinges upon the diaphragm. Figure 48 corresponds to the instant after the reflection when the pressure wave arrives at the next interface above the diaphragm. The interior three elements register essentially zero stress, corresponding to the one-dimensional analysis after the decay of the perturbation due to the diaphragm. Immediately beyond these elements, the doubling effect, due to the rigid gage shoulder, is visible. An elastic shoulder would change this to 1.85 for the time durations shown. Farther out, the incident wave is unaltered, except at the outermost element, which is slightly influenced by the proximity of the free boundary of the test specimen.

The numerical experiment indicates that a diaphragm gage cannot be expected to respond to wave pulse inputs. In measuring waves or other high-frequency content loadings, other gage types should be used, e.g., quartz crystals, etc.

In experimental measurements, a gage response will be noted after reflections within the test specimen initiate a vibratory motion. These readings, however, can not be correlated to the initial pass of the wave front; that is, the measured response cannot be inverted to give a well-behaved initial pulse form. Several pulse forms will lead to the same response, at least to the degree of accuracy that it can be measured.

e. Experimental Shock Test Data and Comparison with Analysis

To verify the predictions of the wave propagation analytical studies, a series of experimental pendulum impact tests was conducted with the uniaxial test specimen No. 2, containing two working 150-psi diaphragm gages. The experimental tests were conducted with the apparatus shown in Figure 49, which was fabricated following that used by Durelli and Riley in Reference 4. The test runs were made with the weight pulled back a distance varying from 2 to 8 inches. Cathode ray oscilloscope records of the dual trace were obtained, each gage trace being obtained against the CEC accelerometer record and the composite record, shown in Figure 50, being made from the various two-trace photographs.

Figure 50 shows typical data traces for the accelerometer, and the two gages with No. 10, the input gage, and No. 5, the output gage.

The data traces shown in Figure 50 must be examined in the light of the analytical gage performance predicted in the previous section of the report. The input waveform, as shown by the accelerometer, typically
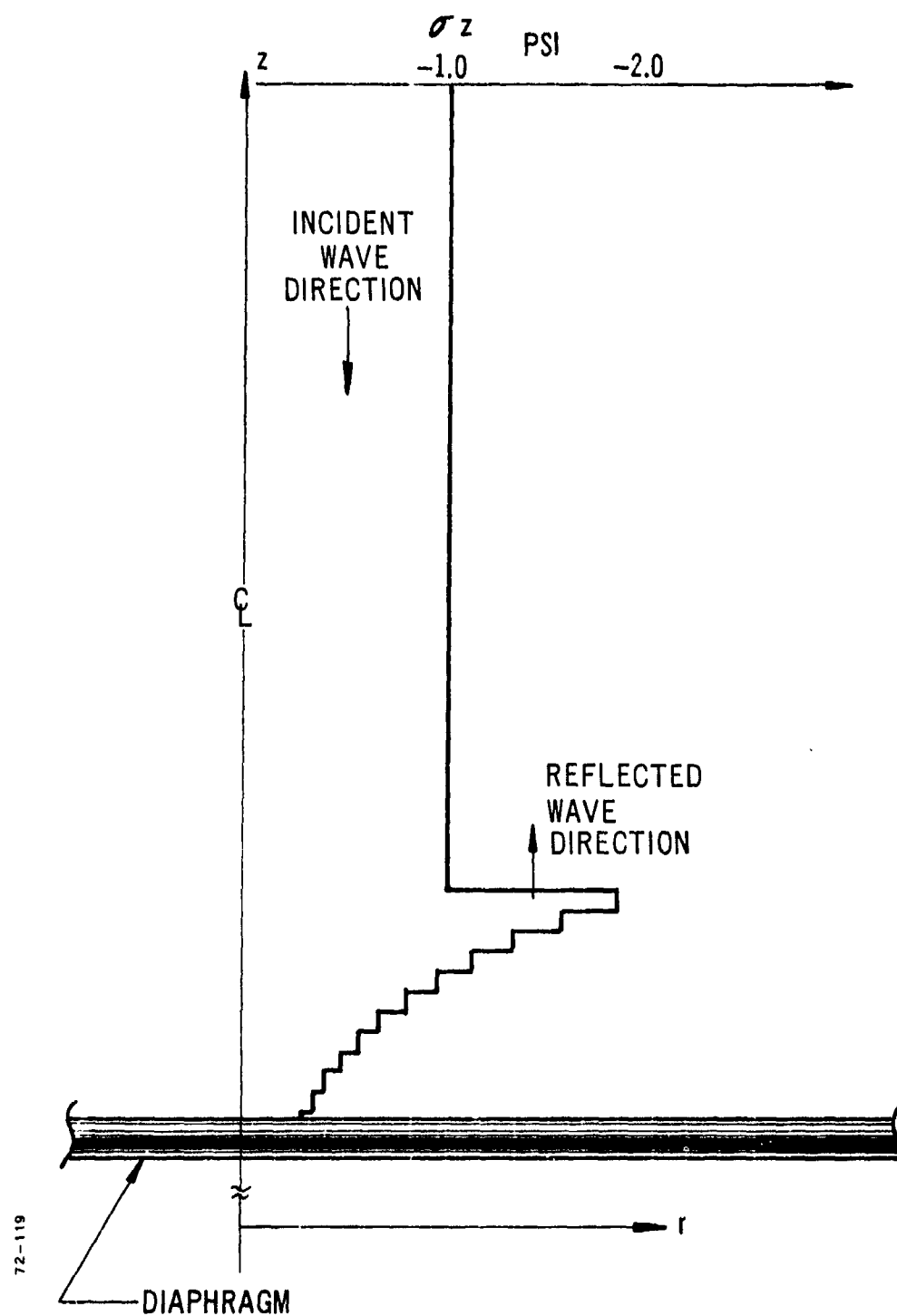
Figure 46.   One-Dimensional Wave Analysis of Gage Neighborhood.
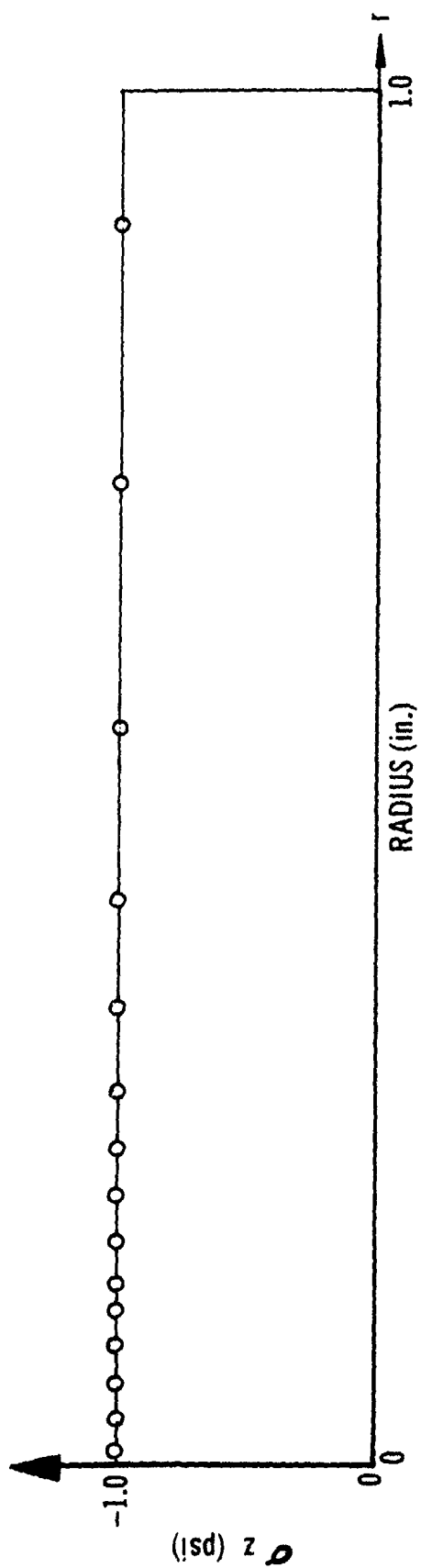
Figure 47. Axial Stress versus Radius at Section A-A; Time = 0.162 x 10⁻⁵ sec.
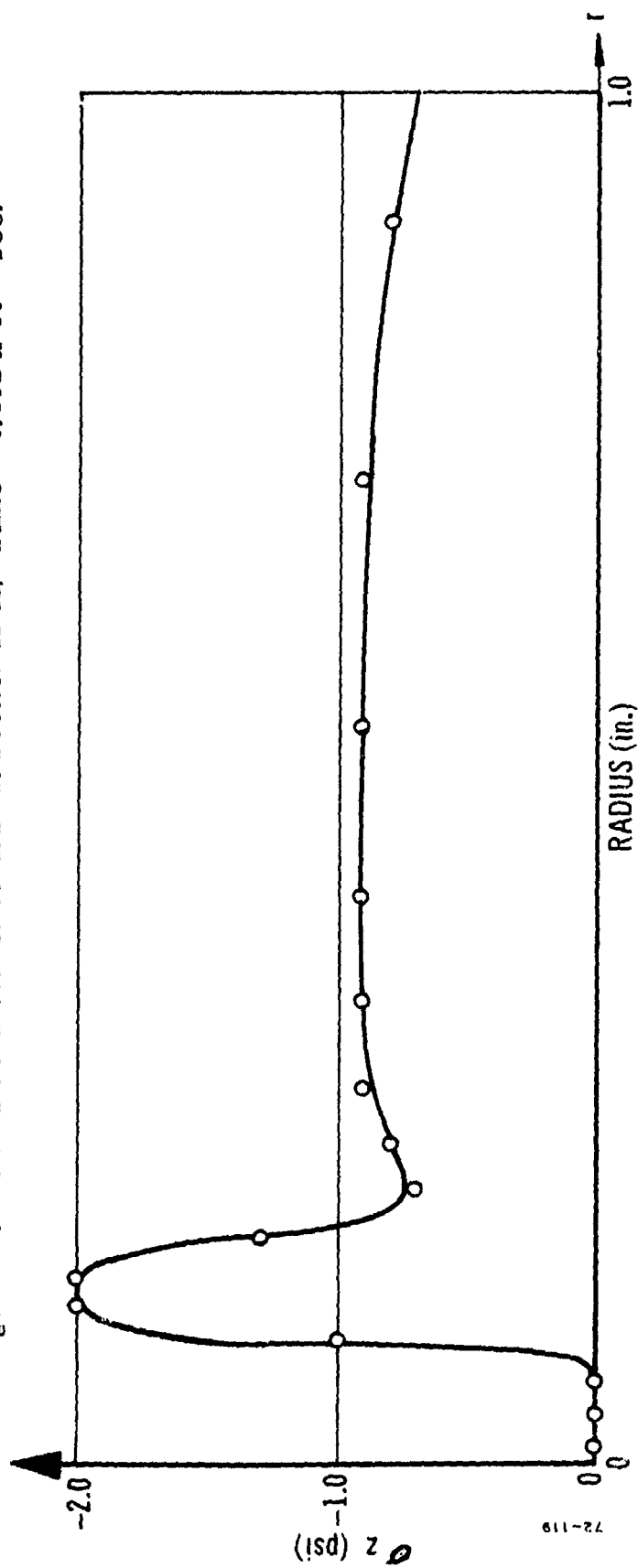
Figure 48. Axial Stress versus Radius at Section A-A; Time = 0.216 x 10⁻⁵ sec.
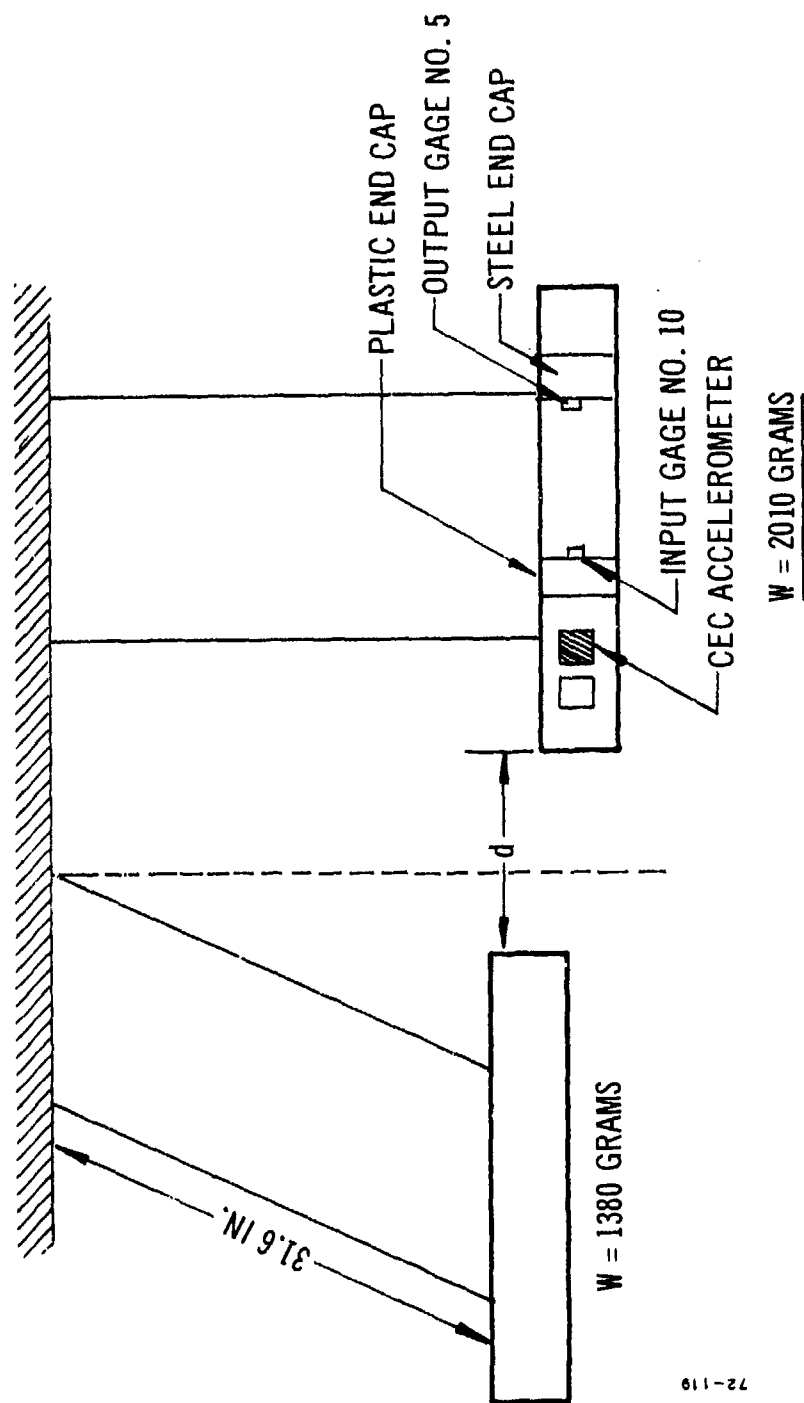
Figure 49. Sketch of Pendulum Shock Test Apparatus.
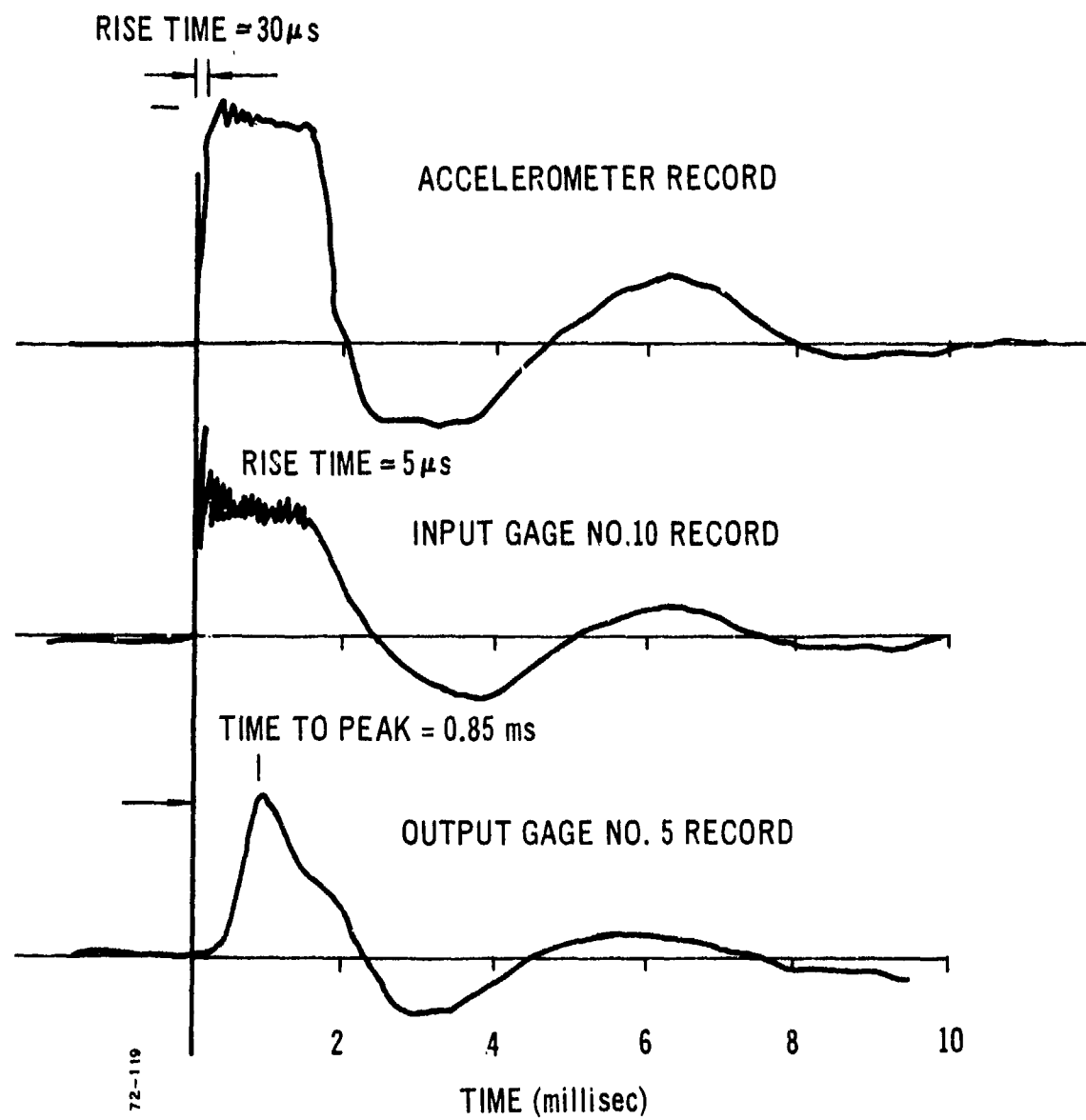
Figure 50. Typical Data Traces for Pendulum Shock Tests.

had a rise time of approximately 30 microseconds and a fairly flat acceleration level for an additional 2.0 milliseconds, with a rapid fall through zero stress to a negative trough of about one-half to one-third of the initial peak. This negative pressure is held for about 1.5 to 2.0 milliseconds, and the wave then becomes positive again. This oscillation appears to die out within two complete cycles as shown.

Gage No. 10, the input gage, follows the initial pressure input rise very well (slightly better than the accelerometer used, in fact). An examination of the initial pressure pulse does reveal the cyclic oscillations predicted theoretically before the signal reaches the flat response region. The gage output waveform thereafter follows the accelerometer waveform reasonably well.

The signal waveform obtained from gage No. 5, the output gage, is distinctly different from that of the accelerometer and from that of gage No. 10. There is first a definite delay of approximately 0.85 millisecond (while the wave front travels along the propellant), and then a single sharp peak is shown by the gage, which falls very rapidly to zero stress at about 2.4 milliseconds and thereafter follows the other two output signals.

It appears that the propellant damping preferentially attenuates the higher frequency gage output, reducing the square shape of the input pulse to the single spike shown and thereafter becoming more nearly a sine wave.

The acceleration obtained during the impact tests is a linear function of the initial displacement of the striker weight, as is shown in Figure 51, wherein the accelerometer output is plotted versus displacement. The mean stress applied to the gage mass is simply given by the acceleration multiplied by the mass. Figure 52 shows the amplitude of the initial peak in the output of gage No. 5 as a function of impact stress. There is a clear relationship between the amplitude and the stress, as will be seen by the data of Figure 52. Because of experimental difficulties associated with triggering the oscilloscope, a similar sequence of data was not obtained for the input gage No. 10.

A later series of impact tests was conducted with a thin sheet of rubber between the striker mass and the gage mass to eliminate the ringing in the accelerometer and gage No. 10 output waveforms during the initial passage of the wave pulse. The effect of the rubber sheet is to reduce the impact acceleration and slow down the initial rise time. Thus, the time to peak acceleration is increased to approximately 0.2 millisecond and the peak acceleration for a 6-inch travel of the striker weight reduces to 21.5 g. The accleration versus displacement with the rubber sheet is also given in Figure 51. Figure 53 shows the peak signal amplitude for gage No. 10 versus impact stress.

It is interesting to note that the sensitivity of the two gages, as determined from the slope of the lines in Figure 52 and 53, is 0.50 and 0.667 mv/psi, respectively, for gage No. 5 and gage No. 10. These sensitivities compare very well with the vibration sensitivities given earlier in Figure 40,
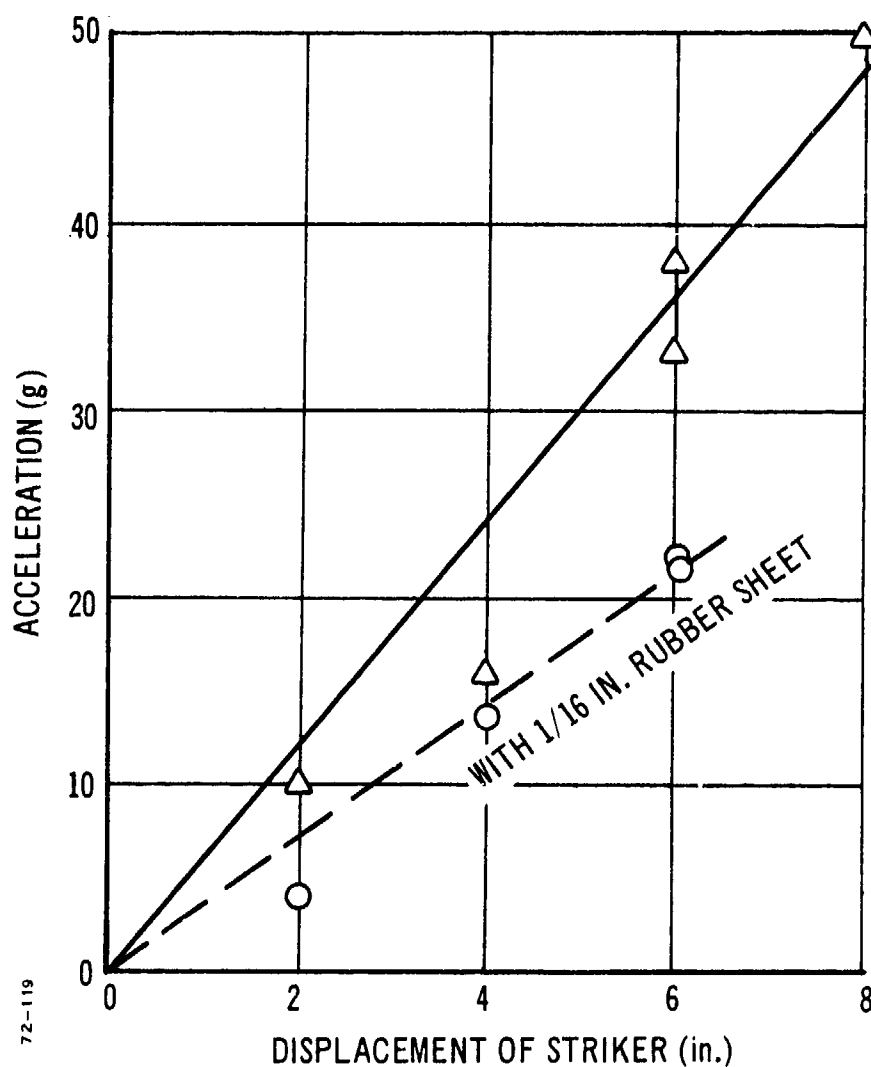
Figure 51. Impact Acceleration versus Striker Displacement.
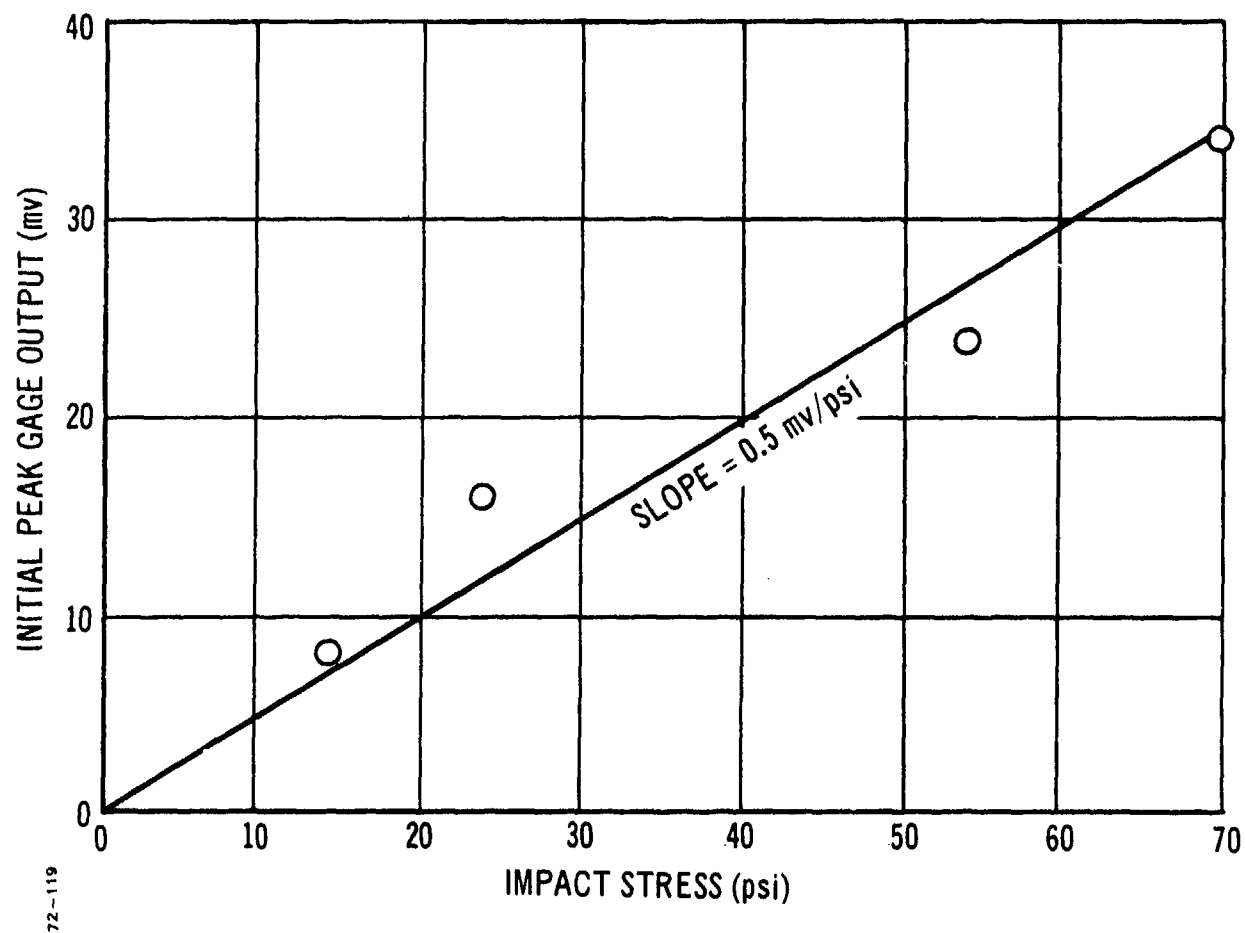
Figure 52.   Gage No. 5 Initial Peak Amplitude versus Impact Stress.
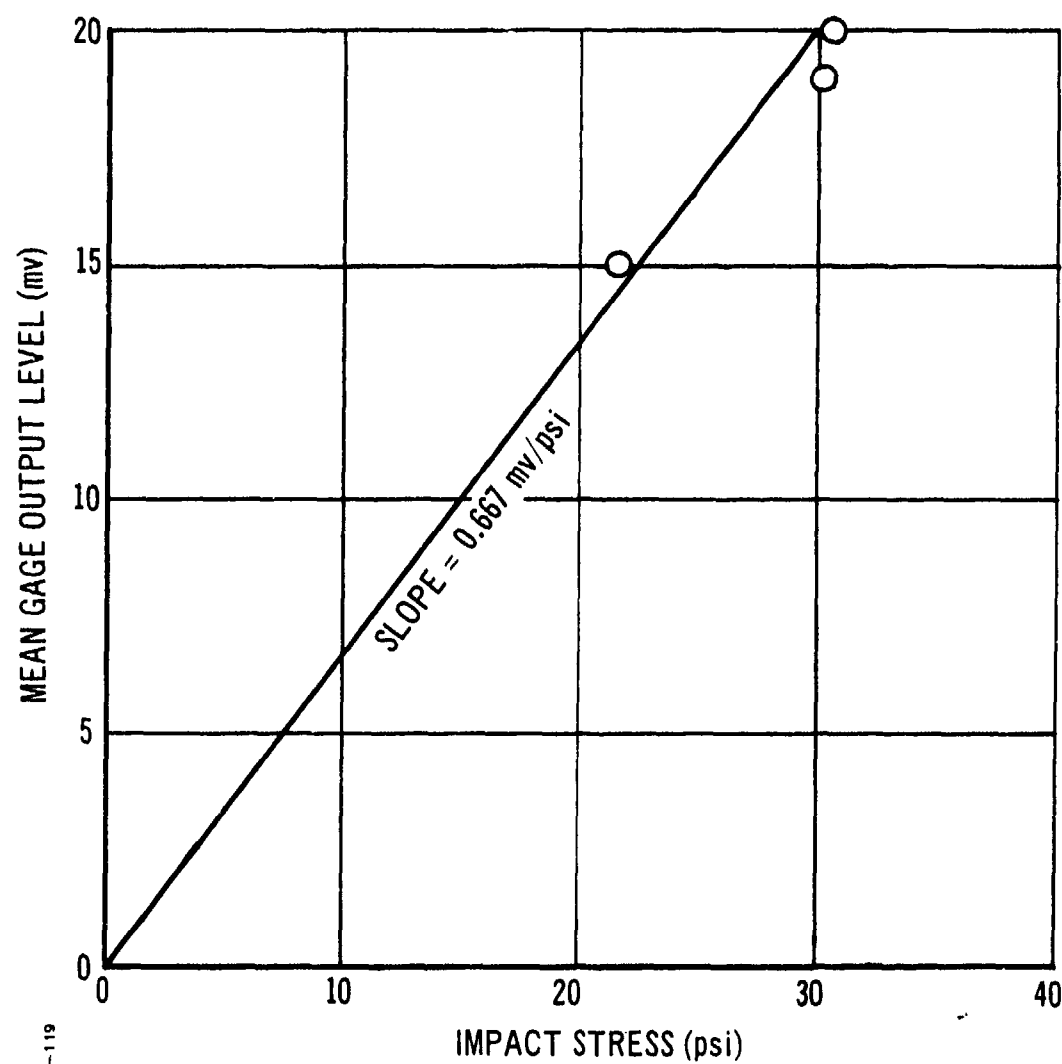
Figure 53. Gage No. 10 Peak Amplitude versus Impact Stress (with Rubber Sheet).

and strongly suggest that the very pessimistic view of the capabilities of the miniature diaphragm gage as a means of detecting high-frequency stresses is too severe. It seems highly probable that the device will respond to reasonably high-rate shock waves involving rise times in the millisecond range. The attenuation of the waves in propellant is so great that it is unlikely that extremely high-rate shock waves will be applied to the gages in a real-life situation.

SECTION IV

EMBEDDED SHEAR GAGE RESPONSE

1. DESCRIPTION OF GAGE AND OPERATING PRINCIPLES

The embedded shear gage considered in this Section is shown in Figure 54. It is the shear cube, and it consists of two strain-measuring sensors mounted perpendicular to each other and at 45 degrees to the mounting plane. Either foil strain gages or semi-conductor strain gages may be used in this shear gage, the latter devices producing a more sensitive shear-measuring gage.

The operating principle of this shear gage is based upon the measurement of the difference between the deformations of the diagonals of a cube of propellant. The strain gages are mounted along the directions of the diagonals so that they respond to some fraction of the strain applied to the cube. The gages are connected in a Wheatstone bridge circuit so that the bridge output is a measure of the difference in the strains in the two gages, as shown in Figure 55. Thus, the application of a normal stress to the cube will give zero output signal if the gage elements are well matched.

It is required to ascertain the relationship between the strain in the sensing elements (the strain gages) and the applied stress or strain in the propellant if the gage were not there.

Two analytical approaches to this problem were investigated. The first was an approximate, simple, closed-form analysis of a flat elastic ribbon enclosed in an infinite elastic sheet, performed by Professors M. L. Williams and W. S. Brown of the University of Utah.

The second analysis, performed by Professors Pister and Taylor of Mathematical Sciences Northwest, consisted of a three-dimensional finite element analysis of the actual shear cube configuration. The results of the two analyses are given next, and are compared with the experimental data in a later section.

2. ANALYSES OF SHEAR CUBE

a. Approximate Strain Analysis of a Flat Elastic Ribbon Enclosed in an Infinite Elastic Sheet

(1) Introduction

In support of an overall study of the strain gage sensitivity of a metallic ribbon in a soft rubber matrix, an approximate strain analysis is desired in order to assess the stiffening effect of the metal ribbon. Expressed alternatively, a strain-sensing element should not disturb the strain field it is sensing. On the other hand, this principle is contradicted to some degree in nearly all mechanical sensing devices. In metal gage elements, bonded to other metal elements, the effect is usually vanishingly

-109-

(A) LPC SHEAR STRAIN TRANSDUCER

(B) SHEAR CUBE CONFIGURATION
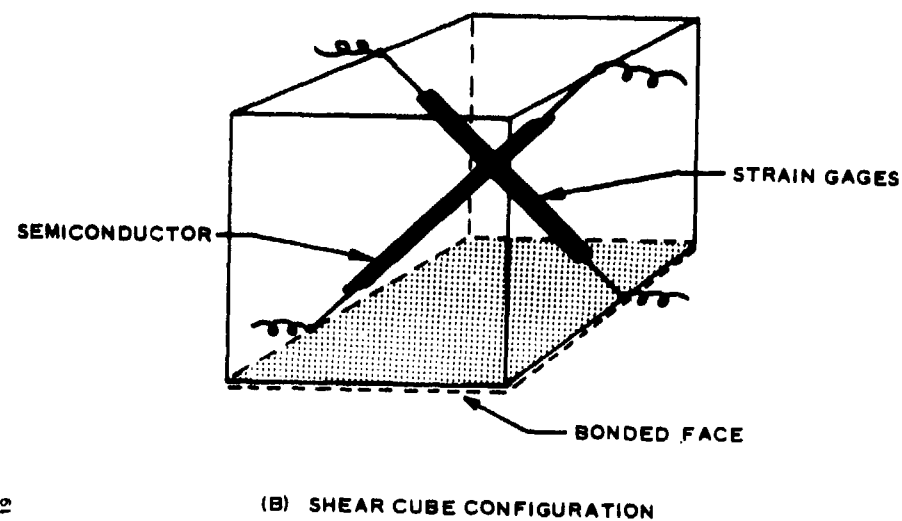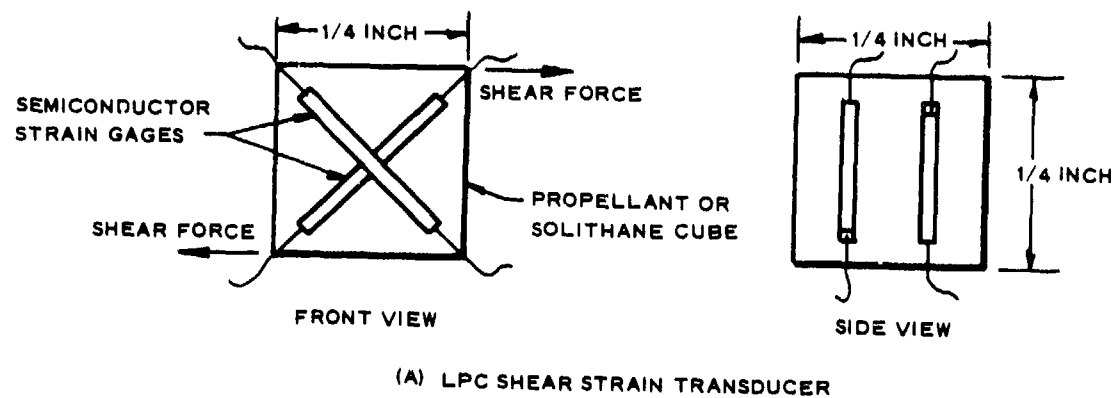
72-119

Figure 54. Shear Cube Configuration.

-110-
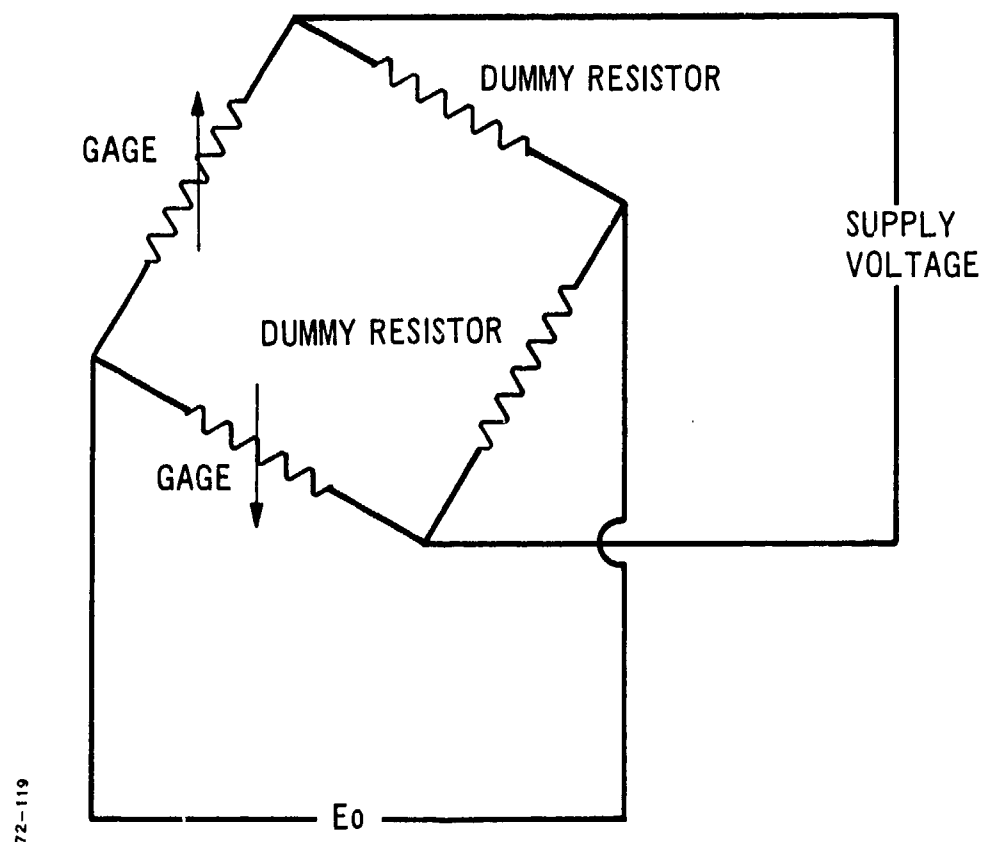
Figure 55. Wheatstone Bridge Circuit for Shear Gage,
            Shear Mode Connection.

small and, depending as it does upon essentially the stiffness ratio $EA/E'A'$, when the modulus ratio $E/E' \approx 0(1)$, then the sensitivity is mainly a function of the area ratio, A/A', of the matrix to gage. For the rubber-to-steel combination, however, the modulus ratio varies characteristically between 10^{-5} and 10^{-2} so that adjustments of the area ratio alone are often not sufficient to neglect the effect of the gage element stiffness.

Under these circumstances, if metallic sensing elements are to be used, it is then necessary to calibrate the response on the basis of a knowledge of those changes in the overall strain field in the rubber caused by the presence of the stiff metallic element. Whereas a reasonably precise elastic analysis can be expected when numerical computational techniques are used, notwithstanding the (mathematically) infinite strain concentrations that exist near the ends of the ribbon element, it would be convenient to have available an approximate but closed-form expression for the gage-matrix interaction for preliminary design purposes.

The purpose of this report is to indicate such a solution and to derive its simplest form, while providing the framework for future improvement in the event that numerical analysis proves unduly intractable or expensive.

(2) The Theorem of Minimum Potential Energy

The solution technique chosen is that of minimizing the potential energy of the combined media system (Ref 6). In its general form, one can deduce the best approximation to the displacement field in an elastic body as follows: First, an admissible set of displacement functions is selected that satisfies the boundary conditions on that part of the boundary over which the displacement boundary conditions are prescribed. Then the potential energy, $V(e_{ij})$, is expressed in terms of the displacements, i.e., their derivatives or strains, requiring $\delta V(e_{ij}) = 0$; specifically

$$\delta V(e_{ij}) = \int_{vol.} \left\{ \frac{\lambda}{2} \left[\epsilon_x^2 + \epsilon_y^2 + \epsilon_z^2 \right] + \mu \left[\epsilon_x^2 + \epsilon_y^2 + \epsilon_z^2 \right] + (\mu/2) \gamma_{xy}^2 \right\} d(vol)$$

$$- \int_{S_\sigma} \overline{\sigma}_{ij} \, \nu_j \, \overline{u}_i \, d \text{ (surface)} \tag{67}$$

where the barred quantities $\overline{\sigma}$ and $\overline{u}$ are the prescribed stresses and the assumed displacements on that part of the surface over which the stresses are given, S_σ. It is important to recognize that the admissible function set is not required to satisfy the equations of equilibrium. (If it did, the exact solution would result.)

(3) The Engineering Problem

The gage-matrix problem visualized is one of plane strain as shown in Figure 56.
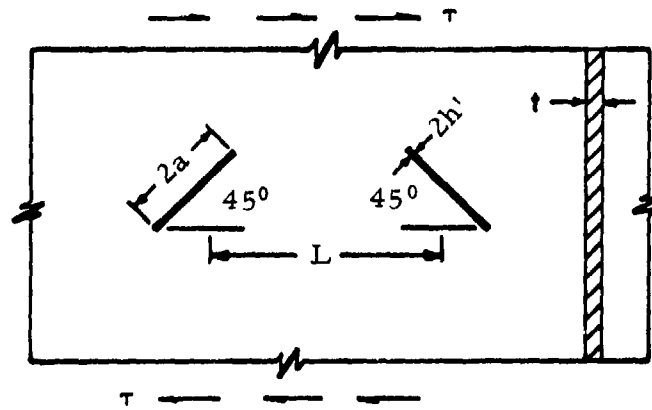
Gage: $E' \approx 10^7$ psi

$\alpha \approx 10^{-6}$ in./in./°F

$\nu' = 0.3$

Matrix: $E \approx 10^{-2}$ to 10^4

$\alpha \approx 10^{-5}$ in./in./°F

$\nu = 1/2$

Figure 56. Gage Configuration.

It is assumed that the length of the gage (of the order of $2a = 0.25$ in.) is small in comparison with the overall dimensions of the assembly and, further, that the gage thickness (of the order of $2h' = 0.0025$ in.) it itself small compared to the gage length. Finally, the gages shown in the figure are considered far enough apart so that their mutual interaction is negligible. From a practical standpoint, $L \gtrsim 2a$.

If the gage element is isolated and the applied shear stress resolved onto planes perpendicular to and parallel with the ribbon gage, one finds that there is no shear applied to the 45-degree resolved element of Figure 57
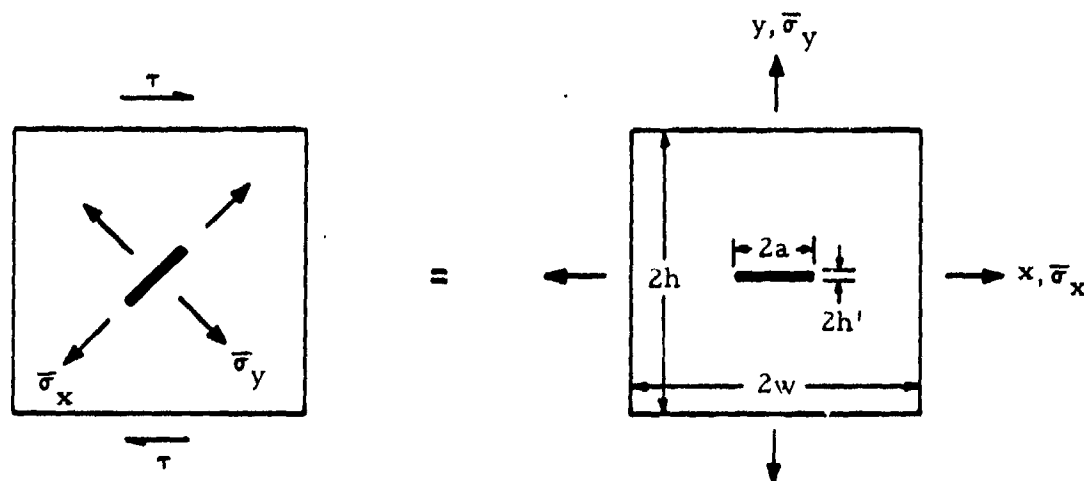
Figure 57. Gage Element Schematic.

and that $\overline{\sigma}_x = -\overline{\sigma}_y = \tau/2$. Hence the behavior of the gage element can be analyzed by studying the plane stress problem of a small, rigid, vanishingly thin inclusion in a bounding incompressible medium, subjected to a biaxial stress field.

(4) Limit Solutions

Considering the properties of the ribbon as denoted by primes, the first limit case is either: (1) that it has vanishingly small stiffness (or is rigid and completely unbonded) such that we recover the standard Griffith problem of a crack of length 2a in an infinite medium (Ref 7) for which the stress field is well known; or (2) the situation of matching material properties and the resulting completely homogeneous medium for which the displacements are

$$u_0(x, y) = E^{-1}\left[\overline{\sigma}_x - \nu\overline{\sigma}_y\right] x \equiv K_x \sigma_0 x \tag{68}$$

$$v_0(x, y) = E^{-1}\left[\overline{\sigma}_y - \nu\overline{\sigma}_x\right] y \equiv K_y \sigma_0 y \tag{69}$$

Indeed it is the latter situation that one desires to be sensed, and the one that will be disturbed by the presence of the element.

The other limit case of interest is for the situation in which the stiffness of the ribbon element is infinitely larger. This problem would be somewhat analogous to the Griffith problem except that along $y = 0$, instead of a free surface with $\sigma_y(x, 0) = \tau(x, 0) = 0$ for $|x| < a$, one would require $u(x, 0) = v(x, 0) = 0$ along $|x| < a$. This problem has been solved in terms of integral equations based upon the solution technique proposed by Ang and Williams (Ref 8). The result can be expressed in terms of Sonine integrals, and for example in the case of $\overline{\sigma}_x = 0$, and an incompressible medium, leads to the expression for the Airy stress function as

$$X(x, y) = \frac{2\nu\overline{\sigma}_y a}{15} \int_0^\infty (1 - 4ty)\, t^{-2}\, e^{-ty}\, J_1(bt) \cos tx\, dt$$

and in particular to a shear stress on the fiber of

$$\tau(x, 0) = -\frac{2\nu\overline{\sigma}_y a}{3} \frac{x/a}{\sqrt{a^2 - x^2}} \quad ; \quad |x| < a \tag{70}$$

or an associated average shear stress, τ_{av}, over the element of

$$\tau_{av} = -\frac{1}{3}\overline{\sigma}_y \tag{71}$$

Furthermore, one can easily deduce the stress normal to the axis if the ribbon at $|x| = a + |\epsilon|$ as

$$\sigma_y = \frac{1}{15} \frac{\overline{\sigma}_y}{\sqrt{2\epsilon/a}} \qquad \text{(rigid ribbon)} \tag{72}$$

which can be compared to the (Griffith) stress for vanishingly small ribbon rigidity of

$$\sigma_y = \frac{\overline{\sigma}_y}{\sqrt{2\epsilon/a}} \qquad \text{(completely flexible)} \tag{73}$$

thus implying a 15:1 stress ratio between the limits of rigidities.

Unfortunately these results are not of immediate value in calculating the strain gage sensitivity because if the ribbon is infinitely stiff, it can not move ($\epsilon_x = 0$) and there will be no area change and thus no resistance change to produce the electrical signal. Indeed, no mathematical analysis is required to make this deduction. On the other hand the specific limiting value of, say, the average shear stress on the gage which, in the elemental aircraft analysis shear lag sense, can be associated with the applied stress in the element of Figure 58
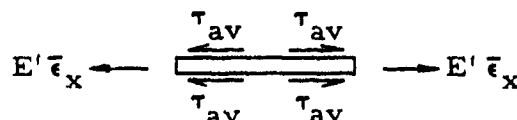
Figure 58. Applied Stress Element.

can give a bounding value for the gage element strain.

(5) Approximate Energy Analysis

The first consideration is to choose an admissible displacement set. Because no displacement boundary conditions are prescribed, there is essentially no restriction except intuitive ones to place upon them. These will be first symmetry conditions that

$$u(0, y) = 0 \tag{74}$$

$$v(x, 0) = 0 \tag{75}$$

and the physical condition that far from the ribbon the displacements should be identical to those that would result under the biaxial stress field if no gage were present, i.e., Equations (68) and (69). For these reasons, and with

-115-

an eye toward simplifying the resultant algebra, e. g., choosing $\exp(-\lambda|y|)$ instead of $\exp(-\lambda y^2)$, consider the simple set

$$u(x, y) = K_x \sigma_0 x \left[1 - c_1 e^{-|x|/a} e^{-\lambda|y|} \right] \tag{76}$$

$$v(x, y) = K_y \sigma_0 y \tag{77}$$

leading to strains of

$$\epsilon_x = K_x \sigma_0 \left[1 - c_1 e^{-|x|/a} \left(1 - \frac{|x|}{a} \right) e^{-\lambda|y|} \right] \tag{78}$$

$$\epsilon_y = K_y \sigma_0 \tag{79}$$

$$\gamma_{xy} = K_x \sigma_0 \lambda c_1 |x| e^{-\lambda|x|} e^{-\lambda|y|} \tag{80}$$

where one may note that the maximum of $\gamma_{xy}(x, 0)$ is at $x = a$. Hereafter, the absolute value signs will be dropped, because the calculations for this symmetric problem will be carried out only in the first quadrant.

The strain energy density in the matrix, assuming incompressibility ($\nu = 1/2$) and plane stress, is

$$W_m = (2E/3) \left[\epsilon_x^2 + \epsilon_x \epsilon_y + \epsilon_y^2 + (\gamma_{xy}/2)^2 \right] \tag{81}$$

$$= (2E/3) \left\{ \left[(K_x + K_y) \sigma_0 - K_x \sigma_0 c_1 \left(1 - \frac{x}{a} \right) e^{-(x/a) - \lambda y} \right]^2 \right.$$

$$- K_x K_y \sigma_0^2 \left[1 - c_1 \left(1 - \frac{x}{a} \right) e^{-(x/a) - \lambda y} \right]$$

$$\left. + K_x^2 \sigma_0^2 (\lambda^2/4) c_1^2 x^2 e^{-(2x/a) - 2\lambda y} \right\} \tag{81a}$$

which, after integrating over the quarter plane, leads to the strain energy of deformation in the matrix, U_m, as

$$U_m = \frac{2E}{3} \left[\left[K_x^2 + K_x K_y + K_y^2 \right] \sigma_0^2 wh \right.$$

$$- \left(2K_x^2 + K_x K_y \right) \frac{c_1 a^2}{\lambda a} \frac{w}{a} e^{-w/a} (1 - e^{-2\lambda h})$$

$$+ \frac{K_x^2 \sigma_0^2 c_1^2 a^2}{4 \lambda a} \left[1 - e^{-2\lambda h} \right] \left\{ \frac{1}{2} \left(1 + \frac{(\lambda a)^2}{4} \right) - \left[\frac{1}{2} - \frac{w}{a} + \frac{w^2}{a^2} \right. \right.$$

$$\left. \left. + \frac{(\lambda a)^2}{8} \left(1 + 2 \frac{w}{a} + 2 \frac{w^2}{a^2} \right) \right] e^{-2w/a} \right\} \right] \tag{82}$$

Next one calculates the strain energy in the ribbon, which is computed from its deformation, namely Equations (76) and (77) evaluated on the plane $y = 0$, or

$$u(x, 0) = K_x \sigma_0 x [1 - c_1 e^{-x/a}] \tag{83}$$

$$v(x, 0) = 0 \tag{84}$$

such that in the ribbon, where properties are primed,

$$
\begin{aligned}
W_R &= \frac{E'}{4(1 + \nu')} \left\{ \frac{2\nu'}{1 - \nu'} + 2 \right\} \epsilon_x^2 \\
&= \frac{E'}{2(1 - \nu'^2)} K_x^2 \sigma_0^2 \left(\frac{h'}{2}\right) \int_0^a [1 - c_1 (1 - \frac{x}{a}) e^{-x/a}]^2 \, dx \\
&= \frac{E' h' K_x^2 \sigma_0^2}{2(1 - \nu'^2)} [a - 2c_1 a \int_0^{a/a} (1 - \xi) e^{-\xi} \, d\xi + c_1^2 a \int_0^1 (1 - \xi)^2 e^{-2\xi} \, d\xi] \\
&= \frac{E' h' K_x^2 \sigma_0^2 a}{2(1 - \nu'^2)} \left\{ 1 - 2c_1 e^{-1} + c_1^2 [(\xi_0 - \frac{1}{2} \xi_0^2 - \frac{1}{2} \xi_0 - \frac{1}{4}) e^{-2\xi_0} \right. \\
&\qquad \left. + \frac{1}{4}] \right\} \xi_0 = 1
\end{aligned}
\tag{85}
$$

Finally the energy contributed by the applied loading, A, is

$$
\begin{aligned}
A &= \int_0^h \bar{\sigma}_x [K_x \sigma_0 w (1 - c_1 e^{-w/a} e^{-\lambda y})] \, dy \\
&\quad + \int_0^w \bar{\sigma}_y [K_y \sigma_0 h] \, dx \\
&= \bar{\sigma}_x K_x \sigma_0 w [h - c_1 e^{-w/a} (1 - e^{-\lambda h}) \frac{1}{\lambda}] + \bar{\sigma}_y K_y \sigma_0 h w
\end{aligned}
\tag{86}
$$

so that for isothermal conditions, the potential energy is

$$
\begin{aligned}
V &= \frac{2E}{3} \left\{ (K_x + K_y)^2 \sigma_0^2 wh - 2(K_x + K_y) K_x \sigma_0^2 c_1 \frac{w}{a} \frac{a}{\lambda} (1 - e^{-\lambda h}) e^{-w/a} \right. \\
&\quad + K_x^2 \sigma_0^2 c_1^2 \frac{a}{2\lambda} (1 - e^{-2\lambda h})[\frac{1}{4} + (\frac{1}{2} \frac{w}{a} - \frac{1}{2} (\frac{w}{a})^2 - \frac{1}{4}) e^{-2w/a}] \\
&\quad - K_x K_y \sigma_0^2 wh + K_x K_y \sigma_0^2 c_1 \frac{w}{a} e^{-w/a} (1 - e^{-\lambda h}) \\
&\quad \left. + \frac{\lambda^2 K_x^2 \sigma_0^2 c_1^2 a^3}{16} \left\{ 1 - [1 + 2 \frac{w}{a} + 2(\frac{w}{a})^2] e^{-2w/a} \right\} \left\{ \frac{1}{2\lambda} [1 - e^{-2\lambda h}] \right\} \right\}
\end{aligned}
$$

$$+ \frac{E'h'K_x^2\sigma_0^2 a}{2(1-\nu'^2)} \left\{ 1 - 2c_1 e^{-1} + c_1^2 \frac{1}{4} (1 - e^{-2}) \right\} \qquad (87)$$

$$- \sigma_x K_x \sigma_0 wh - \bar{\sigma}_y K_y \sigma_0 wh + \bar{\sigma}_x K_x \sigma_0 w \frac{c_1}{\lambda} (1 - e^{-\lambda h}) e^{-w/a}$$

At this point, there are two unknown constants to be determined by minimizing the potential energy [Equation (87)]. Whereas in the general case, one might desire to include in the approximation the effect of finite specimen boundaries, it is sufficient for the present purpose to invoke the fact that the ribbon dimensions are small, sufficiently so that $\exp(-w/a) \ll 1$ and $\exp(-\lambda h) \ll 1$, which leads to the algebraically simpler determining conditions (neglecting also noncontributory terms to $\partial V/\partial c$, and $\partial V/\partial \lambda$, and denoting the remaining ones by V')

$$\frac{3V'}{2E\sigma_0^2 K_x^2 a^2} = \frac{c_1^2}{8\lambda a} \left[1 + \frac{(\lambda a)^2}{4} \right] + \left[\frac{E'h'/(1-\nu'^2)}{Eh/(3/4)} \right] \frac{h}{a} \left[1 - \frac{2}{e} c_1 + \frac{1-e^{-2}}{4} c_1^2 \right] (88)$$

such that

$$\frac{\partial V'}{\partial(\lambda a)} = 0 \qquad - \frac{1}{(\lambda a)^2} + \frac{1}{4} = 0 \qquad (89)$$

$$\frac{\partial V'}{\partial c_1} = 0 = \frac{c_1}{4\lambda a} \left[1 + \frac{(\lambda a)^2}{4} \right] + \left[R\frac{h}{a} \right] \frac{1}{2} (1 - \frac{1}{e^2}) e_1 = \left[R\frac{h}{a} \right] \frac{2}{e} \qquad (90)$$

yielding

$$(\lambda a) = 2 \qquad (91)$$

and

$$c_1 = \frac{1}{\frac{e}{4} \left[1 - \frac{1}{e^2} \right] + \frac{e}{8} \frac{a}{h} \frac{Eh/(3/4)}{E'h'/(1-\nu'^2)}} \qquad (92)$$

where the relative rigidity parameter $(a/h)R^{-1}$

$$\frac{a}{h} \frac{1}{R} \equiv \frac{a}{h} \cdot \frac{Eh/(3/4)}{E'h'/(1-\nu'^2)} \approx \frac{Ea}{E'h'} \qquad (93)$$

explicitly appears in the solution as expected.

The approximate displacement and strain fields can now be obtained by inserting the constants from Equations (92) through (88) into Equations (76) through (80).

-118-

The particular one of interest is the strain in the ribbon. Its displacement is the same as the matrix at $y = 0$; thus

$$u_R(x) = u(x, 0) = K_x \sigma_0 x \left[1 - c_1 e^{-x/a}\right] \tag{94}$$

and because the gage will respond to the average strain $\bar{\epsilon}_R$,

$$\bar{\epsilon}_R = \frac{1}{a} \int_0^a \frac{\partial u_R}{\partial x} \, dx = \frac{u_R(a)}{a} = \frac{\bar{\sigma}_x - \nu \bar{\sigma}_y}{E} \left[1 - \frac{c_1}{e}\right] \tag{95}$$

Equation (92) gives

$$\frac{\bar{\epsilon}_R}{\frac{\bar{\sigma}_x - \nu \bar{\sigma}_y}{E}} = 1 - \frac{1}{\frac{1}{4}\left[e^2 - 1\right] + \frac{e^2}{8} \frac{a}{h} \frac{Eh/(3/4)}{E'h'/(1 - \nu'^2)}} \tag{96}$$

which variation is plotted as the solid line in Figure 59.
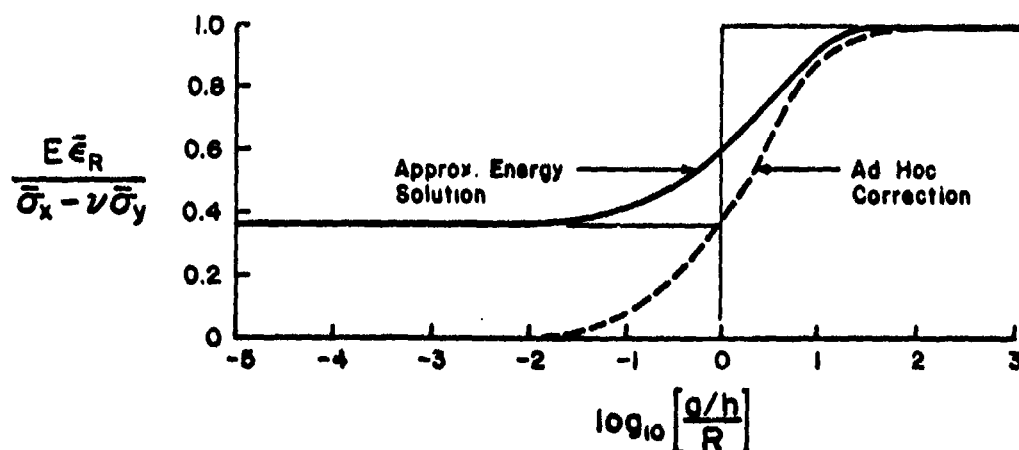
Figure 59. Strain Variation in Ribbon.

Note now the prediction of strain when there is no ribbon, i.e., the situation for which its thickness $h' \to 0$. The correction term vanishes and the strain along $y = 0$, $|x| < a$ is exactly that of the undisturbed field. At the other limit, that of infinite stiffness, for which we know there can (exactly) be no strain in the ribbon, we find from the approximate solution that

$$\frac{E \bar{\epsilon}_R}{\bar{\sigma}_x - \nu \bar{\sigma}_y} = 1 - \frac{4}{e^2 - 1} = 1 - 0.63 = 0.37 \tag{97}$$

instead of zero. Recognizing that the energy solution usually produces a reasonably functional dependence upon the parameters, one may apply an appropriate ad hoc adjustment to Equation (96) by multiplying the second or correction term by an empirical factor to ensure that $\bar{\epsilon}_R = 0$ for $E' \to \infty$ without destroying the correct behavior at the other extreme when $h' \to 0$. The pertinent factor, when included, gives the ad hoc effect of relative ribbon-matrix stiffness upon the gage response shown as the dotted design curve in Figure 59, based on

$$\frac{E\bar{\epsilon}_R}{\bar{\sigma}_x - \nu\bar{\sigma}_y} = 1 - \frac{1}{1 + \frac{e^2}{2(e^2 - 1)} \frac{a}{h} \frac{Eh/(3/4)}{E'h'/(1 - \nu'^2)}} \tag{98}$$

$$= 1 - \frac{1}{1 + 0.58 \frac{Ea}{E'h'}} \tag{98a}$$

which depends on the product of the relative moduli and the thickness-to-length ratio of the ribbon gage. Although this ad hoc correction formula is throught to be satisfactory for the initial design studies, an alternate improvement is possible by enlarging the approximating series [Equations (76) and (77)] and including the w/a and h/a edge effects.

The average shear stress at the gage, using Equation (80) is

$$\tau_{av} = G \int_0^a \gamma_{xy}(x, 0)\, dx = G \left[\frac{\bar{\sigma}_x - \nu\bar{\sigma}_y}{E}\right] (\lambda a)\left(\frac{c_1}{e}\right) = \frac{2}{3} \frac{c_1}{e} (\bar{\sigma}_x - \nu\bar{\sigma}_y) \tag{99}$$

whereupon, evaluating for the infinite rigidity case and $\bar{\sigma}_x = 0$ in order to compare with the exact solution of Equation (71), one has

$$\tau_{av} = \left[-\frac{1}{3} \bar{\sigma}_y\right] 0.63 = 0.63\ \tau_{av}\Big|_{exact} \tag{99a}$$

so that some idea of the stress ratio correction can also be obtained.

b. Finite Element Analysis of Shear Gage Element

(1) Method of Analysis

A typical semiconductor shear gage element is shown in Figure 54. The gage consists of a semiconductor wire embedded in either a Solithane or propellant matrix cube. The experimental calibration of the gage employs the shear calibration specimen shown in Figure 85 of Reference 2. Typical experimental procedures of the calibration method are described in Reference 2.

Because the gage matrix is of the same material as the specimen to be measured, the gage interference is primarily limited to the shear cube itself. The interaction between the cube and the specimen will

be minimal but is influenced somewhat by differences, if they exist, in batch age and cure, etc, of the matrix material. As a result of the above, the analytical aspects of calibration effectively can be split into two problems:

(1) Analysis of the cube with semiconductor elements

(2) Analysis of the shear test fixture

Following is a description of these problems and a numerical solution.

(2) Numerical Solution

A half-inch cube of matrix with an embedded semiconductor strain gage is shown in Figure 60. The function of the semiconductor is to measure the shear stress on the propellant under uniform loading of the cube faces. Ideally, if the gage did not interfere with the deformation pattern in the cube, the correlation between the strain in the semiconductor and the shear stress on the faces could be determined from simple solutions. However, the semiconductor creates a three-dimensional field that must be solved by numerical techniques in order to correlate the semiconductor strain and applied shear stress. In addition, the sensitivity to other induced stress states must be ascertained. To this end, a numerical investigation was undertaken in which four load cases were applied to the cube, as shown in Figure 61. The shear load case is of primary interest because this will furnish information to correlate the gage readings with applied shear stress. The normal loads, cases No. 2 and No. 3, are intended to show their possible effect on the gage readings. The last load case considers the practical problem of gage response under a stress gradient. By means of a general purpose finite element program, which can solve three-dimensional problems, Reference 9, the shear cube gage was modeled through the use of three-dimensional finite elements for the matrix and axial bar elements for the semiconductor wire, Figure 62. The matrix was assumed to be incompressible ($v = 0.5$) and the extensional modulus was taken as 100 psi. The low modulus corresponds to the greatest expected interference by the semiconductor wires. To obtain additional calibration information, the modulus must be varied over the full range of expected values as in Section III.3. However, for long-duration loadings or quasi-static loadings at elevated temperatures, the present analysis provides some basic calibration information.

(3) Results and Discussion

For each load case Table XI lists the average strain in the semiconductor elements and the ratio of this "strain" to the "strain" that would be present without the wires. The low values of these ratios indicates that the wire interferes significantly with the local response in the immediate vicinity of the wires. However, the global deformation pattern on the surfaces of the cube was found to be within 6 percent of that of an equivalent cube with no gage. Thus, there are only minor errors in applying the results to a calibration fixture analysis without the gage.
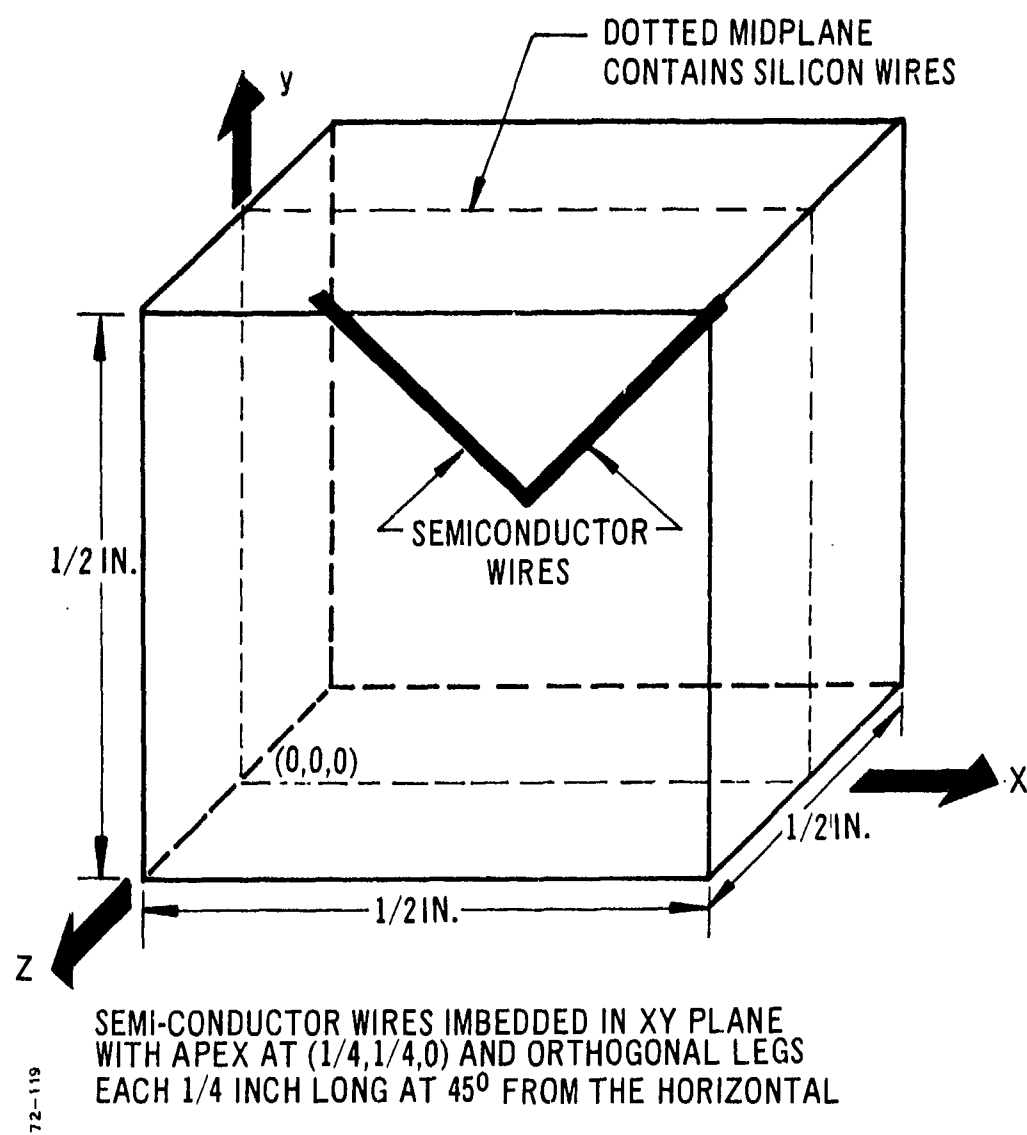
Figure 60. Configuration of Propellant with Semiconductor Elements.

LOCKHEED PROPULSION COMPANY
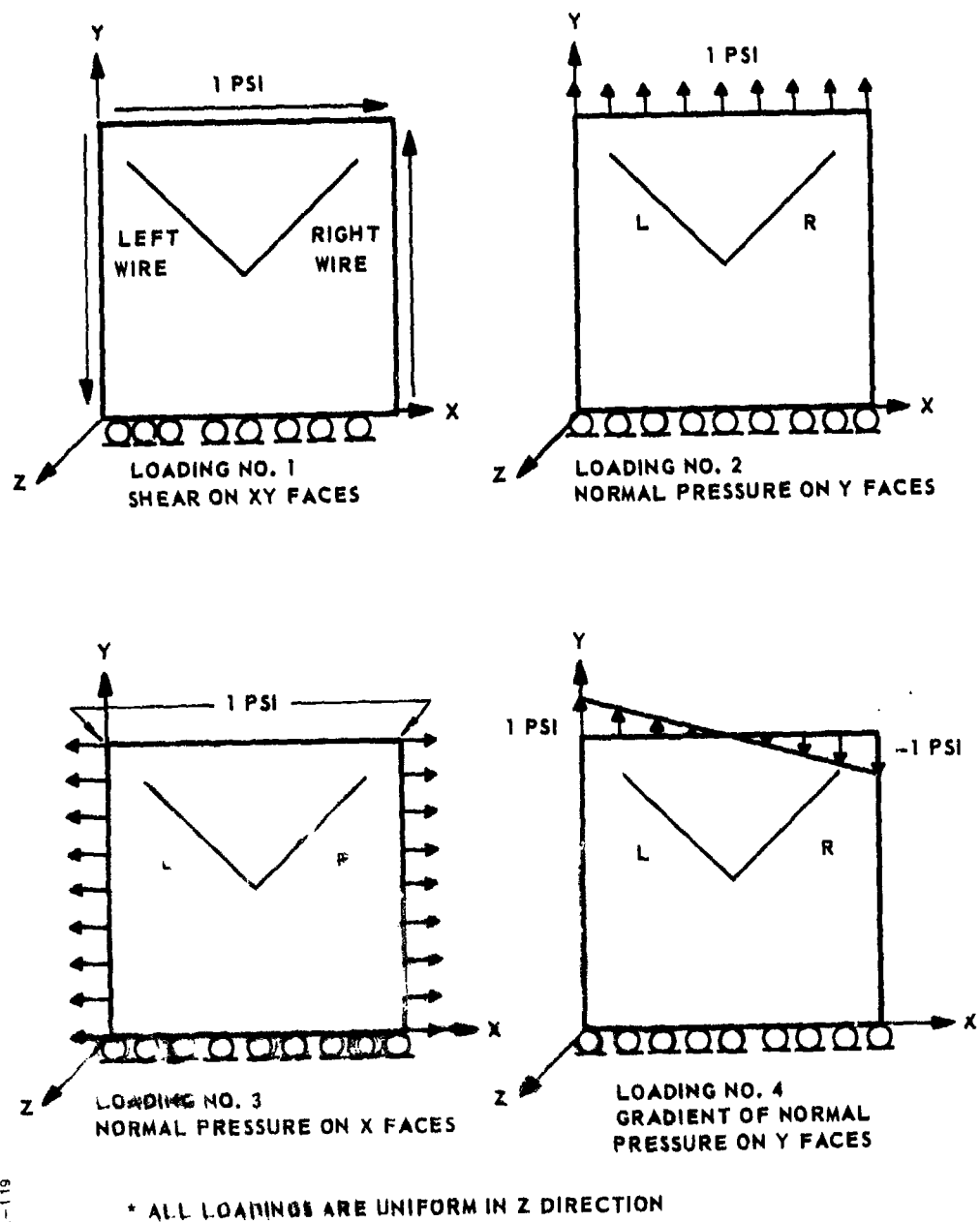
Figure 61. Load Cases Investigated.
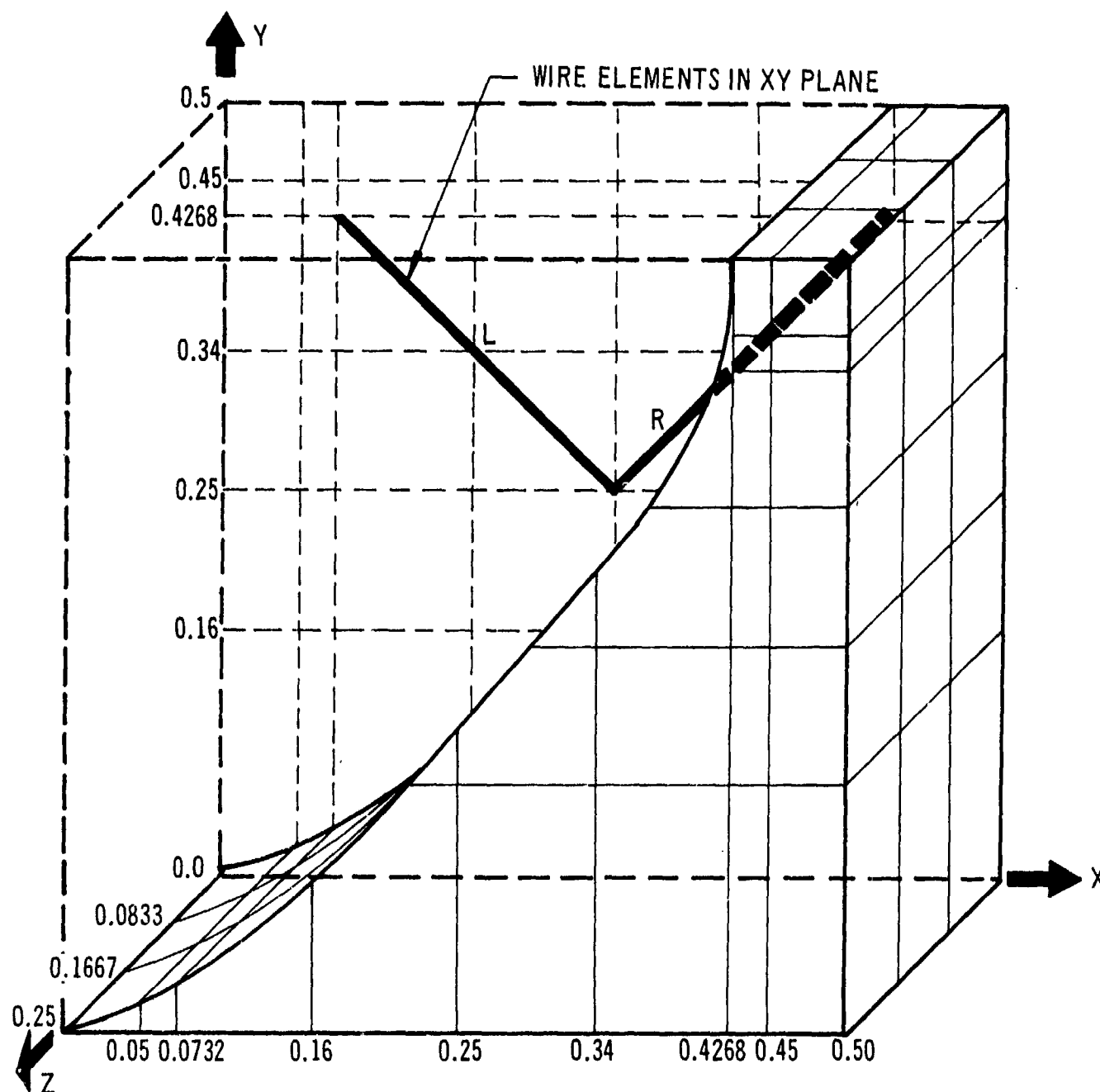
MESH: 144 CONTINUUM ELEMENTS (8 NODE BRICKS) FOR PROPELLANT
4 BAR ELEMENTS FOR SEMI-CONDUCTOR WIRE
268 NODES

MATERIALS: PROPELLANT: E = 100 PSI, ν = 0.5
WIRE: E = 2.7 x 10^6 PSI, AREA = 2.5 x 10^{-5}
(HALF OF WIRE AREA USED IN SYMMETRIC MODEL)

Figure 62. Cutaway View of Symmetrical Half of Propellant Cube with Embedded Wire.

72-119

-124-

TABLE XI

AXIAL STRAINS IN SEMICONDUCTOR ELEMENTS

| | Left Wire | | Right Wire | |
Load Case	Average Strain (in./in. x 10^{-3})	Ratio*	Average Strain (in./in. x 10^{-3})	Ratio*
Shear, No. 1	-2.287	0.15	+2.287	0.15
Normal Y, No. 2	+0.3759	0.15	+0.3759	0.15
Normal X, No. 3	+0.3759	0.15	+0.3759	0.15
Gradient, No. 4	+0.1262	0.14	-0.1262	0.14

* The ratio is determined by dividing the strain listed in the table by the corresponding strain in a cube with no wire.

Inspection of the strain values in Table XI shows that the gage is most sensitive to shear loadings inasmuch as these strains are an order of magnitude higher than strains arising from the other load cases. Moreover, it is evident from the signs of the strains that subtracting the strain of one leg from the other would have the effect of doubling the shear response reading and at the same time eliminating the response from uniform normal pressures. Load case No. 4, normal pressure gradient, does influence the shear reading.

If the gage is utilized in a region of high shear and low normal stress gradients, reasonably accurate measurements should be obtained. If, however, the gage is used in a region of low shear and high normal stress gradient, the gage readings will be unreliable.

The process of discarding "bad" gages, discussed in Reference 2, is suspect. It is possible that considerable normal stress gradients and shears exist in the specimen under normal loads. The fact that the gages give considerable readings is not at all surprising, especially if they are located off the symmetry axis. It has not been possible under this contract to perform all the analyses necessary to "calibrate" the shear-cube test specimen. These analyses are essential for a complete understanding of the system.

3. EXPERIMENTAL DATA

a. Static Tests in Shear Fixture

(1) Shear Test Fixture

Figure 63 shows a sketch of the inert propellant shear test fixture containing four cubes for evaluation. Shear cubes No. 1 and No. 2 were manufactured with Kulite PGP-1000-300 semiconductor gages, 0.30-inch long and 1000-ohm resistance. Shear cubes No. 3 and No. 4 were made with Kulite PFP-500-090 semiconductor gages, 0.09-inch long and 500-ohm resistance. The short 500-ohm, 0.90-inch-long gages are preferred for making shear cubes, but unfortunately they are much more delicate than the 1000-ohm, 0.30-inch-long gages. In fact, gage No. 4 was found to be inoperative after cure of the test fixture, one gage being broken. The remaining three shear cubes were connected into bridge circuits as shown in Figure 64. With a 28-volt supply the 1000-ohm circuits had a bridge voltage of 2.55 volts, whereas the 500-ohm gage had a bridge voltage of 1.83 volts.

Unfortunately, in Shear cube No. 3, made with the delicate 500-ohm semiconductor gages type PFP-500-090, an internal connection broke during the setting up process and the cube became inoperative.

The shear gages also appeared to exhibit variation in sensitivity attributable to poor initial zero reading. For this reason, the shear gage calibration tests were performed by applying shear loads in opposite directions so as to avoid cumulative zero shifts during testing. The loads reversal was obtained in practice by reversing the shear specimen in the test fixture.
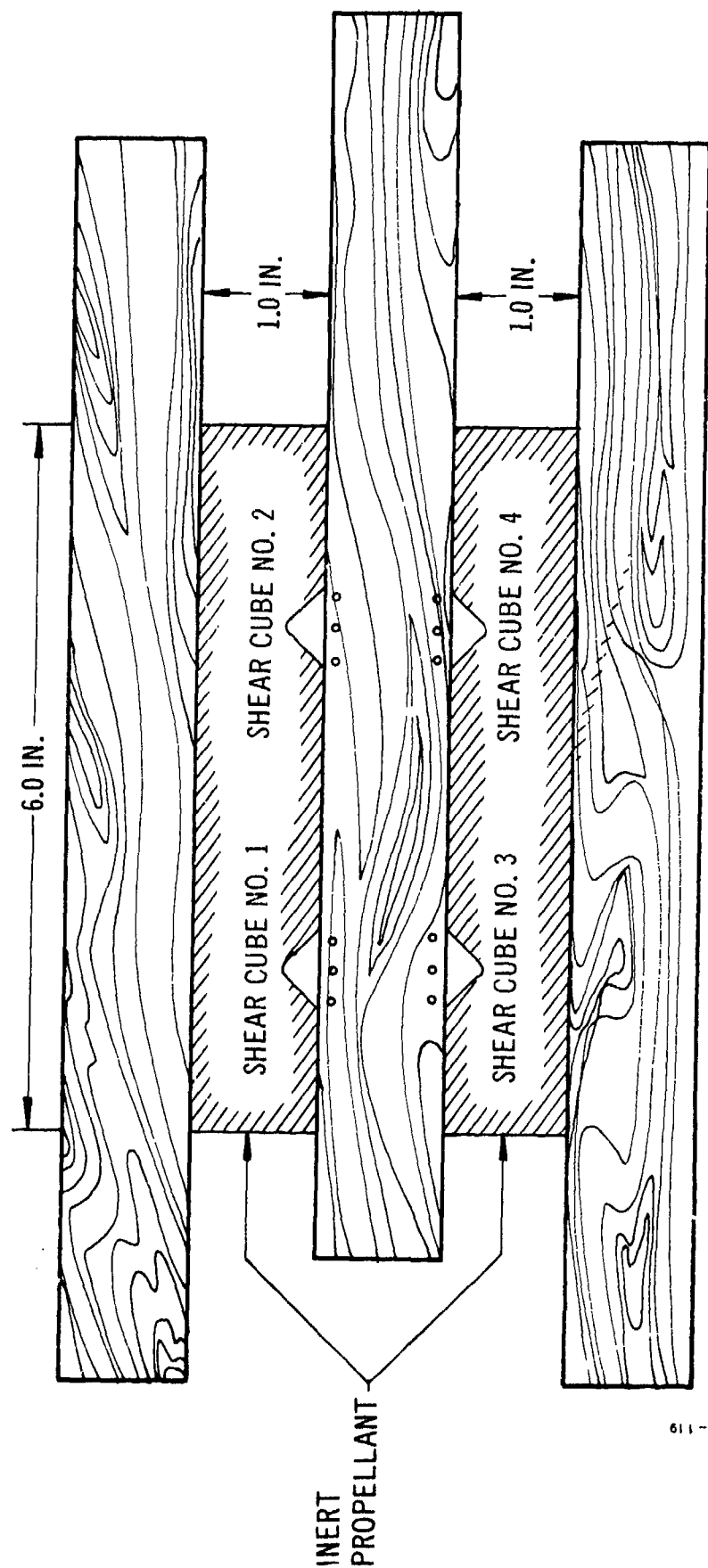
Figure 63. Sketch of Inert Propellant Shear Test Fixture.
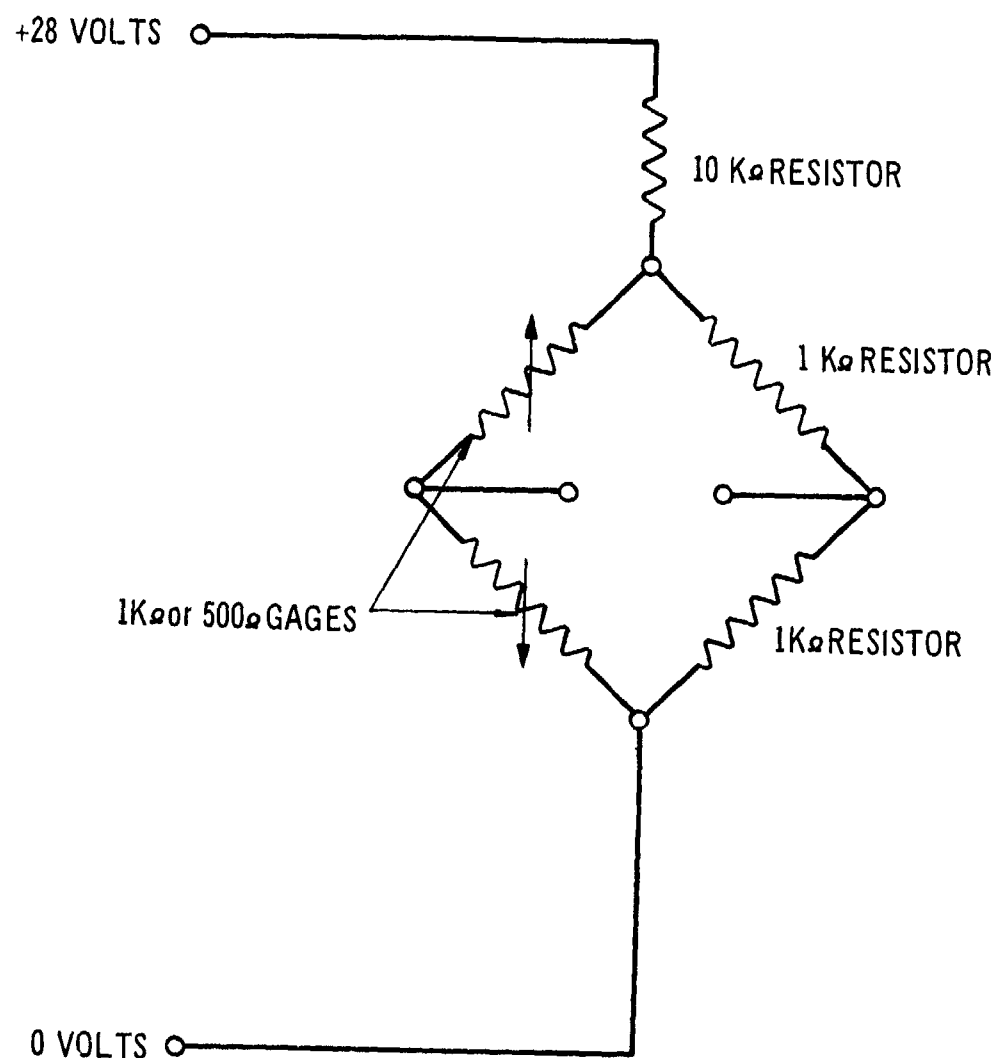
Figure 64. Shear Gage Bridge Circuits.

A later investigation of the difference in sensitivity between the two directions of loading revealed that the most probable cause of the discrepancy was a very small difference in the lengths of the two wooden outer support pieces. Thus, when a load was applied to the center wooden bar of the shear fixture, the loads carried by the two side pieces were not identical, thereby applying slightly different loads to the shear cubes when the text fixture was reversed.

Typical data obtained by the specimen inversion technique just described are presented in Figure 65.

Data from both shear cubes are presented to show their similarity. The variation in gage reading under "zero load" conditions is obvious from the data. Thus for shear cube No. 2, the initial zero load reading was -22.7 mv. After the first shear load was removed, the gage reading reverted to -24.4 mv and, upon inverting of the specimen, the gage reading became -19.0 mv. After removal of the second shear load, the shear cube reading fell to -16.6 mv at the end of the test. Thus an error band of -24.4 to -16.6 mv (i.e., 7.8 mv) was obtained during this test sequence, which represents 0.25-psi total, or a ±0.125-psi error band.

Although this error band is probably small enough to be neglected in practice, it can still make precise laboratory calibrations difficult to perform.

(2) Creep Tests on Inert Propellant Shear Fixture No. 1

A series of constant load creep tests was performed on the inert propellant shear fixture over the temperature range of +166 to -35°F. A 10-pound deadweight was used to produce a step stress of 1.667 psi in the specimen, and an LVDT was mounted to monitor the displacement of the central rod of the specimen. The signals from the LVDT and the two shear gages were recorded on a galvanometer recorder, and the tests were monitored for 10 minutes.

Inverse creep compliance was calculated and the data shifted to produce the master curve of inverse creep compliance versus log reduced time shown in Figure 66. The shift factors obtained are plotted against temperature in Figure 67. It may be noted that the shift factor values are very similar to the uniaxial test data, which are also presented in this figure.

Figure 68 shows the shear gage sensitivity data, mv/psi, plotted against log reduced time. The same shift factors found from the compliance data were used to obtain the reduced data curves. It appears that there is no need for a vertical shift factor to produce a smooth curve. (This is particularly true of gage SH 1; gage SH 2 would benefit from the use of small vertical shift factors between 71 and 10°F.)

A more significant aspect of the shear gage behavior is shown by the data obtained at 166°F. The gages show a distinct loss in sensitivity, attributable, most probably, to a loss of adhesion between the semiconductor strain gage elements and the inert propellant substrate.

-129-
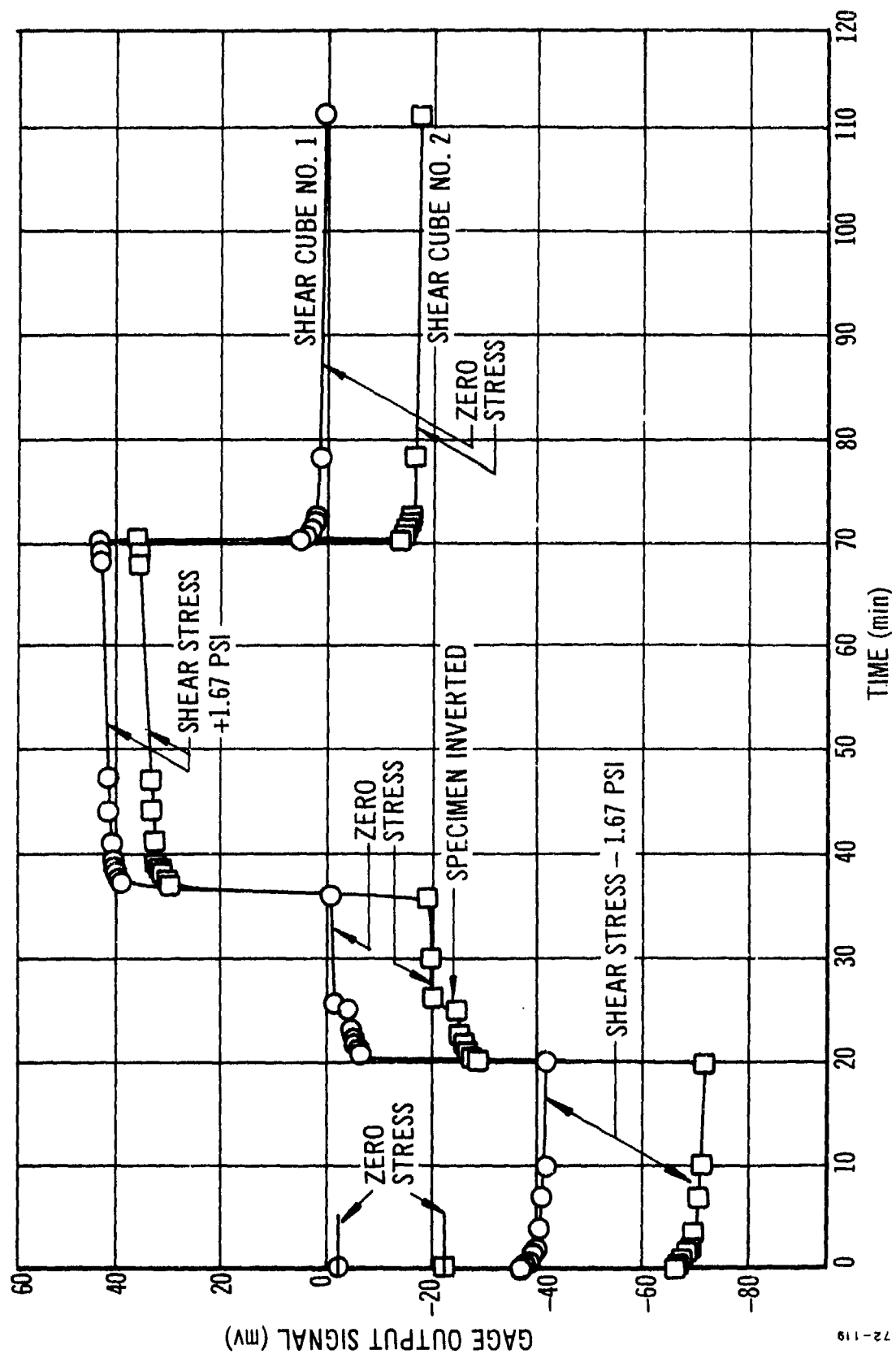
Figure 65. Inert Propellant Shear Specimen No. 1, Tested under Constant Load at 70°F.

72-119
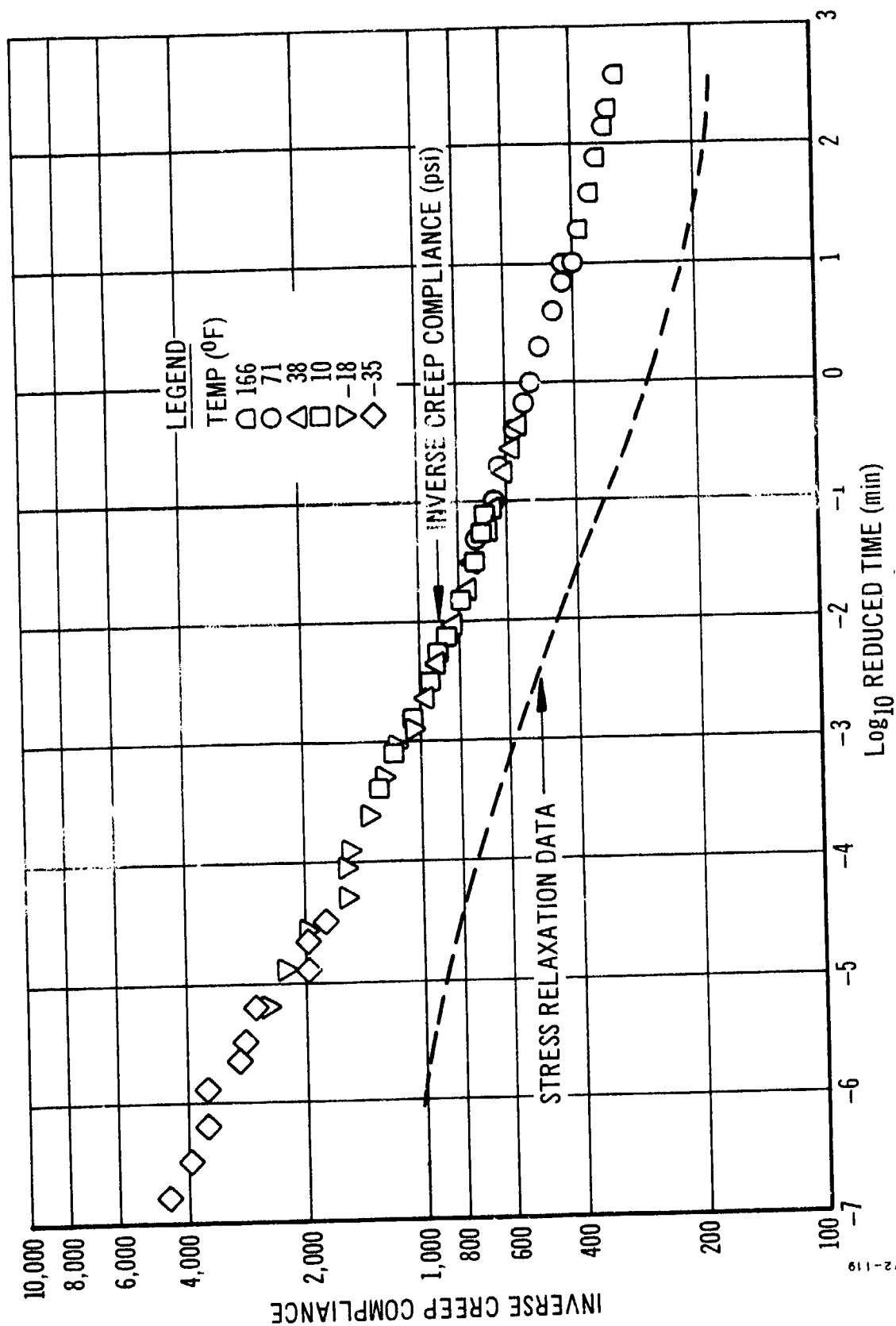
Figure 66. Inverse Shear Creep Compliance versus Reduced Time, Inert Propellant Shear Fixture No. 1.

72-119
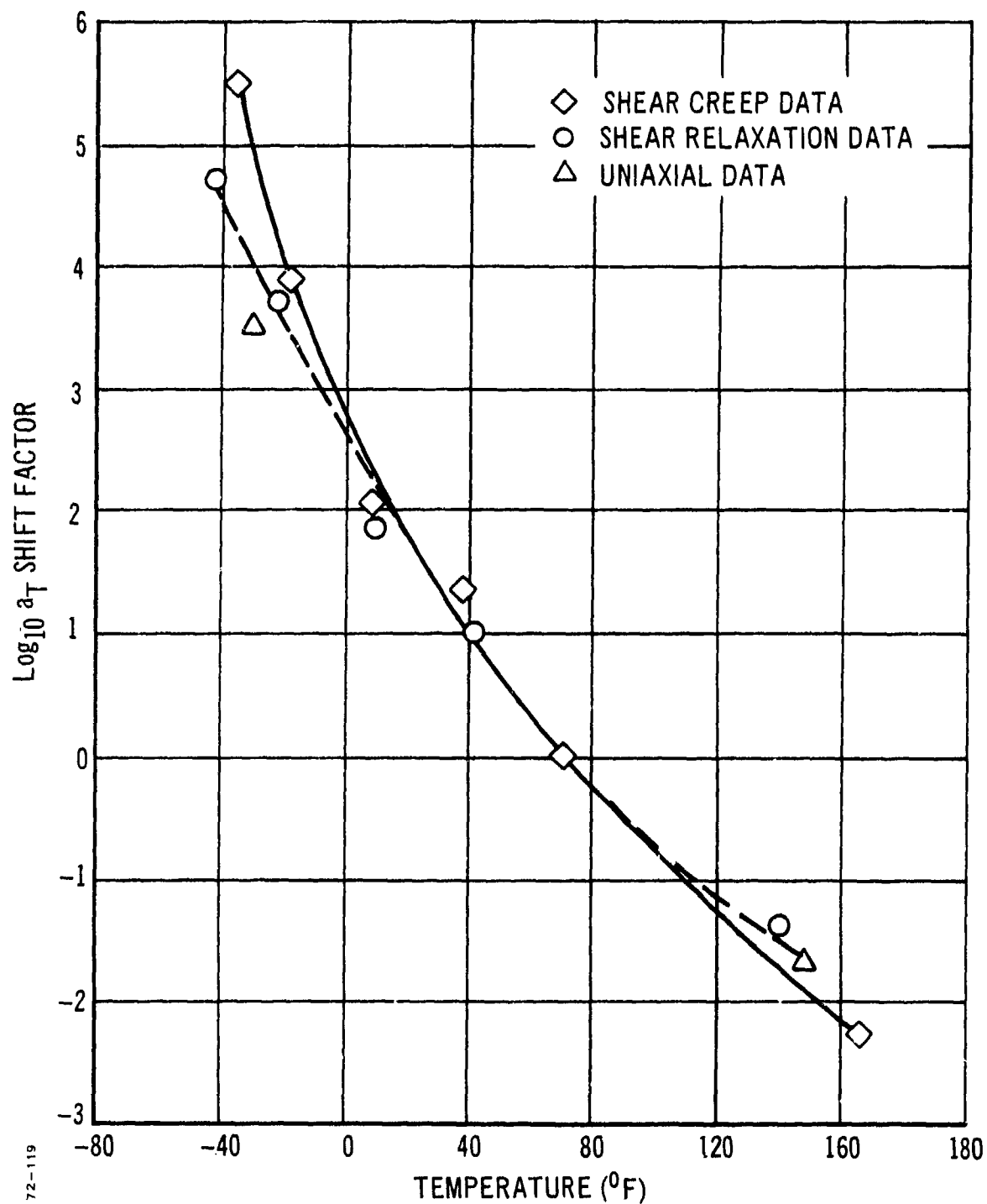
Figure 67. Log a_T Shift Factors versus Temperature, Inert Propellant
Shear Fixture No. 1.
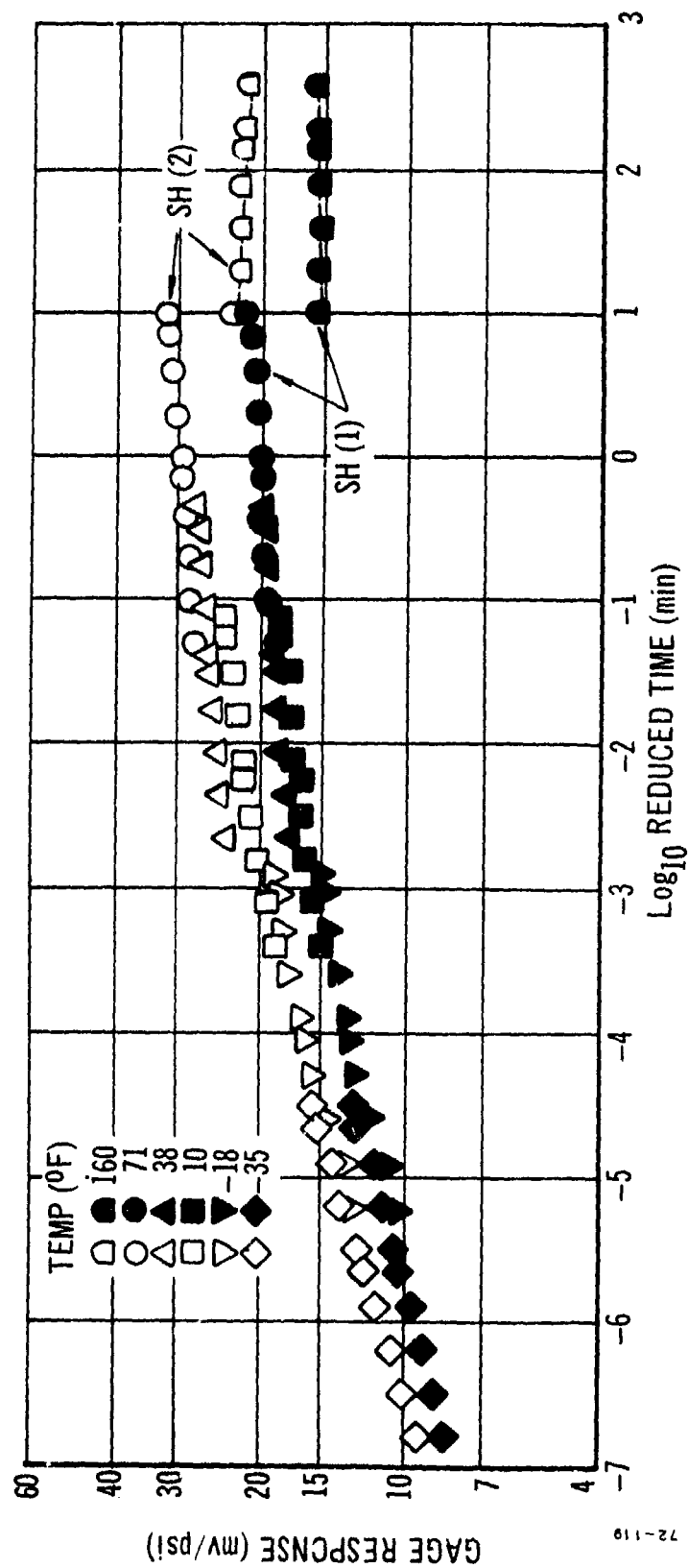
Figure 68. Gage Sensitivity to Stress versus Reduced Time, Inert Propellant Shear Test Fixture No. 1.

Methods of overcoming this problem have not yet been determined. Use of a resin system with a higher cure temperature may produce a better gage than the existing system, but there is no evidence at present that this assumption is correct. There is no doubt that the problem is a function of temperature, because the gage slippage appears to become progressively worse at higher temperatures. The available shear gages may, therefore, produce a higher error in the measured stress/strain values at elevated temperature. For precision in the data, the gages should not be used at temperatures greater than approximately 100^0F.

(3) Relaxation Tests on Inert Propellant Shear Fixture

A series of tests consisting of ramp loading plus constant strain was also performed on the double overlap shear fixture. The data from these relaxation tests are presented in Figures 69 and 70; the log a_T shift factors obtained are plotted on Figure 67. Figure 69 shows the stress relaxation modulus data plotted against log reduced time and the gage sensitivity, in mv/psi, to an applied stress, also plotted against log reduced time.

Gage sensitivity to the applied strain is plotted in Figure 70. Examination of these data curves shows that the gage sensitivity data shift along the log time axis produces relatively smooth reduced data curves without the need, as in the case of the creep test data, for the additional vertical shift factor.

The reduction in gage sensitivity at high temperatures is apparent in the 140^0F test data.

(4) Comparison Between Creep and Relaxation Data

The stress relaxation modulus curve is plotted against the inverse creep compliance data in Figure 66, and the log a_T shift factors for the creep and compliance data are shown together in Figure 67. The log a_T shift factors for the creep and relaxation tests are very similar, as can be observed in Figure 67.

The inverse creep compliance is, however, must larger than the relaxation modulus across the whole reduced time range. Because of this discrepancy, the specimen was again tested in the Instron testing machine with the LVDT (as used for the creep tests) in place to monitor the crosshead displacement, used to determine the stress relaxation modulus. It was found that the LVDT displacement data and the Instron crosshead motion were in close agreement and verified the correctness of the inverse creep compliance data.

It is interesting to note that the discrepancy between the creep and relaxation data, which is of the order of two times at log reduced times between 3.0 and -3.0, increases at short reduced times (log t/a_T = -7.0). This suggests that the flexibility of the Instron testing machine may be partially responsible for the discrepancy. (As the specimen gets colder and stiffer, the Instron frame begins to absorb a portion of the applied load and the actual specimen extension is less than the crosshead movement.)

-134-
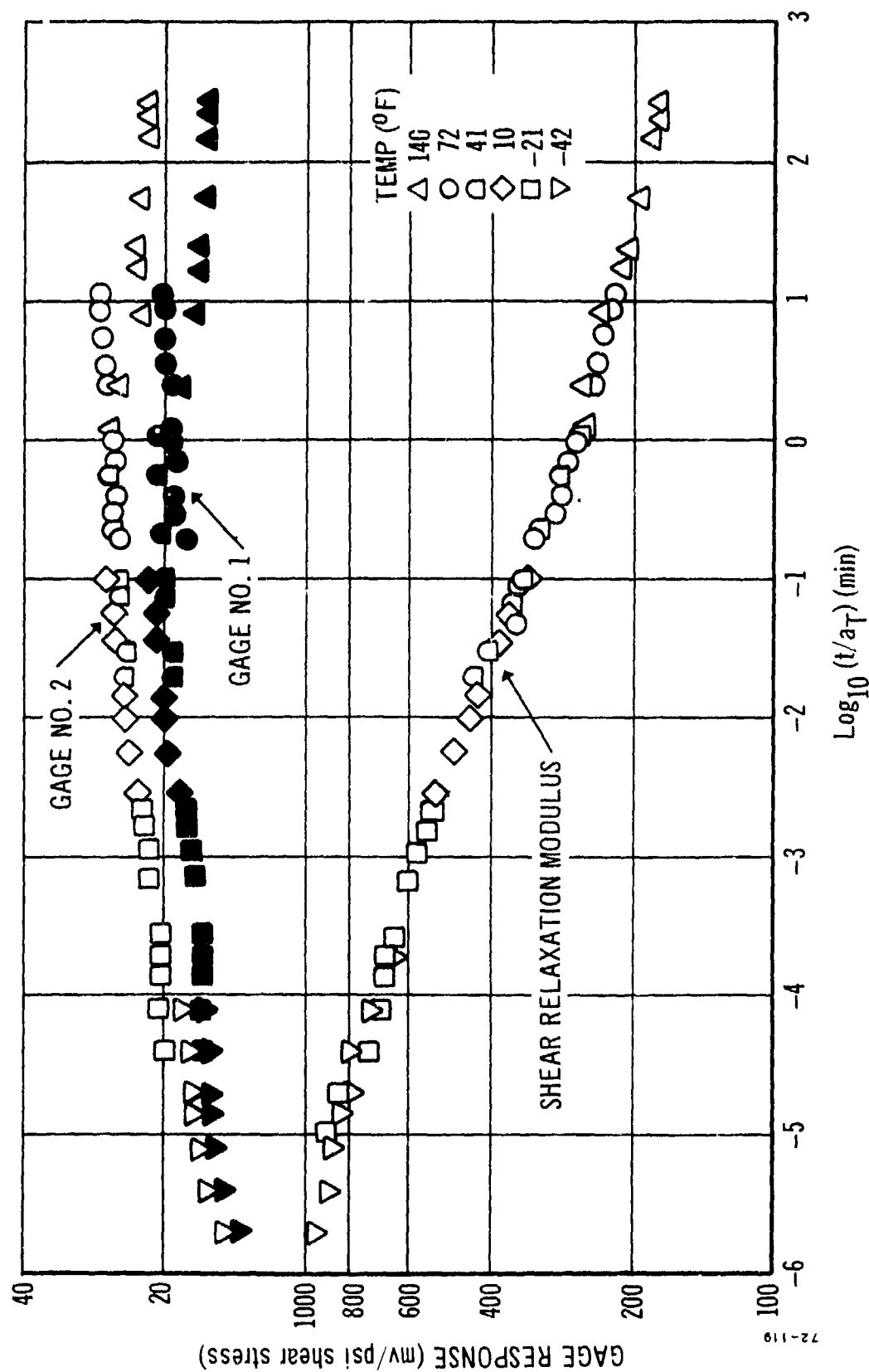
Figure 69. Shear Relaxation Modulus and Gage Sensitivity to Stress versus Reduced Time, Inert Propellant Shear Test Fixture No. 1.
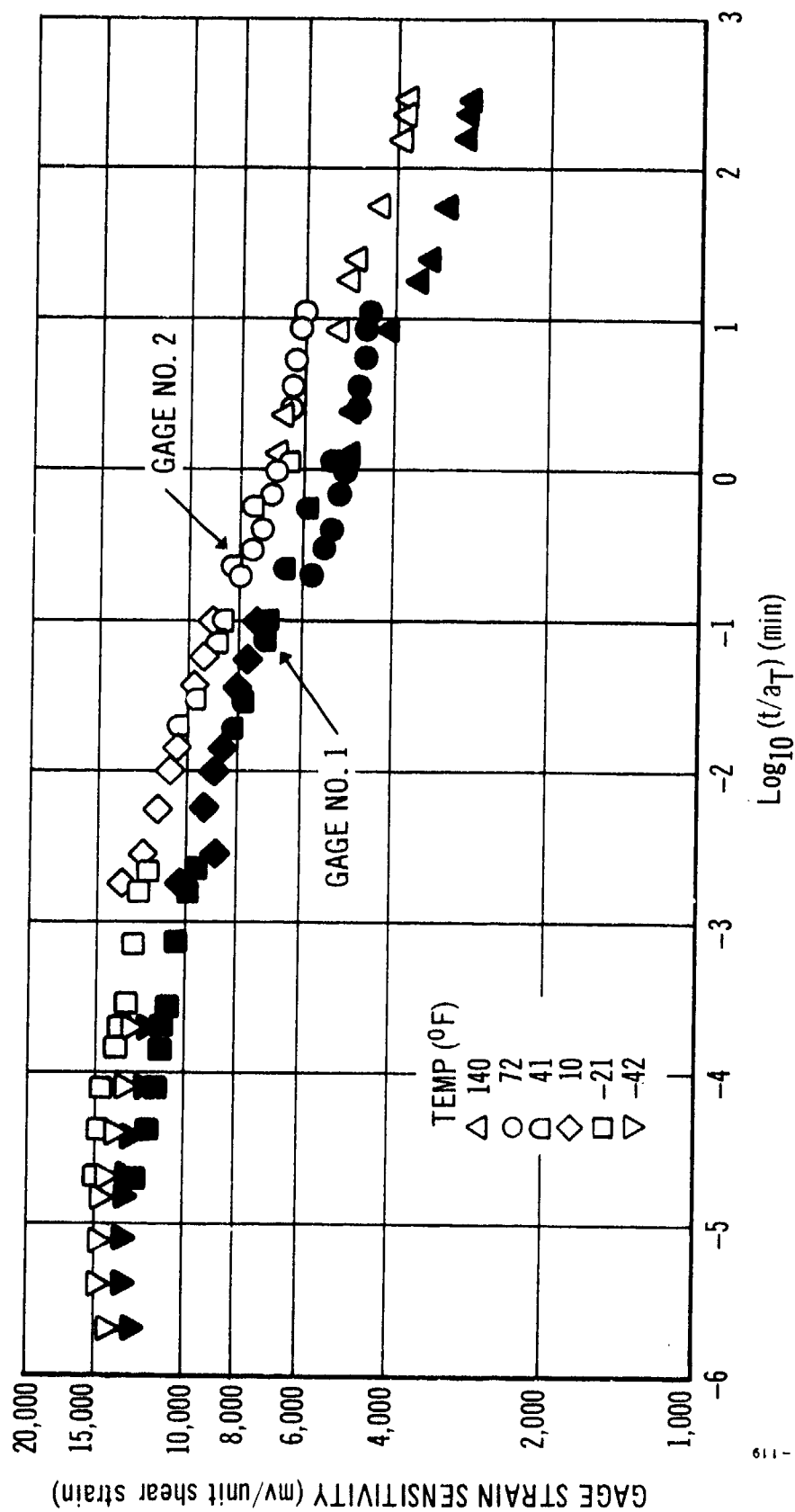
72-119

Figure 70. Gage Sensitivity to Strain versus Reduced Time, Inert Propellant Shear Test Fixture No. 1.

The shear gage sensitivities (mv/psi) obtained during the creep and relaxation tests appear to be quite different on the basis of the data curves of Figures 68 and 69. However, this difference between the gage sensitivities is caused almost entirely by the difference in moduli between the relaxation data and the creep data. This may be observed from Figure 71, in which the gage sensitivities are plotted against modulus (or inverse creep compliance). There is still a difference between the creep and the stress relaxation data, but not as great as appears in the earlier data plots.

Gage sensitivity versus modulus is not the same simple function of modulus that was obtained for the diaphragm gage (see Figure 25). It is, however, a simple type of curve until the higher temperatures are achieved, when the loss in sensitivity with temperature becomes marked.

(5)   Shear Creep Tests on STV Propellant Shear Fixture No. 2

Another double overlap type of shear specimen was made with STV propellant 0064-61E. The specimen was identical to that shown in Figure 63, and contained four shear gages. Three of the gages made with the Kulite PGP-1000-300 semiconductor strain gage sensing elements operated throughout the testing program. As in the case of the data shown in Figures 68 and 69, the shear gages showed almost identical performances throughout the tests. Therefore, only one set of the shear gage data is presented.

The inverse creep compliance and the gage sensitivity to stress (mv/psi) are plotted against reduced time in Figure 72. It was necessary to use a vertical shift factor, b_T, to obtain the smooth curve shown.

The data for log a_T versus temperature are given in Figure 73, and the vertical shift factors are plotted against temperature in Figure 74.

The sensitivity data for the live and the inert propellant specimens are very similar, as may be seen from a comparison of Figures 69 and 72. The live propellant gage is, however, slightly more sensitive. Consequently, the sensitivity values for this gage were factored by 0.733 before being plotted against propellant modulus in Figure 71.

Although the two sets of data are not identical, there is a great similarity between the shear gage sensitivities in the inert and the live propellants. The differences are most probably due to minor adhesion or bridge voltage differences.
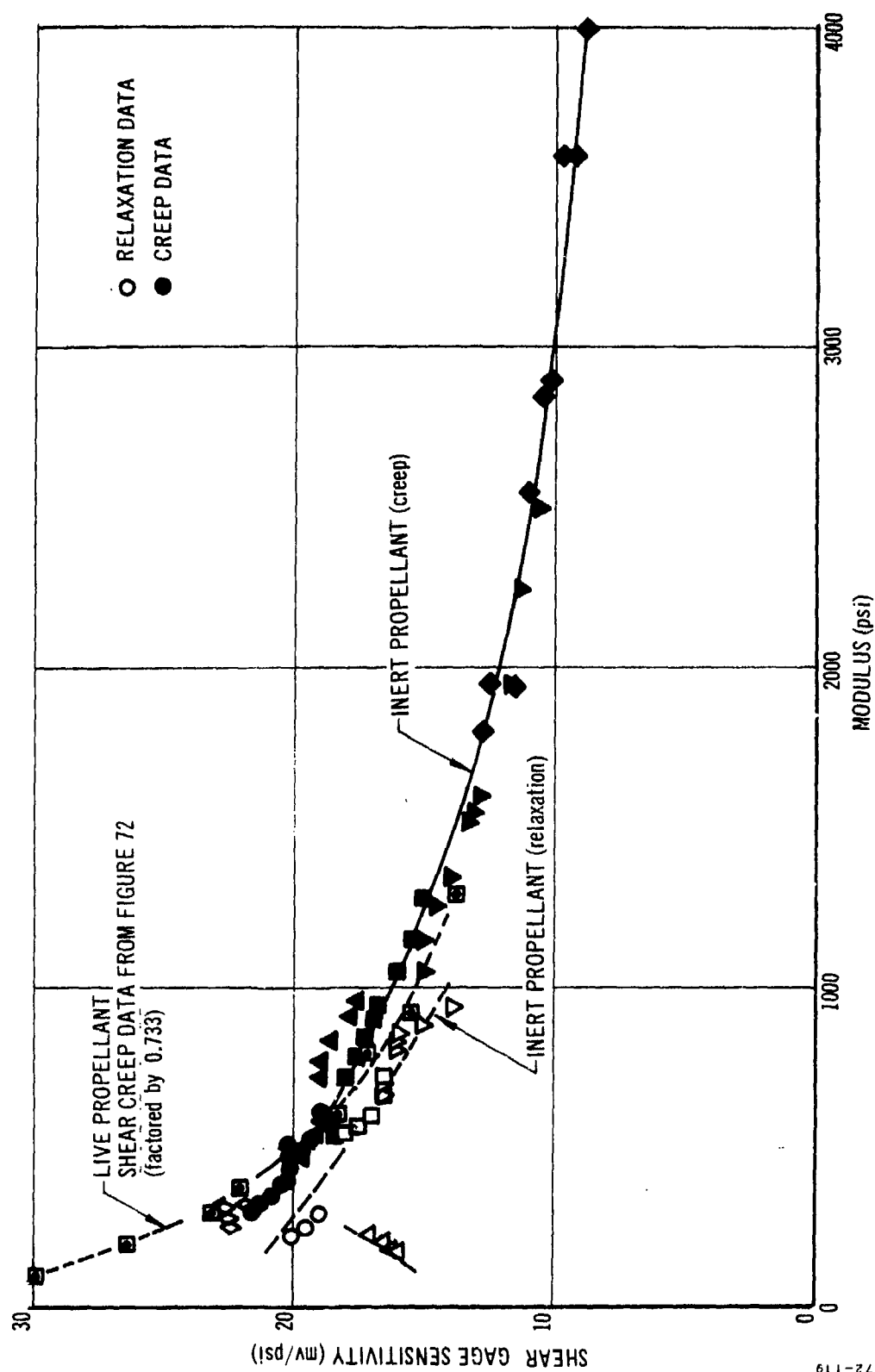
Figure 71. Shear Gage No. 1 Sensitivity to Stress for Creep and Relaxation Tests versus Modulus.

72-119
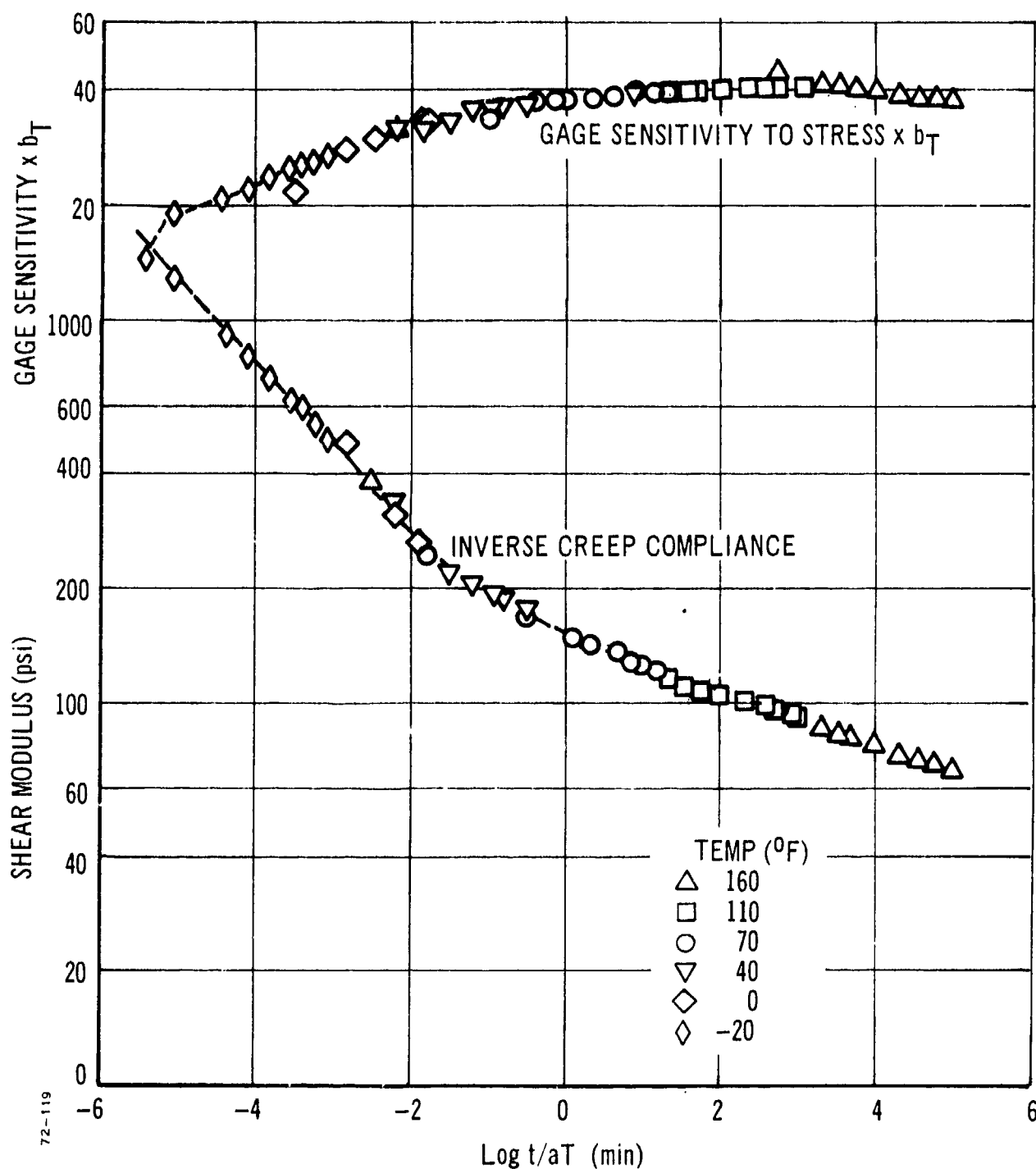
Figure 72. Inverse Creep Compliance and Gage Sensitivity versus Log
Reduced Time for Live Propellant (0064-61E) Shear Specimen.

-139-
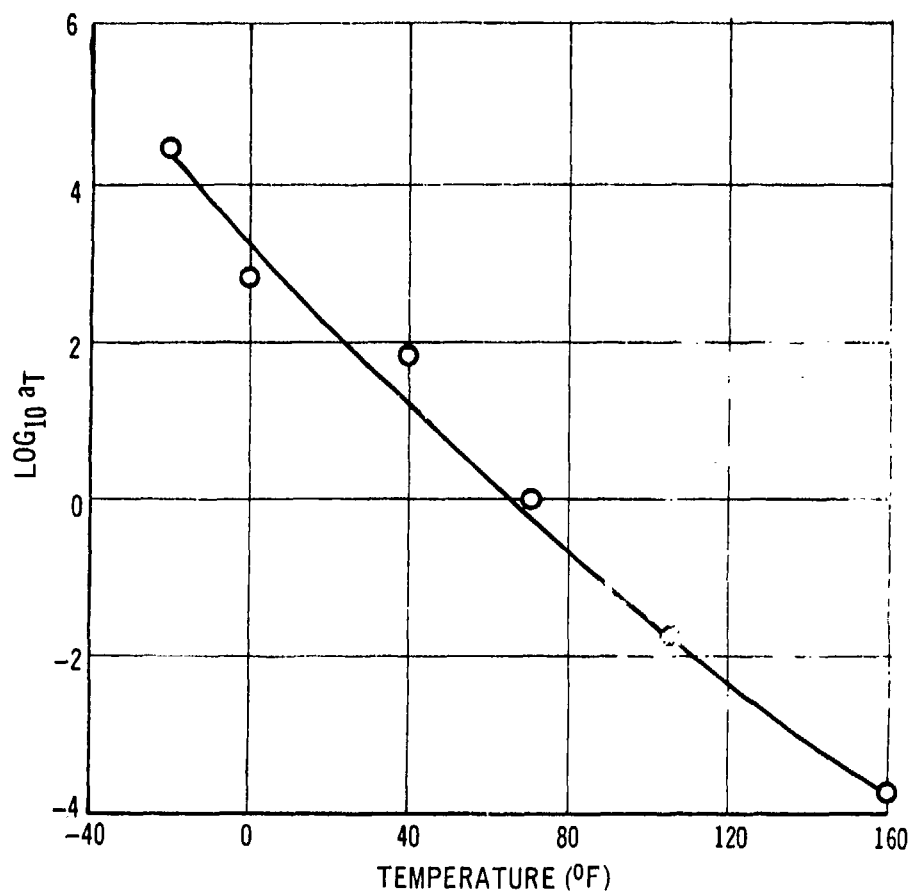
Figure 73. Log a_T Shift Factors versus Temperature, 0064-61E
Propellant Shear Specimen.
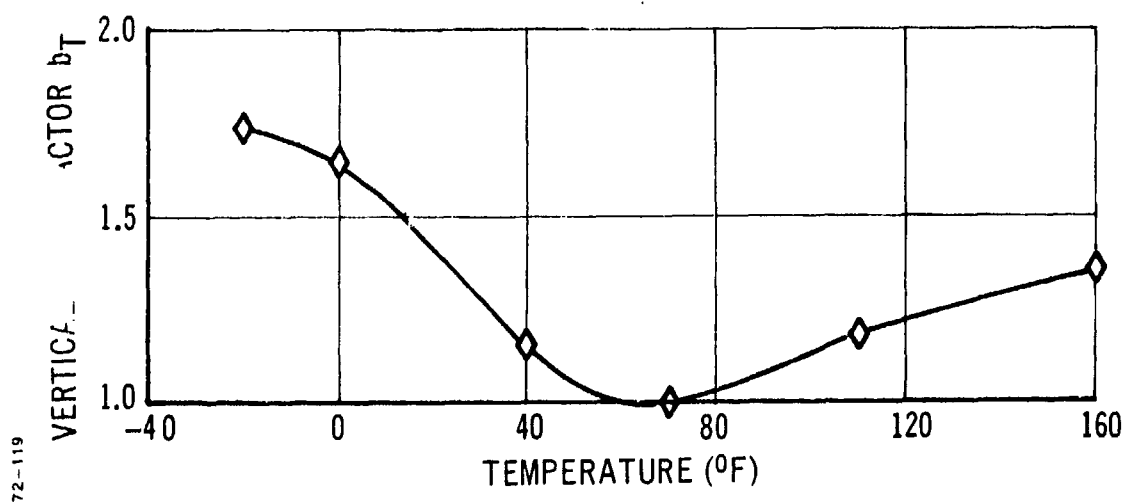
Figure 74. Vertical Shift Factors b_T versus Temperature, 0064-61E
Propellant Shear Specimen.

(6) Normal Stress Tests on 0064-61E Shear Fixture

Normal stress tests were carried out on the live propel-
lant shear test fixture using the experimental test setup illustrated in
Figure 75. Data at three temperatures, plotted against reduced time, are
shown in Figure 76. The gage sensitivity to shear stress is also plotted on
the same figure for comparison purposes. The gage sensitivity to normal
stress is seen to be approximately an order of magnitude less than the sen-
sitivity to shear stress. It is actually better than this at the higher tem-
peratures, where it approaches a factor of 30 times smaller than the shear
sensitivity. Although this appears to be a satisfactory situation, it should
be remembered that the shear gage is extremely sensitive, so that its sen-
sitivity to normal stress is still some 2.5 times greater than that of the 150-
psi diaphragm stress gage at 70^0F. Therefore, under conditions of low
shear and high normal stress, the shear gage will tend to provide misleading
readings.

b. Static Tests on Diametral Compression Specimen

(1) Specimen Details

The diametral compression specimen consists of a 1.0-
inch-thick, 3.0-inch-diameter disc of inert propellant with semiconductor
strain gage elements bonded to the surfaces as shown in Figure 77. One
pair of gages at right angles is mounted on each surface as close to the
center of the disc as possible. This pair of gages comprises a shear gage;
and the shear gage on the opposite face of the specimen is aligned at 45
degrees to the first shear gage, as shown in Figure 77.

Under the action of a vertical compressive load, a vertical
compressive stress $-\sigma_c$ is obtained in conjunction with a horizontal tensile
stress of one-third the magnitude. Therefore, by rotating the disc in rela-
tion to the direction of the applied load, the stresses applied to the shear
cube elements can be varied between $+\sigma_c/3$ and $-\sigma_c$. This test may be
employed to investigate the performance of the shear gages in a complex,
tensile-compressive stress field.

(2) Loads Analysis for Diametral Specimen

Under a vertically applied diametral force F, a vertical
compressive stress

$$\sigma_y = \frac{-6F}{\pi Dt}$$

where D = diameter of specimen and t = thickness of specimen, and a
horizontal tensile stress

$$\sigma_x = \frac{2F}{\pi Dt}$$

are produced at the center of the disc. The third stress σ_z is zero and
there is no shear stress in the x or y directions. The maximum shear stress,
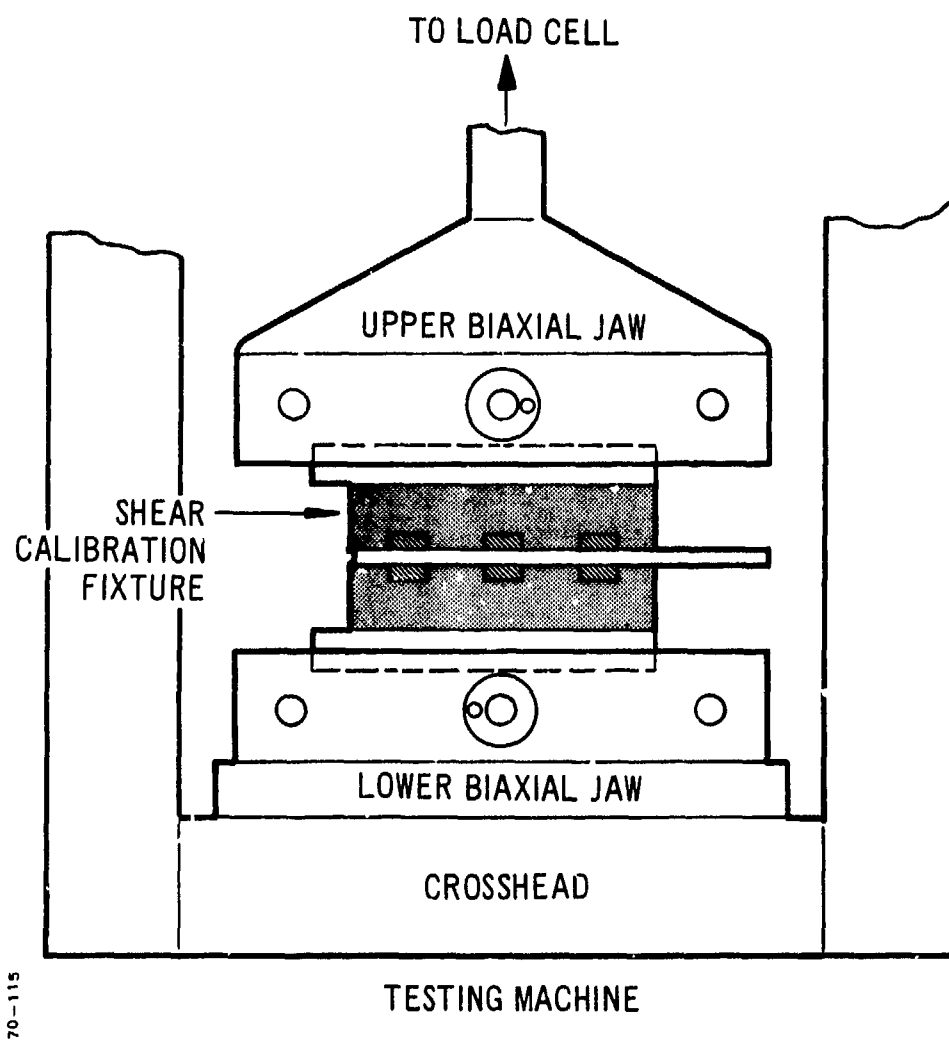
Figure 75. Shear Calibration Fixture Arranged for Normal Shear Test.
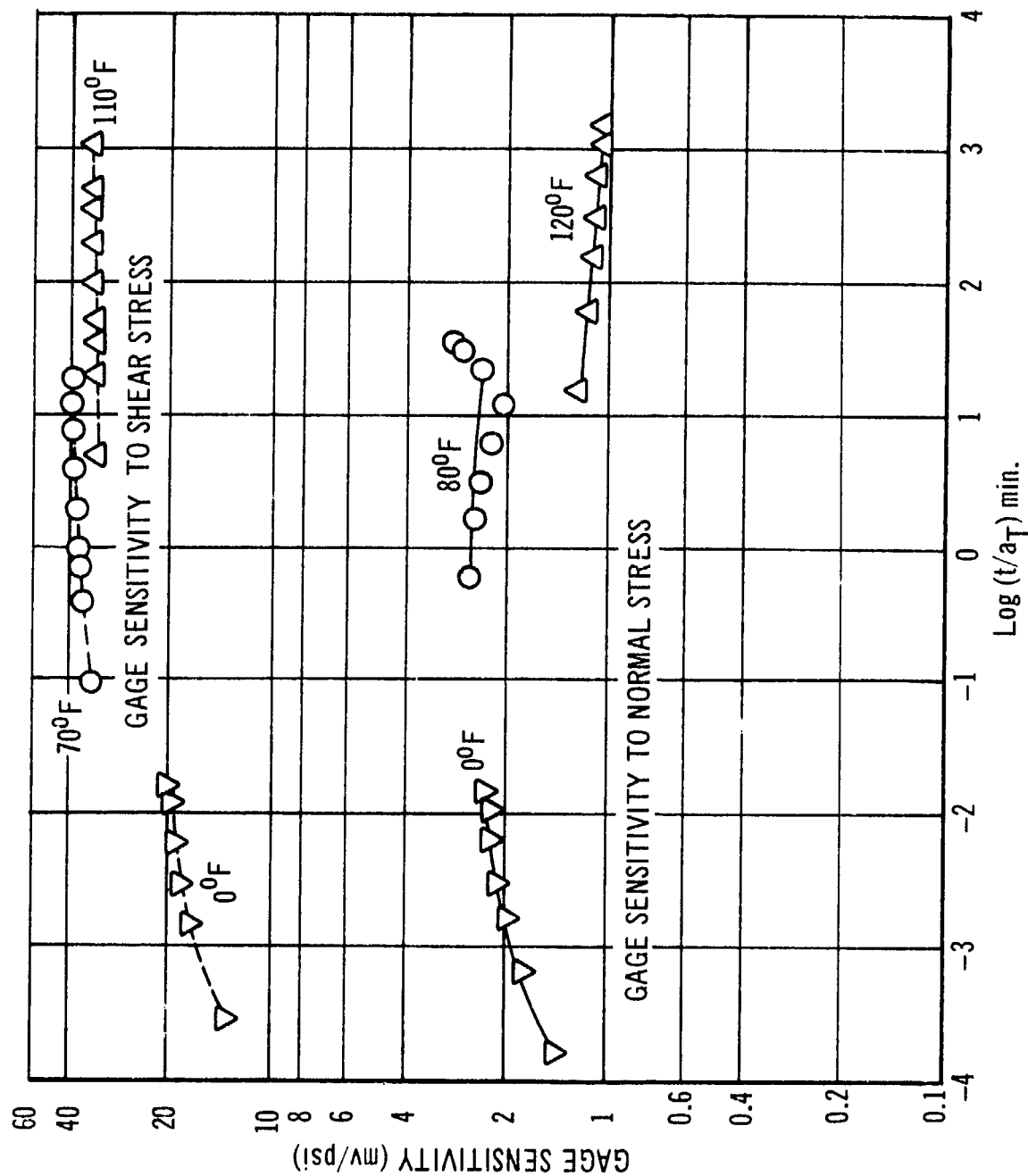
Figure 76. Shear Gage No. 1, 0064-61E STV Propellant Shear Specimen, Sensitivity to Normal Stress versus Reduced Time.
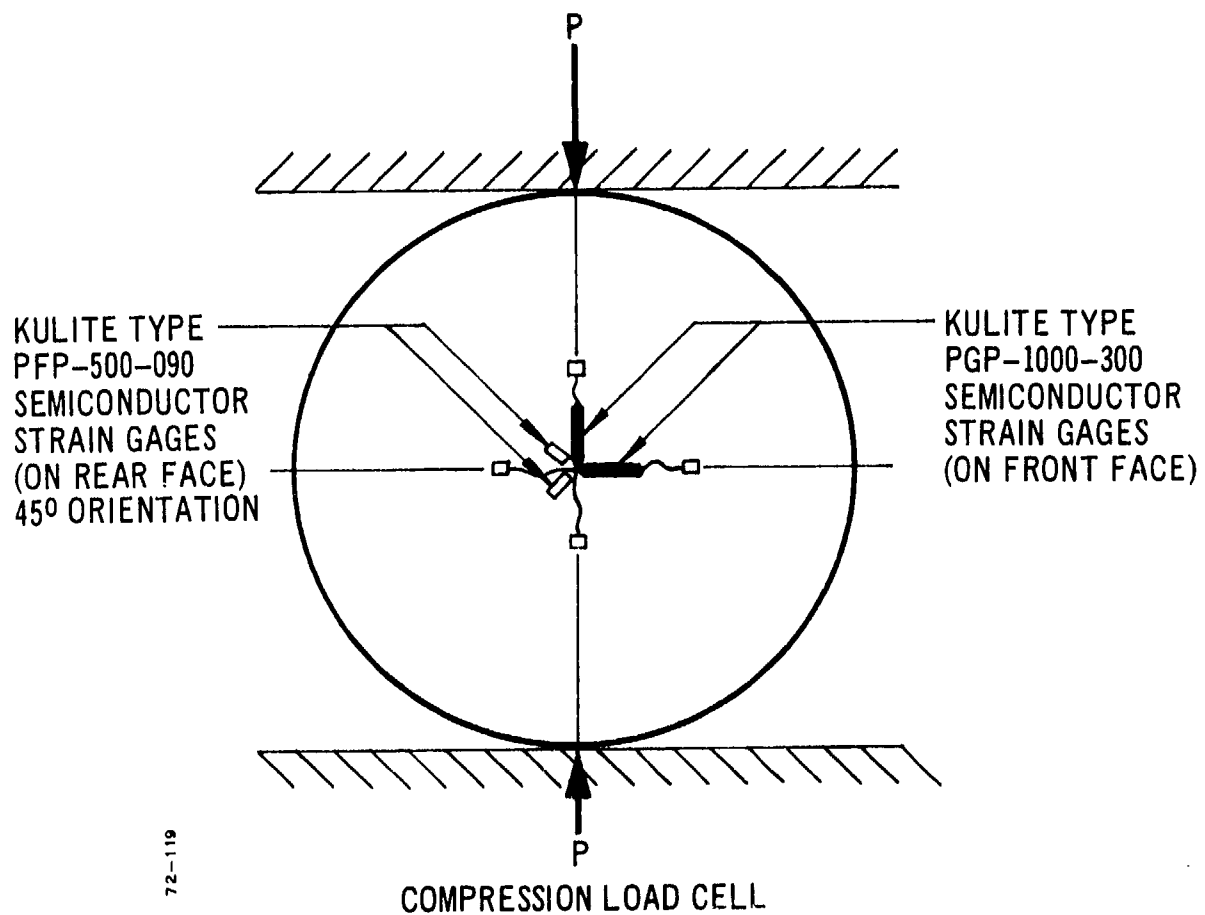
Figure 77. Sketch of Inert Propellant Diametral Shear Gage Specimen.

$$\tau_{xy_{max}} = \frac{4F}{\pi Dt}$$

is obtained at a 45-degree orientation to the applied force. The normal stress on the 45 and 135-degree planes is compressive and is given by the relationship

$$\sigma_{45^0} = \frac{-2F}{\pi Dt}$$

This stress field may be determined from the Mohr Circle diagram of Figure 78, and from these data the shear cube outputs may be calculated for various orientation angles.

When the semiconductor sensing elements are aligned at 0 and 90 degrees to the applied force, the 0-degree gage reacts to the σ_y vertical stress and the 90-degree gage reacts to the σ_x horizontal tensile stress. Thus the gage output

$$E_0 \quad \alpha \quad (\sigma_y - \sigma_x)$$

but

$$\sigma_y - \sigma_x = \frac{2\tau_{xy}}{\sin 2\theta} = 2\tau_{xy_{45^0}} \quad (\theta = 45^0, \sin 2\theta = 1)$$

Thus, the gage output E_0 is proportional to twice the maximum shear stress at a 45-degree orientation to the applied force.

If the semiconductor sensing elements are aligned at 45 and 135 degrees to the direction of the applied force, then the gage output

$$E_{45} = \sigma_{45} - \sigma_{135}$$

and since

$$\sigma_{45} = \sigma_{135} = \frac{-2F}{\pi Dt}, \quad E_{45} = 0$$

i. e., the output of the gage when orientated at 45 degrees to the applied force should be zero.

(3) Experimental Test Results

Tests were made with the diametral specimen at orientations of 0, 45, 90, and 135 degrees. In each case the test consisted of a ramp loading for 1.5 minutes followed by a 10-minute relaxation period, after which the crosshead was lowered at the 0.02 in./min speed to remove the load. Although slight differences were obtained from one test to another, a typical load-versus-time record is as shown in Figure 79. Also shown in Figure 79 are curves for the output of the shear cubes aligned at 0/90 and 45/135 degrees to the direction of the applied force.
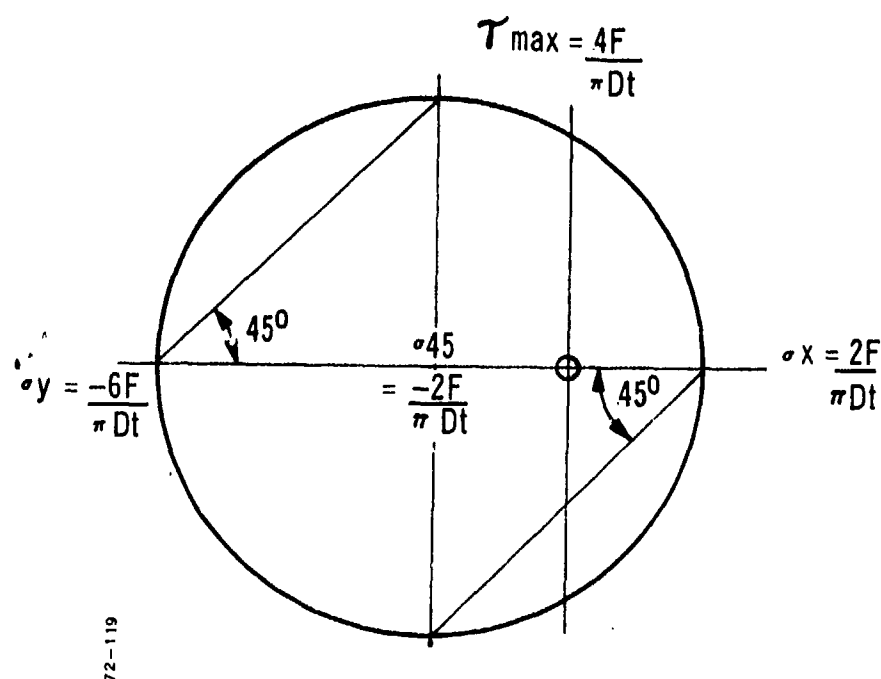
Figure 78. Mohr Circle Diagram for Diametral Compression Test.

-146-
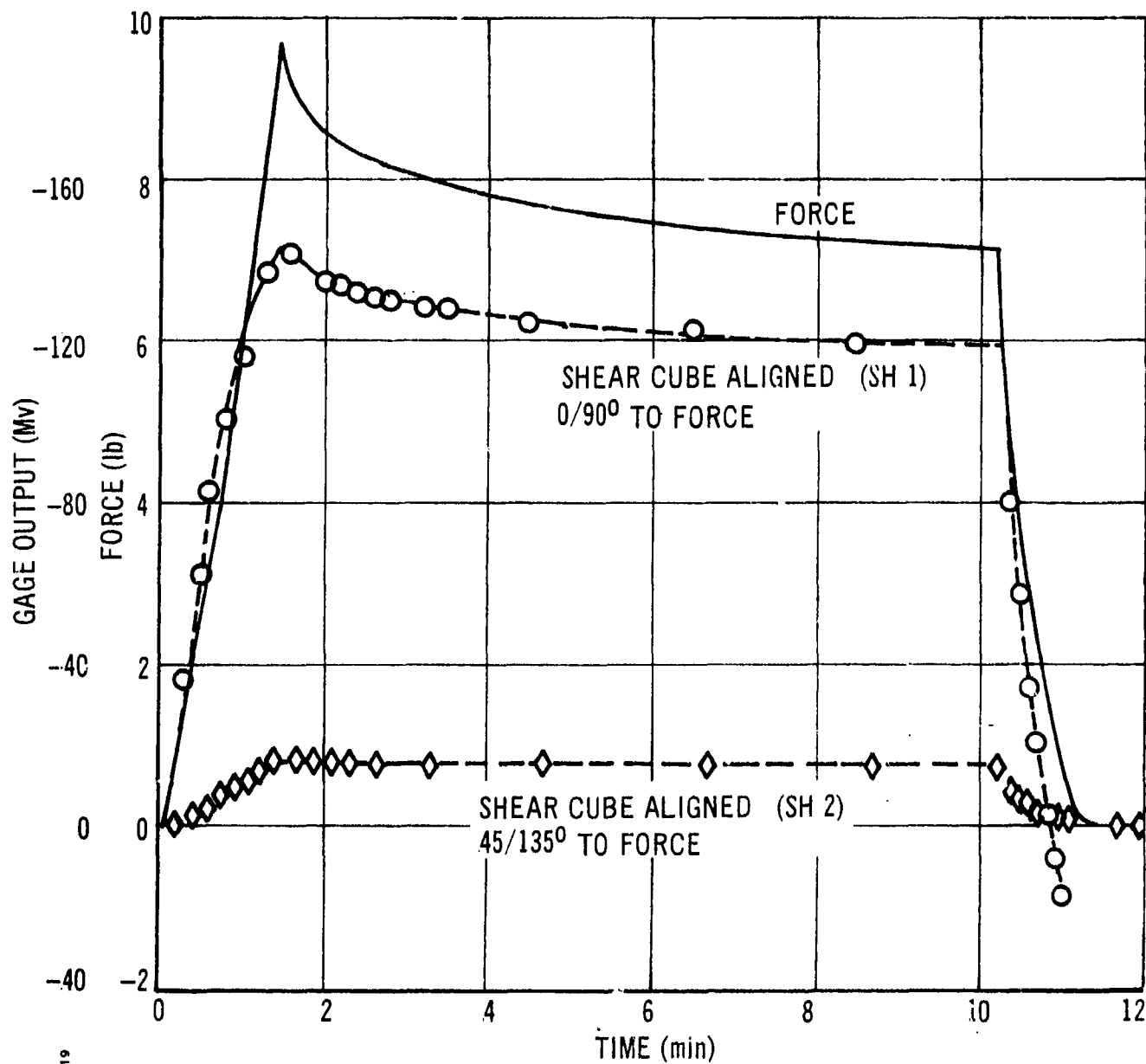
Figure 79. Diametral Compression Test Data.

Figure 80 shows the shear cube sensitivities in mv/psi shear obtained for both gages and for the four test runs.

The following conclusions may be drawn from the results of the tests:

(1) The shear cubes will operate in a biaxial stress field and produce a gage output proportional to the shear stress.

(2) Both gages are imperfect and produce a spurious signal when aligned at 45 degrees to the load, in which case the shear stress should be zero. This cross sensitivity is approximately 10 percent of the normal sensitivity (which agrees with the data of Figure 76).

The data shown in Figure 80 suggest that the gages do not give such accurate data during the ramp loading phase of the test as during the relaxation portion. This problem may be a function of the gages, or, alternatively, it may result from permanent deformation of the disc under the high stresses caused by the near-point loading. This latter explanation is also suggested by the very poor correlation between the stresses and the gage readings under the unloading conditions. The gage readings do not revert to their initial values, almost certainly because of permanent deformation.

To evaluate the performance of the shear gages under ramp loading conditions, the inert propellant shear specimen was tested under a similar ramp loading followed by relaxation test cycle. Tests were performed at crosshead rates of 0.005 and 0.01 in./min; results are given in Figures 81 and 82. Figure 81 shows the Instron force-versus-time curves for the two rates and the corresponding shear gage data-versus-time curves. The similarity between the curves is emphasized in the curves of Figure 82, in which the gage response (mv/psi) is plotted against time. There is no obvious difference between the gage response during ramp loading and during stress relaxation, such as was obtained with the diametral specimen data (Figure 80). Thus the poor correlation for the diametral test ramp loading data is not inherent in shear gages, and there is no reason to assume that the shear gages will not respond properly at high rates of loading.

The results of the diametral compression specimen test show that the shear gages will respond with reasonable accuracy in biaxial tension-compression stress fields.

c. Vibration Tests on Inert Propellant Shear Specimen

(1) Experimental Apparatus

The experimental apparatus used for the vibration tests on the shear specimen was shown earlier in Figure 34. The shear fixture was clamped rigidly along both edges and a small electrodynamic exciter was used to apply a cyclic force to the end of the central rod. In the initial experiments, a small resistor in series with the exciter coil was used to
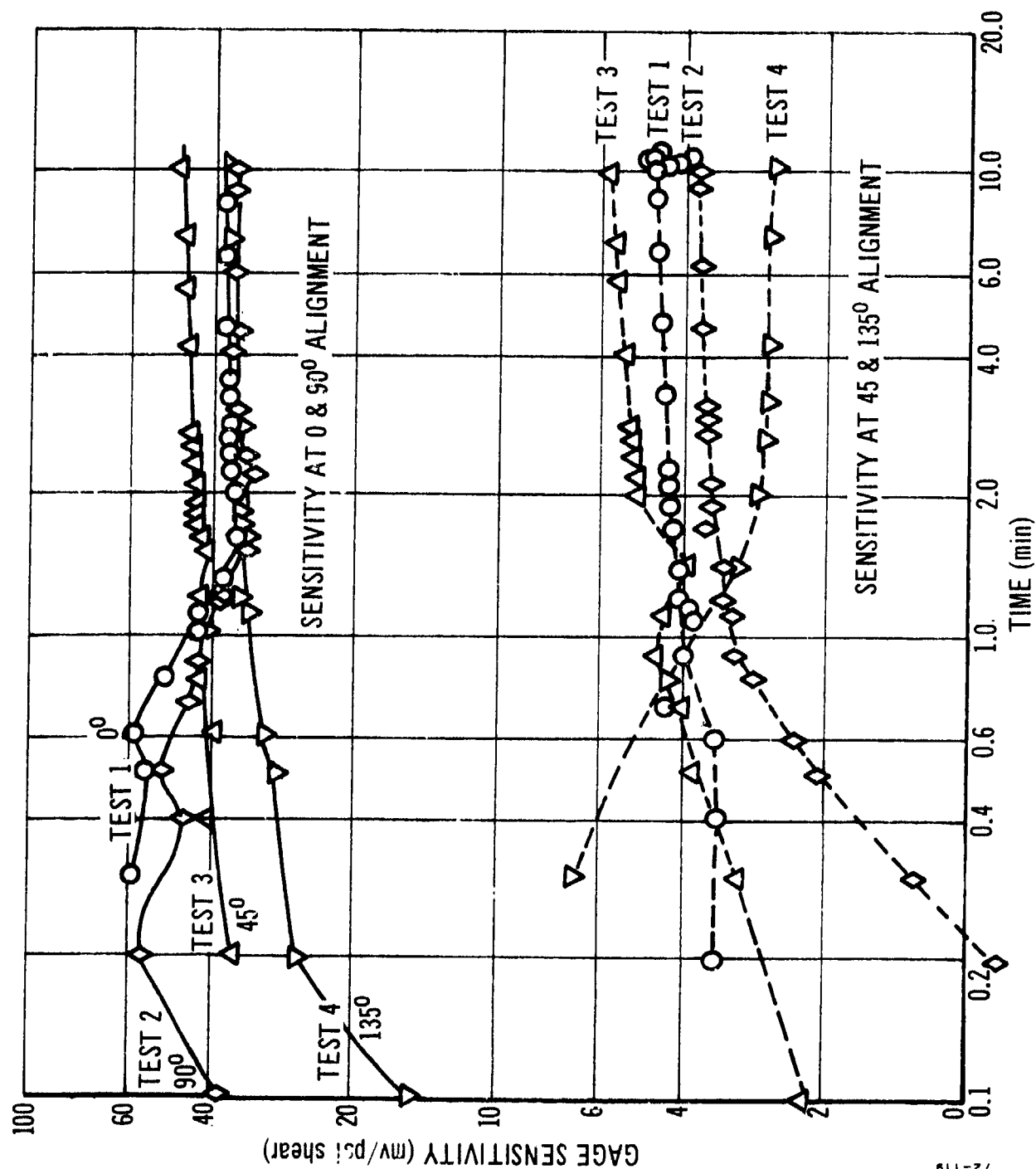
Figure 80. Shear Gage Sensitivity versus Time; Diametral Compression Test Data.

-149-
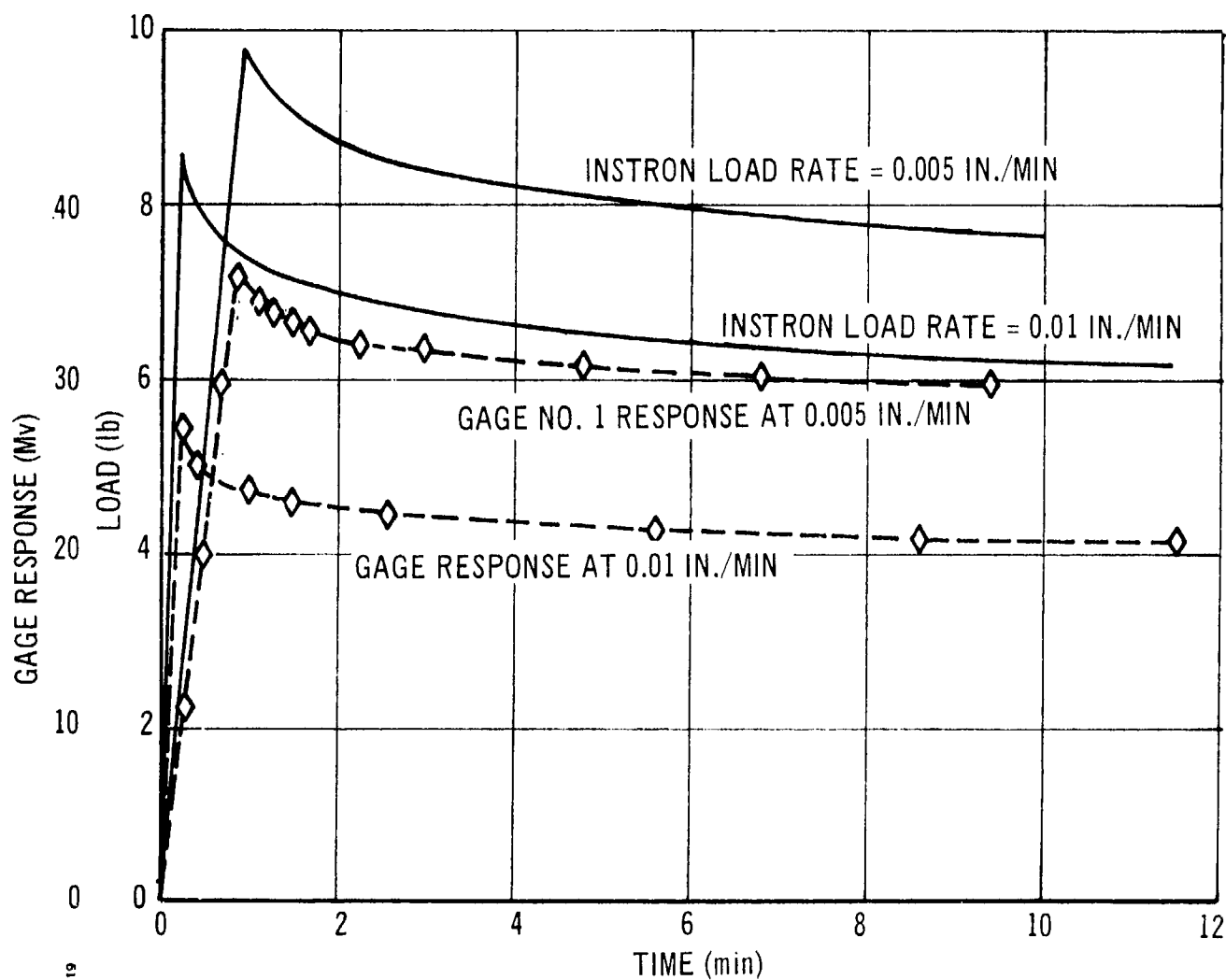
Figure 81.   Instron Load and Shear Gage Response versus Time,
Shear Specimen No. 1.
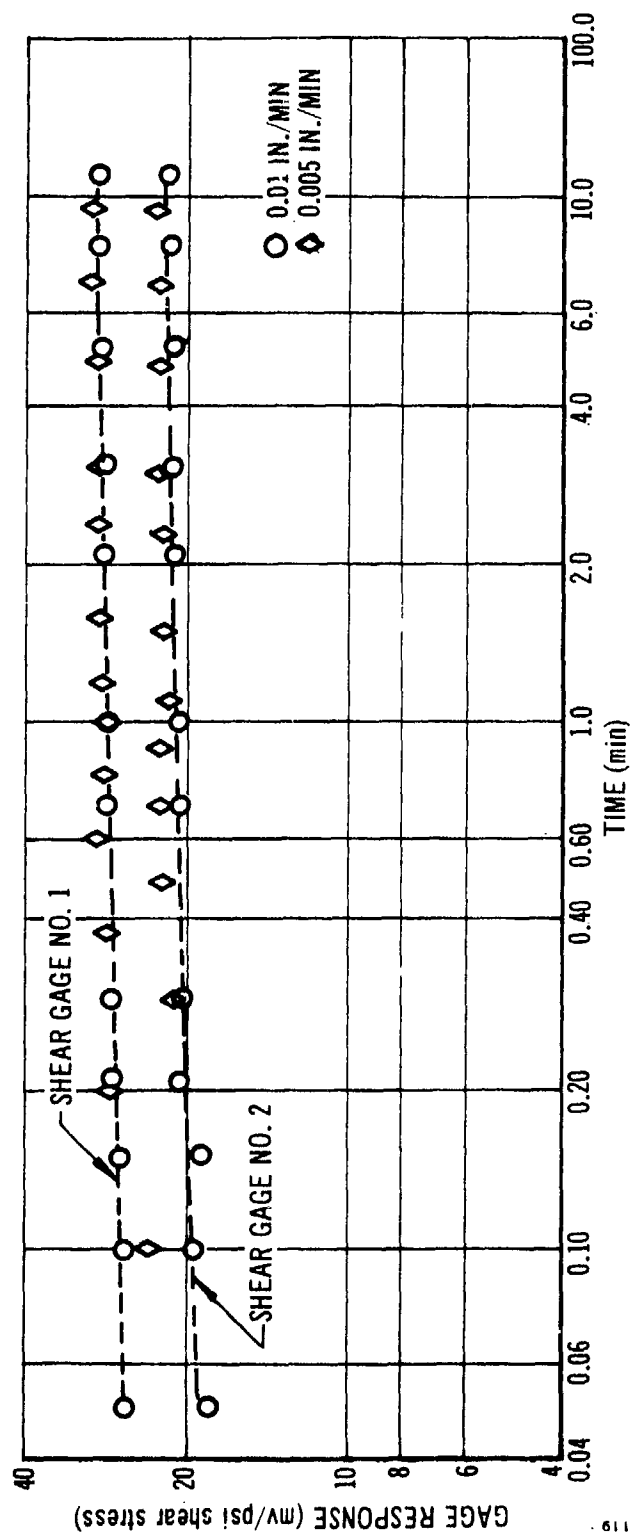
Figure 82. Shear Gage Response versus Log Time, Shear Specimen No. 1 Ramp Loading and Stress Relaxation Tests.

obtain a force signal (proportional to the current through the coil). The resistor output was first calibrated against a load cell at frequencies from 10 to 1000 Hz. A constant cyclic force of 10 pounds (peak to peak) was then applied to the shear specimen, and the force signal and the shear gage output were photographed from the face of a cathode ray oscillograph. Shear gage output and phase lag were determined for a constant force input to the fixture.

In a later series of tests, the displacement of the central rod was measured by means of an LVDT. This enabled values for the dynamic propellant modulus to be determined in addition to the response of the gages for a displacement input.

(2) Experimental Vibration Data

The experimental results obtained from the series of experimental vibration tests on the inert propellant shear specimen are given in Tables XII, XIII, and XIV, and in Figures 83 through 85.

A pronounced reasonance in the test fixture was noted at 390 Hz and the data show this effect: a dip appears in the modulus curve of Figure 83 and sharp peaks are observed in the gage sensitivity curves of Figure 84. This peak is accompanied by a change in phase angle from 14 through 90 degrees at approximately 390 Hz, on to 160 degrees at 700 Hz. The phase angle curves also suggest that another resonance was obtained at approximately 1500 Hz but was not detected experimentally.

The data curves show that the shear gages operate reasonably well for the measurement of dynamic shear stress or strain at frequencies up to approximately 500 Hz, and with reduced sensitivity to stress up to 1000 Hz.

The response to shear strain is the least complex curve shown, and gage sensitivity to strain appears to increase slowly as the propellant modulus increases (with increasing frequency).

As in the case of the uniaxial test fixture, the resonance observed appears to be the simple mass-spring system resonance of the moving parts of the vibrator and the propellant shear specimen (acting as a damped spring).

Based on the results obtained for the uniaxial specimen, it was decided not to perform more tests on the shear fixture at different temperatures. It was anticipated that the results would be very similar to those of Figure 84, except that the resonant frequency would increase as the temperature was decreased. Also, the gage sensitivity to stress would be lower at the lower temperatures because of the higher propellant modulus.

4. COMPARISON BETWEEN ANALYSIS AND EXPERIMENT

The analyses presented earlier in this section do not, unfortunately, give much in the way of concrete data or predicted curves for comparison with the experimental data. These analyses are, in fact, preliminary and

TABLE XII

SHEAR GAGE RESPONSE TO CONSTANT CYCLIC
INPUT FORCE AT 75°F

Frequency (H$_2$)	Force (lb)	Shear Stress (psi)	SH-1		SH-2	
			Response (mv/psi)	Phase Angle (deg)	Response (mv/psi)	Phase Angle (deg)
10	10	1.67	21.0	14	30.6	7
20	10	1.67	-	-	28.8	7
50	10	1.67	16.8	18	24.0	18
100	10	1.67	16.2	14	24.0	14
200	10	1.67	12.3	14	18.0	14
390	10	1.67	28.8	65	46.7	79
500	10	1.67	13.2	108	16.2	135
700	10	1.67	6.5	150	9.0	149
1000	10	1.67	3.84	158	5.8	159
2000	~8	1.33	3.15	65	6.2	58
5000	~4	0.67	6.0	279	6.0	270

TABLE XIII

SHEAR SPECIMEN DYNAMIC MODULUS DATA AT 75°F

Frequency (Hz)	Force (lb)	Shear Stress (psi)	Displacement (in thousands)	Shear Strain (%)	Phase Angle (deg)	Shear Modulus G* (psi)
10	13.6	2.28	3.0	0.30	32	760
20	13.1	2.19	2.2	0.22	36	995
50	13.6	2.26	1.4	0.14	85	1,615
100	22.3	3.72	1.6	0.16	94	2,320
200	45.0	7.50	2.0	0.20	94	3,750
300	18.1	3.02	1.0	0.10	118	3,020
400	20.0	3.33	0.9	0.09	194	3,700
500	53.0	8.75	0.7	0.07	225	12,650
700	45.0	7.50	0.2	0.02	248	37,500
1000	19.0	3.17	0.2	0.02	275	15,850

TABLE XIV

SHEAR GAGE RESPONSE TO CYCLIC STRAIN INPUT AT 75°F

Frequency (Hz)	Displacement (in thousands)	Shear Strain (%)	Gage SH-1 (mv/γ)	Gage SH-1 Phase Angle (deg)
20	2.00	0.20	230	29
50	2.50	0.25	280	63
100	1.50	0.15	533	72
200	1.25	0.125	672	58
300	0.90	0.09	910	79
400	0.60	0.06	1165	87
500	0.60	0.06	1470	90
700	0.25	0.025	1600	84
1000	0.10	0.01	3000	-
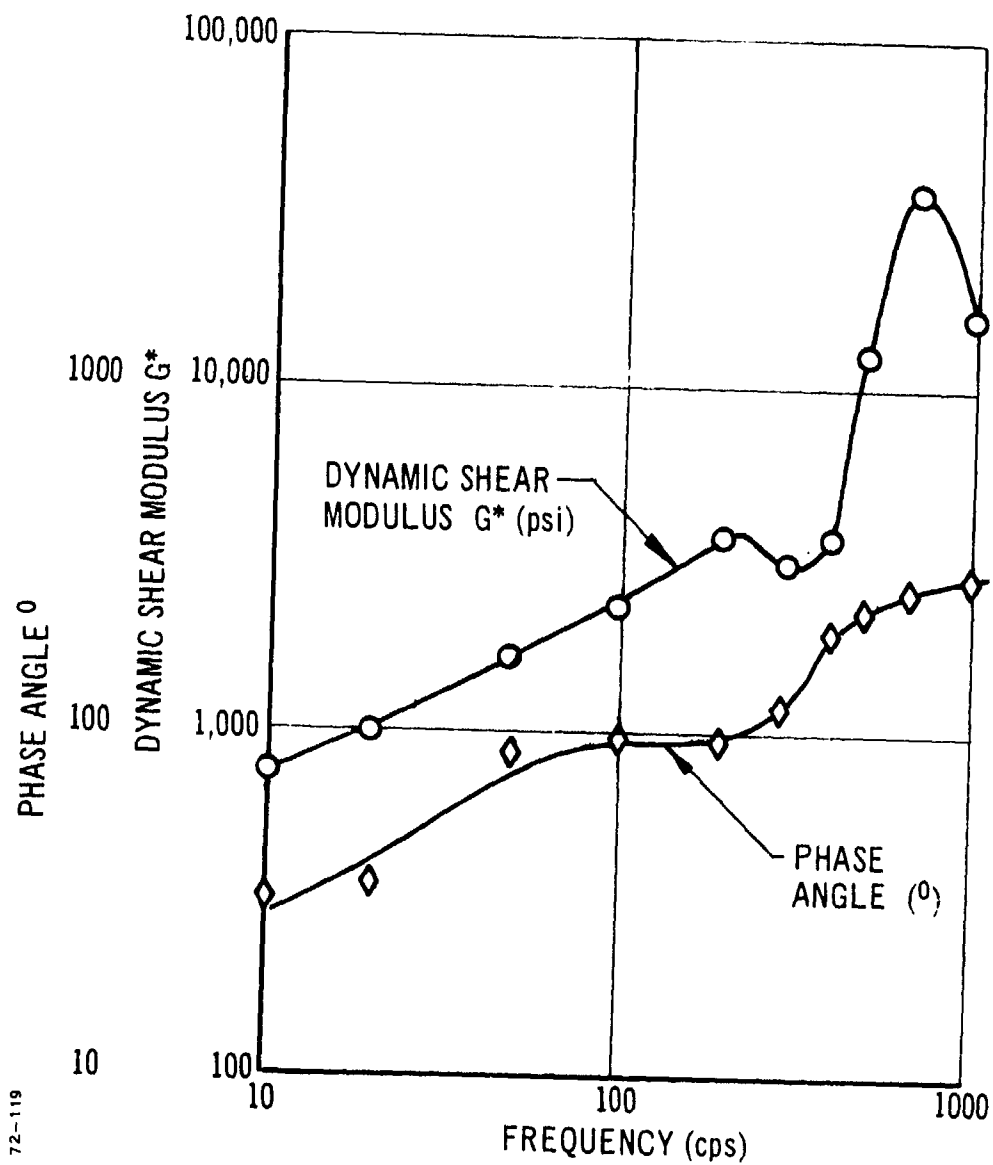
Figure 83. Complex Shear Modulus and Phase Angle versus Frequency, Inert Propellant Shear Specimen.

-155-
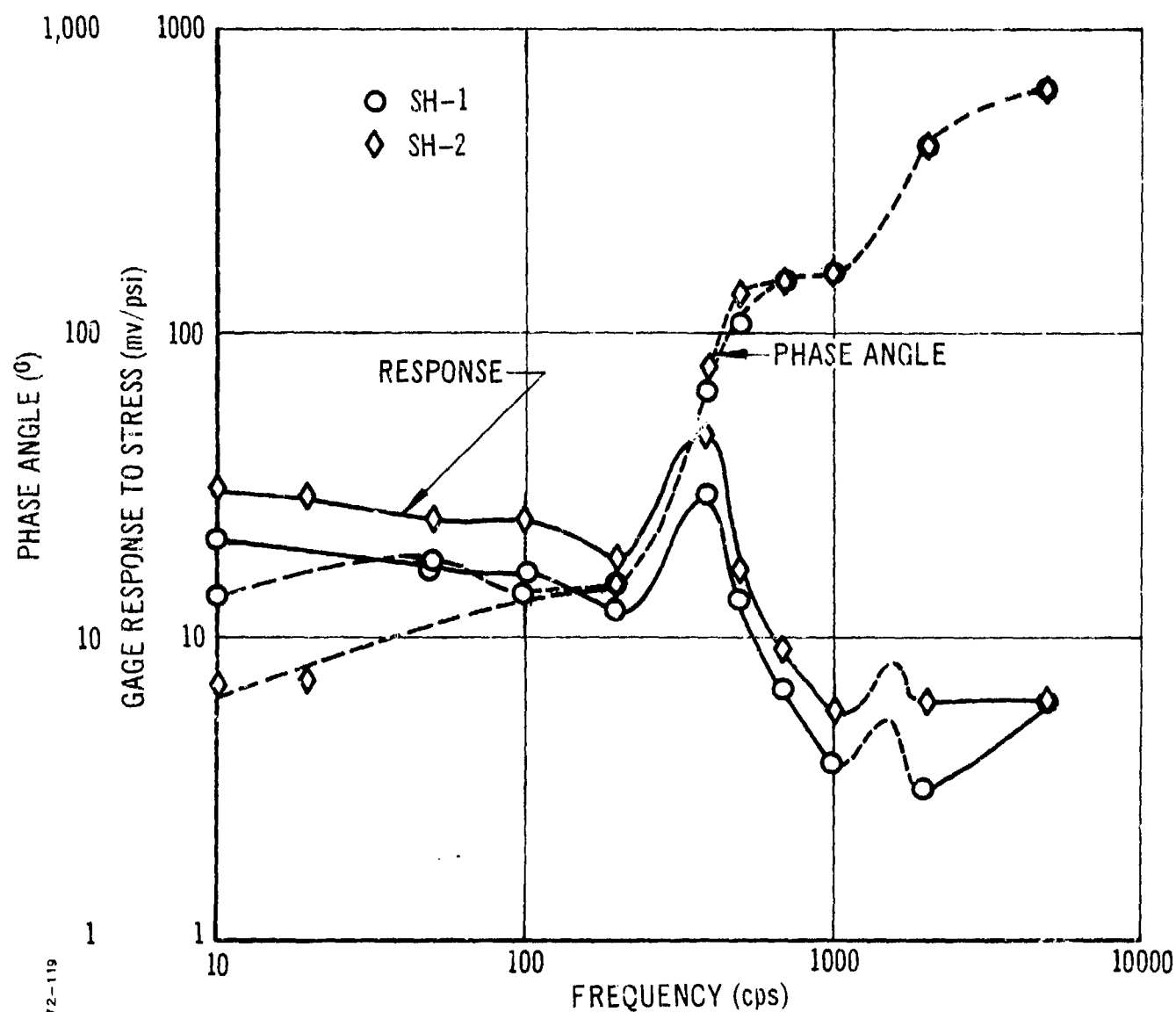
Figure 84. Dynamic Response of Shear Gages to Stress versus Frequency, Inert Propellant Shear Fixture.
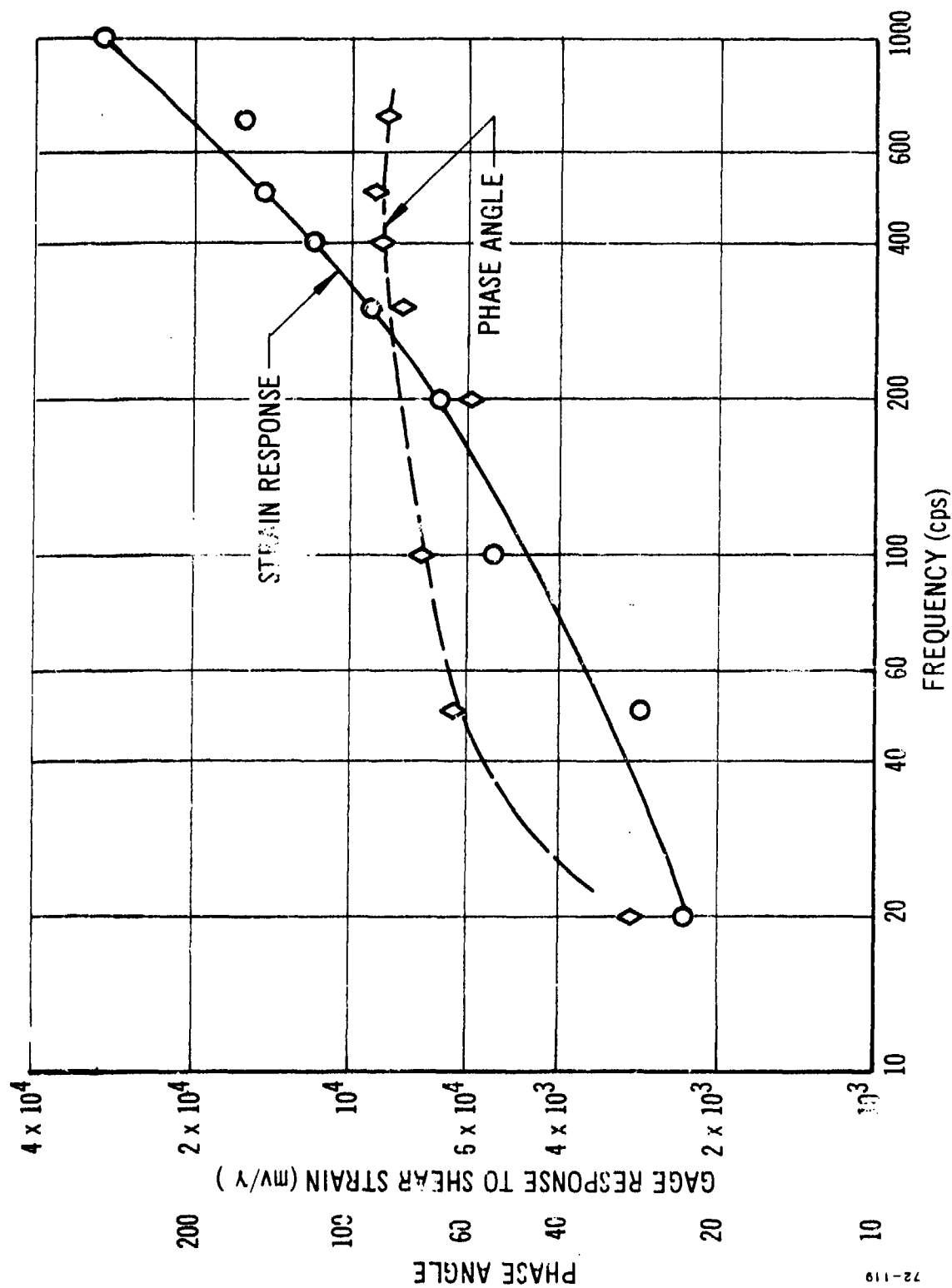
Figure 85. Shear Gage SH-1 Response to Strain versus Frequency, Inert Propellant Shear Fixture.

72-119

need supplementing and extending by more detailed analyses if quantitative data such as that presented for the diaphragm gage in the uniaxial test fixture are required.

In general, the qualitative predictions appear valid. Thus, the analysis predicts that the shear gage should give zero output under normal stress conditions. In practice, because of either stress gradients or because the sensing elements of the shear gages were not precisely oriented at 90 degrees to each other, all the shear gages evaluated in this program showed about a 10-percent cross-sensitivity to normal stress. In many instances, this error will not be significant, but in others--particularly those wherein the shear component is small and strong normal stresses are observed--a large error in the stress readings may be obtained.

Although the analyses at this stage have not proceeded so far as to predict the behavior of the gage for a range of modulus values, the experimental data strongly suggest that there is an intrinsic relation between gage response to stress and the propellant modulus.

SECTION V

NONISOTHERMAL PROPELLANT RESPONSE

1. INTRODUCTION TO PROBLEM

During the past several years various papers have been published (References 1, 2 and 10) in which it has been shown that existing capability to predict the thermal stress induced in a bar or sheet of propellant by restrained thermal cooling, or thermal cooling plus some mechanical deformation, was very poor. Errors in the predicted stress values from thermoviscoelastic analyses ranged from 600 to 2000 percent too low, i.e., the analysis predicted thermal stress levels somewhere between one-half and one-sixth of those measured experimentally.

This is obviously an unsatisfactory state of affairs and this section of the final report is concerned with methods of improving the analytical methods of predicting thermally induced stresses in propellant bars. The approach used herein is to consider the definition of "reduced time" as the main cause of the error and to make use of alternative approaches to defining reduced time.

In a later section of this report, Professor Schapery considers nonlinear propellant behavior due to dewetting as a possible cause of inaccuracy in predicting thermally induced stresses (and strains).

The basis of our contention that the problem lies in the definition of reduced time was presented in last year's final report (Reference 2). The curves shown in Figure 86 are repeated in this section to point out the basic problem. If the thermoviscoelastic computer code is used to predict the stress for the constant strain rate-relaxation-constant strain rate tests shown in Figure 86, then the predicted data are in reasonable agreement with the measured data for temperatures from 77 to -65^{0}F. A maximum error of about 40 percent is obtained under these isothermal test conditions, which is tolerable.

Use of the same input data and the same thermoviscoelastic computer code to calculate the stress under a restrained thermal cooling condition will lead to an error in the calculated thermal stress values of at least a factor of two times, the calculated values being low.

It is believed, therefore, that the error must occur in the determination of the transient modulus for a given time and temperature and this, of course, depends upon the definition of reduced time.

2. MODIFIED DEFINITION FOR REDUCED TIME

The above observations suggest that the problem area with the calculations is in the method of determining the time-dependent modulus during changing temperature conditions.
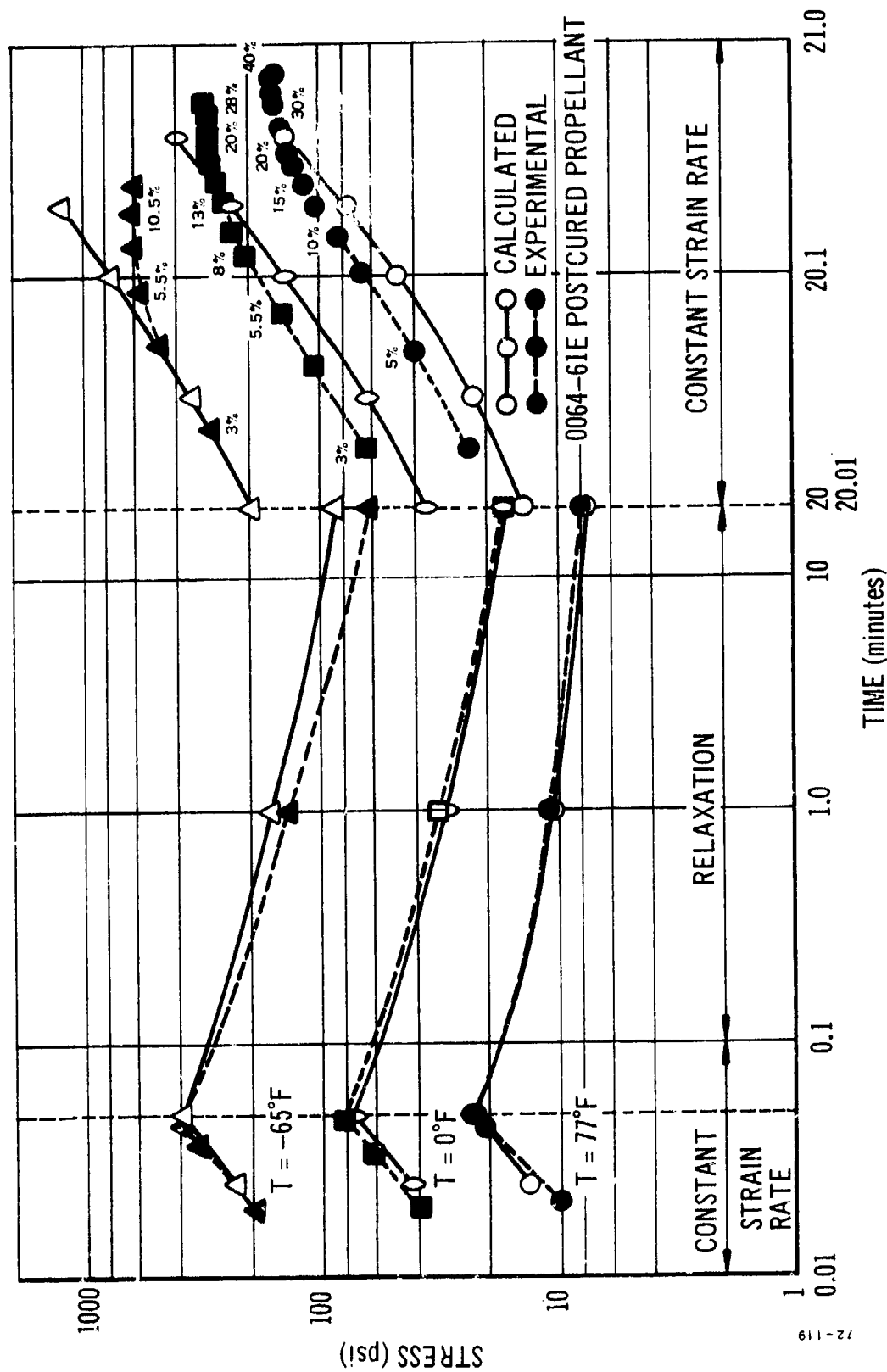
Figure 86. Comparison Between Analytical and Experimental Results for Uniaxial Constant Strain Rate - Relaxation - Constant Strain Rate Tests; Postcured STV Propellant.

The standard technique is based on the postulate of Morland and Lee, which defines the reduced time under transient thermal conditions by means of the simple equation:

$$\xi(t) = \int_0^t \frac{dt'}{a(T(t'))} \tag{100}$$

Under isothermal conditions, this equation reduces to the proper form, i.e.,

$$\xi(t) = \left(\frac{t}{a_T}\right) \qquad \text{(for } T = \text{constant)} \tag{101}$$

Fitzgerald pointed out several years ago that this approach is not the only one available. Starting from the definition of reduced time given in Equation (101), a modified value of reduced time under transient temperature conditions can be obtained as follows:

First write Equation (101) in terms of the inverse shift factor function θ_T, which is equal to $1/a_T$; and we obtain:

$$\xi(t) = t/a_T = t \cdot \theta_T$$

Differentiating this equation:

$$\frac{d\xi(t)}{dt} = \theta_T + t \cdot \frac{d\theta_T}{dt}$$

which, for varying temperature conditions such that

$$\theta_T = \theta_T[T(t)]$$

gives:

$$\left(\frac{d\xi}{dt}\right) = \theta_T + t \cdot \frac{\partial\theta_T}{\partial T} \cdot \frac{dT}{dt} \tag{102}$$

From Equation (102) we obtain the following expression for $\xi(t)$ under transient thermal conditions:

$$\xi(t) = \int_0^t \theta_T \, dt' + \int_0^t t' \frac{\partial\theta_T}{\partial T} \cdot \left(\frac{dT}{dt}\right) \cdot dt' \tag{103}$$

Equation (103) contains two parts, the first being identical to the definition of reduced time proposed by Morland and Lee, Equation (100). The additional term in Equation (103) is concerned with the effects of rate of change in temperature, and the sense of this extra term is to reduce $\xi(t)$ under thermal cooling conditions. This will have the effect of producing

increased modulus values under cooling conditions and decreased modulus values under heating conditions.

However, it is not believed that the changes in stress level that can be obtained through the use of Equation (103) will be sufficient to make experiments and theory agree. The use of Equation (103) is precisely the same as defining reduced time as t/a_T for all conditions, the results of this assumption being well known because it is often used in preliminary modulus determinations.

Another modification to the definition of reduced time was suggested by Professor Pister. This approach makes use of a modified reduced time that is a function of rate of change of temperature as well as temperature. The modified reduced time ξ_m is defined by the equation:

$$\frac{d\xi_m(t)}{dt} = \theta_T (T, \dot{T}) = \theta_T (T) \psi_{\dot{T}} (\dot{T}) \tag{104}$$

where the assumption is made that the effects of temperature and rate of change of temperature are separable into the two independent functions θ_T and $\psi_{\dot{T}}$. The first function is the shift factor under constant temperature conditions, i.e., the inverse of the normal a_T function derived from isothermal test data.

The value of reduced time under transient thermal histories is obtained from the integral of Equation (104):

$$\xi_m(t) = \int_o^t \theta_T [T(t')] \psi_{\dot{T}} \left[\frac{dT}{dt}\right] dt' \tag{105}$$

In order to make use of this equation to calculate the modified reduced time, some functional form must be postulated for $\psi_{\dot{T}}$. The function must be normalized such that at zero rate of temperature change, its value is equal to unity.

In the trial program runs, initial computations were performed using the equation

$$\psi_T = \pm \left[1 + K_1\dot{T} + K_2(\dot{T})^2\right] \tag{106}$$

for comparison with the experimental test case and with the closed form analytical solutions also used as test cases.

Clearly, Equation (106) is merely a simple form of a more general expression that could introduce higher power of rates of temperature change and/or higher order derivatives of temperature.

3. ANALYTICAL TEST CASE

Following some preliminary troubles with the revised computer code for calculating the stress in a uniaxial bar subject to simultaneous straining and thermal cooling, the experimental problem given in last year's final report was rerun with the same input data. These input data represent the highest modulus data for the system and were measured on the uniaxial specimen containing the gage at very low strain levels (0.1 to 0.5 percent).

The modification to the computer code produced slightly different values for the thermal stresses (as discussed later). It was decided to investigate the accuracy of the computer code for a problem with a precisely known (closed form) solution. The problem used was developed last year and consists of the thermal cooling of a bar with the following material properties:

$$\left.\begin{array}{rcl} E_{rel}(t) &=& E_o/\sqrt{t} \\[2mm] \log_e a_T &=& -b\,(T - T_o) \\[2mm] T &=& T_s - K\,t \end{array}\right\} \quad (107)$$

and,

$$\epsilon = R\,t$$

The solution to the thermal cooling problem for this special case is given by the equation:

$$\sigma = 2\,E_o\,(R + \alpha K)\sqrt{\frac{\xi^*}{C^*}}\ \exp\,(t/2\,\xi^*)\ \mathrm{Tan}^{-1}\sqrt{(\exp\,(t/\xi^*) - 1)} \quad (108)$$

where

$$\left.\begin{array}{rcl} C^* &=& C\,\exp\,(bT_s) \\[2mm] \xi^* &=& 1/Kb \end{array}\right\} \quad (109)$$

Analytical solutions were determined for the specific problem of $E_O = 100$, $b = 0.2$, and $K = 25$ and 0.055 deg/min. The calculated data are shown as thermal stress versus temperature in Figure 87.

The revised Knauss computer code was then used to calculate as nearly as possible the same problem, and the resulting data were indistinguishable from the analytical values. The two sets of curves could not be separated on the plot of Figure 87. It seemed, therefore, that the computer code was providing the correct answers to the thermal cooling problems and that the earlier version must have been more approximate in its approach.
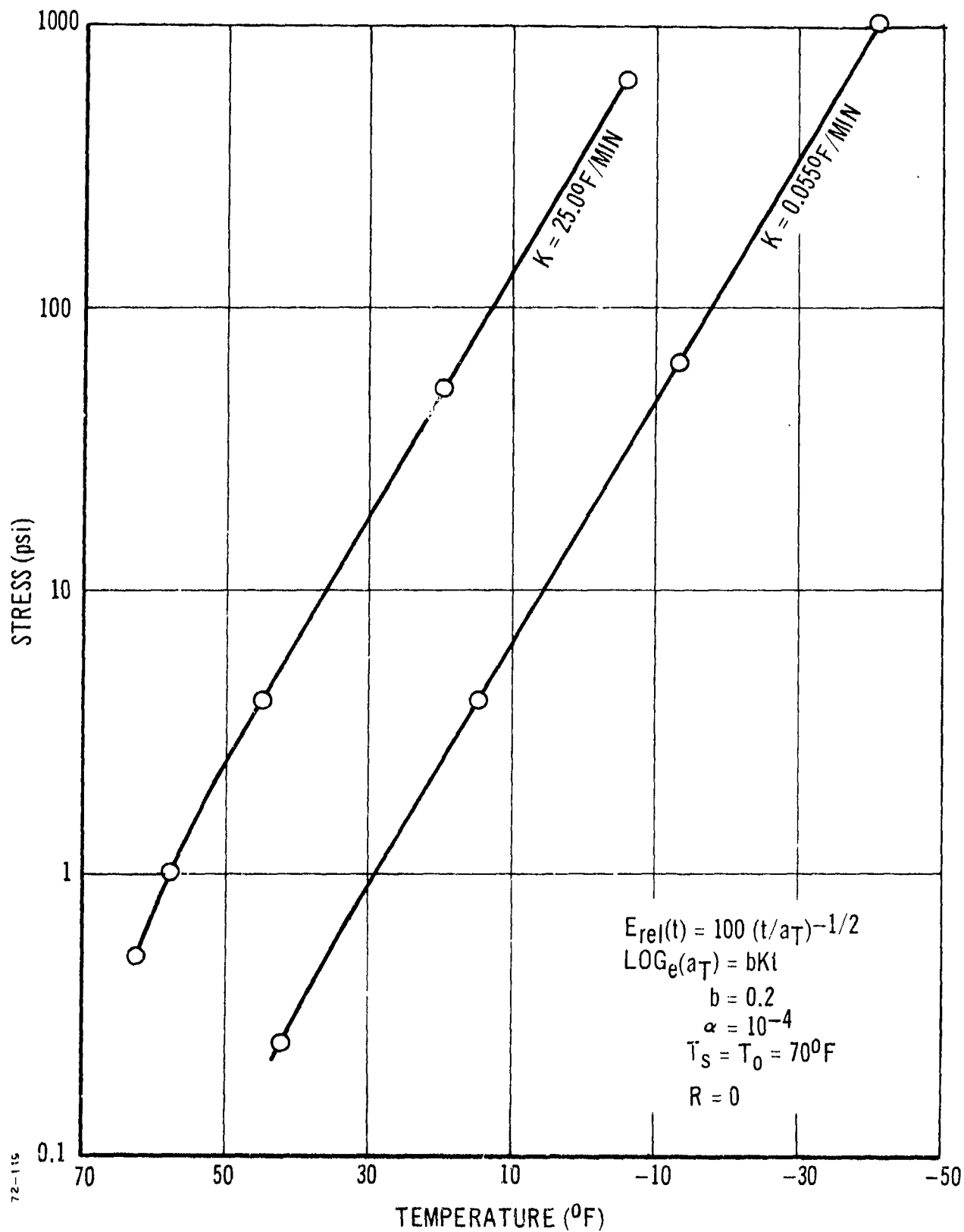
Figure 37. Test Case, Thermal Stresses versus Temperature.

-164-

This analytical test case may be used to illustrate the effects of changing the definition of reduced time by introducing the constants K_1 and K_2 into Equation (106).

Figure 88 shows clearly that the effects of the changes are generally small until a high rate of temperature change is encountered. However, it is possible to provide a considerable increase in the calculated thermal stress values and it remains to be seen whether or not this is sufficient to bring the analysis and experiments into line.

4. COMPARISON BETWEEN ANALYSIS AND EXPERIMENT

a. STV Propellant Bar Containing 25-psi Gage

This is the problem that was analysed last year and discussed in the final report. The input data for the analysis are given in Table XV. Figure 89 shows a comparison between the data calculated with the original Knauss program and the revised data determined with the newer program. The minor differences in the calculated stresses will be apparent in this figure.

Calculated thermal stresses are compared with the measured experimental values in Figure 90. The calculated values are approximately four times lower than the measured data.

Another problem was then run wherein the stress relaxation modulus data were replaced by the creep compliance data with the same time-temperature shift factors retained. As will be observed from Table XVI, the inverse creep compliance values are larger than the stress relaxation modulus values so that a better fit to the measured data was anticipated. The resulting thermal stresses are in fact larger than those derived from the stress relaxation test data, as will be noted in Figure 90. However, the comparison between the computed stress of 24.4 psi and the measured stress of 58.3 psi at the lowest temperature of -75^0F is still not very good. Clearly, other factors must be producing this large discrepancy between theory and experiment.

Several analyses were then performed with different values of K_1 and K_2 used in the expression for the reduced time integral, Equation (106). It should be noted at this time that to give the desired effect, i. e. , an increase in stress with the higher rates of cooling, the sign of the whole bracket in Equation (106) is made negative when values of K_2 alone are employed. The results with K_1 in the equation proved disappointing; if a sufficiently large value of K_1 was employed to give a significant effect, then there was always a chance that the $(K_1 \cdot \dot{T})$ term would be greater than 1.0, which caused the program to break down. Thus, most of the later calculations were performed with the expression $K_1 = 0$, and with K_2 given different values.

Table XVII shows the values of the thermal stress versus time for several different analyses. The values of the constants varied between 0 and 0.02 for K_1, and between 0 and 20.0 for K_2. The effect of the K_1 term
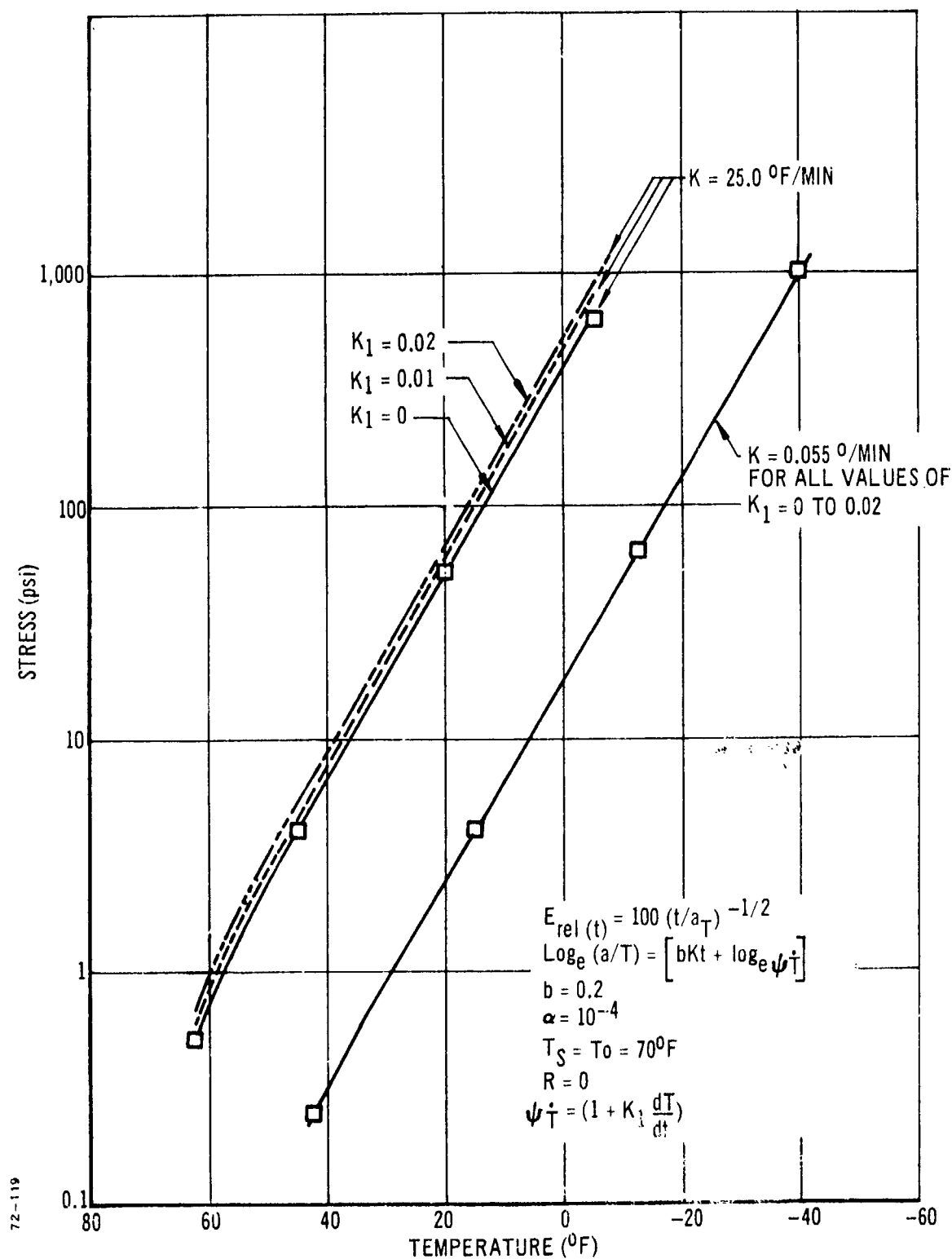
Figure 88. Test Case, Thermal Stress versus Temperature; Revised $\xi(t)$.

TABLE XV

ANALYSIS INPUT DATA FOR
0064-61E PROPELLANT THERMAL COOLING PROBLEM

Log Time (min)	Relaxation Modulus	Log a_T	Temperature (^{0}F)	Time	Temperature (^{0}F)
-12	15,000	8.6	-80	0	146
-10	10,000	7.3	-60	720	104
- 8	7,000	5.8	-40	1010	64
- 6	4,300	4.0	-20	1265	11
- 4	2,500	3.0	0	1495	-11
- 2	1,250	2.0	20	1690	-45
0	640	1.0	40	1880	-75
2	400	0	70	2140	15
4	280	-1.0	100	2600	82
6	200	-2.0	130		
		-3.0	160		

$\alpha_p = 5.67 \times 10^{-5}$

Strain = 0 for all times
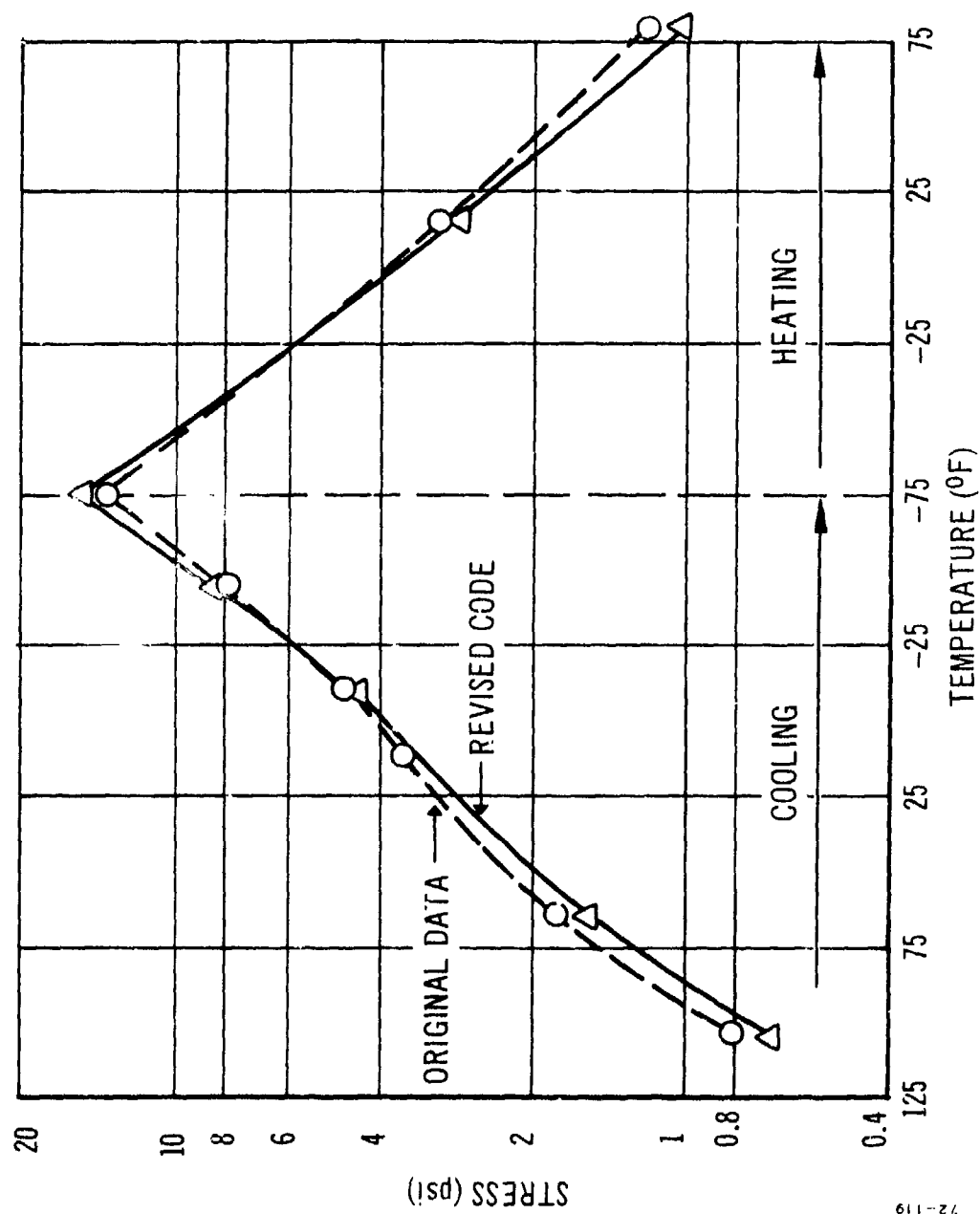
Figure 89. Revised Thermal Stresses for Restrained Uniaxial 0064-61E Test Fixture Containing 25-psi Gage.
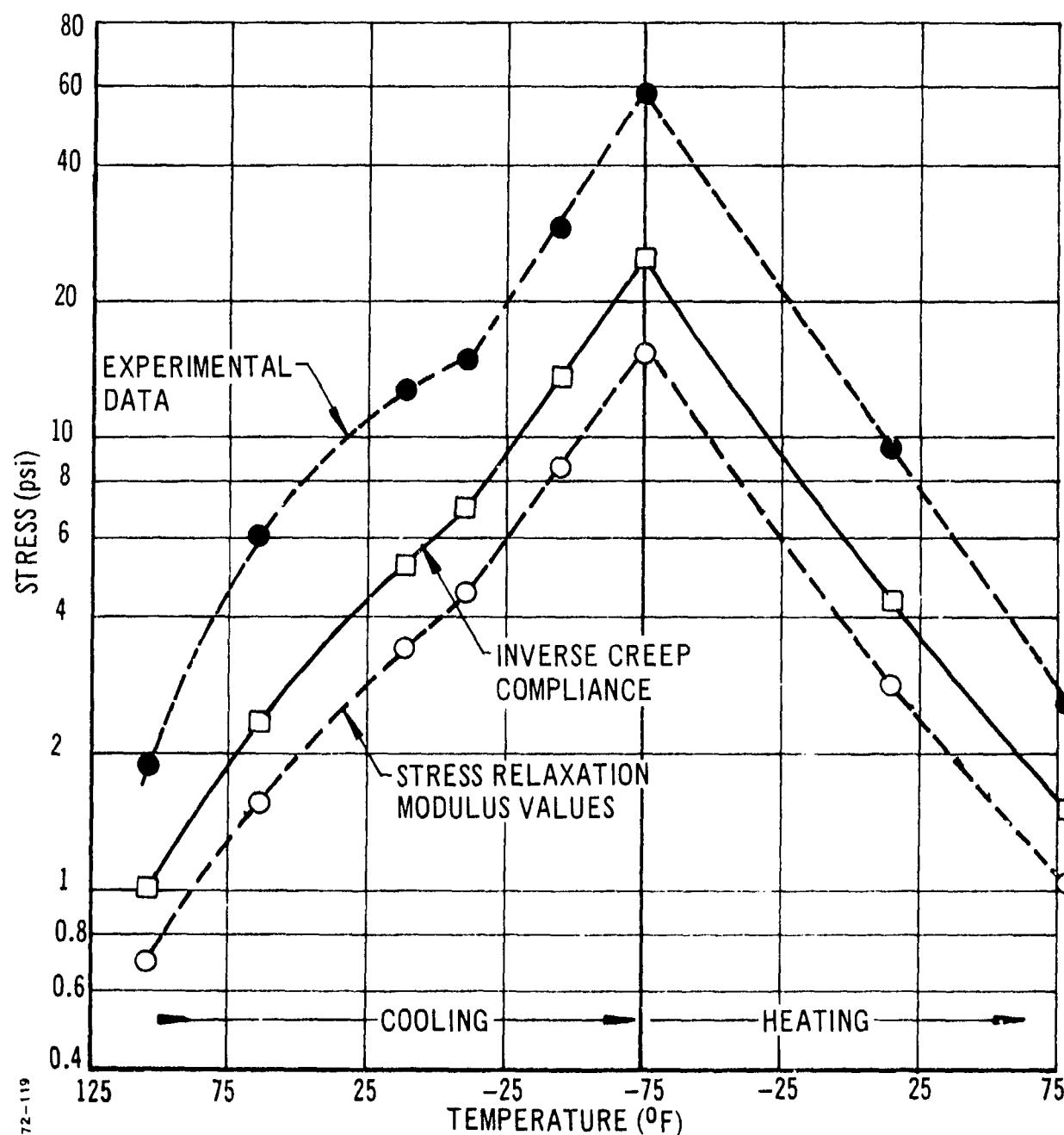
Figure 90. Thermal Stress Values Calculated Using Inverse Creep
Compliance Data for 0064-61E Propellant Uniaxial Test
Fixture Containing 25-psi Gage.

-169-

TABLE XVI

COMPARISON OF STRESS RELAXATION MODULUS
AND INVERSE CREEP COMPLIANCE

(0064-61E Propellant: Data from Uniaxial Test
Specimen Containing 25 psi Gage.)

Log t (min)	Relaxation Modulus (psi)	Inverse Creep Compliance (psi)
-12	15,000	20,000
-10	10,000	15,000
- 8	7,000	11,000
- 6	4,300	7,000
- 4	2,500	4,000
- 2	1,250	1,950
0	640	1,000
2	400	610
4	280	410
6	200	300

TABLE XVII

CALCULATED THERMAL STRESSES FOR UNIAXIAL BAR
OF 0064-61E PROPELLANT UNDER AXIAL RESTRAINT

Time (min)	Calculated Thermal Stresses						Temperature (^{0}F)
	$K_1 = 0$ $K_2 = 0$	$K_1 = 0.01$ $K_2 = 0$	$K_1 = 0.02$ $K_2 = 0$	$K_1 = 0$ $K_2 = 5$	$K_1 = 0$ $K_2 = 10$	$K_1 = 0$ $K_2 = 20$	
720	1.0016	1.0017	1.0017	1.0058	1.0097	1.0168	104
1010	2.3265	2.3268	2.3271	2.3432	2.3586	2.3863	64
1265	5.1900	5.1911	5.1922	5.2700	5.3401	5.4595	11
1495	6.9494	6.9504	6.9515	7.0388	7.1182	7.2555	-11
1690	13.257	13.260	13.263	13.474	13.667	14.000	-45
1880	24.3047	24.309	24.314	25.642	26.690	28.299	-75
2140	4.3250	4.3261	4.3272	4.3623	4.3920	4.4526	15
2600	1.5142	1.5142	1.5142	1.5230	1.5308	1.5487	82

is very small, as will be noted for the maximum stress value, which occurs at a time of 1880 minutes. This stress is increased from 24.3047 to 24.3142 psi as K_1 changes from 0 to 0.02. The effect of changing K_2 from 0 to 20 is to increase this maximum stress value from 24.3047 to 28.2990, which is at least visible.

However, this particular test was conducted at such a low rate of cooling that the rate would not be expected to have a significant effect upon the thermal stress value. Therefore, it appears that if the thermal stresses measured in this test are correct, then the modification to reduced time will not account for the discrepancy between theory and experiment.

Before the conclusion was accepted that rate of temperature change could not have a significant effect on thermal stresses, it was decided that several more thermal cooling experiments should be conducted at various rates of cooling and heating for comparison with the analyses.

b.   Inert Propellant Specimen Containing 150-psi Gage

The inert propellant uniaxial test specimen, containing a single 150-psi gage embedded at one end, was subjected to restrained thermal cooling tests. Three different rates of cooling were employed: a very slow, programmed rate of $7.5^0F/hr$ ($0.125^0F/min$); a moderate cooling rate of 1.0 to $2.0^0F/min$; and a relatively fast cooling rate of 5.0 to $6.0^0F/min$. In point of fact, the latter rate of cooling was higher than could be tolerated and produced a considerable temperature gradient across the specimen. Thus, the load cell reading was unreliable as a measure of the thermal stress, and the embedded gage data would not be expected to give valid results. The two other tests should, however, provide good test data for comparison with the analyses.

Static creep tests had previously been performed on the uniaxial specimen, and the measured inverse creep compliance values were used instead of the relaxation modulus values in the analysis program. Table XVIII presents the thermal analysis input data for the inert propellant tests. A linear coefficient of expansion of 4.5×10^{-5} in./in./^0F was adopted for the analyses.

The experimental and calculated data for thermal cooling tests on the inert propellant specimens are compared in Figures 91 through 93. The data for moderate rate of cooling are presented in Figure 91 and for the very slow cooling rate in Figure 92. Data for the fast cooling rate are given in Figure 93 but are considered less reliable than the other two sets of data.

Consider first the moderate cooling rate data shown in Figure 91. The calculated stress values are approximately one-half of the experimentally measured values over most of the temperature range. The introduction of the modified reduced time with various values of K_2, and with $K_1 = 0$, produces the analytical curves also shown in Figure 91. It seems that the use of the K_2 term produces an almost uniform increase in the thermal stress values, with the calculated data for $K_2 = 20$ being about 1.5 times the thermal stresses for $K_2 = 0$. Reasonable agreement across much of the temperature

TABLE XVIII

MODULUS-TIME AND SHIFT FACTOR-TEMPERATURE
DATA FOR INERT PROPELLANT ANALYSES

Log Time (min)	Modulus (psi)	Temperature (^{0}F)	Log a_T
-10	20,500		
- 9	20,500	-83	8.60
- 8	13,500	-67	6.40
- 7	8,500	-25	3.50
- 6	5,400	75	0
- 5	3,500	146	-1.70
- 4	2,400		
- 3	1,630		
- 2	1,200		
- 1	940		
0	760		
1	640		
2	550		
3	480		
4	430		

$$\alpha_p = 4.5 \times 10^{-5}$$
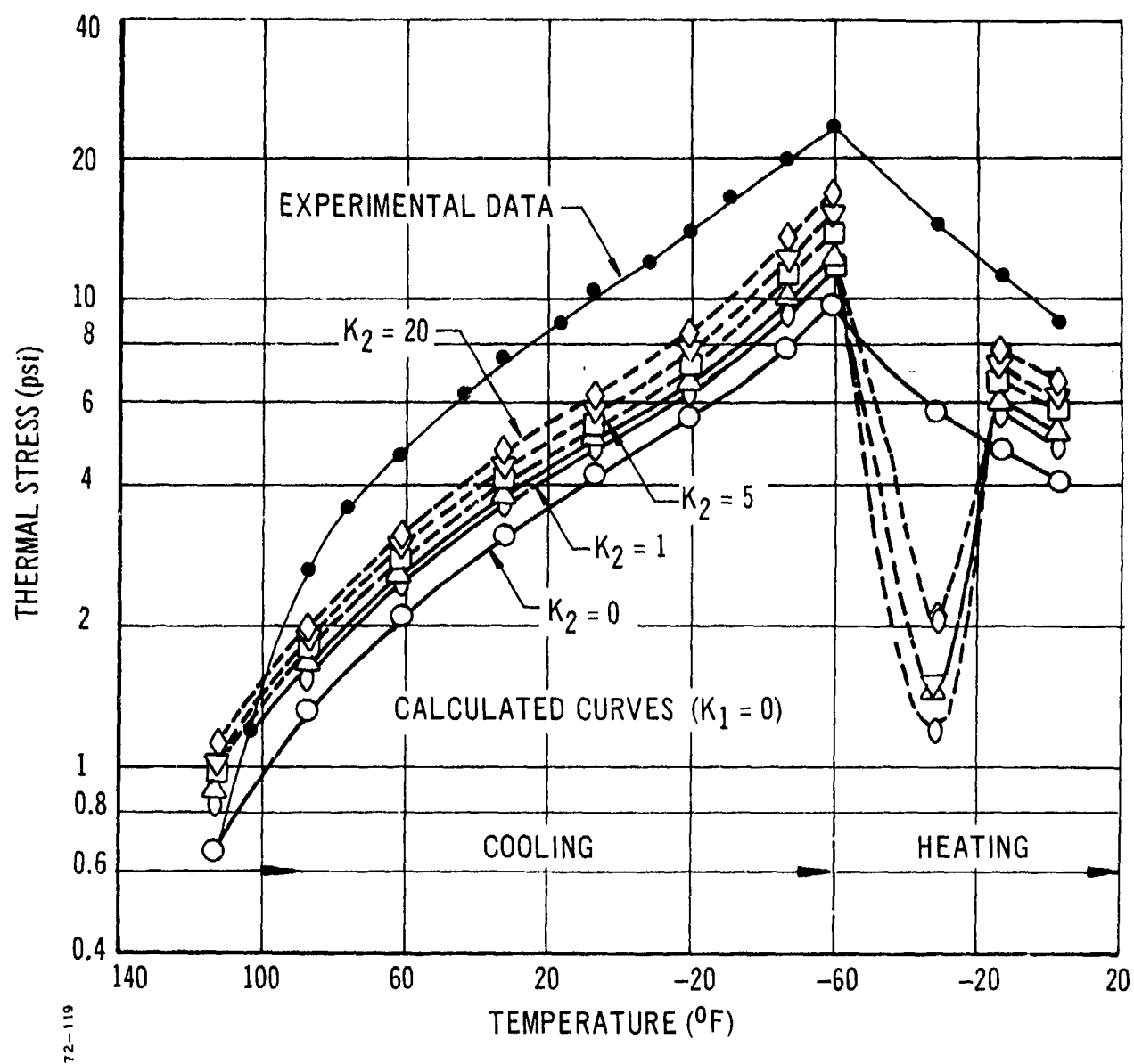
Figure 91. Thermal Stress versus Temperature:
Inert Propellant Specimen Containing 150-psi Gage,
Moderate Cooling and Heating Rate.

-174-
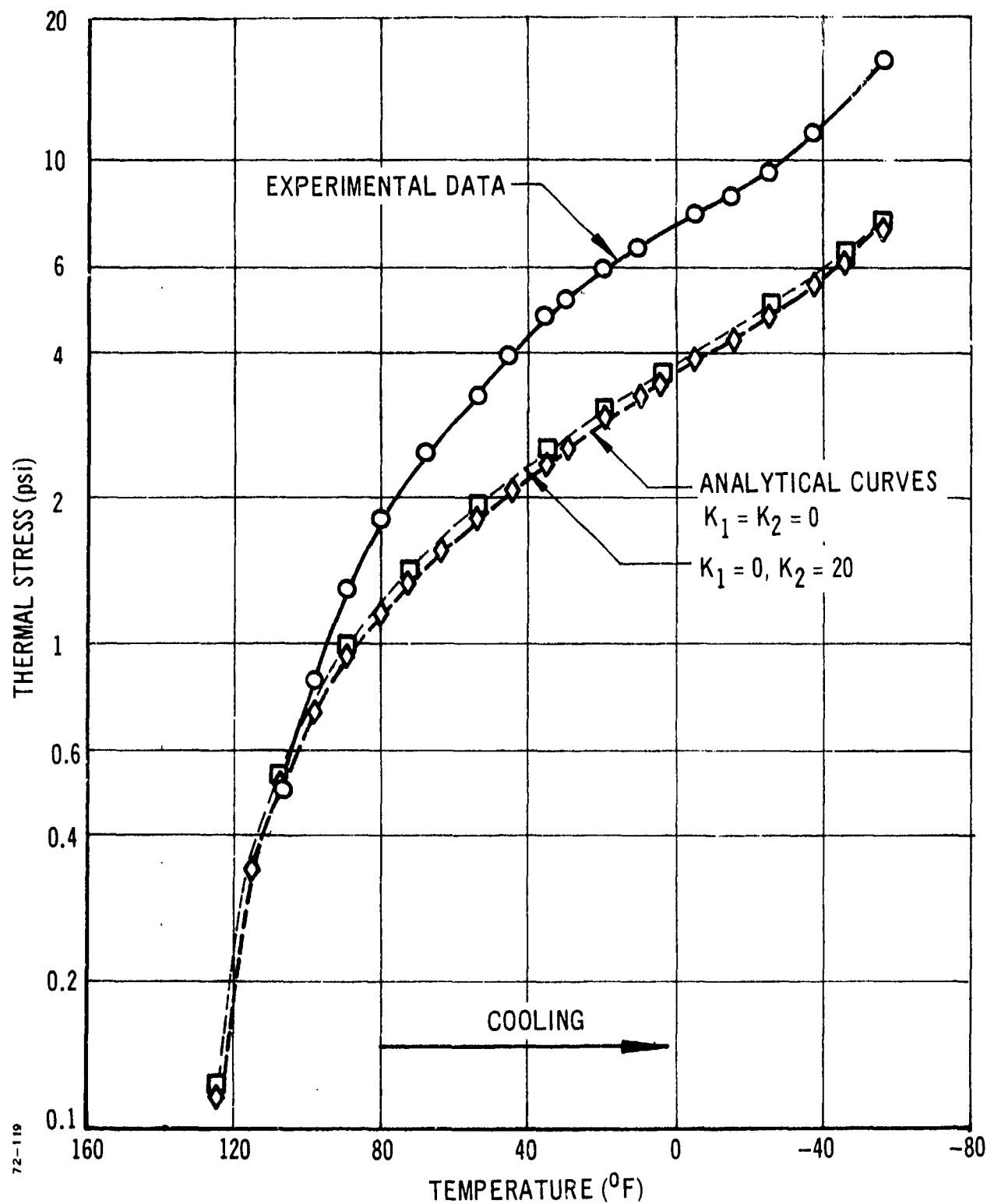
Figure 92.   Thermal Stress versus Temperature:
Inert Propellant Specimen Containing 150-psi Gage,
Slow Cooling Rate.

-175-
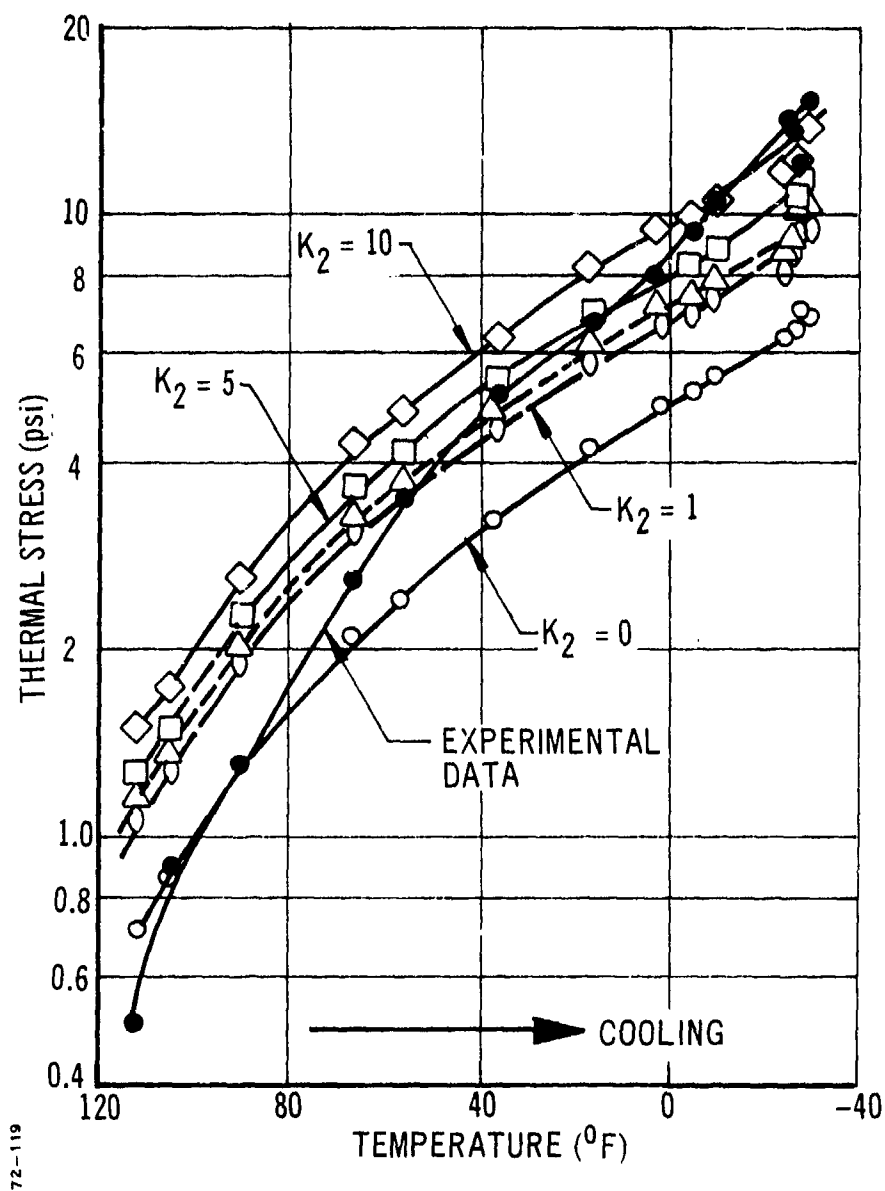
Figure 93. Thermal Stress versus Temperature:
Inert Propellant Specimen Containing 150-psi Gage,
Fast Cooling Rate.

-176-

range could be obtained with a K_2 value of approximately 200 to 400. However, the data would still not appear to fit the measured curve because they would not agree at the higher-temperature end (as will be observed in the curves for the various K_2 values at the 115^0F temperature).

It would appear from the data that the computer program has some difficulties with the calculations when passing through the temperature minimum. The data for $K_2 = 0$ are correct and show a smooth continuous curve, but the curves for K_2 having real values show a spurious data point at the -32^0F temperature. The program appears to recover by the next data point, i.e., the -13^0F temperature point. The cause of this trouble with the program is not known.

The slow cooling rate data of Figure 92 show similar trends in that the calculated thermal cooling stresses are some 50 percent of the measured values for most of the temperature range. Because of the very small rate of cooling, however, the modification to the reduced time has only a very small effect on the stress values, as will be noted. Only the data calculated for $K_2 = 0$ and 20 are shown for clarity. It is clear from these data that even the use of a higher value for K_2, such as 200 or 400, would not result in a reasonable agreement between theory and experiment.

The fast cooling rate data presented in Figure 93 appear to show the best agreement with the analytical data curves. Thus the discrepancy between the experimental calculated data increases to a value of approximately 2 at the lowest temperature of -30^0F; at higher temperatures the error is smaller. However, this apparent better agreement is most probably due to the fact that the temperature was never able to equalize throughout the specimen because of the fast rate of cooling. Thus, the load developed was always smaller than it would have been under slower cooling conditions. The analytical data curves of Figure 93 show that it is relatively easy to produce a significant increase in stress with values of K_2 lower than 10. However, in no case does the calculated data curve bear a close resemblance to the measured data curve.

Considering all the data obtained with the inert propellant specimen containing the 150-psi diaphragm gage, it seems that although it is possible to calculate higher thermal stresses by using the modified definition of reduced time, the measured thermal cooling stresses do not support the view that this is the primary cause of the discrepancy. Additional data would be required to substantiate the hypothesis that rate of change of temperature has a significant effect on thermal stress.

Additional tests were performed with a large block of STV propellant (without a gage) as a specimen. These test results are discussed next.

c.   Tests of Large STV Propellant Specimen

These tests were conducted with two separate objectives. Primarily, the tests were intended to confirm that a single specimen could be used to determine the propellant properties over a wide range of

temperatures, in a manner similar to the technique used to calibrate the gages in a propellant uniaxial specimen. There was some doubt with regard to the validity of the gage calibration data on the ground that performing the calibration tests would damage the propellant and thereby modify the gage-propellant interaction. This objection might be valid if the strain levels used in the tests were high enough.

The second objective of the test series was, therefore, to verify that the use of a large propellant specimen at very low strain levels (not greater than 0.5 percent) would result in valid, repeatable test data with no significant change from test to test. Verification of the fact that propellant could be strained to small strain levels without significant (or measurable) damage would be a valuable indication of the usefulness of the gage calibration tests.

A large propellant specimen was machined from STV propellant 0064-61E to a 2- by 2- by 6-inch size. Large metal end-pieces were post-bonded to the propellant with epoxy adhesive, and a series of constant load creep tests was performed across a wide temperature range from -63 to +144°F. The tests were deliberately not performed in a sequential fashion, and the temperature was switched randomly from high to low. The strains were kept below 0.5 percent, usually around 0.10 to 0.20 percent, by adjusting the applied load as the temperature was changed.

The inverse creep compliance data are presented versus log reduced time in Figure 94, and the corresponding log a_T versus temperature plot is shown in Figure 95. There was no evidence of a shift in the data with time (which was anticipated if the propellant had been damaged during the early tests). There was, however, an apparent change in modulus with strain level, a much larger value being obtained at very small strain levels, of the order of 0.01 to 0.02-percent strain. Higher log a_T values were also required to shift these high modulus curves into line with the other test data, as will be noted from the data for temperatures of 95, -29 and -51°F. The other test data, obtained at strain levels between 0.10 and 0.50 percent, shift reasonably well and produce smooth inverse creep compliance and shift factor curves.

After the creep tests were completed, it was decided to run a restrained thermal cooling test to determine if the low-strain data were any better for the prediction of thermal cooling stresses than the conventional stress relaxation data. Two tests were performed, one at the very low programmed cooling rate (0.125°F/min) and the other at the moderate cooling rate (which was the fastest rate that could be used while maintaining a fairly uniform temperature in the block). The resulting data for thermal stress versus temperature are presented in Figure 96. Both sets of test data are shown, and it is interesting to note that there is very little difference between the low cooling rate and the moderate cooling rate. These data clearly do not support the contention that the thermal stresses are dependent on the rate of cooling. The difference between the curves is simply a function of the different starting temperatures used in the two tests. Thus, cooling for the low-rate test began from an initial temperature of 130°F, whereas cooling for the moderate rate test began from an initial temperature of 64°F.
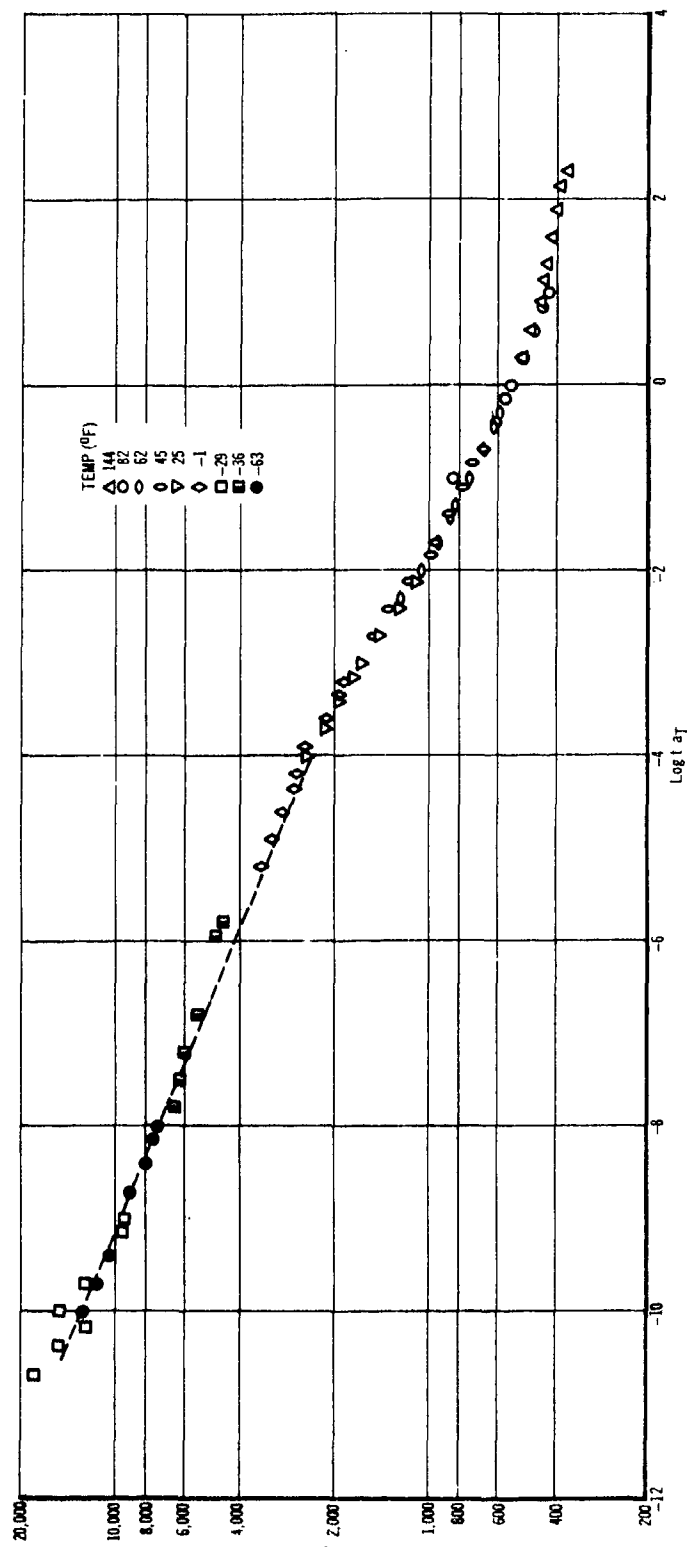
Figure 94. Inverse Creep Compliance versus Reduced Time; Data for Large Block of 0064-61E Propellant.
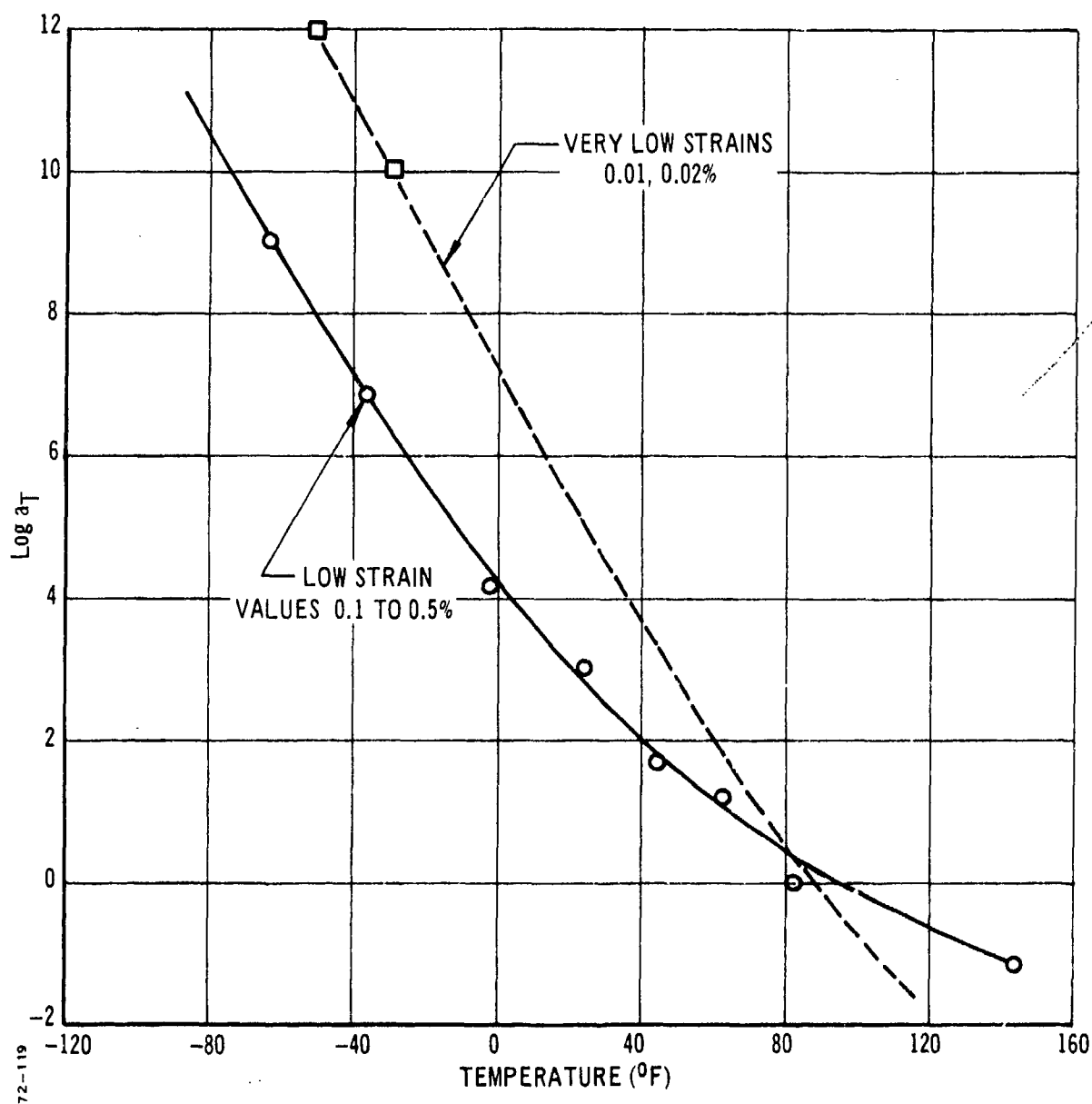
Figure 95. Shift Factors versus Temperature for Large Block of STV Propellant.
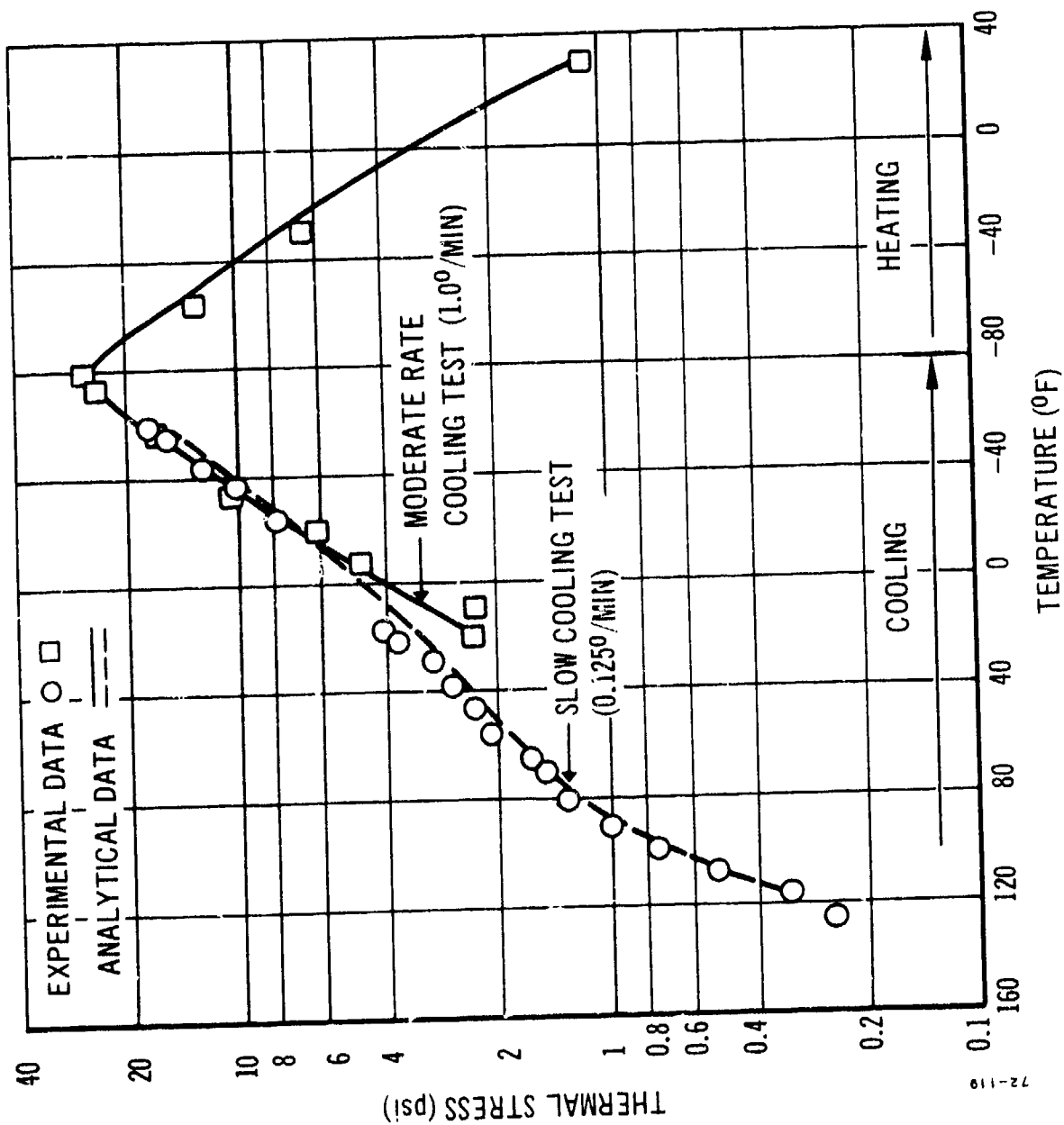
Figure 96. Thermal Cooling Stresses for Large Block of STV Propellant.

The most interesting aspect of the experimental data derived from the large block specimen test is the comparison between the experimental measured data (from the Instron load cell readings) and the calculated data from the revised Knauss computer code. There is very good agreement between the measured and the calculated thermal stress values, for both rates of cooling and with the value of K_2 and $K_1 = 0$, i.e., using the conventional definition of reduced time and ignoring the rate of change of temperature in the calculations. Note that in Figure 96, the points shown are the experimental data and the curves are the analytical predictions.

Thus the data appear to show that the large specimen under very small strain conditions will produce the proper modulus data for use in thermal cooling problems. These data also suggest that if the proper tests are performed to obtain the high, undamaged-propellant modulus data, much better agreement will be obtained between the experimental thermal cooling stresses and the calculated values.

d. Thermal Cooling Analysis with THVINC

In addition to the earlier analyses of the 25-psi test fixture data (from last year's final report), a transient thermal analysis was performed by Mathematical Sciences NorthWest using the revised transient viscoelastic thermal analysis code, THVINC. In this analysis, the experimental conditions were approached even more closely because the temperature history of the outer radius of the propellant, and at the bonded surface between the specimen ends and the propellant, was specified as an input to the program. In addition, the z-component of displacement was set equal to zero along the z = 1.4-inch surface.

The temperature-time history used for the propellant boundary is given in Table XIX. (These data are in some cases linearly interpolated between measured data points.) A stress-free temperature of 146^0F was used.

Average calculated gage stresses are presented in Figure 97 against a temperature base and are compared with the experimental data. The calculated stress values are very similar to those determined earlier (Figure 90) with an assumed uniform temperature throughout the specimen. It is clear, therefore, that the discrepancy between theory and experiment is not due to this approximation.

e. Gage Data from Thermal Tests in Uniaxial Specimens

Data from a 25-psi gage embedded in the STV propellant specimen were reported in last year's final report. Because of the variation in gage response with reduced time, it was necessary to use the Knauss thermoviscoelastic computer program to analyze the test data. Unfortunately, the program was very slow in calculating the gage output data, so that only three data points were obtained to compare with the experimental values.

Using the revised uniaxial thermoviscoelastic computer code with the gage transfer function $\theta(\xi)$ replacing the modulus term, and with

TABLE XIX

TEMPERATURE-TIME HISTORY FOR THVINC ANALYSIS OF 150-PSI GAGE TEST FIXTURE

Time (min)	Temperature (^{0}F)
0	146
10	104
720	104
730	64
1,010	64
1,020	11
1,265	11
1,275	-11
1,495	-11
1,505	-45
1,690	-45
1,700	-75
1,880	-75
1,890	15
2,140	15
2,150	82
2,600	82
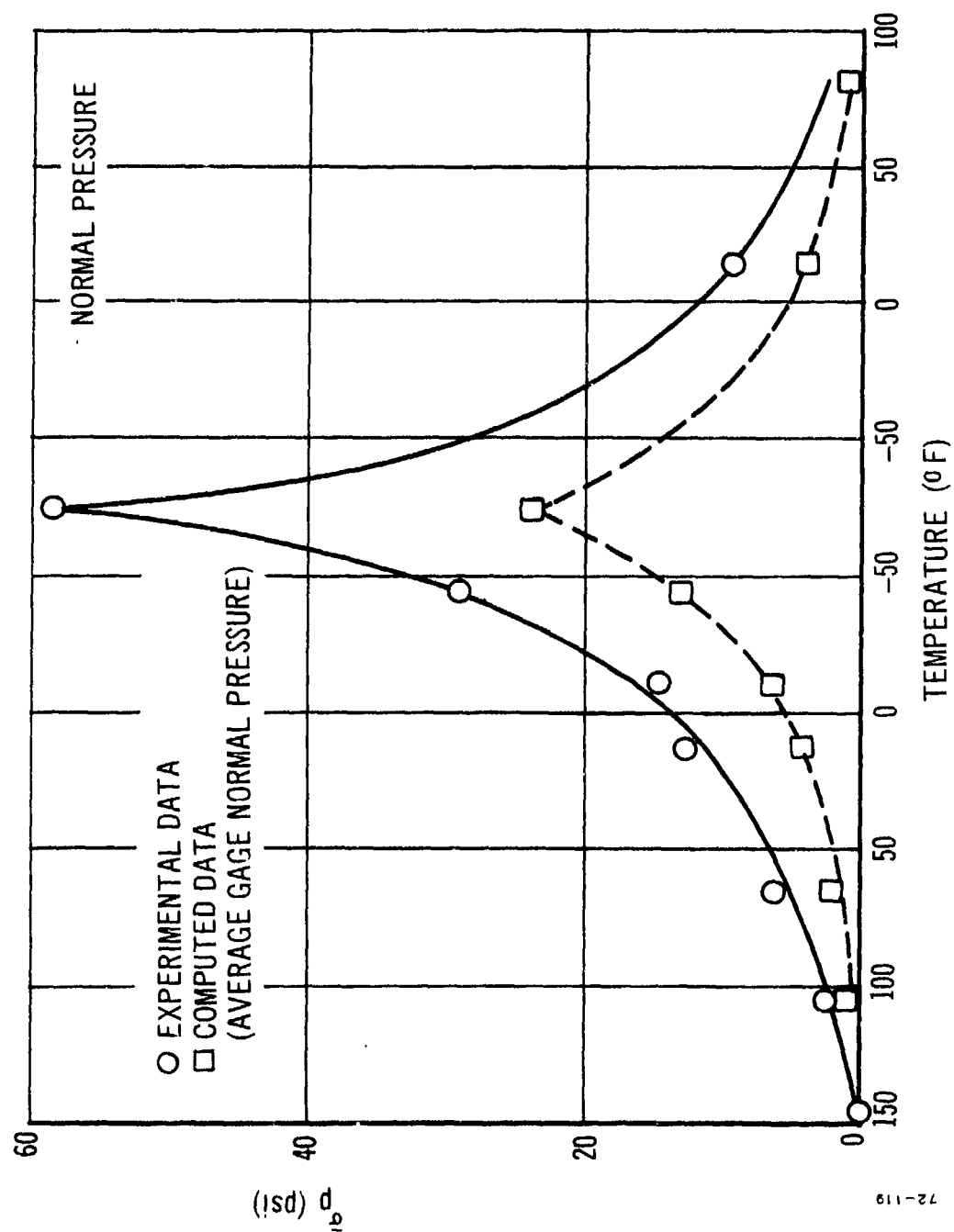
Figure 97. Simulated 150-psi Diaphragm Gage in Uniaxial Calibration Fixture under Restrained Thermal Cooling; THVINC Analysis.

the gage output S(t) replacing the strain term, the thermal stress estimates from the 25-psi gage output signals were calculated. The results are compared in Figure 98 with the measured stresses. The calculated stress values are slightly greater than those presented in last year's report (this year's revised data are believed to be more accurate). The agreement between the analytical gage data and the load-cell-measured stresses is reasonably good across most of the temperature range. The maximum error (27-percent high) occurs at the lowest temperature of -75^0F. Between the temperatures of $+100$ and -45^0F, agreement between the gage data and the measured data is excellent. This is particularly gratifying in view of the fact that the 25-psi gage is not considered suitable for the measurement of thermal stresses in propellant at temperatures approximately below 0^0F.

The newer and much stiffer 150-psi gage was expected to provide accurate thermal stress data in propellant. Data were obtained from the gage embedded in the inert propellant uniaxial test specimen. For these test data, the simplest possible type of data reduction approach was used, i.e., the gage sensitivity was taken to be a constant and independent of temperature. Typical data calcuated from the gage output are shown in Figure 99. Also shown in this figure are the thermal stresses measured with two independent load cells during the same test. A Statham load cell was mounted on the lower end of the specimen, outside the conditioning chamber, as a check on the Instron load cell. The embedded gage gave thermal stress values within 1 psi of the two load cell values at the higher temperatures, and it measured a thermal stress value between the two load cell values at the lowest temperature of -60^0F. This particular test was conducted at the moderate cooling rate so that the gage data would be expected to agree with the measured data. Similarly, the slow programmed cooling rate data shown in Figure 100 also disclose good agreement with the Instron load cell data.

5. CONCLUSIONS OF THERMAL COOLING AND HEATING EXPERIMENTS

Up to the point of the thermal cooling tests on the large STV propellant block specimen, all the data measured in the laboratory tests appeared to confirm the fact that standard analytical techniques were incapable of predicting the stresses induced in a propellant specimen during nonisothermal testing. The calculated data, based upon normal stress relaxation test modulus values, are significantly lower than the measured thermal stresses. The possibility was investigated that this discrepancy was the result of the rate of temperature change producing a pronounced effect on the "reduced time", but results were inconclusive. However, it is certain that the effect of high rate of temperature change is not the only factor involved, even if its effect is measurable.

The later tests performed with the large propellant test specimen suggest that propellant nonlinearity is the basic problem and not the postulate of thermorheological simplicity. Certainly, the use of a large specimen tested at very low strain levels appears to provide more realistic modulus data for computing the thermal stress values.
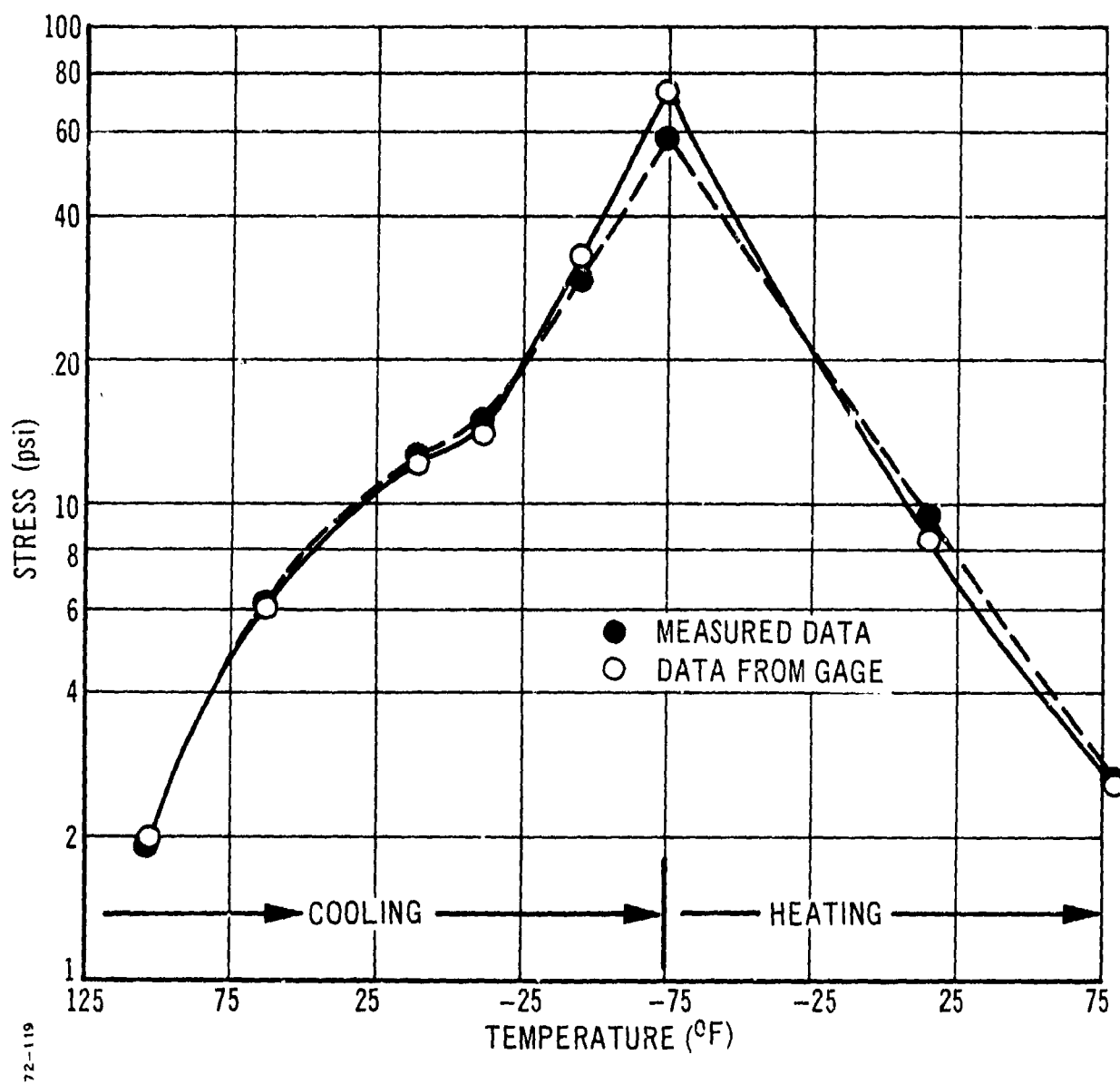
Figure 98. Thermal Stress Values Calculated from 25-psi Gage Data.
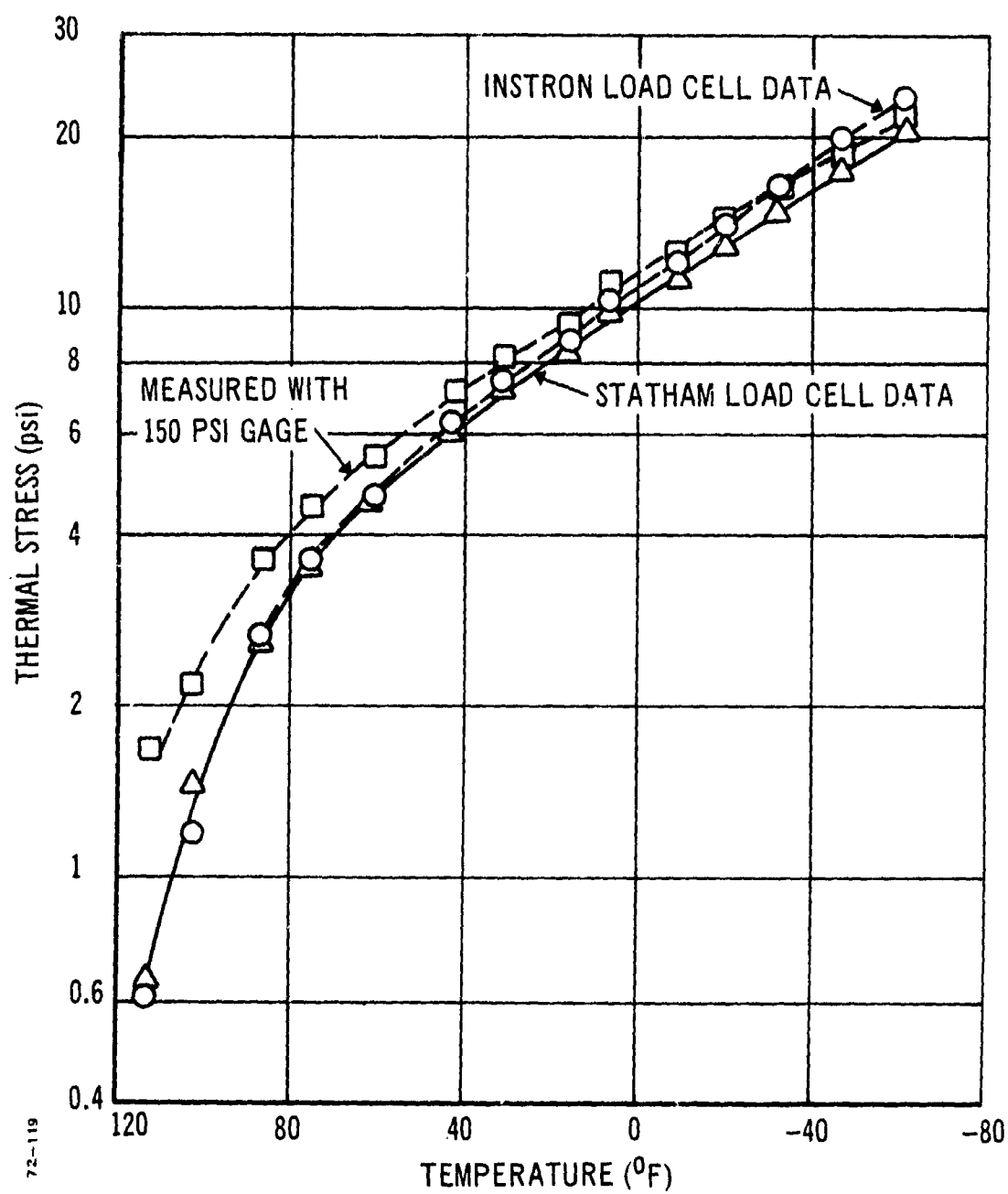
Figure 99. Thermal Stress Values Calculated from 150-psi Gage in Inert Propellant.
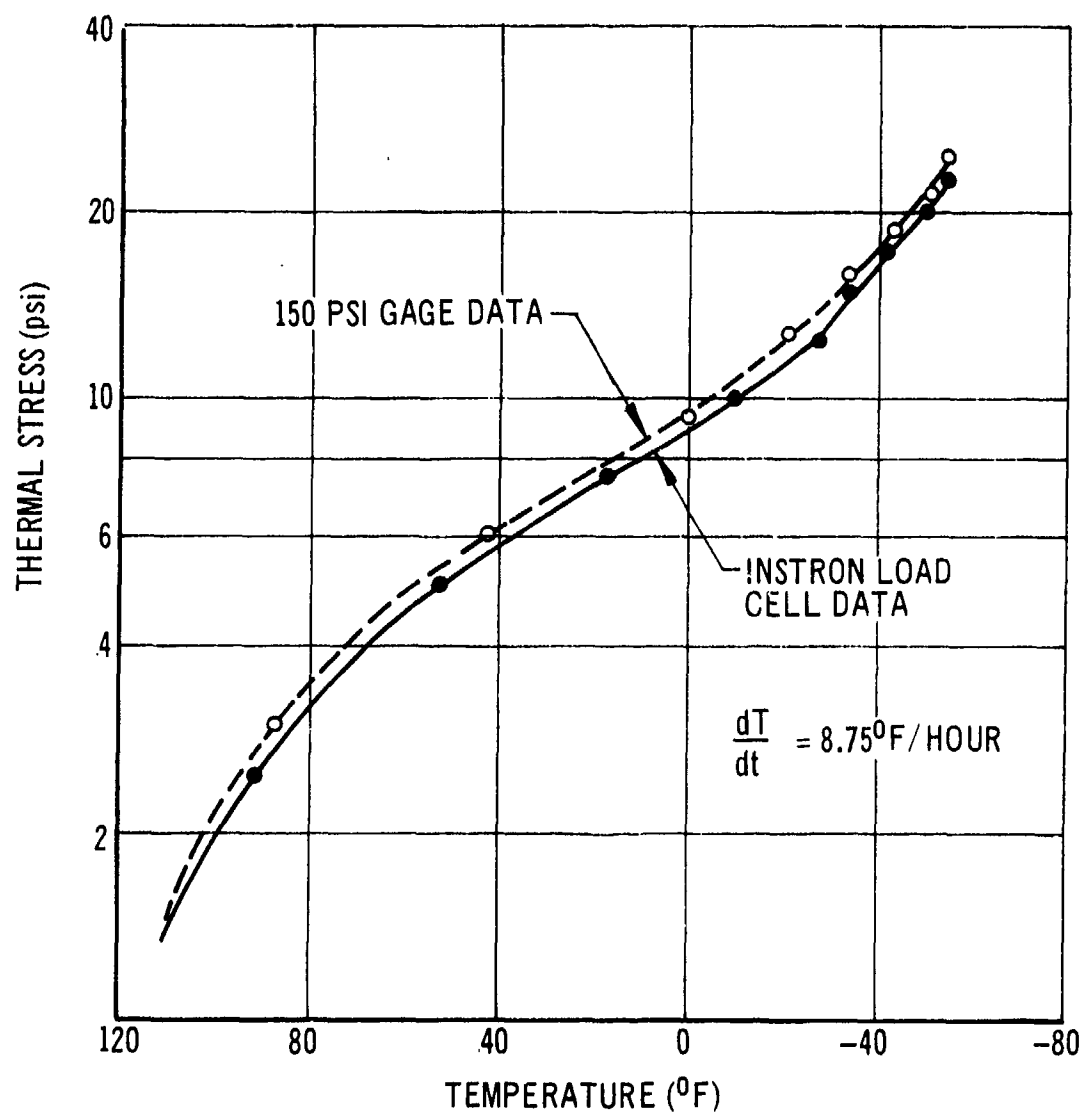
Figure 100. Slow-Cooling-Rate Measured Thermal Stresses
Compared with Gage Values.

A redeeming feature of the experimental test data was the performance of the embedded gages under nonisothermal cooling conditions. It seems that the embedded gage will provide an accurate estimate of the correct thermal stress value, whatever the basic problem involved. This is, of course, one of the major advantages of the use of embedded gages.

(The reverse is blank)

SECTION VI

THERMORHEOLOGICALLY COMPLEX AND NONLINEAR PROPELLANT BEHAVIOR[1]

1. INTRODUCTION TO PROBLEM AREA

The research described in this report grew out of two important findings of the Structural Test Vehicle Program at Lockheed Propulsion Company (Ref 1 and 2): (1) thermal stress predictions made by use of state-of-the-art methods are far below measured values, and (2) bore strain predictions made by use of state-of-the-art methods are, in some cases, significantly different (both qualitatively and quantitatively) from measured values.

Theoretical and experimental investigations were made at Texas A&M University in order to (1) identify the source of these discrepancies, and (2) improve existing analysis methods.

Subsection VI, 2 covers the theoretical investigations. Linear constitutive equations for thermorheologically complex media are given; they are based on a nonequilibrium thermodynamic theory developed in a previous Air Force-sponsored program (Ref 12). These equations contain thermorheologically simple behavior as a special case, and are only slightly more involved than the constitutive equations currently used by solid rocket structural analysts. Moreover, they are capable of predicting stresses that are considerably greater than predicted by thermorheologically simple theory.

Also in subsection VI, 2 a simple method is developed for predicting nonlinear thermal strains and deformations in long, case-bonded, circular port grains. The nonlinear phenomena of vacuole dilatation and large strains are included. This theory predicts the experimentally measured bore strains reported in the STV Final Reports (Ref 1 and 2). In addition, it provides a means for determining bulk propellant properties in a realistic stress state.

The final discussion in subsection VI, 2 is concerned with the relationship between overall and constituent thermal expansion coefficients of composite materials. Equations developed in another Air Force-sponsored program (Ref 13) are given for later use in interpreting experimental observations on the thermal expansion of solid propellant.

The experimental investigations are covered in subsection VI, 3. The poker-chip and strip biaxial specimen tests, which were used to obtain creep, relaxation, and thermal properties in multiaxial stress states, are described. Also presented are two new techniques for measuring changes

---

[1] Section VI was prepared by Professors R. A. Schapery and L. D. Webb and Engineering Research Associate S. W. Beckwith, at Texas A&M University.

Preceding Page Blank NOT FILMED

of very small volume in poker-chip specimens. Results obtained under different stress states are compared with the theoretical interrelationships for propellant with and without preexisting voids. These relationships and poker chip dilatation measurements indicate that the STV propellant has a significant amount of voids.

Concluding remarks are primarily concerned with the effect of preexisting voids on overall mechanical properties, and with the usefulness of instrumented poker-chip specimens for obtaining bulk and uniaxial moduli or compliances.

2. THEORETICAL INVESTIGATIONS

a. Linear Constitutive Equations

Current methods of linear thermoviscoelastic analysis utilize special cases of the following three-dimensional constitutive equations, which are the linearized version of nonequilibrium (irreversible) thermodynamic equations in Reference 12. They are referred here to a cylindrical (r, θ, z) coordinate system; the three normal stress-strain equations are:

$$\sigma_r - \sigma_\theta = 2G_e (\epsilon_r - \epsilon_\theta) + 2a_F \int_0^t \Delta G (\xi - \xi') \frac{\partial (\epsilon_r - \epsilon_\theta)}{\partial \tau} \, d\tau \qquad (110a)$$

$$\sigma_r - \sigma_z = 2G_e (\epsilon_r - \epsilon_z) + 2a_F \int_0^t \Delta G (\xi - \xi') \frac{\partial (\epsilon_r - \epsilon_z)}{\partial \tau} \, d\tau \qquad (110b)$$

$$\sigma_r + \sigma_\theta + \sigma_z = 3K_e (\theta - 3\alpha\Delta T) + 3a_F \int_0^t \Delta K (\xi - \xi') \frac{\partial}{\partial \tau} (\theta - 3\alpha\Delta T) \, d\tau \qquad (110c)$$

where

$$\theta = \epsilon_r + \epsilon_\theta + \epsilon_z$$

and the three shear stress-strain equations are

$$\tau_{r\theta} = G_e \gamma_{r\theta} + a_F \int_0^t \Delta G (\xi - \xi') \frac{\partial \gamma_{r\theta}}{\partial \tau} \, d\tau \qquad (110d)$$

$$\tau_{rz} = G_e \gamma_{rz} + a_F \int_0^t \Delta G (\xi - \xi') \frac{\partial \gamma_{rz}}{\partial \tau} \, d\tau \qquad (110e)$$

$$\tau_{z\theta} = G_e \gamma_{z\theta} + a_F \int_0^t \Delta G (\xi - \xi') \frac{\partial \gamma_{z\theta}}{\partial \tau} \, d\tau \qquad (110f)$$

where ξ and ξ' are "reduced times", defined as

$$\xi = \xi(t) \equiv \int_0^t dt'/a_T, \quad \xi' \equiv \xi(\tau) = \int_0^\tau dt'/a_T \qquad (111)$$

and $a_T = a_T\left[T(r, \theta, z, t')\right]$ is the strongly temperature-dependent shift factor used with thermorheologically simple materials. Furthermore

$$\Delta T = \Delta T(r, \theta, z, t') = \text{difference between grain temperature, } T, \text{ and temperature at which stress} = \text{strains} = 0.$$

$$G_e = G_e(T) \equiv \text{long-time value of shear relaxation modulus}$$

$$\Delta G(\xi) \equiv G(\xi) - G_e = \text{transient component of the shear relaxation modulus}$$
$$\left[\text{note that } \Delta G(\infty) = 0\right].$$

and a_F is a temperature-dependent coefficient; similar definitions apply to the bulk moduli components, K_e and ΔK. Both a_F and a_T are taken to be unity at the same reference temperature, T_R. For unfilled elastomers one usually assumes $G_e(T) = a_F G_e(T_R)$ and $a_F = T/T_R$, which is based on the kinetic theory of rubber elasticity. However, there is no evidence at this time to suggest such simple dependence for propellants.

The bulk response of propellant is normally assumed to be elastic, as defined by the constant bulk modulus, $K \equiv K_e$ (and $\Delta K = 0$), and linear coefficient of thermal expansion, α, in Equation (110c).

The temperature-dependence of the above constitutive equations lends itself to a mechanical model and thermodynamic interpretation (Ref 12). The shear model significance is that $G_e(T)$ defines the temperature-dependence of the equilibrium spring, and a_F defines the temperature-dependence of all remaining springs in that their moduli are functions of temperature through this common factor. The factor a_F is analogous to a_T since the latter one defines a common temperature-dependence of all dashpot viscosities.

Under the assumptions that G_e and K_e are constant and $a_F \equiv 1$, the Equations (110) reduce to those for a thermorheologically simple material (TSM). When one or both of these two conditions are not met, the term thermorheologically complex material (TCM) will be used.

If one assumes $\Delta K \equiv 0$, $a_T \equiv 1$, and $a_F = a_F(T)$, these equations depend on only instantaneous values of temperature. In contrast, if $a_T \neq 1$, the entire temperature history enters Equation (110) through the reduced-time integrals in Equation (111) and the bulk modulus integral (110c).

b.   Specimen Analysis for Constant and Transient Temperatures

The constitutive theory is used here to predict mechanical response of a specimen under (1) constant temperature and strain, (2) constant temperature and stress, and (3) simultaneous cooling (or heating) at constant rates; the temperature rate is assumed to be slow enough to establish essentially a spacewise uniform temperature distribution. Some of these results provide guidelines for reducing the data in subsection VI, 3, and for verifying the theory.

The one-dimensional version of constitutive Equations (110) relating a uniaxial stress σ, strain ϵ, and applied temperature change, $\Delta T \equiv T - T_0$, is

$$\sigma = E_e (\epsilon - \alpha \Delta T) + a_F \int_0^t \Delta E (\xi - \xi') \frac{d(\epsilon - \alpha \Delta T)}{d\tau} \, d\tau \qquad (112)$$

where the argument of ΔE is now $\xi - \xi'$, which is defined by Equation (111), and a_T and a_F are the same functions of temperature that appear in the three-dimensional equations; note that T_0 and T_R are not necessarily the same.

In order to predict behavior of strip biaxial and poker-chip specimens, simply replace the long-time modulus, E_e, and transient modulus, $\Delta E(\xi)$, by the respective effective moduli for these tests; the stress σ and strain ϵ are then interpreted, respectively, as applied force divided by the initial specimen area perpendicular to the loading direction, and the change in grip separation divided by the initial separation.

The quantity

$$\epsilon_T \equiv \epsilon - \alpha \Delta T \qquad (113)$$

in Equation (112) is sometimes called "the strain due to stress," and is actually the specimen strain referred to its unstressed length at the temperature T. In contrast, ϵ is the specimen strain referred to the unstressed length at the initial temperature, T_0.

Through the use of Equation (112) and the definitions that effective modulus, E_{ef}, is

$$E_{ef} \equiv \frac{\sigma}{\epsilon - \alpha \Delta T} \qquad (114)$$

and the effective compliance, D_{ef}, is

$$D_{ef} \equiv \frac{\epsilon - \alpha \Delta T}{\sigma} \qquad (115)$$

the following results were obtained:

Constant temperature and strain:

$$E_{ef} = E_e + a_F \Delta E \left(\frac{t}{a_T}\right) \qquad (116a)$$

Constant temperature and stress:

$$D_{ef} = \frac{1}{a_F} D \left(\frac{t}{a_T}\right) \qquad (116b)$$

-194-

The assumption $E_e = a_F E_e'$ (where E_e' is constant or zero) was used in obtaining Equation (116b) to enable the result to be written in terms of the master curve of creep compliance, $D(t/a_T)$, which is approximately equal to the reciprocal of $E(t/a_T) \equiv E_e + \Delta E(t/a_T)$; in particular, for the power law modulus, Equation (119) below, and $E_e = 0$, it is well known that

$$D\left(\frac{t}{a_T}\right) = \frac{\sin(n\pi)}{n\pi} \; E^{-1}\left(\frac{t}{a_T}\right) \tag{116c}$$

<u>Simultaneous cooling (or heating) at constant rates</u>: Assume for $t > 0$

$$\epsilon = Rt \qquad (R = constant)$$

$$\Delta T \equiv T - T_o = R_T t \qquad (R_T = constant) \tag{117a}$$

$$\alpha = constant$$

Then, we find

$$E_{ef} = E_e + \frac{a_F}{t} \int_0^t \Delta E\,(\xi - \xi')\,d\tau \tag{117b}$$

One important special case of Equation (117) results when we assume $a_T \equiv 1$ and let all temperature dependence be contained in E_e and a_F:

$$E_{ef} = E_e + \frac{a_F}{t} \int_0^t \Delta E\,(u)\,du \tag{118}$$

Although the temperature was assumed to be transient in deriving Equation (118), this equation is also equal to the isothermal secant modulus, $E_s \equiv \sigma/\epsilon_T$, for a constant strain rate at temperature T.

A second important case is one in which ΔE and a_T are expressed as the following power laws:

$$\Delta E = E_1\,\xi^{-n} \; ; \quad a_T = \left(\frac{T_R - T_a}{T - T_a}\right)^m \tag{119}$$

where E_1, n, and m are positive constants, T_a may be a positive or negative constant, and T_R is the temperature at which $a_T = 1$; the temperature T_a is approximately 10 to 20°F below the glass-transition value T_g.[1] Both

___

[1] The constants m and T_a can be found from experimental data as follows: Guess a value of T_a and plot the data in the form $\log a_T$ versus $\log (T - T_a)$. If the points fall approximately on a straight line the guess of T_a is the correct value and m is the magnitude of the log-log slope. If not, guess another value of T_a and repeat the process.

power laws in Equation (119) are very accurate for most solid propellant over broad time and temperature ranges when $T > T_g$ (Ref   ). With these power laws, reduced times, Equation (111), can be analytically integrated; the effective modulus, Equation (117b), then becomes

$$E_{ef} = E_e + I_T \left[E_s - E_e \right] \tag{120a}$$

where

$E_s \equiv$ isothermal constant strain rate secant modulus,
σ/ϵ_T, at temperature T

$$= E_e + \frac{a_F E_1}{1 - n} \left(\frac{t}{a_T} \right)^{-n} = E_e + \frac{a_F a_T^n E_1}{1 - n} t^{-n} \tag{120b}$$

For cooling $(T \leq T_o)$:

$$I_T \equiv \frac{1 - n}{(m + 1)^{1-n}} \left(-1 - \frac{1}{\Delta T_n} \right)^{1-n} (\Delta T_n + 1)^{m+1} \int_{}^{1} (1 - x)^{-n} x^{\left(\frac{m}{m+1} + n - 2 \right)} dx \tag{120c}$$

while for heating $(T \geq T_o)$:

$$I_T \equiv \frac{1 - n}{(m + 1)^{1-n}} \left(1 + \frac{1}{\Delta T_n} \right)^{1-n} \int_{1}^{(\Delta T_n + 1)^{m+1}} (x - 1)^{-n} x^{\left(\frac{m}{m+1} + n - 2 \right)} dx \tag{120d}$$

These results are expressed in terms of the normalized temperature change, ΔT_n, defined as

$$\Delta T_n \equiv \frac{T - T_o}{T_o - T_a} \tag{121}$$

which is a convenient parameter to use in a graphical representation of I_T since, for cooling, $-1 < \Delta T \leq 0$.

The factor I_T is drawn in Figures 101 through 104 for ranges of n and m typical of solid propellant and binders. These are actually the exponent ranges one finds when relaxation data are reduced according to current practice, in which the tacit assumptions $a_F \equiv 1$ and $E_e =$ constant are made. When m = 12, the power-law shift factor, a_T in Equation (119), is very close to the widely used WLF factor over its usual range of validity for solid propellant and binders.
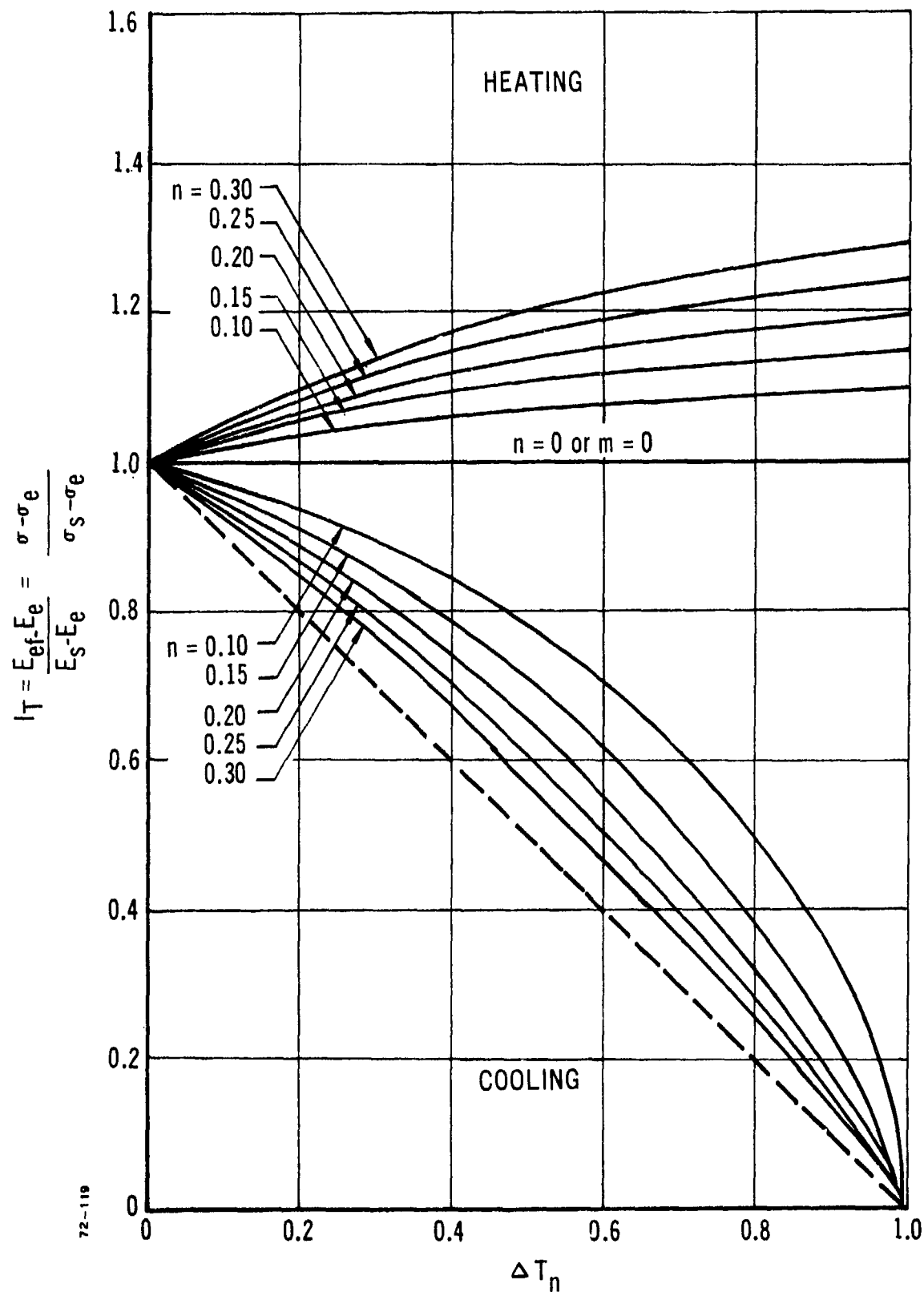
Figure 101.   Modulus and Stress Ratios for Simultaneous
Cooling (or Heating) and Straining, $m = 10$.

-197-
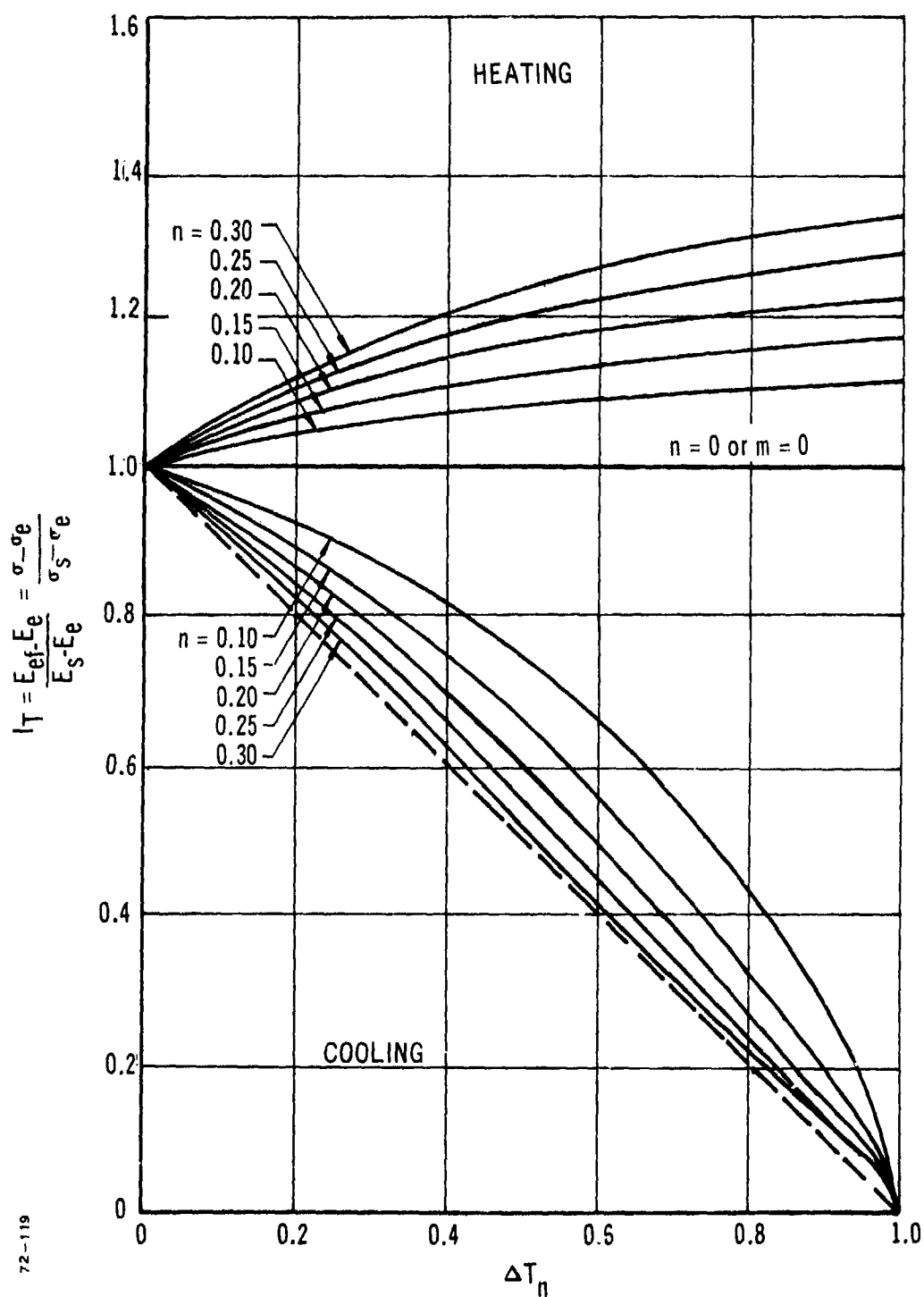
Figure 102. Modulus and Stress Ratios for Simultaneous
Cooling (or Heating) and Straining, m = 12.
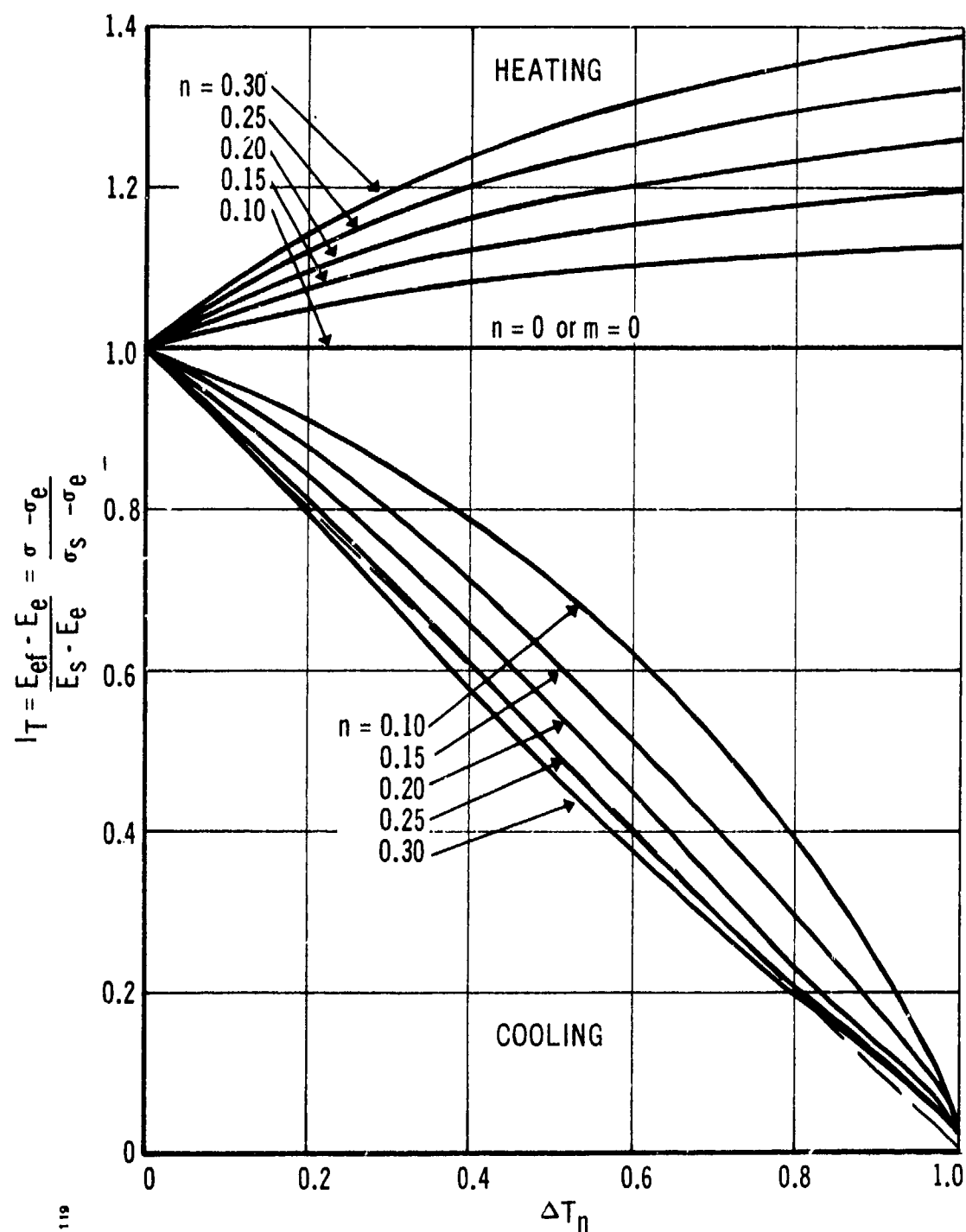
Figure 103.   Modulus and Stress Ratios for Simultaneous
Cooling (or Heating) and Straining, m = 14.
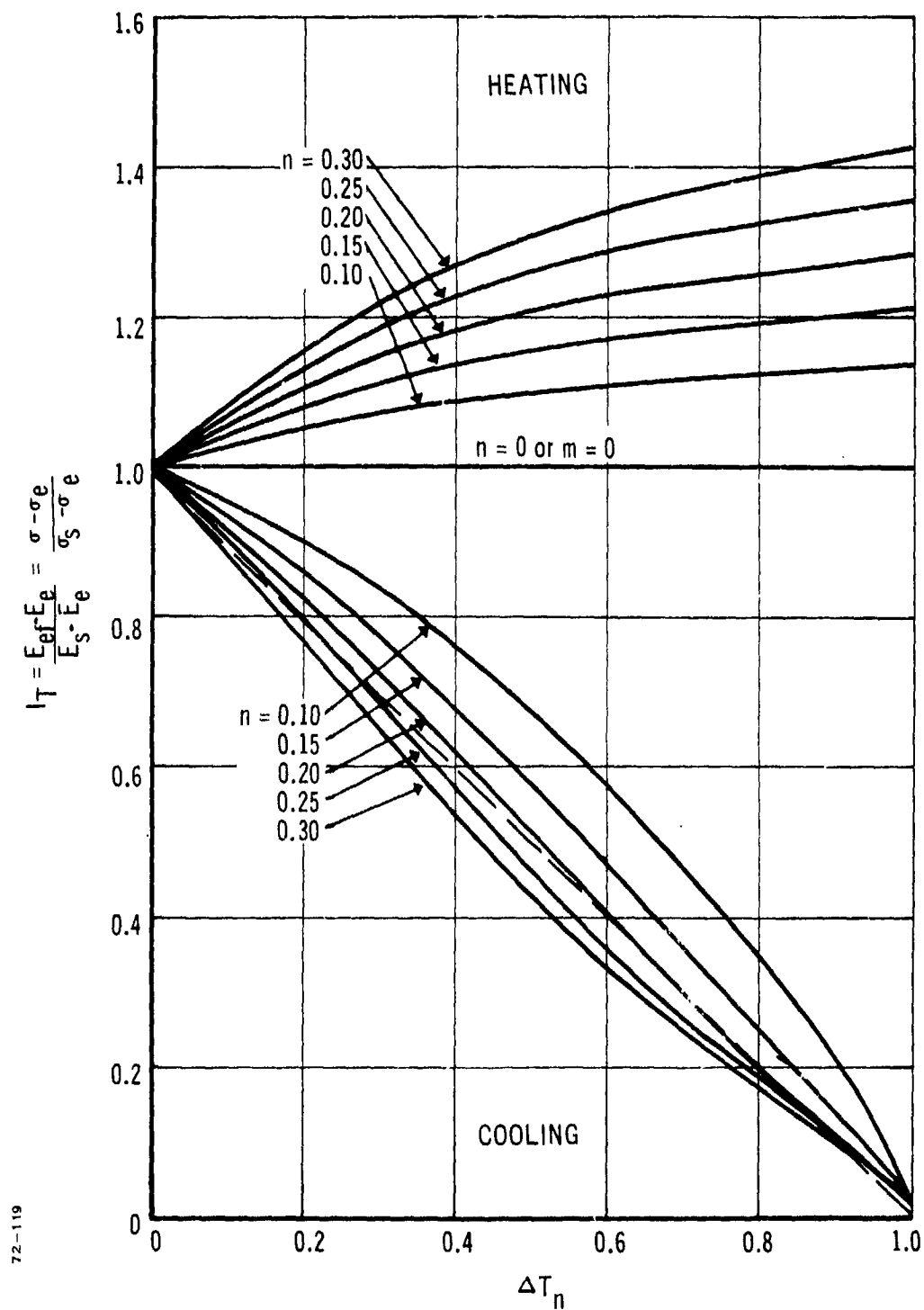
Figure 104. Modulus and Stress Ratios for Simultaneous
Cooling (or Heating) and Straining, m = 16.

It is also important to observe that the ordinate in these figures can be interpreted as the stress ratio $(\sigma - \sigma_e)/(\sigma_s - \sigma_e)$ where

$\sigma \equiv$ actual stress due to simultaneous heating or cooling and straining

$\sigma_e \equiv$ long time elastic stress $= (\epsilon - \alpha\Delta T)E_e$

$\sigma_s \equiv$ stress due a constant strain rate at a constant temperature $= (\epsilon - \alpha\Delta T)E_s$

This statement is verified by multiplying Equations (120a) and (120b) through by the strain due to stress, $\epsilon - \alpha\Delta T$.

The curves in Figures 101 through 104 can be used to:

(1) Calculate the effective modulus and stress in a specimen subjected to constant strain rate and cooling or heating rate, given the secant modulus, E_s, and the condition $a_F \equiv 1$.

(2) Check the assumption $a_F \equiv 1$ (which is used in most current methods of characterization and grain analysis) by comparing the theoretical stress prediction with experimental values. If $a_F \equiv 1$ is not valid, the values of a_F needed to achieve agreement with experimental data can be found from the figures together with Equation (120a); the stress predicted under the assumption that $a_F \neq 1$ is always larger than that for $a_F \equiv 1$ with cooling, or smaller than that for heating.

(3) Correct elastic grain analyses for transient temperature effects. It can be shown that I_T is not restricted to a simple bar under uniaxial stress, but is applicable to actual grain geometries whenever the temperature does not vary appreciably with respect to (r, θ, z); see the following subsection VI, 2, c.

Finally, attention is called to the significance of the $m = 0$ case in the figures, for which $I_T = 1$. In view of Equations (119) and (120a), this value of m implies that: (1) all temperature-dependence is contained in E_e and a_F, and (2) that the effective modulus, E_{ef}, under a transient temperature, $T(t)$, is equal to the isothermal secant modulus, E_s, at temperature $T(t)$; observation (2) also follows from Equation (118), which is not restricted to a power-law modulus.

Inasmuch as a_T reflects the temperature dependence of internal viscosity (Ref 12), one would expect it to be the strongest function of temperature. However, in a nonlinear study on propellant bars subjected to simultaneous cooling and straining (Ref 15), good agreement between experiment and theory was found by using the product of $(\epsilon - \alpha\Delta T)$ and isothermal secant moduli at the instantaneous temperature. This observation implies

for the present linear case that $a_T \simeq 1$. Moreover, it was found that stress in the clamped and cooled bar reported in Figure 2 of Reference 2 could be accurately predicted in the same way. Such agreement may have been fortuitous; this bar problem is reexamined in Section V, wherein it is shown that when very small strain compliance data are used together with the theory for a TSM, theory and experiment are in good agreement.

In view of these comparisons, it appears that the strain level has a significant effect on the type of thermorheological behavior exhibited by propellant. Whether or not Equation (110), in which E_e and a_F may depend on temperature, can be used with confidence to predict stresses within an acceptable degree of accuracy, cannot be answered without a more extensive experimental study. However, the present indications are that these linear constitutive equations are acceptable approximations, at least under monotonic cooling and straining.

c.   Comments on Structural Analysis Methods for Thermorheologically Complex Materials (TCM)

Structural analysis of viscoelastic materials whose constitutive equations are those given in Equation (110), and having both a transient and a nonuniform temperature distribution, generally requires the use of numerical methods that are significantly more involved than those used for elastic media. This observation applies to both a TSM and a TCM; it is based on the fact that the correspondence principle is not valid when temperature varies with respect to both time and space (Ref 16).

If the temperature in the viscoelastic materials is essentially independent of time during the period of application of external loads and/or displacements, the correspondence principle is valid for both TSM and TCM (Ref   ). This means that even with a spacewise nonuniform temperature, important problems (such as grain response to ignition pressure or grain response to aerodynamic heating of the case) can be solved by the simple quasi-elastic method plus superposition (Ref 16).

On the other hand, if the temperature is transient, but is essentially spacewise uniform in the viscoelastic material, there is a difference between the analysis methods that can be used with a TSM and with a TCM. The correspondence principle is applicable in the former case because the constitutive equations, when Laplace-transformed with respect to reduced time ξ, reduce to algebraic relations of the same form as those for elastic materials. This simplification does not result when the Laplace transform is applied to Equation (110) if, G_e, K_e, and/or a_F are functions of temperature (and therefore functions of time). Direct numerical methods of analysis may therefore be needed with a TCM, unless certain conditions, such as those given in the following illustrations, are met.

Consider first the problem of predicting stresses and displacements in a solid propellant grain, in which the following three conditions occur:

(1)   The grain is mechanically incompressible

(2)   The case is mechanically rigid

(3) The difference in temperature between current and
stress-free values is $\Delta T = \Delta T(t)$ in the grain, and
$\Delta T_c = \Delta T_c(t)$ in the case.

Note that ΔT_c and ΔT are not necessarily the same, which allows for the
possibility of short-term aerodynamic heating of the case. It will be shown
that the grain displacements and strains are identical with those in an elastic
grain, and that the grain stresses are the same as those in an elastic grain
with the exception that the elastic Young's modulus, E, is replaced by effective
moduli.

The proof is accomplished by showing that these displacements
and stresses satisfy all of the governing viscoelastic equations for the TCM.
First, it is observed that the elastic grain displacements $(u_r,\ u_\theta,\ u_z)$ have
the form

$$u_r = f_r \delta + g_r \delta_c \tag{122}$$

where

$$\delta = \alpha \Delta T \quad \text{and} \quad \delta_c = \alpha_c \Delta T_c$$

with similar expressions for u_θ and u_z. In general, f_r and g_r are functions
of r, θ, and z, but not of time, grain modulus, and thermal loads δ and δ_c.
This form of the displacements is a result of (1) linearity, which implies
that the solution is proportional to the inputs δ and δ_c; (2) dimensional con-
siderations, in that there is only one modulus (i. e., E) in the problem, and
its units (e. g., psi) are inconsistent with Equation (122) (of course, if the
material were compressible, as defined by the bulk modulus K, the dimen-
sionless ratio E/K could appear in f_r and g_r); and (3) the fact that the time
variable enters the governing equations of elasticity through only T and T_c.
Strains follow directly from Equation (122) by spatial differentiation, and
therefore are independent of E and are proportional to δ and δ_c.

The elastic shear stresses $(\tau_{r\theta},\ \tau_{\theta z},\ \tau_{rz})$ and normal stress
differences $(\sigma_r - \sigma_\theta,\ \sigma_\theta - \sigma_z,\ \sigma_r - \sigma_z)$ follow directly by substituting the
strains into the stress-strain equations. Because the body is incompressible,
the normal stresses are not uniquely defined by the strains, and one must
draw upon the equilibrium equations to complete the solution. These steps
lead finally to normal and shear stresses of the form

$$\sigma_r = \left[m_r \delta + n_r \delta_c \right] E \tag{123}$$

with similar expressions for the five other stresses, where m_r and n_r may
be functions of r, θ, and z, but not of t, E, δ, and δ_c.

For a TCM, it is postulated that the displacements and strains
are identical with those in the elastic grain, e. g., Equation (122), and that
the stresses are of the form

$$\sigma_r = m_r \delta E'_{ef} + n_r \delta_c E''_{ef} \tag{124}$$

-203-

where m_r and n_r are the same functions as in elastic solution Equation (123), and the effective moduli are

$$E'_{ef} = E_e + a_F \; \delta^{-1} \int_0^t \Delta E(\xi - \xi') \; \frac{d\delta}{d\tau} \; d\tau \tag{125a}$$

and

$$E''_{ef} = E_e + a_F \; \delta_c^{-1} \int_0^t \Delta E(\xi - \xi') \; \frac{d\delta_c}{d\tau} \; d\tau \tag{125b}$$

Also,

$$E_e = 3G_e \; , \quad \Delta E = 3\Delta G \tag{125c}$$

The material properties in Equation (125) may, in general, be functions of the transient grain temperature.

The postulated grain displacements satisfy boundary conditions at the case and the incompressibility condition ($\epsilon_r + \epsilon_\theta + \epsilon_z = 3\delta$) because they are independent of material properties and are the same as in the elastic grain. The postulated stresses, e.g., Equation (124), satisfy the stress-free boundary conditions at the grain's free surfaces because m_r and n_r, as derived for the elastic grain, vanish on these surfaces. The remaining equations to be checked are the equilibrium and constitutive equations. Consider, for example, the radial equilibrium equation,

$$\frac{\partial \sigma_r}{\partial r} + \frac{1}{r} \frac{\partial \tau_{r\theta}}{\partial \theta} + \frac{\partial \tau_{rz}}{\partial z} + \frac{\sigma_r - \sigma_\theta}{r} = 0 \tag{126}$$

Now, the elastic stresses satisfy these equations regardless of the magnitudes of δ and δ_c. Therefore the set of functions m (m_r, m_θ, . . .) and the set of functions n (n_r, n_θ, . . .) separately satisfy the equilibrium equations; e.g.,

$$\frac{\partial m_r}{\partial r} + \frac{1}{r} \frac{\partial m_{r\theta}}{\partial \theta} + \frac{\partial m_{rz}}{\partial z} + \frac{m_r - m_\theta}{r} = 0 \tag{127}$$

Substitution of viscoelastic stresses, e.g., Equation (124), into the equilibrium equations obviously leads to equations of the type represented by Equation (127), multiplied by the time-dependent functions E'_{ef} and E''_{ef}; equilibrium is therefore satisfied.

Verification of the constitutive Equations (110) is accomplished in like manner. Namely, substitute the strains, as derived from Equation (122), e.g., into these equations and use the fact that the equations are valid for constant E; from this result and the knowledge that f_r, f_θ, . . . and g_r, g_θ, . . . are all independent of time, the equations are found to be valid.

That the viscoelastic solutions postulated above are the only ones that satisfy all of the governing equations can be shown by using the same technique which is employed to establish uniqueness of elasticity solutions (Ref 17), together with the fact that thermodynamics (Ref 12) places certain restrictions on the material properties in Equation (110).

Observe that effective moduli, Equation (125), reduce to that defined in Equation (117b) when the rate of thermal loading, $d\delta/dt$ and/or $d\delta_c/dt$, is constant. Therefore, if the power laws in Equation (119) are valid here, Equation (120) and Figures 101 through 104 can be used to predict thermal stresses in the grain.

If the restriction of mechanical incompressibility in the preceding example is removed, one cannot necessarily expect the quasi-elastic method of analysis to yield accurate solutions. One situation in which this accuracy can be expected is when the equilibrium bulk modulus K_e and the equilibrium shear modulus G_e are both functions of temperature through the same factor, a_F, that appears in front of the integrals in Equation (110). As proof of this remark, a new set of six stresses σ_r', σ_θ', . . . τ_{rz}', where $\sigma_r' \equiv \sigma_r/a_F$, $\sigma_\theta' \equiv \sigma_\theta/a_F$, etc, is first defined. Then, when all of the governing field and boundary equations are written using these primed stresses, they are found to be identical with those for a TSM. This result, in turn, not only implies that the approximate method of quasi-elastic analysis plus superposition (Ref 16) can be used with confidence in its accuracy, but also that the correspondence principle and its consequences are valid here (Ref 16).

Approximate stress solutions to the problem at hand are the same as shown in Equation (124), except that m_r and n_r are now functions of Poisson's ratio and appear under the integral in the effective moduli, Equation (125) [instead of appearing in front of the moduli in Equation (124)]; Poisson's ratio, ν, for this case is a function of reduced time difference, $\xi - \xi'$, through the relation:

$$\nu = \nu(\xi - \xi') = \frac{1 - (2G'/3K')}{2 + (2G'/3K')} \tag{128}$$

where

$$G' = G_e/a_F + \Delta G(\xi - \xi')$$

$$K' = K_e/a_F + \Delta K(\xi - \xi')$$

The displacement functions, e.g., f_r and g_r in Equation (122), may also depend on Poisson's ratio. In this case, we write, e.g.,

$$u_r = \int_0^t f_r\left[r, \ \theta, \ z, \ \nu\right] \frac{d\delta}{d\tau} \ d\tau$$
$$+ \int_0^t g_r\left[r, \ \theta, \ z, \ \nu\right] \frac{d\delta_c}{d\tau} \ d\tau \tag{129}$$

where ν is given by Equation (128).

-205-

d. Strain Analysis of Long, Circular-Port Grains with
Nonlinear Vacuole Dilatation

When a case-bonded grain is cooled from its stress-free temperature, tensile hoop strains develop which, if large enough, produce vacuole dilatation, usually by a dewetting process. This phenomenon reveals itself as a nonlinear dependence of bore hoop strain and radial displacement on the temperature change. A simple problem is analyzed here, and hoop strain is expressed in terms of dilatation measured on strip biaxial specimens. Comparison with STV data is then made.

(1) Assumptions and the Governing Equations

It is assumed that the grain's temperature distribution is axially symmetric and that the grain is bonded to a mechanically rigid case, which implies that its axial and hoop strains are both equal to

$$\epsilon_c = \delta_c$$

where, as before

$$\delta_c = \alpha_c \, \Delta T_c$$

α_c = case thermal expansion coefficient

ΔT_c = difference between case temperature, T_c, and the stress-free temperature.

The engineering hoop strain, ϵ_θ, is (Ref 18)[1]

$$\epsilon_\theta = \left[1 + 2\left(\epsilon_c + I\right) \frac{b^2}{r_0^2}\right]^{1/2} - 1 \tag{130}$$

where

$$I \equiv -\frac{1}{b^2} \int_{r_0}^{b} \nu_a \, r_0 \, dr_0 \qquad (a_0 \le r_0 \le b) \tag{131}$$

and

b = radius to inside of case (small case strain is assumed)

r_0 = radius to a generic material point in the grain's stress-free state

———————

[1] Plane strain ($\epsilon_z = 0$) is assumed in Reference 18. The solutions in this subsection can be changed to those for plane strain by making the substitutions $\delta_c \longrightarrow \delta_c \left(1 + \nu_c\right)$ and $\delta \longrightarrow \delta + \left[\delta_c \left(1 + \nu_c\right)/3\right]$, where ν_c = case Poisson's ratio $\simeq 0.3$.

$$v_a = \text{local change in area per unit initial cross-sectional area}$$

Also, the radial displacement, u, is

$$u = r_o \epsilon_\theta \qquad (132)$$

So far, these equations for ϵ_θ and u are exact, regardless of strain level and the way in which temperature varies with respect to radius and time. If the grain is mechanically incompressible, the relative area change v_a is

$$v_a = 3\delta - \delta_c \qquad (133)$$

where

$$\delta = \alpha \Delta T$$

$$\Delta T = \text{difference between grain temperature and the stress-free temperature}$$

and the strain, Equation (130), can be found simply be performing the integration in Equation (131). On the other hand, the dilatation is not known a priori when vacuole dilatation exists.

It will now be assumed that the grain's local dilatation, v, consists of only thermal expansion and nonlinear dilatation due to vacuole formation and growth (e. g. , dewetting); volume change due to the sum of the normal stresses is neglected, and v is assumed to be a unique function of only hoop strain and temperature histories; namely,

$$v = v(T, \epsilon_\theta) \equiv 3\delta + v_v \qquad (134)$$

where v_v is the vacuole dilatation. This representation is probably quite good as long as the temperature is a constant or a decreasing function of time. Grain radial stress probably has some effect on the amount of vacuole dilatation, but the stress is smallest where this dilatation is greatest, namely near the bore.

It should be noted that 3δ in Equation (134) is the dilatation in the absence of stress; introduction of a so-called "strain-dependent coefficient of thermal expansion" is not needed because this behavior is implicitly contained in v_v.

At any constant temperature, vacuole dilatation of a specimen for a constant strain rate has the behavior shown in Figure 105 (Ref 19). The abscissa is "strain due to stress," ϵ_T, which is the applied engineering strain referred to unstressed specimen dimensions at temperature, T.
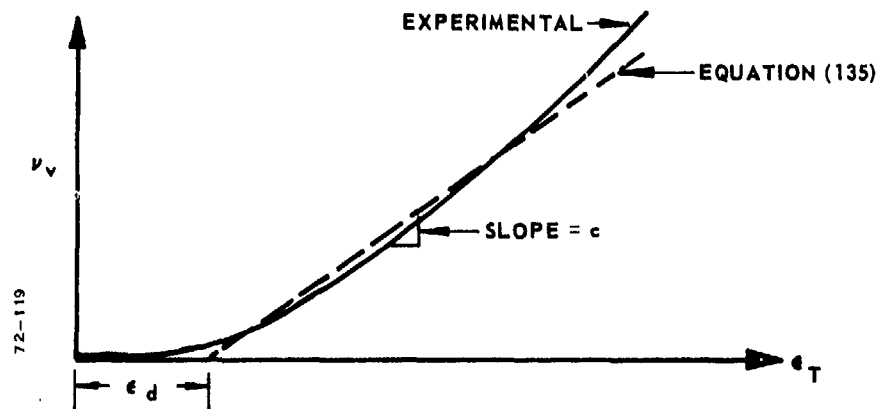
Figure 105   Typical Curve of Nonlinear Vacuole Dilatation versus
Strain of a Tensile Specimen

The term ν_v can be represented quite well by two straight lines:

$$\nu_v = \begin{cases} 0 & ; \quad \epsilon_T < \epsilon_d \\ c(\epsilon_T - \epsilon_d); & \quad \epsilon_T > \epsilon_d \end{cases} \tag{135}$$

where c is the slope of the line and ϵ_d is the "dewetting strain"; both of these material properties may be functions of temperature and possibly of strain and temperature histories.

By combining Equations (134) and (135), and using the fact that the strain due to stress (with $\epsilon_z = \delta_c$) is approximately $\epsilon_\theta - 3\delta/2 + \delta_c/2$, one finds the "dilatational constitutive equation":

$$\nu = 3\delta \qquad \text{for } \epsilon_\theta \leq \frac{3}{2}\delta - \frac{\delta_c}{2} + \epsilon_d \tag{136a}$$

$$\nu = 3\delta + c\left(\epsilon_\theta - \frac{3}{2}\delta + \frac{\delta_c}{2} - \epsilon_d\right) \tag{136b}$$

$$\text{for } \epsilon_\theta > \frac{3}{2}\delta - \frac{\delta_c}{2} + \epsilon_d$$

(2) Grain Dilatation Analysis

For simplicity, in the following discussion the grain and case temperatures are assumed to be equal and spacewise uniform.

First, let us solve the small strain problem; extension to large strain theory will follow. In terms of displacement, the dilatation is

$$\nu = \frac{u}{r_o} + \frac{\partial u}{\partial r_o} + \delta_c \tag{137}$$

-208-

Equate Equations (136) and (137), use the relation $\epsilon_\theta = u/r_o$, and then integrate to find:

● For no vacuole dilatation [condition of Equation (136a) satisfied everywhere]:

$$\epsilon_{\theta l} = \frac{3}{2}\left(\delta - \frac{\delta_c}{3}\right) + \frac{3}{2}\frac{b^2}{r_o^2}(\delta_c - \delta) \tag{138}$$

● For vacuole dilatation between the port radius, a_o, and an intermediate radius, r_d [condition of Equation (136a) satisfied only in the annulus $r_d \le r_o \le b$]:

$$\epsilon_{\theta l} = \frac{3}{2}\left(\delta - \frac{\delta_c}{3}\right) + \frac{2}{2-c}\epsilon_d^{c/2}\left[\frac{3}{2}(\delta_c - \delta)\right]^{\left(1-\frac{c}{2}\right)}\left(\frac{b}{r_o}\right)^{2-c}$$
$$- \frac{c}{2-c}\epsilon_d \tag{139}$$

for $a_o \le r_o < r_d$,

and $\epsilon_{\theta l}$ is given by Equation (138) for $r_o \ge r_d$.

● For vacuole dilatation throughout the web [condition of Equation (136b) satisfied everywhere]:

$$\epsilon_{\theta l} = \frac{3}{2}\left(\delta - \frac{\delta_c}{3}\right) + \left[\frac{3}{2}(\delta_c - \delta) + \frac{c}{2-c}\epsilon_d\right]\left(\frac{b}{r_o}\right)^{2-c}$$
$$- \frac{c}{2-c}\epsilon_d \tag{140}$$

Solution to the finite strain problem is obtained by using Equation (130); namely,

$$\epsilon_\theta = (1 + 2\epsilon_{\theta l})^{1/2} - 1 \tag{141}$$

where, rigorously, $\epsilon_{\theta l}$ is the linear theory strain if there is no vacuole dilatation.

In the presence of vacuole dilatation, Equation (141) is only approximate when $\epsilon_{\theta l}$ is the strain given in Equations (138) through (140). However, it has been found that this approximation is excellent for bore hoop strains as high as 100 percent; this was established by solving the nonlinear equations by the following iteration method:

● Equation (141), which is called the first approximation, is substituted into Equation (136), from which v is calculated.

- The area change ν_a is calculated from the relation $\nu_a = \nu - \delta_c$, and is then substituted in Equation (131) in order to calculate I.

- The second approximation to hoop strain is then calculated by using Equation (130), together with the distribution of I over the web which was found in the second step.

The above three steps are then repeated by starting with the second approximation for hoop strain. This process is repeated until the difference between successive approximations is as small as desired.

A computer program was written to calculate hoop strain by the above iteration technique, and a wide range of examples (b/a_o = 2.71, 5.0, 10.0; $20°F \le |\Delta T| \le 240°F$; $0.10 \le c \le 1.0$; $1.0\% \le \epsilon_d \le 15\%$) was studied in order to determine (1) if the iteration process is convergent and (2) conditions for which the first approximation, Equation (141), is accurate enough for engineering purposes. Figures 106 and 107 show several results for bore hoop strain versus temperature. The solid lines, which are called "exact solutions", are actually the hoop strains predicted after making four iterations. In all cases, it was found that the difference between the third and fourth iterations was less than 2 percent (and often much less) of the hoop strain.

The values of ϵ_d and c used in constructing these graphs were, for simplicity, assumed to be independent of temperature. However, the hoop strain equations, (138) through (141), and the iteration technique, are not restricted in this way. Furthermore, the choice of c = 0.5 was selected because it is typical of the slope normally found for propellant. Also, the difference between the first approximation and the exact solution will usually be much less than shown in the figures because actual b/a_o ratios are generally smaller than 5 or 10.

A conclusion that can be drawn from Figures 106 and 107 is that the first approximation for hoop strain, Equation (141), is sufficiently accurate for most engineering needs. That this equation is so accurate is not very surprising because it is the exact solution for the limiting situations of mechanical incompressibility and/or small strains.

Figure 108 shows the bore strains predicted by using Equations (138) through (141) with two sets of temperature-independent dilatation properties (c, ϵ_d) that are typical of the uniaxial data in Reference 1. It is seen that the vacuole dilatation is sufficient to account for most of the difference between mechanical incompressibility theory and experiment.
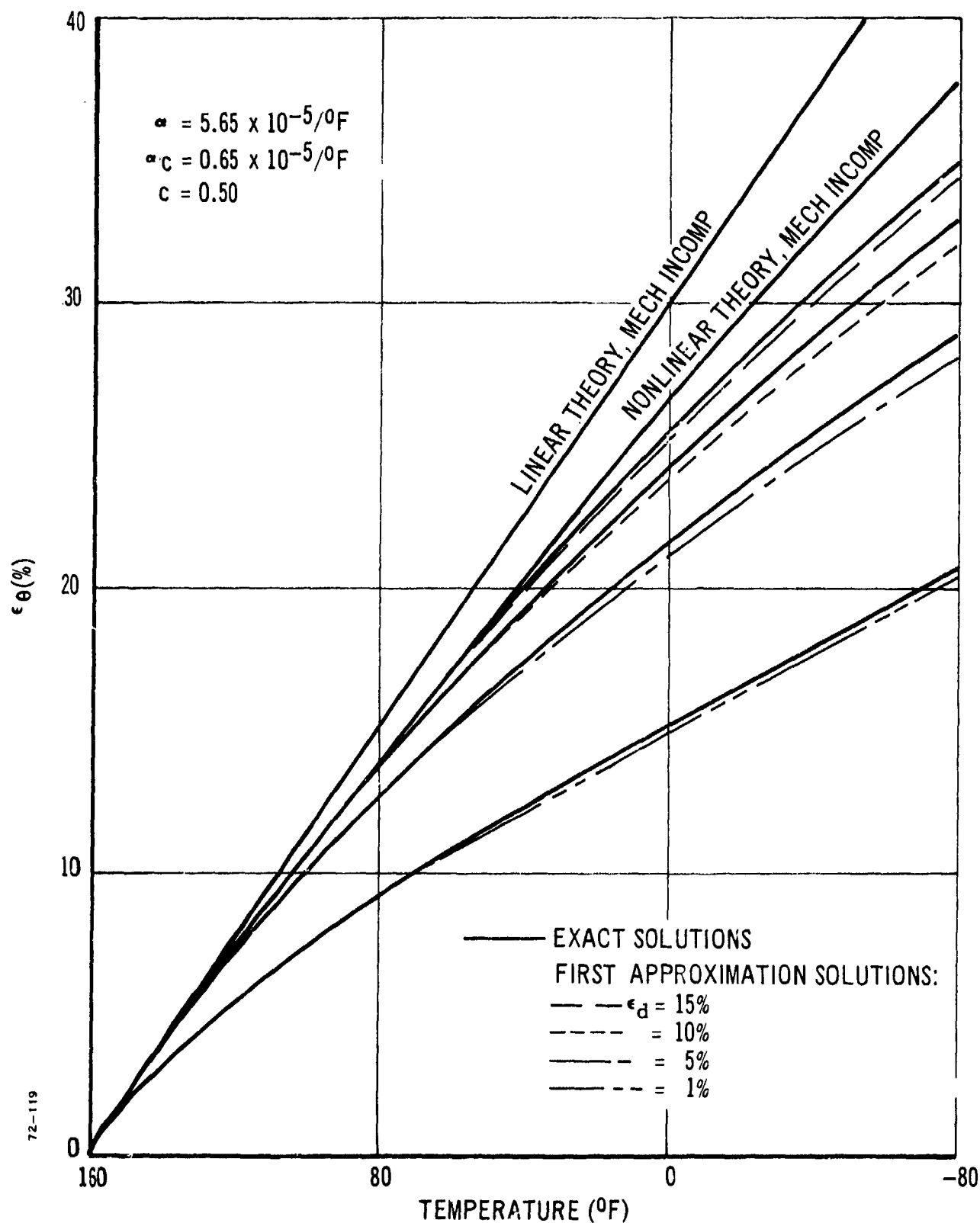
Figure 106. Comparison Between Approximate and Exact Bore Hoop Strains, $b/a_o = 5.0$.
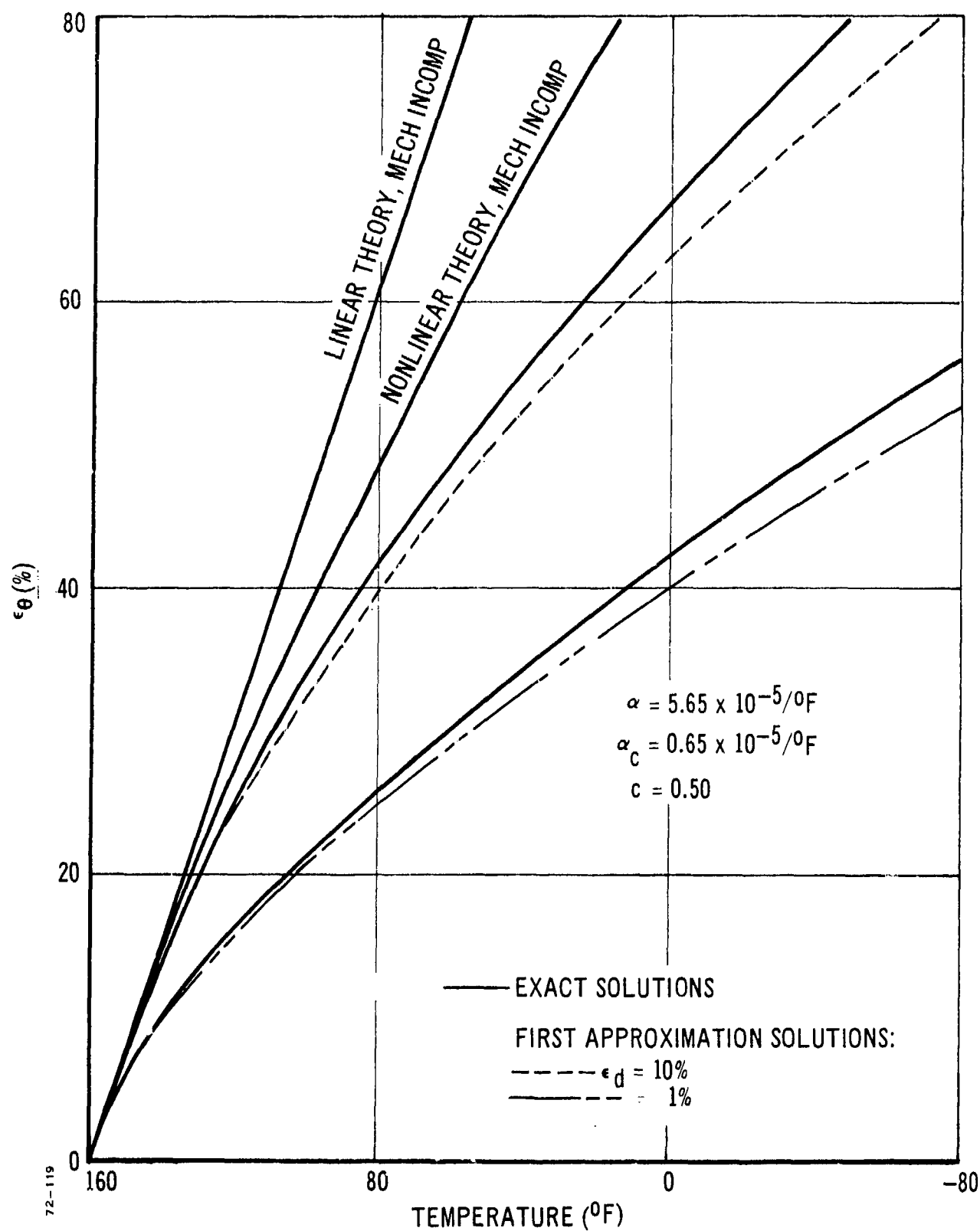
Figure 107. Comparison Between Approximate and Exact
Bore Hoop Strains, $b/a_o = 10.0$.

-212-
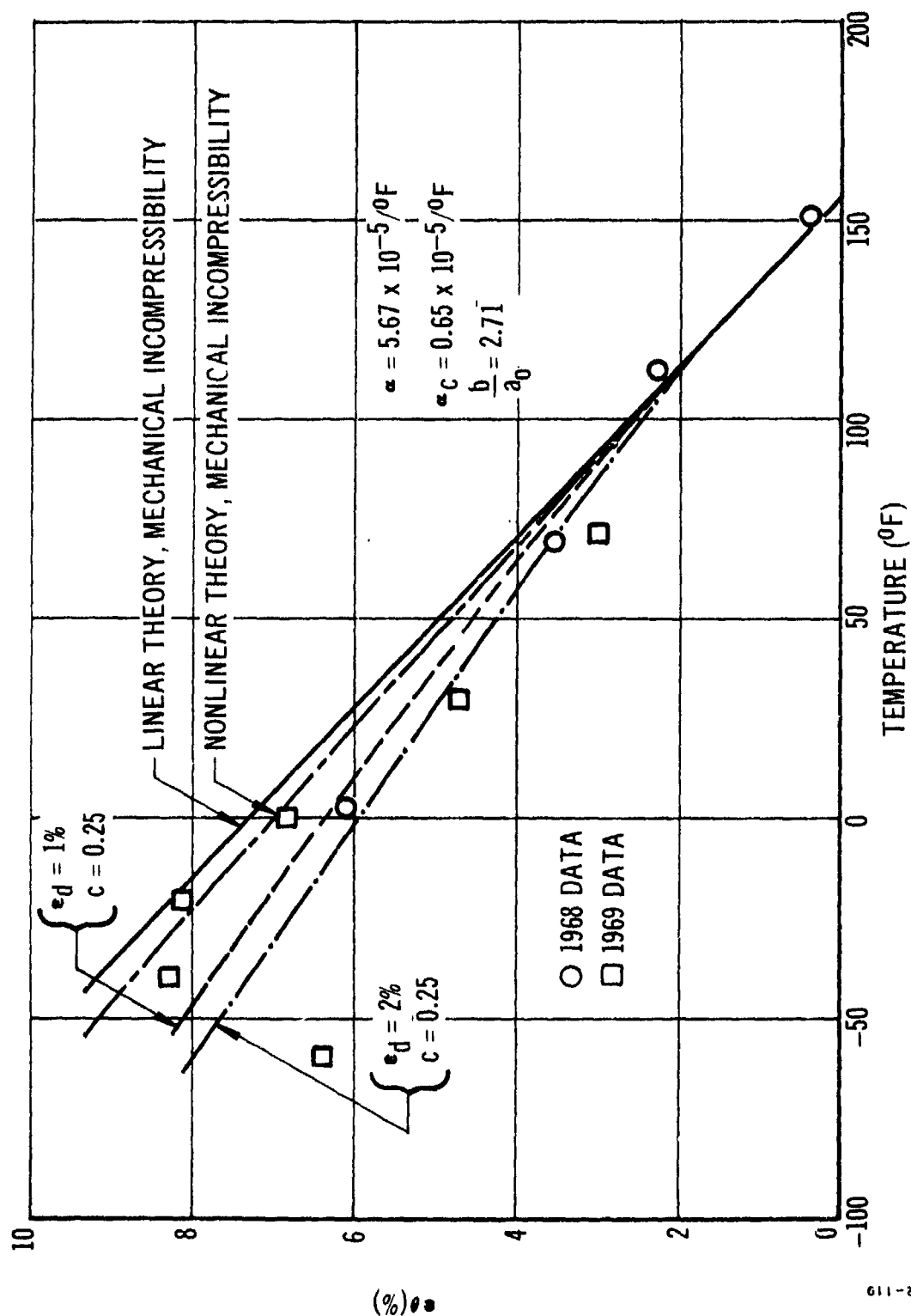
Figure 108. Comparison Between Calculated and Experimental Thermal Bore Hoop Strains at Middle of Steel-Propellant STV No. 2 (Exp Data From Ref 1).

72-119

-213-

e.   Micromechanics Theory of Thermal Expansion

The exact solution for the thermal expansion coefficient of a two-phase, linear elastic composite is (from Ref 13):

$$\alpha = \bar{\alpha} - \frac{\dfrac{1}{K_L} - \dfrac{1}{\hat{K}}}{\dfrac{1}{K_1} - \dfrac{1}{K_2}} (\alpha_1 - \alpha_2) \tag{142}$$

where

$$\frac{1}{K_L} = \frac{v_1}{K_1} + \frac{v_2}{K_2}$$

Also, $\hat{K}$ is the bulk modulus of the composite, subscripts $\underline{1}$ and $\underline{2}$ refer to the phases, and $\bar{\alpha}$ is the rule-of-mixtures value, $v_1\alpha_1 + v_2\alpha_2$ (v_1 and v_2 are the volume fractions).

Prior to dewetting, aluminum plus rubber binder is assumed to be Phase 1, and the oxidizer is Phase 2. After complete dewetting, the vacuoles are assumed to become Phase 2, and Phase 1 is still aluminum plus rubber.

For propellant without any voids, the rule-of-mixtures formula is a very good approximation; viz.,

$$\alpha \simeq \bar{\alpha} \tag{143}$$

This approximation follows from the fact that the binder has a very low shear modulus compared to that of the aluminum and ammonium perchlorate (AP) which, in turn, implies $\hat{K} \simeq K_L$ (Ref 13). It should be added that K_L is a lower bound on the propellant's bulk modulus. This observation, together with the fact that $K_2 > K_1$ and $\alpha_1 > \alpha_2$, implies that rule-of-mixture's formula (143) is actually an upper bound on the expansion coefficient of a void-free propellant.

Similarly, the rule-of-mixtures formula can also be used to predict the expansion coefficient of what has been termed Phase 1 in the above discussion: namely, the two-phase system consisting of the rubber binder plus aluminum. Hence

$$\alpha_1 \simeq v'_{AL}\alpha_{AL} + v'_B\alpha_B \tag{144}$$

where the volume fractions, v'_{AL} and v'_B, are to be calculated here, with only the volume of aluminum plus binder being considered.

-214-

By combining Equations (143) and (144), and referring all volume fractions (v_{AP}, v_{AL}, and v_B) to the total propellant volume, the overall rule-of-mixtures formula becomes

$$\bar{\alpha} = v_{AP}\alpha_{AP} + v_{AL}\alpha_{AL} + v_B\alpha_B \tag{145}$$

When the propellant is in a fully dewetted state, such that there is negligible mechanical interaction between AP and binder, the overall expansion coefficient becomes α_1, Equation (144). This statement follows from the obvious fact that the overall expansion coefficient of a material with holes is equal to that of the material itself.

It should be emphasized that Equation (145) cannot be expected to be valid if any voids exist, regardless of their origin. For example, voids may exist in the propellant as a result of curing conditions, or they may develop under a changing temperature with or without the application of external forces. Therefore, since for typical propellant properties $\bar{\alpha} < \alpha_1$, and assuming that the aluminum and rubber do not debond, one expects the propellant coefficient of expansion measured in the laboratory to fall within the range

$$\bar{\alpha} < \alpha < \alpha_1 \tag{146}$$

Finally, it is to be noted that all constituent thermal expansion coefficients used in the above discussion are, rigorously, in-situ values; i.e., values for the rubber, aluminum, and AP in the chemically and mechanically combined state. The assumption that they are the same as in the uncombined state is probably not serious, and will be used later in this report.

3. EXPERIMENTAL INVESTIGATIONS

a. Approaches Considered

A significant part of this investigation was the review and development (when necessary) of experimental techniques for measuring both propellant specimen deformation and subsequent dilatation. A discussion of the measurement techniques and devices that were considered for possible use in this program can be divided into the three following categories:

(1) Refinement of existing techniques

(2) Combinations of existing techniques into a system whose component parts complement each other to eliminate, define, or minimize the deficiencies of any single technique

(3) The development of new concepts which, although based upon known physical phenomena, may be as yet unused for the measurements desired in this study

In Category 1 would be the capacitive transducer principle. This principle offers a number of advantages over the resistive, inductive, and other types of displacement transducers. The mechanical force requirement is small, the transducer is easily shielded (in contrast to magnetic systems), and the temperature coefficient of air (the dielectric most commonly used in capacitive transducers) is 1 to 2 orders of magnitude smaller than the temperature coefficient of most materials.

Several principles are available for the conversion of capacitive variation into a voltage or current signal, including bridges, electrometric methods, resonance, and frequency variation methods.

The performance of some of the capacitive circuits available on the market is capable of very high sensitivities in terms of displacements perpendicular to a pair of parallel plates. Since the output impedance can be kept small (in the range of several thousand ohms), by suitable choice of circuit resistors, the output current can be measured by a micro- or milliammeter or directly by recorder, without the use of an amplifier, and, therefore, without amplifier noise and possible distortion. Typical values of output current range from -25 to +250 microamperes into a load of 1000 ohms or less for a capacitance variation of ±7 pf (sensitivity 36 micro-amperes/pf).

The sensitivity of some of these transducers, for a variation of the distance d between the two plates of the transducer depends, of course, on the distance between the plates (sensitivity is approximately equal to $1/d^2$). For a two-plate capacitor having a plate distance of about 5/1000 of an inch, the sensitivity is of the order of 2000 volts/inch over a short range of displacement.

The potential use of capacitive devices for dilatation measurements is illustrated in the sketch below. The first sketch shows a biaxial specimen where the dotted region covers a uniform strain field and the dark square is one plate of the capacitor.

-216-
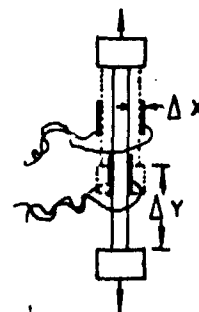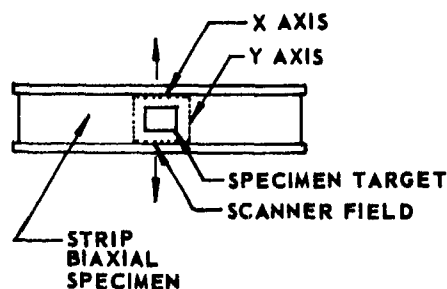
The second sketch shows the reduction in thickness that occurs under load, that causes the plate separation to lessen and the dielectric to change, and that thus causes capacitance changes, which can be measured accurately (i.e., one millionth of an inch induces a 2-millivolt signal). For small plate separations this technique obviously has some potential because of the high sensitivity to displacements. As a result, the technique was considered for use with the strip biaxial specimens. The measuring principle depends on relatively high voltage (approximately 50 volts) to power the capacitance plates for the separation distances commonly seen with strip biaxial specimens (0.375-inch thickness). Voltages of this magnitude were too high to be used safely in an open laboratory.

In addition to the high voltage, the fact that the plates had to be rigidly bonded to the propellant surface presented another drawback, that of localized disturbance of the stress (strain) field. As a result of these disadvantages, plus the fact that specimen dilatation may affect the capacitance, the capacitive devices were not considered further for either the biaxial or poker chip specimens.

In Category 2 are placed conventional measurement techniques such as linear variable differential transducers (LVDTs), linear potentiometers, optical strain gages, etc, along with finesse in specimen selection, construction, and handling. For example, for a poker chip 0.33-inch thick by 4.0 inches in diameter, the change in circumference at its edge center, under a temperature change of 100^0F, is more than 1/10 inch (under the condition that the platens be held rigidly apart during shrinkage).

With this magnitude of circumferential length change and its associated "miniscus" volume change, either change is easily measured (from the standpoint of signal strength).

The obvious advantage of measuring the change in poker chip circumference, rather than the radial motion, led naturally to the device discussed in more detail in subsection VI, 3, b, (2), following.

In Category 3 are the electro-optical devices. In general, electro-optical systems for monitoring displacements incorporate a special photo-multiplier tube to electronically servo-lock on an optical discontinuity. The servo locks on any black-and-white target, sharp edge, or geometrical discontinuity.

In typical operation, the system locks on and tracks a black-and-white target, the image of which is focused on the photocathode by a lens or a telescope. A dark-and-light electron image is emitted from the inner surface of the photocathode and accelerated toward an aperture. The servo holds the edge or boundary of the black-and-white image at the aperture hole, exactly splitting it.

This type of electro-optical tracking system monitors the position of any optical discontinuity perpendicular to the longitudinal axis of the tracker. Although the words black and white have been used to describe the target, it can be any two-color interface capable of providing about a 3:1 contrast ratio.

As the optical image of the area to be monitored is formed on the photocathode by an appropriate lens system, the optical device itself may be remote from the area being monitored. This is especially desirable where thermal transients and hostile environments are to be considered.

The working distance can be as small as 1 inch, allowing resolutions of better than one millionth of an inch. The ultimate resolution of this device appears to be limited by the size and design of the target that the tracker must follow.

Also in Category 3 is placed a method whose feasibility was established in this program. This technique is based upon an electrostatic copying principle and is described in subsection VI, 3, b, (4).

b.   Test Equipment and Procedures

All of the tests were conducted on the original batch of Lockheed Structural Test Vehicle propellant (LPC 0064-61E), which was cast and cured in May 1967. The specimens required for the experimental phase of the program were furnished by the Solid Rocket Division of Rocketdyne. Because of the cost of the samples, only a few specimens were made. Care was taken to ensure that the specimens were kept at relatively low humidity, and load levels were carefully controlled to protect the specimens from unnecessary damage before testing.

(1)   Uniaxial Thermal Expansion Tests

The test specimens used for uniaxial thermal expansion tests were cut from milled biaxial sheets. Each specimen was trimmed to 1/4-inch cross section by holding three sides and the ends clamped while the exposed side was shaved. The specimen was shaved and shaped thusly to avoid mechanical damage. Fine quartz fibers (0.005-inch diameter) were bonded to each end of the specimen. This assembly was suspended inside an Instron environmental chamber (-100 to $+600^0$F) so that specimen hung vertically by the upper quartz fiber. The lower fiber hung through the chamber bottom, where it was attached to the slug (core) of an LVDT. A special, miniature LVDT was chosen to minimize the slug mass (200 mg). With this arrangement the specimen was subjected only to its gravitational loading plus the tiny weight of the slug-fiber string. The LVDT was powered by a Hewlett/Packard carrier amplifier recorder, which enabled displacements of one millionth of an inch to be directly displayed. With this sensitivity, the creep of the propellant under only its own weight could be observed. It was of course necessary to attenuate this sensitivity.

The barrel of the LVDT was mounted on the shaft of a micrometer calibrated in ten-thousandths of an inch, which, through the use of its vernier scale, enabled direct readings to the fifth decimal place. This provided an in-situ calibration scheme and method of determining the range and linearity of the measuring system. At any point in the measurement the calibration could be checked or the instrumentation bypassed by observing micrometer readings. The changes in length of the quartz fibers over the test range were determined with the same apparatus and test

-218-

configuration; the propellant specimen was simply removed and the quartz fibers were linked with a dot of cement characteristic of the size of that holding the fibers to the specimen.

Air currents were deflected away from the quartz fiber/ propellant specimen through the use of a thin tube of plastic and a series of baffles. Measurements were taken only after steady-state temperatures were achieved within the test chamber. At temperatures lower than about -20^0F, frost built up on the quartz fiber and had to be dissipated with a heat gun. However, the use of the heat gun momentarily had little effect on the temperature of the propellant specimen.

(2) Poker Chip Tests

The tests conducted on the poker chip specimens fell into two categories: (1) those designed to measure creep compliance and dilatation under different loading environments and (2) those to measure thermal expansion behavior under a triaxial stress state.

The initial task, and the bulk of the experimental program, was centered around the determination of the creep compliance and mechanical dilatation under both tensile and compressive loading conditions, similar to the stress state at the linear/propellant interface. Test temperatures selected were 0, 70, and 150^0F, although in some cases temperatures of -10 and 140^0F were used because of the availability of several walk-in temperature chambers. Two load levels of 122 and 222 pounds were chosen because these levels were not expected to severely damage the propellant samples, therefore allowing them to be subsequently loaded several times before significant damage occurred. The stress at the center of the poker chip is approximately equal to $2P/A_o$ or, in the case of the selected loads, 19.4 and 35.4 psi, respectively.

Several schemes were explored for measuring the dilatation and axial displacement induced in the poker chip. Included were shadowgraph techniques [subsection VI, 3, b, (4)], optical scanning (such as the Physitech and Martin Tracker type optical devices), and radial profilometers. The best technique proved to be the least exotic, based on conventional techniques for axial displacement and modifications of previous techniques of circumferential measurements. A very sensitive LVDT (0.10-inch range) was used, as shown in Figure 109, to indicate changes in the axial displacement (specimen thickness). The LVDT core was mounted on the lower steel platen and securely held in place with a steel hose clamp. The LVDT slug and calibrating micrometer barrel were firmly fastened to the upper steel platen. Except possibly for load-induced bending, only relatively minor problems were encountered with the measurement of axial displacement.

The authors were aware of previous attempts (Ref 20) to measure the dilatation of poker chip specimens by using LVDTs to measure the changes in the radius. However, the technique was insensitive to the small radial changes and consequently could not detect the dilatation. However, it was believed that the circumference, rather than the radius, would provide more significant changes in dimensions, particularly if
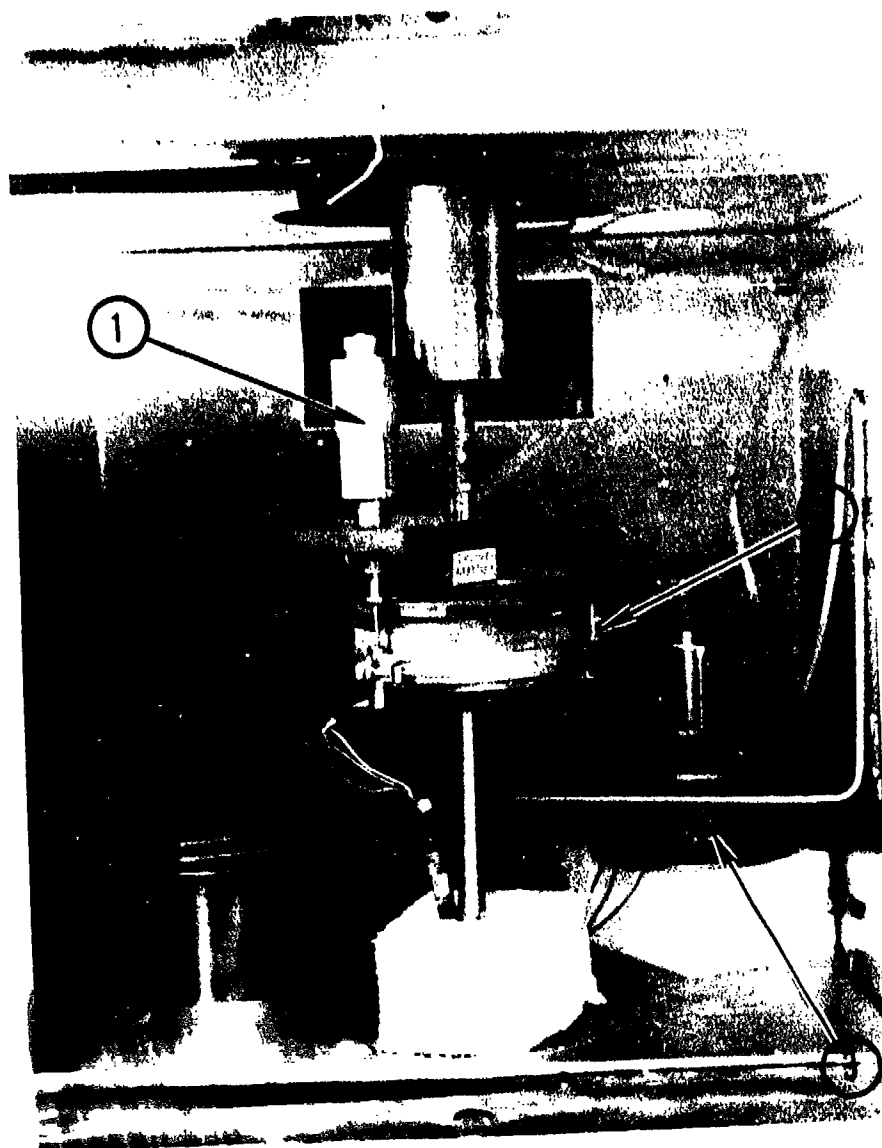
1. THICKNESS-MEASURING LVDT WITH CALIBRATION MICROMETER ATTACHED
2. LEVER ARM AND ATTACHED FIBER PASSING THROUGH THE CHAMBER FLOOR
3. THERMOCOUPLED POKER CHIP FOR INDICATING THE TEMPERATURE-TIME HISTORY

Figure 109.   General Interior View of the Environmental Chamber.

9595

magnified. As a result, the circumference of the poker chip was monitored in all of the creep tests.

The circumferential dimension was monitored around the edge center through the use of a fine quartz fiber as shown in Figure 110. (In later tests, 36-gauge copper thermocouple wire, insulated with Teflon, was used.) One end of the fiber was glued to a small ceramic bead, which in turn was secured to the surface of the propellant by a tiny dot of epoxy adhesive and a short piece of 36-gauge wire strand inserted through the bead into the poker chip. The fiber was wound about the axial center and attached to a lever arm (Figure 111), which served not only to change the direction of motion but also provided a mechanical amplification factor of approximately 6 for the fiber motion. Suspended from the tip of the long arm of the lever was another quartz fiber, which, after passing through the environmental chamber, was bonded to a slug positioned in the LVDT below. The quartz fiber and the LVDT slug were so light that a small additional weight had to be added to the lever arm system to keep the circumferential fiber cinched against the surface of the propellant. The natural resilience of the quartz caused the circumferential fiber to spring away from the propellant surface when the lever arm load was relaxed. This prevented the fiber from sinking (or being driven) into the propellant surface by sustained loading. The fiber was kept at the vertical center of the circumference by placing horseshoe-shaped strands of 36-gauge wire over the fiber, sufficiently far into the poker chip to prevent vertical motion while allowing unhindered circumferential motion.

As shown in Figure 112, both LVDT barrels were mounted on 1/10,000-inch micrometers. In-situ calibration and direct measurements were possible at all times. During one series of tests the recorders were used only as null indicators and the readings were taken directly from the micrometers. The usual procedure was to (1) balance the signal conditioning and recorder equipment, (2) locate and record each LVDT null position, (3) dial known displacements with the micrometers for calibration of the recorder traces, and (4) load the poker chip and observe the dual traces of thickness and change in circumference. Typical data traces are shown in Figure 113.

A hydraulic jack was used to control the tension loading rate. Calibrated weights were supported by a load pan, which in turn was supported by the jack. The loading usually occurred (zero to full load) in $\simeq$ <0.5 second. The specimen was allowed to creep for approximately 180 seconds, at which time the load was quickly removed, and the specimen was allowed to recover for at least 360 seconds.

Figure 114 shows the poker chip specimen that was thermocoupled with two gages imbedded in the propellant (one at center, one at half the radius) and one on the platen surface. Such a dummy unit provided a temperature-time history for another nearby poker chip under test.
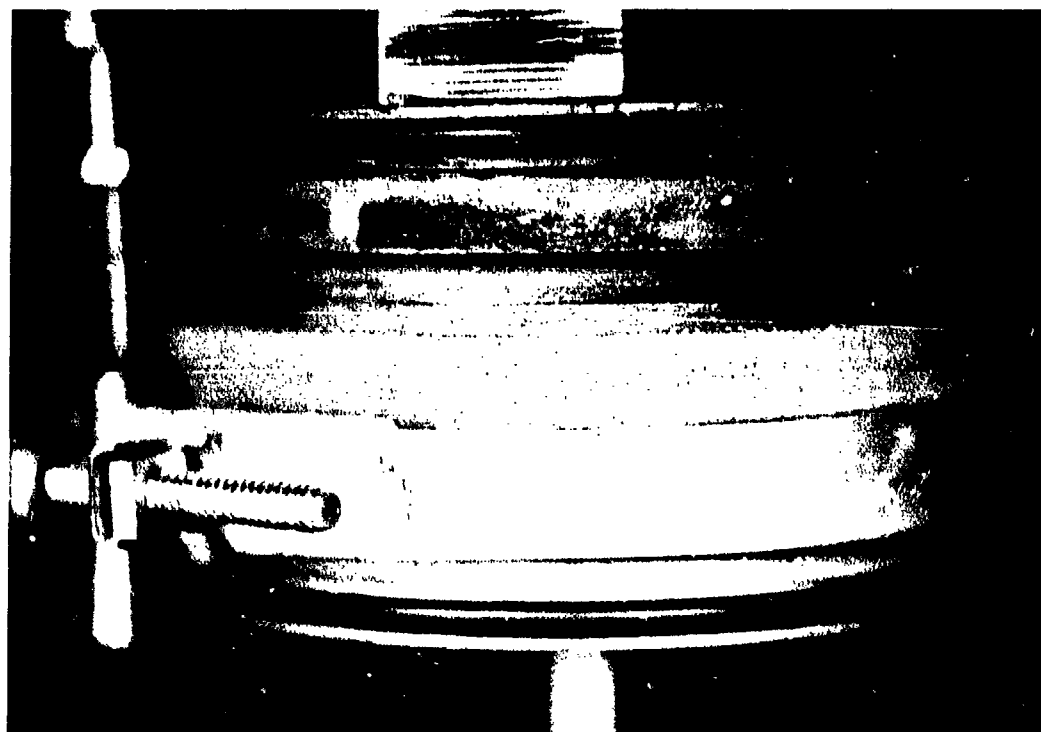
Figure 110.   As-Machined Surface of a Poker Chip with the Quartz Fiber
Circumference Gage Mounted at the Center of the Meniscus.
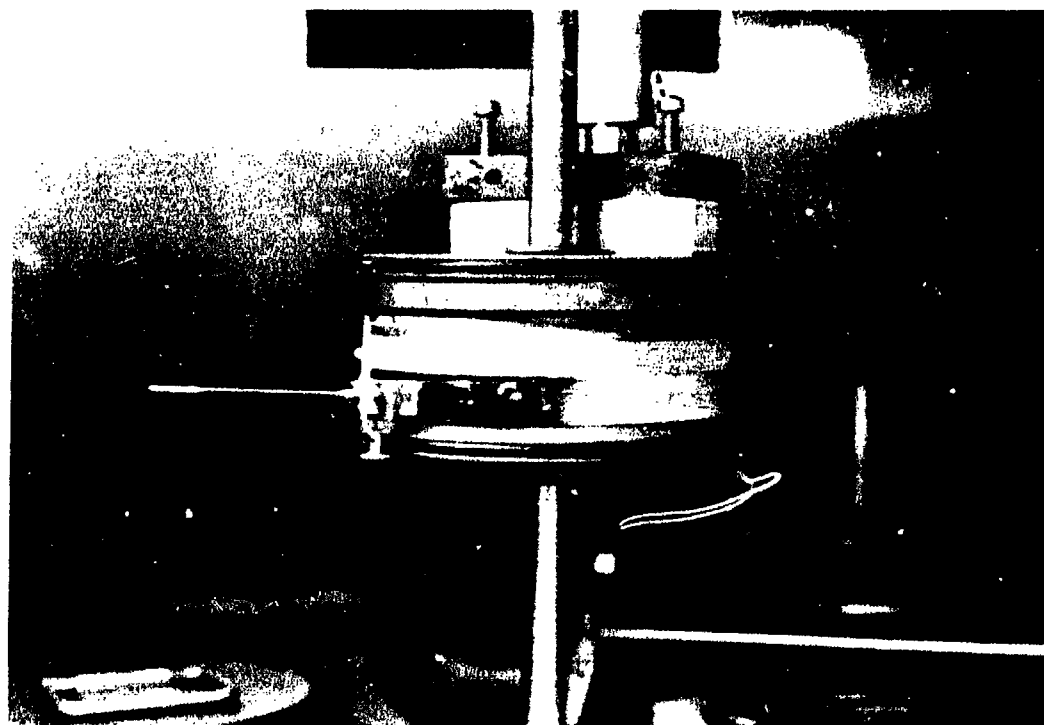
Figure 111.   Poker Chip Rigged for Tension Testing, Showing the
Mounting of the Lever Arm and the Quartz Fiber
Encircling the Propellant.
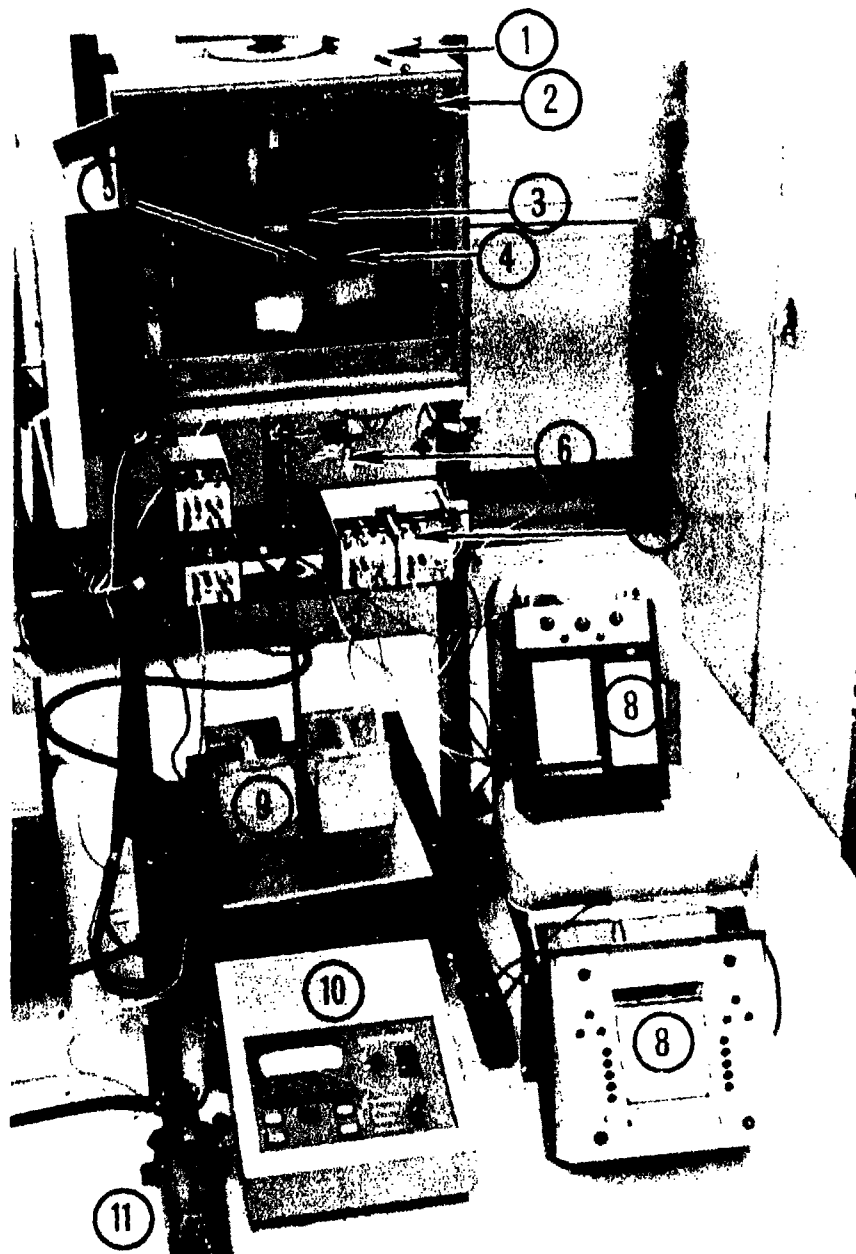
1. THICKNESS MICROMETER ADJUSTMENT ROD
2. INSTRON ENVIRONMENTAL CHAMBER
3. POKER CHIP WITH THICKNESS-MEASURING LVDT AND ATTACHED MICROMETER
4. POKER CHIP WITH IMBEDDED THERMOCOUPLES FOR TIME-TO-TEMPERATURE MEASUREMENTS
5. CHAMBER CONTROL THERMOMETER
6. CIRCUMFERENCE-MEASURING LVDT AND ATTACHED MICROMETER
7. CARRIER AMPLIFIER SIGNAL CONDITIONING UNITS FOR THE LVDTs
8. DUAL CHANNEL RECORDERS
9. LOADING ASSEMBLY (LOAD CELL IS AT TOP OF ENVIRONMENTAL CHAMBER)
10. INSTRON CABINET CONTROLLER
11. HYDRAULIC PUMP AND FLUID RESERVOIR

Figure 112.   Poker Chip Tension Testing Apparatus.
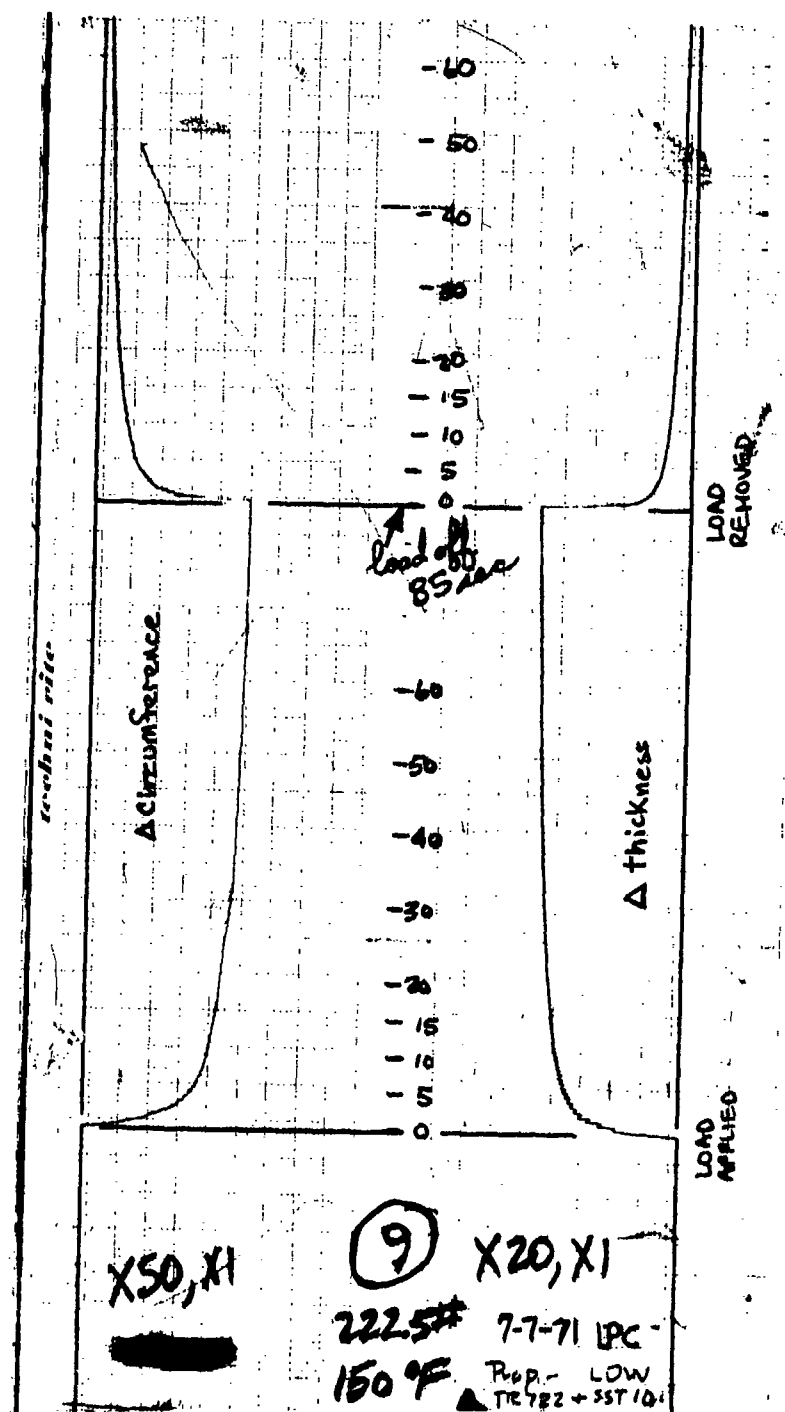
Figure 113. Actual Data Trace Where the Upper Curve is the Circumferential Trace and the Lower Curve Indicates Change in Thickness.

ENVIRONMENTAL TEMPERATURE SENSOR

9596
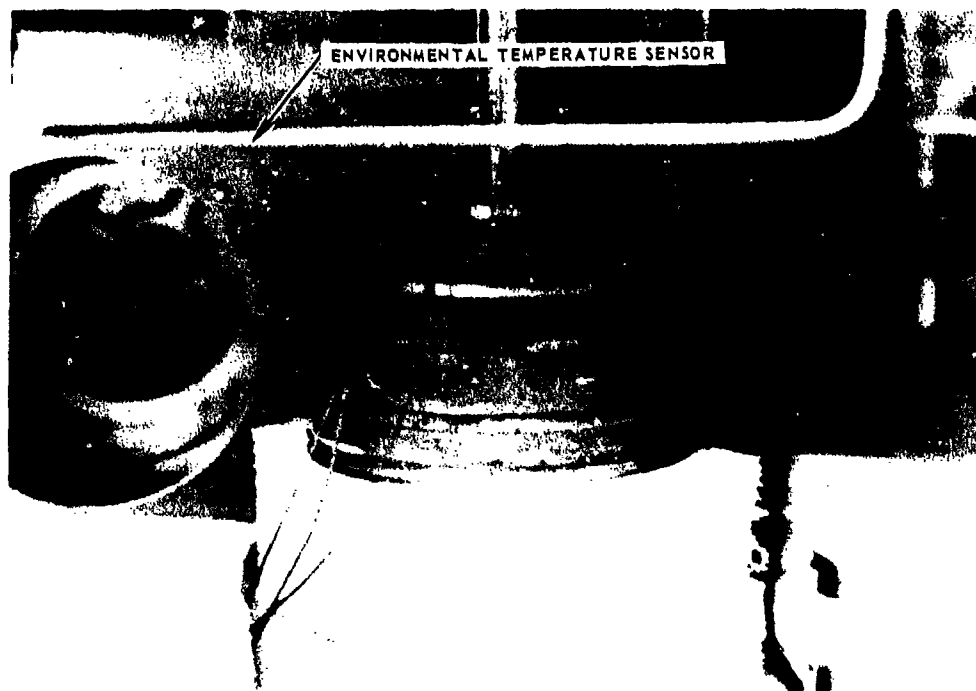
Figure 114. Poker Chip Specimen with Thermocouples
Both Imbedded In the Propellant and Mounted
on the Surface.

The measurement schemes developed for the tension tests
were applied equally as well to the compression tests. Bending was pre-
vented by universal joints and precise load alignment in the tension tests.
However, because universal joints are useless in compression, for the
compression tests a load cage incorporating a point-loading scheme was
fabricated. The specimen was precisely leveled on its support and the
load was transmitted through a ball-bearing center in the top platen of the
poker chip. The data traces for the compression tests are essentially like
those in Figure 113. The compression cage would not fit within the Instron
temperature chamber, and the compression tests therefore were conducted
in the walk-in temperature chambers available at the McNew Materials
Laboratory.

The compression testing sequence for each sample started
first with the higher temperature, either 140 or 150°F. Initial checkout pro-
cedures were conducted with the weight of the loading pan, 22 pounds, used
to calibrate and set up the readout equipment. After the initial setup, several
tests were conducted with the 122-pound load (usually about 4 or 5 tests).
The 222-pound tests were then run next for a similar series, and then the
next lower temperature tests were run in a similar fashion, i.e., low load
first, then high load.

The question of bending was checked out. Several independent tests were connected with two LVDTs mounted 180-degrees apart. Loads were applied to the sample and the axial strains on opposite sides were recorded. After several load cycles, the two LVDTs were rotated to a position 90 degrees from the first series of tests and the load cycles were repeated. The strain variation around the circumference was found to be insignificant for the purposes of the test.

In addition to the creep-recovery tests, the effect of multi-axial stress on thermal expansion was investigated through the use of constrained poker chip specimens. An additional loading fixture was devised for use with poker chip specimens in the determination of the influence of a small, superposed, triaxial compressive stress state on thermal dilatation. Although the effect of superposed tension could be determined in a similar manner, it was not studied in the program. The device, shown in Figure 115, consists of a load cage in which a poker-chip specimen is securely bolted by its lower platen. A compression screw is bolted to the loading fixture above the specimen. The compression screw can be tightened by hand so that the load is applied through the axial center of the specimen, thus eliminating bending. Three short pieces of steel sheet stock were strain-gaged on both sides and each was connected in a half-bridge (Wheatstone) configuration so as to give maximum sensitivity in bending. The three clips were calibrated with a micrometer and then mounted at 120-degree intervals around the poker chip to measure the axially induced strain. A constant strain was held by making relatively minor adjustments to the main compression screw once steady-state temperature was reached. As in the creep tests discussed previously, the circumferential changes were monitored using the quartz fiber/LVDT test configuration.

By holding the platens fixed and cooling or heating the specimen, the free surface will neck-in. Measurements of the resulting changes in circumference, together with Equation (172) [see subsection VI, 3, c, (4)], were then used to calculate α.

(3) Strip Biaxial Tests

Strip biaxial tests were conducted to determine the tension relaxation moduli over the same temperature range as the poker chip specimens. During these tests the dilatation was to be measured and compared with the dilatation measurements found in the poker chip tests. Stress relaxation tests were planned for nominal strain levels of 2.5 and 12.5 percent.

After a review of both the contact and noncontact methods of displacement measurement, such as described in subsection VI, 3, a, it was felt that the available environmental chambers and Instron testing machines would hamper the use of such optical devices as the Physitech and Martin Tracker extensiometer. The possibility of using the capacitor plates as thickness measuring devices was explored further. As indicated previously, the plates were attached in such a manner that the propellant acted as a dielectric whose thickness changed as the stresses were applied. This measuring principle works well, but relatively high voltages (approximately 50 v) used to power the device made the plates a bit dangerous.
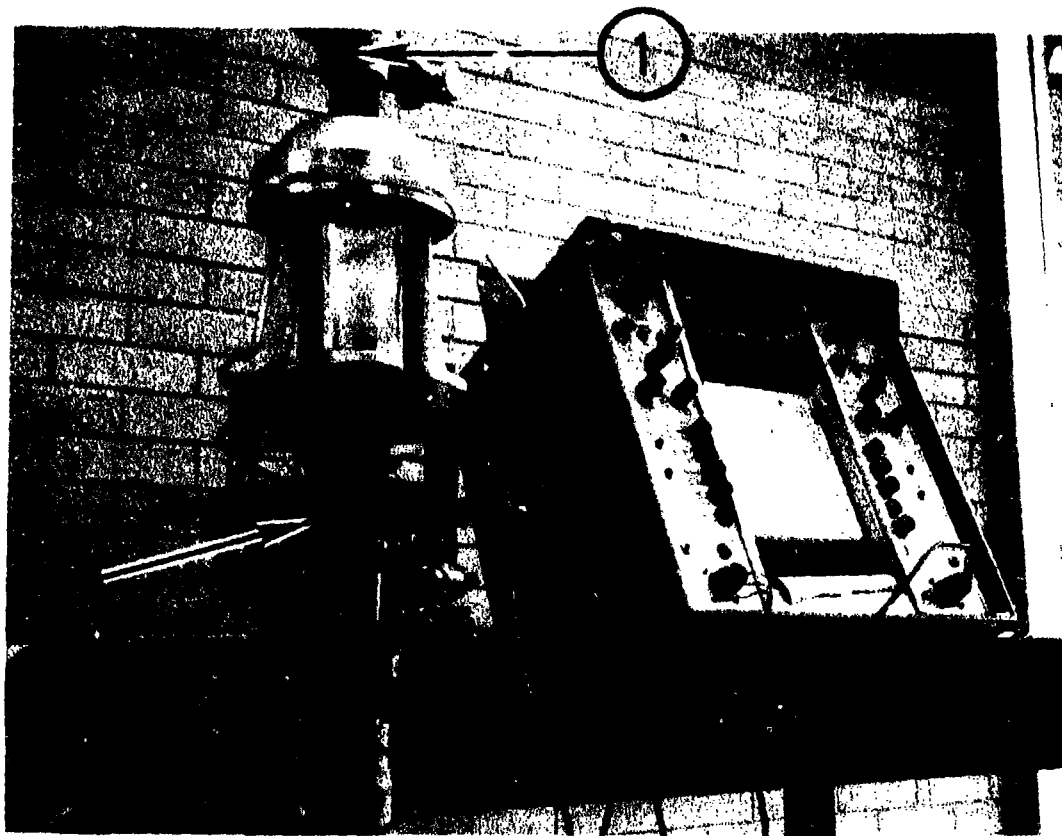
1. MAIN COMPRESSION SCREW
2. LVDT AND CALIBRATION MICROMETER
3. ONE OF THE THICKNESS STRAIN CLIP GAGES

Figure 115.   Carrier Amplifier/Recorder System with the Poker Chip
Fixture Used To Maintain a Fixed Strain During Thermal
Cycling.

9598

-227-

A biaxial dilatometer was then obtained from Hill Air Force Base on a loan basis. The unit as received was in an unworkable condition as originally manufactured by the CETEC Corporation. The unit was completely disassembled, and after extensive modifications, was put in working condition. The dilatometer, shown in Figure 116, was designed to measure dilatation by two methods. The first method relied on direct LVDT measurement of decreases in cross-sectional thickness. The other method was based on state-of-the-art gas dilatometric techniques such as those employed by Farris (Ref 19). The LVDT system consists of spring-loaded probes that ride on the surface of the specimen's sides. Unfortunately, the probes were not only insensitive to the small thickness changes but also damaged the surface at the point of contact. As a result, the LVDT probes were removed entirely. Once the leaks around the lower shaft, main door, and calibration micrometer were sealed, the unit was completely functional. The unit was calibrated before each test by inserting a precision micrometer shaft into the test chamber to simulate a volume change of 0.0707 in.^{3} (for the samples this corresponds to a volume change of about 1.6 percent). It was possible to resolve volume changes of the order of 0.1 to 0.2 percent over a relatively long period, provided the temperature remained stable.

The biaxial strip specimens furnished by Rocketdyne were the standard 14-inch length, which was much too long for the biaxial dilatometer. Several strip biaxial specimens were subsequently cut with the dimensions 7.0 by 1.625 by 0.375 inches. These samples were then cleaned and prepared for bonding following the procedures given in References 21 and 22. The samples were then bonded to aluminum plates and cured for 2 hours at 150°F. Care was taken to create a fillet along the edges in order to provide for good gripping and a gradual load transfer from the grips. Figure 117 shows a typical strip biaxial specimen bonded and ready for testing.

In Figure 118 the biaxial sheet is loaded onto a transfer fixture, which is used both to protect the specimen from flexure and to ensure correct sample alignment and zero strain on the specimen. Upon removal of the specimen, when preset strains are to be maintained, this fixture is also used. The transfer fixture is then pressed against the dilatometer to engage guide pins (shown in Figure 119) with holes in the dilatometer. Figure 119 shows the sample as it is freely moved along the fixture rails until it is loaded and ready for testing. The dilatometer is then sealed and made ready for testing (Figures 120a and 120b) at pressures ranging from ambient to 1000 psi; however, only ambient pressure tests were conducted in this program.

(4) Photoconductive Copying Technique

As noted previously, various techniques are available for the accurate measurement of small displacements. Basically, they are based on the use of either photosensing (visual) or electric-sensing characteristics of such deformation. With some of these techniques, it is theoretically possible to detect several Angstroms of deformation of the specimen, (e. g., electric resistance, semi-conductor strain gages). Despite such high sensitivity, current devices employing such techniques have certain drawbacks.

AFRPL-TR-72-29
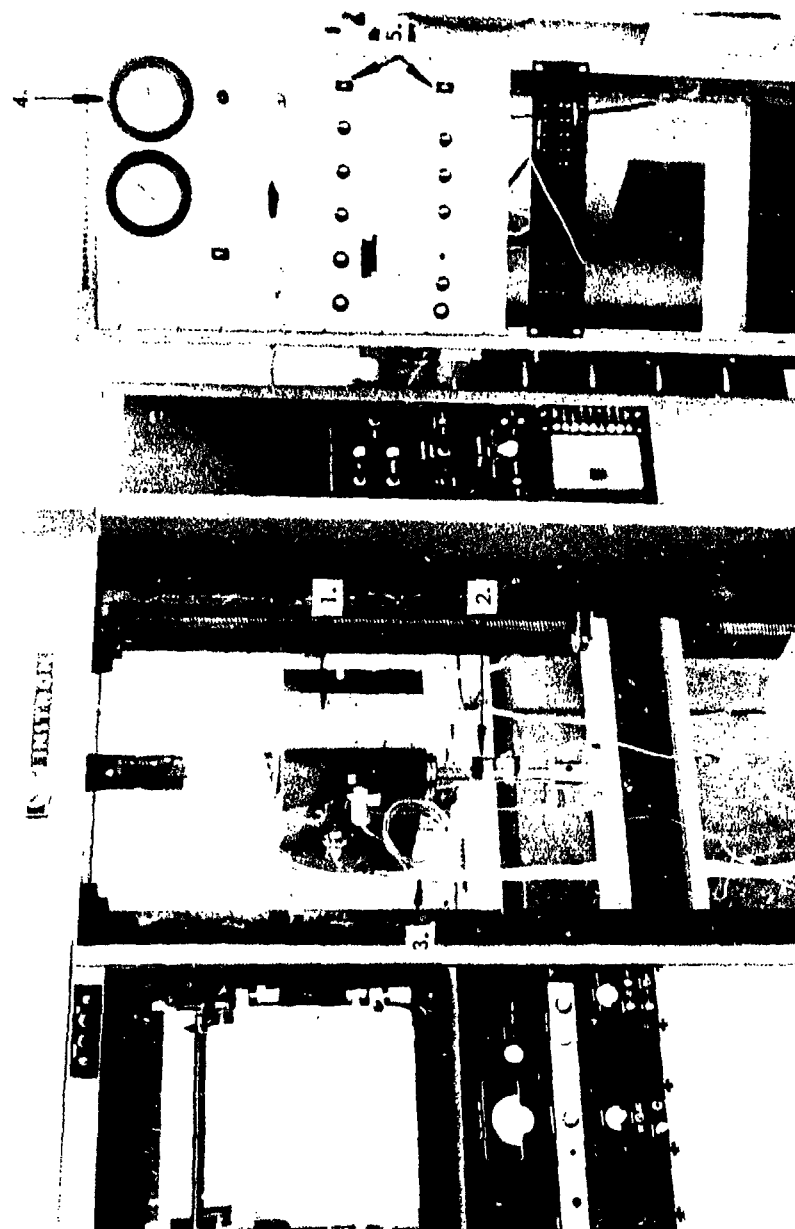
1. SPECIMEN AND REFERENCE CHAMBER MOUNTED IN INSTRON
2. SHAFT VOLUME COMPENSATOR
3. CHAMBER THERMOCUUPLES
4. GAS PRESSURE CONTROL PANEL
5. MEASUREMENT ELECTRONICS

Figure 116.   Biaxial Dilatometer.

-229-

LOCKHEED PROPULSION COMPANY
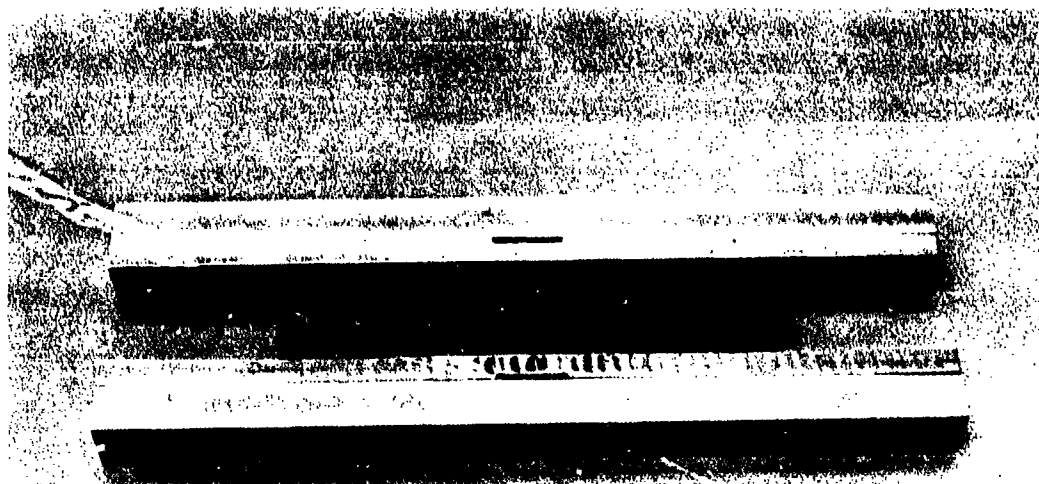
Figure 117.   Strip Biaxial Specimen Bonded to Loading Platen.
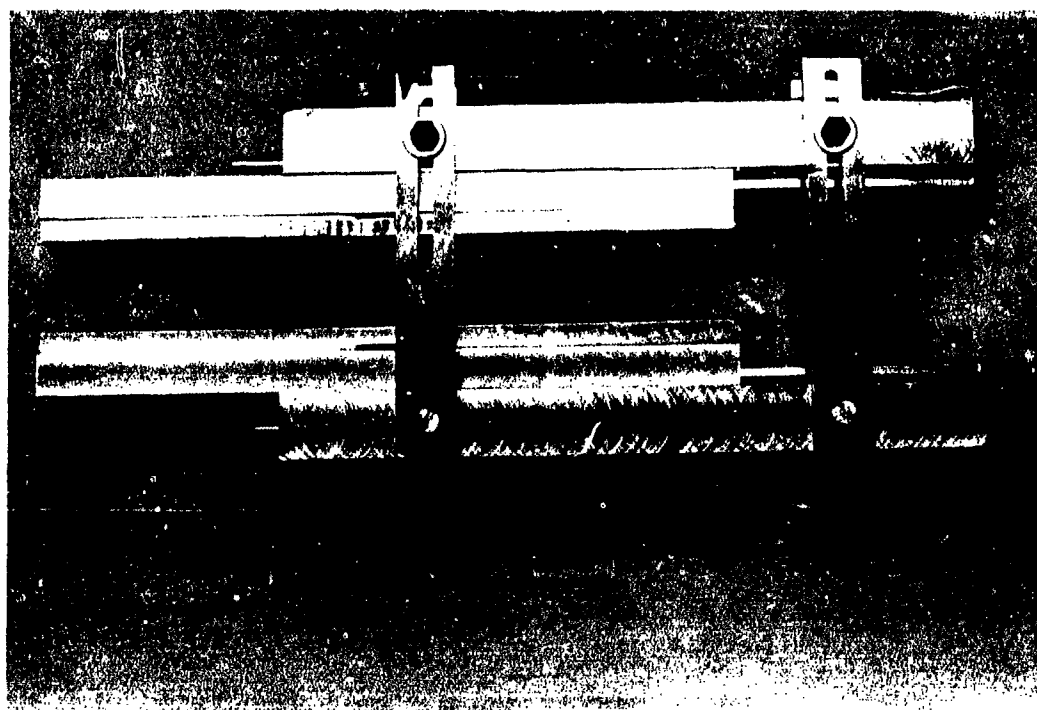
Figure 118.   Strip Biaxial Specimen and Transfer Fixture.
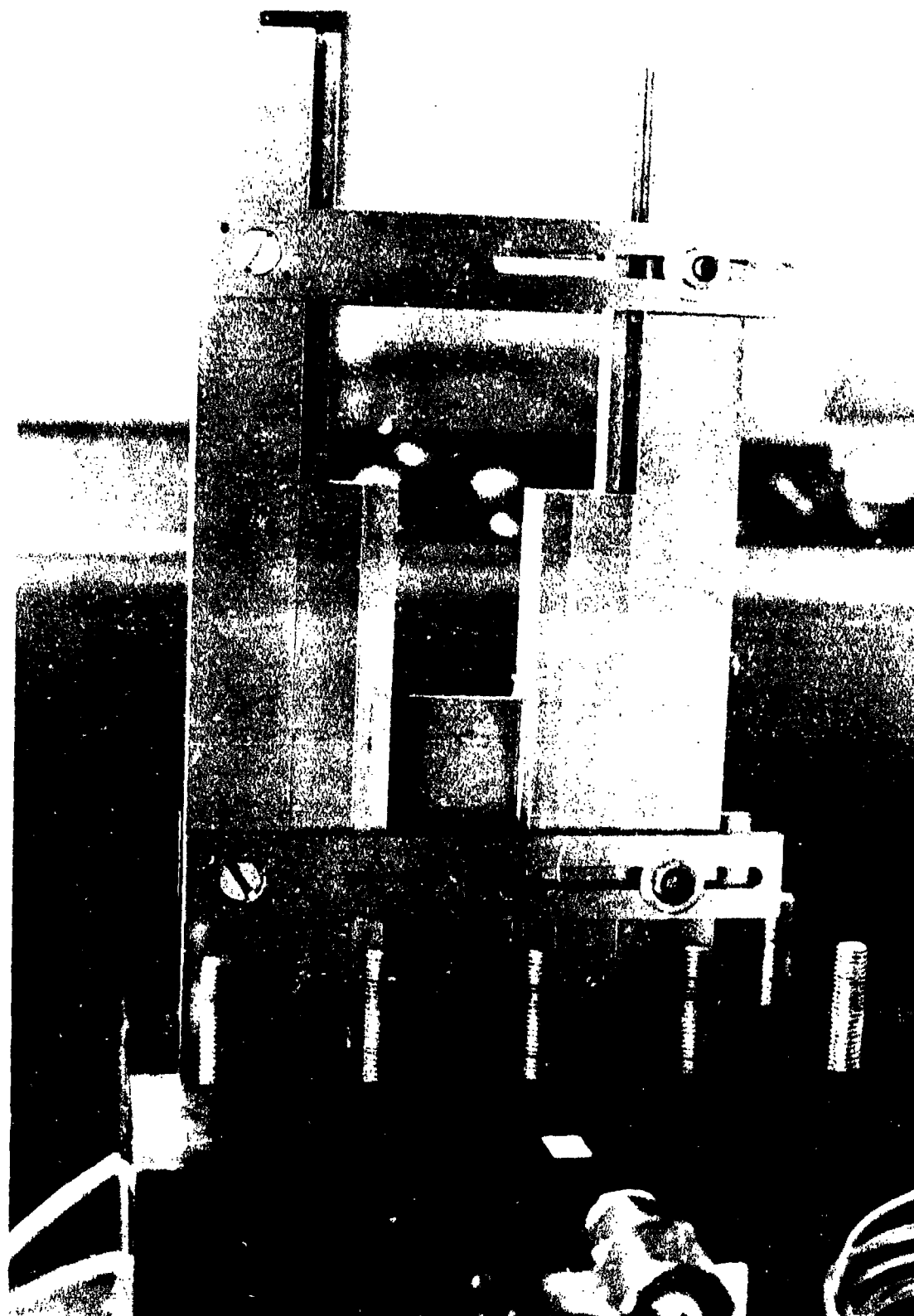
Figure 119.   Closeup of Transfer Fixture and Biaxial Specimen Loaded
(or Extracted Under Strain) in the Dilatometer.

(b) Closeup of Specimen Chamber Showing Mounting Rails and Biaxial Specimen.
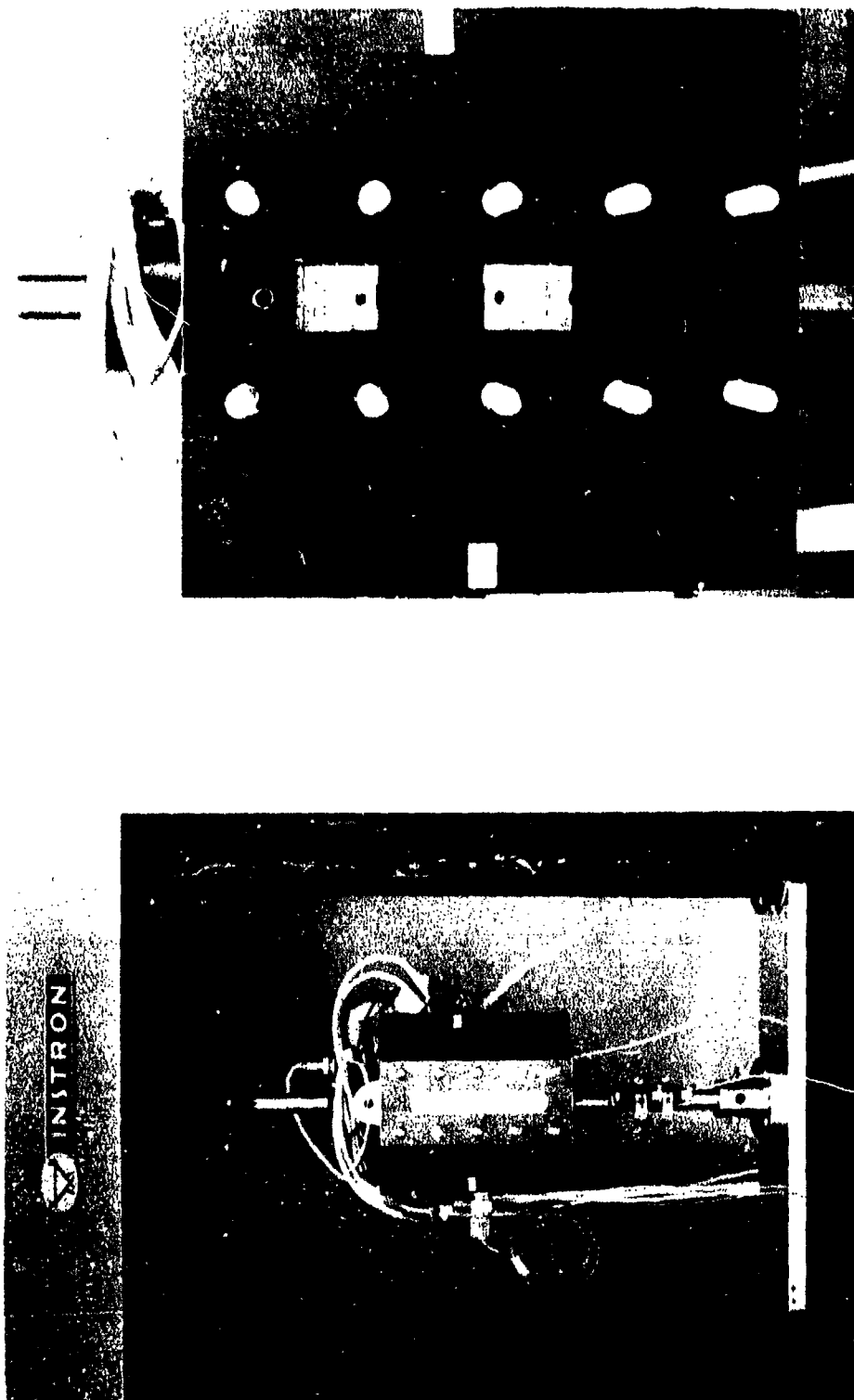
(a) Dilatometer Chamber Showing the Access Port with Slide Plate and Backup Panel.

Figure 120. Dilatometer Chamber and Specimen Detail.

9592

-232-

First, they require physical contact between the detector and the specimen surface. Such physical contact may introduce several undue effects. For instance, if the specimen material is mechanically softer than the detector material, the deformation of the specimen may not be detectable accurately. It is also quite possible to modify the mechanical characteristics of the specimen material by such physical contact. Second, the finiteness of the detector size makes the point measurement impossible. More or less, the presently available techniques have similar drawbacks.

In an effort to resolve these problems, a technique entitled the "Photoconductive Copying Technique for Obtaining the Optical or Electronic Image of the Specimen" was investigated. This technique employs the copying process of typical electrostatic copying machines. The result is the optical image of the specimen, which can be read with the high-resolution microscope or recorded by scanning with an electrometer. This technique offers the following advantages:

(1) Noncontact measurement

(2) Measurement of point deformation as well as of the entire (shadow or edge) deformation of the specimen

(3) Experimental results capable of being copied as well as recorded

(4) Relatively high sensitivity (10^{-4} cm) and high accuracy

(5) Potential for automation of the entire process

(6) Low cost

Research progress. After the decision was made to examine the feasibility of the technique, basic apparatus and materials were obtained. The basic devices and materials for the study were (1) Corona charging device (high voltage source of about 10,000 volts), (2) illumination (or exposure) device, (3) toners (for creating a visual image), and (4) photoconductive materials.

The optical image of the sample can be formed by two exposure methods: "shadow exposure" and "reflection exposure". The present study started with the shadow exposure method, because it required fewer optical systems than the other and also gave general information on the applicability of the proposed technique. As a photoconductive material, zinc oxide-coated paper was employed.

With the shadow exposure method, the following factors have been tested and analyzed:

(1) Desired type of toners

(2) Resolution limit

-233-

AFRPL-TR-72-29

(3) Desired optical system and condition for the optimum
resolution of the sample image

(4) Practical problems associated with the actual Instron-
mounted system

Experimental results indicated that the commercially
available liquid toner was adequate, despite its coarse grain size, for the
desired high-resolution image formation and was preferable to the dry toner
(powdered graphite). Theoretical resolution limit of the optical image (as
limited by grain size) is approximately 10^{-4} cm with visible light, but can
be improved up to 10^{-5} cm with ultraviolet light. Experimental resolution
limit was tested with the reference scale of range 10^{-2} cm to 10^{-3} cm. The
test result showed that the resolution of 10^{-3} cm and 10^{-4} cm can be accom-
plished even under poor conditions if the original reference scales have high
contrast.

To find the desired optical system condition for the opti-
mum result, the actual dimensions of the Instron temperature control box
were measured and two types of shadow exposures were tested, depending
upon whether the light source was placed inside or outside the window of the
box (inside exposure and outside exposure). For each exposure, various
optical devices and problems were studied in detail. The workable condition
for the desired resolution was established for the outside and inside expo-
sures separately and the results have been categorized for future work. In
brief, the shadow exposure method is quite feasible for the desired results,
provided the suggested optical system is used and the working condition is
met.

The final phase of investigation was associated with auto-
mation of the proposed technique. The following problems of the automated
system were researched in some detail:

(1) Advantages of the automated system

(2) Desired photoconductor

(3) Proposed system (functional diagram and its performance)

(4) Design consideration and desired apparatus

No experiment was made on this aspect of the problem.

From the foregoing study the useful nature of the proposed
technique has been demonstrated and basic data have been obtained. How-
ever, there are still problems to be solved in the actual use of the technique.
These may be divided into the two areas discussed below.

Hand-operated system. This system will serve the imme-
diate need of the researcher, and most of the necessary equipment exists in
commercially available forms. For the actual use of this system, however,

the practical problems of proper paper exposure inside the environmental chamber (usually with a fogged window) must be solved. For the inside exposure method (columnated beam), a few more experiments are required to obtain the desired sharp images. For the outside exposure method, mirrors may be needed to direct the columnated beam(s) so as to obtain a sharp and (if desired) undistorted image.

Automated system. Selenium plates were obtained from the Xerox Corporation for use in a series of experiments on automating the image identification. In this system the photoconductive selenium is given an electrostatic charge just as with the zinc oxide-coated paper. The specimen image is cast upon the plate as before and the shadow area remains charged. Instead of developing the image for visual measurement, a charge-sensing probe is used. By using such a device as a Keithley electrometer with a miniature sensor head, and by using the points of intersection of slopes of the resulting trace, results to date show resolutions of at least 10^{-6} inch.
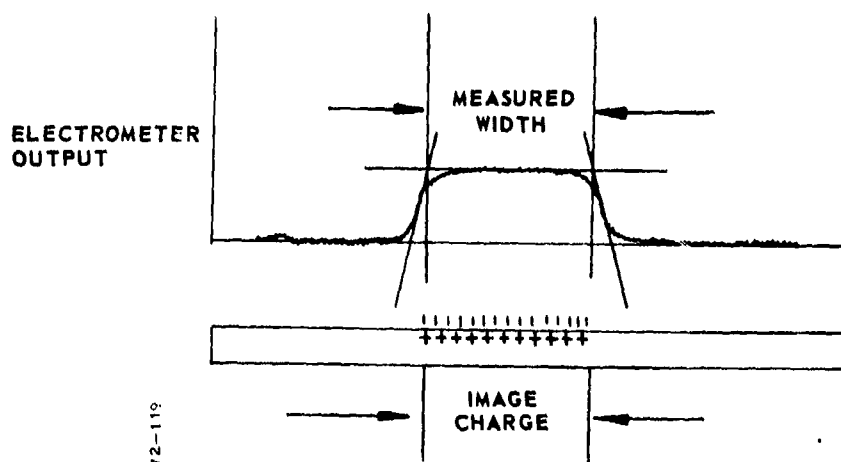
Ultimate resolution may be better, inasmuch as the calibration procedure allowed the head to be positioned only to the nearest 1×10^{-6} inch. These measurements were made by producing contact prints of diffraction gratings. A conceptual device consists of a disc of selenium on which a deformation sequence would be stored much as images are stored on a stereo View Master disc. Following the test sequence, the disc would be rotated at high speed as the sensor head moves radially across the record. This would allow electrical reconstruction, at any desired magnification, of the specimen image. Feeding the electrometer data into a digital processor could yield all necessary conversions into displacement, volume, etc.

-235-

c. Experimental Data and Comparison with Analysis

(1) Uniaxial Thermal Expansion Coefficient

The uniaxial linear expansion coefficient was measured over a temperature range from 135 to -65°F by first heating the sample to 135°F and subsequently cooling it to a lower temperature. The thermal expansion data are shown in Figure 121. Table XX summarizes all of the previously known data on the linear thermal expansion coefficient for this propellant:

TABLE XX

LINEAR THERMAL EXPANSION COEFFICIENT

Temperature Range ($^{\circ}$F)	$\alpha \times 10^5$	Method
200 to 25	6.54	Quartz dilatometer (Ref 1)
25 to -80	5.67	Quartz dilatometer (Ref 1)
75 to -75	5.27	Dupont TMA (Ref 23)

The data in Figure 121 are in good agreement for the lower temperature range (70 to -65°F) but depart considerably at the higher temperatures. In view of the fact that the thermal properties of both the ammonium perchlorate and aluminum are relatively constant over the range of interest, the behavior must be attributed either to changes in the binder thermal expansion coefficient or in the viscoelastic behavior of the overall material. Normally an increase in α occurs with increasing temperature, or at most a relatively constant slope over the higher temperature range. However, what is seen in Figure 121 can be partially attributed to the viscoelastic behavior of the propellant in the manner described below.

As described earlier, the sample measured approximately $\frac{1}{4}$ inch on a side by 2.485 inches in length. The sample was suspended from the top of the environmental chamber by a small quartz fiber, and as a result had a linearly varying tensile stress imposed by gravity-loading. The length-averaged stress due to propellant weight, σ, is given as

$$\sigma_p = \frac{\gamma L_o}{2} \tag{147}$$

where

γ = density of propellant (0.063 lb/in.^{3})

L_o = sample length at room temperature (2.485 inches)
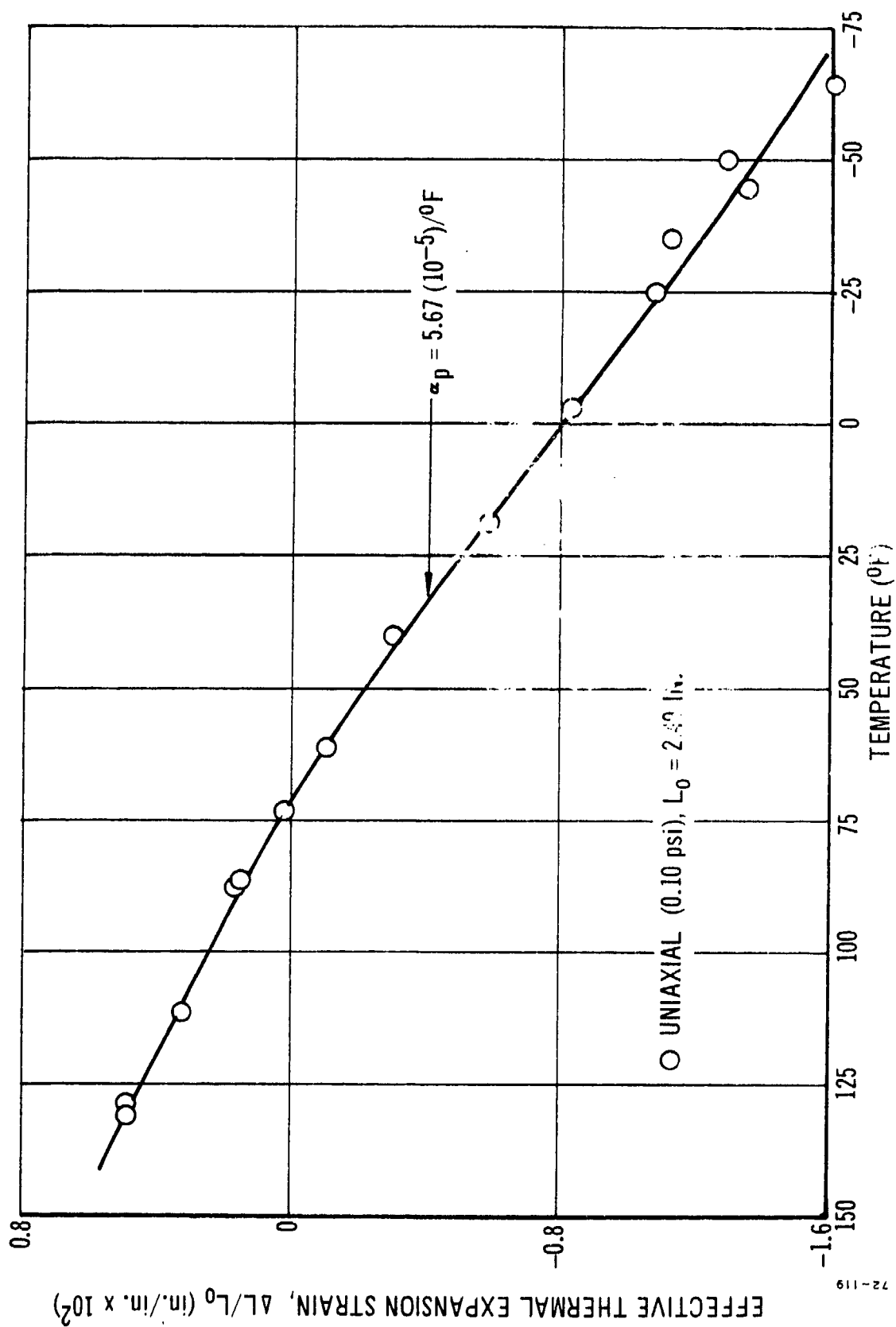
Figure 121   Thermal Expansion Strain for Uniaxial Stress Conditions

$\alpha_p = 5.67 \ (10^{-5})/^\circ F$

○ UNIAXIAL (0.10 psi), $L_0 = 2.50$ in.

EFFECTIVE THERMAL EXPANSION STRAIN, $\Delta L/L_0$ (in./in. x 10^2)

TEMPERATURE ($^\circ F$)

72-119

This stress is found to be about 0.079 psi. In addition to the above stress, the stress due to the LVDT slug, σ_S, is superimposed. The weight of the slug is about 200 milligrams. This corresponds to a stress, σ_S, of about 0.02 psi.

Thus, the total length-averaged stress, σ_g, on the specimen at all times would be about 0.10 psi. The overall axial strain due to gravity, ϵ_g, can be calculated directly from Equation (147):

$$\epsilon_g = \frac{1}{L_o} \int_0^{L_o} \frac{\partial u}{\partial x}\, dx = \frac{D_{crp}}{L_o} \int_0^{L_o} \sigma\, dx = D_{crp}\sigma_g \qquad (148)$$

Starting from room temperature, the sample was heated to about 135^0F and allowed to come to thermal equilibrium. At the highter temperature the amount of creep strain became relatively significant and could not be neglected, as will be shown. The micrometer was zeroed at this temperature and then the oven was allowed to decrease in temperature to the next lower temperature. The cooling rate for the Instron oven within the range of 150 to 70^0F is very slow because the chamber is well insulated. The net result is a decrease in sample length due to thermal expansion, $\alpha \Delta T$, and an increase in creep strain, $\Delta D_{crp}\ g$, where ΔD_{crp} is the change in creep compliance between successive readings. At the high temperature, therefore, the creep strain may be significant in terms of the thermal strains.

As an example, consider the case where the bar is cooled from temperature T_1 to T_2. The measured thermal strain, $\alpha_{m_{12}}\Delta T$, is the sum of the thermal strain in the absence of creep, $\alpha \Delta T$, and the creep strain itself, $\epsilon_{12} = \Delta D_{crp}\sigma_g$,

$$\alpha_{m_{12}}\Delta T = \alpha \Delta T + \epsilon_{12} \qquad (149a)$$

or

$$\alpha_{m_{12}} = \alpha + \frac{\epsilon_{12}}{\Delta T} \qquad (149b)$$

For cooling, $\Delta T < 0$, and Equation (149b) can be rewritten as

$$\alpha_{m_{12}} = \alpha - \frac{\epsilon_{12}}{|\Delta T|} \qquad (149c)$$

This shows that the measured thermal expansion coefficient, $\epsilon_{m_{12}}$, will be lower than the exact coefficient because of the creep strain. Consider the next measurement, taken after cooling the specimen to temperature T_3.

$$\alpha_{m_{23}} = \alpha - \frac{\epsilon_{23}}{|\Delta T|}$$

The creep strain ϵ_{23} will now be less than ϵ_{12} because the propellant creep rate is reduced by lowering the temperature; i.e., $\epsilon_{23} < \epsilon_{12}$, and hence $\alpha_{m23} > \alpha_{m12}$. The measured thermal expansion approches the exact coefficient as the temperature decreases.

The magnitude of ϵ_{12} can be estimated from a knowledge of creep compliance, D_{crp}, at 135^0F. For the imposed stress of 0.10 psi and a measured creep compliance of $10^{-2.1}$ (psi^{-1}), the resulting strain, ϵ, is 0.00079 at 135^0F. In these tests the temperature was dropped 20^0F after about 3 to 4 hours, resulting in a total creep strain of 0.00094. The difference in strain, ϵ_{12}, is then equal to 0.00015. If it is assumed that $\alpha = 5.67 (10^{-5})$, from the values obtained at lower temperatures, then Equation (149c) yields the value of $4.92 (10^{-5})$ for α_{m12}. Although this estimate does not explain the high-temperature value, $4.05 (10^{-5})$, it does show that the creep is at least a factor. Voids are another factor, which is discussed below.

The thermal coefficient decreases at the lower temperatures as the polymer approaches the glass transition temperature of -110^0F. Below about 70^0F, the thermal expansion coefficient becomes relatively constant and the effect of tensile creep is apparently insignificant over the time span of the experiment.

The thermal expansion coefficient can be studied further with the rule-of-mixtures prediction for a three-phase composite system. All that is needed is the volume fraction of each phase, v_i, and the thermal expansion coefficient of the individual phases, α_i, as discussed earlier in subsection VI, 2, e. The volume fractions for this propellant (Ref 23) are:

$$v_{AP} = 0.625$$

$$v_{AL} = 0.110 \tag{150}$$

$$v_B = 0.265$$

Typical values for the thermal expansion coefficients are:

$$\alpha_{AP} = 0.1 (10^{-5})/^0F$$

$$\alpha_{AL} = 1.3 (10^{-5})/^0F \tag{151}$$

$$\alpha_B = 8.0 (10^{-5})^0F \text{ to } 20.0 (10^{-5})/^0F$$

For polybutadiene rubber, α_B is taken as $12.0 (10^{-5})^0F$ (Ref 24).

The rule-of-mixtures gives the thermal expansion coefficient of the composite, α, as the following.

$$\alpha = v_{AP}\alpha_{AP} + v_{AL}\alpha_{AL} + v_B\alpha_B$$

$$= 3.39\,(10^{-5})/{}^0F \tag{152}$$

which, as noted in subsection VI, 2, e, is an upper limit for the composite, provided the propellant is void-free.

The other extreme would be the case where the binder has completely dewetted from the ammonium perchlorate particles and the system behaves as if there were only two phases, aluminum and binder. In this case the volume fractions of the phases, exclusive of ammonium perchlorate, become,

$$v'_{AL} = 0.293$$

$$v'_B = 0.707 \tag{153}$$

and it is found [(see Equation (144)] that:

$$\alpha = 8.87\,(10^{-5}){}^0F \tag{154}$$

The measured value of $\alpha = 5.67\,(10^{-5}){}^0F$ is bracketed by these theoretical values, which implies that (1) the sample has voids and/or (2) the assumed value of $\alpha_B = 12.0\,(10^{-5})/{}^0F$ is low. That the second reason cannot entirely account for the difference between theory and experiment follows from the fact that an unrealistically high value of $\alpha_B = 20.6$ $(10^{-5})/{}^0F$ would be needed to predict the measured value for the propellant without voids.

Let us return now to the earlier discussion on the low value for α shown in Figure 121 at elevated temperatures. If the void volume reduces appreciably with increasing temperature, the behavior shown in Figure 121 would be expected, in that the specimen's α would approach the rule-of-mixtures prediction, Equation (152). One possible explanation for this reduction in void volume is that at high temperatures the binder expands and flows readily to fill in voids between particles that are in contact or at least close to one another.

The existence of appreciable voild content in the unstressed or lowly stressed propellant is further confirmed in the discussion in subsection VI, 3, c, (4) on the poker-chip specimen.

(2) Poker Chip Creep Compliance

The axial displacements measured during both the creep and recovery portions of the loading history on poker chip specimens

subjected to tensile and compressive strain states were used to compute the apparent compliance, D_{pc}. The apparent compliance D_{pc} is given by

$$D_{pc} \equiv \frac{\epsilon_T}{\sigma_o} \qquad (155)$$

where

ϵ_T is the axial strain due to axial stress

σ_o $= P/A$, and A is the area of the poker chip

The creep compliance D_{pc} is shown in Figures 122 and 123 for the 222-pound loading conditions.

The compliance curves were shifted horizontally with respect to the 70^0F creep compliance and displayed in terms of the master curve for creep compliance, $D_{pc}(t/a_T)$, as shown in Figures 124 and 125. The time-temperature shift factors, a_T, which were obtained after the shifting, are shown in Figure 126. These shift factors are in fair agreement with experimental data measured and reported earlier by LPC (Ref 2).

The apparent creep compliance D_{pc}, which is based on the average stress over the bonded surface, can be used to determine the uni-axial creep compliance D_u from the elastic relationships derived in Ref 25. For an assumed mechanically imcompressible elastic material

$$\frac{E_{pc}}{E_u} = 1 + \frac{R^2}{8} \qquad (156)$$

where

E_{pc} $\equiv$ apparent uniaxial modulus

E_u $\equiv$ uniaxial modulus

R $=$ diameter/thickness

It can be shown that Equation (156) is extended to the present problem of creep of an incompressible viscoelastic poker chip by simply writing it in terms of creep compliances; namely

$$\frac{D_u}{D_{pc}} = 1 + \frac{R^2}{8} \qquad (157)$$
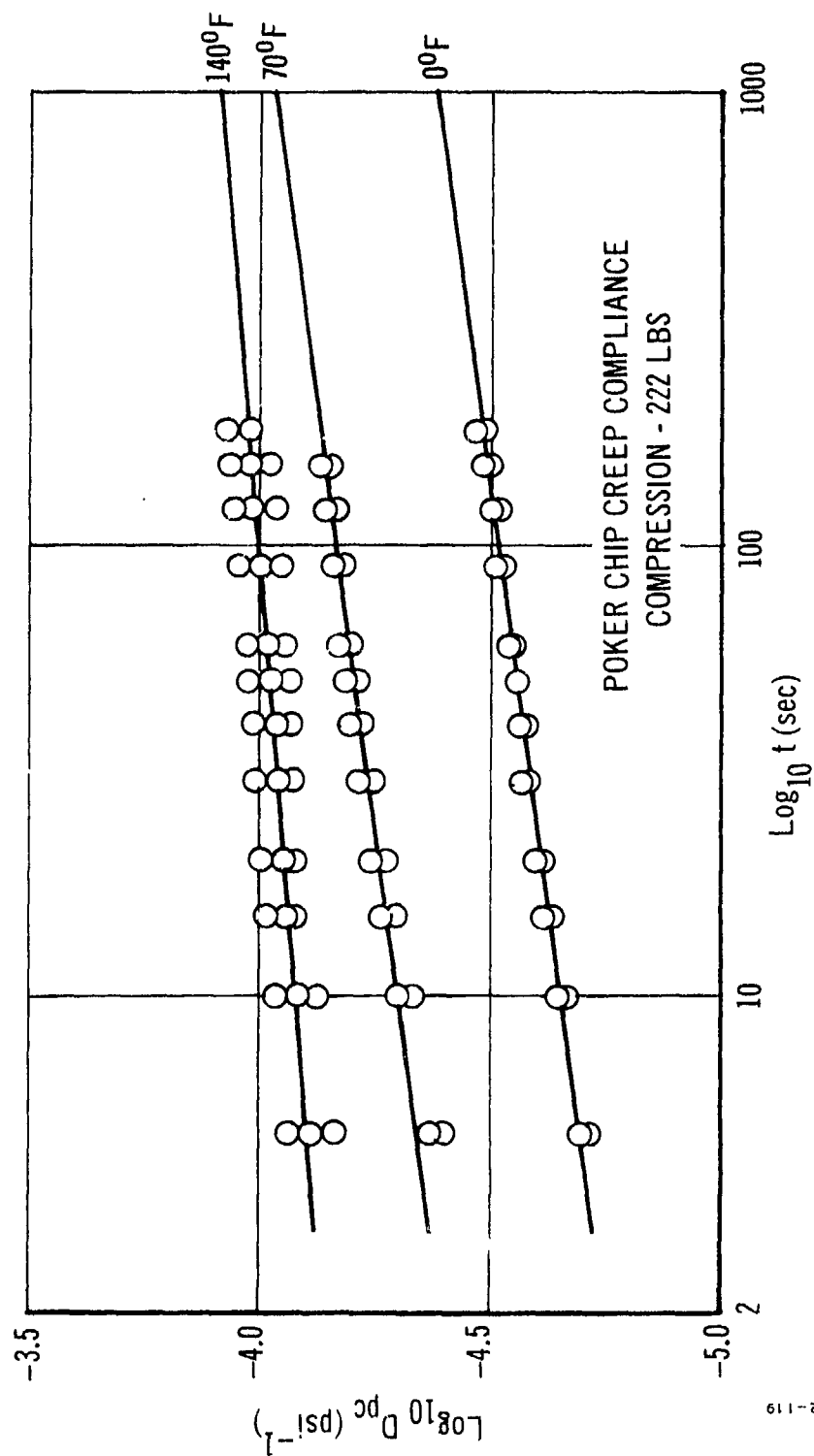
Figure 122. Poker Chip Creep Compliance for 222-Pound Compression Load.

72-119

LOCKHEED PROPULSION COMPANY
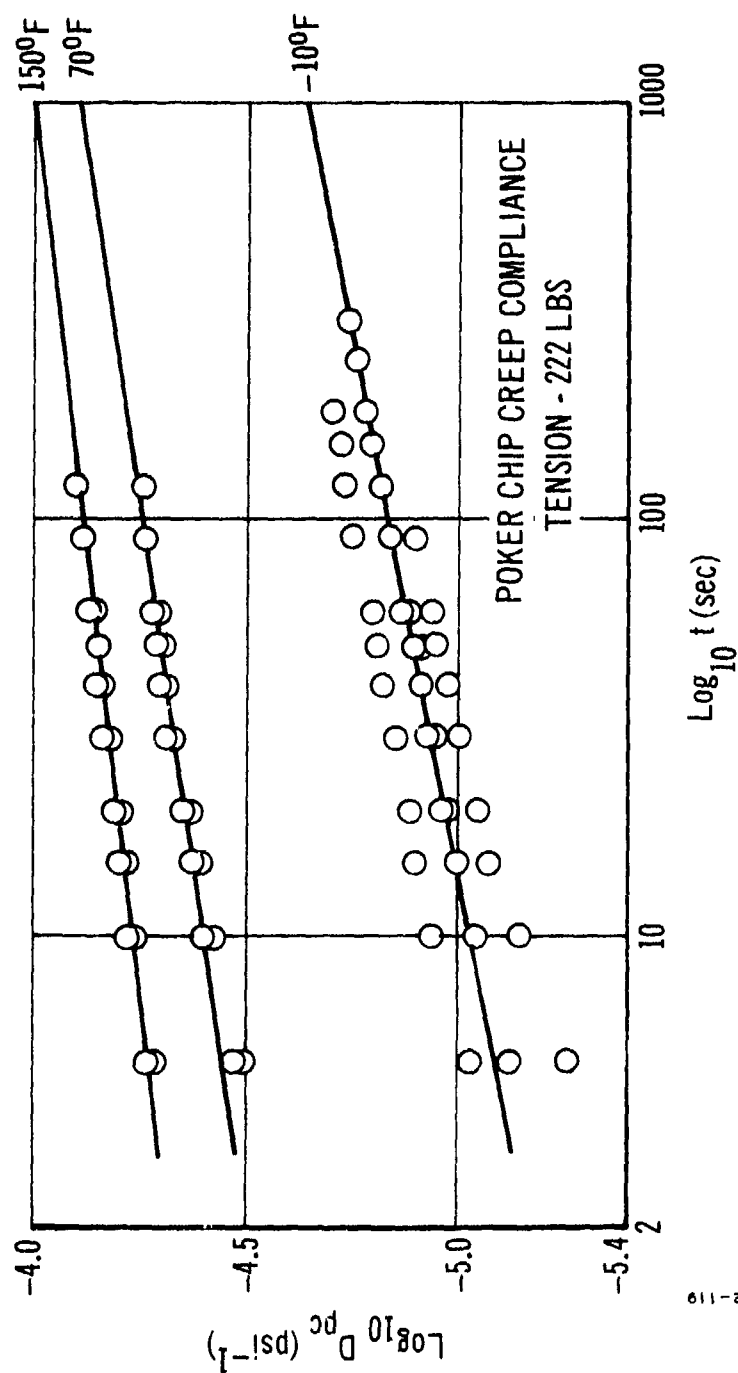
Figure 123. Poker Chip Creep Compliance for 222-Pount Tension Load.

72-119
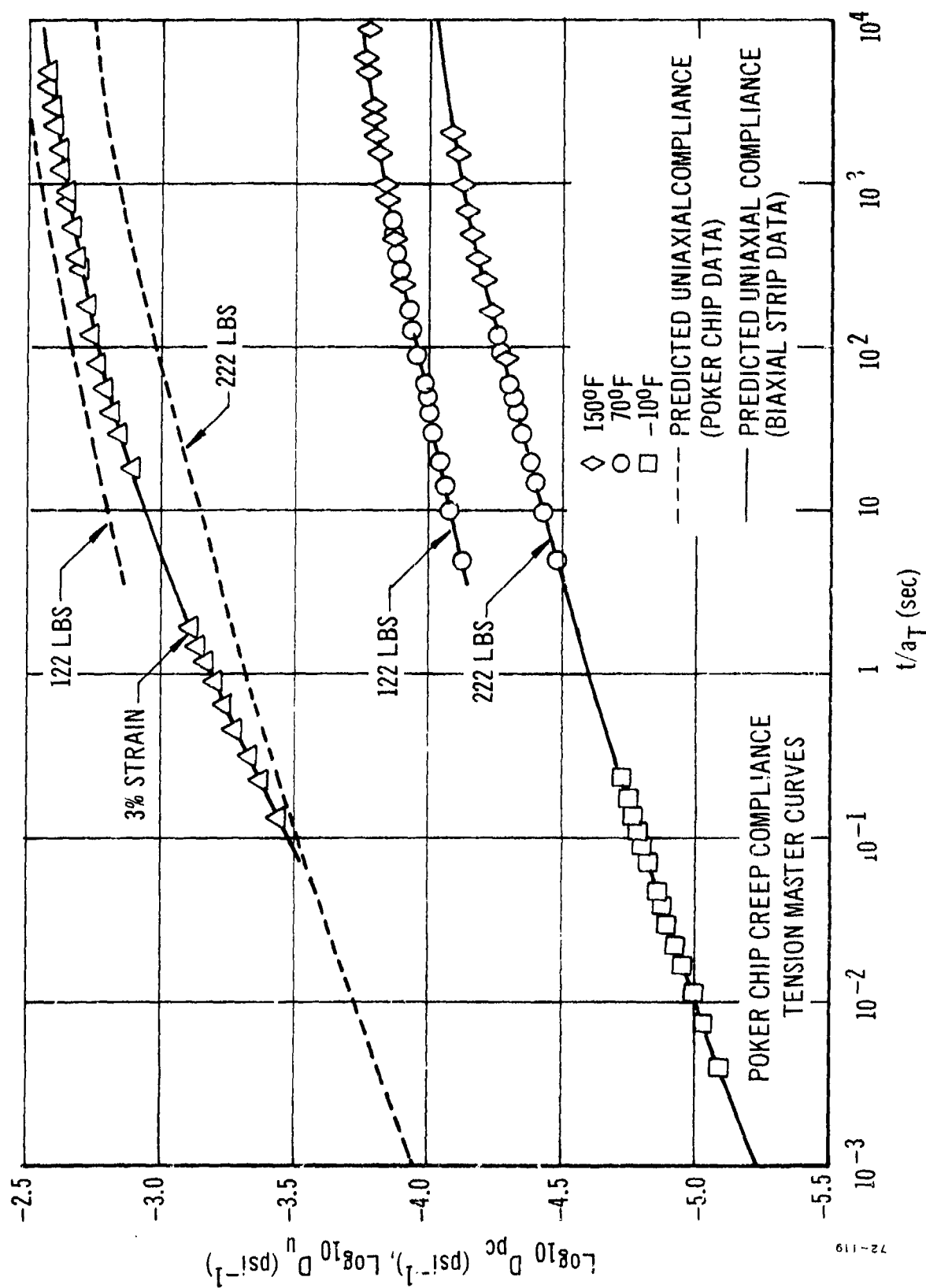
Figure 124. Poker Chip Creep Compliance versus Reduced Time for Tension Loading Conditions and Predicted Uniaxial Creep Compliance.
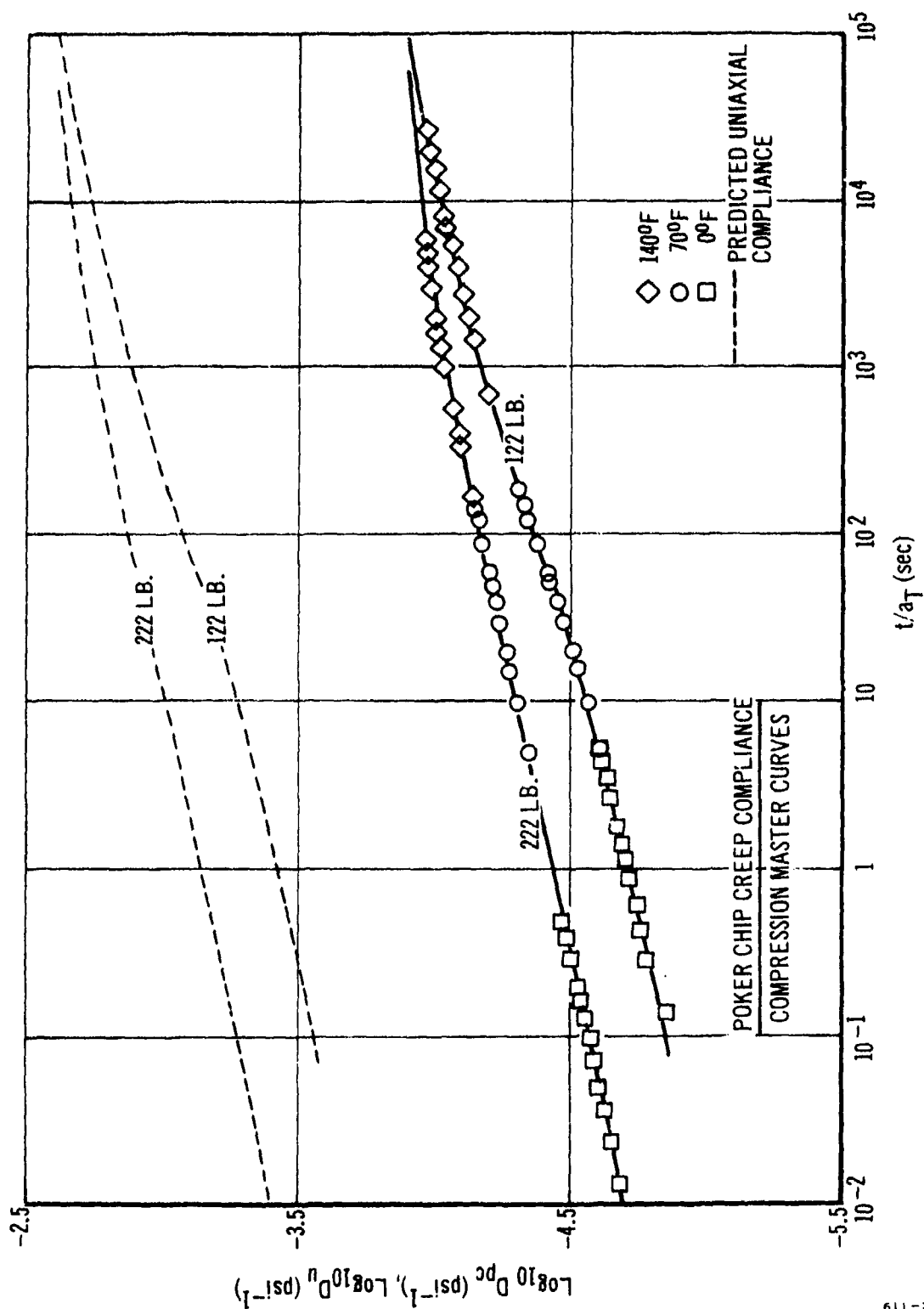
Figure 125. Poker Chip Creep Compliance versus Reduced Time for Compression Loading
Conditions and Predicted Uniaxial Creep Compliance.
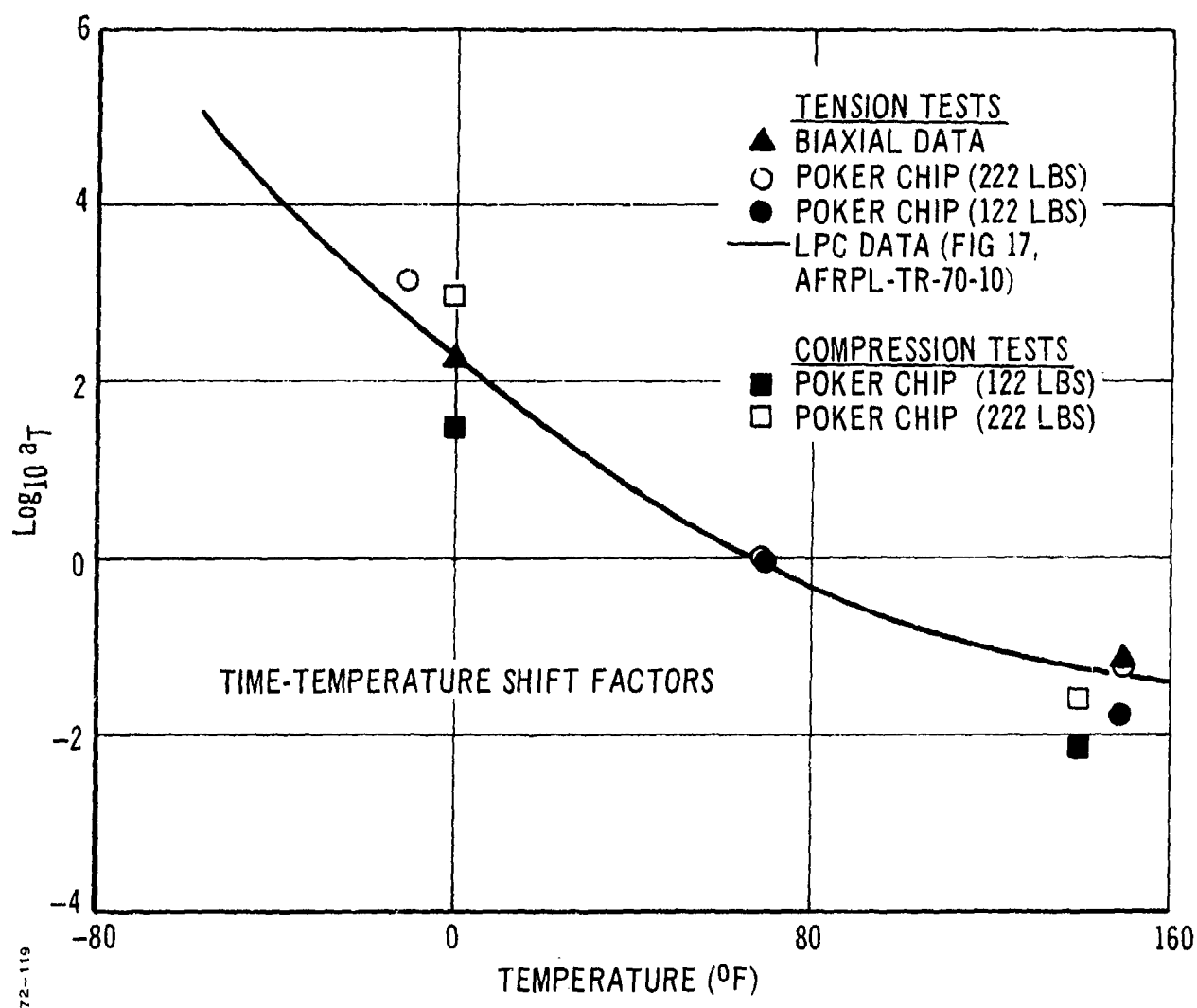
Figure 126. Time-Temperature Shift Factors, a_T, for all Tests;
Biaxial and Poker Chip.

Using the dimensions of the poker chip specimens, one finds that R = 12, and therefore D_u = 19 D_{pc}. The uniaxial creep compliances predicted by Equation (157) are shown in Figures 124 and 125. Later, in subsection VI, 3, c, (4), this equation will be corrected for compressibility of the propellant due to initial voids.

It is surprising to note that the propellant is stiffest at the higher load level in tension, but appears to be softest at the higher load level in compression. This phenomenon was consistent in all of the measurements. For the tensile loads, the response was not particularly unexpected because the low-load-level tests were run on a single specimen following previous tests at 222 pounds. A specimen previously loaded to 222 pounds and then loaded at 122 pounds would be expected to exhibit a higher creep compliance (softer material) because some amount of internal damage has probably occurred in terms of the so-called Mullin's effect.

In addition, the creep compliance was observed to increase with each successive loading cycle in the tension tests. During the first cycle it can be assumed that a significant amount of damage occurs. Upon reloading, without waiting for any possible rehealing, the amount of softening due to damage is not nearly as much. With each successive loading the accumulated damage appears to approach a constant [this behavior under cyclic loading is analogous to that for fiber-reinforced plastics (Ref 26)]. Because only two good poker chip specimens were available, it was necessary to use the specimens several times at both load levels and therefore this fatigue phenomenon could not be fully characterized.

(3) Poker Chip Recovery Compliances

In addition to the compliance obtained during the creep portion of the loading, the poker chip was unloaded completely at time t_c, and the recovery strains were recorded for a period approximately twice as long as the loaded period.

For linear viscoelastic materials, the recovery compliance D_{rec} (which is defined as the ratio of recovery strain to the stress applied during creep), is obtained by adding the compliance $D_{pc}(t)$, which would exist upon loading to a stress level σ_0 at any time Equation (116b) , to the compliance $-D_{pc}(t - t_c)$, which would exist if a stress level of $-\sigma_0$ had been applied at time $t = t_c$. The resulting recovery compliance, D_{rec} is

$$D_{rec} = D_{pc}(t) - D_{pc}(t - t_c) \qquad (158)$$

Figure 127 is representative of the creep-recovery response for a poker chip specimen subjected to a 222-pound tension load. The recovery predictions based on Equation (158) are initially high for both temperatures, although there appears to be a crossover for the 150°F test. The propellant recovers considerably faster initially than linear viscoelastic theory predicts. The departure from the predicted recovery curve is attributed to nonlinearities, rather than to experimental factors, as discussed
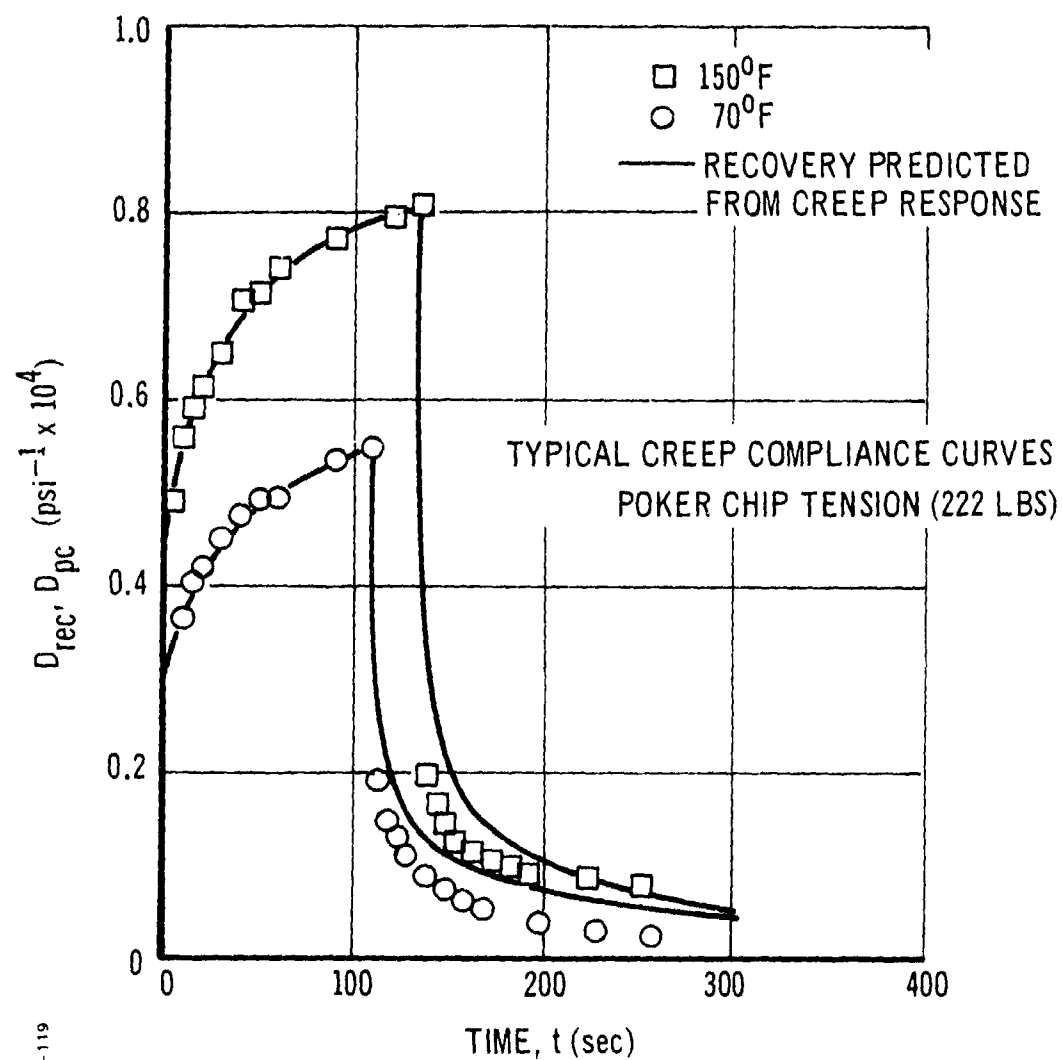
Figure 127. Typical Poker Chip Creep-Recovery Compliance for
222-Pound Tension Load.

-248-

below. The compression creep-recovery response is very similar to the tension data in that the propellant usually recovers faster than linear theory predicts.

As an aid in depicting the nonlinear behavior, the log of typical compression recovery compliances is plotted against log λ in Figures 128 and 129, where

$$\lambda \equiv \frac{t - t_c}{t_c} \tag{159}$$

(Tension data follow a similar pattern and therefore are not shown.) The solid lines in these figures are the predictions based on Equation (158).

Now, for a nonlinear viscoelastic material of the type characterized in Reference 27 and whose strain during the creep phase is represented by the power law

$$\epsilon = \epsilon_1 t^n \tag{160}$$

where ϵ_1 may be a function of stress and temperature (but not time) and n may be a function of temperature (but not stress and time), the recovery compliance is [Ref 27, Equation (42)]

$$D'_{rec} = \left[\frac{g_1^{-1} D'_{pcc}}{D_{pcc}}\right] D_{pcc} \left[(1 + a_\sigma \lambda)^n - (a_\sigma \lambda)^n\right] \tag{161}$$

where D'_{rec} is the nonlinear viscoelastic recovery compliance. Also, D'_{pcc} and D_{pcc} are the nonlinear and linear creep compliances, respectively, at time t_c, and g_1 and a_σ are, in general, material property functions of stress and temperature (but not time); $g_1 = a_\sigma = 1$ for a linear viscoelastic material. Equation (161) predicts that, for a given temperature, the log of nonlinear recovery compliance plotted against log λ may be superposed on the linear prediction through a horizontal translation (log a_σ) and a vertical translation $\left(\log\left[g_1^{-1} D'_{pcc}/D_{pcc}\right]\right)$.

The curves for 70 and 140°F in Figure 128, and the curves for 70°F in Figure 129, require significant upward vertical shifts, but only small horizontal shifts, in order to superpose them on the linear predictions; the unusually rapid decrease in the 0°F compliance in Figure 128 is believed due to experimental error.

It can be shown from the theory in Reference 28 that the required upward vertical shift implies that the springs (in a nonlinear Kelvin model representation) are stiffer under loads of 122 and 222 pounds than under no load. Furthermore, the temperature-averaged spring stiffness is greater under 122 pounds than under 222 pounds. These observations are completely consistent with the creep compliances in Figure 125.
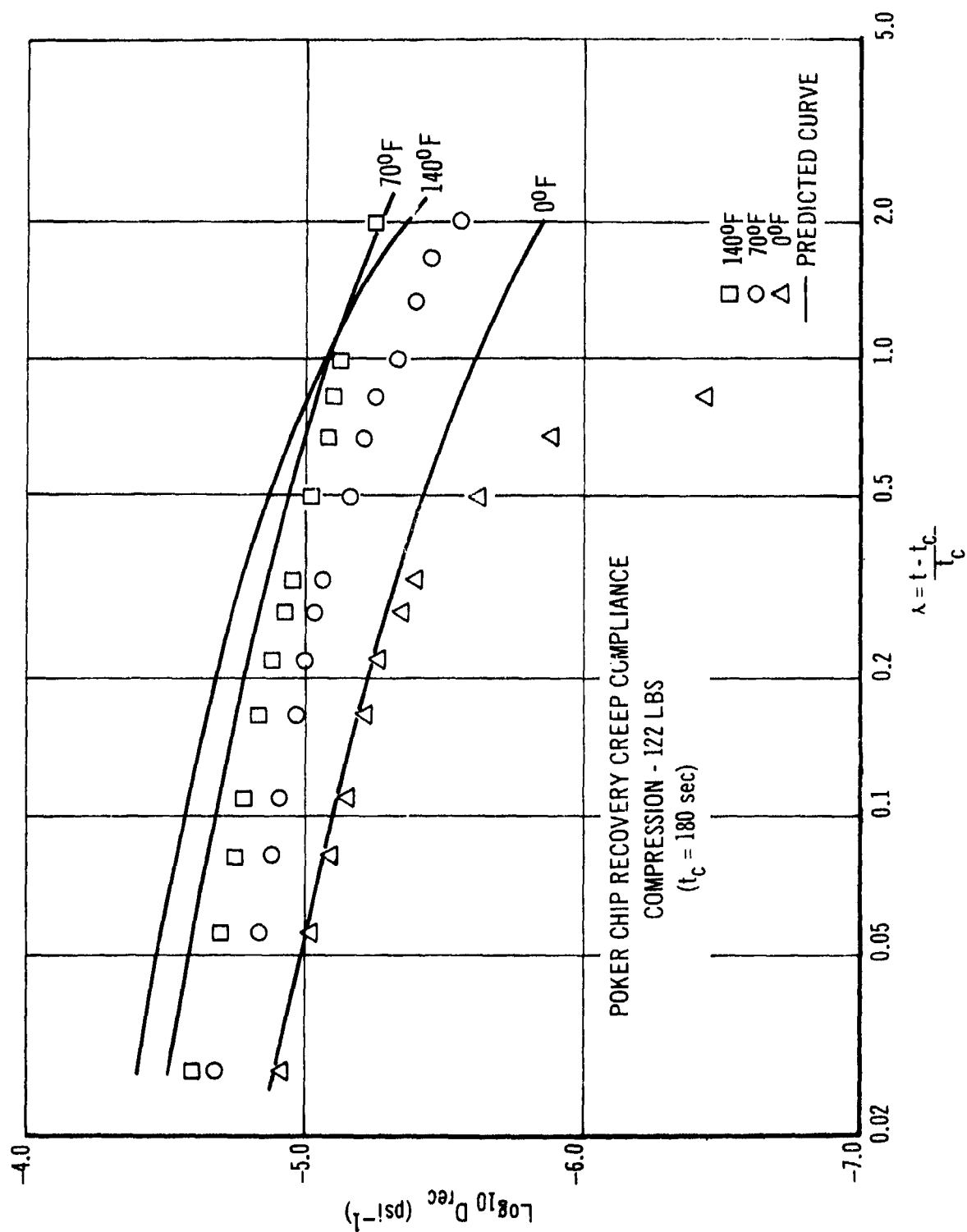
Figure 128. Poker Chip Recovery Compliance for 122-Pound Compression Load.
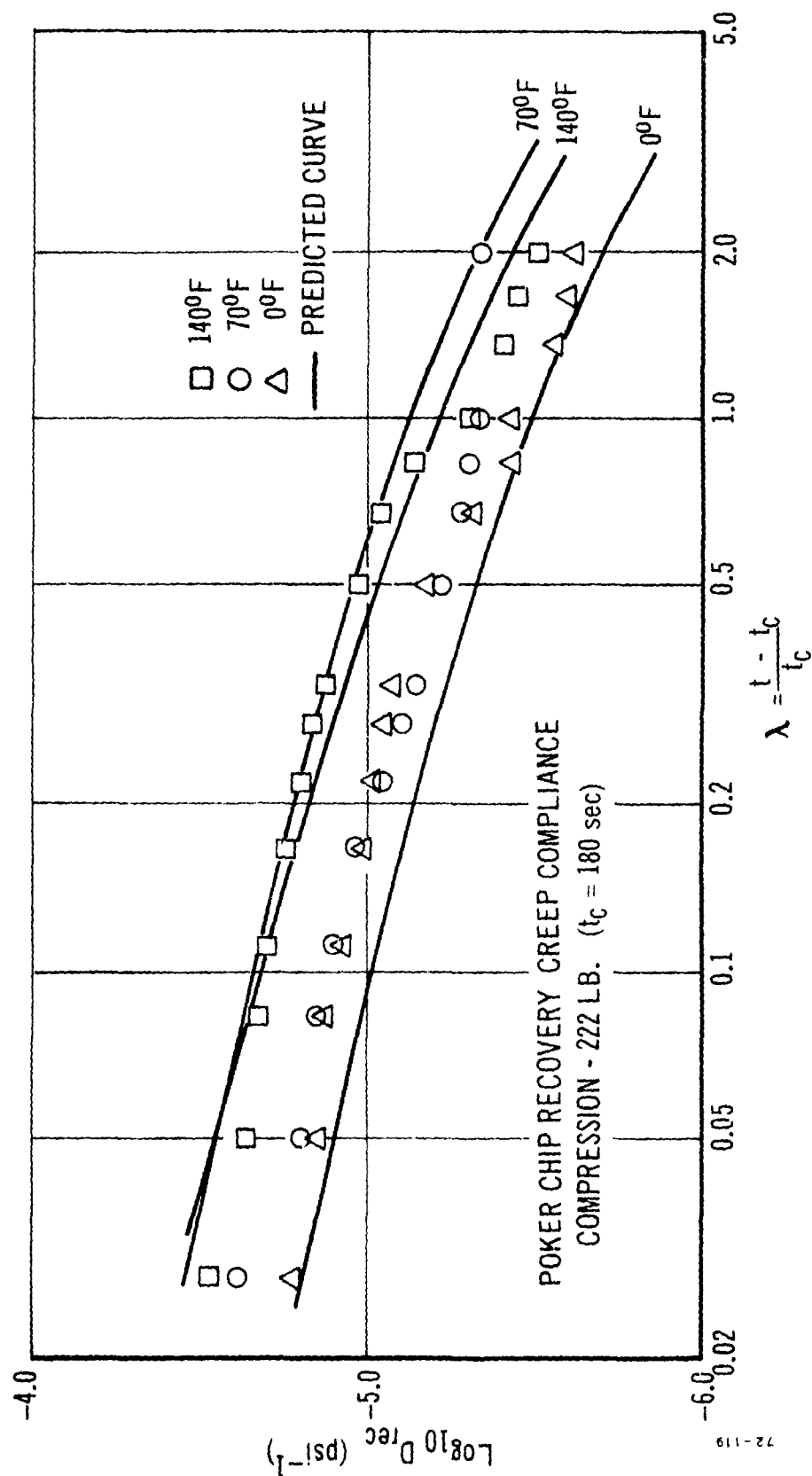
Figure 129. Poker Chip Recovery Compliance for 222-Pound Compression Load.

72-119

The physical basis for this surprising behavior is not at all clear. It may in part be related to the fact that the largest poker chip strains are shear strains (which result from the relatively large displacements parallel to the platens) and these strains are largest under 222 pounds. However, the argument is not supported by the tensile data. Clearly, a more extensive program (using larger and smaller loads in tension and compression and several specimens) is needed to definitely confirm the type of nonlinear behavior reported here and to aid in the development of a physical model of propellant under these combined shear and normal stress states.

(4) Poker Chip Dilatation

Isothermal volume changes. The volume of the poker chip was monitored at all times during the tests. This was done by measuring the axial displacement directly with an LVDT and making a direct correlation with the axial strain ϵ and the poker chip platen separation. In order to compute the change in volume, it was necessary to measure the change in circumference during creep. The technique discussed earlier provided a magnified circumferential displacement, which was used to compute the specimen dilatation.

The dilatation present at any time is determined from a knowledge of V, the sample volume at any given time, and V_o, the initial volume prior to the application of any load. Under a tensile load, the displacement at the extreme radius assumes a parabolic distribution with respect to the thickness direction. The assumption of a parabolic displacement is considered excellent (Ref 25). The change in volume, ΔV, is therefore

$$\Delta V = V_{platen} - V_{parabola} \tag{162a}$$

where

$$V_{platen} = \text{volume displaced by moving platen}$$

$$V_{parabola} = \text{volume swept out by revolving the parabolic area around the loading axis}$$

where, for the small changes in poker chip diameter that exist,

$$V_{parabola} \approx \frac{\pi D_o \Delta D}{3} h_o \tag{162b}$$

and

$$V_{platens} = \frac{\pi D_o^2}{4} h_o \epsilon \tag{162c}$$

-252-

where

D_o = initial chip diameter

h_o = initial poker chip thickness

D = change in mid-plane diameter

ϵ = axial strain

The volumetric responses for the two stress levels and several temperatures are shown in Figure 130 and 131. The dilatation for this propellant is approximately linear with strain, with $\nu \simeq 0.65\,\epsilon$ for both tension and compression stress states at all times and temperatures. Deviations from the straight line appear to be due more to compaction under repeated loads. The existence of initial voids and the compaction phenomenon are also reported elsewhere, as determined in pressurization tests (Ref 29).

Inasmuch as the dilatation response is approximately linear, it is believed the linear elastic poker chip analysis in Reference 25, after being extended to viscoelastic behavior, will be valid for the load range studied.

Estimation of bulk and uniaxial properties. As will now be shown, bulk compliance (or modulus) and uniaxial compliance (or modulus) can be deduced from the measured values of dilatation and effective poker chip compliance. The accurate quasi-elastic method of viscoelastic analysis (Ref 16) will be used to extend the elasticity theory. Specifically, elastic properties will be directly replaced by their time-dependent viscoelastic counterparts after the elasticity analysis is complete. In all cases it will be assumed that $E/3K << 1$ ($E/3K < 0.1$, say) in order to simplify the results; this inequality turns out to be satisfied by the predicted properties.

From Equation (3.2.33) in Reference 25, the change in mid-plane diameter is derived:

$$\Delta D = -\frac{3}{4} D_o f \epsilon \tag{163}$$

where

$$f \equiv \frac{2\,I_1\,(\lambda)}{\lambda\,I_o\,(\lambda)} \tag{164}$$

$$\lambda \equiv R\sqrt{\frac{E_u}{K}} \tag{165}$$

-253-
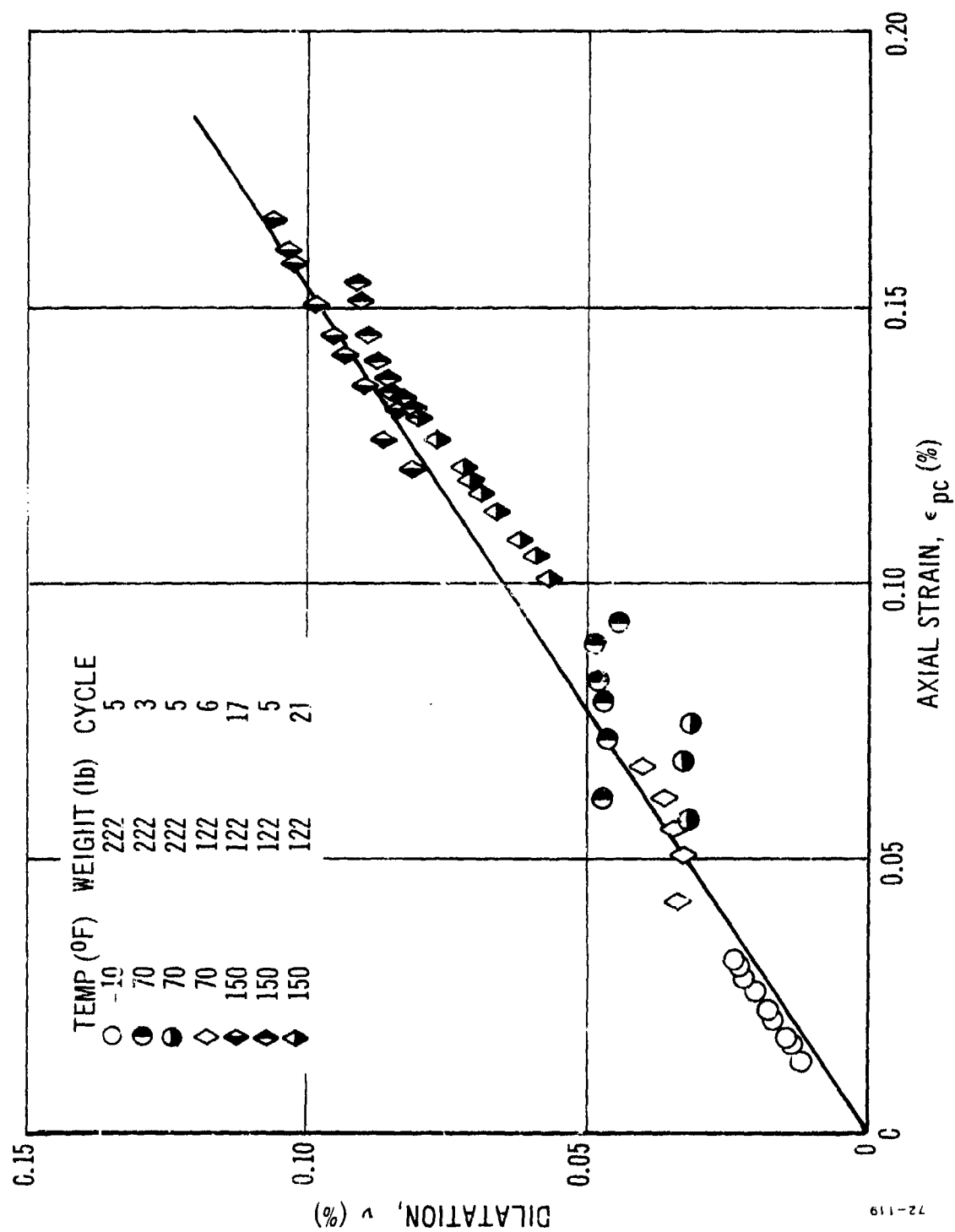
Figure 130. Volumetric Response for Poker Chip Specimen Under Tension Loading.

72-119
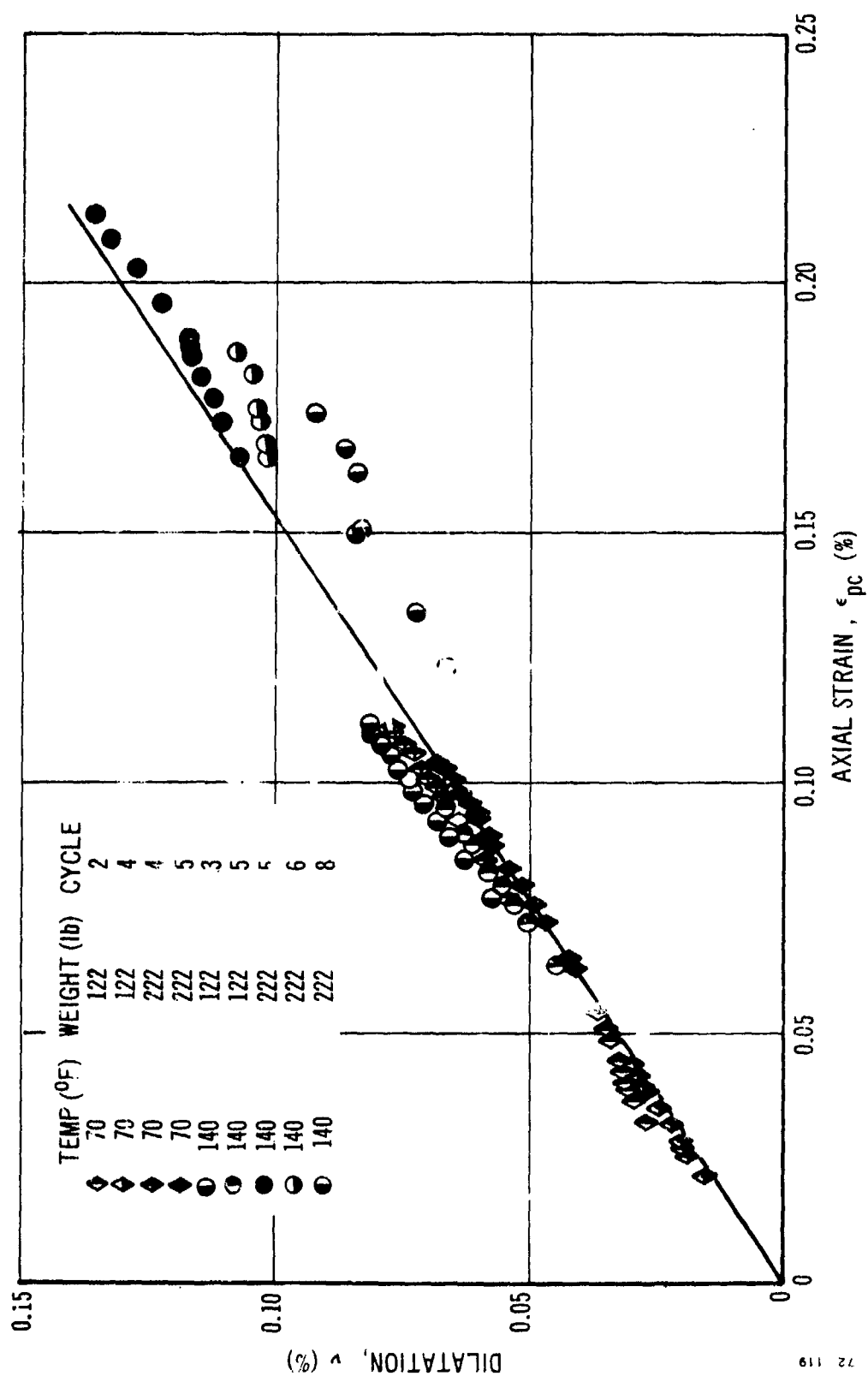
Figure 131. Volumetric Response for Poker Chip Specimen Under Compression Loading.

and

$R \equiv$ initial diameter/initial thickness of poker chip

$K =$ bulk modulus

$E_u =$ modulus in uniaxial tension

Also, I_0 and I_1 are modified Bessel functions of the first kind with argument λ. Substitution of Equation (163) into (162b), and then the result into Equation (162a), yields the overall dilatation:

$$\nu \equiv \frac{\Delta V}{V_o} = (1 - f)\, \epsilon \tag{166a}$$

and dividing through by ϵ,

$$\frac{\nu}{\epsilon} = 1 - f \tag{166b}$$

Also of interest is the effective modulus of the poker chip, E_{pc}, which is obtained from Equation (3.2.35) in Reference 25:

$$\frac{E_{pc}}{E_u} = \frac{K}{E_u}\,[1 - f] + \frac{2}{3}\left\{1 + \left[\frac{\left(1 - \frac{f}{2}\right) f}{1 + \frac{2 E_u}{3K}\left(1 - \frac{f}{2}\right)}\right]\right\} \tag{167}$$

Observe that if E_{pc} and ν/ϵ are known, Equations (166b) and (167) can be used to derive the corresponding values of K and E_u. The method of solution used here was to assume several values of E_u/K, to calculate the resulting values of ν/ϵ and E_{pc}/E_u, and then to plot the results against E_{pc}/E_u, as shown in Figure 132. The ordinate E_{pc}/K was calculated by noting that $E_{pc}/K = (K_{pc}/E_u)(E_u/K)$. Also shown in the figure is the ratio of maximum shear strain (which occurs at the platen near the poker chip's periphery) to axial strain, which was calculated by means of Equation (3.2.28c) in Reference 25. The volume-averaged value of shear strain is approximately $\frac{1}{6}$ the maximum value, and therefore of the same order of magnitude as ϵ for the range indicated in Figure 132.

According to the quasi-elastic method, this figure can be used for viscoelastic materials by simply interpreting E_{pc}/K and E_{pc}/E_u as ratios of inverse creep compliances. Inasmuch as the ratio ν/ϵ was found to be nearly independent of temperature and time, the present theory implies that bulk modulus K and bulk compliance B are proportional to the uniaxial properties E_u and D_u, respectively. One would expect that this direct
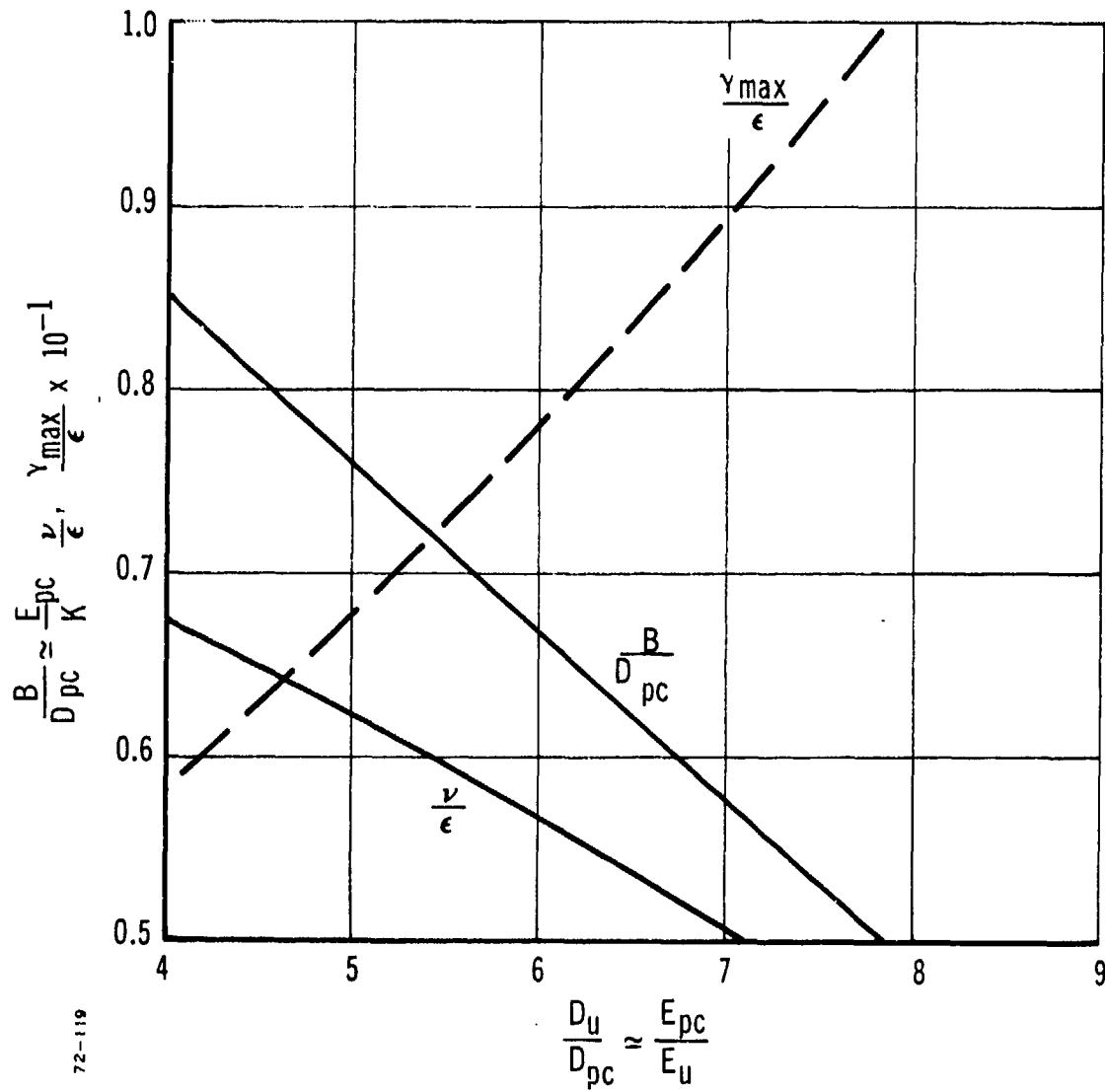
Figure 132. Curves for Determination of Moduli and Shear Strain in a Poker Chip with a Diameter/Thickness = 12.0.

dependence of bulk properties on uniaxial (or shear) behavior of dilatation is largely a result of void compression and expansion.

Tables XXI and XXII show property ratios and reciprocals of predicted values of B and D_u at $t/a_T = 10^{-2}$ sec. and $t/a_T = 10^2$ sec. for the two different dilatation slopes, $v/\epsilon = 0.65$ and $v/\epsilon = 0.50$, the former value corresponds to the solid line in Figures 130 and 131, while the latter one defines an approximate lower bound to the data in these figures. The values of $D_{p\dot{c}}^{-1}$ in the tables are actually averages over all tension and compression compliances at the stated reduced times.

The predicted bulk moduli $(\sim B^{-1})$ are far below the range commonly reported for propellant under moderate and high pressures, which is approximately 500 to 1000 Ksi (see, for example, Reference 29). Furthermore, the theoretical lower bound on bulk modulus K_L in Equation (142) (which applies only if there are no voids) is found to be greater than 500 Ksi. Both of these findings further confirm the presence of a significant amount of initial voids.

That a large drop in bulk modulus can result from even a small void volume will be demonstrated for an idealized model. Specifically, consider the binder to be a homogeneous material having a uniform distribution of noninteracting spherical cavities, and subjected to an external pressure, P_o. The binder material itself is assumed to be linear and mechanically incompressible; binder compressibility can be shown to introduce only a small error. First, deduce the relative volume change $\Delta V_i/V_o$ of a sphere with only one cavity of radius a_i (the sphere's outer radius is b):

$$\frac{\Delta V_i}{V_o} = \frac{9 P_o}{4 \left(1 - \frac{b^3}{a_i^3}\right) E_b} \tag{168a}$$

where E_b is the uniaxial modulus of the unfilled binder. Now, assume the cavity is very small (i.e., $b^3/a_i^3 \gg 1$). Total dilatation, v, of a binder having N voids is therefore

$$v \equiv \sum_{i=1}^{N} \frac{\Delta V_i}{V_o} = - \frac{9 P_o}{4 E_b b^3} \sum_{i=1}^{N} a_i^3 = - \frac{9 P_o}{4 E_b} \frac{v_v}{v_B} \tag{168b}$$

where v_v is the volume fraction of voids referred to total (propellant) volume. The overall (effective) bulk modulus of the binder, K_b, is

$$K_b \equiv - \frac{P_o}{v} = \frac{4 E_b}{9 v_v} v_B \tag{169}$$

TABLE XXI

PREDICTED PROPERTIES FOR DILATATION SLOPE $\nu/\epsilon = 0.65$

$$\frac{B}{D_{pc}} = 0.80; \qquad \frac{D_u}{D_{pc}} = 4.50; \qquad \frac{D_u}{B} = 5.63$$

For $t/a_T = 10^{-2}$ sec., given $D_{pc}^{-1} = 83$ ksi:

$$B^{-1} = 104 \text{ ksi}; \qquad D_u^{-1} = 18.4 \text{ ksi}$$

For $t/a_T = 10^2$ sec., given $D_{pc}^{-1} = 16$ ksi:

$$B^{-1} = 20 \text{ ksi}; \qquad D_u^{-1} = 3.56 \text{ ksi}$$

TABLE XXII

PREDICTED PROPERTIES FOR DILATATION SLOPE $\nu/\epsilon = 0.50$

$$\frac{B}{D_{pc}} = 0.57; \qquad \frac{D_u}{D_{pc}} = 7.10; \qquad \frac{D_u}{B} = 12.5$$

For $t/a_T = 10^{-2}$ sec., given $D_{pc}^{-1} = 83$ ksi:

$$B^{-1} = 145 \text{ ksi}; \qquad D_u^{-1} = 11.7 \text{ ksi}$$

For $t/a_T = 10^2$ sec., given $D_{pc}^{-1} = 16$ ksi:

$$B^{-1} = 28 \text{ ksi}; \qquad D_u^{-1} = 2.25 \text{ ksi}$$

Now, assume that the effect of particle reinforcement on the uniaxial and bulk moduli is the same (namely, $E_b/K_b \simeq E_u/K$) and solve for v_v:

$$v_v = \frac{4}{9} \frac{E_u}{K} v_B \tag{170}$$

Replacing E_u/K with the creep compliance ratio B/D_u, and then referring to Tables XXI and XXII, one finds by using the mean slope, $\nu/\epsilon = 0.65$, that

$$v_v = 2.1 \text{ percent} \tag{171a}$$

and by using the approximate lower limit, $\nu/\epsilon = 0.5$, that

$$v_v = 0.93 \text{ percent} \tag{171b}$$

These void contents are at the upper limit of the magnitudes one finds for many propellants through comparison of theoretical and measured densities (Reference 30); the present high values may be the result of using an over-simplified model.

It is important to note that the uniaxial compliance is predicted in the two preceding tables. This property will not necessarily be the same as found from uniaxial and biaxial tension tests, unless the strains are extremely small in the latter tests. For example, the ratios of poker chip values to those reduced from the 3-percent strip biaxial relaxation modulus in subsection VI, 3, c, (5) are approximately 3.1 and 2.0 when $t = 10^{-2}$ sec, where $\frac{\nu}{\epsilon} = 0.65$ and 0.50, respectively. When $t = 10^{-2}$ sec, the ratios are 6.3 and 4.0, for $\frac{\nu}{\epsilon} = 0.65$ and 0.50, respectively. It is noteworthy that the theoretical prediction of stresses in the restrained cooling test described in Reference 2 is approximately one-fourth of the experimentally determined values. Hence, the above moduli ratios are of the right order of magnitude to bring the theory into line with the experimentally determined stresses.

Observe that the ratio D_u/D_{pc} in the foregoing tables is considerably smaller than predicted by Equation (157) for mechanically incompressible media; in the latter case, the ratio is 19:1. Therefore, the fact that the uniaxial compliances deduced from tensile poker chip tests bracket the one deduced from strip biaxial tests, which is shown in Figure 124, is believed to be fortuitous. In contrast, Figure 3.7 in Reference 25 indicates that when the void content is negligible, the modulus prediction based on mechanical incompressibility is quite accurate for a poker chip with a diameter-to-thickness ratio of 12:1.

Estimation of the linear thermal expansion coefficient. The linear expansion coefficient has been deduced from measurements of the poker chip circumference and a slightly modified form of Equation (163). It can be shown that by making the substitution $\epsilon \rightarrow \epsilon - 3\alpha\Delta T$ in Equation (163), the resulting diameter change is that for a poker chip subjected to a uniform temperature change ΔT as well as to an axial strain ϵ. Proof of this statement is made by introducing thermal expansion into the governing equations

in Reference 25, and then comparing the result with the original isothermal equations. If the platens are prevented from moving, so that $\epsilon \simeq 0$, then α is given by

$$\alpha = \frac{4\Delta D -}{9\, D_o\, \Delta Tf} \tag{172}$$

It should be noted that f is unity only when the material is mechanically incompressible. When, for example, the mean dilatation line $\nu/\epsilon = 0.65$ shown in Figure 130 or 131 is used, Equation (166b) yields

$$f = 1 - \frac{\nu}{\epsilon} = 0.35$$

    The poker chip thermal expansion tests discussed earlier in subsection VI, 3, b, (2) were conducted over a temperature range from -5 to 140^0F under both heating and cooling conditions and under compressive stress. Circumferential measurements were recorded at the beginning and the end of each test, and corrections were made for the thermal expansion of those parts that would affect the reading (circumferential wire, slug wire, etc). The change in circumference was then determined, and the corresponding diameter change was used in Equation (172) to calculate the expansion coefficient. Table XXIII summarizes the values obtained for α under the various test conditions. The relatively low values shown in the table are believed due to platen motion. Therefore, the experimental techniques must be improved before this test can be used to establish its dependence on triaxial stress (and therefore on void content).

TABLE XXIII

POKER CHIP LINEAR THERMAL EXPANSION COEFFICIENT

Temperature Range (^{0}F)	$\alpha \times 10^5/^0$F	Stress (psi)
-5 to 140	3.06	~ 10
73 to -5	4.02	~ 10
75 to 140	2.02	~ 5
140 to 75	2.62	~ 6

(5) Strip Biaxial Modulus and Compliance

    The strip biaxial specimens were strained to a nominal level of 3 percent at a crosshead rate cf 0.2 in./min. The stress relaxation moduli for these tests are shown in Figure 133 for the three test temperatures used in the earlier poker chip tests. Master curves for the stress relaxation moduli are shown in Figure 134 for both the aged (current test data) and the unaged (early Lockheed data given in Reference 1) propellant. The data distinctly show that the propellant has aged, and has in fact hardened with time.
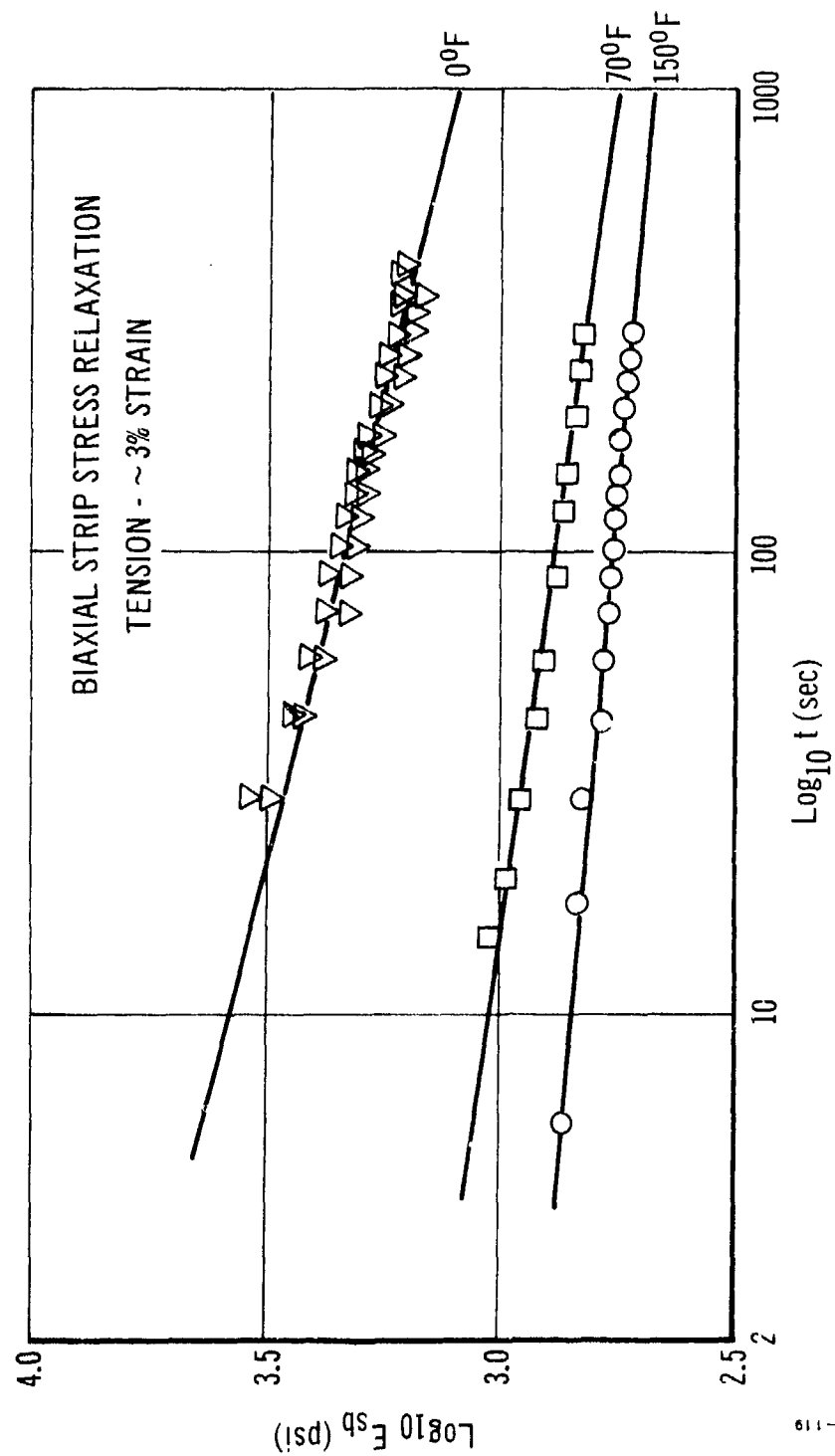
Figure 133. Strip Biaxial Stress Relaxation Modulus for a Nominal Strain of $\epsilon_o \simeq 3$ Percent.
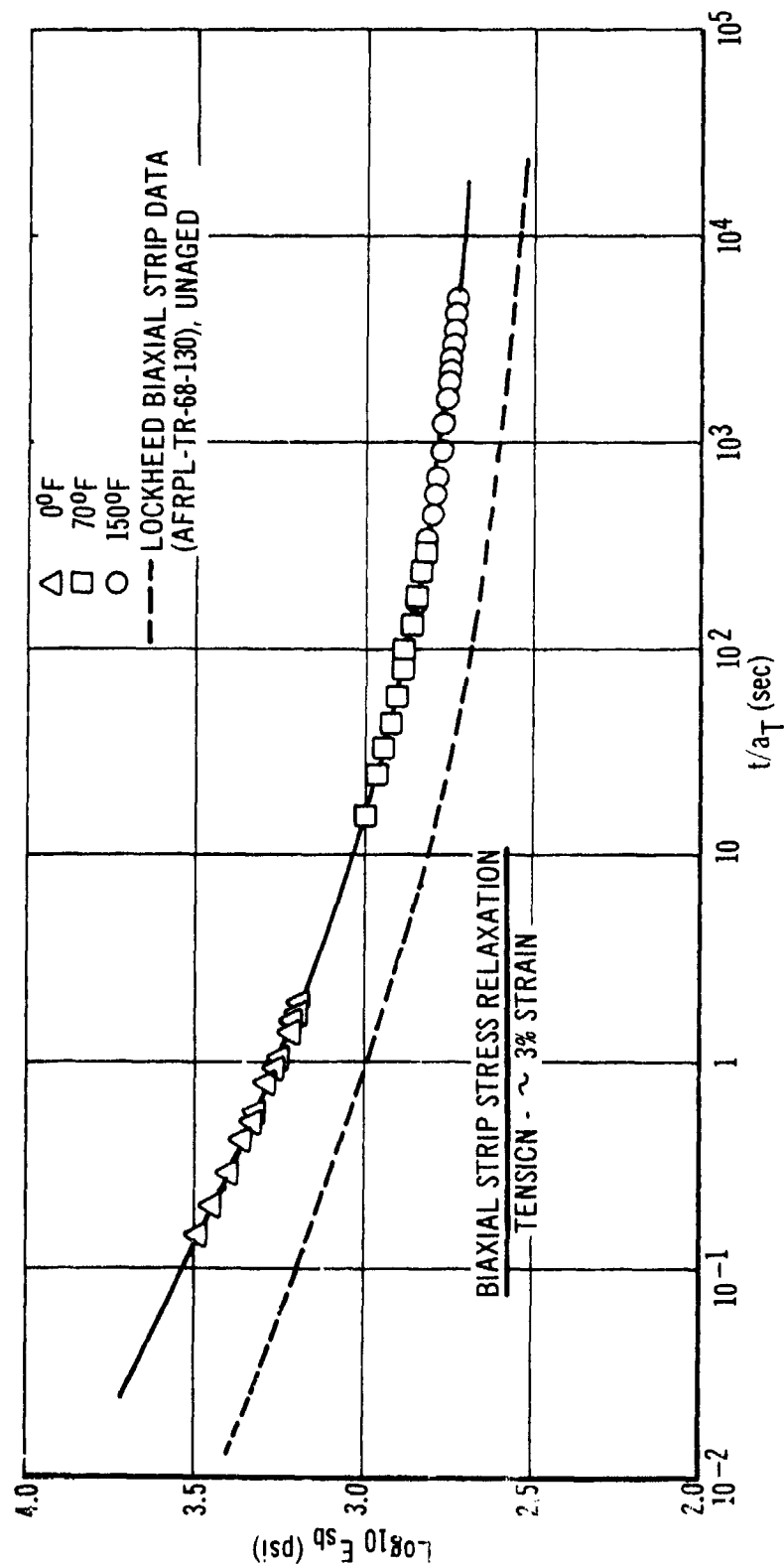
Figure 134. Strip Biaxial Stress Relaxation Modulus versus Reduced Time.

Dilatation was recorded during the complete test, i. e., during both the ramp loading period and the stress relaxation period, for at least 10 minutes. At both 70 and 150°F no measurable dilatation occurred at the 3-percent strain level. The specimens were subsequently strained to about 10 to 12 percent (above which strain level bond separation occurred) and no dilatation was detected. The dilatometer, which is capable of resolving relative volume changes on the order of 0.1 to 0.2 percent, was calibrated both with and without a sample in the chamber, as well as with the loading shaft in motion in order to check for possible leakage. The low strain-level dilatation measured earlier on unaged bars (Ref 1) possibly reflects a lower adhesive strength between ammonium perchlorate and binder than exists in aged specimens.

No dilatation measurements were made at 0°F, because the dilatometer developed a leak around the pull-rod shaft, and the leak could not be eliminated without extensive and timely refabrication.

It is of interest to compare the uniaxial creep compliance predicted from strip biaxial data with that predicted from poker chip data. Assuming $\nu \simeq 0.5$ and linear viscosity, one finds (see Equation (116c),

$$D_u \simeq \left(1 - \nu^2\right)^{-1} \frac{\sin n\pi}{n\pi} E_{sb}^{-1}$$

$$\simeq \frac{4}{3} \frac{\sin n\pi}{n\pi} E_{sb}^{-1}$$

Over the time range of interest for the strip biaxial tests, the slope n varied from 0.8 to 0.33. As a result, the term $\sin n\pi / n\pi$ could not be neglected. Figure 124 compares the predicted uniaxial creep compliances taken from both the poker chip and strip biaxial. The shape of D_u is generally in good agreement with previous Lockheed data; the difference in magnitudes is probably due to aging effects.

4. CONCLUSIONS

The thermorheological and dilatational behavior of STV propellant has been investigated both theoretically and experimentally.

It has been shown that, through a physically based modification of existing, thermorheologically simple, constitutive equations, greatly increased stress magnitudes under transient temperaturing loadings are predicted.

A method of predicting large or small thermal strains in the presence of nonlinear vacuole dilatation (e. g., dewetting) was developed and then applied to circular port motors, including the "steel-propellant" STV No. 2. The previously observed nonlinear dependence of bore strain on temperature in this STV is predicted by this model. An interesting feature of the developed theory is that under some conditions a graph of bore hoop strain versus temperature will appear as if a discontinuity in the thermal expansion coefficient existed. In reality, however, this behavior is a direct consequence of the characteristic shape of the nonlinear "vacuole" dilatation curve of the solid propellant.

Experimental investigations were concerned not only with conventional methods of creep and relaxation testing, but also with new techniques for measuring mechanical and thermal dilatation under biaxial and triaxial stress states. Poker chip dilatational data were obtained during creep tests by simultaneously measuring the circumference of the poker chip's midplane and the platen separation. The method was capable of resolving dilatations as small as 0.01 percent. Strip biaxial tests were conducted with a biaxial dilatometer that could resolve 0.1-percent levels. No dilatation was detected at strains below 10 percent in the dilatometer.

Very precise measurements of poker chip dilatation produced some of the most significant results of the entire program. Specifically, the following were found:

(1) The ratio of dilatation to axial strain is very nearly independent of temperature, stress level, and creep time, and this ratio is the same for tension and compression

(2) The STV propellant has an initial void content indicated by rough analysis to be more than 1 percent

(3) The "low stress" bulk modulus in tension and compression is more than an order of magnitude smaller than the theoretical value for voidless propellant

(4) The bulk modulus is very nearly proportional to the uniaxial modulus, and is, therefore, a strongly viscoelastic function

(5) The uniaxial modulus inferred from low-stress-level poker chip tests was found to be two to six times (depending on the value of reduced time) the modulus obtained from conventional uniaxial and biaxial tests conducted at strains over 1 percent.

5. ACKNOWLEDGEMENTS

The authors wish to acknowledge the very able assistance provided by Dr. J. H. Song in developing the photoconductive copying technique, Larry Lewis in reducing much of the data, and Richard Shankle in performing the compression poker chip tests.

(The reverse is blank)

SECTION VII

STV NO. 6 ANALYSIS AND TEST

1. DESCRIPTION OF STV NO. 6

STV No. 6 was the last STV to be made as a part of the second-year effort. Details of the geometry and instrumentation are shown in Figure 135. The STV contains a four-point star grain port so as to be more representative of a real motor than were the earlier STVs. The grain was cast from LPC-667, an inert propellant formulation based on R-45 hydroxyl-terminated polybutadiene prepolymer. The inert propellant contains 82 wt% solids, consisting of 47 wt% aluminum and 35 wt% ammonium sulphate.

To avoid analytical complexity, the domed head end of the motor case was cast separately and was coated with release agent during casting of the grain proper. The grain therefore has flat, unrestrained ends and a constant cross section and may be analyzed by means of a plane strain strain analysis, at the mid-plane.

Five 150-psi diaphragm normal stress sensors are used in this STV with an additional 600-psi gage used for comparison purposes. The normal stress gages are arranged in two axial lines, in line with the star points (BB) and at 45 degrees to the star points (AA).

Three shear cubes, A.1, A.2, and A.3, were installed in the STV when it was first made. However, shear gage A.1 was broken as a result of an excessive shear force applied during mandrel extraction. Shear gage A.1 was a sensitive device employing unprotected semiconductor strain gages with a corresponding low stress/strain capability. Shear gages A.2 and A.3 were made using Kulite "ruggedized" semiconductor strain gages (i. e. , semiconductor elements sandwiched between epoxy-impregnated glass fiber sheets). These shear gages have a much higher load capacity than the A.1 type of gage, but they also have a lower sensitivity. In operational use in STV No. 6 they have proved very satisfactory with sufficient sensitivity for the requirements.

Two special clip gages, shown in Figure 136, were made to measure bore deformations and changes in star width during the STV tests. Conventional foil gage elements were used on the bore clip gage, but the more sensitive semiconductor type were used on the star-width clip gage.

2. ANALYSIS OF STV NO. 6

Conventional analytical techniques were applied to the analysis of the new STV No. 6 grain. The four-point star bore geometry dictated the use of a generalized plane strain approach, with the results subsequently modified to account for finite length effects.

Figure 137 shows the grain cross section used in the analysis. Because of symmetry, only one quarter of the grain was considered, and a
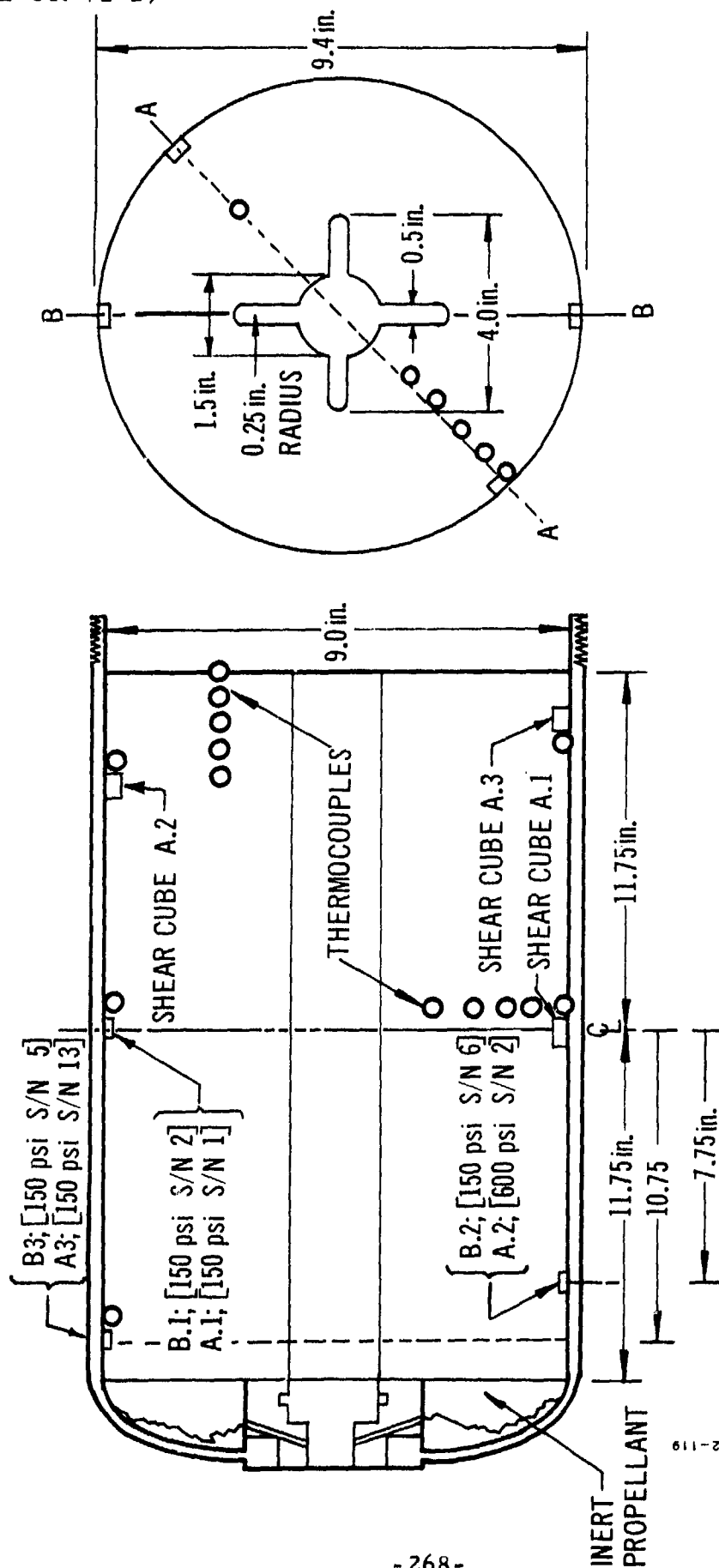
Figure 135. STV No. 6 Instrumentation: Steel Case, Inert Propellant.
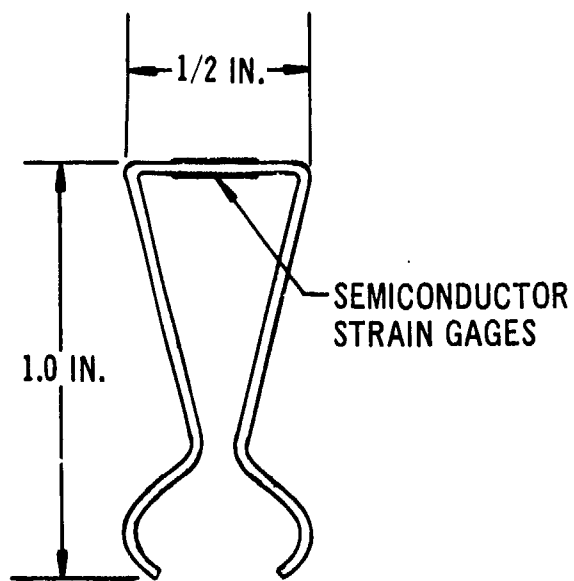
a. STAR CLIP GAGE
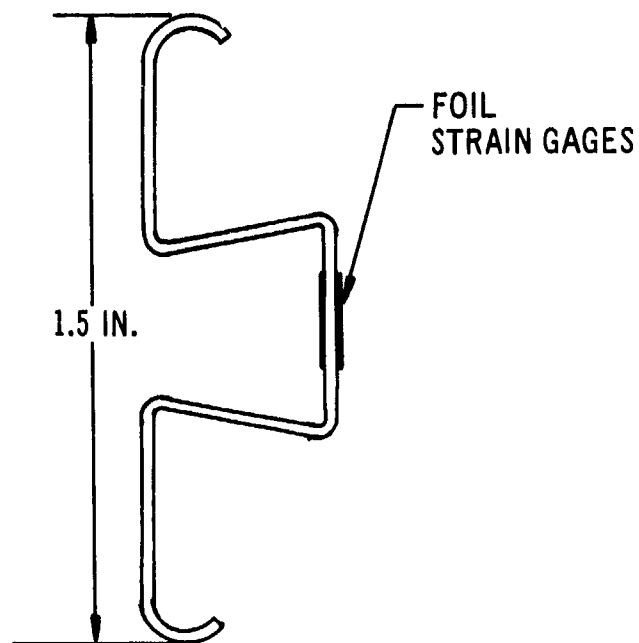
b. BORE CLIP GAGE

Figure 136. Special Clip Gages for STV No. 6.
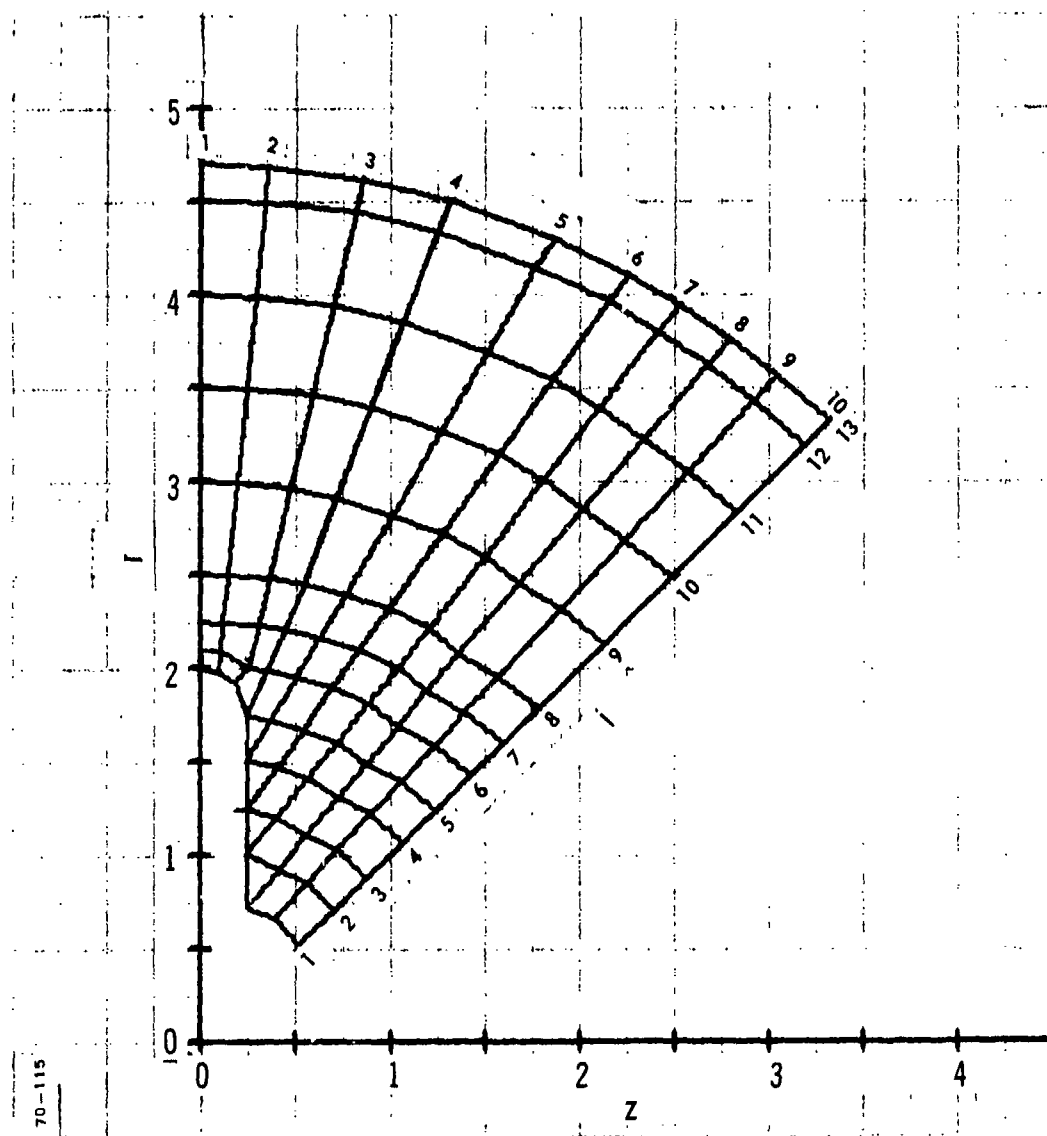
Figure 137. Grain Cross Section Used in Analysis of STV No. 6.

grid was needed for only one eighth, as shown in the figure. Analyses were run for isothermal pressurization and for a thermal cooling condition with a temperature change of 200°F. The analysis was performed with the elastic computer code ANL 800, obtained from the University of California at Berkeley.

Maximum strain values are produced at the tip of the star point, i.e., at nodal point 5.1, under both pressurization and thermal loading conditions. However, because of the small space available within the bore of STV No. 6, the clip gages were placed so as to measure the width of the star valley at the point corresponding to the nodal point 1.7, and the bore clip gages were mounted to measure the diametral changes at the nodal point 1.10.

Similarly, the diaphragm stress gages were arranged to measure the radial stress component at the locations 12.1, and at the 12.10 nodal point. It will be observed from Figure 137 that these correspond to locations in line with the star point and 45 degrees to the star point, respectively.

The analytically predicted pressurization strains at the tip of the star point are shown versus pressure in Figure 138. Figure 139 shows the predicted change in star width and the change in bore diameter as a function of pressure. The latter two curves are of course required for comparison with the experimental observations.

Figure 140 shows the maximum hoop strain generated at the tip of the star point under thermal cooling conditions, and Figure 141 shows the change in width of the star valley and the change in bore diameter as a function of temperature change.

The thermal cooling analysis was based on the assumption that the propellant was incompressible, i.e., $\nu = 0.5$, and the coefficient of thermal expansion was taken from last year's Final Report as 4.25×10^{-5}.

In determining the analytical strains and stresses for the finite length grain, a "Parr Factor" was used to reduce the strains and stresses predicted for the infinitely long plane strain condition. The Parr factors were designed to be used simply with strain measurements and are strictly not valid for predicting stresses. However, it appears that the use of the Parr factor does produce a better estimate of the stress value for a finite-length grain than the plane strain value and for that reason the stresses also have been factored to the lower values.

In lieu of the three-dimensional analysis of the STV No. 6 grain, an approximate approach was used to obtain stress values along the axis of the grain for comparison with the measured gage data. The approximation assumed that the four-point star grain could be represented by an equivalent circular port grain of the same length. The axial stress distribution was then determined for this equivalent grain design and the values at the mid-point of the grain were then factored to agree with the plane strain analysis results for the in-line stresses and stresses at 45 degrees to the star point.
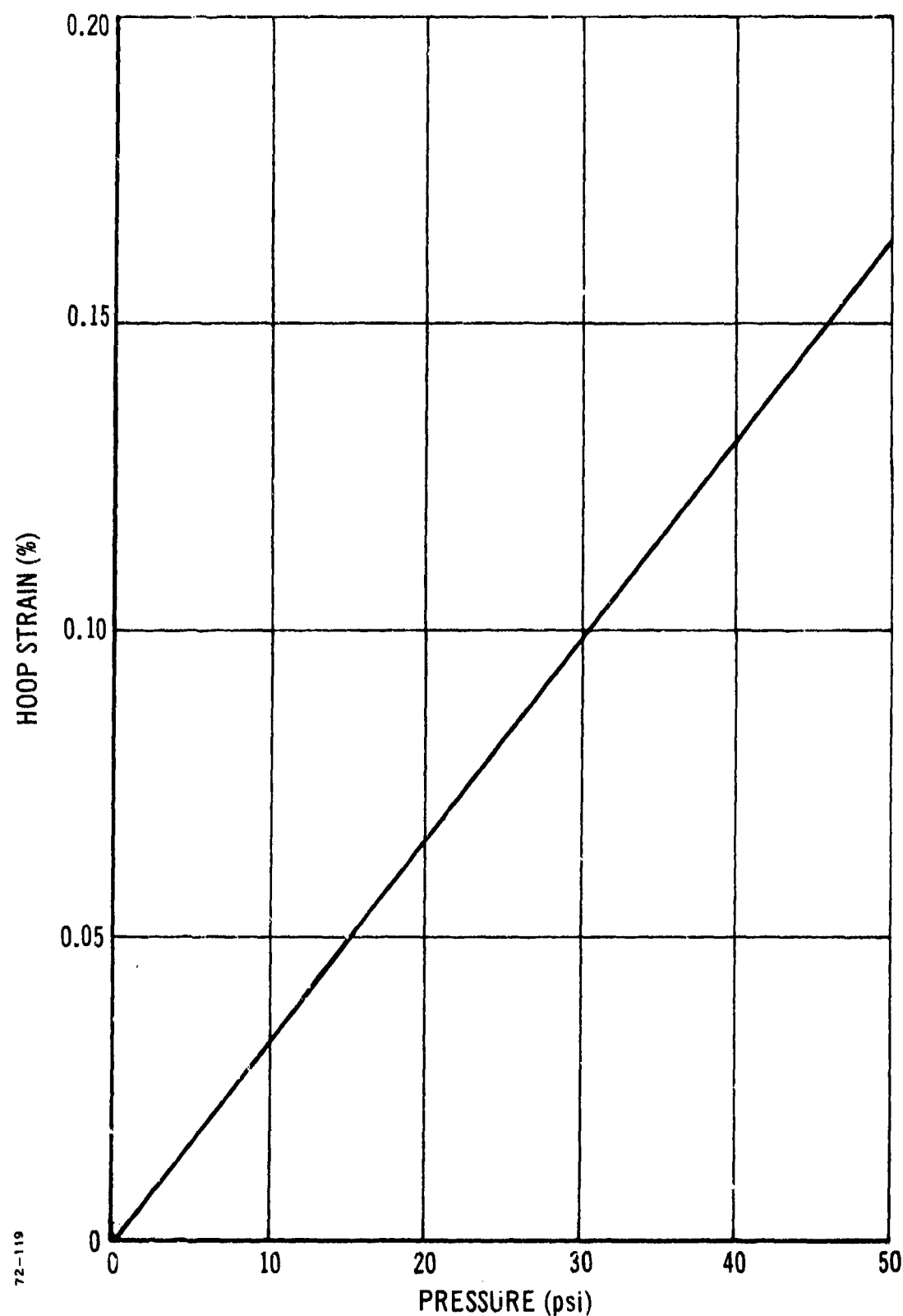
Figure 138. Maximum Hoop Strain at Tip of Star Point Under Internal Pressurization Conditions.
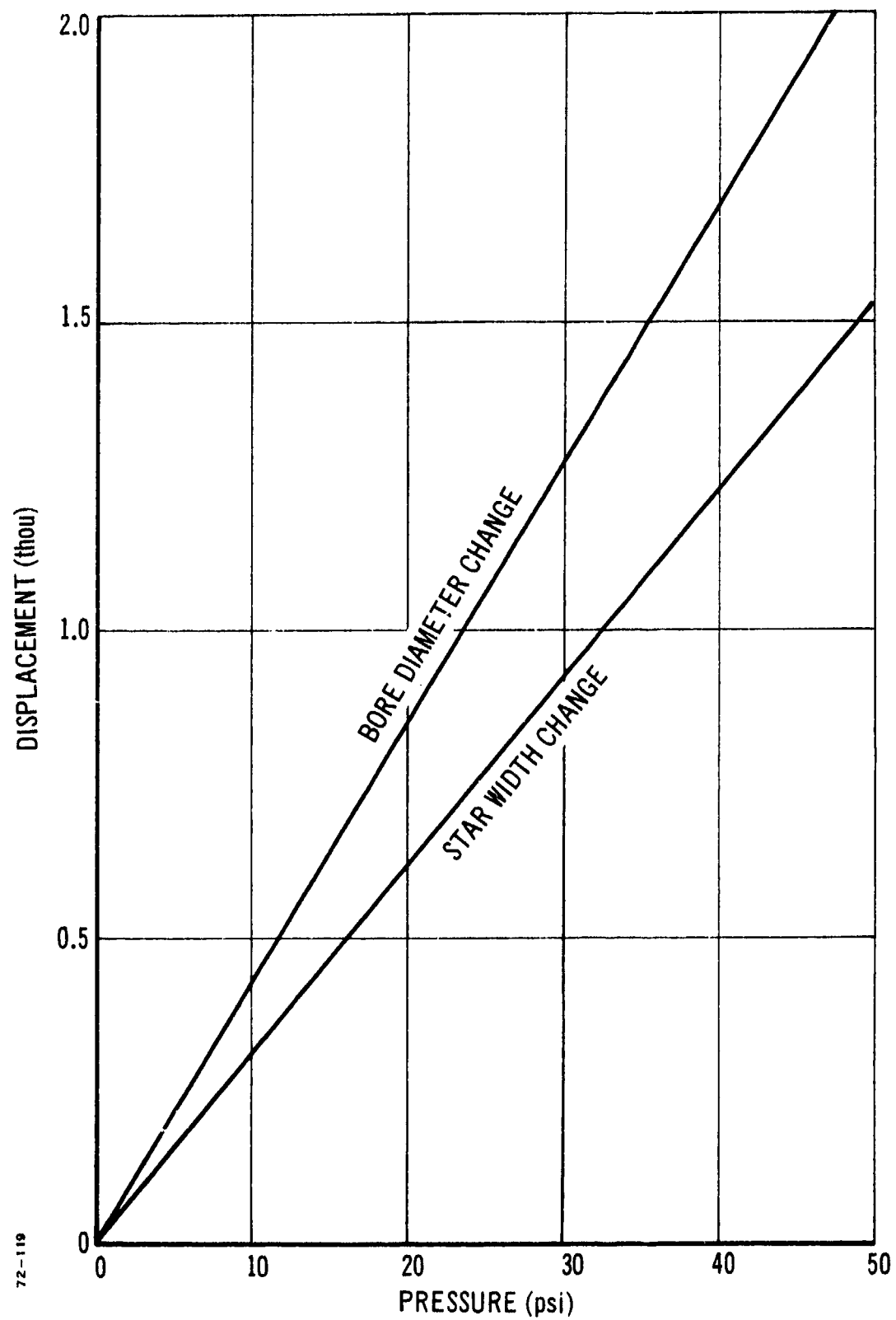
Figure 139. Change in Star Width and Bore Diameter versus Pressure.
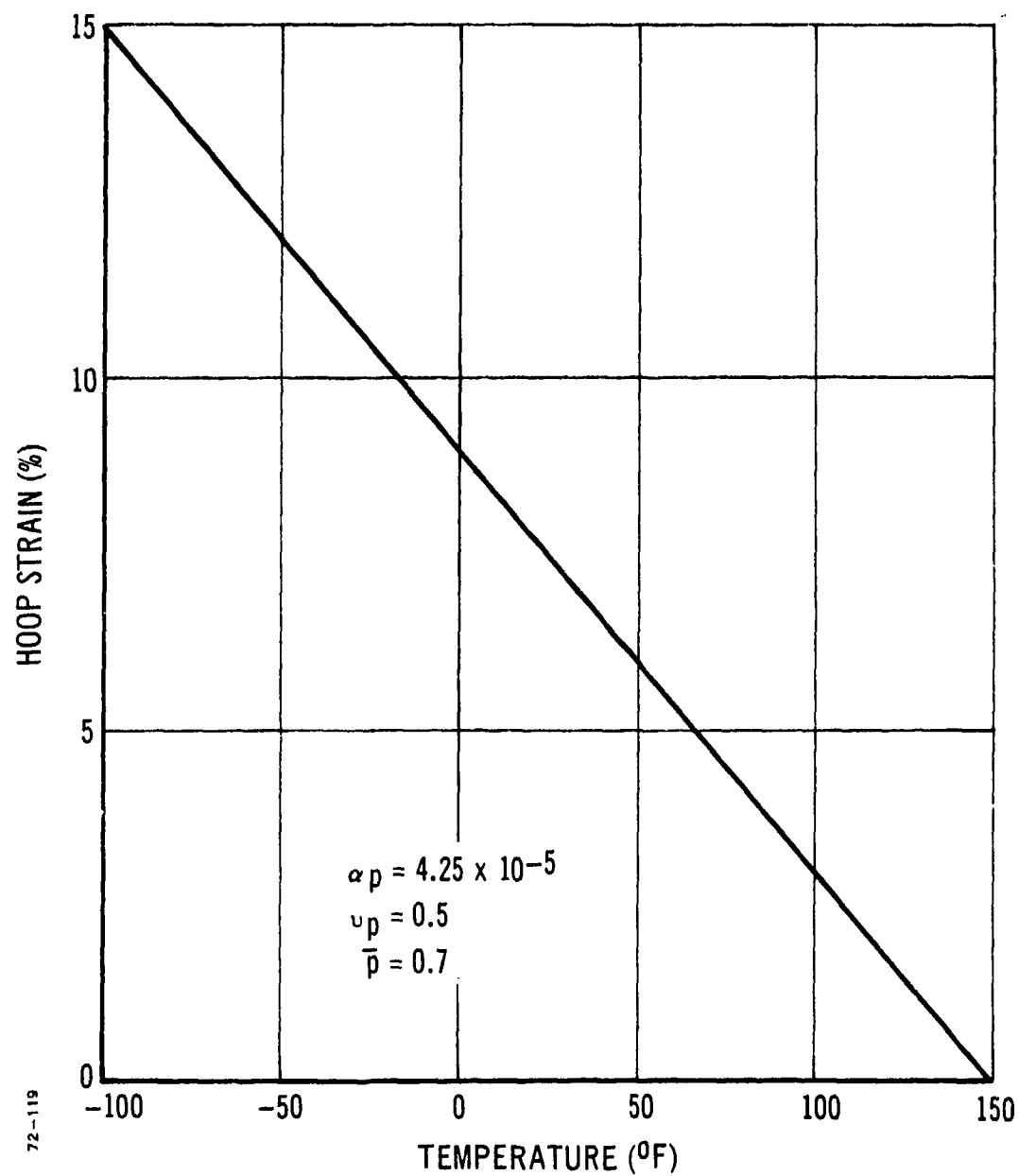
Figure 140. Maximum Thermal Hoop Strain at Star Tip versus
Temperature (Analytical).
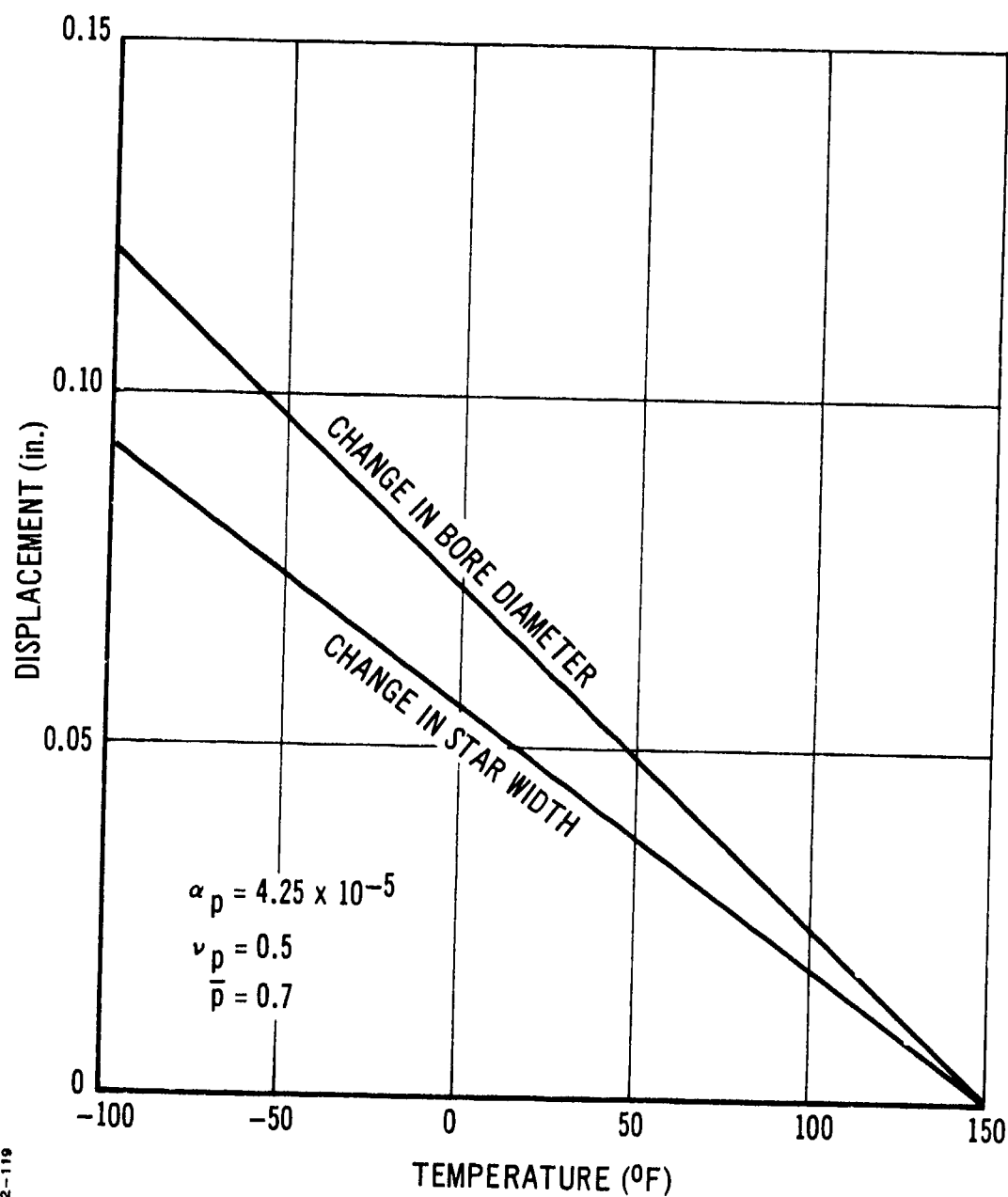
Figure 141. Change in Star Width and Bore Diameter versus
Temperature (Analytical).

The normal radial stresses shown in Figure 142 were determined in this fashion, as were the shear stresses shown in Figure 143.

These stress values were calculated by means of a quasi-viscoelastic approach; the equivalent modulus $E(t/a_T)$ was obtained from the relaxation modulus curves for the inert propellant. The use of the $E(t/a_T)$ modulus instead of the integral form results in higher thermal stress values, so that the calculated values are the largest values that could be predicted.

When the experimental stress values measured on STV No. 6 are compared with the calculated data, the effects of aging must not be ignored. For this reason. the modulus data used to predict the thermal stresses in last year's Final Report were replaced by the aged inert propellant data presented earlier in Table XVII, in order to calculate the stresses for comparison with the more recent experimental tests.

3. EXPERIMENTAL RESULTS FROM STV NO. 6

a. Tests When First Made

Two distinct types of test were conducted on STV No. 6 when it was first manufactured in July 1969. The first type of test was the slow thermal cooldown test with a period of 24 hours between changes in temperature, and with relatively small temperature steps. Later, the STV was placed on test with STV No. 1, which was being temperature-cycled to failure. In this case, the test consisted of a rapid step change in temperature from 150^0F to some low value held for at least 24 hours with a change to 150^0F again for another 24 hours. STV No. 6 was cycled along with STV No. 1 from low-temperature values of -20^0F to a minimum temperature of -65^0F. At this time, the testing on STV No. 6 was terminated for the second year of the STV program.

b. Third Year Tests on STV No. 6

During the third year of the program, similar slow thermal cooling tests were first performed as a means of checking the performance of the instrumentation. Several different runs were required before it was determined that the gages were performing as well as could be expected. The bore strain measuring gage was replaced after the first test runs because it failed to work properly. Similarly, the 600-psi diaphragm gage gave considerable trouble before it was realized that corrosion had attacked the leadwires to the gage and that it was no longer giving reliable data.

Diaphragm gage No. 5 was also found to give erratic data during the third-year tests. This gage, located at the end of the grain, attained a high stress value of 120 psi during the temperature cycling test to -65^0F at the end of the second-year testing program. It seems that this value was reached because the grain began to unbond at the end and, during the third-year tests, it seems that the grain was not bonded to the case in the vicinity of the gage. At any rate this is the most probable explanation for the poor data obtained from gage No. 5 during the later test series.
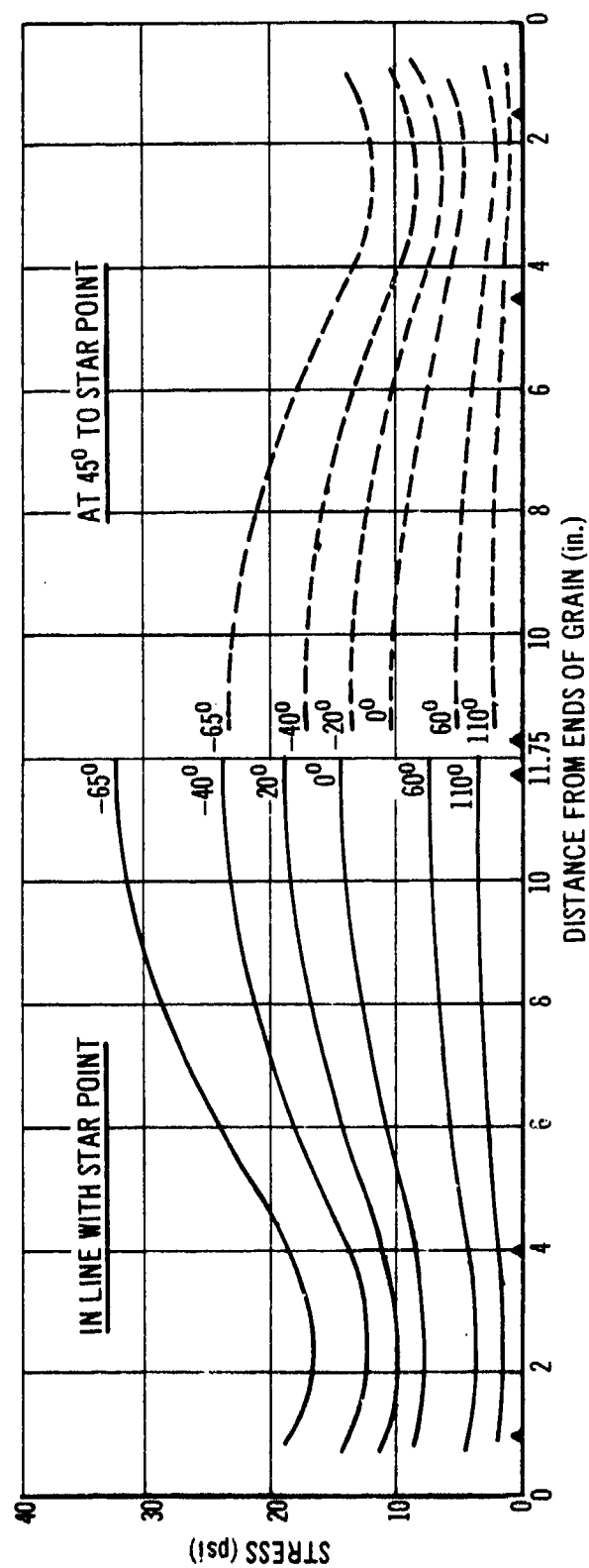
Figure 142. Thermal Radial Normal Stresses Calculated for STV No. 6 versus Temperature (Fresh Inert Propellant).

72-119
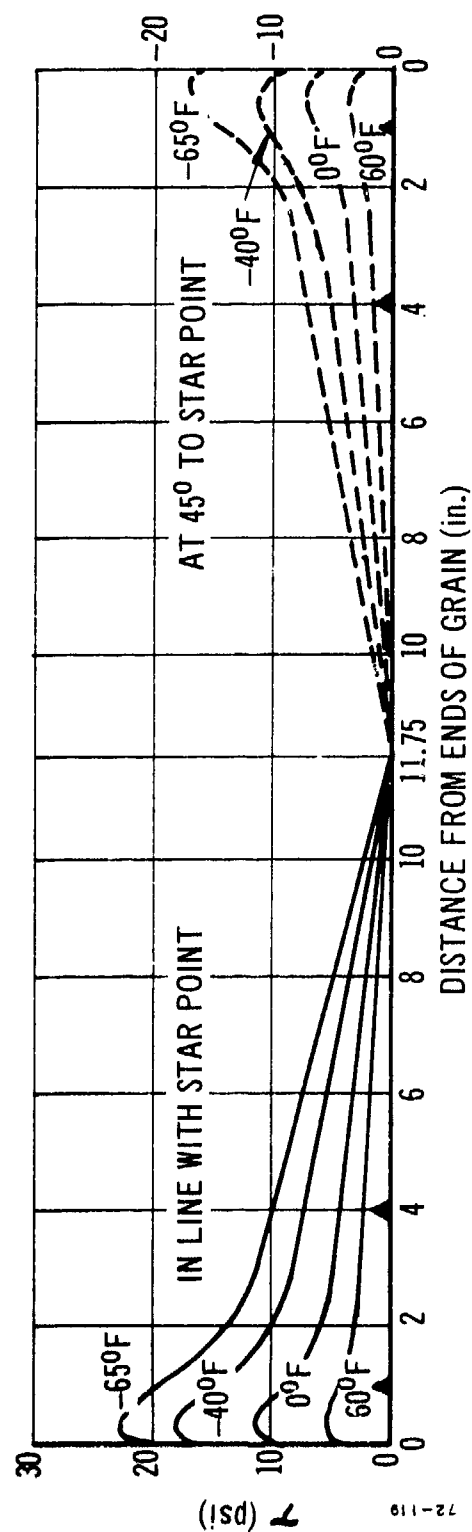
Figure 143. Thermal Shear Stresses Calculated for STV No. 6 for Various Temperatures (Fresh Inert Propellant).

c.   Review of Raw Test Data

Considerable insight into what is happening within STV No. 6 may be achieved merely by examining the raw data from the gages obtained during the tests described earlier. It is not necessary even to convert the gage signals to stress or strain readings, because the trends are apparent from an examination of the gage outputs themselves.

The data measured with some of the gages during the first slow thermal cooling test are much different from the data obtained during the later cycling tests and in the later thermal cooling tests. A reason for this discrepancy was sought.

Two possible reasons are proposed on the basis of the data obtained.

Consider the output data from gage No. 2 located near the end of the grain, and plotted against temperature in Figure 144. The triangles of the lower curve represent the data obtained during the initial slow thermal cooling test, and the circles show the thermal cycling test data. The significant point is the marked change in gage reading at the high temperatures during the thermal cycling tests. Thus, the initial reading at 135^0F is 3.2 mv, which increased to almost 11.0 mv at 160^0F by the end of the thermal cycling tests. The gage appears to be moving into a compressive stress region, if these data are to be believed. A possible explanation for this phenomenon is a rearrangement in the stress pattern through the grain after removal of the mandrel. This rearrangement theory appears sound when the later, third-year thermal cooling data are also examined. By the time of the third-year tests, the STV was 2 years old and the reading from gage No. 2 had moved well into the compressive region. The thermal gage readings did not change significantly during the third-year tests, which suggests that by this time the grain had aged and had achieved a stable configuration.

Simple aging of the propellant unconnected with any mandrel removal appears to be the principal cause of the changes in the shear gage readings presented in Figures 145 and 146. The data show trends very similar to that discussed earlier for the diaphragm gage. Thus, the shear gage readings show a consistent movement at the high temperatures during the thermal cycling tests conducted during the second program year. In this case, however, the drift in the readings is in the same direction as during cooldown, i. e. , the drift is toward an increased shear stress condition and is most probably caused by a continuing cure process involving a slight volume reduction. Again, the later data obtained from the third-year tests show a continuation of the aging process, and there is a new, different thermal cooldown line, which starts from a much higher residual shear stress value.

The significant factor that results from this examination of the raw test data is the fact that the gages can follow the effects of aging within a grain during a relatively long period, i. e. , 2 years. Furthermore, the trends are apparent from merely examining the gage output data and there is
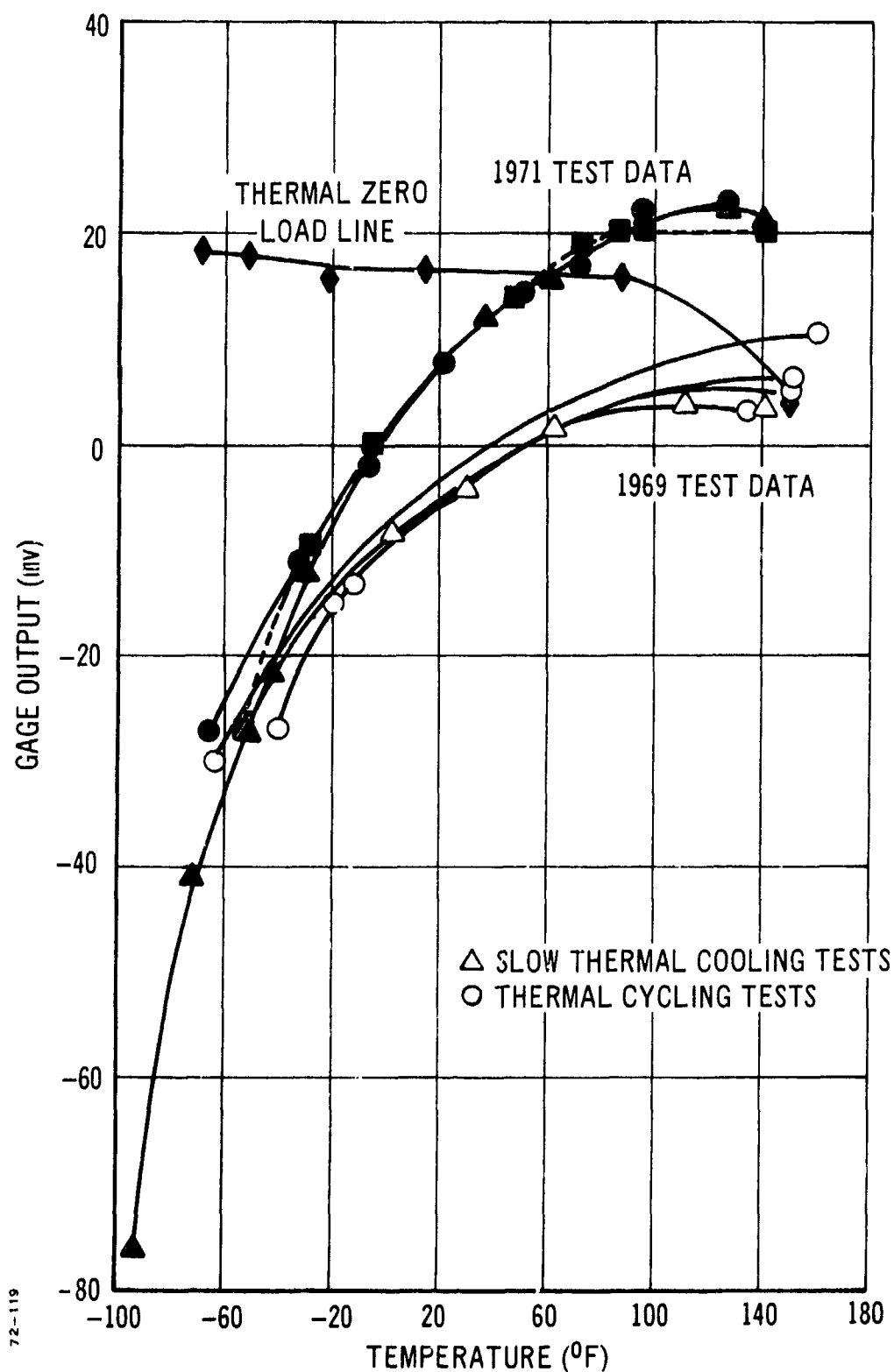
Figure 144. 150 psi Diaphragm Gage No. 2 Output Data from
STV No. 6 versus Temperature.
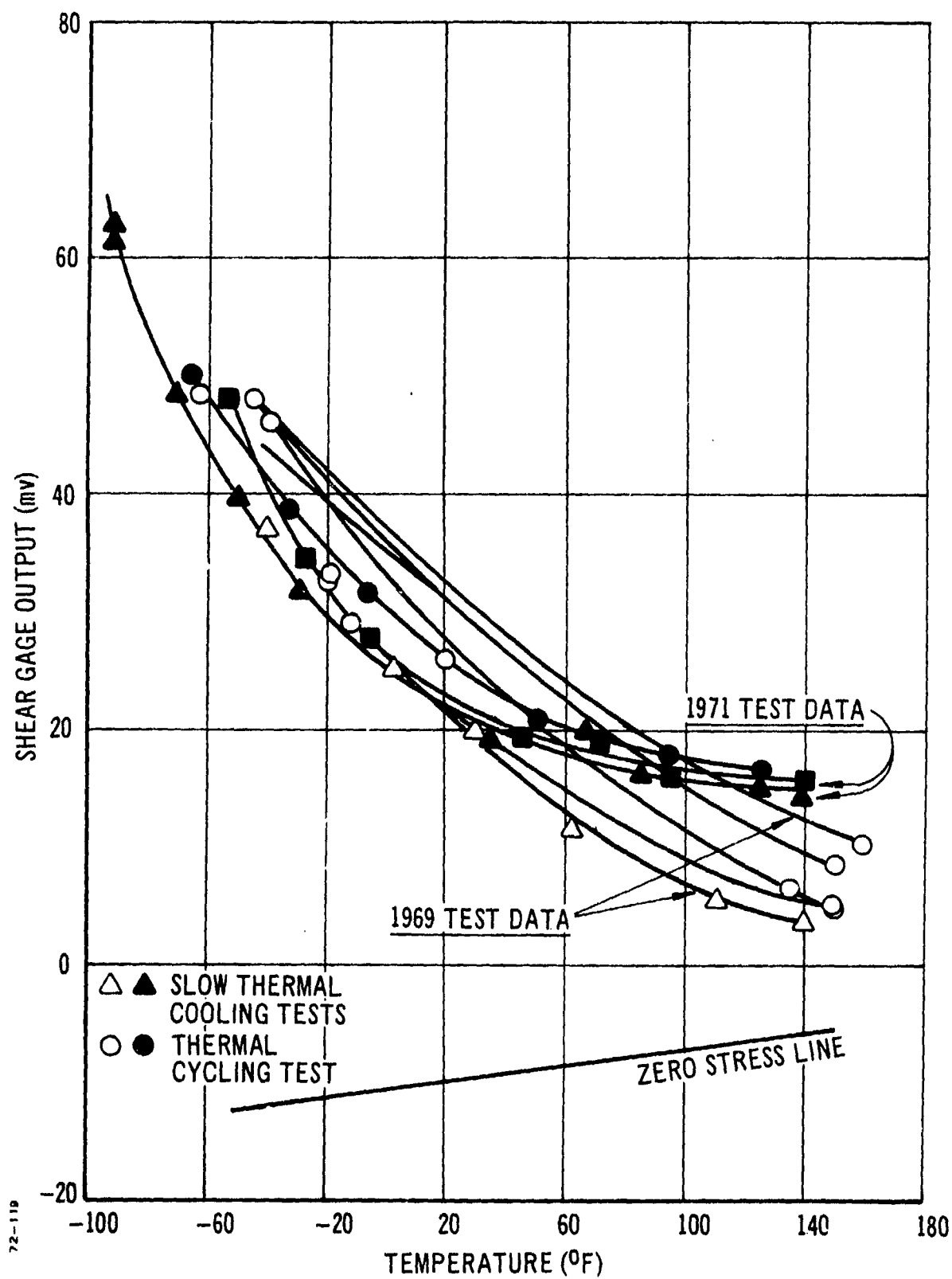
Figure 145. Shear Gage No. 2 Output Data from STV No. 6
versus Temperature.
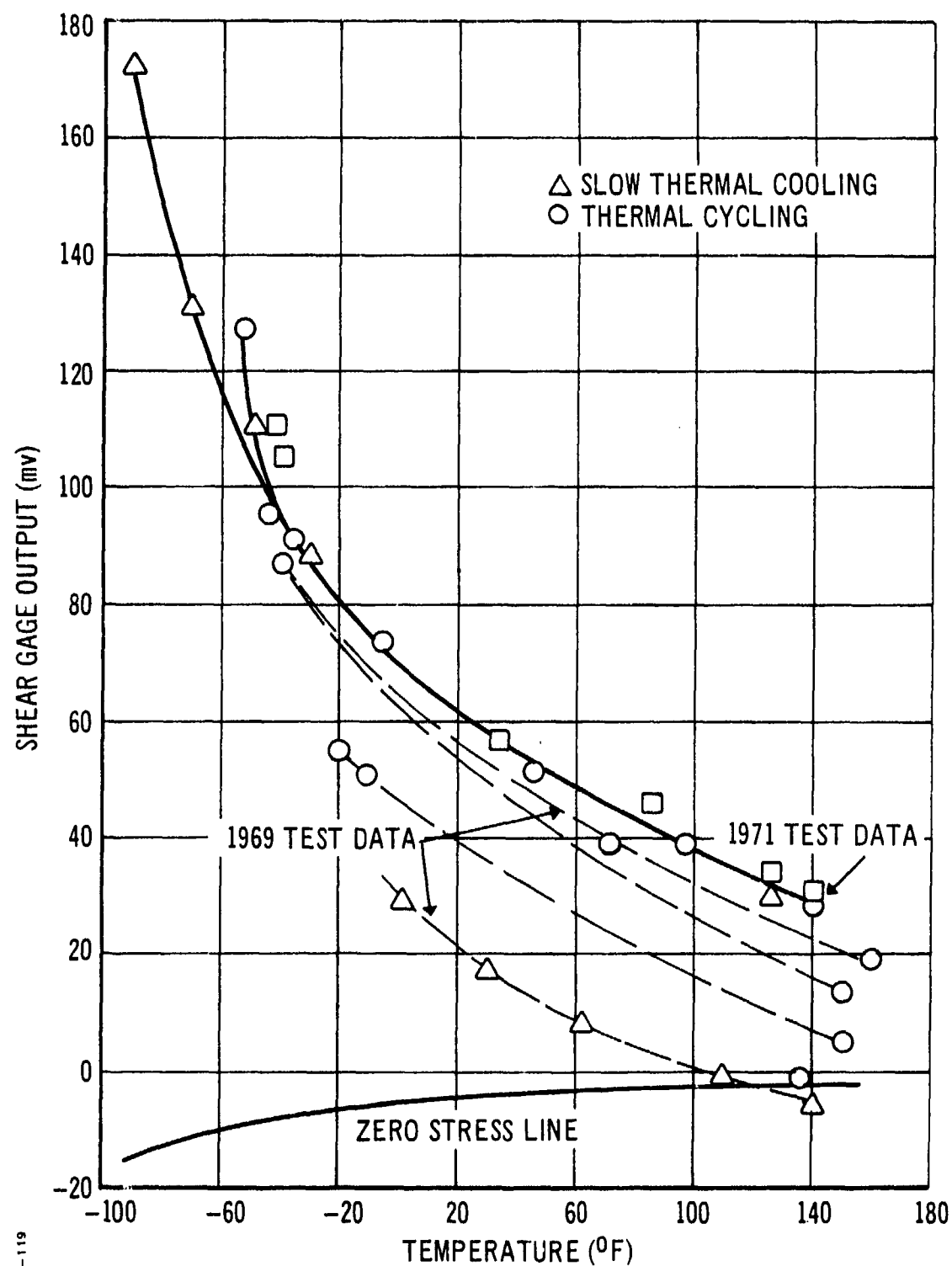
Figure 146. Shear Gage No. 3 Output Data from STV No. 6
versus Temperature.

no need to convert them to engineering units until quantitative values are required for the changes in stress and strain with aging.

Not all of the gages show these marked changes in reading with aging. Most of them, in fact, show very little change from the earliest readings to the last values recorded. Why some gages reveal changes and others do not is yet to be resolved, but there is probably some relatively straightforward explanation for the fact.

4. COMPARISON OF EXPERIMENTAL RESULTS AND ANALYSES

    a. Pressure Test Data

The bore strain measuring gage proved unsuitable for the measurement of pressurization strains because it was simply not sensitive enough to detect the small displacements involved in the low-pressure tests. Good data were obtained from the star-point-width clip gage and some of these data are shown in Figure 147. The measured change in star point width is plotted versus pressure for several temperatures from 140 to 2^0F. At the high temperatures the measured displacements were very small, but they increased as the temperature was reduced from 140 to 60^0F. For the lower temperatures, i.e, 30 and 2^0F, the measured displacements of the star point are smaller than those at 60^0F. This behavior is not anticipated by the analysis, which predicted the dashed line in Figure 147. The agreement between the analysis and the experimental data is not very good. The high temperature data are considerably lower than the predicted values, but the lower temperature data are approximately twice as high as the predicted values.

It is possible that the complex nature of the four-point star geometry makes the prediction of the change in star point width extremely difficult. This does not explain, however, why there is the large variation in displacement readings with the temperature change.

    b. Slow Thermal Cooling Tests

    (1) Strain Data

Two sets of slow-thermal-cooling displacement data are shown in Figure 148, plotted against temperature. The first set of data were obtained when the STV was first built in 1969. The second set of data were measured during the recent thermal cooldown tests during 1971.

It will be noted that there is excellent agreement between the two sets of data; the bore diameter changes and the star width changes appear to be reproducible to within fairly close limits. One or two data points appear suspect, but in general the reproducibility is very good. There does not seem to be any consistent variation in the displacements with aging.

Comparison of the calculated thermal cooling displacement curves and the measured data shows a large discrepancy, with the experimentally measured values being about twice as large as predicted. The
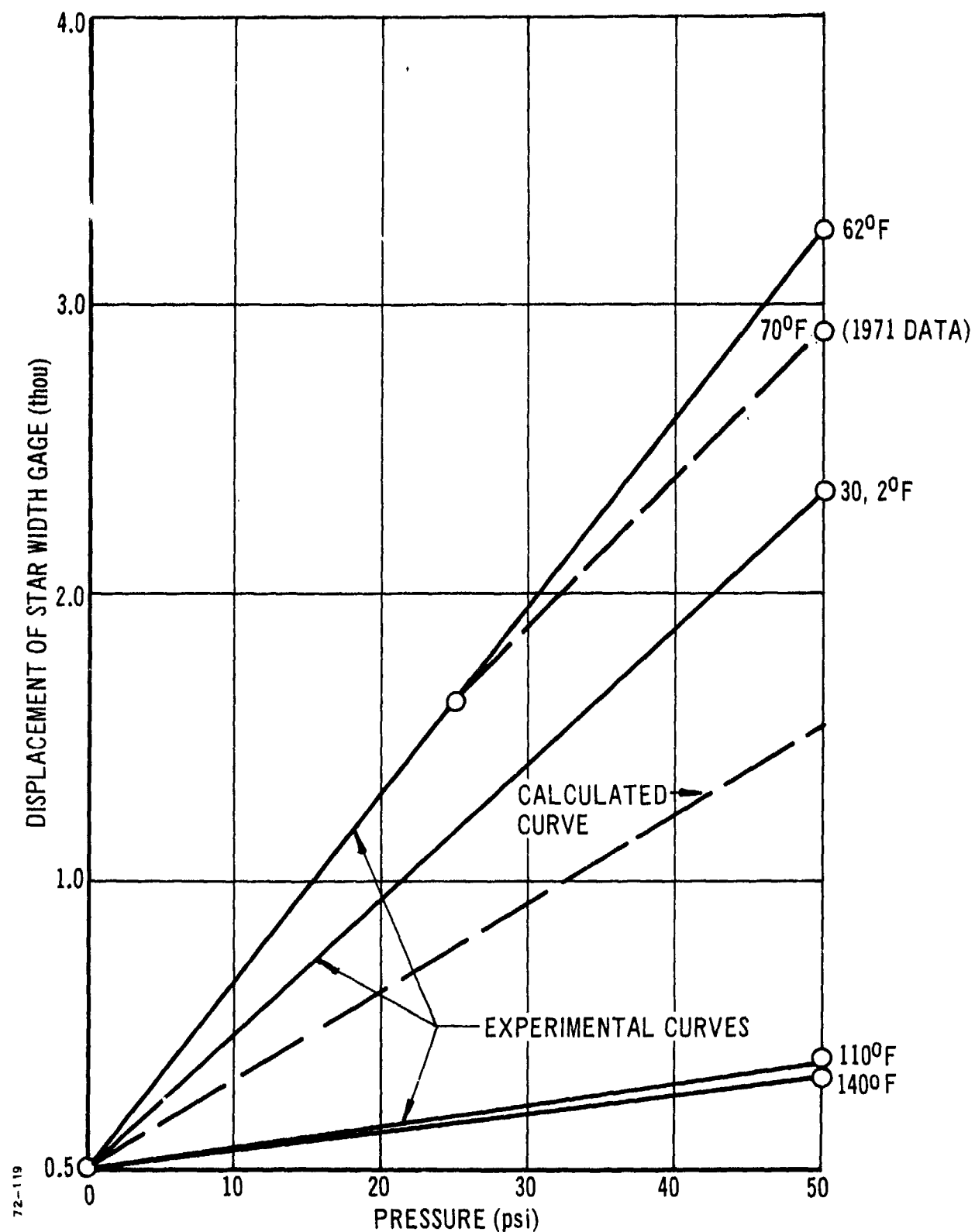
Figure 147. Comparison Between Experimental and Analytical Pressure Strain Data for Star Point.
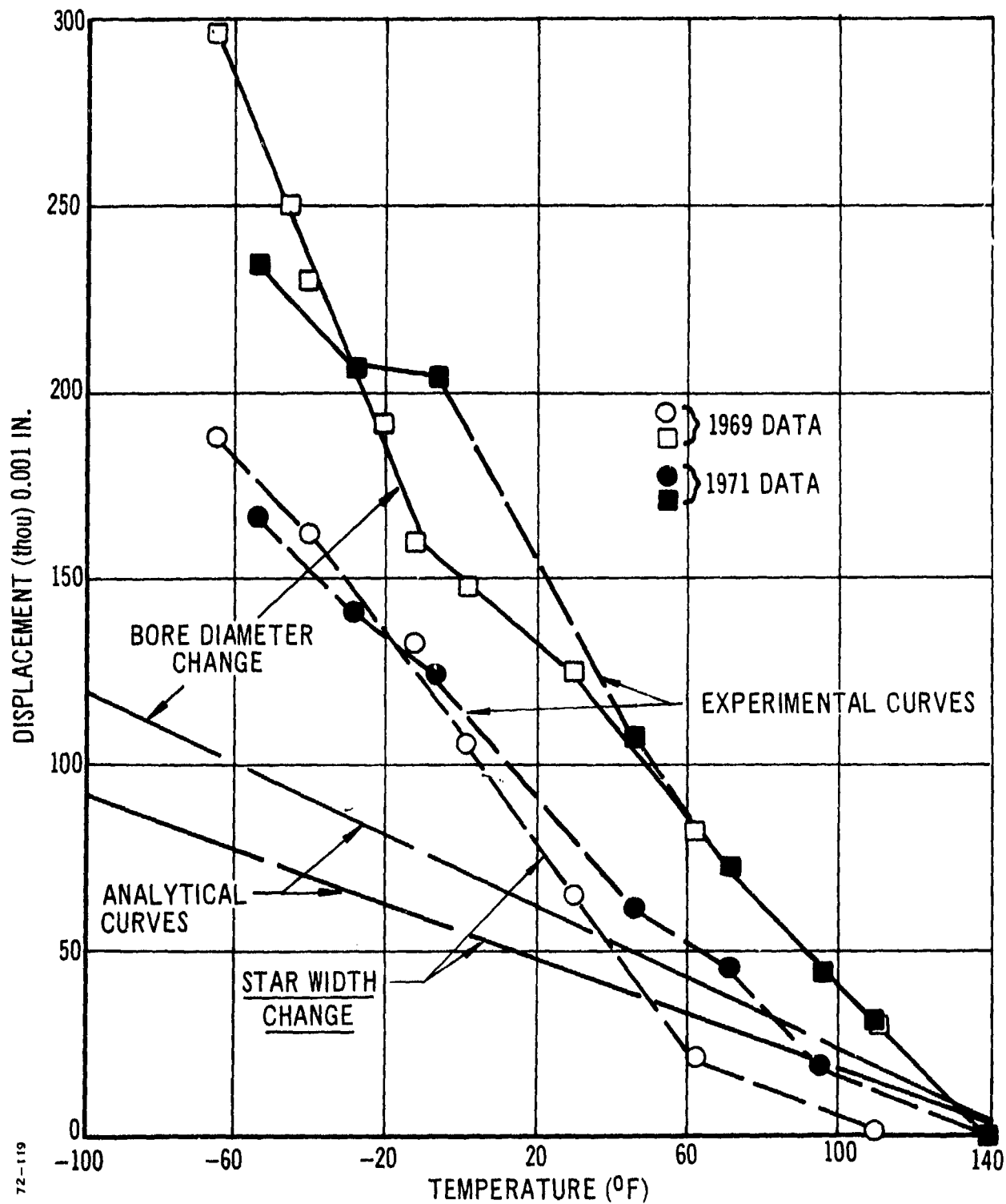
Figure 148. Comparison Between Experimental and Analytical Slow
Thermal Cooling Displacement Data.

experimentally determined data curves seem to exhibit a slight degree of curvature, which would not be expected from the analytical point of view.

(2) Normal Stress Data

A comparison between the calculated and the measured thermal stresses at the midpoint of the STV was presented in last year's Final Report as Figure 111. It is repeated here as Figure 149. It will be observed that the predicted slow thermal cooling stresses are smaller by a factor of 1.5 than those measured. However, the calculated thermal stresses were determined by means of the simple approximation $E(t/a_T)$, but from the unaged inert propellant properties. If the 2-year-old propellant properties are used in place of the unaged properties, then the calculated thermal stresses are increased as shown in Figure 150. Thus, in comparing the measured thermal stress data with the calculated data as in Figure 149, the observed discrepancies can be the result of a higher degree of cure for the propellant in the motor, which would result in higher modulus values similar to the aged propellant modulus data. Thus, the differences between the observed (high) thermal stresses and the calculated (low) stress values can be the result of at least three different effects, as follows:

- The thermal coefficient of linear expansion is greater in the STV than is measured in the small samples in the laboratory. This affects both the stresses and the strains and would tend to being them both into line with measured data.

- The modulus of the unaged propellant as deter- mined from cartons cured with the STV is lower than that of the STV propellant cured in the STV. This problem has been observed before on motors in several different projects. Typically, the carton modulus data are lower than the in-situ motor modulus data.

- The propellant may be nonlinear in its behavior, as demonstrated in many laboratory tests, resulting in modulus data that changes with strain and/or type of loading applied.

As yet there are insufficient data from the STV to allow a decision to be made between these possible causes of the thermal stress and strain discrepancy.

c. Thermal Cycling Tests

Another possibility exists for the discrepancy between the observed thermal stress data and the calculated data. The calculated data values are based on the assumption that the STV is slowly cooled to the lower temperatures in a uniform manner. In reality, however, the propellant may be cooled much faster than say the 20^0F per day assumed, if the STV is placed in a 20^0F temperature differential and most of the temperature change
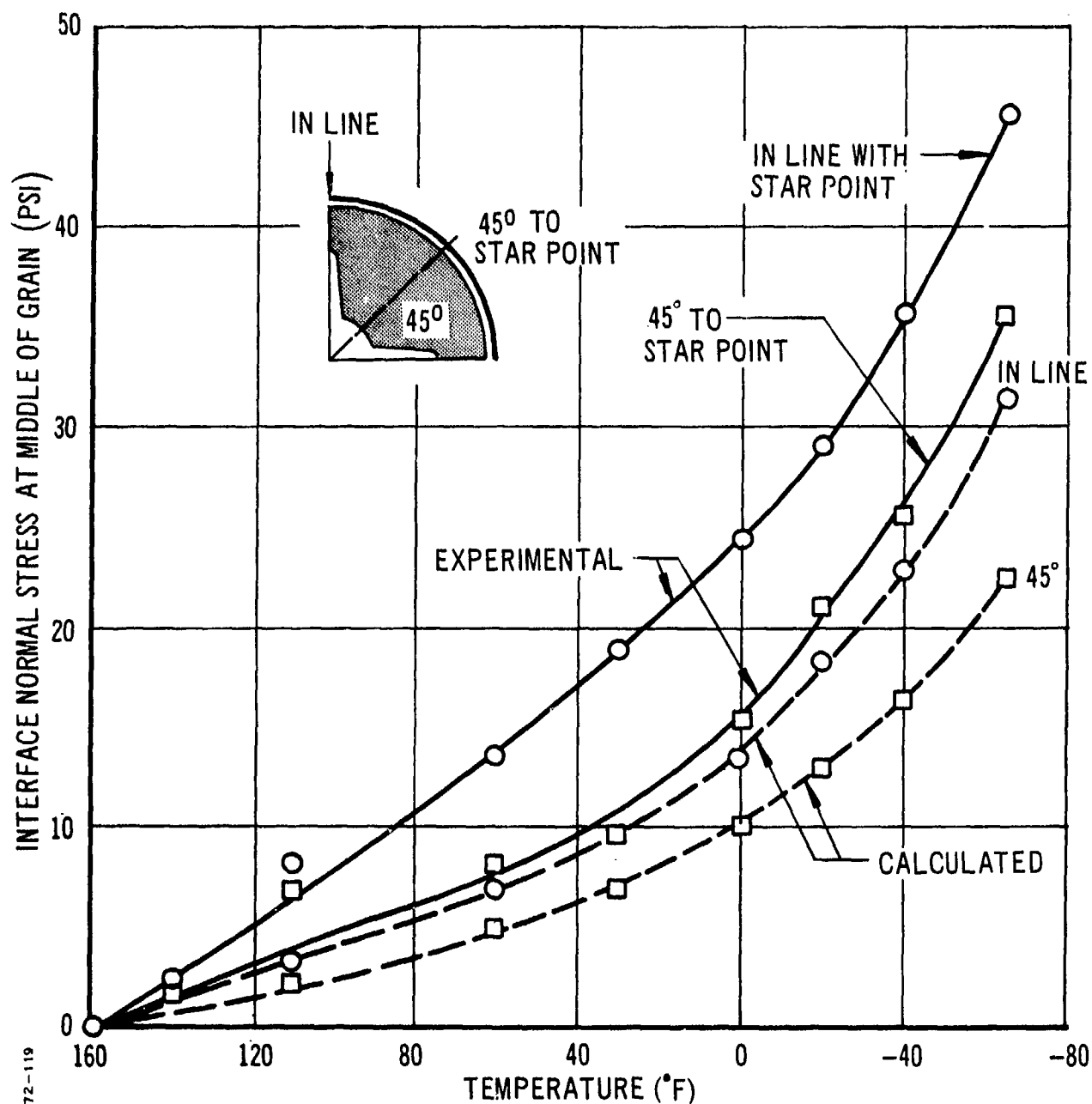
Figure 149. Comparison Between Experimental Thermal Stresses and
Calculated Stress Values from Plane Strain Analysis at
Midpoint of Inert Propellant STV No. 6.
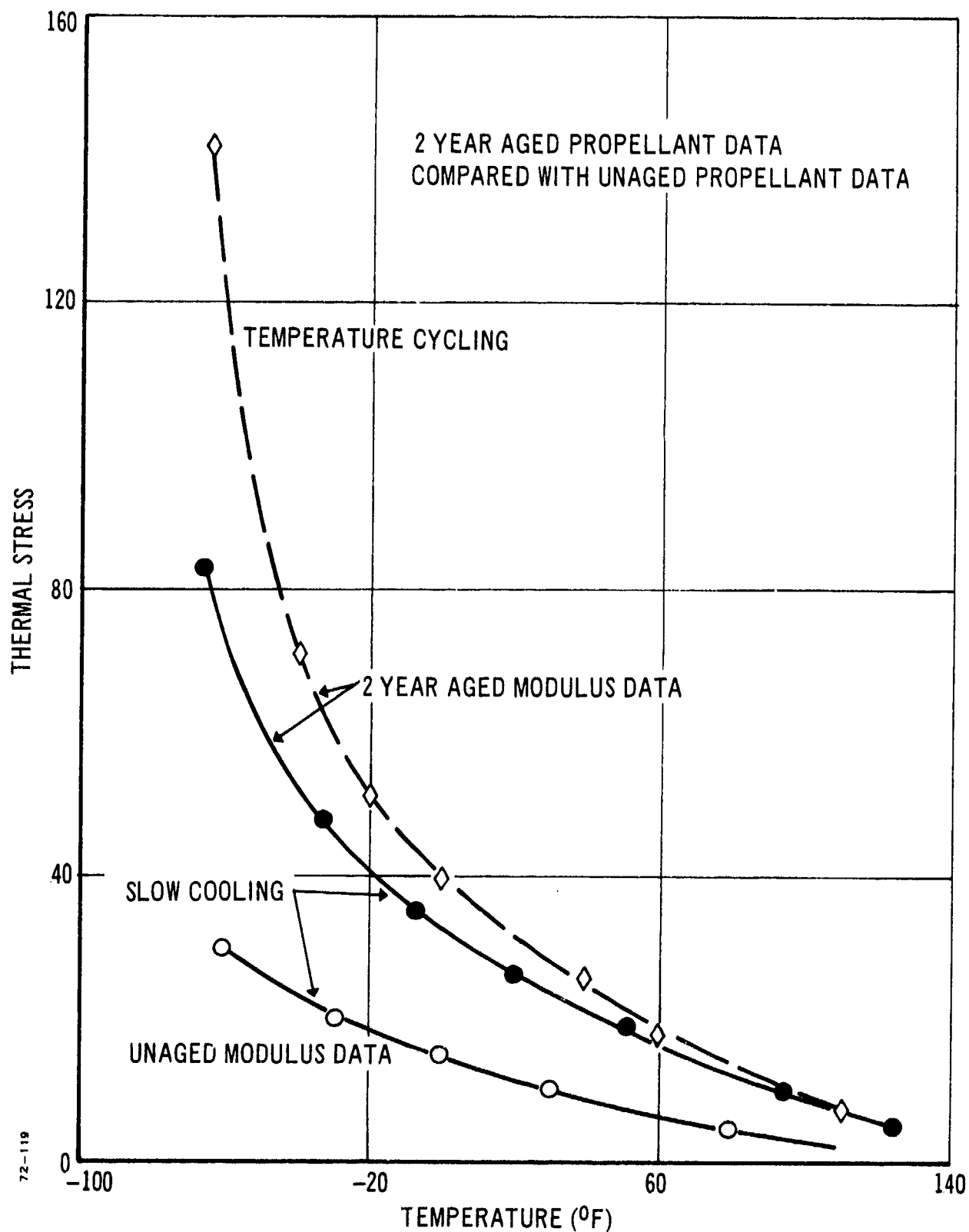
Figure 150. Thermal Stresses Predicted for STV No. 6 in Line with Star Point at Middle of Grain.

occurs in the first portion of the conditioning period. In this case, the rate of cooling of the propellant may be much closer to that obtained under thermal cycling conditions, where it is assumed that the temperature is achieved in a single step from the high (cure) temperature to the low value. The effect of changing from slow thermal cooling to thermal cycling conditions is also shown in Figure 150 for the normal thermal stress at the midpoint of the STV. At moderate temperatures the difference between the slow cooling data and the thermal cycling data is small, but the difference should become much more apparent at low temperatures.

Experimental thermal cycling data from the 1969 tests are presented in Figure 151, and the slow thermal cooling data are also shown for comparison. There is very little difference between the slow thermal cooling data and the thermal cycling data, certainly not as much as would be predicted from the analytical data.

 d. Thermal Shear Stress Data

The raw data from shear gages No. 2 and 3 have already been presented in Figures 145 and 146. The same data, now converted into thermal stress versus temperature, are presented in Figure 151. These data must be compared with the calculated data shown in Figure 152. Curves were calculated on the basis of the "equivalent modulus" at $E(t/a_T)$ from the fresh-propellant data obtained from the propellant cartons cast with the STV, and from the aged-propellant properties determined from the inert propellant test specimen during the third program year. The calculated shear stresses include both slow thermal cooling tests and the thermal cycling tests. It is interesting to note that the differences between the thermal cycling shear stresses and the slow thermal cooling stresses are fairly small for temperatures from 150 to -20^0F, but the differences become significant at the lower temperatures.

To facilitate comparison of the experimental data with the calculated curves, the curves in Figure 151 have been simplified and re-plotted (assuming the shear stress is zero at 150^0F) in Figure 153. Also plotted in this figure are the calculated data.

Considering first the data from shear gage No. 2, it will be noted that the experimental points plotted in Figure 153 do not change greatly whether the test is a slow thermal cooling test or a temperature cycling test. Furthermore, there is not a great deal of difference between the 1969 data and the 1971 data, especially at the lower temperatures. At the higher temperatures, it appears that the postcure reaction has produced an increased shear stress of about 2.0 to 2.5 psi. However, the data are very consistent and are relatively insensitive to the type of test.

The consistency of the experimental data enables a good comparison to be drawn between the calculated data based on the unaged propellant modulus values for a slow thermal cooling type of test. The initial slow thermal cooling test carried out in 1969 gave the highest shear stresses and the largest deviations from the calculated data; the low temperature data approach the thermal cycling calculations instead of the slow thermal cooling
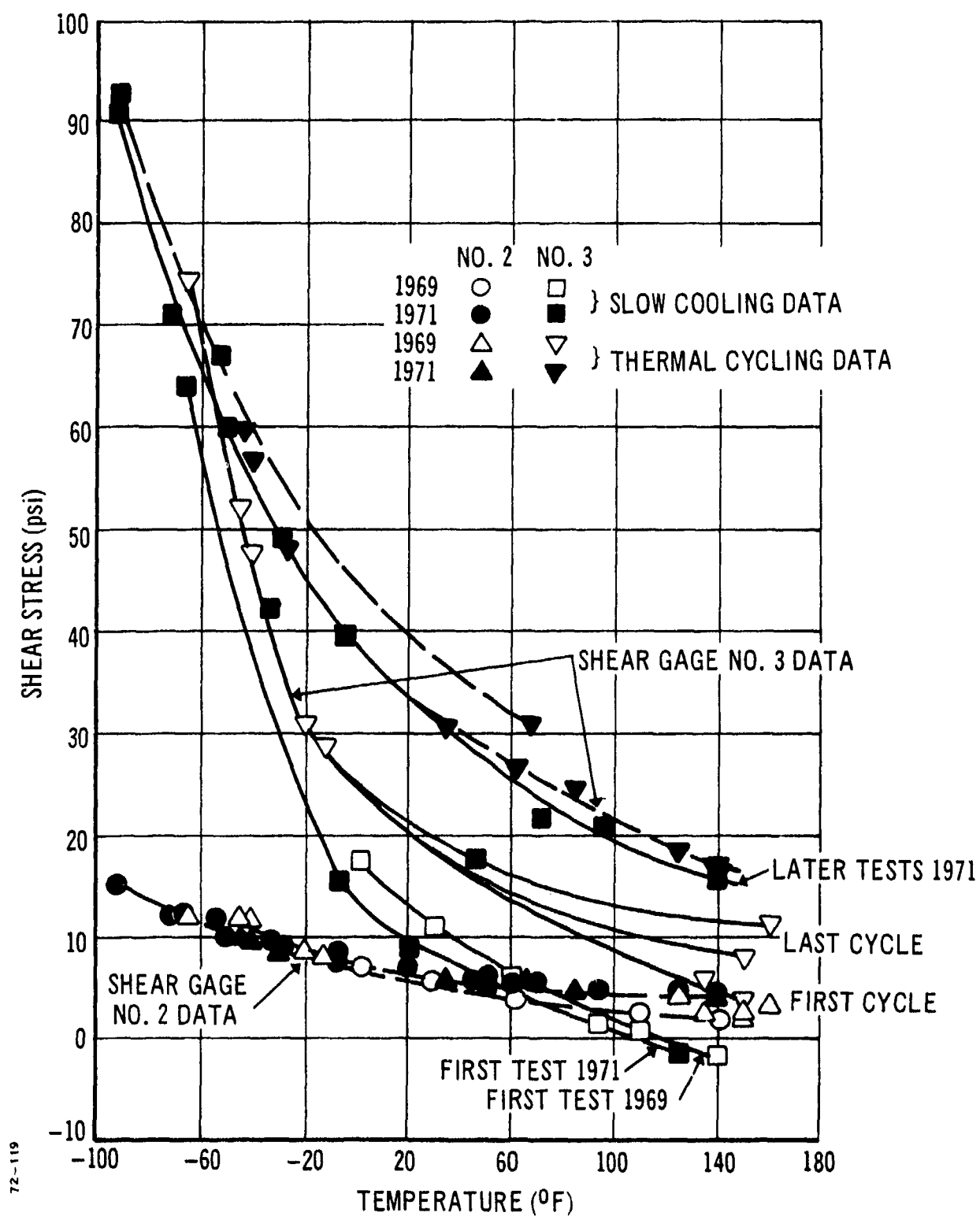
Figure 151. Experimental Thermal Shear Stresses versus Temperature.
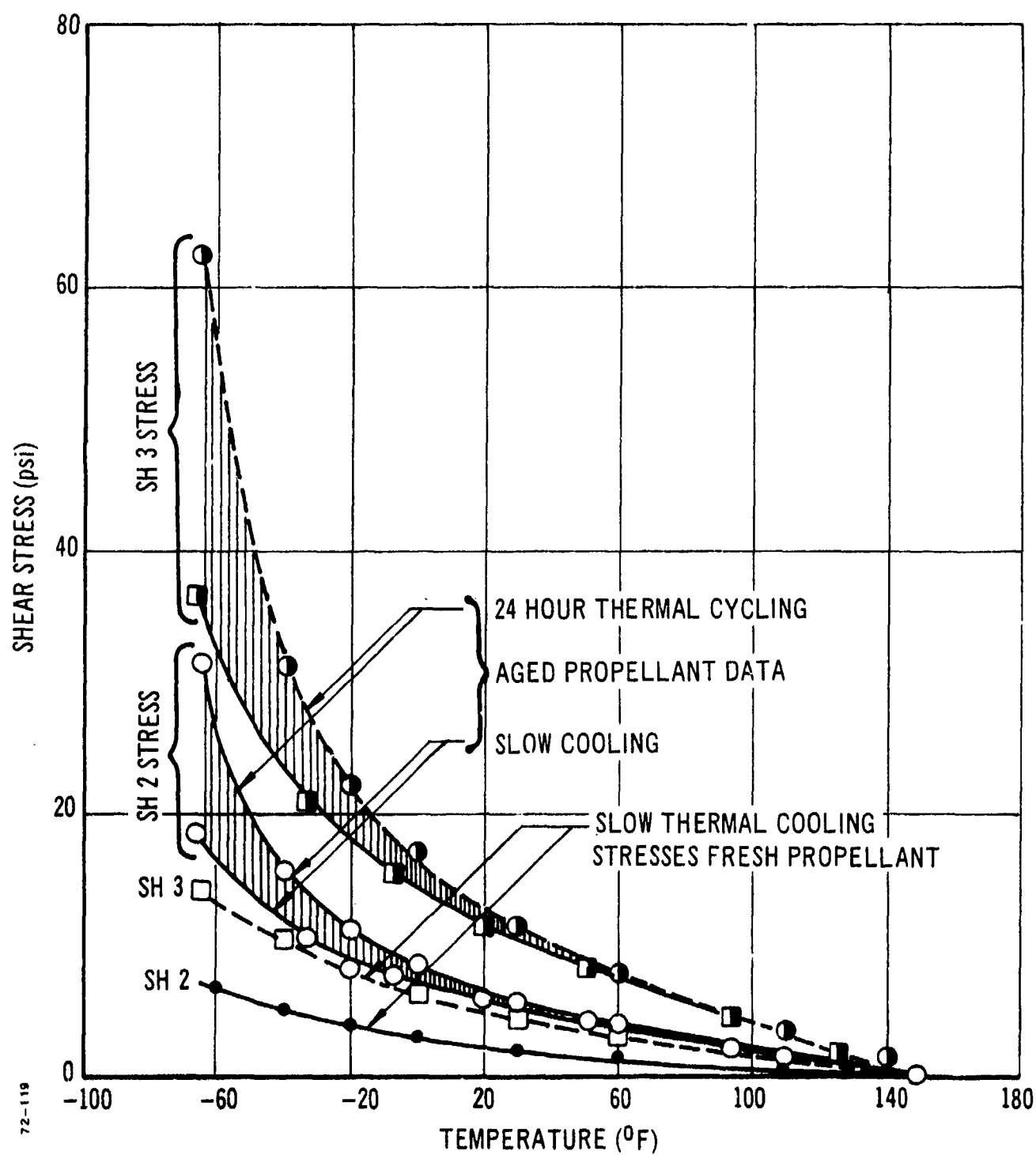
Figure 152. Calculated Thermal Shear Stresses versus Temperature.
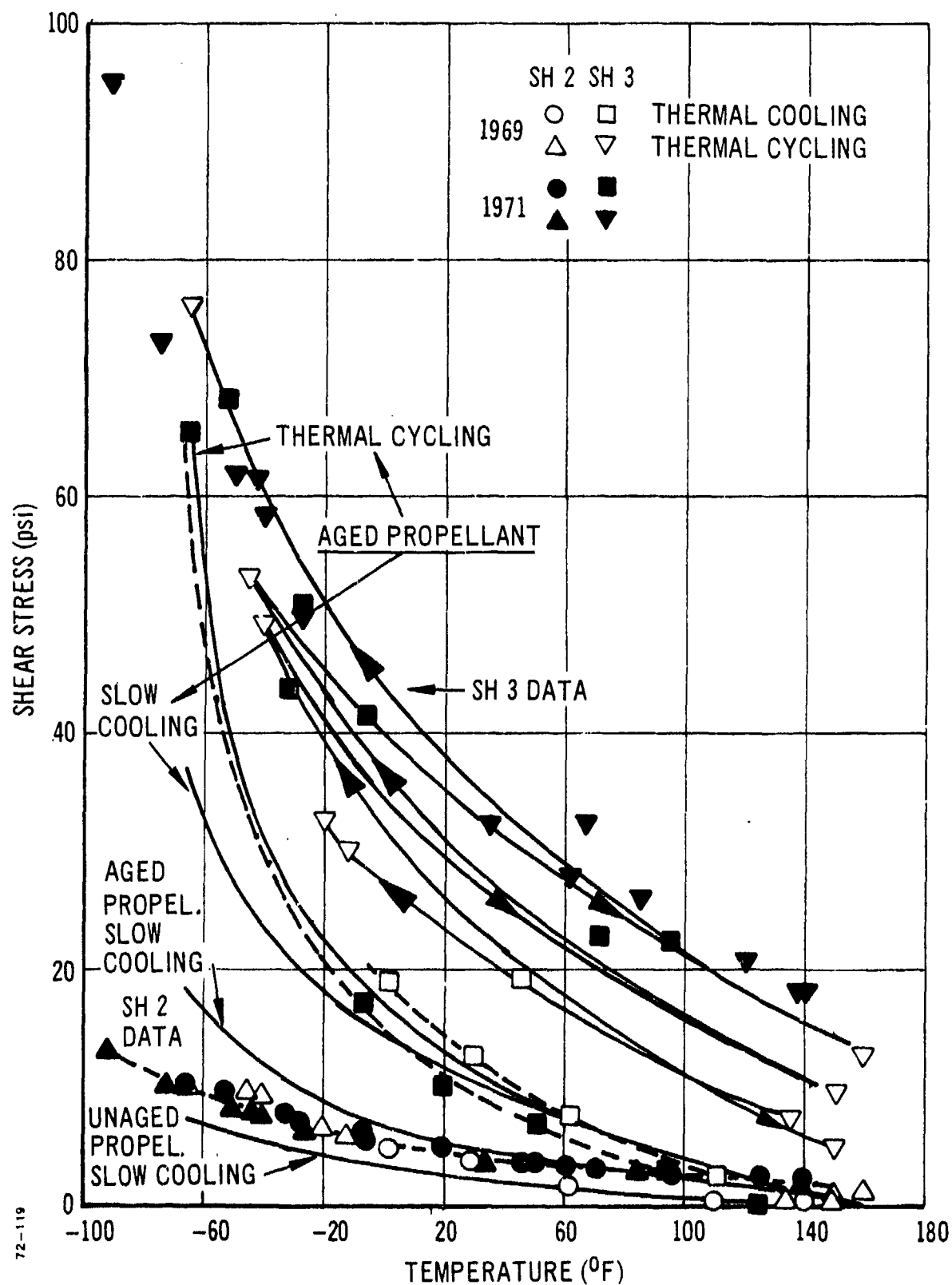
Figure 153. Thermal Shear Stresses Compared with Calculated Data.

curve. The later 1971 data are very close to the slow thermal cooling data but displaced by the amount of the cure shear stress (i.e., about 2.5 psi). There is no evidence of a significant aging effect producing the expected increase in propellant modulus and a corresponding increase in thermal shear stress.

The data obtained from shear gage No. 3 are very different from the No. 2 gage data. Considering first the initial slow thermal cooling test data obtained in 1969, the experimental points are close to the calculated curve for the aged propellant modulus and for the thermal cycling condition. Similarly, the first test performed in 1971, which was another slow thermal cooling test, gave very similar data.

The thermal cycling data measured in 1969 provide the most interesting deviations from the anticipated results. There is strong evidence that the rapid thermal cycling tests did not allow sufficient time for the grain to return to its normal (undistorted) shape when the STV was heated to $140/150^0$F after being cooled to a low temperature. Thus, the thermal shear stress at the high temperature builds up during the thermal cycling to a value of 13 psi. Upon cooling from the high temperature, the stress builds up to a higher value than that calculated, resulting in a set of measured shear stresses considerably higher than those calculated. However, if sufficient time is allowed after the thermal cycling test, then the grain will return to its original shape and the stress will return to zero, as the initial set of test data obtained in 1971 shows.

Again, there is no evidence of a significant increase in stress values with propellant aging; all of the measured stresses are higher than those calculated for the slow thermal cooling condition (which may be realistic for the location of this shear gage near the end of the grain). It is a strong possibility that the temperature of the propellant in the gage locality cools much more quickly than assumed in the slow-cooling calculations.

5. CONCLUSIONS

The agreement between the analytical predictions and the measured stress and strain data from STV No. 6 is not particularly good. However, in view of the fact that the analysis was not a three-dimensional type but relied on approximations to account for the effects of a finite length grain, it is hardly surprising that the agreement was not better.

Part of the reason for the discrepancy between the analysis and the experimental data may be the use of a low value for the coefficient of thermal expansion, α; the measured stress and strain values suggest that the value should have been higher than the value of 4.25 in./in./^{0}F used in the analysis. However this was the value measured in the conventional linear expansion apparatus and there was no good reason for using any other value of α.

The experimental stress and strain data obtained during the testing of STV No. 6 are very consistent. Thus there is little data scatter even between data taken in 1969 and that taken in 1971. This of course tends to make

the stress and strain values measured in the tests somewhat more believable
and they do seem to be rational data.

The most interesting data were noted in the shear cube thermal
cycling test data. During the temperature cycling tests, the data measured
with shear gage No. 3 showed a buildup of thermal shear stress that was not
apparent in the other gage data. During the almost 2-year interval between
the 1969 testing and the 1971 testing of STV No. 6, the grain appeared to
have reverted to its original condition so that the first thermal cooling test
of 1971 gave almost exactly the same data as the 1969 test.

The thermal cycling tests of 1971 were plagued by gage problems so
that the clear stress buildup noted in the 1969 data was not obtained. How-
ever, the increased stress level obtained after the first thermal cooling test
is quite marked.

Because of the type of calibration carried out on the shear gages,
the data have been interpreted as a buildup of shear stress. However, in
view of the data obtained from the shear gages located at the middle of the
diametral compression specimen (see Section IV, 3, b,), it is more probable
that the gage readings are due to shear strains (distortions) developing during
the thermal cycling tests. It takes a finite length of time for the grain shear
distortion to disappear and therefore the gage continues to read a shear
stress/strain value after the load has been removed. In the case of the grain
of STV No. 6, it seems that the shear distortion does not have time to relax
in between the thermal cycles, so that the shear strain gradually increases
with the number of cycles.

It is possible that this phenomenon may contribute to the failure of
the grain during thermal cycling, but there is insufficient evidence at
present to verify this hypothesis.

SECTION VIII

REMOVAL OF GAGES FROM OLD STVs

1. INTRODUCTION

During the STV program it became apparent that unless some technique was developed for the removal of gages from STVs that were no longer in use, they would have to be discarded along with the STVs.

Primarily, the gages of interest are the diaphragm normal stress sensors. They are expensive devices and there is a good chance of recovering them in operational condition. It was determined at an early stage that there was very little chance of recovering the shear cubes from the old STVs. The shear gages are fragile devices and the forces required to remove them from the propellant are generally sufficient to destroy them.

In the case of the miniature diaphragm gages, however, there seemed to be a good chance of recovering the gages in reasonable condition such that a minimum of refurbishing would be required. There was also another reason for wishing to remove the gages from the old STVs: they were not properly calibrated for thermal zero shift before installation (the technique was not established at the start of the STV program). Thus, if the gages could be removed with a piece of the surrounding propellant and case, they might be calibrated for thermal zero effects and thereby enable the old STV data to be analyzed more realistically.

2. TYPES OF STV AVAILABLE

Not all of the STVs posed a problem as far as removal of the gages was concerned. The nylon-encased live propellant STV No. 3 did not appear to present too difficult a problem, and the Solithane grain STV No. 4 certainly did not present a serious safety hazard. The real concern was felt about the removal of the gages from the two live-propellant, steel-case STVs No. 1 and 2. These two steel-encased STVs contained a number of diaphragm gages that were worth recovering and, furthermore, the calibration data for these gages would have proved most useful.

3. TECHNIQUES FOR REMOVING GAGES FROM STVs

a. Nylon-Encased STV

The problem with this STV (No. 3) was that sawing through the nylon case might possibly cause propellant ignition through excessive local heating. For this reason, it was decided to remove the case from the propellant grain and then to take the gages from the live propellant grain in another operation.

The technique adopted was to cool the STV to a low temperature ($-65°F$) until the grain shrank away from the case and could be removed intact. This was achieved with a reasonable degree of success. It required

several cycles to the low temperature before the grain finally became un-
bonded from the grain and then several of the lead wires that were bonded
too well to the case became detached from the gages.

After the removal of the propellant grain from the case, the
various sections of the grain containing the gages were cut from the bulk
of the grain.

b. Steel-Encased Solithane STV No. 4

Because of the inert Solithane grain, there was no problem of
safety with this STV. It was simply necessary to decide whether or not to
try to remove the case from the grain intact, as with the nylon-encased STV
No. 3, or to saw through the case around the gages to keep the case-grain
sections intact.

In the end, it was decided that the best chance of success lay
in simply sawing through the steel case with a standard power saw. This
technique was adopted and the STV case was sawn into small pieces sur-
rounding the gages. Subsequently the Solithane was removed from the steel
case sections without excessive difficulty. Thus, the gages encapsulated in
Solithane elastomer were eventually obtained by this procedure.

c. Steel-Encased Live Propellant STVs No. 1 and 2

These STVs represented the most difficult problem relative to
removing the gages. It was quickly decided that the only possible technique
was to chemically mill the case into small sections containing the gages and
then to cut the propellant away from the gages by hand.

The technique and apparatus used for the chemical milling
operation were similar to those developed at LPC for cutting SRAM motor
cases into sections. The STV case was coated with a layer of RTV com-
pound to prevent the salt solution from attacking the whole of the case wall.
Where the cuts were to be made, the RTV was removed for a distance of
about $\frac{1}{2}$ inch.

A copper pipe was bent into a circle around the STV case.
Small holes in the pipe were arranged to spray the salt solution into the part
of the STV case where the RTV protective coating had been removed. The
salt solution was pumped from a small plastic wading pool by means of a
stainless steel pump. It was sprayed through the copper pipe onto the STV
case and then allowed to flow back into the wading pool by gravity feed. A
large steel drum was arranged around the STV and copper pipe to prevent
loss of salt solution.

A heavy-duty welding apparatus was used to provide a high-
current source for the electro-chemical milling process. The case was con-
nected to the positive electrode (anode) and the copper pipe was connected to
the positive electrode (cathode). The high-current DC flow through the salt
solution resulted in the removal of the steel STV sections that were not pro-
tected by the RTV coating. Experience had shown that the fast-flowing salt
solution spray was effective in removing the heat generated during the chemi-
cal milling operation, and the large surface area of the wading pool was also
used to dissipate the heat.

However, to prevent excessive temperature buildup during the process, several thermocouples were attached to the STV case near the cuts, and the temperature at these locations was monitored continuously during the operation. At the first sign of a serious temperature rise, the current was stopped and the case was allowed to cool to ambient temperature. Because of the high risk of this type of process, the whole operation was conducted at the Potrero testing ground of LPC. A sketch of the apparatus is given as Figure 154.

4.   RESULTS OF GAGE REMOVAL PROCEDURES

On the whole, the removal of the gages from the old STVs proceeded reasonably well. The steel-encased propellant STVs No. 1 and 2 were successfully cut into 4-inch-wide sections surrounding the gages (three per STV). From STVs No. 3 and 4, seven diaphragm gages, enclosed in either live propellant (No. 3), or in Solithane (No. 4), were obtained.

The exercise of removing the gages from the old STVs must be regarded as a feasibility study to determine whether or not the process could be performed. From this viewpoint the operation was a success.

From an economic standpoint, however, it is not likely that the removal of gages from live propellant motors will prove attractive, especially if the cost of new gages can be brought down to a reasonable level. After removal from the STVs or motors, the gages must be separated from the remnants of propellant and sent to the gage manufacturer for any repair and regaging that is required. In the present instance, little was lost if the gages are in fact refurbished at a minimal cost.

The lengthy time required to remove the gages and the cost (in manhours) of the operations prevented the hoped-for recalibration of some of the gages.
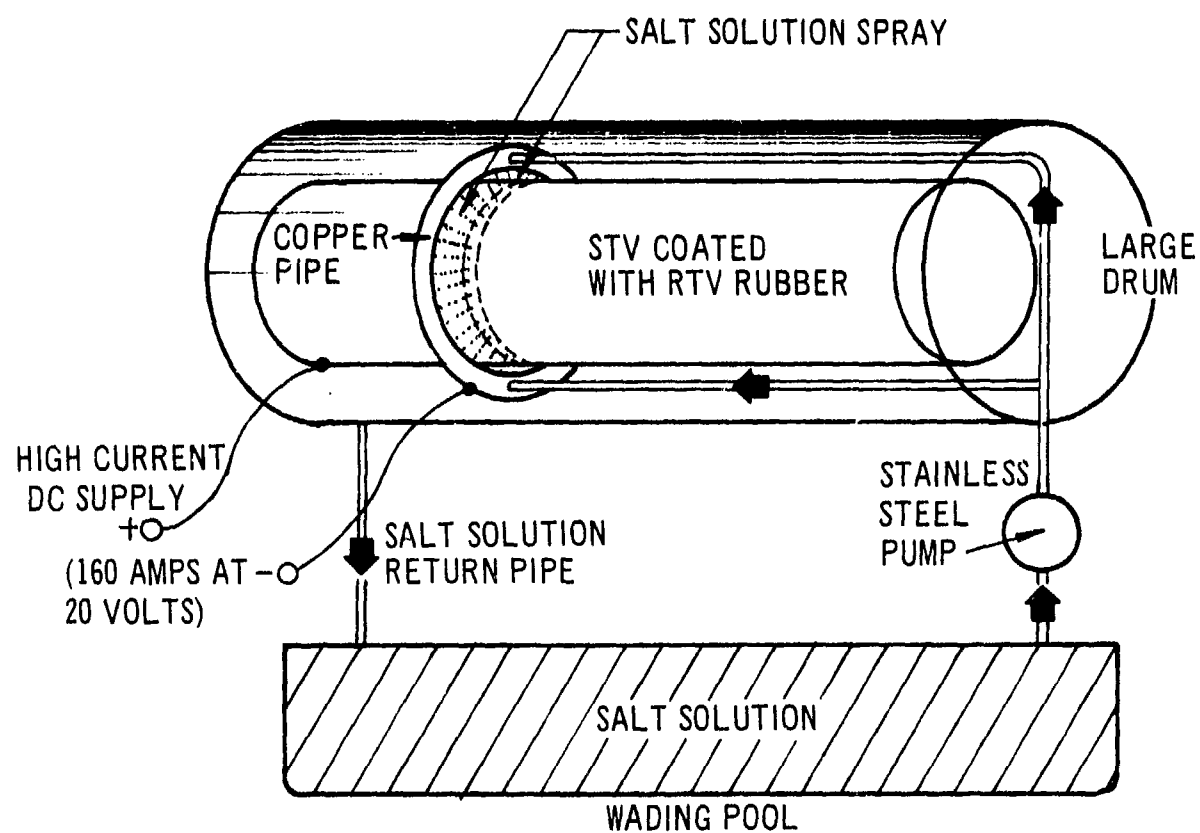
Figure 154. Experimental Setup for Chemically Milling the
Steel-Encased STV.

REFERENCES

1. Leeming, H., et al, Final Report, <u>Solid Propellant Structural Test Vehicle, Cumulative Damage and Systems Analyses</u>, Technical Report No. AFRPL-TR-68-130, Lockheed Propulsion Company, October 1968

2. Leeming, H., et al, Final Report, <u>Solid Propellant Structural Test Vehicle and Systems Analysis</u>, Technical Report No. AFRPL-TR-70-10, Lockheed Propulsion Company, March 1970

3. Leeming, H., <u>Solid Propellant Structural Test Vehicle and Systems Analysis Program</u>, Lockheed Propulsion Company, Monthly Progress Report No. 966-P-5, January 1969

4. Durelli, A.M., and Riley, W.F., "Performance of Embedded Pressure Gages under Static and Dynamic Loading," Symposium on Soil Dynamics

5. <u>Problems in Impact of Solid Rocket Motors</u>, Mathematical Sciences NorthWest, Report No. 70-62-1, Seattle, Washington, August 1970

6. Sokolnikoff, I.S., <u>Mathematical Theory of Elasticity</u>, McGraw Hill, 1956

7. Griffith, A.A., <u>Phil. Trans. Ray. Soc. (A)</u>, <u>221</u>:163, 1921

8. Ang, D.D., and Williams, M.L., <u>J. Appl. Mech.</u>, September 1961, p 372

9. Taylor, R.L., <u>A Finite Element Assembly Program</u>, Report CNME/CR/43, University of Wales, Swansea, Wales, September 1970

10. Bornstein, G.A., "Transient Thermoviscoelastic Analysis of a Uni-Axial Bar," <u>ICRPG Mechanical Behavior Working Group 7th Meeting Bulletin</u>, CPIA Publication No. 177, October 1968

11. Morland, L.W., and Lee, E.H., "Stress Analysis for Linear Visco-elastic Materials with Temperature Variation," <u>Trans. Society of Rheology</u>, Vol 1, p 233, 1960

12. Schapery, R.A., "A Theory of Nonlinear Thermoviscoelasticity Based on Irreversible Thermodynamics," <u>Proc. 5th U.S. Nat. Cong. Appl. Mech.</u>, pp 551-530, 1966

13. Schapery, R.A., "Thermal Expansion Coefficients of Composite Materials Based on Energy Principles," <u>J. Composite Materials</u>, <u>2</u>, pp 380-404, 1968

14. Schapery, R.A., "Effect of Cyclic Loading on the Temperature in Viscoelastic Media with Variable Properties," AIAA J., 2, pp 827-835, 1964

15. Martin, D.L., Jr., "An Approximate Method of Analysis of Nonlinear Transient Thermoviscoelastic Behavior," JANNAF Mech. Behavior Working Group, 8th Meeting, CPIA Pub. No. 193, 1, pp 45-52, 1969

16. Schapery, R.A., "Stress Analysis of Viscoelastic Composite Materials," J. Composite Materials, 1, pp 228-267, 1967

17. Sokolnikoff, I.S., Mathematical Theory of Elasticity, McGraw-Hill, 1956

18. Schapery, R.A., "Approximate Methods for Thermoviscoelastic Characterization and Analysis of Nonlinear Solid Rocket Grains," presented at ICRPG/AIAA 3rd Solid Propulsion Conf., AIAA Paper No. 68-520, June 1968

19. Farris, R.J., "The Influence of Vacuole Formation on the Response and Failure of Highly Filled Polymers," Trans. Soc. Rheol., 12, pp 315-534, 1968

20. Personal communication, E. C. Francis, United Technology Center, 1968

21. Noel, J.S., Burton, J. D., and Harbert, B.C., Fracture Mechanics Approach to Cumulative Damage, Technical Report AFRPL-TR-68-132, December 1968

22. Personal communication, B. C. Harbert, North American Rockwell Corp., Rocketdyne Solid Rocket Division, April 1971

23. Minutes of the Third Cumulative Damage Technical Coordination Meeting, held at Aerojet-General Corporation, February 1-2, 1968

24. Personal communication, H. Leeming, H. Leeming and Associates, February 1972

25. Lindsey, G.H., Schapery, R.A., Williams, M. L., and Zak, A.R., The Triaxial Tension Failure of Viscoelastic Materials, Aerospace Research Laboratories Report No. ARL 63-152, September 1963

26. Lou, Y.C., and Schapery, R.A., "Viscoelastic Characterization of a Nonlinear Fiber-Reinforced Plastic," J. Composite Materials, April 1971

27. Schapery, R.A., "On the Characterization of Nonlinear Viscoelastic Materials," Polymer Engineering and Science, 9, pp 295-310, July 1969

28. Schapery, R.A., _Further Development of a Thermodynamic Constitutive Theory: Stress Formulation_, Purdue U. Report No. 69-2, February 1969

29. Wogsland, N.C., "An Apparatus for Measuring the Bulk Modulus of Solid Propellant," _20th Meeting Bulletin, JANAF-ARPA-NASA Panel on the Physical Properties of Solid Propellants_, pp 317-322, November 1961

30. Personal communication, S. C. Britton, Texas A&M University

(The reverse is blank)

APPENDIX I

MODIFIED APPENDIX A TO AFRPL-TR-69-177: DESIGN OF MICROFILM ACQUISITION, STORAGE, AND RETRIEVAL SYSTEM FOR SOLID PROPELLANT MECHANICAL BEHAVIOR DATA[1]

1. INTRODUCTION

The original Appendix A to AFRPL-TR-69-177, "Design of Micro-film Acquisition, Storage, and Retrieval System for Solid Propellant Mechanical Behavior Data", was considered to require considerable modifi-cation before it could be used successfully for the handling of propellant mechanical behavior data. Thus Mr. E.R. Frost was placed under subcon-tract to perform the required modifications to the system with the assistance of Dr. Leeming, LPC's principal investigator.

Subsequently, it was decided that the scope of the data storage system should be extended so as to encompass gage-propellant calibration data and inert propellant data, neither of which were included in the original scope of the system. These two changes are incorporated in the revised system, which is presented in the later sections of this appendix together with other minor changes also found necessary in the classification of the STV program data.

The original Appendix A to AFRPL-TR-69-177 considered two PCAM cards sufficient to store all of the pertinent solid propellant mechanical behavior data. Card A was to contain proposal information and card B was to contain the material description and the mechanical test data.

At an early stage in the review of Appendix A it became clear that the material description data often would be either proprietary or classified or both. This would involve making the whole of the card B file and the microfiche copies classified. To avoid this situation, it was decided to employ a three-card system in which card A would contain the proposal data as before. Card B would contain the detailed material description data, and card C would employ an abbreviated material description and would contain the mechanical behavior data. With this approach, the A and B cards can be classified and filed separately. The C card, which is used to describe the mechanical test data, contains no classified information and therefore the card file and the microfiche containing the same data need no special handling.

---

[1] This work performed by Edward R. Frost and Associates, under sub-contract to Lockheed Propulsion Company.

The data contained in the C card are printed along the top of the microfiche as a 60-column, two-row heading in the manner shown below:

MICROFICHE HEADING AND INDEX STRIP

Column Number

```
         1111111 1112222222222223 3333333334444444444455 5555 55556
1234567890123456 7890123456789012345678901234567890 1234 567890

1LPCØPC-STV-6461 ØAMBØ100ABØ6M  1BØ1-P165FAMBA-P*ØØ2 BØØØ1-Ø2

Mater· Desc. Fld Agng Cond.Fld Test Type/Cond. Fld  SD Pg No
```

NOTE: Column numbers do not appear on microfiche.

The data consist of five separate sequences of alpha/numeric information or data fields. The first is the Material Description Field, which employs columns 1 through 16. The second is the Aging Condition Field, which employs columns 18 through 30. The third is the Test Type and Condition Field, which employs columns 32 through 51. The fourth is the Source Data Field, which employs columns 53 through 55. The fifth and last is the Page No. Field, which employs columns 56 through 60.

For ease of reading this heading, the data are presented in two rows with the field descriptors printed along the lower row as shown. The coded data symbols are above the printed field descriptor.

Card C contains one additional piece of information that is not printed as part of the index strip of the microfiche. Card columns 70 through 79 contain the microfiche number, which is an arbitrary number assigned sequentially when the data are copied. The microfiche number is photographed with the test card as the first image on the microfiche. Details of the coding system adopted on the C card format are given next.

2. CARD C FORMAT (TEST DATA CARD)

a. Material Description Field, Card Positions 1 through 16

Materials: Numeric, Card Position 1

    1-Propellant (live)
    2-Propellant (inert)
    3-Elastomer
    4-Liner
    5-Insulation
    6-Plastic (e. g., Nylon'
    7-Metal
    8-Structural composite

Manufacturer's Identification Code: Alpha, Card Positions 2 through 4

    LPC-Lockheed Propulsion Company
    AGC-Aerojet-General Corporation

NAR-North American Rockwell Corporation
ARC-Atlantic Research Corporation

Note: AFRPL will assign manufacturer's alpha
designator.

Manufacturer's Designation: Alpha/Numeric, Card
Positions 5 through 11

Examples:

ØØØ586A
ØØØ625A
ØØØØ667
ØØØLPE5
ANB2639
ØØØØSTV-Normal-cure STV propellant
ØPC-STV-STV propellant given additional cure
together with STVs.

Note: Manufacturers will use their own 7-digit
alpha/numeric code.

Hyphenate: Card Position 12

Batch Number: Numeric, Card Positions 13 through 16
(Precede Numeric with Zeros)

Example:

ØØØ1
ØØØ2
ØØØ3
6461- STV propellant Batch No.

Note: Batch numbers will be assigned by manufacturers
in numeric sequence.

Blank Space 1: Card Position 17

b. Aging Condition Field: Card Positions 18 through 30

Aging Temperature: Alpha/Numeric, Card Positions
18 through 22

Example:

P165F - Positive 165^0F
NØ4ØC - Negative 40^0C
ØAMBØ - Ambient (unspecified)

Aging Relative Humidity: Numeric, Card Positions 23 through 25

Example:

$\emptyset$35- 35-percent relative humidity
1$\emptyset\emptyset$- 100-percent relative humidity
AMB- Ambient (unspecified)

Aging Environment: Alpha, Card Position 26

A-Air
B-Nitrogen
C-Argon
D-Oxygen
E through Z reserved

Aging Configuration: Alpha, Card Position 27

Example:

B-Bulk Samples
S-Specimens
M-Motor

i.e., Propellant specimens tested were aged as bulk samples, as specimens, or in motors.

Aging Storage Time: Alpha/Numeric, Card Positions 28 through 30

Examples:

12 H- 12 hours
$\emptyset$2 D- 2 days
$\emptyset$6W- 6 weeks
12M- 12 months
2$\emptyset$ Y- 20 years

Note: Use of V$\emptyset\emptyset$ for data summary sheets, where data from more than one storage period are tabulated.

Blank Space 1: Card Position 31

c. Test Type and Condition Field: Card Positions 32 through 51

Test Type: Numeric, Card Position 32

1- Uniaxial
2- Biaxial
3- Triaxial
4- Shear
5- Fracture mechanics

6- Adhesive
7- Analog
8- Gage calibration test
9- Miscellaneous

Specimen Type: Alpha, Card Position 33

A- Uniaxial JANNAF
B- Tab end JANNAF (ICRPG)
C- Miscellaneous uniaxial
D- Strip biaxial
E- Bubble
F- Diametral compression
G- Poker chip
H- Hollow sphere or ellipse
 I- Hollow cylinder
J- Single lap shear
K- Chevron shear
L- Multiple lap shear
M- Bond in tension
N- Scarf joint specimen
P- Peel specimen
Q- 2-inch cylinder
R- 4- to 6-inch diameter analog
S- Blister peel specimen
T- Center crack strip biaxial
U- Edge crack strip biaxial
V- Radial planar loading specimen (bicycle wheel)
W- Gage/propellant pressurized in motor case
X & Y reserved
Z- Miscellaneous

Test Mode: Numeric, Card Positions 34 and 35

$\emptyset$1- Constant strain rate
$\emptyset$2- Constant stress rate
$\emptyset$3- Constant load/stress (creep)
$\emptyset$4- Constant strain (relaxation)
$\emptyset$5- Mixed rate test
$\emptyset$6- Mixed constant load test   } Cumulative Damage Tests
$\emptyset$7- Mixed constant strain test
$\emptyset$8- Constant pressure
$\emptyset$9- Constant pressure rate
1$\emptyset$- Constant cooling rate
11- Constant cyclic stress
12- Constant cyclic strain   } Fatigue Tests
13- Mixed cyclic stress/strain
14- Small strain dynamic/cyclic
15- Mixed strain plus temperature change
16- Pressurized constant strain rate test
17- Combined pressure/strain calibration test
18 thru 98 reserved
99- Miscellaneous

Hyphenate: Card Position 36

Test Temperature: Alpha/Numeric Card Positions 37
through 41

Example:

   P165F - Positive 165°F
   N04 0C - Negative 40°C
   VARIA - Variable, for data summary sheets

Test Relative Humidity: Numeric, Card Positions 42
through 44

Example:

   020 - 20-percent relative humidity
   100 - 100-percent relative humidity
  AMB - Ambient (unspecified)
  VAR - Various, for data summary sheets

Test Environment: Alpha, Card Position 45

   A - Air
   B - Nitrogen
   C - Argon
   D - Oxygen
   E thru W reserved
   X - To be used for data summary sheets if more than
      one test environment is considered.

Hyphenate: Card Position 46

Test Rate/Strain/Stress/Load: Alpha/Numeric, Card
Positions 47 through 51

Example:

Tensile:

  P0050 - 50 in./min
       - 50-percent strain
       - 50 psi
       - 50 pounds

Note (1): For small strains and low rates, use * to
          indicate position of decimal point.

Example:

P*∅∅2 - 0.002 in./min
N2*5∅ - 2.50-percent strain (compressive) etc

For very low or very high strain rates, use the exponent code as follows:

P 2 E-4 = Tensile, 2×10^{-4} = tensile, 0.0002 in./min
N 5 E+4 = Compressive, 5×10^{4} = compressive, 50,000 in./min

Note (2): For data summary sheet use:

VARIA - Variable, i.e., more than one rate considered on data sheet, or

PMULT - Tensile ⎫
NMULT - Compressive ⎬ multi-rate, multi-strain or stress tests used for cumulative damage experiments, i.e., more than one rate/strain/stress used in a single test.

<u>Blank Space: Card Position 52</u>

d.   <u>Source Data: Card Positions 53 through 55</u>

<u>Source Data: Alpha, Card Positions 53 through 55</u>

Example:

AOO - Raw data (only)
OAO - Computed data (only)
OOA - Graphic data (only)
AAA - Combination of data, i.e., raw, computed and graphical

Note: Explanation and definition of Source Data Coding are as follows:

<u>Raw Data</u>

AOO - Specimen dimension sheet
BOO - Load-time chart (Instron)
COO - Load-displacement chart
DOO - Strain-time chart
EOO - Lateral strain-time chart
FOO - Volume dilation chart
GOO thru ZOO reserved

<u>Computed Data</u> - An Alpha A signifies any or all of the following:

OAO - Failure stress/strain data
     - Relaxation modulus data

-309-

OAO- Creep compliance data
- Constant strain rate data
- Constant stress rate data
- Volume change data
- Cumulative damage calculations
- Add computed data as required

<u>Graphic Data</u> - An Alpha A signifies any or all of the
following:

OOA- Stress versus strain failure envelope
- Failure stress-time locus
- Failure strain-time locus
- Relaxation-time plot
- Creep compliance-time plot
- Failure energy-time plot
- Shift factor-temperature plot
- Add graphic data as required

e. Page Numbering: Card Positions 56 through 60

<u>Page of Pages: Numeric, Card Positions 56 through 60</u>

Example:

$\emptyset$1-1$\emptyset$- Page one of ten pages
$\emptyset$3-$\emptyset$9- Page three of nine pages

<u>Blank Space: Card Positions 61 through 69</u>

f. Microfiche Numbering: Card Positions 70 through 79

<u>Microfiche Number: Numeric, Card Positions 70 through 79</u>

Example:

$\emptyset\emptyset\emptyset\emptyset\emptyset\emptyset\emptyset\emptyset\emptyset$1- Microfiche number one
$\emptyset\emptyset\emptyset\emptyset\emptyset$1$\emptyset\emptyset\emptyset\emptyset$- Microfiche number ten thousand

Note: Microfiche numbers will not appear on the index
strip of the microfiche, but rather on the test
target of the microfiche.

DOCUMENT CONTROL DATA · R & D

(Security classification of title, body of abstract and indexing annotation must be entered when the overall report is classified)

1. ORIGINATING ACTIVITY (Corporate author)	2a. REPORT SECURITY CLASSIFICATION
Air Force Rocket Propulsion Laboratory	Unclassified
Research and Technology Division	**2b. GROUP**
Edwards Air Force Base, Ca. 93523	N/A

3. REPORT TITLE

FINAL REPORT, SOLID PROPELLANT STRUCTURAL TEST VEHICLE PROGRAM

4. DESCRIPTIVE NOTES *(Type of report and inclusive dates)*

Final Report, 1 May 1970 to 30 September 1971

5. AUTHOR(S) *(First name, middle initial, last name)*

H. Leeming, M. L. Williams, W. S. Brown, K. Pister, R. Taylor,
R. A. Schapery, W. D. Webb, W. G. Knauss

6. REPORT DATE	7a. TOTAL NO. OF PAGES	7b. NO. OF REFS
April 1972	310	30

8a. CONTRACT OR GRANT NO.	9a. ORIGINATOR'S REPORT NUMBER(S)
F04611-70-C-0061	AFRPL-TR-72-29
b. PROJECT NO.	
c. N/A	**9b. OTHER REPORT NO(S)** *(Any other numbers that may be assigned this report)*
d.	LPC Report No. 433-F

10. DISTRIBUTION STATEMENT

Distribution limited to U.S. Government agencies only: test and evaluation of military hardware, April 1972. Other requests for this document must be referred to AFRPL (STINFO/DOZ), Edwards, Ca. 93523

11. SUPPLEMENTARY NOTES	2. SPONSORING MILITARY ACTIVITY
N/A	AFFTC Edwards Air Force Base, California 93523

13. ABSTRACT

Results of the third year of the Structural Test Vehicle (STV) Program conducted by Lockheed Propulsion Company for AFRPL are presented. Improved computer codes were used for viscoelastic analyses of a diaphragm gage in a uniaxial propellant specimen subject to constant stress, constant strain, and cyclic tests. A three-dimensional computer code was used to analyze a shear cube under simple loading conditions and to confirm experimental findings that the interference problem is minimal and that a slight cross sensitivity exists. Experimental data show the performance of shear gages in a biaxial (diametral compression) stress field and under cyclical shear loading. Results of restrained cooling and heating tests are presented and compared with analysis. Dilatational experimental and analytical work suggests an improved approach for the determination of thermal strain in a circular port grain. Improved material characterization techniques are also described. Results of thermal cycling and cooling experiments on 4-point-star, inert-propellant STV No. 6 are given. Gage readings measured during the tests are discussed and compared with analysis. A technique for removal of gages from old motors and STVs by chemical milling is discussed. Finally a modified system is described for coding microfilm data of STV, and inert propellant and gage calibration data.

UNCLASSIFIED
Security Classification

14. KEY WORDS	LINK A		LINK B		LINK C	
	ROLE	WT	ROLE	WT	ROLE	WT
Structural Test Vehicles						
Experimental Stress Analysis						
Solid Propellant Grain Analysis						
Stress transducer						
Strain transducer						
Transient Thermal Stresses						

UNCLASSIFIED
Security Classification